CHEMICAL VAPOR DEPOSITION OF THIN FILMS FOR DIFFUSION BARRIER APPLICATIONS

By

OMAR JAMES BCHIR

A DISSERTATION PRESENTED TO THE GRADUATE SCHOOL
OF THE UNIVERSITY OF FLORIDA IN PARTIAL FULFILLMENT
OF THE REQUIREMENTS FOR THE DEGREE OF
DOCTOR OF PHILOSOPHY

UNIVERSITY OF FLORIDA

2004

I would like to dedicate this dissertation to my nephew, Matthew Edward Brown, and to the memory of my grandparents.

ACKNOWLEDGMENTS

On a professional note, I would like to thank my supervisory committee (especially my advisor, Dr. Tim Anderson, and Dr. McElwee-White) for their constant guidance and assistance throughout my Ph.D. work. I would also like to thank the past and present members of Dr. Anderson's, Dr. McElwee-White's and Dr. Norton's research groups, with whom I have collaborated during my time at UF, and Dr. Jianyun Shen, with whom I collaborated on thermodynamic modeling. I would also like to thank Dr. Holloway for use of his 4-point probe device, and the staff at the Major Analytical Instrumentation Center (MAIC), including Eric Lambers, Wayne Acree and Brad Willenburg, for valuable assistance and training with various characterization techniques.

On a personal note, I would like to thank my parents (Sara and Hachemi Bchir) for their encouragement, love and support throughout my life, and for their strong emphasis on the importance of education. I would also like to thank my sister, Annissa Brown, my brother-in-law Eddie, and my nephew Matthew, for their encouragement and support. Thanks also go to my girlfriend Luciana Manfrim for her love and support. Lastly, thanks go to all of the friends that I have made through the years while growing up in Florida, attending Georgia Tech, working at Fluor Daniel and attending UF.

TABLE OF CONTENTS

Page
ACKNOWLEDGMENTS iii

ABSTRACT viii

1 INTRODUCTION
- 1.1 Background 1
- 1.2 Comparison of Diffusivities for Al and Cu in Si 4
- 1.3 Diffusion Barrier Requirements and Properties 6
  - 1.3.1 Film Structure 9
  - 1.3.2 Electrical Properties 11
  - 1.3.3 Conformality 14
  - 1.3.4 Adhesion 16
- 1.4 Dielectric Material Considerations 17
- 1.5 Diffusion Barrier Failure Mechanisms 17
- 1.6 Diffusion Barrier Deposition Techniques 21
  - 1.6.1 Physical Vapor Deposition (PVD) 21
  - 1.6.2 Chemical Vapor Deposition 24
  - 1.6.3 Atomic Layer Deposition (ALD) 37
- 1.7 Copper Deposition Methods 44
- 1.8 Statement of Problem 49
- 1.9 Hypothesis 51

2 REVIEW OF THE LITERATURE
- 2.1 Cu–Si Interconnects without a Barrier 53
- 2.2 Refractory Metal–Based Barriers 54
  - 2.2.1 Unary Refractory Metal Barriers 54
  - 2.2.2 Binary Refractory Metal–Based Barriers 56
  - 2.2.3 Ternary Refractory Metal–Based Barriers 63
- 2.3 Justification for WN_x (and WN_xC_y) as the Barrier Material 71
- 2.4 WN_x Film Properties 72
- 2.5 WN_xC_y Film Properties 75
- 2.6 Amorphous WN_x Film Deposition 77
- 2.7 Demonstrated Uses of WN_x 78
- 2.8 WN_x Deposition Techniques 85
  - 2.8.1 Annealing W in NH_3 85
  - 2.8.2 Plasma Nitridation / Ion Implantation of W 86
  - 2.8.3 Pulsed Laser Deposition 86
  - 2.8.4 Reactively Sputtered WN_x Deposition 87

2.8.5 LPCVD WN_x Deposition 87
2.8.6 PECVD WN_x Deposition 91
2.8.7 MOCVD WN_x Deposition 93
2.8.8 ALD WN_x Deposition 97
2.8.9 ALD WN_xC_y Deposition 99
2.9 Conclusions 100

3 EQUILIBRIUM MODELS FOR WN_x–BASED BARRIERS
3.1 Motivation and Method 101
3.2 Constraints 111
3.3 Degrees of Freedom 111
3.4 Computational Methods 112
3.5 Phase Equilibrium in the W–N System 114
3.6 Previous Studies of the W–N Phase Diagram 125
3.7 W–N Optimization Results and Discussion 126
3.8 Stable Solid Phases in the W–C System 139
3.9 Previous Study of the W–C Phase Model 142
3.10 Equilibrium in the W–C–Cl–H–N System 145
3.11 Optimization of the FCC β–WN_xC_y Gibbs Energy 153
3.12 Degrees of Freedom (DOF) Analysis 168
3.12.1 Homogeneous Gas Phase Speciation 171
3.12.2 Heterogeneous Gas Phase Speciation 177
3.12.3 Heterogeneous Solid Phase Equilibrium 182
3.13 Predicted W–C–N Ternary Phase Diagram 186
3.14 Predicted β–$WC_{0.5}$ – β–$WN_{0.5}$ Pseudobinary Equilibrium 190

4 EXPERIMENTAL APPROACH FOR CVD
4.1 Substrate Preparation 194
4.2 Solvent Tests 195
4.3 Description of CVD System Components 196
4.4 Start–Up 201
4.5 Copper Deposition 201
4.6 Analysis Techniques 202
4.7 Precursor Screening Procedure 208

5 EVALUATION OF $Cl_4(CH_3CN)WN$–*i*–Pr AS A SUITABLE WN_x PRECURSOR
5.1 Synthesis of Isopropyl [$Cl_4(CH_3CN)WN$–*i*–Pr] Precursor 210
5.2 Solvent Selection 211
5.3 Precursor Mass Spectral Pre–Screen 212
5.4 Film Structure 217
5.4.1 XRD Results 217
5.4.2 TEM 223
5.5 Film Composition 225
5.5.1 AES 225
5.5.2 AES Depth Profiling 229

  5.5.3 XPS ... 233
  5.5.4 SIMS Depth Profiling ... 253
5.6 Film Growth Rate (XSEM) ... 255
5.7 Film Incubation Time and Morphology ... 259
5.8 Film Electrical Properties ... 264
5.9 Effect of NH_3 and N_2 Addition to Film Growth ... 267
  5.9.1 Film Structure ... 267
  5.9.2 Film Composition ... 270
  5.9.3 Growth Rate ... 277
  5.9.4 Film Resistivity ... 279
  5.9.5 Sheet Resistance ... 280
5.10 Conclusions for Use of NH_3 and N_2 with i–Pr ... 281
5.11 Effect of Solvent Change on Carbon Content ... 282
  5.11.1 Film Structure ... 284
  5.11.2 Film Composition ... 287
  5.11.3 Carbon Deposition Rate ... 291
  5.11.4 Conclusions On Effect of Solvent Change ... 297
5.12 Conformality Tests ... 298
5.13 Adhesion Tests ... 298
5.14 Conclusions on Use of $Cl_4(CH_3CN)WN$–*i*–Pr to Deposit WN_x ... 299

6 EVALUATION OF $Cl_4(PhCN)W(NPh)$ AS A SUITABLE WN_x PRECURSOR

6.1 Film Growth Studies ... 303
6.2 Synthesis of Phenyl [$Cl_4(PhCN)W(NPh)$] Precursor ... 303
6.3 Solvent Selection ... 303
6.4 Precursor Mass Spectral Pre–Screen ... 304
6.5 Film Structure ... 308
  6.5.1 XRD ... 308
  6.5.2 Lattice Parameter ... 313
  6.5.3 Polycrystal Grain Size ... 315
6.6 Film Composition ... 316
  6.6.1 AES ... 316
  6.6.2 Film Growth Rate (XSEM) ... 320
6.7 Film Electrical Properties ... 322
  6.7.1 Film Resistivity ... 322
  6.7.2 Film Sheet Resistance ... 323
6.8 Conclusions on Use of $Cl_4(PhCN)W(NPh)$ to Deposit WN_x ... 324

7 EVALUATION OF $Cl_4(CH_3CN)WN–C_3H_5$ AS A SUITABLE WN_x PRECURSOR

7.1 Film Growth Studies ... 331
7.2 Synthesis of Allyl [$Cl_4(CH_3CN)WN–C_3H_5$] Precursor ... 332
7.3 Solvent Selection ... 333
7.4 Precursor Mass Spectral Pre–Screen ... 334
7.5 Film Structure ... 336
  7.5.1 XRD ... 336

7.5.2 Lattice Parameter 339
7.5.3 Polycrystal Grain Size 341
7.6 Film Composition 342
7.7 Film Growth Rate (XSEM) 344
7.8 Film Electrical Properties 345
7.8.1 Film Resistivity 345
7.8.2 Film Sheet Resistance 346
7.9 Conclusions on Use of $Cl_4(CH_3CN)WN\text{–}C_3H_5$ to Deposit WN_x 347

8 COPPER TESTS ON BARRIER FILMS FROM $Cl_4(CH_3CN)WN\text{–}i\text{–}Pr$

8.1 Copper Deposition Results 357
8.2 Electrical Measurements 357
8.3 Scotch Tape Tests 358
8.4 Barrier Integrity Tests 358
8.4.1 XRD 359
8.4.2 Electrical Measurements 364
8.4.3 Depth Profiling Analysis 365
8.5 Conclusions Regarding Cu Testing of Deposited Barrier Layers 366

9 RECOMMENDATIONS FOR FUTURE WORK

9.1 Control Film Composition 368
9.2 Decrease Deposition Temperature 371
9.3 Decrease Barrier Thickness 371
9.4 Further Conformality Testing 372
9.5 Further Adhesion Tests 372
9.6 Further Barrier Integrity Analyses 373
9.7 Deposition on Alternate Substrate Materials 375
9.8 Testing of Films for X–ray Absorption Mask Applications 376
9.9 Deposition of Alternate Barrier Materials 376
9.10 System Modifications 376

REFERENCES 378

APPENDIX

A CVD SYSTEM PROCESS FLOW DIAGRAMS 409

B OTHER PRECURSORS TESTED 415

BIOGRAPHICAL SKETCH 419

Abstract of Dissertation Presented to the Graduate School
of the University of Florida in Partial Fulfillment of the
Requirements for the Degree of Doctor of Philosophy

CHEMICAL VAPOR DEPOSITION OF THIN FILMS FOR DIFFUSION BARRIER APPLICATIONS

By

Omar James Bchir

August 2004

Chairman: Timothy J. Anderson
Major Department: Chemical Engineering

The semiconductor industry is transitioning from aluminum to copper as the interconnect material for integrated circuits. Diffusion barriers are essential for preventing copper migration into silicon in the resulting integrated circuits. Metalorganic chemical vapor deposition (MOCVD) is a useful technique for conformal deposition of thin barrier films. By manipulating the molecular structure of the MOCVD precursor(s), it is possible to control the structure and properties of the deposited film.

The focus of this work has been to examine novel precursors for use in MOCVD of thin film diffusion barriers. To date, the suitability of a variety of novel precursors for deposition of tungsten nitride (WN_x) for diffusion barrier applications has been tested. The WN_x precursors were of the form $Cl_4(CH_3CN)WNR$, where R represents the isopropyl, phenyl, and allyl group, among others. Mass spectrometry fragmentation patterns for each precursor were studied to pre-screen candidate precursors. Film properties were examined by several different characterization techniques, including

XRD, AES, XPS, SEM, and 4–Point Probe. Data from these techniques were then correlated to pre-screen fragmentation patterns to determine the impact of the imido (R) group on film deposition. Apparent activation energies for film growth from the allyl, isopropyl and phenyl precursors, for example, were 0.15, 0.84 and 1.41 eV, respectively, and were directly related to the strength of the N-R bond in the precursors.

In addition to experimental testing of new precursors for WN_x deposition, thermodynamic phase equilibria for the W–N–H–C–Cl deposition system was assessed. Modifications were made to the previously reported W–N binary model to include new experimental data from the literature on the desired FCC WN_x phase as well as the SHP WN phase. Once the binary W–N diagram was reassessed, this model was merged with the existing W–H–C–Cl database to create an initial model for solid–gas equilibrium in our system at our experimental conditions. Using a combination of XRD, AES, and XPS data from our films, the W–N–H–C–Cl model was modified to include carbon–nitrogen–vacancy interactions in the face–centered cubic (FCC) WN_xC_y solid phase, so that the new model reflected our experimental results. Finally, the low–temperature ternary W–C–N phase diagram was predicted.

CHAPTER 1
INTRODUCTION

1.1 Background

The semiconductor industry continues to shrink the size of transistors on integrated circuits (ICs) to increase the number of transistors per chip, which translates to increased IC device speed. To shrink these transistors, the sizes of the device features (trenches, vias, etc.) and the metal interconnects ("wires" that connect the individual transistors on the chip) must be decreased. Recent accomplishments have reduced feature sizes to 100 nm, yielding more than 400 million transistors per chip. The International Technology Roadmap for Semiconductors [ITR02] predicts IC feature sizes to shrink continuously over the next several years, in the following steps: 100 nm (in 2003), 90 nm (2004), 80 nm (2005), 70 nm (2006), 65 nm (2007), 45 nm (2010), 32 nm (2013), and 22 nm (2016).

Aluminum (Al) and Al–based alloys have historically been used as the metal interconnect materials on integrated circuits. Al is reaching its usability limit as industry continues to shrink IC features. For a given current flow, decreasing the interconnect cross–section leads to an increase in current flow density. At high current flow density, Al suffers from electromigration, where electrons flowing through the metal interconnect impart enough momentum to carry the metal atoms with them. Once current flow density rises above the critical value (10^6 A/cm^2 for Al), electromigration leads to voids (openings) and hillocks (pileups) in the interconnect wiring (Figure 1-1). Formation of voids in the Al interconnect leads to an open circuit, which causes device failure. Al doped with Cu (termed Al(Cu)) was used to increase the electromigration resistance, but this scheme is also reaching its usability limit. A different interconnect metal is required to meet present and future current flow density demands.

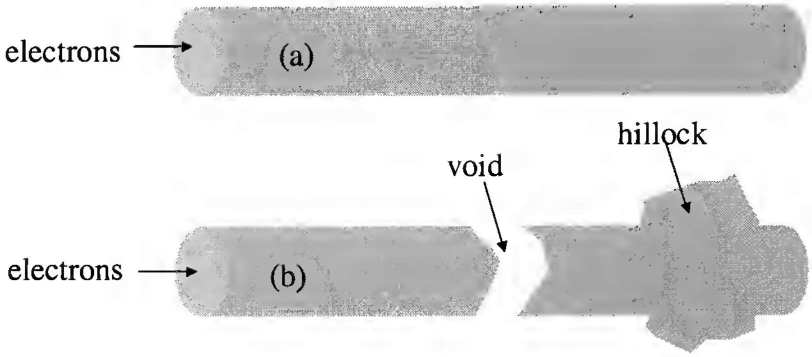

Figure 1-1. Before (a) and after (b) electromigration induced hillock and void formation in an Al interconnect.

Industry has already transitioned to copper as the interconnect material for the intermediate and upper wiring levels on IC devices, due to copper's higher electromigration resistance and 40% lower bulk resistivity (1.67 μΩ–cm for Cu vs. 2.65 μΩ–cm for Al) [Cha89, Kol91]. Copper has ten orders of magnitude higher electromigration resistance than Al, which will increase device lifetime [Mur95], and its lower resistivity will decrease the resistance–capacitance (RC) time constant, which is a large factor in chip performance for ICs with feature sizes below 250 nm [Hu98]. The following relation defines the resistance–capacitance time delay:

$$RC = \frac{\rho l^2 \varepsilon_{ILD}}{t_M * t_{ILD}} \tag{1–1}$$

where ρ is resistivity (Ω–cm), l is the length (cm) of the interconnect line, ε is the electric permittivity (C/V*cm) of the insulating film, t_M is the thickness of the metal interconnect (cm) and t_{ILD} is the thickness of the neighboring insulator (cm). A decrease in the RC time constant leads to higher device switching speed [Pau87], and the switch from Al to Cu may lead to a 15% increase in overall microprocessor speed [IBM97]. While bulk Cu has a resistivity of 1.67 μΩ–cm, the resistivity of IC Cu lines with thickness above 50 nm ranges from 1.7 to 2.0 μΩ–cm [Kal00]. In comparison, Cu–doped Al lines Al(Cu) have resistivities ranging from 3.0 to 3.5 μΩ–cm. In addition to resistivity and electromigration improvements, Cu is said to provide higher IC production yield than Al–based devices with similar design [Sin02a]. Other advantages of switching to Cu interconnects include a decrease in the number of interconnect levels, a roughly 30% decrease in power consumption for operation at a given frequency, and a cost savings of roughly 30% per interconnect level due to integration of dual damascene processing [Nov00]. Silver (Ag), which has an even lower bulk resistivity (1.59 μΩ–cm) than Cu, has been considered for interconnect metallization, but it suffers from poor electromigration resistance [Mur95], making its use as the metallization material unlikely.

The improved electrical properties of Cu are highly desirable, but with these benefits come several drawbacks. These include copper's tendency to corrode under standard fabrication conditions, copper's lack of a stable self–passivating oxide (like Al_2O_3 on Al), the inability to chemically etch Cu, poor adhesion to low dielectric constant (low–k) materials, and rapid diffusion/reaction with Si and SiO_2 [Hu98, Mer01]. Copper diffusion into neighboring layers can cause an increase in contact resistance, a change in the barrier height, leaky p–n junctions, embrittlement of the contact layer, deep level traps and destruction of electrical connections to the chip [Kal00, Wit80]. Copper contamination levels in Si at and above 10^{13} cm^{-3}, for example, are believed to reduce device yield [Ist00].

1.2 Comparison of Diffusivities for Al and Cu in Si

At high temperatures, both Al and Cu diffuse into Si, and when put into direct contact with Si, they will intermix rapidly. While Si is non–reactive with Al [Ram00], it has a small solubility range in Al (0.25 to 1.5% by weight) [Jae88]. At high temperatures (>1000°C), Al diffuses substitutionally into Si, where Al replaces a Si atom in the Si lattice.

Copper, though, has much higher mobility in Si, and is very reactive with Si and SiO_2 substrates [Bau97], forming copper silicide compounds, such as Cu_3Si and Cu_5Si [Bau97, Hym98, Kwo95, Ram00, Rei92], which cause strong deterioration of contact systems [Wan01b]. Copper's high mobility in the Si lattice extends over a wide temperature range. Cu moves into the Si lattice by substitutional diffusion at high temperature (>800°C), but also by interstitial diffusion at low temperature (<700°C), where Cu atoms diffuse between the Si atoms in the lattice (through the interstices). Both interstitial and substitutional diffusion of Cu into the Si lattice occur simultaneously, with interstitial diffusion dominating at low temperature and substitutional diffusion dominating at high temperature.

While the diffusivity of Al in Si at 500°C is less than 1×10^{-20} cm^2/s [Ist00], the diffusivity for Cu in Si depends both on type and concentration of dopants in the Si substrate. The nature of p–type silicon is such that acceptor atoms (such as boron, B) substituted on Si lattice sites have a negative charge (B^-). Since Cu diffuses through Si as a positive ion (Cu^+) [Bai96, Ist00], the negatively charged B^- ions tend to "trap" some of the diffusing Cu ions, giving Cu an apparent diffusivity that is lower than that in intrinsic (undoped) Si. In p–type Si with a boron concentration of 5.0 x $10^{20}/cm^3$, for example, the diffusivity of Cu is 2.0 x 10^{-6} cm²/sec at 500°C, while that in intrinsic Si is 2.0 x 10^{-5} cm²/sec [Ist00]. At room temperature, the diffusivity of Cu in p–type and intrinsic Si, measured by the transient ion drift method [Hei97], ranged from 3.3 x 10^{-13} cm²/s in p–type Si up to 2.7 x 10^{-7} cm²/s in intrinsic Si [Ist98]. This indicates that after 30 minutes at room temperature, Cu can diffuse a distance of 0.5 μm in p–type Si and 400 μm in intrinsic Si.

Since the diffusivity of Al in Si is so small at the processing temperature, the main problem with Al arises when it penetrates the barrier material and accumulates at the barrier–Si interface. This accumulation can lead to formation of Al spikes at the interface, which short out shallow junctions (Figure 1-2a). Copper's high diffusivity in Si, however, means that Cu will not build up at the barrier–Si interface until the Si has reached its saturation value of Cu. Hence, Cu can diffuse into the bulk of the Si wafer and move laterally to contaminate a large area on the wafer [Ist00], as depicted in Figure 1-2b.

While Cu has high diffusivity in Si at room temperature, its solubility is very low (less than 1 Cu atom per cm^3) [Ist00], so formation of a Cu–Si solid solution is unlikely. The diffused Cu will therefore form complexes, precipitates and agglomerates with Si. Four typical reactions can occur for Cu in Si. These include formation of point defects/complexes, copper silicide precipitates, addition to existing defects, and outdiffusion to the Si surface. More information on Cu interdiffusion and reaction mechanisms in Si is available elsewhere [Ist00]. In addition to Si, Cu also diffuses rapidly through SiO_2 under thermal and electrical stress, leading to high leakage currents and dielectric breakdown [Jai99]. Diffusion of Cu atoms into SiO_2 typically occurs due to application of an external electric field, which causes Cu to be ionized (to Cu^+) and accelerated into the SiO_2 [Kri01]. Copper's high diffusivity in Si and SiO_2 makes the need for a robust thin film diffusion barrier to separate Cu from neighboring layers on the IC very critical. Figure 1-2c depicts a stable device structure resulting from use of a diffusion barrier.

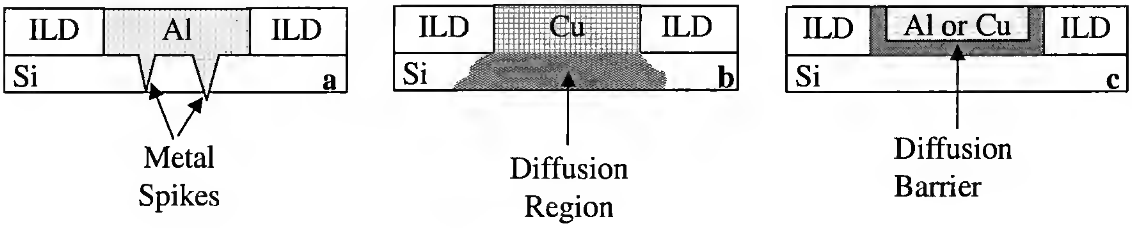

Figure 1-2. Metal to silicon contact layers: (a) Al on Si without a diffusion barrier suffers from junction spiking. (b) Cu on Si without a barrier suffers from massive diffusion (c) Metal to silicon contact with a diffusion barrier remains intact.

1.3 Diffusion Barrier Requirements and Properties

A diffusion barrier is a material used to separate two layers that, if put in direct contact, would interdiffuse and/or react with one another. Diffusion barriers are typically classified into one of three types: passive, sacrificial and stuffed. Passive (ideal) barriers are inert with respect to the layers that they separate, and have low solubility for the neighboring semiconductor and metal. Sacrificial barriers react with one or both of the neighboring layers, and are eventually consumed. The rate of reaction between the barrier and neighboring layers must be slow enough that the lifetime of the barrier is longer than that of the device. If the barrier has a shorter lifetime than the device, the sacrificial barrier will be totally consumed and the device will fail prematurely. Stuffed barriers are polycrystalline films that have their grain boundaries stuffed with a material that blocks diffusion [Wol86]. By stuffing these boundaries, the dominant low–temperature route for diffusion through the barrier is minimized. Stuffing occurs due to both physical and chemical effects. The stuffing “agent” should physically reduce the amount of pore space in the films and should chemically repel the Cu from diffusing through the grain boundary [Par95a]. As an alternative to grain boundary stuffing, high temperature annealing has been used to “cure” deposited barrier films, so that micro–defects such as grain boundaries are removed. Although this technique does decrease the number of grain boundaries in the film, the high temperatures also increase diffusivity of Cu in the barrier film, and can cause Cu penetration [Bai96]. The “curing” properties of a high temperature thin–film anneal are therefore tempered by the increased mobility of Cu in the barrier film at higher temperatures.

In addition to stuffing the grain boundaries, barrier effectiveness can be further enhanced by minimizing the number of grain boundaries in the barrier film. Deposition at low temperatures provides this benefit and several more. First, low temperature deposition minimizes the number of grain boundaries by favoring amorphous film growth. Second, in nitride films, for example, excess nitrogen is retained at lower deposition temperature, and is therefore available to stuff any grain boundaries that may form during thermal cycling. Third, the likelihood of damaging temperature sensitive components (such as low–k dielectric polymers) on the device during barrier deposition is minimized, provided that a temperature ceiling of 400°C is maintained [Eis00a, Ele02, Hau00, Kim03b, Les02, Sun01b]. Deposition above 450°C can increase the compressive stress in Cu films, which is relieved by formation of Cu hillocks [Jai99]. Fourth, low deposition temperatures require a smaller thermal budget. The advantages provided by low temperature deposition can greatly reduce the probability of Cu penetration through the barrier and decrease power consumption. In practice, low deposition temperatures are desirable, but depositing the barrier films at the lowest possible temperature may not be the optimal approach. Depositing the barrier film at the highest allowable processing temperature, assuming that the film structure remains amorphous at this temperature, would prevent significant changes to barrier film structure during subsequent thermal cycling.

During IC processing, the diffusion barrier material is typically deposited between a metal layer (usually Al or Cu) and a semiconductor layer (usually Si or GaAs), a metal and a dielectric (e.g., SiO_2 or low–k), or two metal layers [Lin98a]. The requirements for an ideal diffusion barrier are listed below. Film structure, electrical properties, conformality and adhesion property requirements will be discussed further in the following sections.

- Barrier must prevent diffusion between and be non–reactive with neighboring device layers.
- Barrier should have amorphous film structure to eliminate grain boundaries, which are facile paths for Cu diffusion through the barrier.
- Barrier should be deposited at low temperature to prevent damage to temperature sensitive components on the IC device and to enable amorphous film growth.
- Barrier should have good conformality and uniformity across the wafer, to ensure good barrier coverage over small device features and uniform barrier deposition on all devices across the wafer.
- Barrier should have low bulk electrical resistivity and low contact resistivity to Cu, to minimize resistance to current flow.
- Barrier should have good thermal conductivity to minimize heating of the barrier layer.

- Barrier should have minimal contamination levels; halide impurities can cause corrosion of the Cu layer, while oxygen and free carbon impurities can increase film's electrical resistivity.

- Barrier should have minimum thickness to maximize copper's cross–section in the interconnect and to foster low contact resistance in the metallization stack.

- Barrier should promote adhesion between device layers, as poor adhesion leads to electromigration of Cu at the de–adhered interface.

- Barrier should have high thermal and structural stability, to prevent failure of the barrier during exposure to thermal and mechanical stresses at processing conditions.

- Barrier should enable direct Cu electroplating to eliminate the need for a Cu seed layer, and promote nucleation of the Cu (111) orientation, which has the greatest resistance to electromigration.

- Barrier should be compatible with chemical mechanical planarization (CMP) processes, and act as a good CMP stop layer to eliminate need for a separate stop layer deposition step.

1.3.1 Film Structure

The ideal diffusion barrier structure is a defect free single crystal film [Nic78]. This structure does not contain grain boundaries, which are interface regions ("micro–defects") between crystal grains in a polycrystalline material. Grain boundaries are a "short circuit" path for rapid intermixing of the two neighboring layers, and are the dominant cause for barrier failure at low temperature [Bai96]. In a single–crystal barrier film, all diffusion occurs through bulk defects (including vacancies and dislocations), which is inherently much slower than diffusion through grain boundaries. Deposition of single crystal barrier films is impractical, however, due to low growth rates, lattice mismatch with the underlying substrate, and deposition temperature limitations [Kal00]. The next best solution is to deposit an amorphous, dense, smooth, defect free film [Bai96, Kwo95]. Amorphous films have short–range order (≤ 5 Å), but no long–range order (≥

20 Å) [El190]; therefore no polycrystalline grain boundaries exist to enable rapid diffusion. In addition to having an amorphous microstructure, the density of the barrier material should be as close to the bulk value as possible, to eliminate voids as possible diffusion paths. Polycrystalline films, especially those with a columnar microstructure or those with equiaxial grains of size similar to film thickness, are the poorest performers in diffusion barrier applications. These films contain grain boundaries that can extend from one side of the barrier to the other, meaning an easy diffusion path for Cu through the barrier. Nano–crystalline films, which are polycrystalline films with grain size below ~50 Å [Kal00], are more effective than polycrystalline films with larger grains, but are not as effective as amorphous diffusion barriers. Examples of single–crystal, polycrystalline and amorphous films are shown in Figure 1-3.

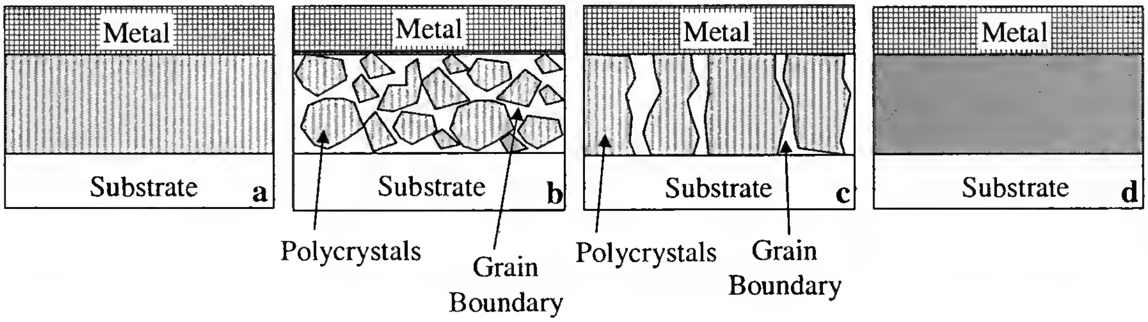

Figure 1-3. Diagram of (a) Single crystal barrier. (b) Polycrystalline barrier with equiaxial grains. (c) Polycrystalline barrier with columnar grains. (d) Amorphous barrier without grain boundaries.

Several different methods are used to deposit amorphous films [Siv95]. The first is to deposit films at low temperature, which enhances sticking probability and suppresses surface diffusion, forcing films toward a disordered state. The second is to deposit films at high nucleation (arrival) rates, so that many small nuclei form on the substrate surface, preventing coalescence of small nuclei into larger polycrystals. The third is to add contaminants (such as N, C, etc.) to impede surface diffusion of the metal species, imparting disorder and decreasing the ability of nuclei to coalesce and grow. In addition to these deposition methods, careful selection of materials can assist formation of an amorphous film. A material's composition may be chosen, for example, so that several stable phases exist together at equilibrium. In a binary system, a film composition should be chosen in a two–phase equilibrium region, while in a ternary system, a three–phase equilibrium region should be selected [Ram00]. The competing stable phases neighboring these regions should be line compounds (have minimal solid solubility regions), have very different compositions, and have complex crystal structures [Ram00]. Compared to a broad solid solution phase, line compounds are inflexible to stoichiometry deviations, which can disrupt polycrystal formation and trigger amorphous growth. In a binary system, then, choosing a film composition in a two–phase equilibrium region bounded by two line compounds should increase the likelihood of amorphous film deposition.

1.3.2 Electrical Properties

To obtain any benefit from the lower bulk resistivity of Cu, the barrier (liner) thickness should be less than 10% of the overall linewidth [Hu98]. A thicker barrier means decreased cross–sectional area of Cu available to conduct current, which causes an increase in the effective resistivity of the Cu line. For a Ti/TiN/Al(Cu)/Ti/TiN sandwich structure, the effective resistivity was estimated to be 4.1 μΩ–cm, due to the high resistivities of the Ti and TiN layers, as well as that for $TiAl_3$, which forms during annealing at the Ti–Al(Cu) interface [Hu98]. For Cu lines with widths ranging from 0.1

to 1 μm, keeping barrier thickness < 10 % of the overall linewidth results in a constant effective resistivity ≤ 2.3 μΩ–cm for the Cu line [Hu98].

The barrier material will typically be used in two types of scenarios on the integrated circuit, which are depicted in Figure 1-4. In the first case, the barrier runs in parallel with the Cu line, as with a trench structure, where the barrier separates the Cu trench from neighboring dielectric layers. In this case, the thickness of the barrier must be minimized, in order to have maximum cross–sectional area for the Cu conductor line. The resistivity of the barrier in this scenario is not critical, however, as electrical current will be flowing through the Cu and not directly through the barrier [Tra03]. In the second case, the barrier will be separating one metal layer from another, as in a via structure, hence the current will pass directly through this intermetal barrier layer. The resistance associated with current flowing from one Cu line through a via (and barrier) to another Cu line is called the via resistance. The barrier film's thickness and bulk resistivity must be minimized to limit the barrier's impact on via resistance. The suggested ideal film resistivity is ≤ 500 μΩ–cm [Ele03], and barrier thickness should be <30 nm [Bai96]. Specific via resistance (Ω–μm² or Ω–cm²), defined as the electrical resistance through the via multiplied by the via's cross–sectional area, is a common measure of barrier impact on current flow through a via. The current, acceptable specific via resistance value for the 100 nm device node is 0.1 Ω–μm² (1 x 10^{-9} Ω–cm²), and this is projected to decrease to <0.01 Ω–μm² (1 x 10^{-10} Ω–cm²) for the 22 nm device node in 2016 [ITR02, Nic95, Tra03].

As an example, the change in specific via resistance with ITRS feature diameter for a fixed 15:1 via aspect ratio was calculated. The via was treated as a cylinder, with

Cu in the center and the barrier layer lining the inside edges of the cylinder. Current is assumed to travel in the Cu cross section of the via, which is the path of least resistance, and then passes through the barrier layer at the via's bottom, as depicted in Figure 1-5.

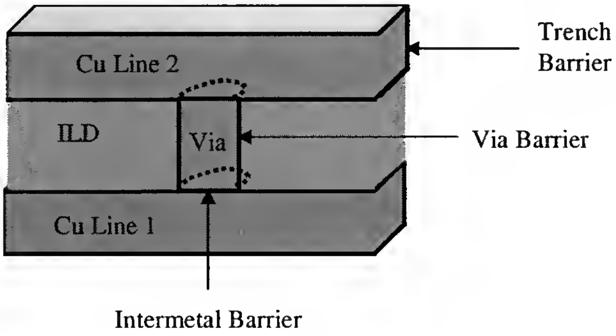
Cu Line 2
Trench Barrier
ILD
Via
Via Barrier
Cu Line 1
Intermetal Barrier

Figure 1-4. Schematic of trench and via applications for barrier materials.

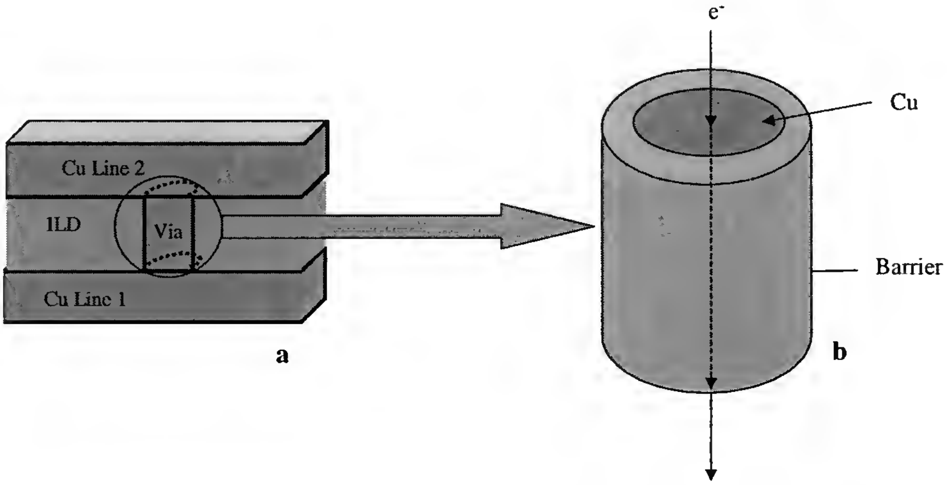
e-
Cu
Cu Line 2
ILD
Via
Cu Line 1
Barrier
a
b

Figure 1-5. a) Cut away view of Cu trenches with via contact. b) Expanded, 3D view of Cu via with barrier layer on sides and bottom.

The thickness of the barrier layer corresponded to ITRS projections for each device node, as follows: 12 nm (in 2003), 10 nm (2004), 9 nm (2005), 8 nm (2006), 7 nm (2007), 5 nm (2010), 3.5 nm (2013), and 2.5 nm (2016). The results for varying barrier resistivities, along with projected requirements from the ITRS Roadmap, are shown in Figure 1-6. The diagram indicates that by the 65 nm node (2007), the barrier layer's resistivity must be ≤ 200 μΩ–cm to meet ITRS projections. Likewise, this value must be ≤ 25 μΩ–cm by the 32 nm node (2013).

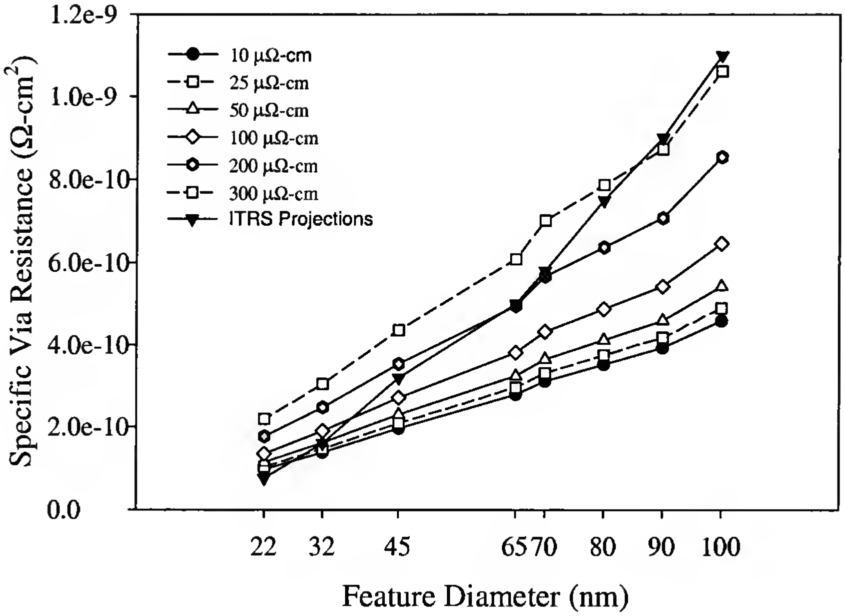

Figure 1-6. Specific via resistance as a function of feature diameter, shown for various barrier layer resistivities. Calculation is for a via with a 15:1 aspect ratio.

1.3.3 Conformality

Conformality (or step coverage) in device microstructures, especially in trenches and vias, is of utmost importance in barrier design. Highly conformal films (approaching 100%) have nearly uniform thickness at all points on a substrate surface (on both the sidewalls and bottom). Film conformality is determined by measuring the film's thickness on the wafer surface (t_s), on feature sidewalls (t_w) and at feature bottom (t_b) (Figure 1-7). Conformality on the sidewall and bottom can be calculated by Equations 1–2 and 1–3, respectively. The feature's aspect ratio, which is the ratio of the feature's height to its width, can be calculated by Equation 1–4.

$$\text{Sidewall conformality } (\%) = \left(\frac{t_w}{t_s}\right) * 100 \qquad (1\text{–}2)$$

$$\text{Bottom conformality (\%)} = \left(\frac{t_b}{t_s}\right) * 100 \tag{1–3}$$

$$\text{Aspect Ratio} = \left(\frac{y}{x}\right) \tag{1–4}$$

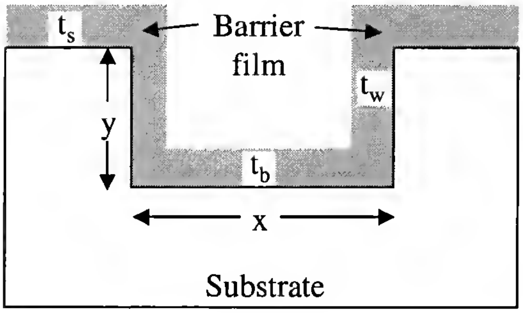
t_s
Barrier film
t_w
y
t_b
x
Substrate

Figure 1-7. Sketch of film dimensions for calculation of conformality.

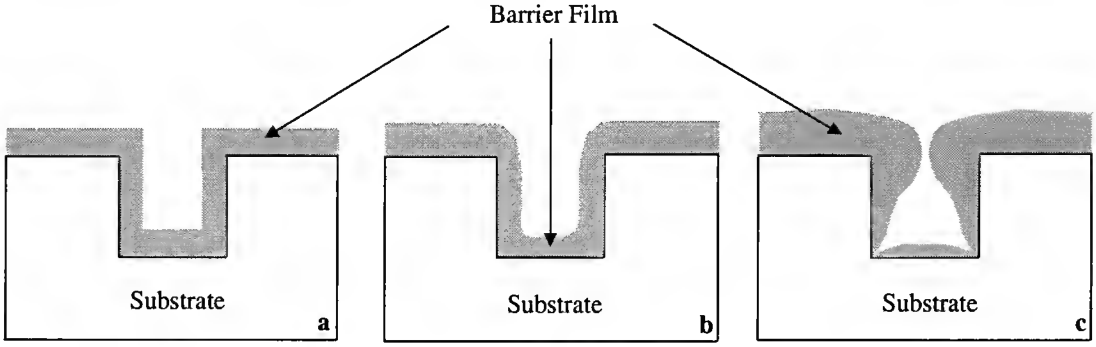
Barrier Film
Substrate
a
Substrate
b
Substrate
c

Figure 1-8. Diagram of (a) Ideal barrier conformality. (b) Good barrier conformality. (c) Poor barrier conformality.

Barriers with poor conformality have uneven thickness, with the film being thinner in certain spots than others. These thin spots are “weak links” in the barrier, which are more susceptible to diffusion than the thicker parts of the layer. Figure 1-8a shows an ideal barrier with 100% conformality. Figure 1-8b shows a practical barrier with rounded edges, while Figure 1-8c shows a poor barrier, with a large overhang near the trench opening and sparse coverage at the trench bottom. Cu can easily penetrate to the underlying Si substrate through the thin barrier at the bottom of the trench.

While device dimensions continue to shrink, the aspect ratio continues to increase, and the ability to conformally cover the bottom and sidewalls of these features becomes even more challenging. Deposition methods and chemistries must be developed to accomplish this task.

1.3.4 Adhesion

The adhesion of the barrier to both the Cu and the neighboring dielectric or semiconductor layers, along with the crystallographic orientation of the deposited Cu (which is affected by adhesion issues), all impact copper's electromigration behavior [Jai99]. Strong Cu adhesion to the barrier layer contributes to good electromigration resistance [Pet03], whereas poor adhesion can cause self–diffusion of Cu along the barrier interface. Self–diffusion of Cu along the interface is even more likely than diffusion along grain boundaries, because grain boundary self–diffusion has a higher activation energy than interface self–diffusion [Llo95]. Copper has an activation energy for bulk self–diffusion of 2.19 eV [Mur95], while the values for grain boundary and interface self–diffusion are 1.2 and 0.8 eV, respectively [Llo95]. Cu (111) is the preferred orientation for the metal, as this plane has minimum surface energy, which results in formation of low–angle grain boundaries [Llo95]. These low–angle grain boundaries minimize flux divergence of electrons flowing through the metal, and therefore minimize electromigration [Jai99]. Aside from the barrier-Cu interface, adhesion at the barrier–dielectric interface can be adversely affected by out–gassing of moisture or other organic materials from the dielectric surface, which can lead to anomalous Cu removal behavior.

1.4 Dielectric Material Considerations

In addition to the changeover to Cu, parallel research is pursuing new, low–k materials, which will also decrease the RC time constant. Historically, SiO_2, with a k value ranging from 3.9 to 4.1, was the dielectric material of choice [Hu98]. Transitioning from Al/SiO_2 devices to Cu/low–k based devices (with k~2) may lead to more than a 400 % reduction in RC delay [Kal00]. New films (such as polyimide, SiLK™, SiOC, etc.), with dielectric constants below 3.9, are being investigated for use as low–k materials, but they cannot tolerate high temperatures during processing [Hu98, Pet03]. The processing temperature limit for these materials, along with the need for good adhesion to Cu, are factors that must be considered when selecting a barrier material to separate them.

Another factor influencing barrier material selection is its compatability with high–k materials, such as those in MOSFET gates or in DRAM capacitors. Barrier materials have been used as top electrodes on high–k gates and DRAM capacitors, and their favorable performance may dictate further use in the future.

1.5 Diffusion Barrier Failure Mechanisms

Thin films typically have higher diffusivity than thicker bulk films, due to a large number of short circuit paths (grain boundaries, dislocations, etc.) distributed over a very small volume [Bal75]. Thinning the barrier film increases the likelihood that these short circuit paths will extend from one side of the film to the other, making it more susceptible to diffusion. Thin film diffusion barriers typically fail in one of two ways. The first is metallurgical failure, where the Cu content of the barrier increases to several atomic percent, changing the barrier layer's composition. The second is electrical failure, where little intermixing with the barrier occurs, but the Cu penetrates the barrier and is present in the semiconductor/dielectric layer in sufficient quantity to alter the characteristics of the device [Ist00]. Most barrier testing techniques, such as depth profiling or SECCO etch tests [Iva99], are suited for detection of metallurgical failure. Use of XRD to detect $CuSi_x$ compounds, for example, is a fairly insensitive detection method, because the bulk concentration of Cu in Si must already be above saturation before the silicide compounds will form.

Measurement of electrical failure is a more sensitive way to determine if Cu has penetrated the barrier and intermixed with the underlying substrate. To detect electrical failure, the electrical properties of devices such as p–n junctions, Schottky diodes or metal-oxide-semiconductor (MOS) capacitors, built under the Cu–exposed barrier or on the wafer surface after the barrier has been removed, are measured. Leakage currents are measured on p–n junctions and MOS devices and compared to Cu–free ones to determine if Cu has penetrated the barrier. Changes in the capacitance and current-voltage (I–V) characteristics of Schottky diodes are measured to determine if Cu has penetrated into the active areas on devices.

Ideally, the performance of different diffusion barrier materials would be tested by comparing the diffusivity of Cu in the different barriers. To determine diffusivity, the migration of atoms, or diffusive flux (J, atoms/cm^2–sec), through the barrier material should be estimated. The flux can be described by Fick's law (Equation 1–5):

$$J = -D\left(\frac{dC}{dx}\right) \tag{1–5}$$

where D is the diffusivity (cm²/sec), C is the atomic concentration (atoms/cm³) and x is the diffusion distance (cm). By measuring flux (J) through the barrier for a given concentration gradient (dC/dx) across the barrier, the diffusivity can be determined. Once this is known, the next level of analysis is to determine whether diffusion through the bulk lattice or the grain boundary dominates. To distinguish between diffusion through the bulk lattice and the grain boundary, two different expressions for diffusivity have been given [Ohr92]. Equation 1–6 gives the expression for lattice diffusivity (D_L):

$$D_L = D_{oL} \exp^{\left({}^{-E_L}\!/_{RT} \right)} \tag{1–6}$$

where E_L is energy per mole for atomic diffusion through the lattice, and D_{oL} is the value for lattice diffusivity at standard conditions. Equation 1–7 gives the expression for grain boundary diffusivity (D_B):

$$D_B = D_{oB} \exp^{\left({}^{-E_B}\!/_{RT} \right)} \tag{1–7}$$

where E_B is the energy per mole for atomic diffusion through the grain boundary, and D_{oB} is the value for grain boundary diffusivity at standard conditions. At low temperature, the diffusion mechanism through a polycrystalline solid is typically controlled by grain boundaries and other defects in the film [Nic78]. Since vacancy–assisted bulk diffusion is negligible below about three–tenths of the solid's melting temperature ($0.3T_m$), diffusion through the grain boundary is the path of least resistance at low temperature. This is reflected by a lower activation energy for grain boundary diffusion relative to bulk diffusion [Cha82, Nic78], with $E_B \approx 0.5E_L$ for FCC metal thin films [Bal75]. As annealing temperature is increased, a changeover from grain boundary controlled diffusion to bulk diffusion occurs. The temperature at which this occurs, called the

Tammann temperature, is typically 0.5–0.66T_m [Nic78]. At higher temperature, the values for D_L and D_B begin to approach each other, and flux through the bulk lattice becomes the dominant route for diffusion, due to the much larger cross sectional area of the bulk lattice relative to that of the grain boundaries.

Experimentally, determination of diffusivity from Cu flux measurements is impractical. Exact measurement of the Cu flux through the barrier is difficult to determine, as failure determination techniques usually focus on qualitative barrier failure. Moreover, issues such as defect density can have a large impact on thin film diffusivity, and can cloud efforts to distinguish between bulk lattice and grain boundary diffusion. Diffusivity in thin barrier films may be estimated with Equation 1–8, which describes diffusion from a limited source at a crystal surface [Wol86]:

$$C_k = \frac{Q_o}{\sqrt{\pi D t}} \exp\left(-\, {d^2}\big/{4Dt}\right) \tag{1–8}$$

where C_k is Cu concentration (cm^{-3}) at distance d (in cm) from the surface, D is the diffusivity (cm^2/s), t is diffusion time (sec), and Q_o (cm^{-3}) is the concentration of Cu at the surface. Since exact Cu concentrations at the two interfaces can be difficult to measure, an apparent diffusivity (D_{app}) is defined by Equation 1–9 [Ist00]:

$$D_{app} = \frac{d^2}{4t} \tag{1–9}$$

where d is the film thickness (in cm) and t is the time (s) for the Cu to appear at the barrier/substrate interface (i.e., the time it takes the barrier to fail). Comparison of apparent diffusivities for different barrier films may be done to determine which barrier is best.

1.6 Diffusion Barrier Deposition Techniques

Diffusion barrier films have been deposited by a variety of methods, including physical vapor deposition (PVD) and chemical vapor deposition (CVD) techniques. The required deposition temperature, substrate characteristics and feature size generally dictate which deposition method is appropriate for a given application. A discussion of some common PVD and CVD techniques to deposit metal nitrides and their inherent advantages and/or disadvantages follows.

1.6.1 Physical Vapor Deposition (PVD)

Typical physical vapor deposition (PVD) methods to deposit barrier films include electron beam evaporation and sputtering. In electron beam evaporation, an electron beam is used to heat a small portion of the solid metal above its melting point. While at high vacuum (10^{-3} to 10^{-4} Torr), the molten metal then evaporates atoms into the gas phase. These atoms diffuse through the chamber's atmosphere and deposit on the susbtrate. One or more reactive gases, such as NH_3 or CH_4, for example, may be introduced into the chamber during evaporation to deposit multi–component films.

The sputtering process involves the use of a plasma gas (typically argon) to physically "knock" atoms off of a metal target and onto a substrate. The sputter chamber operates at low vacuum (~100–120 mTorr), and cations from the plasma impact the metal target cathode to liberate metal atoms, which then deposit on the substrate. In the reactive sputtering process, a reactive gas such as N_2, for example, is introduced into the sputter chamber along with the plasma gas. Once the atoms liberated from the metal target cathode reach the substrate, they can interact with the nitrogen radicals formed by the plasma and deposit either a metal nitride compound or a metal–nitrogen solid solution.

Films produced by PVD processes suffer from high stress, a large number of vacancy defects, excess free volume and poor conformality, leaving spots in the barrier open to diffusion by neighboring species at via and trench sides/bottoms [Aff85, Bau98, Bos91, Kel99, Lee93, Lu98b]. The poor conformality inherent to all PVD processes is due to the directionality imparted to the atoms/clusters traveling toward the substrate. This directionality causes step shadowing, where parts of the substrate surface are not "seen" by the incoming sputter atoms. Step shadowing results in little or no film coverage on certain sections of the substrate. These exposed substrate areas are then vulnerable to reaction with subsequently deposited Cu atoms. Figure 1-9 depicts step shadowing.

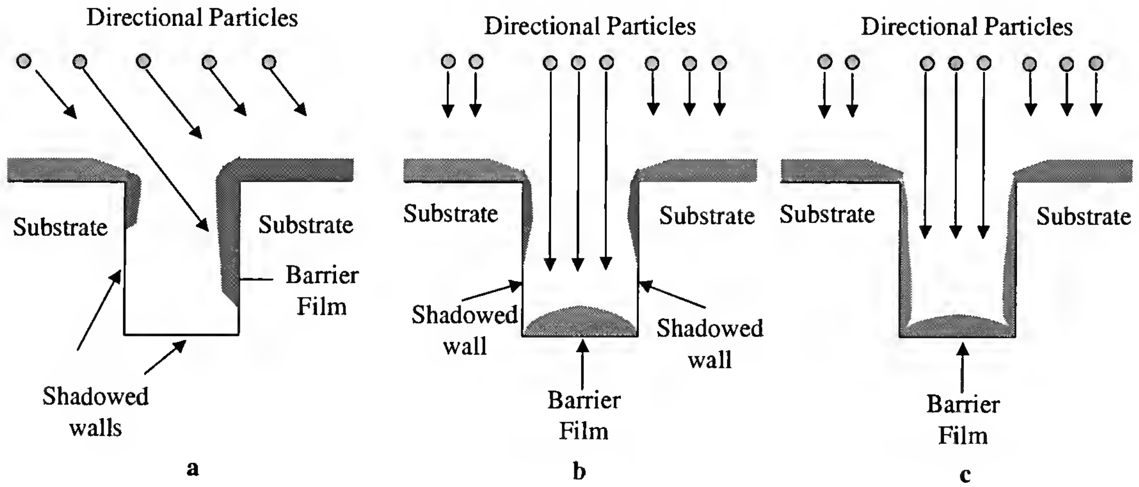
Directional Particles
Substrate
Substrate
Barrier Film
Shadowed walls
a
Directional Particles
Substrate
Substrate
Shadowed wall
Shadowed wall
Barrier Film
b
Directional Particles
Substrate
Substrate
Barrier Film
c

Figure 1-9. Step shadowing effects in small device features due to directional particles arriving at the substrate. a) At an angle to the surface. b) Perpendicular to surface, without resputter. c) Perpendicular, with resputter.

Three variations on sputtering have been developed to extend its applicability to smaller device feature nodes. The first, collimated sputtering, involves the placement of a plate (which contains small holes) between the sputter target and the substrate [Sin02b]. The plate collimates the sputtered atoms/clusters, so that only those traveling parallel to each other in a direction perpendicular to the plate reach the substrate. Once at the substrate, the atoms can deposit or can resputter the metal film at the bottom of a feature (Figure 1-9c), moving it up onto the feature walls to ensure sidewall conformality. The second variation, long–throw sputtering, improves the performance of the sputter deposition system by increasing the distance between the target and substrate, so that only sputtered atoms/clusters travelling in parallel (and perpendicular to the substrate) reach the substrate [Sin02b]. Ionized–PVD (I–PVD) is the third variation used to extend the applicability of sputtering processes beyond the 100 nm device node. I–PVD involves use of a second rf coil to ionize neutral metal atoms that have been liberated from the target by sputtering. These ionized atoms are then accelerated toward the substrate, which is biased to attract the newly ionized metal atoms [Ros01]. Impinging metal atoms resputter the metal that has already deposited on the substrate, and these resputtered atoms can move from the bottom of a feature to the sidewalls and coat them. This leads to improved step coverage in small features compared to other PVD methods. Conformality improvements within the feature from the I–PVD resputter effect are tempered by resputter thinning (beveling) of the feature's top edges (Figure 1-9c). This beveled edge is a weak point in the barrier, and is susceptible to attack by Cu. In addition, although resputter associated with I–PVD improves sidewall coverage, this coverage is still tenuous for films in high aspect ratio features [Vij99]. These extended sputtering techniques, being directional in nature, also have a limited lifespan [Sin02b], and may reach their usability limit at the 45 nm device node in 2010. Among the barrier deposition techniques, only a chemical vapor deposition (CVD) based process offers the conformality required for future device generations, with 100% conformality being the goal for all barriers [Fal98, Fle98, Lev98, Liu00].

1.6.2 Chemical Vapor Deposition

Chemical vapor deposition (CVD) is a widely used film growth technique. It involves the use of one or more gas phase reactants to deposit a solid film on a substrate. The reactant flux at the substrate surface is non–directional in nature, eliminating the possibility of step shadowing in small device features. The substrate promotes reaction between components from the gas phase, and successive reactions lead to film growth. CVD processes typically grow highly conformal films at high growth rates, making them superior to PVD techniques for deposition on aggressive device features. Unlike PVD methods, CVD is capable of area selective growth, which can eliminate a patterning step during device fabrication [Gat96]. CVD techniques are also characterized by high throughput, minimal downtime and easy source changeout, which makes them very attractive for industrial applications. The steps of the CVD process are as follows [Siv95, Vos78]:

- Reactants in the gas phase diffuse through the boundary layer (defined below) to the substrate surface
- Reactants adsorb onto the substrate surface
- Adsorbed species move around surface and settle into available surface sites
- Reactants adsorbed to available surface sites undergo final reactions, which are often catalyzed by the substrate surface, and reaction products are incorporated into the growing film
- By–products from the reaction desorb from the substrate surface

- Desorbed by–products diffuse through the boundary layer and away from the substrate surface

Conversion of gas phase precursors into deposited film can involve both gas phase and surface reactions. Gas phase reactions can involve formation of intermediates and by–products as well as parasitic reactions, such as gas phase nucleation. Surface reactions can involve adsorption/desorption, film formation, and side reactions, which can cause contaminant incorporation into the film. The total pressure in the reactor determines the degree of coupling between gas and surface chemistry [Gat96]. At a total reactor pressure of 1 Torr or greater, homogenous and heterogeneous processes are tightly coupled, while at pressures $< 10^{-4}$ Torr (where $\lambda_{mfp} \approx 50$ cm), the probability of gas phase collisions becomes negligible and the process becomes strictly surface controlled [Gat96]. This surface control at low pressure enables finer control of film properties, such as smoothness and thickness. At higher reactor pressures (>1 Torr), one or more of the gas phase precursors may begin to decompose and/or react to form intermediate gas phase compounds [Gat96]. These precursors (and/or intermediates) can then travel to the substrate surface.

When the precursor (or intermediate) molecules first reach the substrate surface, they can weakly bind (physisorb) to the surface by van der Waals forces or they can immediately react and deposit (chemisorb) [Mas96]. Physisorbed molecules have some degree of mobility, and can diffuse along the substrate surface until they either chemisorb or desorb back into the gas phase. High surface mobility, coupled with the non–directional nature of the reactant flux, are the key CVD features that enable highly conformal film deposition on substrates with varying topography. The probability that an impinging precursor chemisorbs at the initial point of impact on the substrate surface is known as the reactive sticking coefficient. A precursor with high reactive sticking coefficient (approaching unity) and low surface mobility yields a rough film texture, while a precursor with a low reactive sticking coefficient (10^{-3} or less) and high mobility yields a very smooth film [Gat96]. Hence, to deposit smooth films by CVD, a low reactive sticking coefficient coupled with high surface mobility is desirable.

Surface mobility and reactive sticking coefficient are highly dependent on substrate temperature, which must be controlled closely to ensure deposition of films with appropriate structure and properties. Temperature must be high enough to activate the reactions leading to CVD, but cannot be increased indiscriminately. At lower temperature, the sticking coefficient approaches unity and surface diffusivity is minimal [Gat96]. As temperatures increase, the sticking coefficient decreases, while the surface diffusivity and deposition rate typically increase. Higher deposition rates are likely on the flat surface of the substrate, but aspect ratio dependent effects (ARDE) can inhibit deposition in small features. ARDE occur when by–products emanating from the sidewalls and bottom of a small feature inhibit in–diffusion of fresh precursor to the feature. While increasing temperature increases reaction rate on the flat surface, ARDE can lead to a starved condition on the interior walls of the feature. Hence, although increased deposition temperature improves surface diffusivity and decreases sticking coefficient, it can negatively impact film conformality in small diameter, high aspect ratio features (Figure 1-8c).

In addition to optimizing surface mobility and reactive sticking coefficient, the operating regime must be considered when selecting deposition temperature. At lower temperature, the deposition rate is exponentially dependent on substrate temperature, which is indicative of the kinetically controlled regime. Increasing temperature in this regime causes a large increase in film deposition rate, and the slow step in the deposition process is the reaction on the surface. At higher temperature, the deposition rate is relatively insensitive to deposition temperature, which is indicative of the gas–phase mass transfer controlled regime. In this region, the temperature is high enough that essentially all reactants reaching the substrates surface immediately react, and the rate–determining step in the deposition process is transport of reactants to the surface. While the temperature dependence of the deposition rate in this regime is mild (varying from $T^{1.5-2.0}$), the lack of kinetic (surface) control in this regime exacerbates conformality problems. Moreover, higher deposition temperature can alter film structure, causing a shift from amorphous to polycrystalline films, which introduces grain boundaries that can kill barrier performance.

In small features that are to be conformally coated, the surface diffusion length of the physisorbed precursor should be the same order of magnitude as the feature diameter [Coo89]. In larger features, surface diffusion alone is inadequate for conformal coverage, so it must work in tandem with reflection, whereby molecules are reflected back and forth from the sides of the feature until they find a place to chemisorb. Decreasing the precursor's sticking coefficient increases the chance of reflection in a feature. For good coverage, the dimension of the feature should be smaller than the mean free path in the gas phase, so higher pressure (which has a shorter mfp) can be used with smaller device features [Tsa86]. Pressures at and below 500 Torr would be adequate for deposition in a 100 nm feature.

Molecules designed for use as CVD precursors should have high volatility, thermal lability, and have easily (and cleanly) removable supporting ligands [Kod94]. The CVD chemistry should be selected to avoid formation of non–volatile reaction by–products, which can cause particle deposition on the substrate surface and high point defect density [Jai99]. In addition, selection of precursors with low reactive sticking coefficient and high mobility surface species will enhance conformality of the deposited film.

1.6.2.1 Precursor Delivery

During CVD, one or more gas–phase chemical precursors must be delivered to the reactor. The precursors themselves may exist in the gas phase, or they made be put into the gas phase by a number of techniques. Liquid source precursors are typically put into the gas phase by a liquid bubbler system, where a canister containing the liquid precursor sits in a temperature controlled bath (which controls vapor pressure). Carrier gas flows into the bottom of the canister, and bubbles up through the liquid. As the gas bubbles up through the liquid precursor, it becomes saturated with precursor molecules. This carrier gas, saturated with precursor, then flows into the reactor.

There are two typical methods to convey low volatility solid precursors to the reactor: solid source and nebulizer delivery. In a solid source delivery system, the precursor is held in a metal or glass tube. The tube and precursor are heated by thermal or photon energy, and solid precursor near the top of the tube sublimes and is conveyed to the reactor by a carrier gas. As a general rule, a solid precursor must have a vapor pressure higher than 10^{-3} Torr at its melting point to be effectively sublimed and conveyed by a solid source delivery system [Ohr92]. If the vapor pressure is below this value at the melting point, minimal precursor delivery and film deposition will occur.

The second technique, nebulizer delivery, can be used to overcome this vapor pressure limitation. This technique requires dissolution of the solid precursor in a liquid solvent. The solvated precursor is pumped into the nebulizer, which contains a piezoelectric quartz plate. This plate vibrates due to application of a high frequency electrical current, and vaporizes the liquid droplets that contact it. Once the droplets are vaporized into a mist, carrier gas flows through the nebulizer and conveys the mist into the reactor. Figure 1-10 shows a schematic of a nebulizer.

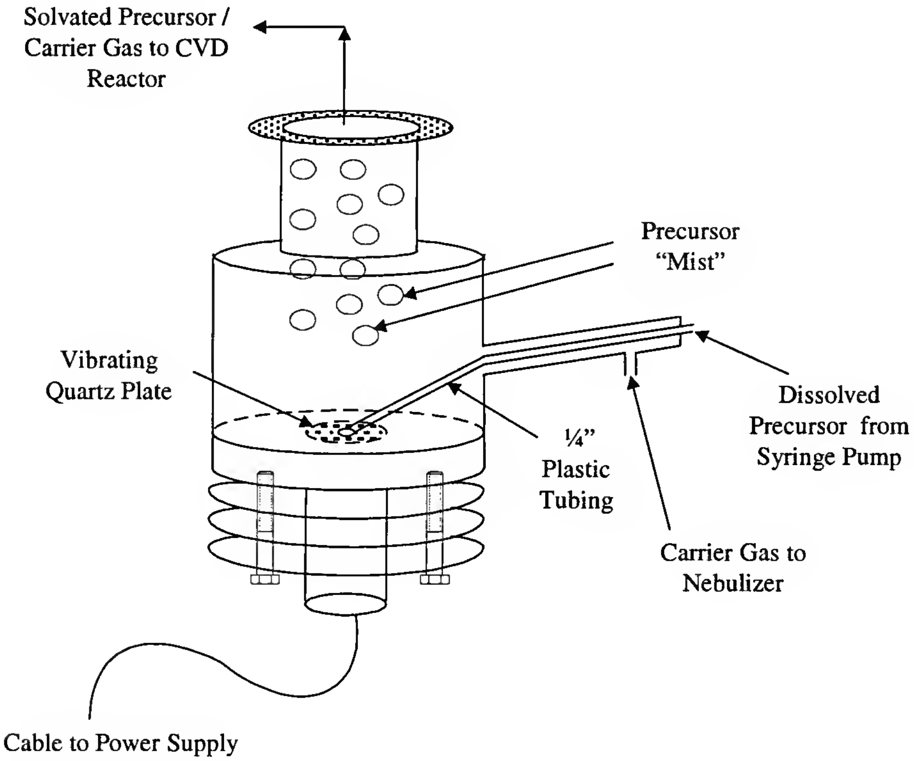
Solvated Precursor / Carrier Gas to CVD Reactor
Precursor "Mist"
Vibrating Quartz Plate
Dissolved Precursor from Syringe Pump
¼" Plastic Tubing
Carrier Gas to Nebulizer
Cable to Power Supply

Figure 1-10. Schematic of a nebulizer delivery system.

1.6.2.2 Variants of CVD

Several variants of CVD are typically used to deposit thin films. The first is low–pressure chemical vapor deposition (LPCVD), which typically relies on metal halide chemistry (e.g., $TiCl_4$, WF_6) to deposit films. This technique usually requires high deposition temperature (>450°C) and suffers from halide incorporation into the barrier films. The presence of halides in the barrier can lead to Cu corrosion, which decreases Cu–barrier adhesion and reduces electromigration resistance [Huo02].

The same halide chemistries used for LPCVD are typically used for plasma–enhanced chemical vapor deposition (PECVD), in which a plasma assists fragmentation of the reactants, thereby lowering the deposition temperature. After fragmentation by the plasma, the precursor fragments travel to the heated substrate, react on its surface and deposit a film. Reduced conformality for PECVD films in high aspect ratio trench features is due to the directional nature of the plasma [Tsa96], as shown in Figure 1-9. Despite the low resistivity and deposition temperatures that PECVD offers, its inability to deposit highly conformal films in high aspect ratio features makes its use in future barrier deposition processes unlikely.

In metalorganic chemical vapor deposition (MOCVD), films are deposited by reaction of one or more carbon–containing vapor phase precursor compounds. MOCVD precursors typically have some or all of the halide ligands common to LPCVD and PECVD replaced with carbon–containing ligands. These precursors afford little or no halide incorporation into the deposited films, and MOCVD has been demonstrated to deposit a variety of films at low temperature. By varying the structure of the precursor molecule, the precursor can be optimized to dissociate in a “clean” fashion (i.e., with minimal oxygen and carbon contamination) and at relatively low deposition temperature. The presence of impurities (O, N, C) is reported to improve stability in contact structures, because the impurities tend to stuff grain boundaries and inhibit diffusion [So88].

Oxygen's "stuffing" effectiveness, however, is lower for Cu than Al, because the reactivity of Cu with O is less than that for Al with O [Kim99c]. Carbon bound to the metal has also been reported to improve thermal stability of the barrier and to foster growth of smaller grains [Wan01b], but free carbon in the films can scatter electrons, increasing film resistivity. Among the challenges for MOCVD of refractory nitride materials are controlling carbon and oxygen contamination, lowering the deposition temperature, and minimizing film resistivity.

1.6.2.3 CVD Reactors

CVD reactors fall into two broad categories: hot wall and cold wall reactors. Hot wall reactors have heated walls, with typically laminar flow profiles. These are preferred for exothermic reactions, since the hot wall temperatures discourage or prevent unwanted deposition on the reactor walls. In contrast, cold wall reactors have steep temperature gradients surrounding the susceptor, which often leads to convection pattern formation in the reactor. These are preferred for endothermic reactions, since the reaction will occur most readily on the hottest surfaces in the system [Vos78].

CVD reactors are typically run in two modes: differential or starved. In a differential reactor (similar to a CSTR), the ratio of reactant out to reactant in is approximately one, so that the composition in the reactor is essentially constant. In a starved (feed rate limited) reactor, the ratio of reactant out to reactant is much less than one, meaning that there are large concentration gradients in the reactor caused by fast reactions [Kod94]. ARDE can cause both differential and starved conditions to exist simultaneously on a substrate with aggressive feature topography. Flat surfaces on the substrate receive adequate precursor flux, and hence operate in a differential condition, while ARDE in small features prevent good precursor flux, starving the sidewalls and bottom. Increasing the deposition temperature increases the concentration disparity between the inside of the feature and the flat surface of the substrate, further degrading the conformality over these features.

1.6.2.4 CVD Transport Issues

Heat and mass transport in a cold–wall CVD reactor can be complex, due to large temperature gradients. Depending on pressure in the reactor, mass transport may occur by fluid flow and/or diffusion [Tim01]. At higher reactor pressures (near atmospheric), both fluid flow and diffusion occur simultaneously. In fluid flow transport, gas molecules follow streamlines through the reactor, while for diffusion transport, concentration gradients drive transport across streamlines. Heat transport occurs by a combination of convection, conduction and radiation in the reactor. Near the deposition surface, the temperature, velocity and concentration vary significantly [Kod94].

Use of an impinging jet to feed reactants onto a small susceptor results in stagnation point flow. The stagnation point is at the center (origin) of the surface, where flow velocities are zero (where y=0 in Figure 1-11). With adequate pressure, a shear layer of uniform thickness develops near the surface of the susceptor [Whi91]. The shear layer, also called the momentum boundary layer, is the relatively stagnant region between the surface of the substrate and the region where the fluid velocity (u) reaches 99 % of the free stream velocity (U_∞, cm/sec). Reactants and by–products travel to and from the substrate surface, respectively, by diffusing through this layer. This boundary layer (δ_M) displaces the outer inviscid flow away from the substrate surface, as depicted in Figure 1-11. Thickening of the low–velocity shear (boundary) layer due to viscous diffusion is balanced by thinning of this layer due to acceleration of the outer inviscid stream, which leads to uniform boundary layer thickness.

The momentum boundary layer thickness (δ_M, cm) in stagnation point flow is approximated by Equation 1–10:

$$\delta_M = 2.4 * \sqrt{\frac{2\nu D_S}{\pi U_\infty}} \tag{1–10}$$

where ν is the kinematic viscosity (cm^2/sec) and D_S is susceptor diameter (cm) [Whi91]. More information on the dynamics of stagnation point flow may be found elsewhere [Whi91].

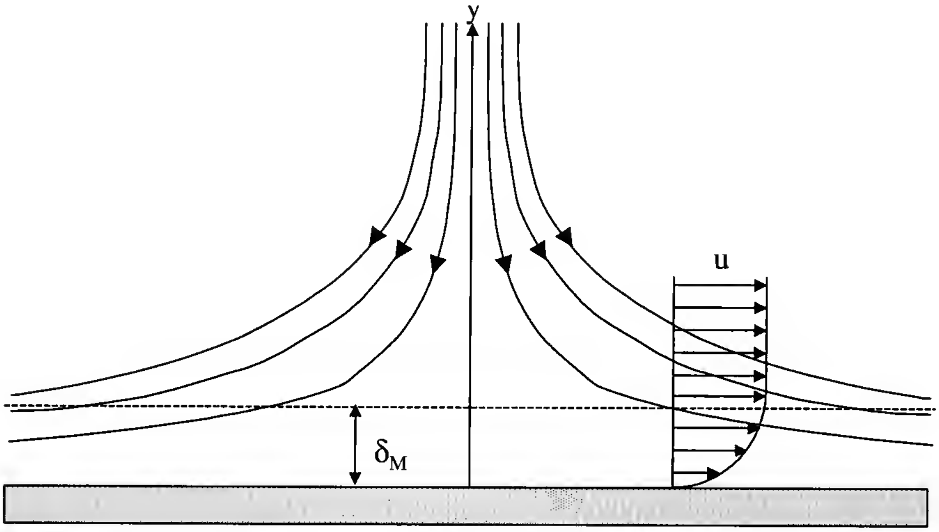

Figure 1-11. Stagnation–point flow [Whi91].

In addition to the momentum boundary layer, concentration and thermal boundary layers, with thickness denoted δ_C and δ_T, respectively, are also defined. The concentration boundary layer extends from the substrate surface to a point where precursor concentration is 99% of the bulk concentration, and likewise, the thermal boundary layer extends to a point where the temperature is 99% of the bulk temperature.

The thickness of the boundary layers depends on several process variables, including gas velocity, temperature, and pressure. Gas phase species outside of these boundary layers (where $y > \delta_M$, δ_C, or δ_T) move by both convection and diffusion. Within the boundary layer (where $y < \delta_M$, δ_C, or δ_T), velocity, concentration, and temperature are non–uniform. As species leave the gas and deposit onto the substrate, their gas phase concentration drops near the substrate surface. To compensate for this drop in concentration near the surface, a net diffusive flux occurs bringing depositing species from regions of higher concentration in the boundary layer to the near–surface region. As the surface reaction generates reaction by–products, the concentration of by–products near the substrate surface is higher than it is at locations farther from the surface. This higher concentration of by–products near the substrate surface leads to a net diffusive flux of by–product away from the substrate. Likewise, temperature varies from the substrate into the gas phase. The temperature at the substrate is high, and this drops steadily through the thermal boundary layer, until it reaches the bulk value. Typical CVD temperature and concentration profiles are depicted in Figure 1-12.

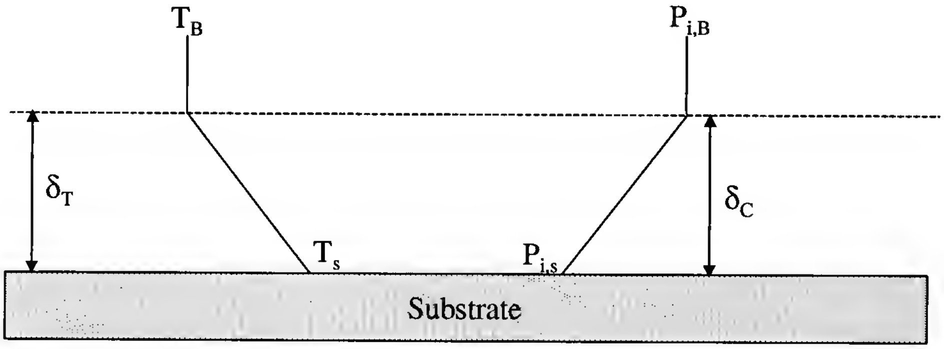

Figure 1-12. Variation of temperature and precursor partial pressure near the substrate in a CVD reactor. Note that while δ_T and δ_C are shown as being equal, this is not always true.

Transport to the substrate during CVD is assumed to occur by diffusion of reactants through the concentration boundary layer at the surface. This boundary layer arises due to consumption of the precursor at the surface, which causes a concentration gradient to form between the surface and the bulk. Flux of reactant through this layer (J, kgmol/m^2–sec) is given by Equation 1–11 [Kel91]:

$$J = \frac{D_o (T_s - T_b)(P_b - P_s)}{\delta_C T_o^2 R \ln\left(T_s / T_b\right)} \qquad (1\text{–}11)$$

where D_o is the diffusion coefficient (m^2/sec) at temperature T_o (K), δ_C is the thickness of the concentration boundary layer (m), P_b and P_s are the bulk and surface partial pressure of the reactant (Pa), T_b and T_s are the bulk and surface temperature (K) and R is the gas constant (m^3–Pa/kgmol–K). Once the reactant species diffuse across the boundary layer, they may or may not be incorporated into the growing film surface. The mass transfer flux (J_{tr}, kgmol/m^2–sec), which is the amount of precursor incorporated at the film surface, is defined in Equation 1–12:

$$J_{tr} = \frac{k_d (P_s - P_{eq})}{R T_s} \qquad (1\text{–}12)$$

where k_d is the mass transfer coefficient (m/sec) and P_{eq} is the equilibrium precursor partial pressure (Pa) at the surface. When the deposition process reaches steady state, the diffusion and mass transfer fluxes are equal, and a dimensionless parameter called the CVD number, N_{CVD}, can be defined [Kel91]:

$$N_{CVD} = \frac{(P_b - P_s)}{(P_s - P_{eq})} = \frac{k_d \delta_C T_o^2 \ln\left(T_s / T_b\right)}{D_o T_s (T_s - T_b)} \qquad (1\text{–}13)$$

The denominator on the left–hand side of the equation represents the degree of precursor supersaturation at the substrate surface. When the amount of supersaturation is small, $P_s \approx P_{eq}$ and $N_{CVD} >> 1$, hence all reactant reaching the substrate reacts immediately. This is known as the mass transfer controlled regime. Conversely, if the supersaturation is large, P_s approaches P_b and $N_{CVD} << 1$, and the species reaching the substrate react very slowly. This is known as the kinetically (or surface reaction) controlled regime. When $N_{CVD} >> 1$, high points on a rough surface have a higher value of P_s, and the growth rate at a high point is increased relative to a low point. This causes rough points on the surface to be amplified by film growth when operating in the mass transfer controlled regime. In contrast, when $N_{CVD} << 1$, P_s approaches P_b everywhere along the surface, so that the growth rate is similar at all points along the surface. This leads to a smoothing of rough spots during film growth when operating in the kinetically controlled regime.

The type of carrier gas used in the reactor can have a significant impact on the films grown during CVD. For fixed bulk and surface temperatures, gases with a lower thermal conductivity will have a sharper temperature profile, meaning less upstream heating of the precursor species as it approaches the substrate. Using a carrier gas with higher thermal conductivity results in a smoother temperature profile, enabling more upstream heating of the precursor. Increased upstream heating promotes pyrolysis, or gas–phase thermal breakdown of the precursor into the intermediate or final reactant species. Increasing the time available for precursors to undergo pyrolysis increases the likelihood that the precursors have decomposed into the intermediate components (if necessary) for final surface reaction. If the precursors undergo sudden pyrolysis very near the substrate surface, they will not decompose as thoroughly, leaving large molecular fragments that can be incorporated into and contaminate the growing film.

Ideally, transport of reactants to and products from the substrate surface should occur in such a way to deposit a “clean” film containing the desired components. In reality, this is unlikely, with atoms from reaction by–products and precursor ligand fragments typically depositing to some degree in the films. Control of contamination by ligand decomposition is extremely important to get films with desirable properties. An example of single–source CVD, which has some contamination from precursor ligands, is depicted in Figure 1-13.

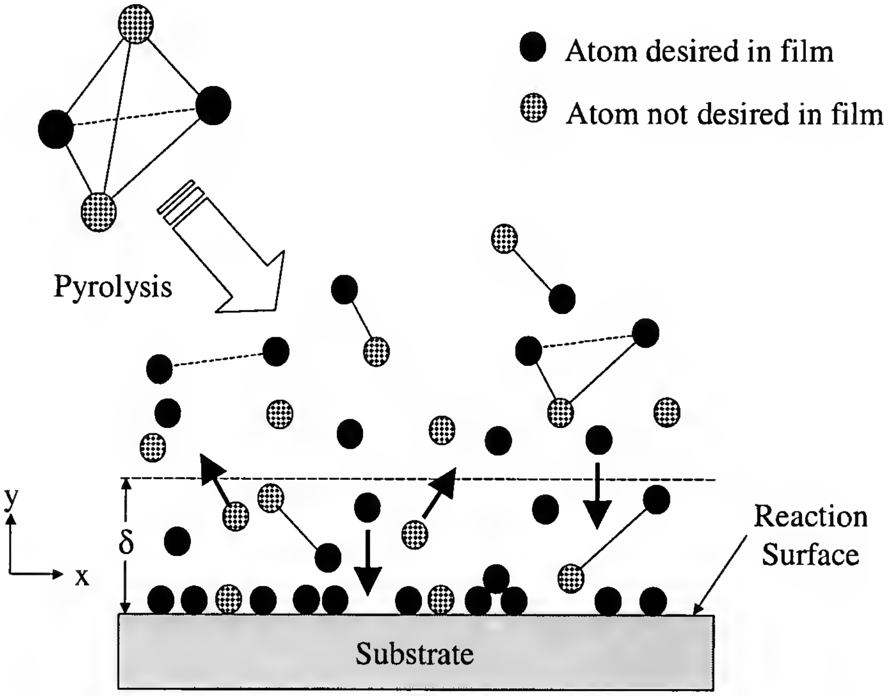

Figure 1-13. Diagram of the CVD process for a single–source precursor.

1.6.3 Atomic Layer Deposition (ALD)

Standard CVD techniques introduce all required precursor gases to the reactor simultaneously, making deposition rate and precise thickness control difficult during film deposition. Although the ITRS roadmap suggests that CVD deposition of barriers will be important in the near term, atomic layer deposition (ALD) methods will emerge as the dominant solutions because of their superior conformality and improved thickness control. As barrier thickness drops below 100 Å, standard CVD techniques will approach their usability limit due to difficulties controlling the deposition rate. Atomic layer deposition (aka ALD, ALE or ALCVD) will be necessary to deposit extremely thin films on the IC devices [Dan02], and its use in IC production at the 65 nm node is projected [Bey02, Cha04]. The highly conformal, ultra–thin barriers afforded by ALD will be essential in the future to minimize the barrier's impact on the resistance per unit length in Cu interconnects [Kap02].

As a variant of CVD, ALD is well suited for deposition of ultra–thin, highly conformal films over small device features. ALD enables monolayer addition with precise thickness and composition control, irrespective of the underlying substrate's topography [Dan02]. ALD has been used to deposit metal, semiconductor, dielectric and seed layers [Dan02, Kla00a–b, Les02]. In particular, ALD has been used to deposit high–k gate dielectrics at the front end and diffusion barriers at the back end of the process. ALD is a "digital" process, involving the stepwise use of two or more gas phase precursors, each of which is self–limiting on the substrate [Ros01]. A single precursor gas is present in the reactor at any given time, so that a uniform layer of the precursor may chemisorb to the substrate surface. Once this chemisorbed layer forms, the chamber is evacuated or swept with inert gas [Sun92]. By minimizing chamber volume, rapid deposition and quick purge/vacuum steps are promoted. This is important to minimize the incorporation of background impurities into the film and also to prevent the process from shifting to CVD mode, which can occur if additional reactant from the previous pulse is in the reactor's atmosphere during the subsequent pulse. A second precursor gas is then introduced to react with the chemisorbed layer from the previous step, forming a new monolayer of material. The second precursor gas is also self–limiting, so that reaction stops after the monolayer of chemisorbed material from the previous step has been consumed. Film thickness is more difficult to control for growth with CVD, which has been reported to close extremely narrow vias rather than depositing conformal films in them [Hau00].

ALD was first reported in 1977 by Tuomo Suntola to deposit ZnS films for electroluminescent displays [Goo86]. Since this first report, the utility of ALD to deposit a variety of materials has been demonstrated. Materials such as metals (e.g., W, Cu, Ni, Co, Ti, Ta, Ru, Pt, Al), metal oxides (e.g., Al_2O_3, ZrO_2, HfO_2) and metal nitrides (e.g., TiN, TaN, WN_x) have been deposited using this technique [Les02]. In contrast to the thin, flat films typically desired by ALD, the process has also been demonstrated to coat porous, high surface area substrates for catalysis [Hau93].

ALD exploits the difference in energy between chemisorption and physisorption to deposit film layers in a self–limiting fashion [Gat96, Goo86]. Temperature is selected so that $E_{chemisorption} > kT > E_{physisorption}$. In other words, the temperature is high enough to overcome physisorption forces to enable desorption of any physisorbed species, but it is also low enough to prevent removal of chemisorbed layers. For an adequate pulse time, complete surface reaction occurs and the film composition is determined by thermodynamics (stable thermodynamic phase forms for the selected conditions).

The precursors must be volatile, thermally stable, self–limiting and highly reactive (fast, complete reactions) with each other and with the substrate. They must also have sufficient purity, have unreactive by–products, and not undergo self–decomposition or cause etching of the film or substrate. The precursors should have a vapor pressure of at least 0.1 Torr for delivery during ALD. Desirable ALD reactions should have large negative ΔG values to ensure rapid surface reaction after the precursor pulse into the reactor [Les02]. High reactivity enables rapid saturation of the film surface, which in turn enables a good deposition rate. The need for high precursor reactivity is contrary to CVD precursors, which require smaller negative ΔG values to prevent gas phase nucleation and particle formation. The precursor dose must be high enough to saturate the substrate surface, which must have reactive adsorption sites [Hau00]. In addition, the reaction temperature must be chosen to enable reaction (chemisorption) between the precursor and reactive sites, while also avoiding gas phase decomposition or condensation of the precursors [Hau00].

The advantages of ALD relative to CVD are excellent conformality (~100%), inherent elimination of pinholes, good thickness uniformity, and elimination of potential gas phase reaction/nucleation [Goo86, Rit03, Sun92, Sun93]. The disadvantages of ALD include slow growth rate (0.06–0.6 μm/hr) [Goo86, Ros01], the possibility for substantial incubation time to deposit the first monolayer of film, contaminant incorporation and the potential for surface reconstructions to adversely affect deposition rate [Ros01, Sun93]. In the most aggressive applications, a diffusion barrier will need to be deposited on four different surface materials simultaneously: two different insulator materials, an etch stop layer (such as Si_3N_4) and Cu [Ele02]. Varying incubation times on the different materials can cause significant deposition difficulty, so choice of precursor and deposition conditions is essential to deal with situations like these. Precursor testing should therefore be done on all possible underlying substrates, to ensure that a given material can be reliably deposited with a given precursor. Another disadvantage is decreased film purity relative to CVD grown films. Background contaminants have considerable time to incorporate into the film during the pulse and purge steps, which can degrade film structure and electrical properties. The purity of purge gases and control of out–gassing from reactor walls and seals are critical, because inadequate control can lead to considerable impurity incorporation causing modification of film structure and properties. Typically, a faster growth rate means less sensitivity to contaminant incorporation [Han03]. ALD must compete with the purity of PVD films, whose growth rates are 2 to 3 orders of magnitude higher in an environment that is 3 to 6 orders of magnitude cleaner [Han03].

Several adjustable parameters are available for the ALD process. The first parameter is the type of ALD reactor system used for deposition. The two main categories for ALD systems are the open type (used with molecular beam epitaxy (MBE)) and the closed type (used with LPCVD) [Sun93]. In the open type system, pressure is fixed, as with an MBE system, which typically operates at ultra–high vacuum (UHV). Precursors are introduced from two or more sources (e.g., Knudsen cell), which are turned on and off to generate the pulsing action. Desorbed surface species collect on the cold walls in the reactor system or by the vacuum pump. In the closed type system, the atmosphere is turned over between reactant exposures to generate the pulsing action; this is done either by evacuating the system (pressure modulation) or by introducing an inert purge gas. In addition to the type of system used, the chamber volume may be adjusted to accommodate more substrates (i.e., to increase throughput) or to decrease purge/vacuum times.

The second adjustable parameter is the type of precursors used for the deposition process. The precursors must be self–limiting, very reactive with each other and with substrate, and generate the desired film structure/stoichiometry. Many precursors have been tested in the literature for various materials, with halide chemistry often being used due to easy removal of the halide ligands (with H_2, NH_3, etc.). In addition to precursor selection, pre–treatment of one or more of the precursors before introduction to the reactor is another adjustable option. For example, Ta films were deposited using plasma–enhanced ALD with sequential pulses of $TaCl_5$ and H_2 [Kim02b]. The H_2 was cracked to atomic H in an rf plasma system before being introduced to the reactor.

The third parameter is substrate temperature, which should be selected to enable chemisorption of first layer and desorption of outer, physisorbed layers [Gat96]. A fourth parameter is the reactant pulse time. A longer pulse time enables more complete surface reaction, and closer approach to thermodynamic equilibrium at the film surface. The last parameter, which is unique to closed type systems, is reactor pressure. ALD process pressure in closed type systems typically ranges from 1 to 10 Torr [Les02], which can be modulated to evacuate the chamber if an inert gas purge is not desired.

The process is depicted in Figure 1-14. The result of running in ALD mode is a linear growth rate with the number of cycles. The number of monolayers grown per cycle (normally <1), multiplied by the number of cycles, gives the film thickness, where one cycle includes one pulse of each of the precursor gases. Several growth cycles are typically necessary to deposit a monolayer of material, because steric crowding on the film surface prevents 100% surface coverage for each pulse. In practice, monolayer by monolayer growth is unlikely, and there may be two or more monolayer levels growing together during deposition. Film growth is dependent on several factors, including reactivity of the precursors, the number of reactive sites available on the substrate/film surface, and the size of the precursor molecule (larger molecules typically yield lower growth rates due to steric hindrance during the reaction cycle) [Hau00]. ALD cycle time typically ranges from 0.5 to 5 seconds.

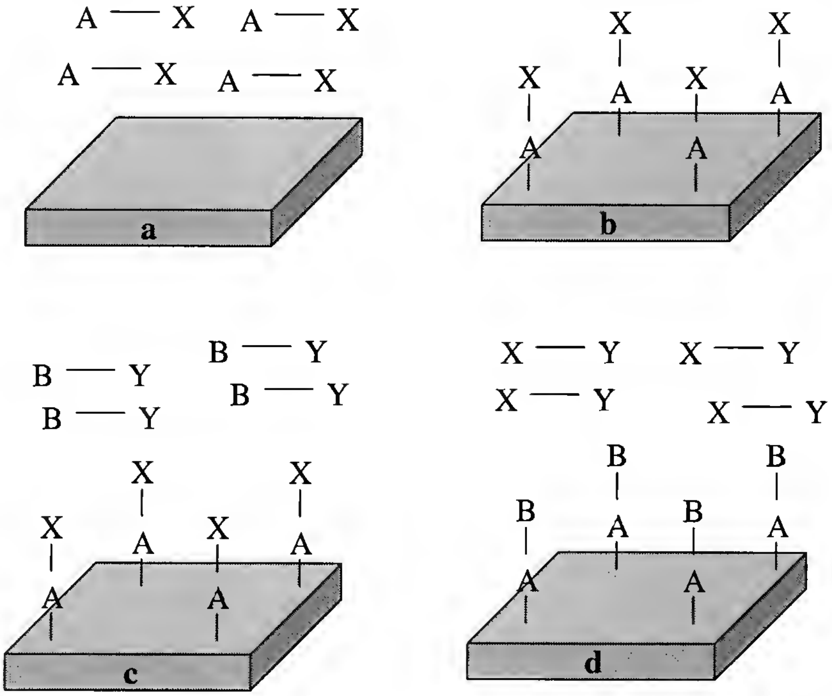

Figure 1-14. Diagram of the ALD process. (a) Introduction of first precursor. (b) Absorption of first precursor. (c) Introduction of second precursor. (d) Complete monolayer deposition of A–B.

The growth rate for an ALD process should be linear with the number of growth cycles. If this is not the case, the process may not be self–limiting. To check this, reactant pulse time can be changed to determine if the experiment is self–limiting, or if longer pulse times result in thicker films. ALD growth reportedly occurs by formation of islands during nucleation, hence the barrier should have thickness at least equal to that required to close the surface of the substrate [Bey02]. This closure thickness depends on the deposition conditions and the barrier materials being used. Electrical measurements (such as 4–point probe) can be used to determine if the deposited film is continuous. Films may have high resistivity until enough cycles have passed that the film is continuous; the film's resistivity will then drop substantially. This is one way to determine if the first monolayer has been completely filled in, if depositing a conductive layer on Si, for example. Extrapolating from a plot of resistivity vs. the number of deposition cycles, one can estimate the deposition cycle after which a continuous film is finally deposited. Ion scattering spectroscopy has also been used to determine when the surface has closed.

The appeal of ALD to industry lies in its ability to manage line resistance and to provide better stress migration performance than PVD films [Pet03]. A thin ALD barrier film at the via bottom is instrumental in lowering via resistance. In addition, Cu seed layers must be ultra–thin, continuous, and have excellent conformality to ensure consistent Cu deposition during ECD, so ALD will be essential for seed deposition. ALD is also excellent for varying the composition of the deposited film with thickness (composition grading), which can be important to ensure a film's compatibility with underlying layers.

1.7 Copper Deposition Methods

Electrochemical deposition (ECD), also known as electrodeposition or electroplating, is the technique currently used in industry to deposit void–free bulk Cu layers on ICs with aggressive topographies [ITR02]. This technique has the advantages of low deposition temperature, high deposition rate, and low manufacturing cost [Chi98]. The ECD process begins with the deposition of a Cu "seed layer" on the barrier surface, because the barrier layer's resistivity is typically too high to enable uniform electrodeposition. Seed layer deposition is currently done by PVD, which is projected to be used down to the 45 nm device node [Pet03]. Once the seed layer is deposited, the sample can be immersed in the electrochemical bath and the ECD process can begin. During Cu ECD, an electrolyte containing Cu cations and sulfate anions (Cu^{2+} and SO_4^{2-}, respectively) is put into contact with the desired deposition surface. Electrons are introduced to the deposition surface (called the cathode) and reduce the Cu^{2+} ions in the ECD solution, causing these ions to plate out as metallic Cu. A Cu seed layer deposited by PVD (prior to the ECD process) is typically used as the cathode, on which Cu^{2+} ions plate out to form Cu(0). The plating reaction is:

$$Cu^{2+} + 2e^{-} \longrightarrow Cu(0) \qquad (1-14)$$

To complete the electrical circuit, an anode is placed in the electrolyte solution. The anode introduces current to the solution, which replaces positive charges lost by the Cu plating reaction, enabling the electrolyte to remain electrically neutral [Rei00]. Since Cu^{2+} ions are present in the plating solutions for ECD, backside protection of the Si wafer from the bath is essential during deposition. Failure to do this can result in massive Cu in–diffusion through the backside of the wafer, which will occur rapidly based on the diffusivity of Cu in Si (as discussed above). At the industrial level, the ECD plating tools have an o–ring around the edge of the wafer, which allows the device side of the wafer to contact the plating solution while preventing the solution from touching the backside. At the research lab level, waxes or glues may be used to protect the backside of the substrate.

The use of special additives enables the ECD technique to fill small features from the bottom up with Cu (superfilling). To ensure deposition of a microvoid–free, uniform thickness Cu layer by ECD, the plating current (and therefore the seed layer thickness) must be essentially constant from edge to center across the wafer [Sin02a]. Hence, high uniformity of the Cu seed layer is essential. The seed layer is usually deposited on the barrier surface by sputtering, however, which is characterized by poor step coverage in small features [And99, Wan03]. A Cu seed layer with poor step coverage leads to poor Cu coverage during ECD. To overcome the conformality challenges associated with sputtering, several different approaches are being pursued.

The first approach is to deposit Cu seed layers by CVD [Nor01]. Generally, Cu CVD precursors are classified into two categories: Cu(I) and Cu(II) compounds. Cu(I) compounds, such as Cu(hfac)(TMVS), where hfac is hexafluoroacetylacetonate and TMVS is trimethylvinylsilane, are typically more volatile, and can be used without a carrier gas or a reducing agent [Nor01]. These compounds tend to be liquids and are capable of deposition below 200°C, but are therefore more reactive and less thermally stable, making control of the deposition rate more difficult. Copper(II) compounds, such as $Cu(hfac)_2$, are more thermally stable, but typically require a reducing agent (such as H_2) to remove the ligands during deposition [Kod94]. In addition, these compounds tend to be solids, requiring a deposition temperature higher than 250°C [Nor01]. The major issue for Cu CVD from both Cu(I) and Cu(II) precursors is incorporation of halides and carbon from the precursor ligands into the Cu film, which can have detrimental effects on film properties such as adhesion and resistivity. More detail on Cu CVD precursors and deposition is available elsewhere [Kod94].

Deposition of a Cu seed layer by CVD followed by PVD and reflow of Cu has also been reported [Fri99a, Jai99]. Cu reflow typically involves the deposition of Cu by PVD methods, especially sputtering, followed by subsequent annealing of the device. The annealing process enhances surface diffusion of Cu, which enables Cu transport into and filling of small features [Fri99a]. The driving force for this diffusion is the chemical potential gradient associated with differences in surface curvature along the surface of the deposited Cu. To minimize the total free energy on the Cu surface, Cu atoms diffuse along the surface from convex regions to concave ones [Fri99a]. The net result is thinning of convex overhang regions at the tops of features and filling of concave parts of the features, such as via/trench sidewalls and bottoms. This diffusion–mediated process is good for movement of Cu to fill submicron feature sizes. Anneal time can be modified by changing the anneal temperature, but the anneal temperature cannot be higher than the temperature stability limits for the device, and must be low enough to prevent bulk Cu diffusion, which can lead to delamination and a change in Cu texture. Typically, Cu is annealed for 13–14 minutes at 450°C during the reflow process [Fri99a].

Another approach is to deposit Cu seed layers by ALD. Several different precursors have been tested for ALD Cu seed deposition, including Cu(hfac)(TMVS), $Cu(hfac)_2$, $Cu(thd)_2$, $[Cu(C_3H_7)NC(CH_3)N(C_3H_7)]_2$, and CuCl, where thd is tetramethyl heptanedionate [Kod94, Lim03, Nor01]. The first four compounds are bulky, metalorganic sources, which have a very low growth rate per cycle due to steric hindrance. In addition, the first two compounds contain F, making the possibility of F incorporation into the deposited Cu film an issue. The last compound, CuCl, is a solid with very low vapor pressure, hence transport to the reactor is very challenging. [Huo02, Jup97, Nor01].

Electroless Cu plating, which deposits Cu without use of a sputtered Cu seed layer, may also be used [Wan03]. This technique involves deposition of Cu from an ionic solution, where the deposition surface catalyzes a redox reaction, without any external electrodes [Sha95]. A specific component from the solution (e.g., glyoxylic acid) serves as a reducing agent, and is oxidized on the catalytic surface, releasing one or more electrons [Wan03]. These electrons reduce Cu^+ ions from the solution, causing the Cu to plate out as a film on the deposition surface. While this technique has been used to deposit Cu seed layers with good conformality and low resistivity (1.7 $\mu\Omega$–cm), and has also been used to do Cu filling [Lee98a], control of the deposition rate is not as precise as sputtering. More detail on this deposition technique is available elsewhere [Sha95, Sha97].

The last approach is seedless ECD [ITR02, Sin02a], where Cu is directly electroplated onto the underlying barrier material using an external electrode, but without any seed layer. This technique is the most technologically and economically promising, because it eliminates the seed layer deposition step from the current IC metallization process and does not require new equipment expenditures. Selection of a diffusion barrier material that enables seedless Cu electrodeposition could result in significant cost savings to the metallization process.

1.8 Statement of Problem

The three main challenges of shifting to Cu interconnects on IC devices are: a) Cu deposition technique b) patterning method for the Cu layer, and c) which barrier material and deposition method will prevent Cu–Si interdiffusion while fostering adhesion to neighboring layers [And99].

The first challenge has been addressed by use of ECD. Since Cu is resistant to chemical etching, the application of standard reactive ion etching (RIE) techniques used to pattern Al is not feasible for Cu. The second challenge, patterning of Cu interconnects, has therefore been addressed by the dual–damascene deposition process. In this process, Cu is deposited across a pre–patterned wafer by one of the aforementioned deposition techniques. Chemical mechanical polishing (CMP) uses a grinding pad and slurry to remove excess Cu, leaving only the desired spots (e.g., trenches and vias) filled with metal. Since the dual–damascene process deposits Cu in both trenches and vias, the need for tungsten (W) plugs at the upper levels of the IC, which are used to fill vias on Al based devices, is eliminated. Removing this W plug lowers the electrical resistance of the device, both because Cu has a lower resistivity than W and because the Cu–W interface is eliminated.

The third challenge, barrier material and deposition technique, is an ongoing issue as device features continue to shrink. Ti/TiN barriers, deposited by sputtering, are still used at the contact level with W plugs, where TiN protects the contact from F in the WF_6 precursor and improves W adhesion [ITR02, Kal00]. Ti reacts with Cu to form cuprides, making Ti thermodynamically unstable as a diffusion barrier for Cu [Ram00]. Moreover, if TiN films are Ti rich, the excess Ti can react with Cu and lead to failure of the TiN barrier. In addition, TiN barriers with thickness below 20 nm reportedly fail to prevent Cu diffusion due to grain boundary diffusion [Kal00].

A Ta/TaN dual layer barrier structure is currently used as the Cu diffusion barrier at the intermediate and upper wiring levels on IC devices. Cu has good adhesion to Ta, which encourages deposition of low–resistivity Cu (111) on its surface [Pet03], while TaN has good adhesion to the dielectric layer [ITR02, Sin02a]. The Ta/TaN dual layer barriers are deposited by modified sputtering methods [ITR02, Sin02a], however, which have a finite lifetime due to aforementioned step shadowing issues. Barrier deposition takes place on the industrial scale in a cluster tool, which contains several chambers connected by a common vacuum transfer chamber. The barrier is deposited in one chamber, and the wafer is then moved in-vacuo to a separate Cu seed layer deposition chamber. Once the Cu seed layer is deposited, the wafer is pulled out of the cluster tool and put into a separate system for Cu ECD.

The "holy grail" of diffusion barrier research is a robust material / deposition method couple that meets all of the above listed barrier requirements and is extendable to future device generations. In addition, a material/deposition pair which would enable Cu metallization to extend from the upper levels of the device down to the contact level would eliminate the need for Al metallization at the local level and the use of W contact plugs, yielding greater device speed. The interconnect structure's features (trenches and vias) become increasingly more aggressive (narrower diameter and higher aspect ratio) as the wiring levels get closer to the contact level. Research should therefore focus on meeting coverage requirements at device level feature dimensions to enable future extension of Cu throughout the IC.

1.9 Hypothesis

It is evident that a variant of CVD will be required to meet future demands for conformal diffusion barrier deposition on aggressive IC device topographies. New precursors will be required to meet the increasingly stringent demands on film properties. In an effort to avoid halide incorporation, synthesis and testing of novel WN_x and WN_xC_y MOCVD precursors were pursued in this work, for reasons that will become clear in Chapter 2.

Depositing WN_x and WN_xC_y films from novel precursors by MOCVD should minimize halide content, have low temperature deposition, enable good adhesion to neighboring layers, and enable a single–step CMP process. In addition, these materials appear to be useful for direct, seedless electroplating, and have been reported to resist Cu diffusion. WN_x is also reported to deposit in amorphous form more easily than TaN_x [Ram00], and the addition of C to form WN_xC_y should enhance the ability to deposit amorphous films even further.

Eventually, a shift from CVD to ALD will be necessary to meet conformality requirements in small device features. Hence, our strategy is to initially pursue WN_x and WN_xC_y films by MOCVD and to eventually transition to precursor development and testing for ALD.

The film growth and procedure and characterization techniques used to analyze the films will be discussed in Chapter 4. Data, analysis and conclusions for each precursor will be presented in a separate chapter, while the thermodynamic analysis for the W–N–C–H–Cl system is presented in Chapter 3. Cu diffusion results for barriers deposited with an isopropylimido-based W complex will be discussed in Chapter 8, and future work will be discussed in Chapter 9.

CHAPTER 2
REVIEW OF THE LITERATURE

From a thermodynamic standpoint, a barrier material must be chosen so that the chemical potential (the thermodynamic description of reactivity) at each interface ensures little or no reaction. A major thermochemical difference between Al and Cu is their reactivity with silicon. Al can exist in equilibrium with Si, while Cu cannot, readily reacting to form silicides [Ram00]. This non–equilibrium suggests that the thermodynamic driving force for diffusion in the Cu–Si system is larger than that in the Al–Si one. An ideal barrier separating Cu from Si must therefore be stable to and non–reactive with both Cu and Si. Moreover, the barrier should be stable with other potential materials in the IC, such as low–k and high–k dielectrics.

Many materials have been examined to determine their potential as diffusion barriers for Cu metallization schemes. A comprehensive list of various materials tested as diffusion barriers can be found in previous review articles [Jai99, Kal00, Kim03b].

2.1 Cu–Si Interconnects without a Barrier

Ideally, the easiest route to IC device fabrication would be to deposit Cu directly onto any neighboring layers. Hymes et al. [1998] formed copper silicide compounds by sputtering Cu onto thin films of Si, with the goal of using these compounds as passivation layers to prevent further Cu–Si interdiffusion and reaction. At room temperature, Cu_3Si and Cu_5Si formed, while all Cu_3Si decomposed to Cu_5Si after annealing at only 300°C. The Cu_5Si compound disappeared after annealing at 500°C, leaving only pure Cu and dissolving the Si into the Cu layer. The inability to form a thermally stable Cu–Si passivation layer highlights the instability of the Cu–Si interface and underscores the need for a diffusion barrier to separate these materials.

2.2 Refractory Metal–Based Barriers

The term refractory refers to a material with a melting point above 1800°C [Pie96]. Due to their low self–diffusion coefficients, refractory metal–based materials have been frequently studied for use as diffusion barriers [Liu00], with current refractory metals of interest for diffusion barrier applications including Ti, Ta, W and Ru.

2.2.1 Unary Refractory Metal Barriers

Unary refractory metals have been explored as potential barrier materials, due to their low self–diffusivity and low electrical resistivity. Some drawbacks associated with these materials include their tendency to crystallize (enabling grain boundary diffusion) and to react with Si at temperatures greater than 450°C [Joh00a]. The applicability of several unary refractory metals as barriers will be discussed in the following sections.

2.2.1.1 Ti Barriers

While Group V and VI transition metals (e.g., Ta and W) are stable and non–reactive with Cu, Group IV transition metals such as Ti are unstable, forming several cuprides, including Cu_4Ti, Cu_4Ti_3, CuTi and $CuTi_2$ [Ram00]. For this reason, Ti is not a viable choice for a Cu diffusion barrier, as its reaction with Cu would degrade the barrier structure and lead to rapid device failure.

2.2.1.2 Ta Barriers

Tantalum (Ta) does not react with Cu [Wan94], and has demonstrated good oxidation resistance and enhanced Cu (111) texturing during Cu ECD [Chi02]. Ta generally fails to suppress Cu diffusion, however, because grain boundaries readily form during deposition and subsequent thermal cycling of the Ta layer. In addition, Ta reacts with Si to form silicides, making the Ta–Si interface unstable, and disqualifying Ta metal as a potential single barrier layer material to separate Cu and Si.

2.2.1.3 W Barriers

Tungsten (W) is another transition metal that does not react with Cu [Ram00, Wan94]. It does, however, react with Si [Ram00]. W reportedly failed as a Cu barrier due both to a silicidation reaction above 670°C [Tak97b] and crystallization, which causes grain boundary formation [Cha97c]. Sputtered W barriers have also been reported with columnar grains, which extended across the entire barrier thickness and caused barrier failure above 700°C [Mer97]. While PECVD W has been reported with very low resistivity (10 μΩ–cm) [Cha97b], films deposited at 350°C had an open grain boundary structure, which led to a low activation energy (0.46 eV) for Cu diffusion [Gup95]. Metallic W has also been deposited by ALD, using WF_6 and Si_2H_6 precursors over a temperature range of 30 to 350°C [Ela01]. Below 100°C, some Si surface species were left on the surface and remained unconsumed by the WF_6 precursor exposure.

2.2.1.4 Ru Barriers

Ru, like Ta and W, is non–reactive with Cu [Chy03], and has been tested as a Cu diffusion barrier material. The tested Ru barriers were deposited by PVD methods, however [Jos03], which have a limited lifespan, as mentioned in Chapter 1. In addition, Ru silicides are reported to form after annealing at 500°C [Jel03]. A sputtered Ru layer sandwiched between two TiN layers reportedly did not enhance the barrier's ability to prevent Cu diffusion [Kim03c]. Ru deposited by CVD has been studied for use as the metal electrode for DRAM capacitors [Aoy99, Lee00a, Mat02], and Ru has also been deposited by ALD [Aal03]; reports of CVD and ALD Ru as Cu diffusion barriers, however, have not been given.

2.2.2 Binary Refractory Metal–Based Barriers

To overcome the limitations associated with unary refractory metal barriers, binary compounds containing Ti, Ta and W have been widely studied. The addition of a second, nonmetal element to the refractory metal tends to increase the likelihood of depositing amorphous films, because the nonmetal element disrupts the crystallization process. The non–metal also generally increases film resistivity, however. The properties and applicability of several refractory metal carbides and nitrides will be discussed in the following sections.

2.2.2.1 Refractory Metal Nitrides (M–N)

Adding nitrogen to refractory metals gives rise to refractory metal nitrides, where the term nitride refers to compounds formed between nitrogen and other elements with equal or lower electronegativity [Pie96]. Three characteristics play a role in the formation of metal nitrides: the size ratio of nitrogen to the other element, the electronegativity difference between nitrogen and the metal, and the electronic bonding characteristics between nitrogen and the metal [Pie96]. Below a N/metal radius ratio of 0.59, interstitial nitrides form, while above 0.59, covalent nitrides (such as Si_3N_4) typically form [Pie96]. The early transition metals (Groups IV, V and VI) have a large enough host lattice to enable formation of interstitial nitrides, where the nitrogen atoms sit on interstitial sites in the metal lattice. The atomic radius of N is 0.74 Å, while that for W, for example, is 1.394 Å, yielding a N/W radius ratio of 0.53. The nitrogen and metal atoms have a large electronegativity difference, so the N atoms "nest" in the interstitial sites of the metal lattice [Pie96]. Interstitial nitrides have bonding with a combination of metallic, covalent and ionic character, high hardness and strength, and high thermal and electrical conductivity. These nitrides tolerate nonmetal vacancies, making them susceptible to the presence of interstitial impurities such as oxygen. Most early transition metals have a BCC structure, which cannot accommodate significant nitrogen levels at the interstices. To form an interstitial nitride, the metals switch to a close–packed structure, such as FCC or HCP, to ensure adequately sized interstitial sites that can accommodate N. Close–packed FCC transition metals have both tetrahedral and octahedral interstitial sites, but since the tetrahedral sites are too small to accommodate the N atoms, N only occupies the octahedral sites [Pie96].

Nitrogen addition suppresses crystallization in the films, and helps to repel the advance of Cu through the grain boundaries, due to a repulsive interaction between Cu and N [Eks01, Tak97a]. Excess nitrogen in these films migrates from the bulk polycrystals to the grain boundaries, where repulsive interactions between Cu and nitrogen "stuff" the boundary and halt Cu diffusion [Eks01, Sha89]. Formation of copper nitride (Cu_3N) by reactive sputtering has been reported, but this compound is unstable, decomposing to Cu and N under vacuum at 100°C [Liu98, Mar95].

Refractory metal nitrides tend to have high hardness, good chemical stability and high conductivity [Lev98, Nag93]. Three nitrides of current interest are FCC titanium nitride (TiN), FCC tantalum nitride (TaN), and FCC tungsten nitride (WN_x). While FCC TiN and TaN have melting points of 2950 and 3093°C, respectively [Pie96], FCC WN_x does not melt, but instead decomposes to BCC W and N_2 gas under vacuum at elevated temperature (850°C) [Suh01]. Since this decomposition temperature is substantially higher than the typically processing window for ICs, FCC WN_x is a viable diffusion barrier candidate material. The barrier properties of TiN, TaN and WN_x are discussed in more detail below.

2.2.2.1.1 TiN

Titanium nitride (TiN) was widely used as a diffusion barrier for the Al–Si system, and its reported resistivity ranges from 20 to 2000 μΩ–cm [Par96]. PVD has dominated TiN barrier deposition, resulting in non–uniform coverage of high aspect ratio structures and a columnar grain structure [Gal99, Kal00]. TiN performs poorly with Cu metallization due to this columnar microstructure [Nic95], which enables rapid Cu diffusion through the barrier [Gal99]. Plasma treatment and exposure to SiH_4, however, have been reported to improve TiN's resistance to Cu diffusion [Jos02]. Another difficulty involves the reactivity of Ti rich TiN films with Si and Cu. For TiN films with a Ti/N ratio > 1 (i.e., film is unsaturated with nitrogen), the excess Ti will react with Si or Cu, leaving the barrier permeable to Cu and the device vulnerable to rapid failure [Kim92, Lee94a, Ram00].

To avoid the problems associated with PVD TiN, several different CVD techniques have been tested. Liu et al. [2000] used LPCVD of $TiCl_4$ + NH_3 at high deposition temperature (630°C), but the resulting films had a columnar grain structure and suffered from halide incorporation. MOCVD TiN has shown only 40–50% conformality in small contact structures [Fal98], has high impurity incorporation, and requires an additional plasma–processing step to stabilize the films in low resistivity form [Gal99]. MOCVD TiN films deposited below 450°C were very porous, with low density and high resistivity, and had poor resistance to Cu diffusion [Par95b]. Capping the film with an ultra–thin Si_3N_4 layer has also enhanced performance of porous TiN films deposited by MOCVD of tetrakisdimethylamido tantalum (TDMAT). This thin capping layer improves barrier capability without significantly increasing the film resistivity, but adds another step to the barrier deposition process [Lu98a].

While oxygen stuffing of the TiN barrier (due to air exposure) helps it to resist Al in–diffusion (due to aluminum oxide formation), it does not prevent Cu in–diffusion, due to the lack of a stable, passivating Cu oxide layer [Par95a]. In addition, TiN was not suitable for Cu electroless plating, as its redox potential was higher than that of the Cu electrode, preventing the initial displacement reaction from occurring at the TiN surface [Wan03].

2.2.2.1.2 TaN

TaN is a proven Cu diffusion barrier, and is reportedly stable against Cu–Si interdiffusion up to 720°C [Wan94]. Copper with a PVD Ta/TaN dual layer barrier is currently used as the interconnect scheme for intermediate and upper level wiring on IC devices. The dual layer barrier is required to overcome adhesion difficulties: Cu adheres well to Ta, but not to TaN, while SiO_2 and most dielectrics adhere well to TaN, but not Ta. [ITR02, Sin02a]. In addition, the TaN layer promotes deposition of the low resistivity (20–30 $\mu\Omega$–cm) α–Ta phase, whereas the high resistivity (180 $\mu\Omega$–cm) β–Ta phase forms when Ta deposits directly on SiO_2 [Tra03]. But, since PVD TaN has much higher resistivity (~200 to 250 $\mu\Omega$–cm [Sun98a, Tra03]) than Ta, the TaN layer thickness should be held to a minimum. A 7 Å thick TaN film was found to foster α–Ta deposition and to prevent Cu interdiffusion [Tra03]. The lifespan of this bilayer deposition technique is limited, however, due to the inability of PVD processes to deposit conformal films at ever shrinking device dimensions.

LPCVD routes to TaN deposition have been examined as well, as this deposition method provides superior conformality to sputtering techniques, which are projected to reach their usability limit at the 65 nm node in 2007 [Han03]. CVD of TaN was reported by reacting halide precursors, including $TaBr_5$, TaF_5 and $TaCl_5$, with NH_3 [Kal99, Hil00]. Resistivities ranged from 395 to 5000 μΩ–cm depending on the precursor used, with the lowest value corresponding to $TaCl_5$ [Kal99, Che99b, Hil00]. Halide incorporation, however, ranged from 0.5 to 4.5 at. %, with a value of 1.0 at. % for the $TaCl_5$ precursor [Kal99, Hil00, Che99b], While plasma assisted CVD reduced the resistivity of films deposited by $TaBr_5 + NH_3$ to 150 μΩ–cm, an increase in Br content up to 3 at.% occurred [Che99a].

Attempts to grow TaN by MOCVD resulted in films with high resistivity and some carbon contamination. When pentakis(dimethylamido)tantalum (PDMATa) was used for MOCVD of TaN, the resulting films contained the insulating Ta_3N_5 phase [Fix93]. Pentakis(diethylamido)tantalum (PDEATa) was also tested, but the films also had very high resistivity (7000–60000 μΩ–cm) [Cho98, Cho99]. MOCVD using tert–butylimido–tris(diethylamido)tantalum (TDEATa) has also been tested, resulting in good step coverage (~100%) but high deposition temperature (up to 650°C) and resistivity (900–2000 μΩ–cm) [Tsa95]. Low film density and grain boundary formation were the typical causes of barrier failure in MOCVD TaN [Kal00].

One study of an ALD TaN/PVD Ta barrier has also been given [Ho04]. The precursors used in this study were not disclosed, but the barrier scheme was shown to work with a 65 nm Cu back–end–of–line (BEOL) interconnect structure. The ALD TaN barrier had good yield and reliability, and a 16% reduction in RC time delay over a PVD TaN/PVD Ta barrier scheme was demonstrated.

2.2.2.1.3 WN_x

As mentioned above, N has been added to W to deposit WN_x films. These films show promise as thermodynamically stable, stuffed barriers for separation of Cu and Si and have been demonstrated as excellent glue layers for W/Si and W/SiO_2 interfaces [Gal97, Kim92]. Many deposition techniques, including ion implantation, sputtering, LPCVD, PECVD, MOCVD and ALD have been used to deposit WN_x films. A detailed discussion of WN_x films deposited by these techniques will be deferred until Section 2.7 below, as we have chosen to focus on this material for our work.

2.2.2.2 Refractory Metal Carbides (M–C)

Unlike the nitrides, refractory metal carbides from all three Groups (IV, V and VI) tend to be hard, wear–resistant materials with high melting points and good chemical resistance [Pie96]. The Group IV, V and VI refractory metals form interstitial carbides, with crystal structures similar to those for the nitrides. The electrical resistivity of carbides is typically lower than that for nitrides with equivalent crystal structure, due to weaker bonding between the metal and C relative to bonding between metal and N [Nak87]. While these properties make the carbides interesting diffusion barrier candidates, C, unlike N, does not exhibit a repulsive interaction with Cu, making the carbides less resistant to Cu diffusion. The barrier properties of TiC, TaC and WC_x are discussed below.

2.2.2.2.1 TiC

One report of TiC (deposited by sputtering) as a Cu diffusion barrier has been given [Wan01a]. While the TiC resisted metallurgical failure at temperatures up to 650°C, the same films suffered electrical failure after annealing at temperatures just above 500°C.

2.2.2.2.2 TaC

Sputter deposited TaC films have also been tested as Cu diffusion barriers [Ima97, Lau02, Mor98]. While these films had low resistivity (210 μΩ–cm for 100 nm thick film), carbon–rich TaC films contained low–density carbon regions surrounding TaC grains [Ima97]. These low–density regions are facile paths for Cu penetration through the barrier, with 7 nm TaC films failing to prevent Cu diffusion above 550°C [Lau02]. This indicates that C, unlike N, lacks the ability to chemically repel Cu diffusion through the film, and is reflected in TaC's lower activation energy for Cu diffusion as compared to W_2N or TaN [Mor98].

2.2.2.2.3 WC_x

The bulk resistivity of β–WC_x is slightly lower than that for β–WN_x, with reported values of ~ 41 μΩ–cm and ~50 μΩ–cm, respectively [Lee93, Nic78]. MOCVD WC_x from $W(CO)_6 + C_2H_4$ has been tested as a Cu diffusion barrier [Sun01b, Vel00]. Deposition temperatures ranged from 250 to 510°C, with 50 nm thick films deposited at 290°C having resistivity of 250 μΩ–cm. A 70 nm thick WC_x film annealed for 8 hours at 400°C resisted Cu diffusion. Sputtered WC_x with resistivities ranging from 200 to 1000 μΩ–cm were also tested as Cu diffusion barriers, with the incorporation of C resulting in smaller grain sizes relative to pure W films [Vel00, Wan01b]. The onset of silicide formation above 700°C, however, indicated the instability of the WC_x/Si interface and also compromised barrier integrity against Cu diffusion. Kim [2003a] reported deposition of tungsten carbide (WC_x) films by plasma assisted ALD (PAALD) using the bis(tert–butylimido)bis(dimethylamido)tungsten $[(^tBuN)_2(Me_2N)_2]W$ precursor with H_2 and N_2 carrier gas. The films were deposited on SiO_2/Si substrates at 250°C, and had growth rates ranging from 0.4 to 0.7 Å/cycle, 100 % conformality in 0.15 µm features with a 15:1 aspect ratio, and resistivities ranging from 295 to 22000 µΩ–cm. The films contained 63 at.% W, 28 to 42 at.% C, 2 to 7 at.% N, and 1 to 6 at.% O. Cu barrier integrity tests were not reported, however.

2.2.3 Ternary Refractory Metal–Based Barriers

The addition of a third element to a binary refractory metal nitride matrix tends to further disrupt the microstructure, increasing the likelihood of nanocrystalline or amorphous phase formation [Ist00, Jai99, Ram00]. C, Si and B are the most examined third elements added to metal nitride films.

2.2.3.1 Refractory Metal Carbonitrides (M–C–N)

The addition of C to refractory nitrides has two general purposes: to increase the likelihood of amorphous film deposition, and to decrease film resistivity relative to the binary nitride. The C and N intermix on the interstitial sublattice of the host metal, and lattice structures are similar to those for the nitrides and carbides. The advantages of adding C to the N on the non–metal sublattice are tempered by the decreased ability of C (relative to N) to chemically repel Cu diffusion. The composition and microstructure of the films must therefore be carefully controlled to deposit low resistivity films with high stability against Cu diffusion. Free carbon (C not bound to W), in particular, should be minimized, as it has minimal impact on Cu diffusion and detrimentally affects film resistivity.

2.2.3.1.1 TiCN

One report of a TiCN Cu barrier, deposited by MOCVD of tetrakis(dimethylamino)titanium (TDMAT), has been given [Eiz94a]. While the films resisted Cu in–diffusion after annealing at 600°C, they had high resistivities, ranging from 3000 to 20000 μΩ–cm for 200 Å films.

2.2.3.1.2 TaC_xN_y

TaC_xN_y films deposited by sputtering of a TaC target in an Ar/N_2 atmosphere were also tested as Cu diffusion barriers [Sun01a]. TaC_xN_y was found to have superior thermal stability to the respective binary phases, and its resistance to Cu diffusion was greater than TaC due to stuffing of the grain boundaries with N. The films had relatively low resistivity (~300 μΩ–cm), and prevented Cu diffusion after a 30 min anneal at 600°C. Jun [1996] used pentakis(diethylamido)tantalum to deposit TaC_xN_y films by MOCVD, but resistivity was high (≥ 6000 μΩ–cm) and the barrier failed after annealing for 1 hour at 500°C. MOCVD of TaC_xN_y films was also done using a mixture of pentakis(dimethylamido)tantalum and pentakis(diethylamido)tantalum [Hos00]. These films prevented Cu diffusion after a 30 min anneal at 500°C, but had high resistivity (≥ 4000 μΩ–cm).

2.2.3.1.3 WN_xC_y

The bulk resistivity of β–WC_x is somewhat lower than β–WN_x, and as expected, the resistivity of β–WN_xC_y is reportedly lower than that for β–WN_x. Carbon and nitrogen in these films can deposit at interstitial lattice sites (i.e., bind to W) or as free C or N. Given a choice, free N is more desirable, because although it increases film resistivity (as does free C), it also repels Cu diffusion. Free C also increases resistivity, but is less effective at preventing Cu diffusion. The difficulty, then, is to minimize or eliminate deposition of free C, while encouraging some N to deposit interstitially and allowing some to deposit as free N. This should give minimum film resistivity and maximum Cu resistance.

WN_xC_y films were deposited by non–reactive sputtering of W–C and W–N targets, with the resulting films being amorphous, but maintaining some short–range order [Vie02]. These films were not tested for Cu barrier reliability, however.

MOCVD was used to deposit WN_xC_y as a barrier for Cu metallization in a patent application [Fuk00]. Amorphous WN_xC_y films were deposited by reacting a gas containing W, such as WF_6, $W[N(CH_3)]_6$, or $W[N(C_2H_5)]_6$, with a hydrocarbon gas, such as CH_4, and a nitrogen supply source, such as a nitrogen plasma, at 360°C. X–ray diffraction indicated a peak between 36 and 38 $2\theta°$ and a second position between 42 and 44 $2\theta°$, both of which are indicative of FCC WN_xC_y deposition. While resistivities down to 275 $\mu\Omega$–cm were reported, details of Cu barrier testing were not included.

Several studies have reported ALD deposition of WN_xC_y. The deposition used sequential reactions of WF_6, NH_3 and Et_3B [Ele03, Kim03d, Li02, Li03, Pet02, Smi02]. The lowest reported resistivity was 210 $\mu\Omega$–cm for a film deposited at 350°C [Ele03, Li02]. One group reported that a 120 Å thick WN_xC_y film was stable for a 30 min anneal up to 700°C [Kim03d]. These ternary films had high density and excellent adhesion to copper, but contained some amount of F (0.5–1 at.%) [Ele03, Li03].

2.2.3.2 Other Ternary Refractory Metal Compounds

Several ternary silicide systems, including $TiSi_xN_y$ [Bai96, Chi01, Eis00b, Jos02], $TaSi_xN_y$ [Lee99, Som97], and WSi_xN_y [Bla97, Hir01], have been examined for diffusion barrier applications. While the addition of Si promotes amorphous film growth and improves Cu adhesion [Har01], it also increases film resistivity and can decrease failure temperature [Kal00]. The ratio of metal/Si must be greater than 1.67 to ensure stability with Cu [Nic95]. The failure mechanism in these films tends to be grain boundary diffusion after barrier crystallization [Nic95], and the stability of these films is questionable due to the potential for Si out–diffusion into and reaction with the neighboring Cu layer. These barriers are also reported to have poor adhesion to low–k dielectrics [Pet03], and the majority of research on ternary silicide barriers has relied on PVD methods, which will have limited use in the future.

2.2.3.2.1 TiSiN

TiSiN films were deposited by reactively sputtering a Ta–Si target in an Ar/N_2 gas mixture [Iij95, Rei94]. Reid et al. [1994] deposited amorphous films with a stoichiometry of $Ti_{0.34}Si_{0.23}N_{0.43}$ and resistivity of 680 μΩ–cm. These films resisted Cu diffusion after a 30 min anneal at 650°C. Iijima et al. [1995] deposited amorphous films with a stoichiometry of $Ti_{0.31}Si_{0.19}N_{0.50}$ and resistivity of 500 μΩ–cm. These films resisted Cu diffusion after a 30 min anneal at 600°C.

LPCVD of $TiCl_4+SiH_4+NH_3+H_2/Ar$ at 500°C was also reported [Bla97]. As–deposited films were microcrystalline, with a composition of $Ti_{0.47}Si_{0.07}N_{0.46}$. Chlorine and oxygen contamination levels ranged from 3 to 5 at.%. This film prevented Cu diffusion after a 600°C anneal for 1 minute.

MOCVD of TiSiN films has been reported with multiple precursor schemes, including TDMAT + SiH_4 + NH_3 [Chi01, Jos02] and TDEAT +SiH_4 + NH_3 [Bai96]. A 50 Å thick TiSiN film had good wettability to Cu and low resistivity (350 μΩ–cm) [Chi01]. The Si was suggested to improve Cu adhesion when thin oxidized layers are present on the barrier, and also to reduce Cu agglomeration [Pet03]. TiSiN films deposited by a combination of MOCVD and plasma assisted CVD, however, allowed Cu to diffuse through after annealing at 500°C [Jos02]. Amorphous TiSiN films deposited at 400°C contained ~3 at.% C and O, and had high resistivity (>2000 μΩ–cm) [Bai96].

Metalorganic ALD of TiSiN films was reported using TDMAT, NH_3 and SiH_4 at 180°C [Min00]. The film contained small crystallites in an amorphous phase, and film stoichiometry was $Ti_{0.32}Si_{0.18}N_{0.50}$, but barrier film resistivity and Cu testing were not reported.

2.2.3.2.2 TaSiN

Several reports of TaSiN thin films as Cu diffusion barriers have been given. TaSiN films were deposited by reactive sputtering of a Ta–Si target in N_2 [Har01] and Ar/N_2 [Kim97a, Kol91, Lee99] gases. This ternary layer had better barrier performance and better adhesion to Cu than a Ta/TaN dual layer barrier, but details of the barrier's performance and electrical properties were not given. Lee et al. [1999] deposited films with $Ta_{0.43}Si_{0.04}N_{0.53}$ stoichiometry, with a failure temperature of 825°C (decomposing to Cu_3Si +TaN_x + $TiSi_2$ above this temperature) but the film had high resistivity (1419 μΩ–cm). Kolawa et al. [1991] deposited 100 nm thick amorphous films with a stoichiometry of $Ta_{0.36}Si_{0.14}N_{0.50}$. The films had high thermal stability, preventing interdiffusion between neighboring Cu and $TiSi_2$ layers up to 900°C, had O content below 3 at.%, and had resistivity of 625 μΩ–cm. Kim et al. [1997a] varied the N content of the TaSiN films to determine the impact on barrier performance. Films with N content greater than 40 at. % resisted Cu diffusion after an 800°C anneal, while those with lower N levels failed after a 700°C anneal. Information on film resistivity was not provided, however.

LPCVD of $TaCl_5$+SiH_4+NH_3+H_2/Ar at 500°C was also used to deposit TaSiN [Bla97]. As–deposited films were microcrystalline, with a stoichiometry of $Ta_{0.35}Si_{0.11}N_{0.54}$, and contained Cl and O levels ranging from 3 to 5 at.%. The films failed to prevent Cu diffusion after a 1 minute, 600°C anneal, however.

2.2.3.2.3 WSi_xN_y

Several reports of WSi_xN_y thin films as Cu diffusion barriers have been given. Reactive sputtering of a W–Si target in N_2/Ar gas was used to deposit amorphous $WSi_{0.6}N$ films [Min96, Shi97], which crystallized after annealing at 850°C [Shi97]. Film resistivity was 430–450 μΩ–cm, and the $WSi_{0.6}N$ film blocked Cu diffusion after a 30 min anneal at temperatures up to 600°C.

WSi_xN_y films were also deposited by N_2 plasma nitridation of sputtered WSi_x thin films [Hir98, Hir99, Hir01]. As–deposited films were amorphous, and their effectiveness decreased with increasing film crystallinity. A WSiN(6 nm)/WSi_x(14 nm) bilayer resisted Cu diffusion after annealing for 1 hour at 400°C [Hir99]. Electrical properties of the barrier film were not reported, however. WSi_xN_y thin films were inadvertently formed by annealing a W/WN_x/poly–Si structure at 800°C [Nak97]. The resulting W/WSi_xN_y/poly–Si structure was stable up to 950°C, above which silicidation of the W layer occurred. The ternary film was not tested as a Cu diffusion barrier, however, and bulk resistivity of this film was not reported.

WSi_xN_y films were also deposited by LPCVD of WCl_6+SiH_4+NH_3+H_2/Ar at 500°C [Bla97]. As deposited films had a stoichiometry of $W_{0.54}Si_{0.12}N_{0.34}$, contamination levels of Cl and O ranging from 3 to 5 at.%, and high resistivity (1000 μΩ–cm). These layers prevented Cu diffusion after a 600°C anneal for 1 minute, and crystallized at 900°C.

Amorphous WSi_xN_y thin films were also deposited by PECVD of WF_6+ N_2 + H_2 + SiH_4 at 380 to 400°C [Eck03]. While film resistivity was low (308 μΩ–cm), layer uniformity and thermal stability was poor, as films crystallized after a 1 hour anneal at 600°C. Amorphous WSi_xN_y thin films were also deposited by PECVD of WF_6+Si_2H_6+NH_3 at 350°C [Gok99]. Films with compositions of $W_{1.21}Si_{0.14}N$ and $W_{0.96}Si_{0.24}N$ were deposited, which crystallized after annealing at 800°C for 30 min. Film resistivities below 200 μΩ–cm were reported after annealing at 450°C, but film performance with Cu was not reported.

2.2.3.2.4 WB_xN_y

Several reports of WB_xN_y thin films as Cu diffusion barriers have been given. WB_xN_y films with a variety of stoichiometries were deposited by reactive sputtering of a W–B target in N_2/Ar gas [Rei95]. A $W_{0.64}B_{0.20}N_{0.16}$ film showed the best resistance to Cu diffusion, preventing it after a 30 min anneal at 800°C. This stoichiometry also had a low resistivity of 220 μΩ–cm. WB_xN_y films were also deposited by reactive sputtering of W and W_2B_5 targets in N_2/Ar gas, with substrate temperature ranging from 25 to 500°C [Lee01b, Par00]. Film stoichiometries ranged from $W_{0.90}B_{0.05}N_{0.05}$ to

$W_{0.57}B_{0.05}N_{0.38}$, with resistivities as low as 140 μΩ–cm obtained for the stoichiometry with the lowest N content. As–deposited films were amorphous, crystallizing after a 700°C anneal [Par00], and resisted Cu diffusion after a 30 min anneal at 800°C [Lee01b]. WB_xN_y films deposited by reactive sputtering of a W_2B_5 target in N_2/Ar gas at 35°C were used to form Schottky contacts to GaAs [Kim98b].

WB_xN_y films were formed by ion implantation of BF_2^+ into WN_x thin films, which were deposited by PECVD of $WF_6 + NH_3 + H_2$ on Si (100) at 300°C [Kim97b, Kim99a]. The ternary film was amorphous, and resisted N out–diffusion after annealing at 800°C. As–deposited ternary bulk film resistivity was 200 μΩ–cm, which was slightly higher than the value for the binary WN_x film, and the ternary film resisted Cu diffusion after annealing at temperatures up to 750°C.

Deposition of WB_xN_y thin films by PECVD of $WF_6 + NH_3 + B_{10}H_{14} + H_2$ on Si (100) at 350°C has also been reported [Kim97b, Kim98a, Kim02a]. As–deposited film stoichiometries ranged from $W_{0.90}B_{0.05}N_{0.05}$ to $W_{0.38}B_{0.42}N_{0.20}$, depending on the $B_{10}H_{14}$/ NH_3 ratio, with the optimal film stoichiometry being $W_{0.46}B_{0.25}N_{0.29}$. Resistivity ranged from 100 to 844 μΩ–cm, with a value ~700 μΩ–cm for a 2000 Å thick film with optimal stoichiometry. Films with optimal stoichiometry remained amorphous even after annealing at 800°C, and resisted Cu–Si interdiffusion up to this temperature. Tungsten rich as–deposited films were polycrystalline, and B atoms reportedly out–diffused even faster during annealing that did the N atoms. Both the $W_{0.90}B_{0.05}N_{0.05}$ and $W_{0.80}B_{0.15}N_{0.05}$ stoichiometries failed to resist Cu diffusion after annealing above 600°C.

2.3 Justification for WN_x (and WN_xC_y) as the Barrier Material

The microelectronics industry already uses Ti, Ta and W in one form or another (such as TiN barriers, Ta/TaN barriers and Ta_2O_5 capacitors, and W plugs) for memory and processor devices [Jai99]. TiN is used as a barrier for Al based metallization, but TiN is unsuitable for Cu metallization, as mentioned earlier. Cu diffusion barrier research has focused on TaN and WN_x, with WN_x appearing to have technological advantages over TaN as a Cu diffusion barrier. WN_x is known to be an effective diffusion barrier against copper penetration at temperatures up to 750 °C [Pok91], and adhesion of CVD Cu to WN_x is stronger than that to TaN [Iva99]. In addition, WN_x outperforms TaN as a liner material for seedless electrochemical deposition (ECD), as ECD Cu shows stronger adhesion to WN_x film layers [ITR02, Sha01, Sin02a]. A suitable liner material would enable seedless ECD of Cu. Elimination of the Cu seed layer, typically deposited by sputtering, would increase throughput by removing a process step, as well as remove the complications associated with sputtering in ever–shrinking device features. The combination of these steps would result in cost savings per wafer, higher wafer throughput, and higher quality devices for a WN_x based system as compared to its TaN counterpart [Gal99].

In addition, to enable electroless plating of Cu onto the barrier materials, TaN barrier layers require a pre–deposition HF etch, while WN_x barriers do not. Tungsten oxide, present on the WN_x surface due to air exposure, is readily dissolved in the electroless plating solution, hence the pre–deposition etch step is unnecessary [Wan03].

There are also processing advantages for WN_x. During chemical mechanical polishing (CMP), TaN is removed at a rate 18 times slower than Cu, while WN_x is removed 1.5 times faster [Gal99]. One report gives WN_x removal rates of ~100 Å/min for CMP pressures below 0.5 psi, while comparable removal rates for TaN require polishing pressures close to 2 psi [Tak02]. The slow removal rate of TaN means that the pad must be in contact with the Cu/TaN surface for an extended period of time to planarize the wafer. This extended contact time leads to dishing of the copper, where excessive copper is removed from the device. Dishing of both the Cu and dielectric layers impacts line resistance and planarity of the device [Jai99]. A time–consuming two–step CMP process, which includes a slurry and pad changeout, is required to minimize copper dishing during planarization of TaN.

From the above discussion, it is evident that WN_x films are the most promising candidates for diffusion barrier materials. The resistivities for these films are reasonably low, and WN_x has shown good adhesion to Cu and other potential neighboring materials. CVD and ALD routes to low–resistivity WN_x have been established, although the precursors must be optimized to minimize halide contamination and to control carbon levels. Recent studies have examined WN_xC_y for diffusion barrier applications, due to its ability to deposit in amorphous form, its lower resistivity relative to WN_x, and its excellent adhesion to Cu. A review of the properties of WN_x, along with a brief discussion of WN_xC_y films, follows.

2.4 WN_x Film Properties

The four commonly seen phases for tungsten nitride are BCC WN_x, FCC β–WN_x, HCP WN_x, and SHP–WN [Gui93, Nak87, Wri89]. The structure and properties of these phases are discussed in more detail in Chapter 3. FCC β–WN_x is the desired phase for Cu diffusion barriers because it has the lowest bulk resistivity (~50 $\mu\Omega$–cm) of the various tungsten nitride phases [Lee93]. The structure of FCC WN_x is NaCl type, with W atoms at FCC sites and N atoms at octahedral interstitial sites. The FCC β–WN_x phase, with $x \approx 0.5$ (also called β–$WN_{0.5}$ or β–W_2N) has lattice constant a=4.126 Å, hence it has a lattice mismatch of –24% with Si (a=5.431 Å) and –27 % with GaAs (a=5.653 Å) [JCP88]. The β–$WN_{0.5}$ stoichiometry is described as a defective NaCl–type structure, with half of the octahedral interstitial sites filled with N and half of them vacant [Hon00]. Bonding in metal nitrides is complex, with both metallic (valence electrons delocalized; non–directional bonding) and covalent (valence electrons shared; highly directional bonding) characteristics, due to the combination of metal–metal and metal–nonmetal interactions [Tot71]. Hones et al. [2000] described metal–nonmetal bonding in NaCl type structures as having π–like and σ–like bands due to overlap of the d and 2p orbitals from the metal and nonmetal, respectively. These bands (called pd_π bands) have ionic character, with bonds having more ionic character when this band is populated and more covalent–metallic character when the band is depopulated [Hon00]. Shen et al. [2000a], using transmission electron diffraction (TED), found W–N and W–W nearest neighbor distances of 2.08 and 2.92 Å, respectively, in sputter deposited β–W_2N films. The β–W_2N lattice parameter (4.126 Å) represents the distance between centers of W atoms at the corners of an FCC unit cell, while the 2.92 Å W–W correlation represents the distance between centers of the corner and face centered W atoms in the FCC unit cell (Figure 2-1). The theoretical density of FCC β–$WN_{0.5}$, based on 4 tungsten and 2 nitrogen atoms per unit cell, is 18.0 g/cm³, while experimentally determined densities range from 8.0–17.9 g/cm³ [Bos91, Gal97, Hec02, Mar93, Sam80, Sot03].

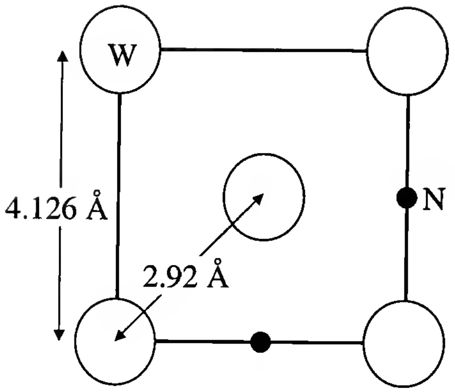

Figure 2-1. Distances between W atoms in the FCC face of the β-W_2N phase.

Shen and Mai [2000b] have reported that binding energy shifts (per XPS) for W and N in polycrystalline β–$WN_{0.5}$ films indicate an ionic bonding character in the films (consistent with $W^{\delta+}$–$N^{\delta-}$). The apparent binding energy difference between the metal and N atom, from XPS, gives an idea of the degree of charge transfer. A large binding energy difference infers greater bond ionicity [Pri95]. Moreover, adding more nitrogen to the films has been suggested to cause a decrease in the number of free electrons provided by W in the solid film [Sot03], which is consistent with increasing film resistivity with nitrogen content. At lower N levels, the metal's band structure is retained, so that metal nitrides show metallic properties [Muk93]. Matsuhashi and Nishikawa [1994] reported FCC β–WN_x films to have a work function before annealing of 5.0 eV, where work function is a measure of the energy required to remove an electron from the material to a state of rest outside the material (i.e., at the vacuum level). Transmission electron diffraction (TED) intensities were also used to determine the concentration of W–N neighboring pairs in the β–WN_x films. Results showed that the concentration of W–N neighboring pairs did not increase when bulk N content was increased above x~0.5 [Shen00b]. This indicates that excess N in the films migrated to the polycrystalline grain boundaries rather than filling the remaining vacant interstitial sites in the FCC lattice. Shen et al. [2000c] reported no SHP δ–WN formation, even for WN_x with x=1.22, which shows that excess N migrated to the grain boundaries in the polycrystalline FCC films.

Other reported properties for the binary nitride include a compressive stress of 4.3 ± 0.5 GPa, nanohardness of 30 GPa, and a Poisson's ratio assumed to be 0.25 for films with the $WN_{0.6}$ stoichiometry [Hon00]. In addition, depending on the W/N ratio, thick WN_x films were reported with refractive indices and absorption coefficients ranging from 3.20 to 4.00 and 1.20 to 3.95, respectively, as determined by ellipsometry [Boh90].

Oxygen impurities tend to form solid solutions with metal carbides and nitrides [Tot71], and oxygen is reported to oxidize the surfaces of polycrystals [Par96]. Impurities such as O, N and C are reported to enhance the stability of diffusion barrier films [Cha97c, Cha99, Lee94a]. Various stoichiometries of tungsten oxynitride have been reported. The JCPDS powder diffraction standard indicates two phases of $W(N,O)_x$, one with x=0.62 and a=4.138 Å, and the other with x= 0.57 and a=4.126 Å [JCP88]. A $WN_{1.34}O_{0.42}$ phase with a=4.153 Å has also been reported [Sel95].

2.5 WN_xC_y Film Properties

Little information is available in the literature on the structure and properties of WN_xC_y films. In going from nitrides to carbides, electron density increases around the metal atomic sphere and decreases around the non–metal atomic sphere, consistent with more ionic bond character for the nitrides and more covalent bond character for the carbides [Gub94]. This is also consistent with the higher resistivity of β–WN_x relative to β–WC_x [Kim03a, Nak87]. Adding carbon to the nitride phase therefore leads to a decrease in film resistivity. The FCC WN_xC_y phase, with N and C intermixing on the interstitial sublattice of FCC W, has been predicted by thermodynamic analysis [Fri99b, Hua97, Jon93], and has been studied for diffusion barrier applications. A detailed experimental analysis of the composition, structure and electrical properties of these films has not been reported, however.

WN_xC_y film deposition was reported using WF_6+NH_3+$B(C_2H_5)_3$ at 350°C [Ele03, Li03]. The film composition was $W_{0.55}N_{0.15}C_{0.30}$, and films had a nanocrystalline β–WC_x or β –WN_x cubic structure in an amorphous matrix along with low resistivity (210 to 400 μΩ–cm). The films had F, O and B impurities below 0.5 at.%, H content < 4 at.%, density of 14 g/cm³ and resistivity of 300 to 400 μΩ–cm [Li03]. Another report using the same chemistry gave a film composition of $W_{0.57}N_{0.13}C_{0.30}$ and resistivity ranging from 600 to 900 μΩ–cm, but deposition temperature was not given [Smi02].

Kim et al. [2003d] also reported deposition of WN_xC_y films using WF_6+NH_3+ $B(C_2H_5)_3$ at 350°C. Film composition from RBS was 48 at.% W, 32 at.% C and 20 at.% N, and film density was 15.37 g/cm³. The film had low resistivity (350 μΩ–cm), and had an electron diffraction pattern that closely matched those for β–$WN_{0.5}$ and β –$WC_{0.6}$. One HR–TEM lattice fringe spacing was 2.39 Å, which was between the interplanar spacings for (111) β–$WN_{0.5}$ (2.38 Å) and β –$WC_{0.6}$ (2.43 Å). The other lattice fringe spacing was 2.08 Å, which was between the interplanar spacings for (200) β–$WN_{0.5}$ (2.06 Å) and β –$WC_{0.6}$ (2.11 Å). These values support the presence of a ternary WN_xC_y solid solution. Moreover, a 12 nm WN_xC_y film prevented Cu diffusion during annealing up to 700°C.

Vlakhov et al. [1995] deposited W, WC and WN_xC_y films to study their electrical resistivities, and stated that bulk tungsten nitrides, carbides, and carbonitrides were good superconductors [Vla95]. The W films were deposited from both $W(CO)_6$ and WCl_6, the WC films were formed by annealing the W films in a carbon–containing atmosphere, and the WN_xC_y films were deposited by co–reacting $W(CO)_6$ +NH_3 + CH_3COCH_3 [Vla95]. The room temperature (300 K) resistivities of W, WC and WN_xC_y films with thickness of 0.4 μm were compared. The W and WC films had similar resistivities, ranging from 109 to 191 μΩ–cm, while the WN_xC_y films had a much higher resistivity of 651 μΩ–cm.

2.6 Amorphous WN_x Film Deposition

Incorporation of smaller solute atoms into a metal matrix will cause a crystalline solid solution to become unstable above a certain solute concentration, fostering amorphous film growth [Ell90]. To enable amorphous film deposition in binary systems, the atomic radii of the two elements must differ by more than 10 % [Ell90]. The atomic radius of N is 0.74 Å, while that for W is 1.394 Å, hence N is 47% smaller than W, and so WN_x should be able to deposit in amorphous form. Moreover, nitrogen can act as a roadblock to trap diffusing W on the film surface, or can serve as a nucleation site for lattice defects. The trapped W and permanent defects caused by N incorporation prevent crystallization, and amorphous growth occurs [She00b].

Several reports of amorphous WN_x deposition by a variety of deposition techniques have been given. These include reactive sputtering, LPCVD, PECVD, MOCVD, annealing W in NH_3, PLD and ion implantation. FCC β–WN_x films with $x < 0.5$ were typically amorphous, while those with $x \approx 0.5$ contained polycrystalline

β–$WN_{0.5}$, and those with x > 0.5 contained β–$WN_{0.5}$ and additional N at the grain boundaries [She00e,f].

Depending on their composition, amorphous WN_x films have been reported to crystallize at temperatures ranging from 480–620°C [Suh01]. Additional contamination from C will likely increase the crystallization temperature of WN_xC_y films.

2.7 Demonstrated Uses of WN_x

WN_x as a Diffusion Barrier

Kilbane and Habig [1975] first reported growth of WN_x thin films by reactively sputtering a W target in a mixture of Ar/N_2 gas. Reichelt and Bergmann [1975] also studied deposition of WN_x thin films by RF sputtering. Ten years later, two reports were published describing the use of sputter deposited WN_x films as diffusion barriers [Aff85, Kat85]. Since then, many studies of WN_x as a diffusion barrier separating Cu and Si have been reported. References for some of these reports are listed in several review articles [Jai99, Kal00, Kim03b].

The use of WN_x as a diffusion barrier on low–k materials has also been examined. The interaction between WN_x and the low–k material hydrogen silsesquioxane (HSQ) has been studied [Zen00a]. Retention of H in the HSQ film is very important, as the dielectric constant (k) of the film is a strong function of H content (as Si-H). A W_2N barrier film deposited by PECVD of $WF_6+N_2+H_2$ prevented the release of H (as H_2) from HSQ more effectively than its TaN counterpart deposited by PVD [Zen00a]. Adhesion strength between WN_x and two other low–k dielectrics, an aromatic hydrocarbon (SiLK^{TM}, from Dow Chemical) and a polyarylene ether–based polymer (Flare 2.0^{TM}, from Allied Signal), has also been studied [Lan00]. TiN, TaN and WN_x all had similar adhesion strengths to these low–k materials, suggesting that a similar bonding mechanism exists between the barriers and these low–k films [Lan00]. These barriers are expected to have stronger adhesion than Cu to the polymer layers, because Cu, unlike the refractory metals, has fewer unfilled d–orbitals available for bonding to the surface [Lan00].

WN_x films have also been tested to separate Cu from the low–k material fluorine doped silicon oxide (SiOF) [Lee98c]. WN_x had poor adhesion to SiOF layers which had not been pre–treated with O_2 plasma at 300°C, and failed to prevent Cu–SiOF intermixing. When the SiOF layer was pre–treated, however, WN_x had good adhesion to and prevented Cu diffusion into SiOF for a 30 second anneal at 900°C. Surface oxidation and densification of the SiOF, caused by the plasma pre–treatment, are believed to enhance barrier capability on pre–treated SiOF [Lee98c].

WN_x films have also been tested as diffusion barriers between the Ni and W layers in an $In_xGa_{1-x}As$/Ni/W contact structure for use with GaAs [Uch97]. These reactively sputtered WN_x films prevented out–diffusion of In from the $In_xGa_{1-x}As$ layer, and also lowered the contact resistance from (4 to 1 Ω–cm).

WN_x formed by nitridation of an amorphous CVD–W layer using N_2 plasma was used as a barrier in the multilayer structure Cu/amorphous–WN_x/amorphous–W/p^+n–Si diode [Cha99]. The structure maintained its integrity after annealing at 725°C. The same group determined the upper limit for a Cu/amorphous–WN_x/amorphous–W/Si multilayer structure to be 750°C [Cha97a, Cha97c].

WN_x as Gate Electrode in MOSFET Devices

Historically, metal oxide semiconductor field–effect transistor (MOSFET) devices have used SiO_2 as the gate dielectric. Shrinking device sizes are forcing a decrease in SiO_2 layer thickness. Devices formed with SiO_2 layers less than 3 nm thick suffer from high leakage current due to direct tunneling of electrons through the oxide, hence an alternative material with higher permittivity is required to prevent tunneling [Lee01c]. Ta_2O_5 is a potential alternative due to its high dielectric constant (20–25) relative to SiO_2 (3.9) [May90, Par98a]. New contact materials, including WN_x, are being investigated for devices with Ta_2O_5 gates. WN_x/Ta_2O_5 structures had lower leakage current than TiN/Ta_2O_5 structures after annealing at 900°C [Lee01c]. In addition, the WN_x/Ta_2O_5 structure had no interfacial reaction, while the TiN/Ta_2O_5 interface degraded after annealing. The superior performance of WN_x is reportedly due to diffusion of N from WN_x into the Ta_2O_5 layer, which suppresses Ta and O out–diffusion [Lee01c]. Diffusion of N into Ta_2O_5 did not occur for the TiN/Ta_2O_5 structure.

WN_x has also been used as a diffusion barrier and W source in poly–Si gate stack structures [Gal00, Yan02]. Without a barrier, W reacts readily with Si, forming a highly resistive WSi_x phase [Kas94]. Kasai et al. [1994] formed a W/WN_x/Poly–Si gate structure with a 50 Å thick layer of WN_x. The sheet resistance of W in this gate structure was low (1.6 Ω/) compared to one without the barrier layer (18 Ω/), which suffered from silicide formation. First, PECVD WN_x was deposited on poly–Si and annealed to form a W–Si–N layer. Then, the structure was annealed at temperatures up to 1000°C in either an Ar or N_2 atmosphere to convert some of the remaining WN_x layer to W. The newly formed layer of W can then be used as the contact metal for the gate. While as–deposited WN_x films had sheet resistance of 19.2 Ω/ , the W layer produced by annealing had sheet resistances as low as 1.28 Ω/ [Gal00]. Sputtered WN_x was tested in a similar manner; formation of WSi_2 was suppressed due to formation of a Si_3N_4 layer at the WN_x–Si interface after a rapid thermal anneal (RTA) at 1000°C [Yan02]. Kang et al. [2001,2002] used a sputtered, 100 Å thick WN_x film as a barrier layer in a W/WN_x/poly $Si_{1-x}Ge_x$ gate structure for use in a CMOS–FET. Takagi et al. [1996] used a W/WN_x polysilicon gate electrode to produce a CMOS device. The WN_x layer suppressed silicide formation after a 30 second anneal at 950°C, and the specific contact resistance for a W/WN_x/poly–Si structure was 10^{-7} Ω–cm² [Tak96]. In addition, the sheet resistance of WN_x deposited on poly–Si was reported to be an order of magnitude lower than that for WSi_x [Cho02].

WN_x as a Gate Electrode in MESFET Devices

Rectifying (Schottky) contacts for GaAs self–aligned gate field–effect transistors (SAGFETs) must have good thermal stability, good adhesion to GaAs, and high Schottky barrier height [Lee95, Pac91]. WN_x Schottky contacts formed by PECVD of WF_6+NH_3+H_2 on GaAs maintained their interface integrity after a 30 second, 1000°C RTA [Lee95]. Yu et al. [1988] sputter deposited thin WN_x films for use as a Schottky contact to GaAs, while Boher et al. [1990] deposited thick WN_x films. Kim [1994] used PECVD of WF_6 + NH_3 + H_2 at 350°C to deposit WN_x Schottky contacts to GaAs. WN_x nucleated easily on GaAs and had higher thermal stability than W films, maintaining the W_2N stoichiometry and blocking As out–diffusion during a RTA at 1000°C for 30 seconds [Kim94]. Grain boundaries in the PECVD WN_x films were stuffed by excess N, preventing Ga and As out–diffusion, and this Schottky contact structure was stable up to

850°C. Paccagnella et al. [1991] examined the effect of GaAs pre–treatment on the performance of WN_x/GaAs Schottky diodes. Schottky barrier height was highest for WN_x/GaAs diodes annealed at 800°C, where GaAs was pretreated by H_2 plasma [Pac91]. Sputter deposited WN_x has also been used as a gate metal in GaAs SAGFETs [Nag94, Gei86, Uch86]. In particular, $WN_{0.04}$ was found to produce Schottky barriers with excellent stability after annealing for 20 min at 810°C [Gei86]. WN_x films have also been deposited onto 4H–SiC to form Schottky contacts with high temperature stability [Pec97, Kak99]. The contacts, deposited by room temperature magnetron sputtering of a W target in Ar/N_2 gas, remained rectifying up to 1200°C despite formation of the W_5Si_3 and W_2C phases [Pec97].

WN_x as an Ohmic Contact in HBT Devices

Thermally stable, low resistance ohmic contacts are critical to produce high speed, high frequency devices such as heterojunction bipolar transistors (HBTs). Park et al. [1998b] deposited the Au/Pt/Ti/WN_x metal contact structure onto n–InGaAs, which is a cap layer used for AlGaAs/GaAs HBTs. The minimum contact resistivity for the Au/Pt/Ti/WN_x/n–InGaAs structure was 9.5×10^{-8} Ω–cm², which was obtained after annealing at 400°C [Par98b]. In addition, the morphology of the contact remained smooth over a wide annealing range.

WN_x as a Top Electrode in DRAM Devices

WN_x films have also been investigated as top electrodes for Ta_2O_5 dynamic random access memory (DRAM) capacitors [Cho01, Mat94]. Cho et al. [2001] deposited both TiN and WN_x by reactive sputtering in Ar/N_2 ambient to test their stability as a diffusion barrier at the interface in a W/Ta_2O_5 gate structure. The structures with WN_x

barriers had higher thermal stability, as they were more resistant to Ta and O out–diffusion than TiN. The increased stability was presumably due to migration of N from the WN_x film to the WN_x/Ta_2O_5 interface, which prevented Ta and O from diffusing out of the Ta_2O_5. Suzuki et al. [1998] used WF_6 with two different N sources, NH_3 and NF_3, to deposit WN_x thin films by PECVD. When tested as top electrodes in DRAM capacitors, these films had leakage currents that were an order of magnitude lower than PVD TiN top electrodes. Matsuhashi and Nishikawa [1994] tested sputtered WN_x, TiN and TaN as top electrodes in Ta_2O_5 DRAM capacitors. After annealing for 30 min at 800°C, the WN_x/Ta_2O_5 structure exhibited lower leakage current than structures with TiN or TaN electrodes [Mat94]. Kim et al. [2001] used a W/WN_x/Poly–Si gate stack to produce polysilicon based DRAM devices.

WN_x as an X–ray Absorber Mask

The use of amorphous WN_x films in absorber masks for X–ray lithography has also been demonstrated [Lee97, Lee98b]. WN_x has good stress controllability, strongly attenuates x–rays, and has a coefficient of thermal expansion (CTE) very close to common x–ray membrane materials such as SiC, BN, SiN_x, and CN, making it a desirable x–ray mask material [Lee98b]. WN_x masks were grown by reactive sputtering of a W target in an Ar/N_2 atmosphere on room temperature indium tin oxide (ITO) coated Si substrates. Film microstructure depended on the nitrogen content of the films, with 20 at. % N being the upper limit for the amorphous phase. As N levels increased above this, film microstructure shifted to polycrystalline β–$WN_{0.5}$.

WN_x as a Liner for Cu Deposition

Sputtered WN_x films were also shown to be good liner materials for seedless electrochemical deposition, due to strong Cu–WN_x adhesion and high Cu nucleation density on the WN_x surface [Sha01]. ECD Cu was deposited on air–exposed WN_x films, and the composition of the ECD bath was controlled to strip off surface oxides [Sha01]. Use of TiN as a seed layer for electroless Cu deposition resulted in only sporadic Cu coverage on the barrier layer [Mur95], while electroless Cu deposition occurred readily on WN_x films [Wan03]. For the same bath temperature (70°C), electroless Cu deposition occurred more rapidly on WN_x than on TaN [Wan03]. Moreover, Cu deposited by CVD had low via resistance on WN_x, but high via resistance with Ta based barriers [Jai99].

Other WN_x Uses

β–$WN_{0.5}$ has found use in bulk form (i.e., powder) as a catalyst for quinoline hydrodenitrogenation [Abe93], n–heptane isomerization [Sel95], deamination of 2–octylamine and alcohol dehydration [Lee92, Luc96]. Reactively sputtered amorphous WN_x films have also been deposited and used as a means to form equiaxed, low resistivity W films in W/poly–Si gate structures [Lee03]. Amorphous WN_x films annealed at 1273 K released nitrogen to form BCC W with a resistivity of 12 $\mu\Omega$–cm, which was similar to the value for pure, sputtered W. The presence of a small amount of residual N in the films at 1273 K suppressed silicide (WSi_x) formation, enabling the W film to retain its low resistivity.

WN_x Etching

Several etching studies have been done on WN_x films. Lee [98b] first reported use of SF_6 + Ar + N_2 in an inductively coupled plasma (ICP) etching system to anisotropically etch WN_x thin films. Etch rates ranged from 4000 to 14000 Å/min. Vijayendran et al. [1999] used an NF_3/N_2 reactive ion etch (RIE) to remove WN_x films. Reyes–Betanzo et al. [2002] used SF_6 + Ar to anisotropically etch W and WN_x films.

2.8 WN_x Deposition Techniques

A variety of techniques to deposit WN_x have been tested in order to optimize key film properties, which include film resisitivity and deposition temperature. Ideal film resistivity was reported to be 500 μΩ–cm, [Ele03], while a temperature ceiling of 400°C has been given for IC production by numerous reports [Eis00b, Ele02, Hau00, Kim03b, Les02, Sun01b]. Depositing the barrier at the absolute minimum temperature, however, may not be the best solution, as other processes occurring during IC processing will typically take the device temperature up to ~400°C. If the barrier is deposited at much lower temperature than the processing temperature ceiling, significant shift in barrier structure can occur during subsequent high temperature processing, leading to Cu diffusion and potential barrier failure.

The reported deposition techniques include reactive sputtering, annealing of W in NH_3, plasma nitridation of W, LPCVD, PECVD, MOCVD, and ALD. Reports of each of these techniques to deposit WN_x are discussed below.

2.8.1 Annealing W in NH_3

Deneuville et al. [1989] reported formation of WN_x by annealing sputtered W films on Si in an NH_3 atmosphere from 500 to 1100°C. The N/W ratio increased with temperature, going from 0.37 to 1.85 across the aforementioned temperature range. While several polycrystalline structures were postulated based on film composition, XRD results were not given to support them. High temperature and pressure, along with long anneal times, are required to form WN_x in this manner, making this an undesirable deposition technique for IC manufacturing.

2.8.2 Plasma Nitridation / Ion Implantation of W

W films, deposited by CVD of $WF_6 + SiH_4 + H_2$ were nitrided to form thin WN_x films using an in–situ N_2 plasma treatment [Yeh96]. This nitride layer prevented WAl_{12} formation after annealing at 550°C, where WAl_{12} formation can degrade contact structures using W plugs between Al and Si. WN_x films were also formed by N^+ ion implantation into W metal substrates [Zha99]. Barrier testing with Cu was not done for either of these films, however. N^+ ion implantation was also done on W films deposited by PECVD of $WF_6 + H_2$ to form amorphous WN_x films [Kwo95]. These films resisted Cu penetration after a 30 min anneal at 800°C, while polycrystalline PECVD WN_x films failed. The nitridation technique is directional in nature, however, meaning that good conformality will be difficult in highly aggressive future device topographies. Chang [1997a–c, 1999] reported N^+ ion implantation into W films deposited by CVD of $WF_6 + SiH_4$. The films had resistivity of 198 $\mu\Omega$–cm and resisted Cu diffusion for annealing temperatures below 700°C, but had poor adhesion to the underlying Si substrate.

2.8.3 Pulsed Laser Deposition

Soto et al. [2003] first reported pulsed laser deposition of tungsten nitride films from a W target in the presence of N_2. Films were deposited on n–type Si (111) and on Corning glass slide substrates, at N_2 pressures ranging from 1×10^{-8} to 1×10^{-1} Torr. Films contained W, N and some O, believed to originate from W target contamination, and had higher density than films produced by DC magnetron sputtering. This technique, like plasma nitridation, is also directional, making its ability to deposit highly conformal films in future device generations questionable.

2.8.4 Reactively Sputtered WN_x Deposition

Typically, sputtered WN_x films are formed by sputtering a W target in a N_2/Ar atmosphere. A variant of this, known as nitrogen ion beam sputter deposition (IBSD), has also been reported [Eiz94b, Gal93], where a nitrogen ion beam, rather than an Ar+ ion beam, is used to liberate W atoms from the W target. Nitrogen ions or radicals backscattered from the target are then incorporated with W at the substrate to deposit WN_x. Both variants enable amorphous film deposition due to the decreased mobility of W in the presence of N on the substrate surface. N can inhibit W mobility on the substrate surface by blocking W diffusion or by trapping W. Decreased W diffusivity leads to defect formation, failure of crystal growth and amorphization of the growing film [She00b]. Sputtering can be done at low deposition temperature (at or near ambient), which protects temperature sensitive components from thermal damage during the barrier deposition process.

Many reports of sputtered WN_x deposition have been given in the literature. The key properties of these films are summarized in Table 2-1. While sputter deposited WN_x films are generally contaminant free, the major drawback of sputtering, as mentioned in Chapter 1, is poor conformality in small, high aspect ratio device features.

2.8.5 LPCVD WN_x Deposition

LPCVD of WN_x has been researched as a possible alternative to sputtering for smaller device features with high aspect ratios. Many reports of LPCVD WN_x films have

Table 2-1. Key properties of sputtered WN_x films reported in the literature

Sputter Target / Gas Composition	Dep. Temp. (°C)	Resistivity Range (μΩ–cm)	Conformality (%)	Contam. Levels (at %)	Dep. Rate (Å/min)	Adhesion	Failure Temp. with Cu (°C)	References
W (target) + Ar/N_2 gas	25–400	40–11000	N/A	Ar <1% O 1–12%	17–700	Excellent on Si (scotch tape test), Poor on GaAs above 21 at.% N, Poor on quartz	600–900	[Aff85, Bak02, Bou97, Cha89, Cho01, Cho02, Gei86, Gic83, Hon03, Hub88, Kak99, Kat85, Kil75, Kol87, Lee90, Lee97, Lee00b, Lee03, Lin90, Lip03, Mig01, Mor98, Pac91, Pec97, Pok91, Rei75, Rey02, Sha01, She00a–f, So88, Sot03, Suh99, Suh01, Tak97a, Uch86, Uek96, Vu90, Yu88]
W (target) + N^+ ion beam	20-600	200–540	N/A	N/A	9–90	N/A	N/A	[Bos91, Eiz94b, Gal93, Zha99]
W (target) + Ne/N_2	25	132–15685	N/A	N/A	12–63	N/A	N/A	[Hub88]

been given in the literature. The key properties of these films are summarized in Table 2-2.

As evident from Table 2-2, LPCVD reactions are based on halide chemistry, and include the reduction of WF_6, WO_3, or WCl_6 by NH_3 or NF_3 in a H_2 atmosphere [Chi93, Gon02, Mar93, Nag93, Nak87, Sak96, Suz98, Vol85]. Nagai and Kishida [1993] reported that use of WCl_6 as the tungsten precursor for reaction with NH_3 and H_2 was more thermodynamically favorable than using WF_6, as the Gibbs free energy change was larger for the chloride precursor reaction. Marcus et al. [1993] have reported high LPCVD deposition rates, ranging from 1800–4500 Å/min.

One report (not included in the table) of the "indirect" deposition of β–WN_x has been given, where this phase formed after annealing a metastable W_3N_5 phase [Zha97]. Reacting $WNCl_3$ with ZnN_2 produced the W_3N_5 phase at 400°C, and subsequent annealing at 600°C resulted in formation of the β–WN_x phase.

The halide precursors used for LPCVD can create difficulties during barrier deposition and subsequent device processing. WF_6 is reported to consume Si during the reaction, forming SiF_4, which leaves vacancies on the Si substrate [Kim91, Kim92, Lai98a]. In addition, there are concerns that residual F and Cl in the barrier contribute to corrosion of metal interconnects [Fal98, Kel99, Raa93]. Contamination levels of 0.1–0.9% F have been reported for LPCVD films [Mar93]. Moreover, reactive by–products (e.g., hydrogen halides) resulting from LPCVD are a material handling concern [Cur92, Kim91].

Adduct formation is another difficulty associated with LPCVD. Adducts are compounds produced by chemical addition of two or more reactants. These adducts can settle onto the substrate and barrier film during deposition, resulting in dislocations and/or pinholes in the film that can lead to barrier failure. Gas phase adducts such as

$WF_6{\cdot}4NH_3$, NH_4F_2, and NH_4F have been reported during LPCVD reactions [Nak87, Suz98, Tsa96].

Table 2-2. Key properties of LPCVD WN_x films reported in the literature

LPCVD Deposition Chemistry	Dep. Temp. Range (°C)	Resistivity Range (μΩ–cm)	Conformality (%)	Contam. Levels (at %)	Dep. Rate (Å/min)	Adhesion	Failure Temp. with Cu (°C)	References
$WF_6 + NH_3$	450–700	900–2800	N/A	F 0.1–0.9 %	1800–4500	Good (scotch tape)	N/A	[Mar93, Wan03]
$WF_6 + NH_3 + H_2$	400–700	N/A	N/A	N/A	N/A	N/A	N/A	[Nak87]
$WF_6 + NH_3 + H_2$ by photo–assisted LPCVD (PACVD)	600	800–1000	N/A	N/A	N/A	N/A	N/A	[Par97a]
$WF_6 + NH_3 + SiH_4$	325–450	200–15000	45–100% (Diam: 0.2μm, AR: 3.0–9.8)	N/A	400	Excellent (scotch tape) after Ar plasma	450	[Gon02]
$WCl_6 + NH_3 + H_2$	500–900	N/A	N/A	N/A	N/A	N/A	N/A	[Nag93, Nag00]
$WO_3 + NH_3$	700–1000	N/A	N/A	N/A	N/A	N/A	N/A	[Vol85]*

*Note: bulk β–W_2N powder, rather than film, produced in this report

2.8.6 PECVD WN_x Deposition

The same halide chemistries used for LPCVD are also used for PECVD, whereby the plasma assists fragmentation of the reactants, lowering reaction temperatures considerably. After fragmentation by the plasma, the precursor fragments travel to the heated substrate, react on its surface and deposit a film. Many reports of PECVD WN_x films have been given in the literature. The key properties of these films are summarized in Table 2-3.

Films deposited by PECVD show excellent adhesion, with resistivities as low as 70 μΩ–cm. Growth rates are moderate, ranging from 300–400 Å/min [Gal97], and conformality up to 70 % has been reported for trench holes with diameter ≥ 0.30 μm [Kim93].

PECVD films suffer from reduced conformality in small diameter, high aspect ratio trench features, however, due to the directional nature of the plasma [Joh00a, Tsa96]. Despite the low resistivity and deposition temperatures that PECVD offers, its inability to deposit highly conformal films in high aspect ratio features makes its use in future barrier deposition questionable. Moreover, PECVD films, like LPCVD films, suffer from halide impurities. Concerns about halides contaminating the barrier films also exist for PECVD, since the same reactants are often used for both LPCVD and PECVD. Contamination levels up to 4 at.% F, which are higher than those for LPCVD, have been reported for PECVD films [Lee93]. Another difficulty associated with PECVD is gas phase adduct formation; adducts such as $(WF_6)_x(NH_3)_x$ and NH_4F have been reported during WN_x PECVD [Lu98b, Suz98]. These adducts can contaminate films grown by PECVD and deposit particles on the film surface, both of which can

Table 2-3. Key properties of PECVD WN_x films reported in the literature

PECVD Deposition Chemistry	Dep. Temp. Range (°C)	Resistivity Range (μΩ–cm)	Conformality (%)	Contam. Levels (at %)	Dep. Rate (Å/min)	Adhesion	Failure Temp. with Cu (°C)	References
$WF_6 + N_2 + H_2$	275–475	190–240	36–70% (0.3 μm, 3:1 AR),	F: ≤ 1 at.% C: ~1 at.% O: ≤ 3.4 at.%	600–1800	Good (Scotch tape)	400–700	[Eck02, Gan00, Hec02, Jin99, Lai98a , Li00, Lu98b, Vij99, Zen00a,b]
$WF_6 + NH_3 + H_2$	25–620	90–550	33% (0.15 μm, 9:1 AR), 70% (2 μm, 2:1 AR), 60% (0.35 μm, 3.5:1 AR)	F: ~2 at.% O: ~2 at.%	210–400	N/A	500–800	[Bai03, Gal97, Iva99, Kim91, 92, 93, Kwo95, Lee93, 94a–c, Lee98c, Lin98a–b, Lin99, Meu98, Par97b, Par98a]
$WF_6 + NF_3$	350	175	N/A	N/A	N/A	N/A	N/A	[Suz98]

cause premature device failure. The difficulties associated with sputtering, LPCVD and PECVD have shifted attention to the use of metalorganic precursors for WN_x barrier deposition. At present, several metalorganic WN_x precursors have been reported in the literature. Our research has focused on the thermal decomposition of novel single–source precursors via MOCVD.

2.8.7 MOCVD WN_x Deposition

MOCVD of WN_x has many desirable properties. Films deposited by metalorganic complexes such as $(^tBuN)_2W(NH^tBu)_2$ or $W(CO)_6$+NH_3 do not contain halides, which can etch subsequent metallization layers when incorporated into the barrier film. By varying the structure of the MOCVD precursor molecule, the precursor can be optimized so that it dissociates in a "clean" fashion (i.e., with minimal oxygen and carbon contamination) and at relatively low deposition temperatures. Temperatures down to 200°C have been demonstrated for MOCVD film deposition [Chi93, Kel99]. The presence of impurities (O, N, C) is reported to improve stability in contact structures, because the impurities tend to stuff grain boundaries and inhibit diffusion [So88]. Oxygen's "stuffing" effectiveness, however, is lower for Cu than Al, because the reactivity of Cu with O is less than that for Al with O [Kim99c]. Carbon has also been reported to improve thermal stability of W barriers and foster growth of smaller grains [Wan01b]. Although these impurities may stabilize the film and decrease polycrystal size, they may also act as electron scattering sites, increasing film resistivity. The challenges for MOCVD of refractory nitride materials include minimizing carbon and oxygen contamination, minimizing film resistivity, and lowering the deposition temperature.

Kelsey et al. [1999] reported the use of $W(CO)_6$+NH_3 to deposit WN_x films. The metalorganic precursor was fed from a solid source delivery system, and was mixed with NH_3 in the reactor, over a deposition temperature range of 200 to 350°C. The deposited films were polycrystalline β–W_2N, with growth rates ranging from 40 to 100 Å/min. Resistivities as low as 123 μΩ–cm were observed, which coincided with carbon and oxygen contamination levels below 5%, and step coverage was greater than 90% on 0.25 μm feature sizes. Barrier integrity tests for a sample with an annealed metallization overlayer have not been reported for films grown by this precursor scheme, however. The merits of growth with $W(CO)_6$ are tempered by the possibility that decomposition of the precursor's CO byproduct can cause oxygen contamination in the films.

Typical strategies for CVD of multi–element barrier materials involve the use of co–reactant precursors. Co–reactant deposition uses a separate precursor for each element desired in the film; hence, bonds between these elements must be formed by intermolecular processes during deposition. In contrast, a single–source precursor already has bonds established between the elements that will comprise the film prior to deposition. This approach is particularly useful when the bond strengths in the individual precursor candidates, and thus decomposition temperatures, are quite different. Another advantage to using a single source precursor include elimination of the need for multiple reactants so that flow ratio control is eliminated as a process variable. In addition, gas phase adducts, which have been reported for many LPCVD processes, are no longer a concern, because multiple gas phase reactants are not being introduced to the reactor. Our research involves the use of novel single–source metalorganic precursors to deposit WN_x thin films.

Table 2-4. Key properties of MOCVD WN_x films reported in the literature

MOCVD Deposition Chemistry	Dep. Temp. Range (°C)	Resistivity Range (μΩ–cm)	Conformality (%)	Contam. Levels (at %)	Dep. Rate (Å/min)	Adhesion	Failure Temp. with Cu (°C)	References
$(^tBuN)_2W(NH^tBu)_2$	450 –650	620 – 7000	85 (Diam: 0.40 μm, AR: 3)	C: 6 at.% O: 3 at.%	20 – 100	Poor	N/A	[Chi92, Chi93, Cur92, Nug80, Tsa96]
$W(CO)_6 + NH_3$	200 – 350	123	90 (Diam: 0.25 μm, AR:4)	C: < 5 at.% O: < 5 at.%	40 – 100	N/A	N/A	[Kel99]
$CH_3(CH_2)_2CH(CH_3)NCW(CO)_5 + N_2 + NH_3$	250 –400	N/A	N/A	N/A	N/A	N/A	N/A	[Gor00]

Nugent et al. [1980] first reported synthesis of the $(^tBuN)_2W(NH^tBu)_2$ molecule, which would later be the first single–source molecule tested for MOCVD of WN_x. Currie et al. [1992] used this molecule to deposit a W/W_2N composite coating. The precursor was dissolved in hexane solvent, and the liquid mixture was used to coat the substrate. The solvent was then evaporated off and the precursor–coated substrate was subjected to heat treatment up to 1200°C. The resulting film was a composite mixture of α–W/β–W_2N. No growth rates or resistivities were reported for these films, however.

Chiu et al. [1993] reported use of the same molecule as a single–source MOCVD precursor to deposit WN_x films. The precursor was transported to the reactor by a solid source delivery system, and the depositions were done by thermal decomposition over a temperature range of 450 to 650°C. The resulting films were polycrystalline β–W_2N, with growth rates ranging from 20 to 100 Å/min, and lattice parameters ranging from 4.14 to 4.18 Å. Tsai et al. [1996] later reported that these films were nitrogen rich, with additional N expanding the lattice parameter above the 4.126 Å standard for β–W_2N films. These films had resistivities ranging from 620 to 7000 $\mu\Omega$–cm, with step coverage for a 0.40 μm diameter feature up to 85%. Resistivity increased with an increase in the N/W ratio of the film, while the N/W ratio increased with decreasing deposition temperature. Oxygen and carbon contamination levels of 3 and 6 at.%, respectively, were given for these films. Crane et al. [2001] later studied the reaction mechanism for WN_x deposition from this precursor. Barrier integrity tests with an annealed metallization overlayer have not been reported, however, for films grown by this precursor.

Gordon et al. [2000] reported deposition of WN_x thin films from tungsten (0) pentacarbonyl 1–methylbutylisonitrile ($CH_3(CH_2)_2CH(CH_3)NCW(CO)_5$). A nebulizer vaporized the liquid phase precursor, and this vapor was conveyed to the reactor by a carrier gas mixture containing N_2 and NH_3. Substrate temperatures ranged from 250 to 400°C, and the reactor pressure was atmospheric. Films were amorphous per XRD, and Rutherford backscattering (RBS) showed the film stoichiometry to be near $W_{0.67}N_{0.33}$.

One report of indirect β–W_2N deposition (not included in the table) from a MOCVD precursor has been given [Zha97]. The MOCVD precursor $[WNCl_3{\cdot}NCCH_3]_4{\cdot}2CH_3CN$ was used to deposit a metastable W_3N_5 phase, which was then annealed to form β–W_2N. Key properties from several reports of MOCVD WN_x films are summarized in Table 2-4.

2.8.8 ALD WN_x Deposition

The use of ALD in mass production is suggested to be necessary by the 65 nm node for diffusion barriers [Bey02, Han03] and by the 45 nm node for high–k gate dielectrics and the first few metal layers [Han03, Cha04]. In the front end, step coverage is not an issue, but ALD is very useful to deposit ultrathin films of high–k dielectric materials. In the back end, ALD is useful due to its excellent conformality, which is required to deposit seed and barrier layers in high aspect ratio vias and trenches.

ALD of WN_x films by sequential reaction of adsorbed WF_6 with NH_3 on Si(100) and SiO_2 substrates has been reported [Ele02, Kla00a–b]. Deposition of a WN_x monolayer occurred by 2 half–cycles. In the first half cycle, WF_6 was introduced into the reactor. After monolayer adsorption onto the substrates, any remaining WF_6 in the reactor atmosphere was pumped out. In the second half cycle, NH_3 was introduced into the reactor to convert the adsorbed WF_x monolayer into W_2N. Klaus et al. [2000a,b] reported a linear deposition rate of 2.5 Å/cycle for reaction temperatures ranging from 600 to 800 K, but the films had very high resistivity (4.5 x 10^6 μΩ–cm). Elers et al. [2002] reported a deposition rate of 0.42 Å/cycle at 350°C (623 K), along with high resistivity (4500 μΩ–cm) and 2.4% F content. Conformality data were not presented for these films.

Nitride growth with ammonia by ALD is reported to have a low growth rate, which is due either to a small number of NH_x groups left on surface after NH_3 pulse or due to adsorption site blocking by readsorbed reaction byproduct HCl [Les02]. Sim [2003] used WF_6 and a pulsed plasma NH_3 to deposit WN_x thin films by ALD at 350°C on Si and non–Si substrates. The pulsed plasma NH_3 provides reactive radicals such as NH^+, NH_2^+, NH_3^+ and H^+, which prevent fast reaction of WF_6 with Si. The deposition rate was 2.2 Å per cycle (on both Si and TEOS), and a 220 Å thick barrier prevented Cu diffusion after a 30 min anneal at 700°C.

ALD of WN_x thin films using the metalorganic precursor bis(tert–butylimido)bis(dimethylamido)tungsten $(^tBuN)_2(Me_2N)_2)W$ and NH_3 was recently demonstrated in the temperature range of 250 to 350°C [Bec03a, Bec03b]. The growth rate for WN_x films was 1 Å per cycle, with no incubation period, and films were deposited on silicon, glass quartz, glassy carbon, stainless steel, aluminum, gold and copper substrates. The W:N stoichiometry of the films was shown to be ~1:1 per RBS, and the films adhered very well to Cu deposited on their surface by ALD. The films resisted Cu in–diffusion up to 600°C, but converted to pure W after a 30–minute anneal at 725°C. Step coverage was 100 % in a feature with an aspect ratio greater than 200:1.

A mechanism for the ALD reaction was proposed, in which it was suggested that NH_3 did not react with the metalorganic precursor, but instead catalyzed the removal of the alkyl groups on the precursor itself. Pyridine was used in place of NH_3, and WN films were again deposited.

2.8.9 ALD WN_xC_y Deposition

ALD of a WN_xC_y ternary solid solution onto Cu and SiO_2 substrates by sequential reaction of WF_6, NH_3 and Et_3B has also been reported [Pet02, Smi02]. A 70 Å thin film was deposited with a growth rate of 0.8 Å/cycle and an AES composition of 57% W, 30% C and 13% N. Conformality on 0.25 μm vias was 100% on the feature bottom and sidewalls, while film resistivities ranged from 600 to 900 μΩ–cm. Cu seed deposition by PVD was performed ex–situ before bias temperature stress (BTS) testing was performed on the samples. WN_xC_y had marginal adhesion on SiO_2, but via resistance with this barrier was about half that of PVD Ta [Smi02]. The same chemistry was used to deposit FCC β–WN_xC_y nanolaminates at 350°C, which had resistivity of 210 μΩ–cm and excellent adhesion to Cu [Ele03, Li02].

Li et al. [2003] also deposited WN_xC_y films with WF_6 + NH_3 + $(Et)_3B$, varying deposition temperature from 275 to 325°C. The films had a growth rate of 0.8 to 0.9 Å/cycle, and step coverage in 130 nm features with a 40:1 aspect ratio was > 90 %.

Kim et al. [2003d] reported deposition of WN_xC_y films using ALD of WF_6+NH_3+TEB at 350°C. Film composition from RBS was 48 at.% W, 32 at.% C, and 20 at.% N, and film density was 15.37 g/cm^3. The film had low resistivity (350 μΩ–cm), and had an electron diffraction pattern that closely matched those for β–$WN_{0.5}$ and β–$WC_{0.6}$. A 12 nm film survived a Cu anneal up to 700°C.

2.9 Conclusions

Continuous scaling down of barrier thickness will make material selection a critical issue. In thicker barrier films, deposition of an equiaxial, small–grained microstructure provides good barrier performance, because the diffusion path is very tortuous, hence Cu cannot penetrate through the barrier. Barrier thickness at the 100 nm node is 12 nm (120 Å), however, and will shrink to 7 nm (70 Å) by the 65 nm node in 2007 and eventually to 2.5 nm (25 Å) at the 22 nm device node in 2016 [ITR02]. By 2016, the barrier layer thickness will correspond to ~ 5 monolayers of barrier material. Barrier layers will become so thin in future device nodes that manipulating the microstructure (i.e., amorphizing the film) alone will not be enough to prevent Cu penetration, as any defects in the film will be weak points for Cu diffusion. The addition of an element such as nitrogen, which chemically repels Cu and stabilizes the metal against silicide formation, will be essential to bolster barrier resistance at weak points such as defects. Ru, for example, is a promising barrier and direct ECD candidate, but it does not chemically repel Cu, readily forms silicides, and could be susceptible to Cu diffusion through defects in film structure. The stuffed barrier concept, therefore, should likely be extended down as barrier layers are thinned. Along with stuffed barrier materials, the future barrier deposition technique will most likely be ALD, due to the inability of PVD and CVD methods to produce ultra–thin, highly conformal films.

CHAPTER 3
EQUILIBRIUM MODELS FOR WN_x–BASED BARRIERS

3.1 Motivation and Method

The CVD process involves a gas phase, containing one or more species, interacting with a solid substrate, which may catalyze a reaction(s) leading to film formation. The CVD process is complex, with transport phenomena (energy, mass and momentum) and reaction kinetics controlling the rate of approach to thermodynamic equilibrium to determine which phase(s) will form and their extent. Transport phenomena govern the ability of the precursor(s) and any intermediate(s) to reach the reaction surface (substrate), while reaction kinetics address the ability of and pathway for the precursor(s) and intermediate(s) to react and lead to deposition of a film on the substrate surface. The parameters that affect transport phenomena in the reactor are the applied boundary conditions (e.g., susceptor temperature, reactor pressure, reactor inlet flowrates), the system geometry, and the thermophysical properties [Vos78]. Understanding the available kinetic pathways in the system is very important, as kinetic barriers (pathways with high activation energies) can prevent the growth of certain solid phases in favor of others or the incorporation of impurities. Kinetic limitations may prevent concentrations at the growth surface from being at their equilibrium values, and should be taken into consideration when predicting the phases expected to form in the film. Chemical equilibrium studies are useful to determine which solid phase(s) and gas species would form during CVD at specific process conditions (temperature, pressure and inlet compositions), barring any kinetic or transport constraints. Depending on the conditions in the reactor system, the process may or may not be close to equilibrium. While transport and kinetic constraints must be taken into account to form a complete CVD model, transport effects and especially kinetic pathways in the reactor are very difficult to unravel.

Computing the thermodynamic equilibrium state in the reactor system is therefore a logical first step toward forming a complete CVD model. Thermodynamic modeling is an important tool used to estimate the equilibrium set of phases and their composition for a system at specific reaction conditions. Experimentally, achieving thermodynamic equilibrium may be impractical, due to kinetic constraints, transport issues, and short time scales for reactant exposure to the substrate. To approach true thermodynamic equilibrium in the reactor, temperature should be maximized to overcome kinetic constraints, and the reactant exposure time should be maximized. If equilibrium conditions are assumed for a given process, the film provides a record of the growth condition at the interface, assuming the temperature is sufficiently low to quench the film. Then, the equilibrium composition of the solid phase(s) formed during the reaction can be determined ex–situ, by a combination of characterization techniques such as XRD and XPS. Exclusion of certain solid phases evident from these techniques, such as surface oxides, may be needed if they form due to post–growth air exposure. The equilibrium composition of the vapor, however, must be determined in–situ, due to the disappearance of many high temperature species upon cooling to room temperature [Vos78].

CVD tends to be a non–equilibrium process due to kinetic limits and short residence times of vapor species. Although CVD is a non–equilibrium process, equilibrium thermodynamic calculations can give us a preliminary idea of solid, liquid and gas phase composition in a multi–component system [Raz95], and hence can be used as a guide in choosing process conditions [Smi82]. In addition, an equilibrium thermodynamic model may be useful when rates of change are rapid (e.g., at high temperature). At high temperature, a mass–transfer limited regime typically exists. If the mass transfer coefficients of the various reactants through the boundary layer are similar, then the reactant concentrations at the growth surface are equal to that in the bulk, and the surface conditions are a good equilibrium approximation. This utility diminishes at lower temperature, as reactor kinetics limit the rate [Smi82]. When performing a thermodynamic equilibrium analysis care must be taken to identify species whose formation is both thermodynamically and kinetically favorable. Each of the proposed species and phases should have a kinetic pathway to form and take part in the equilibrium.

Several experimental variables are useful and necessary to carry out a thermodynamic equilibrium analysis. For a system operating at constant pressure, these variables include the system's temperature, pressure, and elemental makeup. Once these variables are specified, a list of potential species and phases present in the system is drafted. This list must then be checked and modified to include only those species and phases whose formation is kinetically possible. Finally, a set of equilibrium variables (e.g., temperature, pressure, moles of elements) must be specified to generate an equilibrium CVD phase diagram.

The general criterion for equilibrium in an isolated system is that G', the overall Gibbs energy, be minimum [DeH93]. This is described mathematically as [DeH93, Kat97]:

$$G' = \sum_{\alpha=1}^{p} G'^{\alpha} = \text{minimum} \tag{3–1}$$

where G'^{α} is the total (not per mole) Gibbs energy of the α phase, and p is the total number of phases in the system. If G' is minimum at equilibrium, dG' must be zero:

$$dG' = \sum_{\alpha=1}^{p} dG'^{\alpha} = 0 \tag{3–2}$$

The expression for the change in overall Gibbs energy (G') for an arbitrary change in state in a system is [DeH93]:

$$dG' = -S'dT + V'dP + \sum_{k=1}^{c} \mu_k dn_k \tag{3–3}$$

where μ_k is the chemical potential, defined as the change in overall Gibbs energy with a change in the amount of component k present, holding temperature, pressure and composition of other components constant:

$$\mu_k = \left(\frac{\partial G'}{\partial n_k} \right)_{T,P,n_{j \neq k}} \tag{3–4}$$

In a system with two components (1 and 2) and two phases (α and β) at equilibrium, for example, which is constrained to constant temperature and pressure (so that dT and dP are zero), the above expression for dG' becomes [DeH93]:

$$dG' = dG'^{\alpha} + dG'^{\beta} = \mu_1{}^{\alpha} dn_1{}^{\alpha} + \mu_1{}^{\beta} dn_1{}^{\beta} + \mu_2{}^{\alpha} dn_2{}^{\alpha} + \mu_2{}^{\beta} dn_2{}^{\beta} = 0 \tag{3–5}$$

where μ_1^{α} is the chemical potential of component 1 in the α phase. In a two–phase non–reacting system, for example, $dn_1^{\alpha} = -dn_1^{\beta}$, so that the number of moles of each component is conserved. Substituting this into the above equation yields:

$$dG' = (\mu_1^{\alpha} - \mu_1^{\beta})dn_1^{\alpha} + (\mu_2^{\alpha} - \mu_2^{\beta})dn_2^{\alpha} = 0 \qquad (3\text{–}6)$$

For the above equation to be valid, it is seen that the coefficients on dn_1^{α} and dn_2^{α} must be zero at equilibrium, since transport of components 1 and 2 between the α and β phases can occur (i.e., dn_1^{α} and dn_2^{α} are non–zero). This implies that the chemical potential for a given component in the α phase must equal its chemical potential in the β phase at equilibrium. This result is general and can be applied to any number of components and phases, and is the criterion used to construct phase diagrams.

Before setting up a phase diagram, though, the basis for Gibbs energy expressions (e.g., G'^{α} and G'^{β}) for different phases must be established. To calculate a thermodynamic equilibrium, expressions describing the Gibbs energy of each phase must first be defined. If the system is assumed to be maintained at constant pressure (as in our experimental system), the effect of temperature on Gibbs energy can be examined. To begin, write the expressions for Gibbs energy, enthalpy and entropy for a simple single–component system at constant pressure [DeH93]:

$$G = H - TS \qquad (3\text{–}7)$$

$$\Delta S = \int_{T_1}^{T_2} \frac{C_p}{T} dT \qquad (3\text{–}8)$$

$$\Delta H = \int_{T_1}^{T_2} C_p dT \qquad (3\text{–}9)$$

$$\Delta G = \int_{T_1}^{T_2} C_p dT - T\left(\int_{T_1}^{T_2} \frac{C_p}{T} dT\right) \tag{3–10}$$

This expression gives the Gibbs energy for a single component in terms of two experimentally measured variables, constant pressure heat capacity (C_p), which is typically measured by calorimetric methods, and temperature (T). Beginning with a list of values for the heat capacity as a function of temperature for a pure component, an equation may be fitted to this data to obtain a temperature dependent expression for heat capacity. Some common models for the heat capacity expression are shown in Equations 3–11 to 3–14 [Gur89]:

$$\mathrm{C_p(T) = a + bT - \frac{c}{T^2}} \tag{3–11}$$

$$\mathrm{C_p(T) = a + bT - \frac{c}{T^2} + dT^2} \tag{3–12}$$

$$\mathrm{C_p(T) = a + bT - \frac{c}{T^2} + dT^2 + eT^3} \tag{3–13}$$

$$\mathrm{C_p(T) = a + bT - \frac{c}{T^2} + dT^2 + eT^3 + fT^4} \tag{3–14}$$

Fitting experimentally determined heat capacity data to one of the heat capacity expressions above, and substituting this expression into Equation 3–10, enables calculation of Gibbs energy changes.

For pure component phases, the Gibbs energy expression can often be determined experimentally by such techniques as calorimetry, gas phase equilibria measurements or electromotive force (EMF) measurements [Sau98]. Thermodynamic assessment, which is an alternative, stepwise approach, may be used when experimentally determined Gibbs energies are unavailable. The first step is to represent the Gibbs energy for the component(s) of interest by a power series in terms of temperature, as follows [Din91]:

$$^{o}G_i^{\varphi} = a + bT + cT\ln T + \sum^{n} d_n T^n \tag{3-15}$$

where $^{o}G_i^{\varphi}$ is the Gibbs energy of a pure component and n typically has the values of 2, 3 and −1. In addition, a pressure dependent term may be added to the series if warranted. The values of n are determined during the procedure of thermodynamic optimization to obtain the best possible fit between the calculated and experimental compositions. Assessment involves modifications to the coefficients in the Gibbs energy expressions, so that the shape and position of phase boundary regions on the diagram, along with the thermodynamic properties (heat capacity, enthalpy, etc.) calculated from the Gibbs energy, are consistent with experimental observations, where available. The coefficients of the Gibbs energy expressions have physical meaning corresponding to such thermodynamic properties as enthalpy, entropy, and heat capacity, hence any expression resulting from an optimization should be validated against experimental values (when available) for these properties. If experimental property data are unavailable, the optimization can still be done, but equilibrium phase and composition data must be used to delineate the phase boundary regions, so that the resulting phase diagram is as accurate as possible. Estimation of the coefficients may be done by trial–and–error or mathematical methods [Kat97]. In this study, both the PARROT module within ThermoCalc and trial–and–error methods were used to optimize coefficients in the Gibbs energy expressions of interest.

Multi–component mixtures have a more involved expression for Gibbs energy. The general expression for the Gibbs energy per mole of a solution phase containing i components is shown below:

$$G^{\varphi}{}_{\text{mix}} = \sum_i x_i G_i^{o} + RT\sum_i x_i \ln x_i + G_{\text{mix}}^{xs} \qquad (3\text{–}16)$$

where x_i is the mole fraction of component i, R is the gas constant and T is absolute temperature. The $G^{\varphi}{}_{\text{mix}}$ term is the sum of three terms on the right hand side. The first term represents the contribution to Gibbs energy from pure components (also called the mechanical mixing term), with G_i^{o} being the Gibbs energy of pure component i per mole at its reference state (temperature, pressure and phase). The second term represents the Gibbs energy change upon mixing to form an ideal solution, and for a solid solution assumes that components may mix on any position available in the phase without preferential site occupation [Sau98]. The third term, called the excess Gibbs energy of mixing, represents non–ideal mixing interactions. The excess Gibbs energy can take several different forms, depending on which model one chooses to follow. The regular solution model, for example, assumes that any non–ideal interactions between constituents in the solution depend only on temperature, and are not composition dependent. The excess Gibbs energy for a binary mixture of A and B using the regular solution model takes the following form:

$$G_{\text{mix}}^{xs} = x_A x_B L \qquad (3\text{–}17)$$

where L is a temperature dependent parameter describing A–B interaction [Sau98]. A positive value for L indicates repulsive interaction between the components, while a negative value indicates an attractive interaction [Swa72]. The next level of complexity is for the interaction energies to incorporate composition dependence. An example is the sub–regular solution model, which assumes that interaction energies change linearly with composition [Sau98]:

$$G_{mix}^{xs} = x_A x_B \left(L^A x_A + L^B x_B\right) \tag{3–18}$$

where L^A is the parameter describing A–B interaction on the A side of the composition range. More complex expressions for excess Gibbs energy are available, and are reviewed in detail elsewhere [Sau98].

Gibbs energies for some phases (e.g., unstable phases, multi–component phases) cannot be easily determined by calorimetric methods, and are determined instead by optimizing the diagram to fit experimentally observed equilibrium composition data. Once a Gibbs energy expression has been defined for each component included in the equilibrium, the overall Gibbs energy of the system must be minimized at every point over the entire temperature and composition range. Minimizing the Gibbs energy at every point then leads to equilibrium compositions at different conditions, the basis for the phase diagram. Tie lines and regions made up by them on the phase diagram represent two–phase equilibria resulting from the two phases having equal component chemical potentials at a given set of conditions.

Use of a metalorganic precursor to deposit WN_x films can lead to appreciable C contamination into the films, especially at higher deposition temperature, and can cause unintentional deposition of W–C–N solid solution or line compounds, along with free C in the film. The presence of C in our metalorganic precursor ligands and solvent makes the formation of a ternary W–C–N solid phase, rather than the binary WN_x, highly probable. Recent reports, however, indicate interest in the FCC β–WN_xC_y phase as a potential barrier material, as detailed in Chapter 2 [Ele03, Li02, Smi02]. While one benefit of depositing β–WN_xC_y films is lower resistivity than the binary nitride, the presence of free carbon in the films can increase film resistivity, negating this benefit. Moreover, as mentioned in Chapter 2, free C regions in the film were reported to be facile paths for Cu to penetrate the barrier [Ima97], due to carbon's inability to chemically repel Cu. An equilibrium phase diagram for the ternary W–C–N system at low temperature and pressure, consistent with MOCVD process conditions, would be a useful guide to select deposition conditions for β–WN_xC_y that minimize free carbon in the films.

The elements contained in precursor, solvent, and carrier gas molecules used in this work are W, C, Cl, H and N, with solid and gas phases being in contact during the CVD reaction, while purposely avoiding a liquid phase. Modeling of the experimental results from this work therefore requires inclusion and analysis of the W–C–N ternary system. While the experimental data from this work indicate the presence of ternary FCC β–WN_xC_y polycrystals in the films, the deposition mechanism that gives rise to them involves solid–gas equilibrium in the W–C–Cl–H–N system. This analysis must therefore model W–C–Cl–H–N solid–gas equilibrium, adjusting parameters for the ternary FCC β–WN_xC_y phase within this system to ensure its formation at our reactor conditions. From the results of this analysis, the equilibrium phase diagram for the ternary W–C–N system can then be predicted. Before the 5–component analysis can begin, models for the binary W–N and W–C systems must first be reviewed. Existing W–N and W–C phase diagrams, along with new literature data, will be analyzed to determine if the solution model parameters need to be revised. Once the binary analyses are complete, a degrees of freedom (DOF) analysis for the 5–component system will be done to determine the effect of varying specific conditions in our reactor on the predicted equilibrium. The ternary W–C–N phase diagram will then be predicted, and lastly, the $\beta-WC_{0.5}-\beta-WN_{0.5}$ pseudobinary system will be discussed.

3.2 Constraints

To perform an equilibrium analysis, several calculational constraints must be addressed. These include mandatory constraints that are independent of the particular system of interest, and specific constraints that define the parameters of a specific system. The mandatory constraints include conservation of elemental species in the system, and the non–negativity constraint, which dictates that the number of moles of any species in the system must be either positive or zero [Smi82]. The elemental species conservation constraint can be represented by a set of equations as follows:

$$\sum_{i=1}^{N} a_{ki} n_i = b_k ; k = 1,2 \ldots E \qquad (3-19)$$

where a_{ki} is the subscript of the kth element in the molecular formula of component i, n_i is the number of moles of component i, b_k is the fixed number of moles of element k in the system, N is the number of components, and E is the number of elements. Specific constraints typically include temperature, pressure, and elemental moles, which must be given at the outset before the analysis can be done. The elemental species conservation constraints are linear in the mole numbers of the species present, while the chemical potential functions are not, meaning that any solution scheme will be iterative [Smi82].

3.3 Degrees of Freedom

The Gibbs phase rule defines the degrees of freedom for a system, F, as the number of independent variables required to describe the state of the system [DeH93]. For a non–reacting system, this is defined as F=C–P+2, where C is the number of components (in our case, elements) and P is the number of phases. This relation is useful when examining a phase diagram or a system with a known number of phases. When running a thermodynamic analysis, however, the number of phases at a given set of conditions is typically an unknown, desired quantity. "True" degrees of freedom as defined by ThermoCalc [Sun95] is C+2, which represents the number of components (C) input to the system plus temperature and pressure. Finally, stoichiometric degrees of freedom (R) is the number of species (S, which includes molecules, line compounds, non–stoichiometric phases, gas species, etc.) being considered in an equilibrium analysis minus the number of components in the system, R=S−C [Smi82]. The value of R represents the number of independent chemical reactions relating the components in the system.

Internal degrees of freedom are a separate issue, and do not affect the overall DOF for the system. In the FCC β–WN_xC_y phase, for example, the values of x and y are internal DOF for the phase. Setting the values of x and y fixes the composition of the phase, but does not eliminate a DOF for the system.

3.4 Computational Methods

Before starting a thermodynamic equilibrium analysis, the list of potential species in the solid, liquid, and gas phases must be assembled. In ThermoCalc, this list of species and their relevant thermodynamic data are assembled into a thermodynamic database (tdb) file. To begin the analysis, the "true" degrees of freedom must equal zero, hence the temperature, pressure, and elemental composition must be input to begin the calculation. Once these inputs are given, the value of R and the list of R independent chemical reactions among the specified elements in the tdb file must be determined. The general solution for the elemental species conservation equation above is of the form:

$$n_i = n_i^o + \sum_{j=1}^{R} \nu_{ij}\xi_j \qquad i = 1,2\ldots N \tag{3-20}$$

where n_i is the final equilibrium mole number for species i, $n_i°$ is the initial mole number of species i, and ν_{ij} and ξ_j are the stoichiometric coefficient and the extent of reaction parameter, respectively, for species i in the jth independent reaction among the species. After the list of R independent chemical reactions is determined, all values of ν_{ij} are known, and the optimization process focuses on solving for ε_j. The computational method to solve for the equilibrium composition in a complex system has its origins in work done by Brinkley [1946] and White [1958]. This stoichiometric algorithm method is outlined in section 4.3.3 of Smith and Missen [1982]. ThermoCalc, the software used for this thermodynamic modeling, does this procedure automatically.

The sublattice model will be used to describe the solid phases in the W–C–Cl–H–N system. This model is phenomenological, and considers a given solid to be composed of separate, interlocking sublattices. Each sublattice has certain elements that may mix on it. Vacancies may also be added to each sublattice to model homogeneity ranges in the solid phases. This model is very useful to describe metallic systems with interstitial atoms, such as metal carbides and nitrides, where carbon and nitrogen occupy interstitial sites in the metal lattice. The metal atoms are treated as one sublattice, while the interstitial carbon and nitrogen atoms are treated as a second, interlocking sublattice. Since the sublattice model is a construct that uses different composition variables, the use of the sublattice model requires modifications to the Gibbs energy expression listed in Equation 3–16 above. A modified expression for the Gibbs energy of a solution phase, adapted for a two sublattice model (metal on one sublattice and interstitial atoms on the other) with mixing only taking place on the interstitial sublattice, is shown below:

$$G^{\varphi}{}_{m} = \sum_{i} y_i{}^{I} G_i^{o} + zRT \sum_{i} y_i{}^{I} \ln y_i{}^{I} + G^{xs}_{mix} \tag{3–21}$$

where y_i^I is the site fraction of element i on the interstitial (I) sublattice. The term z is the number of available interstitial sites per metal atom, and depends on the structure of the metal sublattice. Incorporation of vacancies into the sublattice model enables us to consider homogeneity ranges among the atoms mixing on a given sublattice. Vacancies will be incorporated into the interstitial sublattice, which contains nitrogen and carbon, but will be ignored for the tungsten sublattice, per previous analyses in the literature.

3.5 Phase Equilibrium in the W–N System

While many recent studies examining crystal structure and film composition have been reported, a suitable phase diagram for the W–N system incorporating these results has not been assembled. A previous study of phase equilibrium in the W–N system generated a solid–liquid equilibrium diagram [Gui93]. The liquid phase has not been observed experimentally. Furthermore, no liquid phase has been reported during tungsten nitride deposition from a process that involves a gas phase. For the range of temperatures and pressures of interest to CVD, a solid–gas equilibrium phase diagram for the W–N system would be a useful guide for choosing deposition conditions to grow these barrier films.

To assemble the W–N solid–gas phase diagram, the solid and liquid phases that may potentially form, as well as any species that may appear in the gas phase, must first be specified. Then, expressions describing the Gibbs energy of each phase must be defined.

3.5.1 Pure Components in the W–N System

The pure, stable phase of tungsten at 298 K and 10^5 Pa is the body–centered cubic (BCC) form (also called α–W). This phase has a lattice parameter of 3.165 Å [JCP88], a melting point of 3422°C, density at 20°C of 19.25 g/cm³ [Sha96] and a resistivity of 5.65 μΩ–cm [Mur95]. Pure tungsten in face centered cubic (FCC) and hexagonally close packed (HCP) forms has been discussed in the literature, but both are considered to be metastable. A second element, such as interstitial C or N, is typically needed to stabilize the tungsten atoms into an FCC or HCP configuration. The stable phase of pure nitrogen at 298 K and 1 atm is N_2 gas, which has a boiling point of 77.35 K.

3.5.2 Stable Solid Phases in the W–N System

Several stable forms of solid tungsten nitride have been identified in the literature. Wriedt [1989] considered four solid phases to be stable in the W–N equilibrium system. These phases were BCC WN_x (terminal solid solution), face–centered cubic (FCC) WN_x (β–phase), simple hexagonal packed (SHP) WN (δ–phase) and orthorhombic WN_2 (δ_R^V–phase) [Gol67, Tak97a, Wri89]. Subsequent work excluded the latter phase in favor of a hexagonal close packed (HCP) WN_x (δ_H^{II}) phase, which is referred to as HCP W_2N when $x = 0.5$ [Fri99b, Hua97]. This is analogous to the HCP WC_x phase, which was described as a random interstitial solution of carbon in HCP tungsten [Gus86]. Schematic diagrams of the reported stable solid phases in the W–N system are shown in Figure 3–1.

The BCC WN_x phase (Figure 3–1) is stable up to 3422°C, and has a lattice parameter near 3.165 Å. The solubility of N in BCC WN_x varies, as denoted by the subscript "x," and is reported to range from 1.7×10^{-5} to 5×10^{-3} at. % N over the temperature range of 1200 to 2400°C at 10^5 Pa pressure [Wri89]. Wriedt [1989] adopted the following equation from Jehn and Ettmayer [1980], which fits the concentration of nitrogen in BCC WN_x to Sievert's Law (Equation 3–22):

$$\log C_N = \frac{1}{2}\log(P_{N_2}) - 1.38 - \frac{9520}{T} \tag{3–22}$$

where P_{N_2} is the nitrogen pressure (in Pa) and T is temperature (K). Since the composition dependence of BCC WN_x on temperature and pressure has been thoroughly examined, the existing Gibbs energy expression for this phase [Gui93] will not be modified for this analysis.

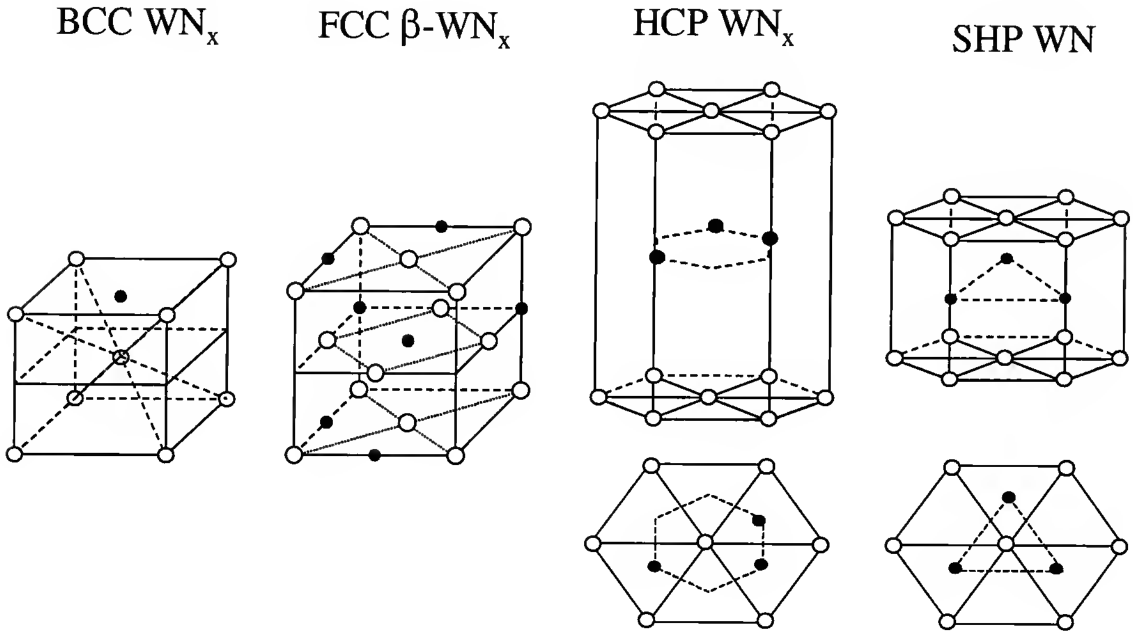

Figure 3–1. Schematic of the reported stable solid phases in the W–N system (not to scale). Open circles are W atoms, while black circles are N atoms.

The FCC β–WN_x phase (Figure 3–1) has a defective NaCl structure, with W atoms at the FCC sites, N atoms and vacancies at the interstitial octahedral sites, and a lattice parameter of 4.126 Å for x = 0.5 [Gol67, Hon00, JCP88, Tot71]. For the FCC β–$WN_{0.5}$ stoichiometry (used interchangeably with FCC β–W_2N or FCC β–$W_{0.67}N_{0.33}$), half of the interstitial sites are vacant. The theoretical density for this phase and stoichiometry is 18.0 g/cm³, while experimentally determined densities range from 15.0 to 17.9 g/cm³ [Aff85, Bos91, Gal97, Sam80]. BCC WN_x contains minimal nitrogen, which is required in appreciable amounts for this application to repel Cu diffusion through the film. Hence, FCC β–WN_x is the desired phase of tungsten nitride for its barrier potential. Furthermore, it has a relatively low bulk resistivity (~50 μΩ–cm) [Lee93] despite considerable nitrogen content, presumably because the metal atoms are arranged in the close–packed FCC configuration. Nitrogen atoms are assumed to locate randomly on the interstitial sublattice, as no evidence of N ordering on the interstitial sublattice has been reported. Due to a significant vacancy concentration on the interstitial sublattice, this phase has a substantial homogeneity range, which is denoted by the subscript x. A range of x values has been reported for the β–WN_x phase in the literature; this will be discussed in more detail in Section 3.7 below.

The SHP δ–WN phase (Figure 3–1) has a simple hexagonal packed structure similar to WC, with lattice parameters a=2.893 Å and c=2.826 Å [Sch54]. This phase is considered a stable stoichiometric line compound with formula WN [Gui93, Lee95, Sch54, She00a, Tot71, Zha99]. The calculated theoretical density for this phase is 16.0 g/cm³, while experimentally determined densities range from 12.1 to 15.9 g/cm³ [Sam80]. Experimental observations of this phase are discussed in more detail in Section 3.7 below.

The hexagonal close–packed HCP WN_x phase (Figure 3–1), referred to as the ε phase, has lattice parameters a=2.89 Å and c=22.85 Å with a theoretical density of 12.0 g/cm³ for x=0.5 [Gui93, Pea67, Tot71]. An experimental density has not been reported for this phase, which contains a random interstitial solution of nitrogen in HCP tungsten. For the HCP $WN_{0.5}$ stoichiometry (HCP W_2N), half of the interstitial sites are vacant. Guillermet [1993] considered this phase to be metastable, but included it in their calculation of the W–N phase diagram. Huang [1997], however, considered this phase to be stable in her calculation of the Nb–W–C–N phase diagram, because the analogous HCP WC_x phase is stable. A similar approach will be adopted for this analysis; hence this phase will be included in the assessment of the W–N phase diagram. The previously reported Gibbs energy expression for this phase [Gui93] will not be modified, however, as no experimental data have been reported for this phase in the literature. Several other tungsten nitride solid phases were identified but described as metastable [Wri89], hence they will not be included in this thermodynamic analysis.

Liquid–solid phase equilibria data have not been reported for the W–N system. Guillermet [1993] modeled the W–N liquid phase using a substitutional solution model, which assumes that components can mix on any available position in the phase without any preferential site occupation (i.e., ideal mixing) [Sau98]. Additionally, the regular solution approximation was used, which assumes that interaction energy is independent of composition.

3.5.3 Liquid Solution in the W–N System

The W–N liquid phase was previously modeled using a substitutional solution model [Fri99b, Gui93, Hua97]. The regular solution approximation was applied, which assumes that component interactions are independent of composition. No experimental data have been reported for a W–N liquid phase, but only inferred for liquid–solid phase equilibria data, hence the existing liquid model [Gui93] will be included in the present study without modification.

3.5.4 Gas Phase in the W–N System

The gas phase species included in this analysis were N, N_2, N_3 and W, following previous work [Gui93]. The gas phase was treated as an ideal mixture, with Gibbs energies for the gas species taken from the SGTE database [Ans87].

3.5.5 Equilibrium Modeling Basis

Solid Phase Model

Expressions describing the sublattice model are shown in Table 3-1, and are in the form $(W)_1(N,Va)_z$. Tungsten (W) sits on its own sublattice, while nitrogen (N) and vacancies (Va) mix on the interstitial sublattice sites. The subscript on the interstitial sublattice, z, indicates the number of interstitial sites available per W atom, and depends on the structure of the metal (W) sublattice. For the BCC phase z = 3, while z = 1 for the FCC and SHP phases and 0.5 for the HCP phase [Gui93, Gus86].

Table 3-1. Sublattice Models for the Solid Phases in the W–N Binary System

Solid Phase	Sublattice Model Expression
BCC solid solution	$(W)_1(N,Va)_3$
FCC (γ or β) nitride	$(W)_1(N,Va)_1$
HCP (ε) nitride	$(W)_1(N,Va)_{0.5}$
SHP (δ) nitride	$(W)_1(N)_1$

Use of the sublattice model to describe the BCC, FCC, and HCP WN_x solid solution phases requires modification of the standard expression for the Gibbs energy of mixing. This modification restricts mixing of N and Va to the interstitial sublattice, and assumes that all sites on the metal sublattice are filled. The modified expression for Gibbs energy of a solid solution phase, adapted for the two–sublattice model, is shown in Equation 3–23:

$$G_m^{\varphi} = y_N{}^I G_{W:N}^{\varphi} + y_{Va}{}^I G_{W:Va}^{\varphi} + zRT\left(y_N{}^I \ln y_N{}^I + y_{Va}{}^I \ln y_{Va}{}^I\right) + G_{mix}^{xs} \qquad (3\text{–}23)$$

where G_m^{φ} is the Gibbs energy (per mole of formula units, where the formula contains 1+z atoms) for the φ solution phase (φ=BCC, FCC or HCP), $y_N{}^I$ and $y_{Va}{}^I$ are the site fractions of N and Va on the interstitial (I) sublattice, respectively, and $G_{W:N}^{\varphi}$ and $G_{W:Va}^{\varphi}$ are the Gibbs energies for the φ phase if all interstitial sublattice sites were filled by N and Va, respectively. The last term, G_{mix}^{xs}, is the excess term addressing N–Va interaction on the interstitial sublattice, and in this study is expanded in the following form [Sau98]:

$$G_{mix}^{xs} = y_N{}^I y_{Va}{}^I \sum_v ({}^oL_{W:N,Va}^{\varphi,v})(y_N{}^I - y_{Va}{}^I)^v \qquad (3\text{–}24)$$

where ${}^oL^{\varphi}$ is the parameter describing non–ideal N–Va interactions on the interstitial sublattice, and v typically takes values from 0 to 2. If G_{mix}^{xs} is independent of composition (i.e., regular solution approximation), v = 0 and Equation 3–24 simplifies to:

$$G_{mix}^{xs} = y_N{}^I y_{Va}{}^I \, {}^oL_{W:N,Va}^{\varphi} \qquad (3\text{–}25)$$

The regular solution approximation was used previously to model the solid solution phases in the W–N system [Fri99b, Gui93, Hua97], and is used in this work as well.

Dinsdale [1991] reviewed the thermodynamic data available in the literature for the pure W and N phases. The Gibbs energy expressions describing the various phases of pure tungsten (with all interstitial sites vacant) are shown in Table 3-2 below [Din91, Gui93, Gus85, Gus86]. The expressions are valid over the temperature range $298.15 \leq T \leq 6000$ K unless noted otherwise. The $V_m(T,P)$ term is molar volume, which is both temperature and pressure dependent. This term was modeled with an analytical expression, as reported by Gustafson [1985] and Dinsdale [1991]. Expressions for the various solid phases of tungsten nitride (with all interstitial sites occupied by nitrogen), modeled with the ThermoCalc software by Guillermet [1993], are listed in Table 3-3.

Table 3-2. Gibbs Energy Expressions (J/mol) for Pure Solid Phases of W [Gui93, Gus86].

Phase	Sublattice Model Layout	Gibbs Energy Expression T(K)
BCC α–W	$(W)_1(Va)_3$	${}^{o}G^{BCC}_{W:Va} - H^{SER}_{W} = GHSERW = -7646.311 + 130.4T$ $- 24.1T\ln T - .001936T^{2} + 2.07x10^{-7}T^{3} + 44500T^{-1}$ $- 5.33x10^{-11}T^{4} + \int_{0}^{P} V_{m}(T, P)dP$ (for $298.15 \leq T \leq 3695$) ${}^{o}G^{BCC}_{W:Va} - H^{SER}_{W} = GHSERW = -82868.801 + 389.362335T$ $- 54T\ln T + 1.528621x10^{33}T^{-9} + \int_{0}^{P} V_{m}(T, P)dP$ (for $3695 \leq T \leq 6000$)
FCC β–W	$(W)_1(Va)_1$	${}^{o}G^{FCC}_{W:Va} - H^{SER}_{W} = 19300 + 0.63T + GHSERW$
HCP ε–W	$(W)_1(Va)_{0.5}$	${}^{o}G^{HCP}_{W:Va} - H^{SER}_{W} = 14750 + GHSERW$
SHP δ–W	$(W)_1(Va)_1$	Not Reported

The $\Delta^{o}G^{BCC}_{W:N_3}$ term is the temperature dependent Gibbs energy of formation for BCC WN_3, which is BCC WN_x with all available interstitial sites (z=3 for BCC WN_x) filled by N. The $\Delta^{o}G^{FCC}_{W:N}, \Delta^{o}G^{HCP}_{W:N_{0.5}}$, and $\Delta^{o}G^{SHP}_{W:N}$ terms are defined similarly. H^{SER}_{W} and H^{SER}_{N} represent the enthalpy of W and N at the stable element reference (SER) conditions (298.15 K and 10^5 Pa), i.e., solid BCC W and N_2 gas, respectively, at 298.15 K and 10^5 Pa, with all subsequent Gibbs energy expressions referenced back to these pure component stable forms. For these elements in their stable reference state at 298.15 K, H^{SER}_{W} and H^{SER}_{N} are defined to be zero.

Table 3-4 shows Gibbs energy models for the W–N solid solution phases. The first three solid phases are solid solutions, each with their own nitrogen homogeneity range on the interstitial sublattice. The fourth phase, SHP (δ) nitride, is a line compound with a fixed nitrogen stoichiometry. Its Gibbs energy expression is listed in Table 3-3 rather than Table 3-4, because no mixing occurs on the interstitial sublattice in this phase.

Table 3-3. General Gibbs Energy Expressions per mol of Formula for Solid W–N Phases.

Phase	Sublattice Model Layout	Gibbs Energy Expression
BCC α–WN$_x$	$(W)_1(N)_3$	${}^{o}G^{BCC}_{W:N} = H^{SER}_{W} + 3H^{SER}_{N} + \Delta{}^{o}G^{BCC}_{WN_3}$
FCC β–WN$_x$	$(W)_1(N)_1$	${}^{o}G^{FCC}_{W:N} = H^{SER}_{W} + H^{SER}_{N} + \Delta{}^{o}G^{FCC}_{WN}$
HCP ε–WN$_x$	$(W)_1(N)_{0.5}$	${}^{o}G^{HCP}_{W:N} = H^{SER}_{W} + 0.5H^{SER}_{N} + \Delta{}^{o}G^{HCP}_{WN_{0.5}}$
SHP δ–WN	$(W)_1(N)_1$	${}^{o}G^{SHP}_{W:N} = H^{SER}_{W} + H^{SER}_{N} + \Delta{}^{o}G^{SHP}_{WN}$

Table 3-4. Mixing Gibbs Energy Expressions per mol of Formula for W–N Solid Solution Phases.

Phase	Sublattice Model Layout	Binary Gibbs Energy Expression
BCC α–WN$_x$	$(W)_1(N,Va)_3$	${}^{o}G^{BCC}_{m} = y_N {}^{o}G^{BCC}_{W:N} + y_{Va} {}^{o}G^{BCC}_{W:Va} +$ $3RT[y_N \ln y_N + y_{Va} \ln y_{Va}] + {}^{xs}G^{BCC}_{m}$
FCC β–WN$_x$	$(W)_1(N, Va)_1$	${}^{o}G^{FCC}_{m} = y_N {}^{o}G^{FCC}_{W:N} + y_{Va} {}^{o}G^{FCC}_{W:Va} +$ $RT[y_N \ln y_N + y_{Va} \ln y_{Va}] + {}^{xs}G^{FCC}_{m}$
HCP ε–WN$_x$	$(W)_1(N, Va)_{0.5}$	${}^{o}G^{HCP}_{m} = y_N {}^{o}G^{HCP}_{W:N} + y_{Va} {}^{o}G^{HCP}_{W:Va} +$ $0.5RT[y_N \ln y_N + y_{Va} \ln y_{Va}] + {}^{xs}G^{HCP}_{m}$
SHP δ–WN	$(W)_1(N, Va)_1$	–

In the three solid solution phases, W occupies one sublattice, and does not undergo mixing, which is evident from a fixed W stoichiometry. The second sublattice contains a combination of N and Va. The Gibbs energy models for the three W–N solid solutions describe mixing of N and Va on the interstitial sublattice of metallic W. The different phase structures result from the variation in structure of the metallic W sublattice with temperature and N content. To account for the N homogeneity range, both N and Va are incorporated into the model for the interstitial sublattice. Table 3-5 shows the temperature dependent expressions for $\Delta^{o}G^{\varphi}_{W:N}$ and $^{o}L^{\varphi}_{W:N,Va}$ reported by Guillermet [1993]. The expressions are based on the regular solution model to address N–Va interactions on the interstitial sublattice, and the value for $^{o}L^{FCC}_{W:N,Va}$ was assumed to be independent of temperature (i.e., strictly regular). A value for $^{o}L^{HCP}_{W:N,Va}$ was not reported.

Table 3-5. Reported Gibbs Energy Parameters per mol of Formula for the Stable W–N Solid Phases [Gui93].

Phase	Sublattice Model Layout	Gibbs Energy (G) and Excess Gibbs Energy (L) Expressions
BCC α–WN$_x$	$(W)_1(N)_3$	$\Delta^{o}G^{BCC}_{W:N} = -268828.908 + 444.62002T$ $-72.7446506\,T\ln(T) + 1079965T^{-1} - .0251743468T^{2}$ $^{o}L^{BCC}_{W:N,Va} = 83285 - 69.977T$
FCC β–WN$_x$	$(W)_1(N)_1$	$\Delta^{o}G^{FCC}_{W:N} = -40752.746 + 259.88468T - 45.443666T\ln T$ $+ 237083T^{-1} - .0046519123T^{2}$ $^{o}L^{FCC}_{W:N,Va} = -61824$
HCP ε–WN$_x$	$(W)_1(N)_{0.5}$	$\Delta^{o}G^{HCP}_{W:N} = -12811.336 + 186.68879T$ $-34.217887T\ln(T) + 105601T^{-1} - .004509875T^{2}$
SHP δ–WN	$(W)_1(N)_1$	$\Delta^{o}G^{SHP}_{W:N} = -66519.085 + 272.76021T - 45.64545T\ln T$ $+ 392513T^{-1} - .0035306184T^{2}$

Note: above expressions are applicable over the temperature range 298.15≤T≤6000 K.

3.5.6 W–N Liquid Phase Model

The Gibbs energy expression for the liquid phase in Equation 3–26 is based on the ideal mixing model, as no experimental data are available to assess any deviations from ideality for the liquid phase:

$$G_m^{liq}(T,P) = x_N\,{}^oG_N^{liq} + x_W\,{}^oG_W^{liq} + RT\left(x_N \ln x_N + x_W \ln x_W\right) \qquad (3\text{–}26)$$

where x_N is the mole fraction of N in the liquid phase and ${}^oG_N^{liq}$ and ${}^oG_W^{liq}$ are temperature and pressure dependent Gibbs energies for pure liquid N and W, as reported previously [Din91,Gus85].

3.5.7 W–N Gas Phase Model

The molar Gibbs energy for each species in the gas phase is represented by Equation 3–27, which assumes ideal gas behavior and is both temperature and pressure dependent:

$${}^oG_{i,m}^{Gas}(T,P) - H_{i,m}^{SER} = {}^oG_{i,m}^{Gas}(T) + RT\ln P \qquad (3\text{–}27)$$

where ${}^oG_{i,m}^{Gas}$ (T,P) is the Gibbs energy per mole of species i at temperature T and pressure P, and $H_{i,m}^{SER}$ is the enthalpy for the pure, stable form of species i at 298.15 K and 10^5 Pa. The ${}^oG_{i,m}^{Gas}$ (T) term can be expanded as follows [Gus85]:

$${}^oG_{i,m}^{Gas}(T,P) - H_{i,m}^{SER} = \left(a + bT + cT\ln T + dT^2 + eT^3 + gT^{-1}\right)_{i,m} + RT\ln P \qquad (3\text{–}28)$$

An expression in the form of Equation 3–28 is generated for each species, and these are put into Equation 3–29 to get an overall Gibbs energy for the gas phase (G_m^{Gas}(T,P)):

$$G_m^{Gas}(T,P) = \sum_i x_i\left({}^oG_{i,m}^{Gas}(T,P) - H_{i,m}^{SER}\right) + RT\sum_i x_i \ln x_i \qquad (3\text{–}29)$$

where x_i is the mole fraction of species i in the gas phase.

3.6 Previous Studies of the W–N Phase Diagram

A phase diagram for the binary W–N system was previously reported, and is shown in Figure 3–2 [Gui93]. This diagram does not consider the presence of the gas phase at low pressure (≤ 10^5 Pa).

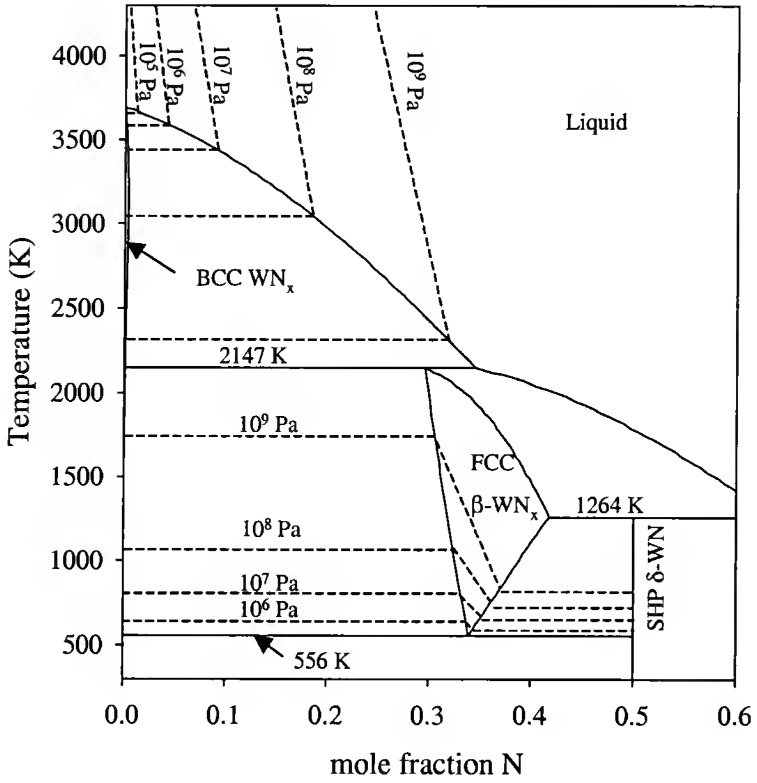

Figure 3–2. Binary phase diagram for the W–N system [Gui93]. The gas phase was not included in this phase diagram.

Adding the gas phase into Guillermet's model while maintaining the pressure at 10^5 Pa (Figure 3–3), it is seen that the liquid phase is replaced by gas, and the FCC β–WN_x phase disappears. The formation of stable FCC β–WN_x in the presence of N_2 gas has been reported, however, (Table 3-6), hence the model used to generate Figure 3–2 and 3–3 must be modified to account for this.

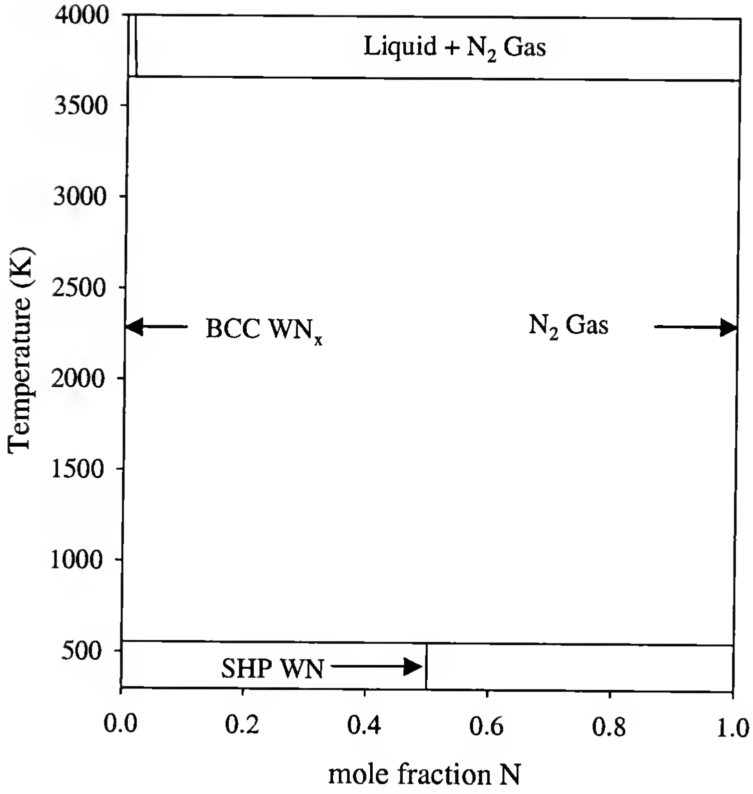

Figure 3–3. Binary phase diagram for the W–N system using Guillermet's model, with the gas phase included.

In addition, the $\Delta^{o}G_{W:N}^{FCC}$, ${}^{o}L_{W:N,Va}^{FCC}$ and $\Delta^{o}G_{W:N}^{SHP}$ terms are modified in this analysis to reflect recently reported experimental data on solid–gas equilibria in the W–N system for the FCC and SHP solid phases. Existing Gibbs energy expressions for the BCC and HCP solid phases, as well as the liquid and gas phases, will not be modified, as no new experimental data have been reported for these.

3.7 W–N Optimization Results and Discussion

FCC β–WN_x Stability Data

As mentioned previously, the desired W–N solid phase for a barrier material is FCC β–WN_x, but in the amorphous state. Various temperatures, pressures and deposition methods have been used to form the FCC β–WN_x phase, and a range of x values in the resulting films has been reported. The temperature, pressure, and stoichiometry ranges reported in the literature must be reflected in the modified phase diagram. Many reports in the literature describe deposition of amorphous WN_x films, with subsequent annealing at various temperatures and pressures leading to formation of one or more of the aforementioned W–N solid phases. In many cases, if the initial amorphous film was nitrogen rich (x in $WN_x > 0.5$), FCC β–$WN_{0.5}$ polycrystals formed with excess N migrating to the grain boundaries, which are disordered regions between the polycrystals in the films. Various techniques, including XPS [Nag93, Nak87] and transmission electron diffraction (TED) [She00b], have been used to differentiate between N at the grain boundary and in the polycrystal. Since grain boundaries are inherently non–equilibrium regions in the film, only data that is available for polycrystalline materials will be used to optimize the phase diagram. Table 3-6 shows the representative temperature, pressure, and stoichiometry ranges for the polycrystalline FCC β–WN_x phase, as reported in the literature, which were used in this assessment. Stable pressure and temperature ranges include conditions during deposition and during post–growth anneals. Operating outside of the stable temperature and pressure ranges for each of the respective references resulted in deposition of multiple phases or phases other than FCC β–WN_x.

As evident in Table 3-6, the upper and lower limits for x in β–WN_x, which were used in this assessment, are 0.72 and 0.43, respectively. Schonberg [1954] first reported a stoichiometry range of $0.5 \leq x \leq 0.72$ for FCC β–WN_x, formed by NH_3 nitridation of W at 800°C. Although the pressure for this process was not specified, Banik et al. [1979] reported a pressure of 1×10^8 Pa to form FCC β–$WN_{0.5}$ by NH_3 nitridation of W. The

Table 3-6. Stable Existence Regions for FCC β–WN$_x$ Used in Assessment

Value of x in FCC β–WN$_x$	Stable Temperature Range (K)	Stable Pressure Range (Pa)	FCC β–WN$_x$ Deposition Method	Reference
$0.43 \le x \le 0.72$	$556 \le T \le 2147$*	$10^5 \le P \le 10^9$	N/A (Assessment of Lattice Parameter Data)	[Gui93]
x=0.5	473	7	Sputtering	[Lin90]
x=0.5	$473 \le T \le 1073$	$6.6\times10^{-5} \le P \le 7.9\times10^{-1}$	Sputtering	[She00b]
x=0.5	613	Not reported	PECVD (WF_6+N_2+ H_2)	[Li00]
x=0.5	673	2.6×10^{-1}	Sputtering	[Tak97a]
x=0.5	≤ 923	1.3	Sputtering	[Kat85]
x=0.5	≤ 1073	$6.6\times10^{-1} \le P \le 2.0$	Sputtering	[So88]
x=0.5	≤ 1123	6.6×10^{-1}	Sputtering	[Suh99, Suh01]
$0.5 \le x \le 0.71$	500 ± 20	0.66	Sputtering	[Hon03]
$0.5 \le x \le 0.72$	1073	Not reported	NH_3 Nitridation of W Powder	[Sch54]
0.54	723	Not reported	Sputtering	[Bak02]

*Note that the gas phase was not included in the equilibrium calculation for this system at low pressures ($\le 10^5$ Pa).

pressure used by Schonberg is therefore assumed to have been substantially higher than atmospheric, which precludes use of this temperature and pressure data point in our analysis. The stoichiometry range, however, will be used, as it was recently confirmed by low–pressure sputter deposition (Table 3-6 [Hon03]). Guillermet [1993] generated a W–N phase diagram depicting the FCC β–WN$_x$ phase, which was referred to as the γ nitride, with a homogeneity range of $0.43 \le x \le 0.72$. This range was based on a review by Wriedt [1989], which incorporated lattice parameter data from several reports [Hag30, Khi59, Kie51, Sch54]. This phase diagram, however, excluded the gas phase at low pressures, and focused only on solid–liquid equilibrium, with pressures ranging from 10^5

to 10^9 Pa. Experimentally, the liquid phase is not observed at 10^5 Pa, as N prefers to exist in the gas phase as N_2 at high temperature, rather than forming a melt with W. Recent experimental studies have indicated that the stability range for formation of FCC β–WN_x at low pressures (10^5 Pa and below) extends from 473 (200°C) to 1123 K (850°C) [She00b, Suh01]. Hones et al. [2003] reported that the highest nitrogen content for FCC β–WN_x was $x=0.71$, and increasing nitrogen content to $x\approx0.75$ caused formation of a second phase, SHP δ–WN. These reports indicate that the stability region for FCC β–WN_x is larger than previously thought, and that previously accepted thermodynamic stability limits for this phase may have actually been kinetic limits on the formation of this phase due to experimental design. Previous thermodynamic assessments of the W–N system typically involved experimental formation of FCC β–WN_x by NH_3 (or N_2) nitridation of BCC W at high temperature and pressure over long periods of time (typically several weeks) [Sch54, Ban79]. The formation of FCC β–WN_x from BCC W and N_2 gas was predicted to occur at 1100°C and 10^8 Pa, with the high temperature and pressure required to dissociate N_2 [Ban79]. These processes required high temperature and pressure, owing to the need to break W–W bonds in the solid and N–H or N–N bonds in the gas before W–N bonds could form. After overcoming any strain energy in the solid and breaking the W–W bonds, nitride formation was then able to occur. While formation of FCC β–WN_x by these routes requires high temperature and pressure, this likely reflects a kinetic barrier to the NH_3 (or N_2) nitridation process, rather than a thermodynamic stability limit. Newer deposition techniques, such as sputtering, PECVD, LPCVD, MOCVD, and ion implantation have established low temperature and low–pressure kinetic routes to the formation of FCC β–WN_x. Sputtering, for example, uses plasma energy to break the strong bond in gaseous N_2, liberating atomic nitrogen, which is then free to react with W atoms emanating from the sputtered target to form tungsten nitride films. Sputtered films containing the FCC β–WN_x phase have been deposited at a temperature as low as 200°C [She00b], and are reported to remain intact after annealing at temperature to 850°C under UHV conditions (6.6×10^{-5} Pa) [She00b, Suh99, Suh01]. Recent reports use high temperature vacuum anneals (typically 30 min) to establish temperature stability limits for the deposited phases. Although annealing for a longer time (days or weeks) would give more confidence that equilibrium existed, the data are only available for these short anneals. Hence, these high temperature anneals will be assumed to approximate equilibrium to assess the system at low pressure. Considering available experimental data in the literature, the most robust low–pressure phase diagram should contain an FCC β–WN_x solid solution with a temperature range of 473 to 1123 K (200 to 850°C), a composition range $0.43\leq x\leq0.72$, and be stable at a total system pressure of 6.6×10^{-5} Pa.

Several other reports on the stoichiometry and temperature stability of β–WN_x phase were considered but excluded from this analysis. In addition to the stoichiometry range reported in Table 3-6, Hones et al. [2003] also reported the deposition of overstoichiometric ($x>1$) FCC β–WN_x films, where additional N incorporated into tetrahedral holes in the interstitial sublattice. Substoichiometric films had increasing hardness with x, while hardness dropped for overstoichiometric films, which were partially delaminated from their substrates. The overstoichiometric films are therefore considered to be metastable, and are not included in this assessment. One report of MOCVD grown FCC β–$WN_{1.0}$ was given based on an XRD lattice parameter of 4.154 Å and composition ratios from WDS [Chi93]. Reported AES concentrations were 12 at. % for both C and N, which did not agree with WDS values [Chi92]. The presence of C in these films suggests that formation of a β–WN_xC_y solid solution, where C intermixes with N on the polycrystal's interstitial sublattice [Hua97, Jon93], may have occurred. Incorporation of C on the interstitial sublattice expands the polycrystal lattice, resulting in a larger lattice parameter for β–WN_xC_y films relative to β–WN_x, assuming a fixed number of occupied interstitial sites. Their reported lattice parameter expansion, interpreted as a binary β–$WN_{1.0}$ stoichiometry, may have actually been due to the formation of a ternary β–WN_xC_y solid solution, hence this data point will be excluded from the phase diagram analysis.

A report of FCC β–$WN_{0.5}$ deposition at 150°C and 27 Pa has also been given [Bai03]. The film was deposited by PECVD, using WF_6, NH_3 and H_2 on a SiO_2 substrate. Their XRD spectrum, however, suggests formation of W_3O rather than FCC β–W_2N. The formation of this oxide was likely due to the presence of oxygen in the SiO_2 substrate. Another report on PECVD grown β–WN_x films indicated an upper stability limit of 1000°C after annealing for 60 sec in a N_2 atmosphere [Gal00]. The annealing pressure was not specified, however, so this data point was omitted. Another report gave 1050°C as the upper stability limit for FCC β–$WN_{0.5}$ [Vie02]. While an XRD spectrum indicated peaks consistent with FCC β–$WN_{0.5}$ after heating to 1050°C, the heating process was done in a differential scanning calorimeter (DSC) under an $N_2 + H_2$ atmosphere, at an unreported pressure. Since this temperature limit may reflect enhanced stability of FCC β–$WN_{0.5}$ due to the pressure of the $N_2 + H_2$ atmosphere, this data point will also be excluded from the analysis.

SHP δ-WN Stability Data

Table 3-7 shows representative temperature, pressure, and stoichiometry ranges for the polycrystalline SHP δ–WN phase, as reported in the literature, which were used in this assessment. Stable pressure and temperature ranges include conditions during growth and annealing. Lee [1995] formed the SHP δ–WN phase by PECVD of WF_6+NH_3+H_2. XRD results for their as–deposited films indicated SHP WN in equilibrium with FCC β–$WN_{0.5}$ and β–W, but the SHP δ–WN peak disappeared after annealing at 500°C and 6.6×10^1 Pa. Shen et al. [2000a] also reported formation of SHP δ–WN, with subsequent decomposition to β–$WN_{0.5}$ + N_2 after annealing at 550°C at 6.6×10^{-5} Pa. Considering available information in the literature, the most robust low–pressure phase diagram should contain the SHP δ–WN phase with an upper temperature limit of 823 K (550°C) at a total system pressure of 6.6×10^{-5} Pa.

Table 3-7. Stable Existence Regions for SHP δ–WN Used for Assessment.

Stable Temperature Range (K)	Stable Pressure Range (Pa)	SHP δ–WN Deposition Method	Reference
$0 \leq T \leq 1264$*	$10^5 \leq P \leq 10^9$	N/A (assessment)	[Gui93]
473	7	Sputtering	[Lin90]
500 ± 20	6.6×10^{-1}	Sputtering	[Hon03]
≤ 773	6.6×10^1	PECVD WF_6+NH_3+H_2	[Lee95]
≤ 773	2.7×10^{-1}	Sputtering	[Uek96]
≤ 823	$6.6\times10^{-5} \leq P \leq 7.9\times10^{-1}$	Sputtering	[She00a]

*Note that the gas phase was not included in the equilibrium calculation for this system at low pressure (≤ 10^5 Pa).

Several other reports on the stoichiometry and temperature stability of δ–WN phase were considered but excluded from this analysis. Schonberg [1954] reported the formation of SHP δ–WN in equilibrium with BCC W and FCC β–$WN_{0.5}$ by NH_3

nitridation of W at 800°C, but the pressure for this process was not specified. Schonberg also reported rapid decomposition of the SHP δ–WN phase during a 600°C anneal in "vacuum." Banik et al. [1979] reported a pressure of 1×10^{8} Pa to form FCC β–$WN_{0.5}$ by NH_3 nitridation of W. The pressure used by Schonberg is therefore assumed to have been substantially higher than atmospheric; hence this data point will be excluded in this low–pressure assessment. Zhang et al. [1999] reported the formation of SHP δ–WN by N ion implantation into a W surface at 3.4×10^{-3} Pa, but the substrate temperature was not specified. One report of δ–WN deposition by sputtering onto a room temperature (T=20°C) GaAs substrate was also given [Gal93]. This report relied solely on SIMS data for the deposited film, and inferred the crystal structure based on W/N ratio. Since XRD analysis was not provided for this film, the data point will be excluded from this analysis.

Assessed W-N Phase Diagram

As mentioned above, the new literature data indicates that the FCC β–WN_x solid solution should have a temperature range of 473 to 1123 K (200 to 850°C), a composition range $0.43\leq x\leq0.72$, and be stable at a total system pressure of 6.6×10^{-5} Pa. Moreover, the SHP δ–WN phase should have an upper temperature limit of 823 K (550°C) at a total system pressure of 6.6×10^{-5} Pa. The values for $\Delta^{o}G^{FCC}_{W:N}$, $^{o}L^{FCC}_{W:N,Va}$ and $\Delta^{o}G^{SHP}_{W:N}$ terms were modified through use of ThermoCalc's Parrott optimization module to reflect the new data.

Figure 3–4 shows the new W–N solid–gas phase diagram based on the assessment of the data listed in Table 3-6 and 3–7, at the lowest reported stable pressure for the FCC and SHP phases. The left side of the diagram contains a very narrow existence region for BCC WN_x between 0 and 3695 K, which is not visible. Above 3695

K, the left side of the diagram contains a narrow region representing a liquid W–N solution, which again is not visible. The right side of the diagram is N_2 gas over the entire temperature range. The FCC β–WN_x phase, which did not previously appear in equilibrium with the gas phase (Figure 3–3), now appears with a finite homogeneity range. The FCC β–$WN_{0.5}$ phase/stoichiometry exists in equilibrium with BCC WN_x and SHP WN at 473 K. The horizontal line at 1123 K represents a three–phase equilibrium between BCC WN_x, FCC β–WN_x, and N_2 gas. FCC β–$WN_{0.5}$ is reported to decompose under vacuum to BCC W and N_2 gas at 1123 K (850°C) [Suh99, Suh01], but a small concentration of dissolved N likely remains in the BCC W, as indicated by the BCC WN_x phase on the left side of the diagram. The SHP δ–WN phase is known to decompose to FCC β–$WN_{0.5}$ and N_2 gas at high temperature under vacuum [Gol67, She00d], and this is

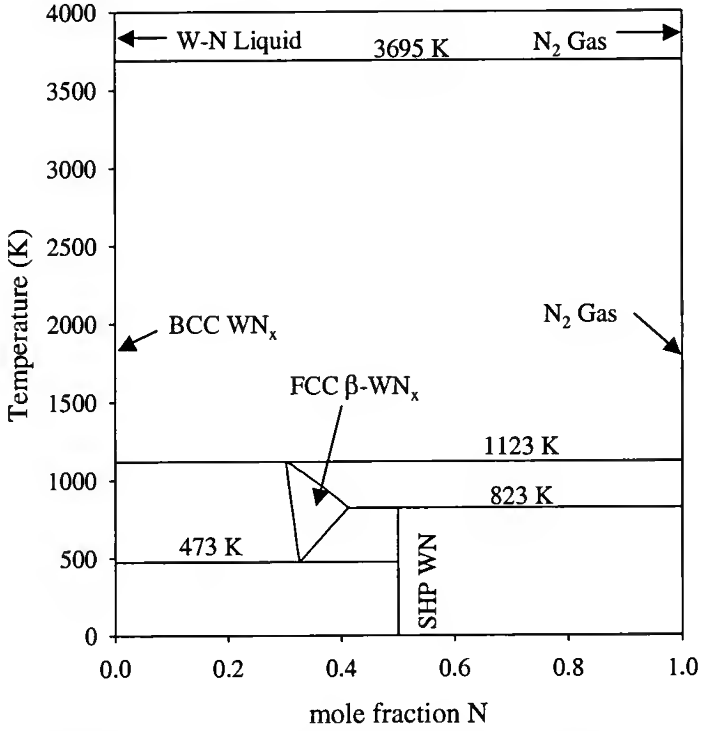

Figure 3–4. Binary phase diagram for the W–N system at 6.6×10^{-5} Pa, using new data with the gas phase included.

indicated on the new diagram. The upper temperature limit for the SHP δ–WN phase, previously 651 K (Figure 3–3), is now 823 K, reflecting enhanced stability for this phase per recent experimental reports.

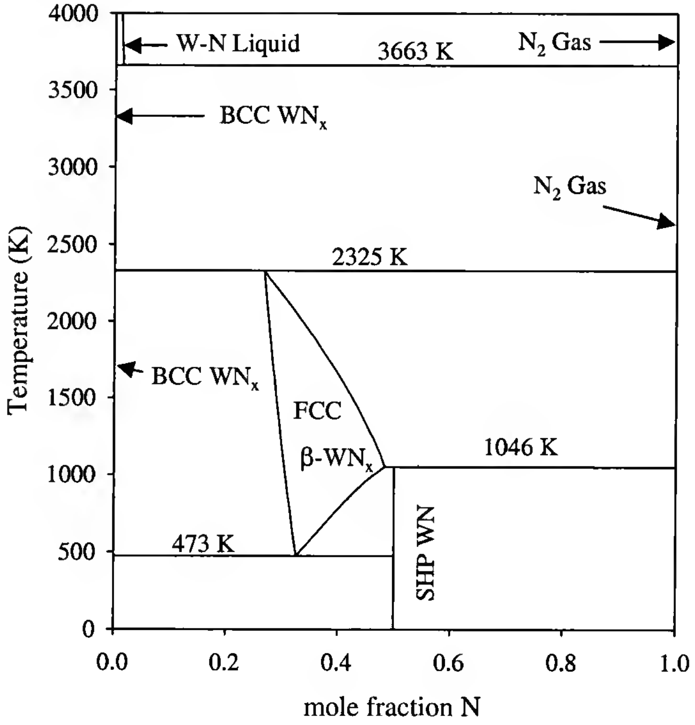

Figure 3–5. Binary phase diagram for the W–N system at 10^5 Pa, using new data with the gas phase included.

Increasing pressure in the W–N solid–gas system from 6.6×10^{-5} to 10^5 Pa causes an expansion in the stability range of FCC β–WN_x (Figure 3–5). The upper temperature limit for this phase increases from 1123 K at 6.6×10^{-5} Pa to 2325 K at 10^5 Pa. Interestingly, this upper temperature limit is close to 2147 K, the upper limit reported for the FCC β–WN_x phase in the solid–liquid system at 10^5 Pa [Gui93]. In addition to the increased upper temperature limit, the upper solubility limit of N in the FCC β–WN_x phase increases with increased pressure, increasing from x=0.72 to x=0.92, which is approaching the stoichiometry for SHP δ–WN formation. The upper temperature limit for the SHP δ–WN phase also increased with pressure, rising from 823 K at 6.6×10^{-5} Pa to 1046 K at 10^5 Pa.

The new expressions for $\Delta^{o}G_{W:N}^{FCC}$, ${}^{o}L_{W:N,Va}^{FCC}$ and $\Delta^{o}G_{W:N}^{SHP}$ generated by this assessment are listed in Table 3-8. To achieve an adequate fit for the model to the new experimental data, the parameter describing N–Va interactions on the FCC interstitial sublattice was given a temperature dependent expression, whereas this was previously assigned a constant value by Guillermet [1993].

Table 3-8. Modified W–N Gibbs energy expressions (J/mol of formula) generated by this work.

Phase	Sublattice Model Layout	Gibbs Energy (G) and Interaction Parameter (L)
FCC β–WN$_x$	$(W)_1(N)_1$	$\Delta^{o}G_{W:N}^{FCC} = -124063.4 - 100.74T$ ${}^{o}L_{W:N,Va}^{FCC} = -68362.39 - 9.01T$
SHP δ–WN	$(W)_1(N)_1$	$\Delta^{o}G_{W:N}^{SHP} = -163975.23 - 63.38T$

Note: the above expressions are applicable over a temperature range of $298.15 \leq T \leq 6000$.

If Equation 3–23 is written for the FCC phase, Equation 3–30 results:

$$G_m^{FCC} = y_N{}^I G_{W:N}^{FCC} + y_{Va}{}^I G_{W:Va}^{FCC} + RT\left(y_N{}^I \ln y_N{}^I + y_{Va}{}^I \ln y_{Va}{}^I\right) + y_N{}^I y_{Va}{}^I\, {}^{o}L_{W:N,Va}^{FCC} \quad (3–30)$$

To obtain the Gibbs energy for the FCC β–WN$_{0.5}$ stoichiometry, for example, substitute $y_N{}^I = y_{Va}{}^I = 0.5$, the expression for $G_{W:Va}^{FCC}$ from Table 3-2, and the expressions for $\Delta^{o}G_{W:N}^{FCC}$ and ${}^{o}L^{FCC}$ from Table 3-8. Simplifying gives Equation 3–31:

$$\begin{aligned} G_m^{FCC} &= -73295.45 + 7.13T - 12.05T\ln T - 9.68\times10^{-4}T^2 + 1.04\times10^{-7}T^3 \\ &+ \frac{22250}{T} - 2.67\times10^{-11}T^4 \end{aligned} \quad (3–31)$$

This value is in J/mol of formula for FCC β–$WN_{0.5}$ (1 mole W + 0.5 mol N). To convert this Gibbs energy to J/mol of formula units for β–W_2N, this value must be multiplied by 2.

A comparison of the enthalpies of formation for the FCC and SHP phases reported in the literature against those generated by this assessment is shown in Table 3-9. Lakhtin [1979] and Neumann [1934] gave ΔH_f values for FCC β–W_2N in units of J/mol of formula (i.e., 2 W atoms, 1 N atom). Their values were divided by 2 to convert them to a J/mol of formula for FCC β–$WN_{0.5}$.

The new $\Delta°H_f$ (298) values for FCC β–$WN_{0.5}$ and SHP δ–WN generated by this work, as shown in Table 3-9, indicate greater stability of these phases than previously reported. This reflects the ability of new deposition techniques to overcome kinetic barriers to form these phases, as discussed above.

Table 3-9. Comparison of reported and calculated heats of formation ($\Delta°H_f$) for FCC β–$WN_{0.5}$ and SHP δ–WN phases.

Phase & Formula	$\Delta°H_f$ (298), kJ/mol of formula	Basis	Reference
FCC β–$WN_{0.5}$	−18.9	Assessment	[Gui93]
	−33.0	Ab Initio Calculation	[deB88]
	−36.0	Assessment	[Lak79]
	−35.6	Calculation based on experimental data of non–W metal nitrides	[Neu34]
	−69.5	Assessment	This Work
SHP δ–WN	−15.0	Ab Initio Calculation	[deB88]
	−24.0	Assessment	[Gui93]
	−82.0	Assessment	This Work

Figure 3–6 plots the trend of $\Delta°H_f(298)$ for nitrides of neighboring metals on the Periodic Table. The slope of the line connecting $\Delta°H_f(298)$ for ZrN, NbN and MoN is 158, while the slope for the line connecting HfN, TaN and our value for β–$WN_{0.5}$ is 150.

Table 3-10. Enthalpies of Formation for Several Neighboring FCC Nitrides

Compound	Atomic Number of Metal	$\Delta°H_f$ (298), kJ per mole of metal atom	Reference
FCC ZrN	40	−365	[Pie96]
FCC NbN	41	−229	[Ino01]
FCC MoN	42	−49	[Fri91]
FCC HfN	72	−369	[Pie96]
FCC TaN	73	−215	[Fri98]
FCC $WN_{0.5}$	74	−70	This Work
FCC $WN_{0.5}$	74	−35	[Neu34]
FCC $WN_{0.5}$	74	−18	[Gui93]

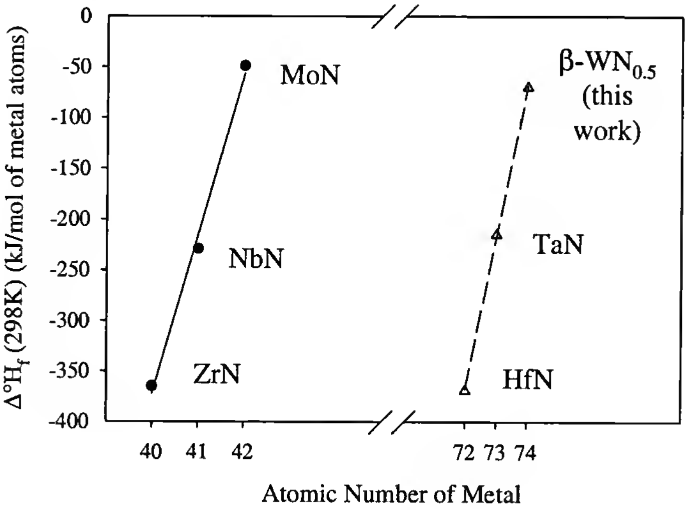

Figure 3–6. Trend of $\Delta°H_f$ (298) for nitrides of neighboring metals on the Periodic Table.

Replacing our value of $\Delta°H_f(298)$ with that for β–$WN_{0.5}$ from Guillermet [1993] gives a slope of 176, while the value from Neumann [1934] gives 167. The trend on the periodic table suggests that the value generated by this work, and that given by Neumann [1934], are closer to the trend than that given by Guillermet [1993]. Since our new value incorporates experimental composition data rather than being based on assessment of neighboring nitrides, it would appear that our new $\Delta°H_f(298)$ may be closer to the actual value than that suggested by Neumann [1934].

3.8 Stable Solid Phases in the W–C System

The same solid phase structures discussed previously for the W and the W–N system also apply to the W–C system, with C replacing N on the interstitial sites in the metal sublattice. The pure, stable form of C at 298.15 K and 10^5 Pa is solid graphite.

The same solid phases described for the binary nitride exist for the binary carbide. The Gibbs energy model describing these phases is given in Table 3-11. The general Gibbs energy expressions for the solid W–C phases are given in Table 3-12, while the specific expressions for the W–C solid solution phases are given in Table 3-13. Gibbs energy parameters reported in the literature for the W–C solid phases are given in Table 3-14. The BCC WC_x phase is stable at all temperatures up to the solidus (3422°C), and has a lattice parameter of 3.158 Å [Gol63]. The reported solubility of C in BCC WC_x, based on experimental measurements, ranges from 0.05 at. % at 2273 K (2000°C) to a maximum of 0.7 at.% at the eutectic temperature, 2983 K (2710°C) [Geb66, Gol63]. The relationship between temperature and carbon solubility in the BCC WC_x phase was reported as:

$$\ln c_{max} = 4.67 - \frac{15x10^3}{T(K)} \qquad (3\text{–}32)$$

where c_{max} is maximum concentration in at. % and T is temperature in K.

The FCC β–WC_x phase (also called β–WC_{1-x}) has a defective NaCl structure, with a lattice parameter of 4.236 Å for β–$WC_{0.6}$ [Gus86, JCP88, Rud67, Tot71]. Toth [1971] reported this phase with 38 at.% C (x in β–WC_x is 0.61), while Gustafson [1986] reported C content ranging from 37 to 39 at. % ($0.59 \leq x \leq 0.64$). Pauleau [1992] found the maximum C content in β–WC$_x$ to be ~ 40 at. % ($x = 0.67$), while Sara [1965] reported this phase with an "approximate" maximum of 41 at.% C ($x=0.70$). Overall, this phase has a reported C content ranging from 38 to 41 at. %, corresponding to a homogeneity range in β–WC$_x$ of $0.60 \leq x \leq 0.70$ [Gus86, JCP88, Rud67, Sar65, Tot71].

The SHP δ–WC phase has a hexagonal structure with lattice parameters a=2.906 Å and c=2.837 Å [Tot71]. Gustafson [1986] considered this phase to be a stoichiometric line compound with formula WC, as did Toth [1971].

Table 3-11. Solid Phases Considered in the W–C Binary Model

Condensed Phase	Sublattice Model Layout
BCC solid solution	$(W)_1(C,Va)_3$
FCC (γ or β) carbide	$(W)_1(C,Va)_1$
HCP (ε) carbide	$(W)_1(C,Va)_{0.5}$
SHP (δ) carbide	$(W)_1(C)_1$
Graphite	$(C)_1$

Table 3-12. General Gibbs Energy Expressions (J/mol of formula) for Solid W–C Phases.

Phase	Sublattice Model Layout	Gibbs Energy Expression
BCC α–WC$_x$	$(W)_1(C)_3$	$^{o}G^{BCC}_{W:C} = H^{SER}_{W} + 3H^{SER}_{C} + \Delta^{o}G^{BCC}_{WC_3}$
FCC β–WC$_x$	$(W)_1(C)_1$	$^{o}G^{FCC}_{W:C} = H^{SER}_{W} + H^{SER}_{C} + \Delta^{o}G^{FCC}_{WC}$
HCP ε–WC$_x$	$(W)_1(C)_{0.5}$	$^{o}G^{HCP}_{W:C} = H^{SER}_{W} + 0.5H^{SER}_{C} + \Delta^{o}G^{HCP}_{WC_{0.5}}$
SHP δ–WC	$(W)_1(C)_1$	$^{o}G^{SHP}_{W:C} = H^{SER}_{W} + H^{SER}_{C} + \Delta^{o}G^{SHP}_{WC}$

While the HCP WC$_x$ phase is considered stable, three separate forms of this phase have been reported. The high temperature form exists above 2750 K, the low temperature phase exists below 2350 K, and the third phase exists between these temperatures [Gus86]. Gustafson [1986] treated this as a single phase containing a random interstitial solution of carbon in HCP tungsten, with a stoichiometry range of

$0.37 \leq x \leq 0.50$. A similar approach will be taken here. Lattice parameters near a=3.00 Å and c=4.73 Å have been reported for the HCP W_2C stoichiometry [JCP88, Gus86, Tot71]. Huang [1997] and Frisk [1999b] considered this phase to be stable for calculation of the Nb–W–C–N and Ta–W–C–N phase diagrams, respectively.

Table 3-13. Mixing Gibbs Energy Expressions (J/mol of formula) for W–C Solid Solution Phases.

Phase	Sublattice Model Layout	Binary Gibbs Energy Expression
BCC WC_x	$(W)_1(C,Va)_3$	${}^{o}G_{m}^{BCC} = y_C {}^{o}G_{W:C}^{BCC} + y_{Va} {}^{o}G_{W:Va}^{BCC} +$ $3RT[y_C \ln y_C + y_{Va} \ln y_{Va}] + {}^{xs}G_{m}^{BCC}$
FCC β–WC_x	$(W)_1(C, Va)_1$	${}^{o}G_{m}^{FCC} = y_C {}^{o}G_{W:C}^{FCC} + y_{Va} {}^{o}G_{W:Va}^{FCC} +$ $RT[y_C \ln y_C + y_{Va} \ln y_{Va}] + {}^{xs}G_{m}^{FCC}$
HCP WC_x	$(W)_1(C, Va)_{0.5}$	${}^{o}G_{m}^{HCP} = y_C {}^{o}G_{W:C}^{HCP} + y_{Va} {}^{o}G_{W:Va}^{HCP} +$ $0.5RT[y_C \ln y_C + y_{Va} \ln y_{Va}] + {}^{xs}G_{m}^{HCP}$
SHP δ–WC	$(W)_1(C, Va)_1$	–

Table 3-14. Reported Gibbs energy parameters (J/mol of formula) for the stable W–C solid phases [Gus86].

Phase	Sublattice Model Layout	Gibbs Energy (G) and Excess Gibbs Energy (L) Expressions
BCC WC_x	$(W)_1(C)_3$	$\Delta {}^{o}G_{W:C}^{BCC} = 3.751x10^5 - 35.87T$
FCC β–WC_x	$(W)_1(C)_1$	$\Delta {}^{o}G_{W:C}^{FCC} = -17864 + 1.875T$ ${}^{o}L_{W:C,Va}^{FCC} = -17.98T$
HCP WC_x	$(W)_1(C)_{0.5}$	$\Delta {}^{o}G_{W:C}^{HCP} = -13430 - 13.3T$ ${}^{o}L_{W:C,Va}^{HCP} = 8330$
SHP δ–WC	$(W)_1(C)_1$	$\Delta {}^{o}G_{W:C}^{SHP} = -58192 + 287.16T - 46.48T\ln T$ $-.0021435T^{2} - 9.2217x10^{-8}T^{3} + 590500T^{-1}$

Note: above expressions are applicable over temperature range of $298.15 \leq T \leq 6000$ K.

3.8.1 Liquid Solution in the W–C System

The W–C liquid phase was previously modeled using a substitutional solution model [Fri99b, Gus86, Hua97]. The regular solution approximation was applied, which assumes that component interactions are independent of composition. No experimental data for a W–C liquid phase have been generated by our work, hence the existing liquid model will be included in the present study without modification.

3.8.2 Gas Phase in the W–C System

The gas phase model for the W–C system is constructed in the same manner as that for the W–N system. The gas phase species included in this analysis were C_1, C_2, C_3, C_4, C_5 and W, following previous work [Jon96b]. The gas phase was treated as an ideal mixture, with Gibbs energies for the gas phase species taken from the SGTE database [Ans87].

3.8.3 W–C Liquid Solution Model

The Gibbs energy for the liquid phase is based on the ideal mixing model, as no experimental data are available to assess any deviations from ideality for this phase:

$$G_m^{liq}(T,P) = x_C\,{}^{o}G_C^{liq} + x_W\,{}^{o}G_W^{liq} + RT\left(x_C \ln x_C + x_W \ln x_W\right) \qquad (3\text{–}33)$$

where x_c is the mole fraction of C in the liquid phase and ${}^{o}G_C^{liq}$ and ${}^{o}G_W^{liq}$ are temperature and pressure dependent Gibbs energies for the pure liquid C and W phases, as reported previously [Din91, Gus85].

3.9 Previous Study of the W–C Phase Model

The reported binary W–C diagram, which was modeled with ThermoCalc and assessed against experimental data, is shown in Figure 3–8 [Gus86]. The HCP, SHP and FCC phases are all evident in the diagram. While a small homogeneity range is evident for FCC β–WC_x between 2800 and 3000 K, this phase does not appear at the low temperature end of the phase diagram.

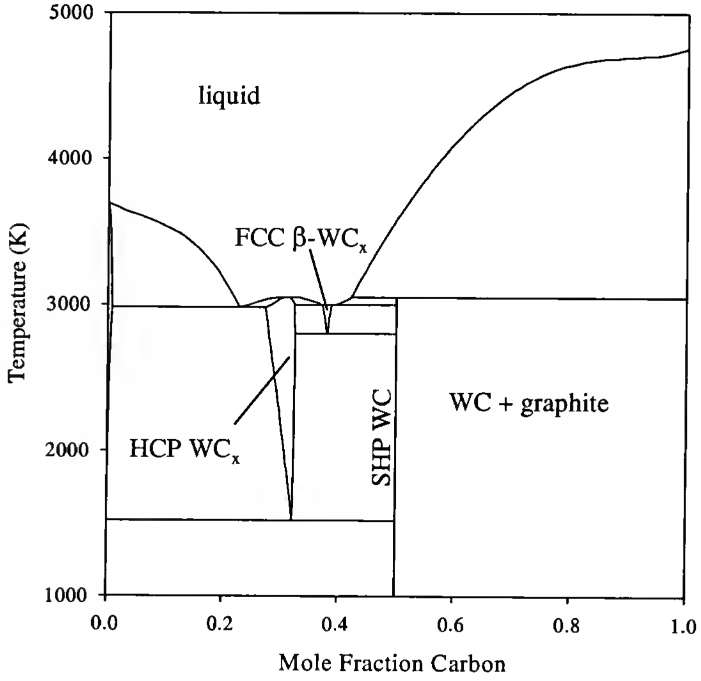

Figure 3–7. Binary phase diagram for the W–C system [Gus86]. The β–WC_x phase was labeled "WC_{1-x}" in the original diagram by Gustafson.

As shown in Table 3-15, however, recent experimental results indicate the existence of a low–temperature stability region for FCC β–WC_x. Qin et al. [1998] found β–WC_x composition to vary from β–$WC_{0.2}$ (β–$W_{0.83}C_{0.17}$) to β–$WC_{0.6}$ (β–$W_{0.62}C_{0.38}$) for films deposited by PECVD of $W(CO)_6$ + H_2 at 330°C. Carim et al. [1989] formed the β–WC_x phase at 4×10^{-3} Torr by sputtering alternating layers of W and C onto a Si (111) substrate. The bulk sample temperature was ~150°C, but the temperature at the surface was not measured, and may have been slightly higher. Moreover, Pauleau and Gouy–Pailler [1992] reported formation of the β–WC_x phase on polished stainless steel substrates by reactive sputtering of a tungsten target in an Ar/CH_4 gas mixture. The substrate temperature ranged from 200 to 250°C. Srivastava et al. [1984] also reported deposition of β–WC_x films by RF magnetron sputtering. These films were deposited on stainless steel substrates at 400 to 500°C and a pressure of 2×10^{-2} Torr. Reniers [1996] reported formation of β–WC$_x$ by reactive sputtering of an Ar/CH$_4$ gas mixture onto W foil. Vieira [2002] reported formation of β–WC$_x$ by sputtering of a W–C target. This phase decomposed at 845°C to form SHP WC + HCP W$_2$C, although the pressure for this transformation was not given. One report, which was not included in Table 3-15, gave an XRD spectrum with a broad peak near $2\theta = 38°$ [Sun01b]. While they reported deposition of SHP WC and HCP WC$_{0.5}$, the peak location actually suggests FCC WC$_x$ deposition. Overall, these reports indicate the possibility of β–WC$_x$ formation at much lower temperature than reported in the existing phase diagram [Gus86], which indicates the ability of sputtering, as a "kinetic helper," to form these phases at low temperature. This indicates a need for reassessment of the low temperature end of the W–C binary phase diagram; the currently available data, however, are inadequate to establish the temperature, pressure and composition boundaries of the FCC β–WC$_x$ phase.

Table 3-15. Stable Low Temperature Existence Regions for FCC β–WC$_x$

Value of x in FCC β–WC$_x$	Stable Temperature Range (K)	Stable Pressure Range (Pa)	FCC β–WC$_x$ Deposition Method	Reference
$0.20 \le x \le 0.60$	603	NR	PECVD W(CO)$_6$+H$_2$	[Qin98]
$x = 0.67$	473–523	NR	Sputtering of W in CH$_4$/Ar	[Pau92]
NR	~423	0.53	Sputtering of W and graphite	[Car89]
NR	673–773	2.7	Sputtering of W in C$_2$H$_2$/Ar	[Sri84]
NR	1118	NR	Sputtering of W–C target	[Vie02]
NR	NR	NR	Sputtering of W in CH$_4$/Ar	[Ren96]

NR = not reported

3.10 Equilibrium in the W–C–Cl–H–N System

To model equilibrium in our reactor, all of the stable solid, liquid and gas phase species in the W–C–Cl–H–N system were included. Stable solid phases in the binary W–N and W–C systems were discussed above, but a C–N phase diagram, which would address the third binary side of the ternary W–C–N phase diagram, is unavailable. While carbon nitride (CN_x) deposition has been reported, these phases are typically amorphous and/or metastable [Jel00, Nin02]. Hence, carbon nitride solid phases will be excluded from this analysis in favor of tungsten carbides, nitrides and carbonitrides with various lattice structures. In addition, other potential solid phases formed by addition of Cl and H to the ternary W–C–N subsystem will be included. While some CVD equilibrium models exclude the liquid phase from consideration due its presumed absence during reaction, all potential liquid and gas phase species from the Sub94 database will be included in this analysis for completeness.

3.10.1 Stable Solid Phases in the W–C–Cl–H–N System

Thermodynamic properties for several solid phases, including tungsten chlorides of different stoichiometries and ammonium chloride (NH_4Cl), were taken from the Sub94 database in ThermoCalc. Gibbs energy expressions for pure, solid W, graphite and diamond–like C phases were taken from the SGTE database [Din91]. In addition to these phases, several stable forms of tungsten nitride and carbide, as discussed above, as well as tungsten carbonitride, have been reported in the literature. The solid species included in this analysis are listed in Table 3-16. As shown in Table 3-16, no evidence of new ternary W–C–N phases has been given, but mixing of C and N on the interstitial sublattices of the previously described W–N and W–C solid phases (Figure 3–1) has been reported [Fri99b, Hua97, Jon93, 96b]. Implicit in the description of the stable HCP carbonitride phase is the assumption that the HCP WN_x phase is considered to be stable due to the stability of its HCP carbide analog. Jonsson [1993, 1996b] first predicted phase equilibrium in the W–C–N system, although no experimental data were available for assessment. Two W–C–N phase diagrams were generated at 2873 K; one excluded the gas phase from consideration, while the other included the gas phase at 1000 bar pressure. Both diagrams indicated the presence of ternary SHP WN_xC_{1-x} and HCP

Table 3-16. Solid Phases Considered in the Model for W–C–Cl–H–N

Solid Phase	Data Source
NH_4Cl_1	[Lid85], [Sub 94 Database]
NH_4Cl_2	[Lid85], [Sub 94 Database]
WCl_2	[Sub 94 Database]
WCl_3	[Sub 94 Database]
WCl_4	[Sub 94 Database]
WCl_5	[Sub 94 Database]
WCl_6 (α1)	[Sub 94 Database]
WCl_6 (α2)	[Sub 94 Database]
WCl_6 (β)	[Sub 94 Database]
Graphite	[Din91]
Diamond–like carbon	[Din91]
BCC α–W	[Din91]
FCC β–W	[Gus85]
HCP ε–W	[Gus85]
BCC α–WN_x	[Gui93]
FCC β–WN_x	This Work
HCP ε–WN_x	[Gui93]
SHP δ–WN	This Work
BCC α–WC_x	[Gus86]
FCC β–WC_x	[Gus86]
HCP ε–WC_x	[Gus86]
SHP δ–WC	[Gus86]
BCC α–WN_xC_y	[Fri99b, Hua97, Jon93, 96b]
FCC β–WN_xC_y	[Fri99b, Hua97, Jon93, 96b]
HCP ε–WN_xC_y	[Fri99b, Hua97, Jon93, 96b]
SHP δ–WN_xC_{1-x}	[Fri99b, Hua97, Jon93, 96b]

WN_xC_y phase fields, but neither indicated an FCC β–WN_xC_y phase field. None of these models included C–N or C–N–Va interaction parameters, but instead assumed ideal mixing on the interstitial sublattice.

Several quaternary thermodynamic analyses involving the W–C–N subsystem have also been performed, including the Ti–W–C–N, Nb–W–C–N and Ta–W–C–N systems [Fri99b, Hua97, Jon93, 96b]. These reports contained phase diagrams that included the BCC, FCC, SHP and HCP metal carbonitride phases. Jonsson, Huang and Frisk each described the metal–W–C–N quaternary system using the two sublattice model, with metal and W mixing on one sublattice and C, N and vacancies (where applicable) mixing ideally on a second, interstitial sublattice. To date, interaction parameters describing C–N or C–N–Va interactions on the W interstitial sublattice have not been reported.

As detailed in Chapter 5, our experimentally deposited films contain a mixture of FCC β–WN_xC_y and amorphous carbon, but do not contain the BCC, SHP or HCP carbonitride phases. Oxygen in the films is due to post–growth in–diffusion, and is therefore excluded from this equilibrium analysis. Our experimental data will therefore be used to estimate Gibbs energy and interaction parameter values for the FCC (W)(N,C,Va) phase, while the published Gibbs energy values for the BCC, SHP and HCP carbonitride phases will not be modified. To examine the thermodynamic stability of β–WN_xC_y, the two–sublattice model will again be invoked. The metal sublattice contains W atoms, while the interstitial sublattice contains a mixture of N, C and Va. This model is represented by the notation $(W)_1(N,C,Va)_z$, where z is the number of available sites in the interstitial sublattice per W atom. For the FCC carbonitride, the model takes the form $(W)_1(N,C,Va)_1$. The FCC β–WN_x and FCC β–WC_x phases are both reported to have a defective NaCl–type structure, with vacancies intermixing on the interstitial sublattice. For these phases, the most commonly reported stoichiometries are FCC β–$WN_{0.5}$ and FCC β–$WC_{0.6}$, respectively, indicating that some of the interstitial sites are vacant. A range of x values have been reported for both of these phases, as indicated in Table 3-6 and Table 3-15.

The lattice parameter of the β–WN_xC_y polycrystals is highly dependent on the composition of the interstitial sublattice. Experimentally determined lattice parameters, along with the concepts of fractional site occupation and Vegard's law may be used to estimate the composition of these polycrystals [Kos93]. Zhang [1994] used lattice parameter data to determine the content of C and N on the interstitial sublattice in ternary TiN_xC_{1-x} polcrystals, which had a rock salt (NaCl) structure. In addition, Vegard's Law was used to estimate the C and N content of carbonitrides with the general form (Nb,Ti,V)(C,N) [Ino01] and Zr(C,N) [Bin95]. Interaction parameters and phase equilbria generated with the Vegard's Law approximation were in good agreement with experimental data.

3.10.2 Liquid Solution in the W–C–Cl–H–N System

Thermodynamic properties for pure liquid W, C and N were taken from the SGTE database [Ans87, Din91]. Thermodynamic properties for several other species in the liquid phase, including CCl_4, C_6H_5Cl, NH_4Cl and the tungsten chlorides, were taken from ThermoCalc's Sub94 database. The W–N and W–C liquid phases were previously modeled using a substitutional solution model [Gui93, Gus86], and no new ternary W–C–N liquid species have been reported. The regular solution approximation, which assumes that component interactions are independent of composition, was applied for the W–N and W–C liquid phases. The substitutional, regular solution model will be extended to model the liquid phase in our system. The liquid phase species included in this analysis are summarized in Table 3-17.

Table 3-17. Liquid Phase Species Considered in the W–C–Cl–H–N Model

Liquid Phase	Data Source
CCl_4	ThermoCalc Sub 94 Database
C_6H_5Cl	ThermoCalc Sub 94 Database
NH_4Cl	ThermoCalc Sub 94 Database
WCl_5	ThermoCalc Sub 94 Database
WCl_6	ThermoCalc Sub 94 Database
C	[Ans87, Din91]
N	[Ans87, Din91]
W	[Ans87, Din91]

3.10.3 Gas Phase in the W–C–Cl–H–N System

All of the 110 potential gas phase species in ThermoCalc's Sub94 database were included in the W–C–Cl–H–N calculation, but a truncated list of the major gas species is

Table 3-18. Selected Gas Phase Species Considered in the W–C–Cl–H–N Model

Species	Data Source
CH_4	Sub 94 Database
N_2	Sub 94 Database
NH_3	Sub 94 Database
HCl	Sub 94 Database
H_2	Sub 94 Database
C_2H_2	Sub 94 Database
C_2H_4	Sub 94 Database
C_2H_6	Sub 94 Database
C_3H_6	Sub 94 Database
C_6H_6	Sub 94 Database
C_4H_8	Sub 94 Database
HCN	Sub 94 Database
C_G	Sub 94 Database
N_G	Sub 94 Database
W_G	Sub 94 Database

shown in Table 3-18 for brevity. The gas phase was treated as an ideal mixture, with Gibbs energies for the gas species taken from the SGTE database [Ans87].

3.10.4 W–C–Cl–H–N Solid Phase Model

Dinsdale [1991] reviewed the thermodynamic data available in the literature for the condensed phases of pure W, C, and N. The Gibbs energy expressions therein are valid over a temperature range of $298.15 \leq T \leq 6000$ unless noted otherwise. Gibbs energy expressions for NH_4Cl and the various stoichiometries of tungsten chloride were taken from ThermoCalc's Sub94 database.

The two–sublattice model was used to describe the solid phases in the W–C–N system. Expressions describing the sublattice model are shown in Table 3-19 below, and are in the form $(W)_1(N,C,Va)_z$ [Hua97]. W sits on its own sublattice, while N, C and Va mix on the interstitial sublattice sites. The subscript on the interstitial sublattice, z, is again the number of interstitial sites available per W atom.

Table 3-19. Sublattice Models for the Ternary Solid Phases in the W–C–N System

Solid Phase	Sublattice Model Expression
BCC α–WN_xC_y	$(W)_1(N,C,Va)_3$
FCC β–WN_xC_y	$(W)_1(N,C,Va)_1$
HCP ε–WN_xC_y	$(W)_1(N,C,Va)_{0.5}$
SHP WN_xC_{1-x}	$(W)_1(N,C)_1$

The Gibbs energy models for the three W–C–N solid solutions describe mixing of N, C and Va on the interstitial sublattice of metallic W. The different phase structures result from the variation in structure of the metallic W sublattice with temperature and nonmetal content. To account for the homogeneity range, vacancies are again incorporated into the model for the interstitial sublattice.

Use of the sublattice model to describe the BCC, FCC and HCP W–C–N solid solution phases requires modification of the standard expression for the Gibbs energy of mixing. This modification restricts mixing of N, C and Va to the interstitial sublattice, and assumes that all sites on the metal sublattice are filled. The modified expression for Gibbs energy of the ternary solid solution phase, adapted for the two–sublattice model, is shown below:

$$\begin{aligned} G^{\varphi}_{m} &= y_{N}{}^{I} G^{\varphi}_{W:N} + y_{C}{}^{I} G^{\varphi}_{W:C} + y_{Va}{}^{I} G^{\varphi}_{W:Va} \\ &\quad + zRT\left(y_{N}{}^{I} \ln y_{N}{}^{I} + y_{C}{}^{I} \ln y_{C}{}^{I} + y_{Va}{}^{I} \ln y_{Va}{}^{I}\right) + G^{xs}_{mix} \end{aligned} \tag{3–34}$$

where G^{φ}_{m} is the Gibbs energy (per mole of formula units) for the φ solution phase (φ=BCC, FCC or HCP), $y_N{}^I$, $y_C{}^I$ and $y_{Va}{}^I$ are the site fractions of nitrogen and vacancies on the interstitial (I) sublattice, respectively, and $G^{\varphi}_{W:N}$, $G^{\varphi}_{W:C}$ and $G^{\varphi}_{W:Va}$ are the Gibbs energy for the φ phase if all interstitial sublattice sites were filled by N, C and Va, respectively. The last term, G^{xs}_{mix}, is the excess term addressing interactions on the interstitial sublattice, and can be expanded in the following form for the solid solution phases (φ=BCC, FCC or HCP) [Sau98]:

$$\begin{aligned} G^{xs}_{mix} &= y_{N}{}^{I} y_{Va}{}^{I} \sum_{v} ({}^{o}L^{\varphi,v}_{W:N,Va})(y_{N}{}^{I} - y_{Va}{}^{I})^{v} + y_{C}{}^{I} y_{Va}{}^{I} \sum_{v} ({}^{o}L^{\varphi,v}_{W:C,Va})(y_{C}{}^{I} - y_{Va}{}^{I})^{v} \\ &\quad + y_{N}{}^{I} y_{C}{}^{I} y_{Va}{}^{I} \sum_{v} ({}^{o}L^{\varphi,v}_{W:N,C,Va}) \end{aligned} \tag{3–35}$$

where ${}^{o}L^{\varphi}_{W:N,C,Va}$ is the ternary parameter describing non–ideal N–C–Va interactions on the interstitial sublattice of the solid solution, and v typically takes values from 0 to 2. For the line compound phase (φ=SHP), the excess energy would have the form:

$$G^{xs}_{mix} = y_{C}{}^{I} y_{N}{}^{I} \sum_{v} ({}^{o}L^{SHP,v}_{W:C,N}) \tag{3–36}$$

If G^{xs}_{mix} is dependent on temperature and independent of composition (i.e., regular solution approximation), v = 0 and Equations 3–35 and 3–36 simplify to Equations 3–37 and 3–38, respectively:

$$\begin{aligned} G^{xs}_{mix} &= y_N{}^I y_{Va}{}^I\,{}^oL^{\varphi,0}_{W:N,Va} + y_C{}^I y_{Va}{}^I\,{}^oL^{\varphi,0}_{W:C,Va} \\ &\quad + y_N{}^I y_C{}^I y_{Va}{}^I\,{}^oL^{\varphi,0}_{W:N,C,Va} \end{aligned} \tag{3–37}$$

$$G^{xs}_{mix} = y_C{}^I y_N{}^I\,{}^oL^{SHP}_{W:C,N} \tag{3–38}$$

The regular solution approximation was used previously to model solid solution phases in the W–C–N system [Fri99b, Hua97], and is used in this work as well. Values for ${}^oL^{\varphi,0}_{W:C,Va}$ and ${}^oL^{\varphi,0}_{W:N,Va}$ were discussed above, while a value for ${}^oL^{FCC}_{W:N,C,Va}$ is addressed in this analysis to incorporate our experimental data for equilibrium in the W–C–Cl–H–N system.

Table 3-20. Gibbs Energy Expressions for W–C–N Solid Solution Phases

Phase	Sublattice Model Layout	Ternary Gibbs Energy Expression
BCC WN_xC_y	$(W)_1(N, C, Va)_3$	${}^oG^{BCC}_m = y_N{}^oG^{BCC}_{W:N} + y_C{}^oG^{BCC}_{W:C} + y_{Va}{}^oG^{BCC}_{W:Va} +$ $3RT[y_N \ln y_N + y_C \ln y_C + y_{Va} \ln y_{Va}] + {}^{xs}G^{BCC}_m$
FCC β–WN_xC_y	$(W)_1(N, C, Va)_1$	${}^oG^{FCC}_m = y_N{}^oG^{FCC}_{W:N} + y_C{}^oG^{FCC}_{W:C} + y_{Va}{}^oG^{FCC}_{W:Va} +$ $RT[y_N \ln y_N + y_C \ln y_C + y_{Va} \ln y_{Va}] + {}^{xs}G^{FCC}_m$
HCP WN_xC_y	$(W)_1(N, C, Va)_{0.5}$	${}^oG^{HCP}_m = y_N{}^oG^{HCP}_{W:N} + y_C{}^oG^{HCP}_{W:C} + y_{Va}{}^oG^{HCP}_{W:Va} +$ $0.5RT[y_N \ln y_N + y_C \ln y_C + y_{Va} \ln y_{Va}] + {}^{xs}G^{HCP}_m$
SHP WN_xC_{1-x}	$(W)_1(N, C)_1$	${}^oG^{SHP}_m = y_N{}^oG^{SHP}_{W:N} + y_C{}^oG^{SHP}_{W:C} +$ $RT[y_N \ln y_N + y_C \ln y_C] + {}^{xs}G^{SHP}_m$

3.10.5 W–C–Cl–H–N Liquid Phase Model

The Gibbs energy per mole for the liquid phase ($G_m^{liq}(T,P)$) is based on the ideal mixing model, as no experimental data are available to assess any deviations from ideality for this phase:

$$G_m^{liq}(T,P) = \sum_i^j x_i\,{}^{o}G_i^{liq} + RT\left(\sum_i^j x_i \ln x_i\right) \qquad (3\text{–}39)$$

where x_i is the mole fraction of species i in the liquid phase and ${}^{o}G_i^{liq}$ is the temperature and pressure dependent molar Gibbs energy for the pure liquid species i, as reported previously [Din91, Gus85]. Existing Gibbs energy expressions for species in the liquid phase will not be modified, as no new experimental data have been reported.

3.10.6 W–C–Cl–H–N Gas Phase Model

The W–C–Cl–H–N gas phase model is similar to that for the model for the W–N gas phase, described above, although many more species are incorporated for this five–component system. Existing Gibbs energy expressions for species in the gas phase will not be modified, as no new experimental data have been reported for them.

3.11 Optimization of the FCC β–WN_xC_y Gibbs Energy

Several reports of tungsten carbonitride formation have been given in the literature, but an analysis of the polycrystal's structure and composition has not reported. Chitica [1996] reported WN_xC_y deposition by laser ablation of a W target in either CH_4 or C_3H_8 with small amounts of N_2. The WN_xC_y phase had minimal N content, but considerable levels of carbon, which increased with pressure, rising from $y = 0.08$ to 0.34 over a pressure range of 0.05 to 0.2 Pa. The crystal structure was not indicated, however. Gogova et al. [1998] reported deposition of WN_xC_y films for use as barriers to Co diffusion. Two different methods were used to deposit the films; the first was to heat CVD–W thin films in NH_3, CH_4 and Ar at 1050°C, and the second was to react $W(CO)_6$, CH_3COCH_3 and NH_3 at 400°C. RHEED analysis of the films showed that the WN_xC_y was crystalline, but d–spacing values did not correspond to either SHP WC or BCC W. Neither a chemical analysis of the crystalline WN_xC_y phase before and after annealing nor the pressures for these processes were given, however.

Wang et al. [2000] reported thin films containing the cubic β–WC_x, HCP W_2C and SHP WN phases by N^+ ion irradiation of a sputtered C film on a W substrate. The pressure during ion bombardment was 3.4×10^{-3} Pa, but substrate temperature was not measured. While they assigned a broad XRD peak near $2\theta = 37$ ° to the cubic WC_x phase, the peak's position suggests deposition of β–WN_xC_y; elemental analysis of the polycrystals to confirm this, however, was not reported. Moreover, although W4f and C1s XPS peaks were assigned to the suggested phases, a plot of the N1s peak was not shown. In addition, the phase described as SHP WN may actually have been SHP WN_xC_{1-x}. The formation of carbonitride upon irradiation with N^+ ions, but not with Ar^+ ions, suggests a strong, attractive C–N interaction on the interstitial sublattice of W. This also infers greater stability of the carbonitride relative to the nitride or carbide for these deposition conditions.

As mentioned in Chapter 2, a patent application reported the use of MOCVD to deposit β–WN_xC_y films [Fuk00]. X–ray diffraction indicated a peak between 36 and 38 2θ° and a second position between 2θ°= 42 and 44, both of which are consistent with FCC β–WN_xC_y deposition. ALD was also used to deposit FCC β–WN_xC_y films, as mentioned in Chapter 2 [Kim03d]. Bulk film composition from RBS was 48 at.% W, 32 at.% C, and 20 at.% N, and the HR–TEM lattice fringe spacing was 2.39 Å, which is between the interplanar spacings for the (111) orientation of β–$WN_{0.5}$ (2.38 Å) and β –$WC_{0.6}$ (2.43 Å). The other lattice fringe spacing was 2.08 Å, which was between the interplanar spacings for the (200) orientation of β–$WN_{0.5}$ (2.06 Å) and β –$WC_{0.6}$ (2.11 Å), respectively. In another ALD study, β–WN_xC_y was deposited with a bulk composition of 55 at.% W, 15 at.% N, and 30 at.% C [Li02, Smi02]. While these studies support the presence of a ternary FCC β–WN_xC_y solid solution, a detailed compositional analysis of the β–WN_xC_y polycrystals has not been done.

To begin the analysis of our experimentally deposited FCC β–WN_xC_y polycrystals, the modified expression for Gibbs energy for the FCC solid solution phase is shown below:

$$\begin{aligned} G_m^{FCC} &= y_N{}^I G_{W:N}^{FCC} + y_C{}^I G_{W:C}^{FCC} + y_{Va}{}^I G_{W:Va}^{FCC} \\ &+ zRT\left(y_N{}^I \ln y_N{}^I + y_C{}^I \ln y_C{}^I + y_{Va}{}^I \ln y_{Va}{}^I\right) + G_{mix}^{xs} \end{aligned} \tag{3–40}$$

where

$$\begin{aligned} G_{mix}^{xs} &= y_N{}^I y_{Va}{}^I \, {}^oL_{W:N,Va}^{\varphi,0} + y_C{}^I y_{Va}{}^I \, {}^oL_{W:C,Va}^{\varphi,0} \\ &+ y_N{}^I y_C{}^I y_{Va}{}^I \, {}^oL_{W:N,C,Va}^{\varphi,0} \end{aligned} \tag{3–41}$$

The fractional site occupations of N, C and Va on the interstitial sublattice are denoted $y_N{}^I$, $y_C{}^I$, $y_{Va}{}^I$, and are subject to the constraint that they sum to one:

$$y_N{}^1 + y_C{}^1 + y_{Va}{}^1 = 1 \tag{3–42}$$

To convert from mole fraction (x_i) to site fraction (y_i) for the same two–sublattice model, Equation 3–43 may be applied [Sau98]:

$$x_i = \frac{N^M y_i^M + N^I y_i^I}{N^M(1 - y_{Va}^M) + N^I(1 - y_{Va}^I)} \qquad (3\text{–}43)$$

where x_i is the overall mole fraction of component i, and the superscripts M and I refer to the metal and interstitial sublattices, respectively. N^I is the total number of sites on the interstitial sublattice, while y_i^I and y_{Va}^I are the site fraction of i atoms and vacancies, respectively, on the interstitial sublattice. Incorporation of vacancies into the sublattice model enables us to consider homogeneity ranges among the atoms mixing on a given sublattice. Vacancies will be incorporated into the interstitial sublattice, which contains nitrogen and carbon, but will not be considered for the tungsten sublattice. Equation 3–43 above can therefore be simplified, noting that $y_{Va}^M = 0$ and $N^I = zN^M$:

$$x_i = \frac{\frac{N^I}{z} y_i^M + N^I y_i^I}{\frac{N^I}{z} + N^I(1 - y_{Va}^I)} = \left(\frac{y_i^M + z y_i^I}{1 + z(1 - y_{Va}^I)}\right) \qquad (3\text{–}44)$$

Moreover, assuming that all mixing occurs on the interstitial sublattice, and that tungsten is the only element on the metal sublattice, $y_W^M = 1$ and $y_W^I = y_N^M = y_C^M = 0$. Therefore, expressions for x_W, x_N and x_C in terms of z and interstitial site fractions can be written, noting that $y_{Va}^I = 1 - y_N^I - y_C^I$:

$$x_W = \left(\frac{1}{1 + z(y_N{}^I + y_C{}^I)}\right) \qquad (3\text{–}45)$$

$$x_N = \left(\frac{z y_N^I}{1 + z(y_N{}^I + y_C{}^I)}\right) \qquad (3\text{–}46)$$

$$x_C{}^I = \left(\frac{z y_C^I}{1 + z(y_N{}^I + y_C{}^I)}\right) \qquad (3\text{–}47)$$

The latter two equations can be solved simultaneously for y_N^I and y_C^I, given the overall mole fractions for C and N in the polycrystal. Note, however, that the mole fraction of carbon in this expression is denoted x_C^I, which represents the mole fraction of carbon residing in the interstitial sites of the polycrystals. Experimentally, C incorporates into both the polycrystal's interstitial sites and at grain boundaries, as indicated by XPS results. Film composition was determined by AES, which is an area–averaged technique that cannot differentiate between C in the grain boundary and interstitial C. The value for x_C provided by AES therefore is an "average" value, including both interstitial and grain boundary carbon, and can be described by the following equation:

$$x_C = x_C^{\,I} + x_C^{\,GB} \tag{3–48}$$

where x_C^{GB} is the mole fraction of C at the grain boundary. Any difference between x_C^I and x_C indicates leftover "free" carbon not residing in the polycrystal, which therefore resides at the grain boundary (denoted x_C^{GB}). Since x_C, as determined by AES, cannot be directly related to y_C^I, another method is required to determine the C content in the β–WN_xC_y phase.

The site fraction of C in the β–WN_xC_y phase, y_C^I, may be estimated through the application of Vegard's Law, which represents a linear relationship between the lattice constants of end members in alloys. This Law requires the end members to have the same crystal structure. To find the lattice constant of an alloy mixture (a_{alloy}) containing these three components mixing on the interstitial sublattice, Vegard's law takes the form:

$$a_{alloy} = a_1(y_N^{\,I}) + a_2(y_C^{\,I}) + a_3(y_{Va}^{\,I}) \tag{3–49}$$

where a_1, a_2, and a_3 are the lattice constants for phases 1, 2, and 3, respectively. The three end–member phases of interest are β–W, β–$WN_{0.5}$ and β–$WC_{0.6}$. The β–W phase has an

FCC W lattice structure, with all interstitial octahedral sites containing vacancies. This phase is not observed experimentally, but is useful for the application of Vegard's Law, and should not be confused with experimental reports of β–W, which actually have the W_3O stoichiometry [Hag54]. The β–$WN_{0.5}$ and β–$WC_{0.6}$ phases contain N and C atoms, at 1/2 and 3/5 of the available interstital octahedral sites in the FCC W lattice, respectively, while the remaining sites are vacant. Since the three phases are derived from the same FCC β–W lattice structure, Vegard's law may be applied to determine the shift in lattice parameter with interstitial site occupation. Vegard's law for the lattice parameter of the ternary W–C–N solid solution may be written:

$$a_{\beta\text{-WNxCy}} = a_{\beta\text{-WN}}(y_N{}^I) + a_{\beta\text{-WC}}(y_C{}^I) + a_{\beta\text{-W}}(y_{Va}{}^I) \qquad (3\text{–}50)$$

where $a_{\beta\text{-WN}}$, $a_{\beta\text{-WC}}$ and $a_{\beta\text{-W}}$ are the lattice parameters for β–WN, β–WC and β–W, respectively, which are hypothetical FCC W phase compositions with all interstitial sites completely filled by N, C and Va, respectively. The term on the left, $a_{\beta\text{-WNxCy}}$, is the experimentally determined lattice parameter of the deposited films (per XRD), while a lattice constant of 3.875 Å for $a_{\beta\text{-W}}$ was calculated based on a W atomic radius of 1.37 Å [Sha96]. Values of 4.377 and 4.477 Å for $a_{\beta\text{-WN}}$ and $a_{\beta\text{-WC}}$, respectively, were extrapolations based on the calculated 3.875 Å for $a_{\beta\text{-W}}$ and reported lattice parameters of 4.126 and 4.236 Å for $a_{\beta\text{-WN0.5}}$ and $a_{\beta\text{-WC0.6}}$, respectively. Combining these values with Equation 3–50 gives:

$$a_{\beta\text{-WNxCy}} = 4.377(y_N{}^I) + 4.477(y_C{}^I) + 3.875(1 - y_N{}^I - y_C{}^I) \qquad (3\text{–}51)$$

There is now one equation with 2 unknowns, $y_N{}^I$ and $y_C{}^I$. To solve this equation, an assumption regarding the site occupation of N must be made. Per XPS results for film growth (Chapter 5), N is only present in the film's polycrystals. N1s XPS peaks at higher binding energy (above 400 eV), which indicate N at the grain boundaries, do not appear for any of our films deposited over the experimental temperature range. Films deposited with NH_3 as a co–reactant to boost N content also lack higher binding energy N1s peaks. Therefore, all N detected by AES is assumed to reside in the polycrystals, with none at the grain boundaries. All N detected by AES is therefore considered to preferentially occupy interstitial sites in the polycrystals rather than grain boundaries. This assumption allows us to determine the fractional site occupation of N atoms (y_N^I) on the interstitial sublattice. Once this has been determined, Equation 3–51 is solvable. Before calculating y_N^I, though, the conversion from overall film mole fraction, x (which is given by AES), to site fraction, y, must be addressed. To convert from mole fraction to site fraction for a two–sublattice model, the Equation 3–52 may be applied [Sau98]:

$$x_j = \frac{\sum\limits_S N^S y_j^S}{\sum\limits_S N^S (1 - y_{Va}^S)} \tag{3–52}$$

where x_j is the overall mole fraction of component j, N^s is the total number of sites on sublattice s, y_j^s is the site fraction of component j on sublattice s, and y_{Va}^s is the site fraction of vacancies on sublattice s. Denoting the metal sublattice "M" and interstitial sublattice "I," the equation for the overall mole fraction of N is:

$$x_N = \frac{N^M y_N^M + N^I y_N^I}{N^M (1 - y_{Va}^M) + N^I (1 - y_{Va}^I)} \tag{3–53}$$

This expression can be simplified by noting some properties of the $(W)_1(N,C,Va)_z$ model. First, only W resides on the M sublattice, so $y_N^M=0$. Next, no vacancies are considered on the M sublattice, so y_{Va}^{M}=0. Moreover, the number of sites on sublattice M is related to those on the interstitial sublattice I through the factor z by the following expression:

$$N^{I} = zN^{M} \tag{3–54}$$

Lastly, since at first only nitrogen addition to the W sublattice is being considered:

$$y_{N} + y_{Va} = 1 \tag{3–55}$$

Now, Equation 3–53 can be rewritten:

$$x_{N} = \frac{zy_{N}^{I}}{1 + zy_{N}^{I}} \tag{3–56}$$

Solving for y_N^I:

$$y_{N}^{1} = \frac{x_{N}}{z(1 - x_{N})} \tag{3–57}$$

Now, Equation 3–51 can be rewritten in terms of z and x_N, which are knowns:

$$a_{\beta\text{-WNxCy}}(\text{Å}) = 4.377\left(\frac{x_{N}}{z(1-x_{N})}\right) + 4.477\left(y_{C}^{I}\right) + 3.875\left(1 - \frac{x_{N}}{z(1-x_{N})} - y_{C}^{I}\right) \tag{3–58}$$

Now, solve for y_C^1, the carbon site fraction in the β–WN$_x$C$_y$ polycrystals:

$$a_{\beta\text{-WNxCy}}(\text{Å}) - 4.377\left(\frac{x_{N}}{z(1-x_{N})}\right) - 3.875\left(1 - \frac{x_{N}}{z(1-x_{N})} - y_{C}^{I}\right) = +4.477\left(y_{C}^{I}\right) \tag{3–59}$$

Simplifying:

$$y_{C}^{I} = \frac{a_{\beta\text{-WN}_{x}C_{Y}} - 0.502\left(\frac{x_{N}}{z(1-x_{N})}\right) - 3.875}{0.602} \tag{3–60}$$

This expression gives the site fraction of carbon in the β–WN$_x$C$_y$ polycrystals. This can be converted to mole fraction of carbon in the polycrystal, x_C^I, by use of Equation 3–47. Experimental values for film composition and lattice parameter are shown in Table 3-21, while calculated polycrystal stoichiometries based on these data are shown in Table 3-22. These lattice parameters were derived from XRD spectra shown in Figure 5–31 in Chapter 5.

As with most CVD deposition systems, there is some question about the reactor system's proximity to "true" equilibrium conditions. To minimize uncertainty regarding the reactor's proximity to equilibrium, only data for the highest deposition temperature (700°C) was included in Table 3-22 above. Higher temperature enables more kinetic barriers to be overcome, and is therefore a better approximation to equilibrium than depositions at lower temperature. Film deposition with NH_3 is mass transfer controlled across the entire 450 to 700°C temperature range (Figure 5–36 in Chapter 5); in this regime, if the mass transfer rates of the various reactants are similar (as expected), the composition of reactants at the surface should be similar to that in the bulk gas phase. Thus, the film composition for deposition with NH_3 at the highest temperature (700°C) will be taken as the closest approach to equilibrium, and will be used in the Gibbs energy determination for the ternary β–WN_xC_y phase. Hence, the calculated β–$WN_{0.16}C_{0.43}$ ($W_{0.63}N_{0.10}C_{0.27}$) stoichiometry will be taken as the experimental equilibrium value for deposition at 700°C. The film composition was determined by AES, which has an accuracy of ± 5 at. %, hence the polycrystal stoichiometery is a rough estimate both due to compositional inaccuracy and to a lesser extent the use of Vegard's Law approximation. Lack of any literature data for the FCC W–C–N ternary phase made this necessary, however. Data from Rutherford Backscattering Spectroscopy (RBS) were collected to improve compositional accuracy, but the poor resolution provided by the specific RBS instrument used for measurements made interpretation of the RBS data impossible.

Table 3-21. Experimental Bulk Composition and Lattice Parameter Data Used for Assessment of FCC β–WN_xC_y

MOCVD Deposition Chemistry	Deposition Temperature (°C)	Lattice Parameter at Ambient Temp., (Å)	Bulk Composition in Film (at. %)			
			W	N	C	O
i–Pr + PhCN in H_2	700	4.163	46.3	2.7	48.6	2.4
i–Pr + PhCN + NH_3 in H_2	700	4.160	47.9	8.9	41.5	1.7

Table 3-22. Estimated Equilibrium Compositions for FCC β–WN_xC_y Polycrystals

MOCVD Deposition Chemistry	Deposition Temp. (K)	Deposition Pres. (Pa)	x in β–WN_xC_y	y in β–WN_xC_y	Normalized Stoichiometry
i–Pr + PhCN in H_2	973	4.67×10^4	x = 0.04	y = 0.46	$W_{0.67}N_{0.02}C_{0.31}$
i–Pr + PhCN + NH_3 in H_2	973	4.67×10^4	x = 0.16	y = 0.43	$W_{0.63}N_{0.10}C_{0.27}$

Based on AES, XPS, and XRD data (Chapter 5), it was determined that films deposited at 700°C, regardless of NH_3 addition, contained β–WN_xC_y and amorphous C, along with minute amounts of WO_3. Oxygen incorporation is believed to occur by post–growth exposure to air, hence the oxygen content and oxide phase will excluded from consideration in the thermodynamic model. This leaves β–WN_xC_y and amorphous carbon as the deposited phases to be considered for the model. Amorphous C, however, is inherently a metastable phase, so it will be approximated as being in its stable form (graphite) at experimental conditions for modeling purposes. Deposition of amorphous C rather than graphite may reflect kinetic constraints during deposition that prevent graphite, which is considered stable at our experimental conditions, from forming. For purposes of the equilibrium model, β–WN_xC_y, graphite and gas will be assumed to exist in equilibrium during deposition in the W–C–Cl–H–N system, hence the final model should reproduce this equilbrium at 700°C, with the appropriate stoichiometry in the carbonitride phase.

To model the formation of FCC $\beta\text{–}W_{0.63}N_{0.10}C_{0.27}$ in equilibrium with graphite and a gas phase at 700°C, several solid–phase parameters had to be modified. Modified low–temperature expressions for $^{o}G^{FCC}_{W:C}$ and $^{o}L^{FCC}_{W:C,Va}$, along with a new value for $^{o}L^{FCC}_{W:N,C,Va}$, were generated to accurately model the experimental system; the new values are shown in Table 3-23, and are compared to the original values reported by Gustafson [1986]. In addition, the Gibbs energy and interaction parameter expressions for several neighboring FCC transition metal carbides are listed for comparison; these expressions are truncated to the first three terms (a + bT + CTlnT), where for the Gibbs energy expressions, a=H_o (enthalpy at standard conditions) and –(b+c) = S_o (entropy at standard conditions). Comparing the new values for $^{o}G^{FCC}_{W:C}$ from this work to the original values reported by Gustafson [1986], it is apparent that the new value for S_o is only ~8% larger than the existing one, while the new value for H_o is ~30% larger. The differences between the values of H_o and S_o generated in this work for FCC WC_x and those reported for FCC TiC_x and NbC_x are due to the inability of W to form a stable monocarbide in FCC form [Pie96]. The composition ranges for FCC TiC_x and NbC_x near 1000 K extend from $Ti_{0.65}C_{0.35}$ to $Ti_{0.52}C_{0.48}$ [Bin95] and $Nb_{0.60}C_{0.40}$ to $Nb_{0.50}C_{0.50}$ [Hua97], respectively. Similarly, that for FCC TaC_x ranges from $Ta_{0.53}C_{0.47}$ to $Ta_{0.50}C_{0.50}$ [Fri98]. In fact, all of the Group IV, V and VI metals, with the exception of W, can form stoichiometric FCC carbides and nitrides [Pie96]. Stable, stoichiometric WC and WN only exist in SHP form, however. Since the FCC carbides of all Group IV, V and VI metals (except W) have homogeneity ranges extending up to the stoichiometric limit ($Metal_{0.50}C_{0.50}$), their minimum vacancy concentration is $y_{Va}\approx 0$. As shown in Figure 3–7 and Table 3-15, the stoichiometry of FCC β–WC_x at maximum C content, however, is β–$W_{0.60}C_{0.40}$ (or β–$WC_{0.67}$), which corresponds to a minimum vacancy site fraction of $y_{Va}\approx 0.33$. Since no ordering has been reported for C on specific interstitial sites in these FCC carbides, the higher minimum value for y_{Va} in FCC WC_x suggests that this phase should have higher positional entropy relative to the other Group IV, V and VI FCC carbides, which are not reported to be ordered. This is reflected in the higher S_o value generated by this work.

Figure 3–8 shows a plot of the metal's atomic number (Ti=22, Nb=41 and W=74) vs. H_o for several FCC carbides. The solid circles are the reported H_o values for FCC TiC_x and FCC NbC_x, while the open circle is a calculated value for FCC W:C generated by extrapolation from the FCC TiC_x and NbC_x values. The open triangle data point is the value from the existing model for FCC WC_x, while the open square is the new value generated by this work. Our new value for H_o falls well above the trend predicted by extrapolation from values for FCC TiC_x and NbC_x (solid line), but is slightly closer to the trend than the existing value from Gustafson [1986]. This indicates that FCC β–WC_x in our model is slightly more stable than reported previously by Gustafson.

The original value reported by Gustafson [1986] for ${}^{o}L^{FCC}_{W:C,Va}$ in FCC WC_x would be –17,980 J/mol at 1000 K, which is significantly less negative than values for the other Group IV, V and VI FCC carbides (Table 3-23). The higher minimum value for y_{Va} in FCC β–WC_x means that the interaction parameter describing C–Va interactions in FCC W, ${}^{o}L^{FCC}_{W:C,Va}$, should actually have a larger negative value than that for the other Group IV, V and VI FCC carbides, reflecting stronger C–Va attraction in FCC β–WC_x. The new, low temperature value for ${}^{o}L^{FCC}_{W:C,Va}$ (−260,000 J/mol) indicates a much stronger C−Va attraction in FCC β−WC_x relative to the other carbides.

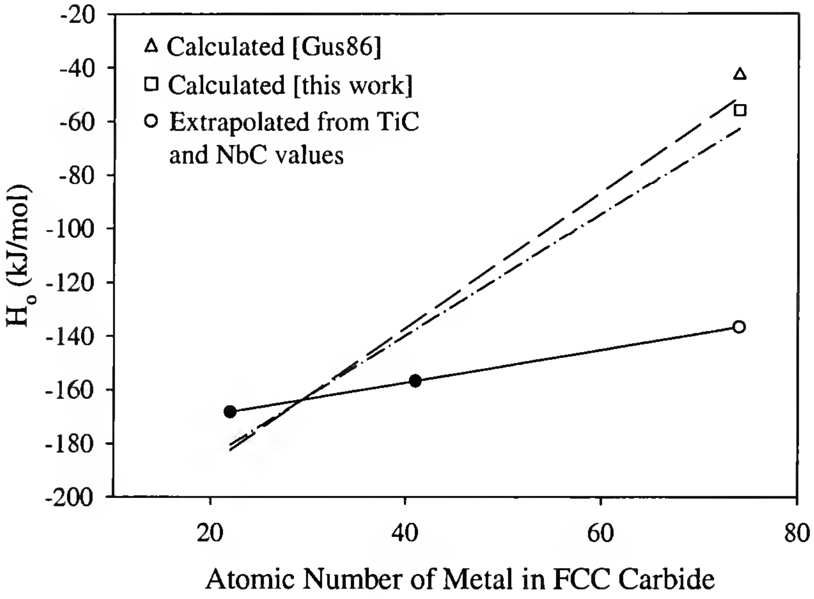

Figure 3−8. H_o values for the FCC carbides of Ti [Jon96a], Nb [Lee01a] and W [Gus86, this work].

Modifications to the ${}^{o}G^{FCC}_{W:C}$ and ${}^{o}L^{FCC}_{W:C,Va}$ values resulted in enhanced stability of the FCC β−WC_x phase at low temperature, consistent with recent experimental reports discussed in Table 3-15. Although parameters addressing C−N and C−N−Va interactions on the FCC W interstitial sublattice have not been reported, they have been given for other refractory metals, as detailed in Table 3-24. Interestingly, C−N and C−N−Va interaction parameters in the Ti and Nb carbonitride systems are generally very attractive, having large, negative values. For FCC NbN_xC_y, the reported interaction parameter is variable, depending on the vacancy site fraction on the interstitial sublattice. As listed above, the FCC NbC_x stoichiometry corresponding to minimum C concentration near 1000 K is

$Nb_{0.60}C_{0.40}$ [Hua97], which translates to a maximum vacancy site fraction of $y_{Va} \approx 0.33$. The stoichiometry corresponding to minimum N concentration in the analogous nitride,

Table 3-23. Gibbs Energy and Interaction Parameter Expressions (J/mol of formula) for Several FCC Metal Carbides.

Phase	Sublattice Model Layout	Gibbs Energy (G) and Excess Gibbs Energy (L) Expressions (J/mol)	Reference
FCC NbC_x	$(Nb)_1(C)_1$	$\Delta ^oG^{FCC}_{Nb:C} = -156735 + 284*T - 46*T\ln T$ $^oL^{FCC}_{Nb:C,Va} = -94050 + 23T$	[Lee01a]
FCC TaC_x	$(Ta)_1(C)_1$	$\Delta ^oG^{FCC}_{Ta:C} = -163844 + 267*T - 45*T\ln T$ $^oL^{FCC}_{Ta:C,Va} = -60408 + 4T$	[Fri96]
FCC TiC_x	$(Ti)_1(C)_1$	$\Delta ^oG^{FCC}_{Ti:C} = -168261 + 294*T - 48*T\ln T$ $^oL^{FCC}_{Ti:C,Va} = -52702 - 5T$	[Lee01a]
FCC ZrC_x	$(Zr)_1(C)_1$	$\Delta ^oG^{FCC}_{Zr:C} = -224785 + 297*T - 48*T\ln T$ $^oL^{FCC}_{Zr:C,Va} = -41870 - 36T + 6T\ln T$	[Gui95]
FCC β–WC_x	$(W)_1(C)_1$	$\Delta ^oG^{FCC}_{W:C} = -42879 + 303*T - 48*T\ln T$ $^oL^{FCC}_{W:C,Va} = -17.98*T$	[Gus86]
FCC β–WC_x	$(W)_1(C)_1$	$\Delta ^oG^{FCC}_{W:C} = -55879 + 330*T - 48*T\ln T$ $^oL^{FCC}_{W:C,Va} = -260000$	This Work

FCC NbN_x, is $Nb_{0.55}N_{0.45}$, which translates to a maximum interstitial vacancy site fraction of $y_{Va} \approx 0.2$. Assuming that the maximum vacancy fraction for the binary carbide would also be the maximum value in the ternary carbonitride, the maximum value for the ternary interaction parameter is $^oL^{FCC}_{Nb:C,N,Va} = -(0.33*(312985)) \approx -104328$ J/mol. The reported ternary interaction parameter values for $^oL^{FCC}_{Ti:C,N,Va}$ and $^oL^{FCC}_{Nb:C,N,Va}$, along with the new value for $^{o}L^{FCC}_{W:C,N,Va}$ from this work, are plotted in Figure 3–9. The new value for $^{o}L^{FCC}_{W:C,N,Va}$ from this work fits the trend of the reported Ti and Nb values, as the goodness of fit (R^2 value) for this line is 0.96.

Table 3-24. Interaction Parameters for Several Refractory Metal Carbonitrides

Compound Model	Interaction Parameter Expression (J/mol)	Reference
FCC $Fe_1(C,N)_1$	$^{o}L^{FCC}_{Fe:C,N} = -14545$	[Du91]
FCC $Nb_1(C,N)_1$	$^{o}L^{FCC}_{Nb:C,N} = 12.5922*T$	[Lee01a]
FCC $Ti_1(C,N)_1$	$^{o}L^{FCC}_{Ti:C,N} = -54176$	[Jon96a]
FCC $Nb_1(C,N,Va)_1$	$^{o}L^{FCC}_{Nb:C,N,Va} = -y_{Va}*312985$	[Lee01a]
FCC $Ti_1(C,N,Va)_1$	$^{o}L^{FCC}_{Ti:C,N,Va} = -121744$	[Jon96a]
FCC $W_1(C,N,Va)_1$	$^{o}L^{FCC}_{W:N,C,Va} = -90000$	This Work

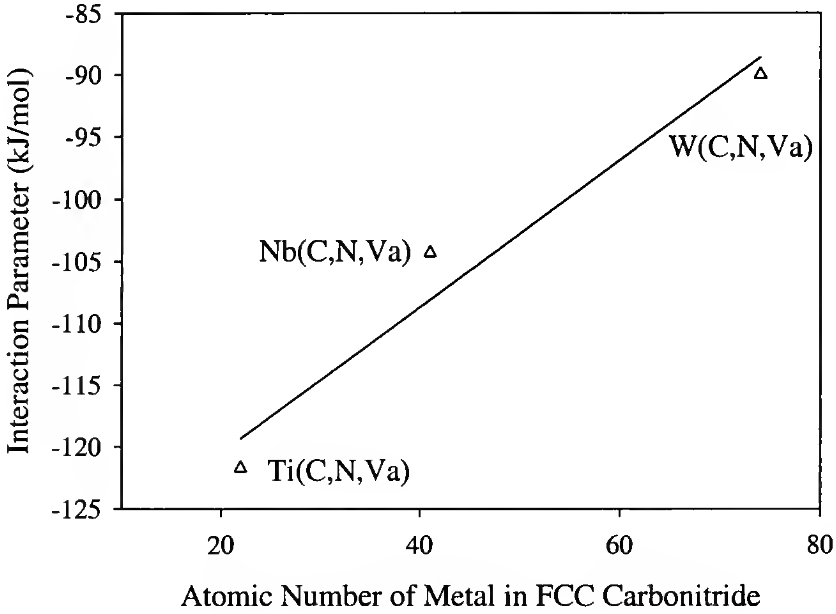

Figure 3–9. C–N–Va interaction parameter trend based on reported values for Ti [Jon96a] and Nb [Lee01a] and the new value for W from this work.

Our experimental XPS results also indicate attractive C–N interaction on the interstitial sublattice of the WN_x polycrystals, as discussed in Chapter 5, but evidence of ordering is not present. Moreover, the ternary FCC TiN_xC_y and FCC HfN_xC_y phases are reported to have broader homogeneity ranges than their binary metal nitride and metal carbide counterparts [Bin95], which is further evidence of attractive C–N and C–N–Va interaction on the interstitial sublattice of these metals.

3.12 Degrees of Freedom (DOF) Analysis

The CVD process involves a mixture of gaseous precursors and products contacting a solid substrate surface. For this reason, gas phase chemical equilibrium calculations are useful to estimate the makeup of the gas taking part in the reaction at the substrate surface. Equilibrium calculations can be done for a homogeneous gas phase system, which represents the scenario in a reactor system before deposition begins, and for a heterogeneous gas–solid phase system, which represents the equilibrium after deposition has begun.

The mixture of precursor, solvent, and carrier gas examined in this study contain W, C, Cl, H and N atoms. Both H_2 and N_2 were tested experimentally as carrier gases, but N_2 did not afford low temperature deposition, and prevented deposition when added as a co–reactant to H_2 carrier gas. N_2 is assumed to be inert over the entire experimental temperature and pressure range, due to a large kinetic barrier to its dissociation/reaction, so this result was not surprising. N present in any equilibrium phases or species therefore originates from decomposition of the precursor and/or solvent. Since i–Pr + PhCN in H_2 carrier gas provided the best experimental film results, this will be used as the basis for our thermodynamic analysis. As a base condition, the initial input values were the mole fractions of W, C, Cl, H and N present in a mixture containing 75 mg of the isopropyl precursor $Cl_4(CH_3CN)W(N^iPr)$, 10 mL of benzonitrile (PhCN) solvent, and 1000 standard cm³/min (sccm) of H_2 carrier gas, as shown in Table 3-25.

W–C–Cl–H–N equilibrium calculations were done for temperatures ranging from 300 to 1200 K and pressures ranging from 0 to 1×10^5 Pa. Temperature and pressure, the two easiest variables for us to manipulate experimentally, were varied to determine their impact on homogeneous and heterogeneous gas phase speciation. The most important input atom ratios, along with temperature, were also varied to determine their effect on solid phase deposition at certain equilibrium conditions. Atom ratios considered in the DOF analysis are listed in Table 3-26, along with the values of these ratios in a basis mixture of i–Pr + PhCN + H_2 carrier gas, and the inputs for the calculation. The CVD phase diagrams generated by this DOF analysis are useful to determine which direction one must go experimentally, with respect to variable manipulation, to deposit the desired solid phase(s).

Table 3-25. Elemental Composition for $Cl_4(CH_3CN)WN$–*i*–Pr in PhCN with 1000 sccm H_2 Carrier Gas

Element	Amount Present in i–Pr Precursor (gmol/min)	Amount Present in PhCN (gmol/min)	Amount Present in Carrier Gas (gmol/min)	Total (gmol/min)	Input Mole Fraction
W	1.18×10^{-6}	–	–	1.18×10^{-6}	2.23×10^{-5}
C	5.90×10^{-6}	4.53×10^{-3}	–	4.53×10^{-3}	8.55×10^{-2}
Cl	4.72×10^{-6}	–	–	4.72×10^{-6}	8.90×10^{-5}
H	1.18×10^{-5}	3.23×10^{-3}	4.46×10^{-2}	4.78×10^{-2}	9.02×10^{-1}
N	2.36×10^{-6}	6.46×10^{-4}	–	6.49×10^{-4}	1.22×10^{-2}

For a system containing 5 elements, there are 7 “true” degrees of freedom (number of elements + 2) that must be satisfied before the equilibrium calculation can begin. For the homogeneous and heterogeneous speciation calculations, the input moles of each of the five species were fixed to the basis value (Table 3-25). For isobaric calculations with variable temperature, the pressure was fixed and an initial temperature value was input to generate an initial equilibrium. From this initial equilibrium data point, the temperature was varied to determine its effect on the partial pressure of the gas phase species produced. For isothermal calculations with variable pressure, the temperature was fixed and an initial pressure value was input to generate an initial equilibrium. Pressure was then varied to determine its effect on partial pressure of gas species produced.

Table 3-26. Ratios and Inputs Used for Heterogeneous Solid Phase Equilibrium DOF Analysis

Input Ratio	Ratio in Basis Mixture	Inputs for Calculation (status during mapping)
$\left[\frac{\text{moles N}}{\text{moles N} + \text{moles W}}\right]$	0.998	Temperature (variable) Pressure (fixed) moles W + N (fixed) moles W (variable) moles C (fixed) moles Cl (fixed) moles H (fixed)
$\left[\frac{\text{moles C}}{\text{moles C} + \text{moles W}}\right]$	0.999	Temperature (variable) Pressure (fixed) moles W + C (fixed) moles W (variable) moles Cl (fixed) moles H (fixed) moles N (fixed)

For heterogeneous solid phase equilibrium (CVD phase diagrams), the atom ratios of interest, along with temperature, were varied to determine their impact on the solid phase deposited. To vary the atom ratio, the sum of the two atoms of interest was set to a fixed value, as were the individual values for the remaining three atoms. By fixing the sum of the two atoms of interest, the ratio of atoms within this sum could be varied in a stepwise manner. An initial value for one of the elements in the sum was supplied, which brings the degrees of freedom to zero so that the calculation may begin. After an initial equilibrium is calculated, the quantity of one element in the sum is varied, which automatically varies the value for the other element in the sum, since their total is fixed. In addition to element ratio, the temperature is also varied so that the CVD phase diagram can be mapped. Table 3-26 shows the input ratios studied, as well as the input values and their status (fixed or variable) during calculation of the CVD phase diagram.

3.12.1 Homogeneous Gas Phase Speciation

Homogeneous gas–phase equilibrium was calculated by considering all potential gas phase species (per ThermoCalc's SUB94 database) in equilibrium with solid W, which has minimal vapor pressure at the temperatures of interest and has minimal impact on the gas species. Mole fractions for the precursor/solvent mixture in 1000 sccm of H_2 carrier gas are shown in Table 3-25. This is the basis concentration of reactants during deposition, without any co–reactants such as NH_3 or N_2 added. The values in this table serve as the initial conditions input to ThermoCalc for it to begin the equilibrium calculation.

Figure 3–10 shows the variation of partial pressure with temperature for gas species in the $Cl_4(CH_3CN)WN$–*i*–Pr + PhCN + H_2 carrier gas system. The bulk of the gas phase is made up of H_2. The dominant carbon containing species was CH_4, which is a stable and desirable reaction product in MOCVD. CH_4 is an effective gas phase carbon sink that limits the amount of carbon available to contaminate the film. The concentration of CH_4 was fairly steady over the temperature range examined. A variety of other C containing species are also present in the homogeneous equilibrium, as shown in Figure 3–10.

The dominant equilibrium Cl–containing species in the gas phase was HCl, and its equilibrium concentration was unchanged with increasing temperature. Interestingly, the presence of Cl_2 is not predicted in appreciable concentration. The predominance of HCl is due to excess H_2 carrier gas, which is available to react with Cl ligands leaving the precursor to form HCl.

Below 500 K, the dominant N containing species is NH_3, while N_2 is dominant above 500 K. The NH_3 level steadily decreases above 500 K, which is indicative of its tendency to decompose (presumably to N_2 and H_2) with increasing temperature. The concentration of N_2 increases up to 600 K and then levels off with increasing temperature, which is indicative of its high thermal stability in this temperature range. While N_2 and NH_3 are the principal species through which N escapes from the film, HCN and HNC are two other N–containing species in the homogeneous equilibrium through which N may desorb from the films. HCN first appears near 800 K, and overtakes NH_3 in concentration above 1000 K. HNC appears above 1000 K, but its concentration remains below that for N_2, NH_3 and HCN up to 1200 K.

The impact of overall system pressure on the gas phase equilibrium was also examined. Figure 3–11 shows the dependence of gas phase speciation on total system pressure as a function of temperature. The levels of H_2, N_2 and HCl are essentially constant over the entire pressure range for the four temperatures shown. Increasing overall system pressure tends to decrease the variety of gas species present in appreciable concentration. Figure 3–11 indicates that an increase in total pressure causes an increase in the NH_3 concentration, however. The concentration of NH_3 increases steadily with total system pressure at the four temperatures shown (Figure 3–11a–d). The drop in NH_3

concentration with increasing temperature, discussed above, is again evident when moving from Figure 3–11a to d. The increase in NH_3 concentration with pressure is expected, as increased pressure drives the following equilibrium to the left per Le Chatelier's principle.

$$2NH_3 \rightleftharpoons N_2 + 3H_2$$

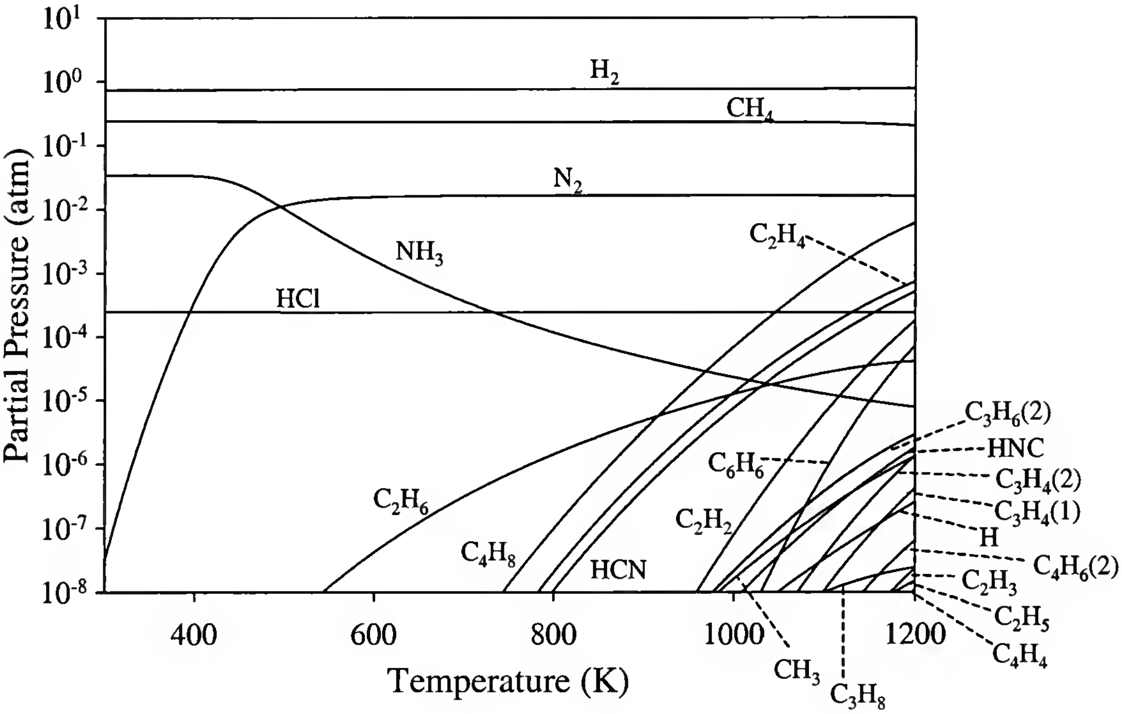

Figure 3–10. Effect of temperature on homogeneous gas phase equilibria for a mixture of the i–Pr precursor in benzonitrile solvent, with H_2 carrier gas flowrate of 1000 sccm at 4.67×10^4 Pa (350 Torr).

In this case, the equilibrium constant, K, is proportional to $1/P_{total}^2$, hence increasing the total system pressure decreases the tendency of NH_3 to dissociate. While the above equilibrium suggests that N_2 and H_2 should combine to form NH_3 at higher pressure, a large kinetic barrier to the decomposition of N_2, coupled with our relatively low operating pressures during CVD, make this unlikely during deposition.

The concentration of CH_4 also increases with total system pressure; this increase is especially noticeable at 1200 K. This is presumably due to a shift in equilibria similar to that discussed above for NH_3. Equilibria leading to formation of C_2H_4 and C_4H_8, for example, may be written:

$$2CH_4 \rightleftharpoons C_2H_4 + 2H_2$$

$$4CH_4 \rightleftharpoons C_4H_8 + 4H_2$$

To form C_2H_4, 2 moles of reactant (CH_4) are converted to 3 moles of product (1 mole C_2H_4, 2 moles H_2). For both of these equilibria, the equilibrium constant, K, is proportional to $1/P_{total}$, hence increasing the total system pressure decreases the tendency of CH_4 to form products.

HCN first appears in Figure 3–11b at 800 K for pressures below 0.5 atm, but its concentration also decreases with increasing system pressure. Equilibria based on both N_2 and NH_3 can be written which give rise to formation of HCN:

$$2CH_4 + N_2 \rightleftharpoons 2HCN + 3H_2$$

$$2CH_4 + 2NH_3 \rightleftharpoons 2HCN + 6H_2$$

To form HCN from CH_4 and N_2, for example, 3 moles of reactant (2 moles CH_4, 1 mole N_2) are converted to 5 moles of product (2 moles HCN, 3 moles H_2). For these equilibria, the equilibrium constant, K, is proportional to $1/P_{total}^2$ and to $1/P_{total}^4$, respectively, hence increasing the total system pressure decreases the tendency to form HCN.

As evident in Figure 3–11d at 1200 K, high temperature fosters formation of a large variety of C containing species. The concentration of all of these species, with the exception of CH_4, C_2H_6 and C_3H_8, decreases with increasing total system pressure. The increase in the concentration of CH_4, C_2H_6 and C_3H_8 with total pressure can again be explained by a shift in equilibrium to decrease the total number of moles at higher pressure. Formation of other C containing species from C_2H_6 and C_3H_8 follows equilibrium behavior similar to that for CH_4. For example:

$$C_2H_6 \rightleftharpoons C_2H_4 + H_2$$

$$4C_3H_8 \rightleftharpoons 3C_4H_8 + 4H_2$$

To form C_2H_4, 1 mole of reactant (C_2H_6) is converted to 2 moles of product (1 mole C_2H_4, 1 mole H_2). Likewise, to form C_4H_8, 4 moles of reactant (C_3H_8) is converted to 7 moles of product (3 moles C_4H_8, 4 moles H_2). For these equilibria, the equilibrium constant, K, is proportional to $1/P_{total}$ and to $1/P_{total}^3$, respectively, hence increasing the total system pressure favors formation of C_2H_6 and C_3H_8.

A comparison of the behavior for CH_4, C_2H_6 and C_3H_8 with pressure results in the following equilibria:

$$2CH_4 \rightleftharpoons C_2H_6 + H_2$$

$$3CH_4 \rightleftharpoons C_3H_8 + 2H_2$$

The total number of moles in the gas phase is conserved per these equilibria, so increasing total system pressure should not favor formation of C_2H_6 or C_3H_8 over CH_4, and vice versa. The concentration of each of these species increases with pressure due to decomposition of the other C containing species at higher pressure. In these equilibria, K is independent of pressure, hence increasing the total system pressure will not favor formation of reactants or products.

Homogeneous speciation calculations indicate that operation at lower temperature and higher pressure yield maximum CH_4 concentration, which is the most abundant gas phase C sink. Increasing deposition temperature and decreasing pressure leads to the largest variety of C containing species in the gas phase. The concentrations of these

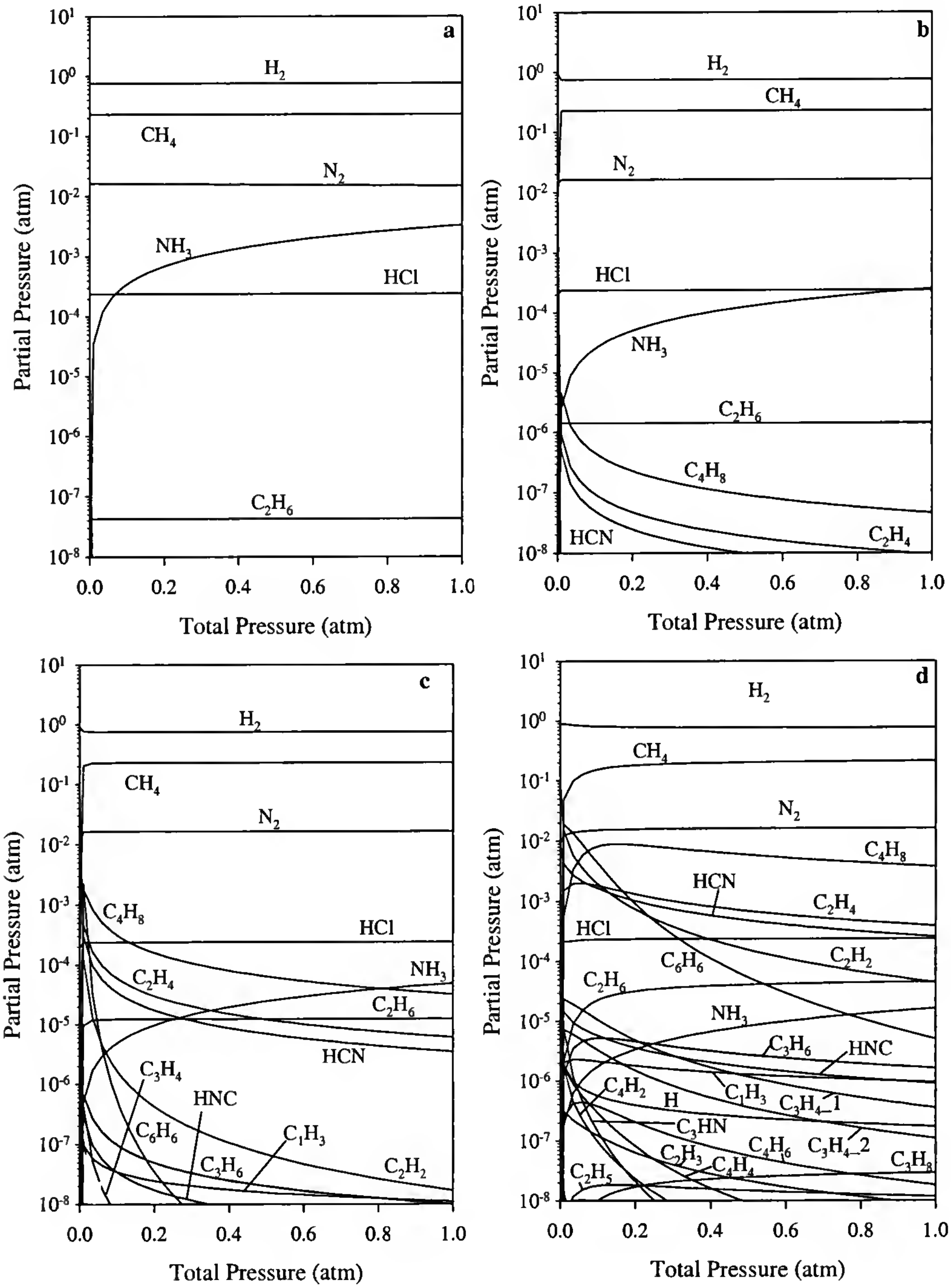

Figure 3–11. Effect of total system pressure on homogeneous gas phase equilibria for a mixture of the i–Pr precursor in benzonitrile solvent, with H_2 carrier gas flowrate of 1000 sccm. (a) 600 K (b) 800 K (c) 1000 K (d) 1200 K.

various species, however, are orders of magnitude lower than that for CH_4, so operating in a region to maximize CH_4 content appears to be the best way to maximize the amount of C in volatile form.

3.12.2 Heterogeneous Gas Phase Speciation

Heterogeneous gas phase speciation is shown in Figure 3–12. H_2 and CH_4 are the dominant H and C containing species, respectively, while the variety of carbon containing species with concentrations $\geq 10^{-8}$ atm are considerably less for heterogeneous speciation relative to the homogeneous case. H_2 concentration is steady at lower temperature, but increases above 800 K, which suggests increased alkyl decomposition at higher temperature. The decrease in concentration for most C containing species at higher temperature, as well as the smaller variety of C containing species, is consistent with increasing C deposition in the films at higher temperature. The dominant Cl containing species is again HCl, but rather than having a constant concentration as in the homogeneous case, the HCl level drops rapidly below 425 K. This is due to the stability of solid NH_4Cl at low temperature, which serves as a solid phase sink for Cl.

N_2 and NH_3 behave in a similar fashion in both the homogeneous and heterogeneous equilibria. Interestingly, the CH_4, C_2H_6 and C_4H_8 concentrations drop substantially above 800 K. This coincides with the appearance of solid graphite near 800 K, which serves as a solid sink for C at higher temperature. Two other C containing species, C_2H_4 and HCN, appear near 800 K and increase steadily with temperature. These two species were reported to form during MOCVD of TaN_xC_y from the pentakisdimethylamido tantalum precursor at 780 K [Slo99]. While both of these species could serve in addition to CH_4 as gas phase carbon sinks, HCN has been reported to deposit carbon into films at higher temperature (discussed further in Chapter 5). Hence, operating below 800 K (527°C) may help to decrease formation of HCN, which can subsequently decompose to deposit C in the films.

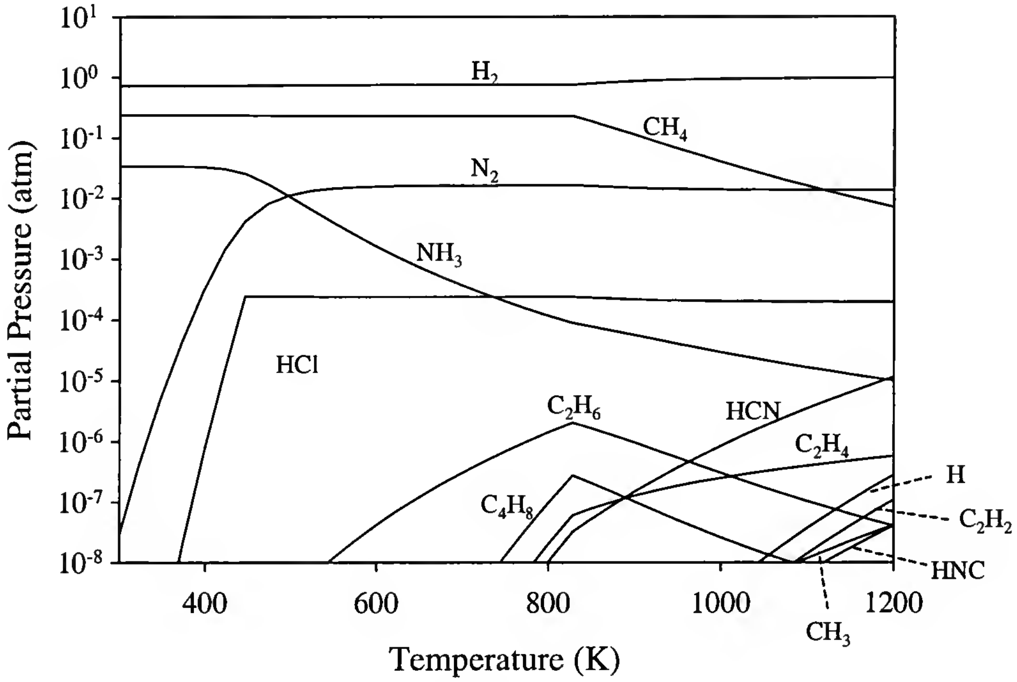

Figure 3–12. Effect of temperature on heterogeneous gas phase equilibria for a mixture of the i–Pr precursor in benzonitrile solvent, with H_2 carrier gas flowrate of 1000 sccm at 4.67×10^4 Pa (350 Torr).

The effect of total system pressure on heterogeneous gas phase speciation was also examined. Figure 3–13 shows species partial pressure vs. total system pressure at 600, 800, 1000 and 1200 K. H_2, N_2 and HCl levels were essentially constant over the entire pressure range explored. As in the homogeneous case, the concentrations of NH_3 and CH_4 increase with total system pressure. While HCN concentration decreased with increasing pressure for the homogeneous case, its concentration was unchanged with pressure at 1000 and 1200 K. Moreover, HCN concentration increases with temperature, suggesting that this may be an important pathway for N and C desorption at higher temperature.

In contrast to the homogeneous case, the concentration of many gas species increases with increasing pressure, especially at the two higher temperatures (Figure 3–13c–d). For several of these species (e.g., C_2H_4, C_4H_8), this behavior runs contrary to Le Chatelier's principle, described above. This is evidence of the solid phases, especially the carbides, carbonitrides and graphite, taking part in the equilibrium and affecting speciation in the gas phase above it.

Experimentally, both N_2 and H_2 were tested as carrier gases. Deposition temperatures $\geq$ 800°C were necessary to deposit films from the i–Pr precursor in N_2 carrier gas. Use of H_2 as the carrier gas, though, allowed for deposition down to 450°C. This is most likely due the thermal conductivity difference between H_2 and N_2. The thermal conductivities of H_2 and N_2 at 500°C are 404 and 53 W/m–K, respectively [Inc90]. Higher carrier gas thermal conductivities cause more upstream heating of the precursor. This improves the gas–phase thermal decomposition of the precursor into desired intermediates, which then react on the substrate surface to deposit WN_x films.

Addition of NH_3 and/or N_2 to the H_2 carrier gas would appear to help suppress the evolution of N from the precursor and the films. Experiments have shown that addition of NH_3 to the reactor system led to increased N content in the deposited films (Chapter 5). This result, however, is likely caused by reaction between NH_3 and the precursor molecule/growing film, rather than a shift in the above equilibrium. Similar experiments with N_2 (which is inert at our experimental conditions) in place of NH_3 led to poor films with minimal nitrogen content. The N_2 co–reactant may have actually blocked surface sites rather than suppressing evolution of N, thereby inhibiting film deposition.

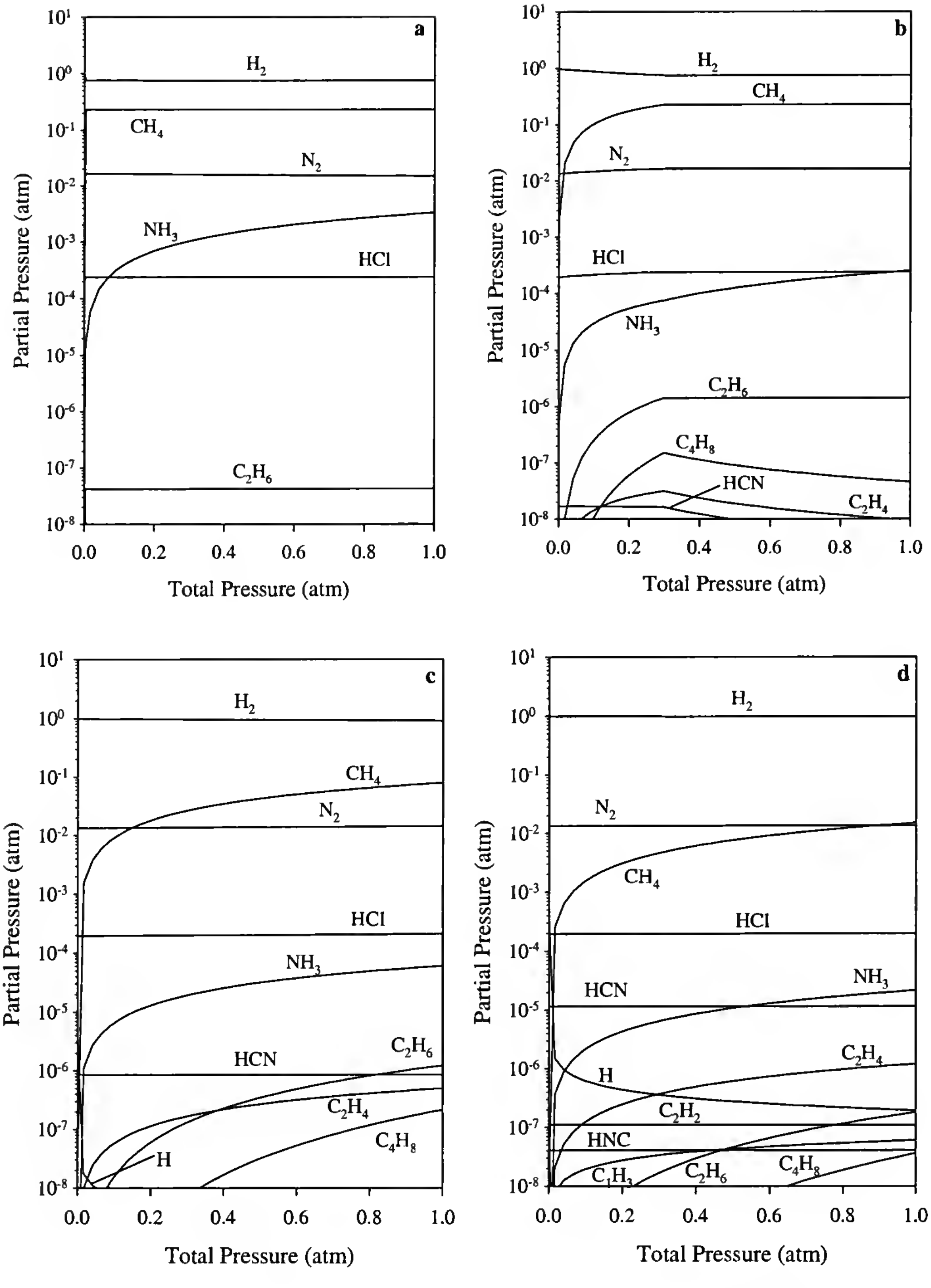

Figure 3–13. Effect of total system pressure on heterogeneous gas phase equilibria for a mixture of the i–Pr precursor in benzonitrile solvent, with H_2 carrier gas flowrate of 1000 sccm. (a) 600 K (b) 800 K (c) 1000 K (d) 1200 K.

Residual gas analysis (RGA) data for deposition with $Cl_4(CH_3CN)WN$–*i*–Pr + PhCN + H_2, discussed further in Chapter 5, indicate the presence of C_2H_2, C_6H_4, HCN, PhCN, HCl, and H_2. The presence of C_2H_2 and C_6H_4 during deposition resulted from thermal decomposition of PhCN in the reactor. As discussed in Chapter 5, concentrations for PhCN decomposition products were adjusted to eliminate contributions from PhCN cracking in the RGA. The remaining signal was therefore due to thermal processes in the reactor. C_2H_2 is predicted to form during heterogeneous equilibrium for high temperatures ($\geq$ 1100 K), while C_6H_4 is not predicted to form in appreciable concentration. Experimental RGA results indicate the presence of PhCN and C_6H_4 at 873 K, however. This suggests that PhCN decomposition in our reactor is incomplete and does not occur near equilibrium, which is supported by the kinetically limited character of the carbon deposition process with PhCN solvent, as discussed in Chapter 5.

The presence of HCl and HCN in the reactor is qualitatively consistent with heterogeneous equilibrium calculations. HCl is believed to be the major desorption route for Cl leaving the precursor molecules; RGA data and equilibrium calculations support this, and indicate that Cl_2 is not present in significant concentration. While HCN seems to be an alternate pathway for N and C desorption at increasing temperature, literature reports suggest that it decomposes on surfaces containing W, and hence may be responsible for adding C and N to the films (Chapter 5 has more detail).

CH_4, the most abundant C containing species in the equilibrium model, may have been present in the reactor in significant quantity. Both CH_4 and O have the same m/z value (m/z = 16) in our RGA, however, hence a peak at 16 is likely to be a convoluted signal, making the relative concentration of CH_4 in the reactor unclear. Oxygen presumably emanates from fragmentation of background O_2 or H_2O in the system. N_2 was the carrier gas for RGA studies, so the amount generated during reaction is unknown.

NH_3 may also have been present in the reactor in significant quantity, as a peak at m/z=17 was present during deposition. Since NH_3 and $[OH]^+$ have the same m/z value (m/z=17), however, this signal is likely to be convoluted, including signals for both NH_3 and $[OH]^+$. The presence of $[OH]^+$ is likely due to cracking of background H_2O in the RGA.

Heterogeneous equilibrium calculations, like the homogeneous ones, indicate that operation at lower temperature and higher pressure yields maximum CH_4 concentration. Again, increasing deposition temperature and decreasing pressure leads to the largest variety of C containing species in the gas phase, although the number of gas species is much lower relative to the homogeneous case, especially at higher temperature. The concentrations of these various species, as in the homogeneous case, are orders of magnitude lower than that for CH_4, however. Hence, operating conditions that maximize CH_4 concentration appear to be the best way to maximize the amount of C in volatile form, thereby minimizing the amount of C deposited in the film. Operation at lower temperature and higher pressure maximizes the CH_4 content in the system, and should therefore minimize the amount of C deposited in the films.

3.12.3 Heterogeneous Solid Phase Equilibrium

The effect of varying two input atomic ratios on the solid phase equilibrium was also examined. The goal was to determine which values of these ratios would favor deposition of the FCC phase, without any second phase present. The first ratio considers changes to the number of N atoms relative W atoms in the input mixture. The plot in Figure 3–14 shows the effect of varying temperature and N/N+W on the deposited equilibrium solid phases. Note that the gas phase is in equilibrium with all solid phases shown on the diagram, but is not included on the diagram. Four solid phases are evident in the diagram: FCC β–WN_xC_y, SHP WN_xC_{1-x}, graphite, and NH_4Cl. The roughly horizontal line extending from 770 to 828 K delineates two regions. Graphite is stable above this line, but does not appear below it. At the highest temperature, for all values of N/N+W, a mixture of FCC and graphite is stable. As temperature decreases toward the graphite demarcation line, a two–phase and a three–phase solid region appear. The two–phase solid region contains a mixture of SHP and graphite, and is present at higher values of N/N+W. The three–phase region consisting of FCC, SHP and graphite exists at lower values of N/N+W. Below the graphite demarcation line, graphite disappears, while the FCC and SHP phases remain. For N/N+W values above 0.5 and temperatures between 484 K and the graphite line, a single SHP phase region exists, while a two–phase SHP + NH_4Cl region exists below 484 K, with NH_4Cl existing in two different forms. Per JANAF [Lid85], NH_4Cl undergoes a second order transition at 457.7 K, which is evidenced by a change in heat capacity of the solid at this temperature. This is reflected in the diagram, where NH_4Cl_1 exists with SHP above this transition temperature, while NH_4Cl_2 exists with SHP below it. Moving below N/N+W = 0.5, the equilibrium shifts to a two–phase solid mixture of FCC and SHP. The small, triangular region between ~ 550 and 770 K, with N/N+W $\leq$ 0.04, contains a single FCC phase, which is the most desirable phase for barrier deposition. The operating window in which pure FCC phase material can be deposited at equilibrium is relatively narrow. This suggests that during low–temperature (<770 K) equilibrium deposition conditions, the amount of available N input to the reactor should be decreased relative to our current input amount, to avoid formation of the high resistivity SHP phase. Even for depositions at 450°C (723 K), however, FCC (presumably, based on inference from XPS data) + amorphous carbon is deposited. This suggests that kinetic constraints at this low temperature may cause a surface limited process that inhibits formation and/or desorption of C as a volatile species. Inadequate CH_4 production and/or desorption, for example, could lead to amorphous C deposition even at the lowest temperature.

Experimentally, use of $Cl_4(CH_3CN)WN$–*i*–Pr + PhCN + H_2 causes the minimum value of the N/N+W ratio to be ~0.998, as shown in Table 3-26. By adding an N bearing co–reactant (such as NH_3), this ratio can be increased essentially to 1. Conversely, if an N–free solvent were used in place of PhCN, the ratio above would reach a minimum value of 2/3, due to each i–Pr precursor molecule containing one W and two N atoms (imido N and N in CH_3CN trans ligand). The trans ligand could be changed to one without N, which would decrease this ratio to 1/2. To lower the ratio any further, the number of W atoms in the precursor molecule must be increased or the single source chemistry would need to be abandoned in favor of a co–reactant scheme, with separate precursors providing the W and N atoms.

The second ratio considers changes to the number of C atoms relative W atoms in the input mixture. The plot in Figure 3–15 shows the effect of varying temperature and C/C+W on the deposited equilibrium solid phases. Note again that the gas phase is in equilibrium with all solid phases shown on the diagram, but is not included on the diagram. Four solid phases are also evident in this diagram: FCC β–WN_xC_y, SHP WN_xC_{1-x}, graphite and NH_4Cl. The line extending from 518 to 438 K delineates two regions: NH_4Cl is stable below it (with SHP), but does not appear above it. Moving above this line, a single phase SHP field exists. The curve extending from C/C+W=0.1

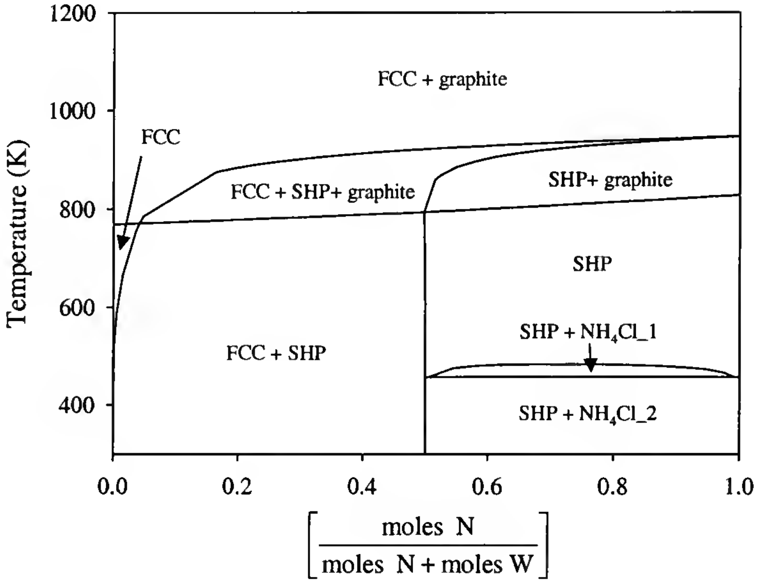

Figure 3–14. CVD phase diagram for variable temperature and N to W ratio; the gas phase is in equilibrium with all solids shown in the diagram, but is not indicated on the diagram.

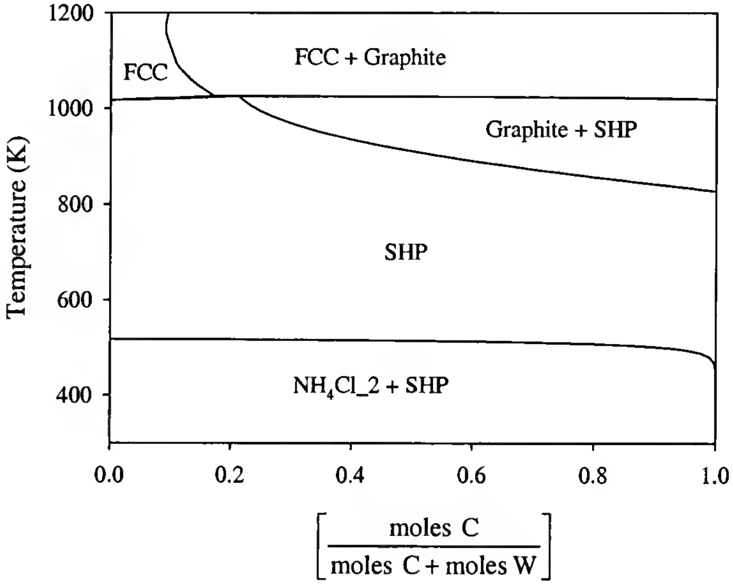

Figure 3–15. CVD phase diagram for variable temperature and C to W ratio; the gas phase is in equilibrium with all solids shown in the diagram, but is not indicated on the diagram.

at T=1200 K to C/C+W=1 at T=828 K, with a discontinuity near T=1020 K, delineates the regions with and without graphite. Graphite appears to the right of this curve, in equilibrium with FCC at higher temperature and SHP at lower temperature. The appearance of graphite at higher temperature and C content makes intuitive sense, as moving toward higher temperature and C levels in our system leads to greater C contamination in the films. The line that is slightly concave down and intercepts the axes on either side of the diagram at T=1020 K delineates regions with (above the line) and without (below the line) the FCC phase. At lower values of C/C+W above 1020 K (747°C), FCC exists as the single solid phase. This suggests that the amount of C in our system should be decreased significantly from the normal value of C/C+W = 0.999 (Table 3-26), and that operation at temperatures greater than 1020 K is required. To decrease the C content, a change in precursor ligands and, more importantly, solvent, would be required. Operating at high temperature favors polycrystalline film deposition, however, which leads to poor barrier performance. Based on the CVD diagrams in Figure 3–14 and Figure 3–15, it appears that fixing the C input to current levels and lowering both the input N level and temperature is the likely route to equilibrium deposition of the FCC phase. Kinetic constraints on the formation and desorption of volatile C containing species, however, may make this difficult, as moving toward lower temperature, which is required for barrier deposition, inherently moves the reactor conditions further away from equilibrium.

3.13 Predicted W–C–N Ternary Phase Diagram

Using the database generated for the W–C–Cl–H–N system, ternary phase diagrams for the W–C–N subsystem can be predicted. The predicted ternary equilibrium for the W–C–N system at 700°C (973 K) and 1×10^5 Pa is shown in Figure 3–16. Four solid phases and one gas phase are present on this diagram. The four condensed phases are FCC BCC W, FCC β–WN_xC_y, SHP WN_xC_{1-x} and graphite, while the gas phase is N_2. Interestingly, the HCP WN_xC_y phase does not appear in the diagram, nor did it appear in either of the CVD phase diagrams. A sizable homogeneity range exists for the single phase field of FCC β–WN_xC_y, which is similar to homogeneity ranges reported for the FCC phase in the Ti–C–N, Zr–C–N [Bin95] and Nb–C–N [Lee01a] systems. The FCC β–WN_xC_y region is broader at the C–rich end of its range, suggesting enhanced stability of this phase at lower x and higher y values.

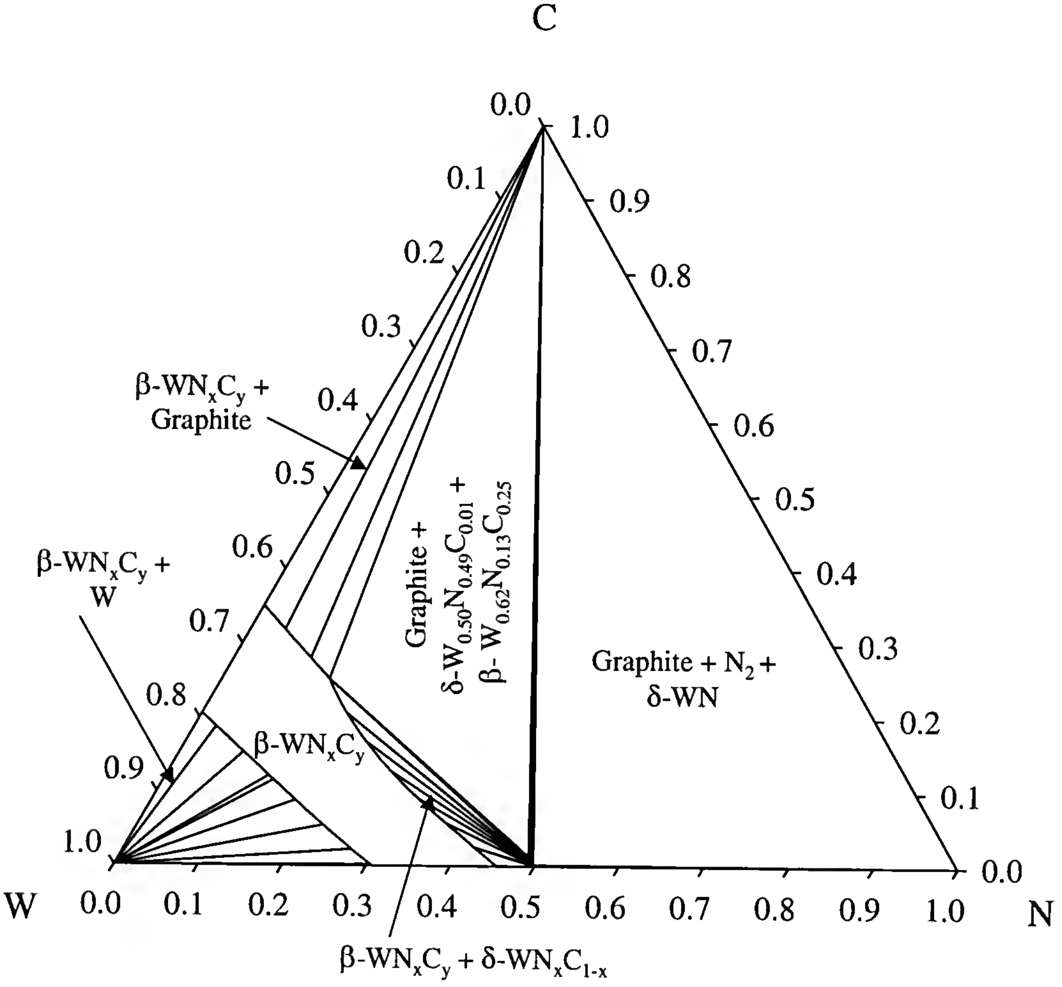
C
0.0
0.1
0.2
0.3
0.4
0.5
0.6
0.7
0.8
0.9
1.0
1.0
0.9
0.8
0.7
0.6
0.5
0.4
0.3
0.2
0.1
0.0
W 0.0 0.1 0.2 0.3 0.4 0.5 0.6 0.7 0.8 0.9 1.0 N
β-WNxCy + Graphite
β-WNxCy + W
β-WNxCy
Graphite + δ-W0.50N0.49C0.01 + β- W0.62N0.13C0.25
Graphite + N2 + δ-WN
β-WNxCy + δ-WNxC1-x

Figure 3–16. Predicted ternary equilibrium phase diagram for the W–C–N system at 973 K and 1×10^5 Pa.

Three two–phase regions are present on the diagram. The triangular shaped region in the bottom left corner of the diagram extending from W to β–$W_{0.8}C_{0.20}$ to β–$W_{0.69}N_{0.31}$ is a two–phase region containing the BCC W and FCC β–WN_xC_y phases in equilibrium. Another two–phase region exists between the single phase FCC β–WN_xC_y field and the line connecting δ–WN with δ–$W_{0.50}N_{0.49}C_{0.01}$. The third two–phase region exists between graphite and the FCC β–WN_xC_y phase.

Two three–phase regions are also present on the diagram. The triangular shaped region on the right of the diagram is a three–phase invariant region bounded by SHP δ–WN, graphite, and N_2 gas. The other three–phase invariant region is bounded by graphite, β–$W_{0.62}N_{0.13}C_{0.25}$ and δ–$W_{0.50}N_{0.49}C_{0.01}$.

In application to CVD, this diagram suggests that the W/C and W/N ratios should initially be made large to drive deposition into the two–phase W + FCC β–WN_xC_y field, where W could be easily detected by XRD. The initial growth temperatures should be relatively high to produce films which are easy to characterize. It is noted that the boundary between the two–phase region and the single FCC β–WN_xC_y field is only weakly dependent on temperature. Thus, the strategy would then be to increase the W/N and possibly W/C ratios, until the W metal phase disappears. The next step then would be to lower the processing temperature to foster deposition of an amorphous FCC β–WN_xC_y film.

The predicted ternary equilibrium diagrams for the W–C–N system at 1×10^5 Pa are shown for temperatures of 500°C (773 K) and 300°C (573 K) in Figure 3–17 and Figure 3–18, respectively. Interestingly, the two–phase graphite + FCC β–WN_xC_y region shrinks with decreasing temperature through growth of the two–phase FCC

β–WN_xC_y + δ–WN region. The increase in area of the FCC + δ two–phase region with decreasing temperature follows the trend on the binary W–N diagram, in which the FCC region narrows with decreasing temperature below 1046 K while the two phase FCC + δ region grows (Figure 3–5). The tested precursors were unable to deposit films at 300°C, requiring higher temperature to trigger film growth. Hence, no experimentally grown film is available for comparison against this diagram.

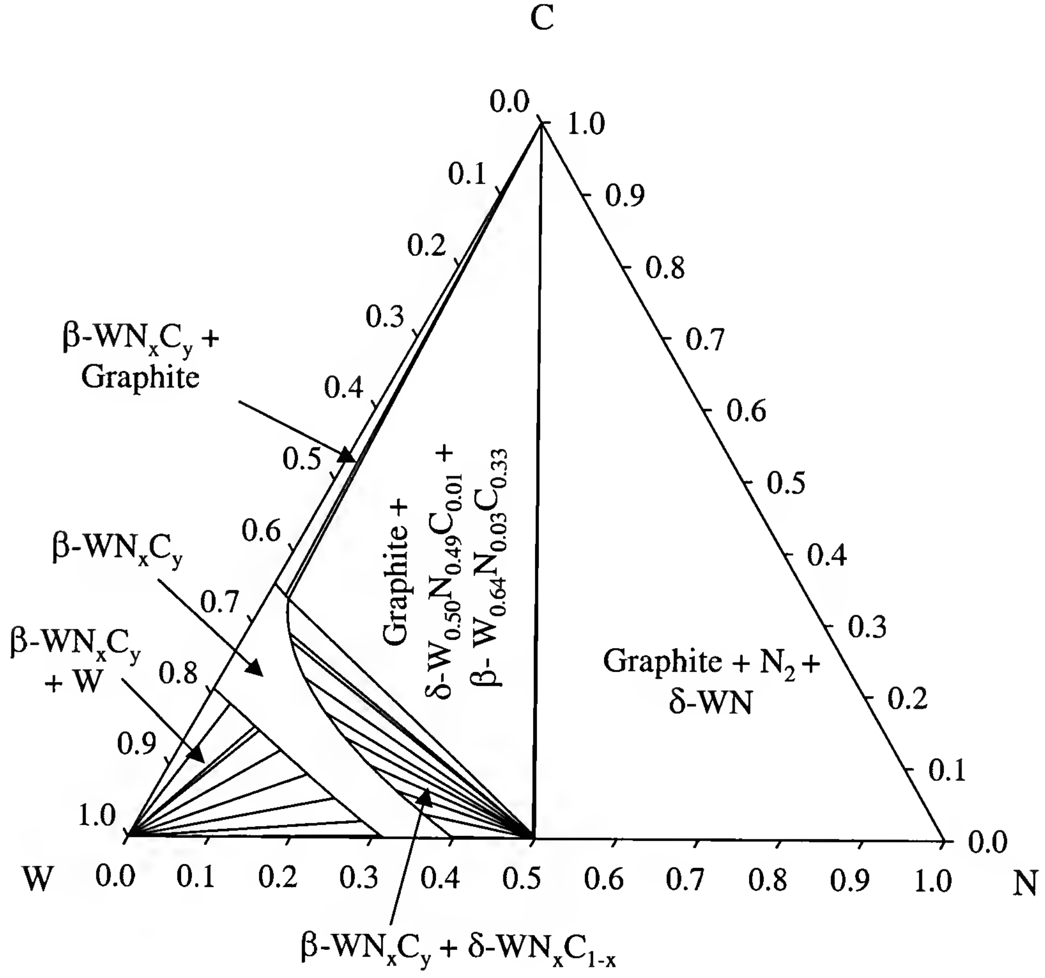
C
0.0
0.1
0.2
0.3
0.4
0.5
0.6
0.7
0.8
0.9
1.0
1.0
0.9
0.8
0.7
0.6
0.5
0.4
0.3
0.2
0.1
0.0
W
0.0
0.1
0.2
0.3
0.4
0.5
0.6
0.7
0.8
0.9
1.0
N
β-WN_xC_y + Graphite
β-WN_xC_y
β-WN_xC_y + W
Graphite + δ-$W_{0.50}N_{0.49}C_{0.01}$ + β- $W_{0.64}N_{0.03}C_{0.33}$
Graphite + N_2 + δ-WN
β-WN_xC_y + δ-WN_xC_{1-x}

Figure 3–17. Predicted ternary equilibrium phase diagram for the W–C–N system at 773 K and 1×10^5 Pa.

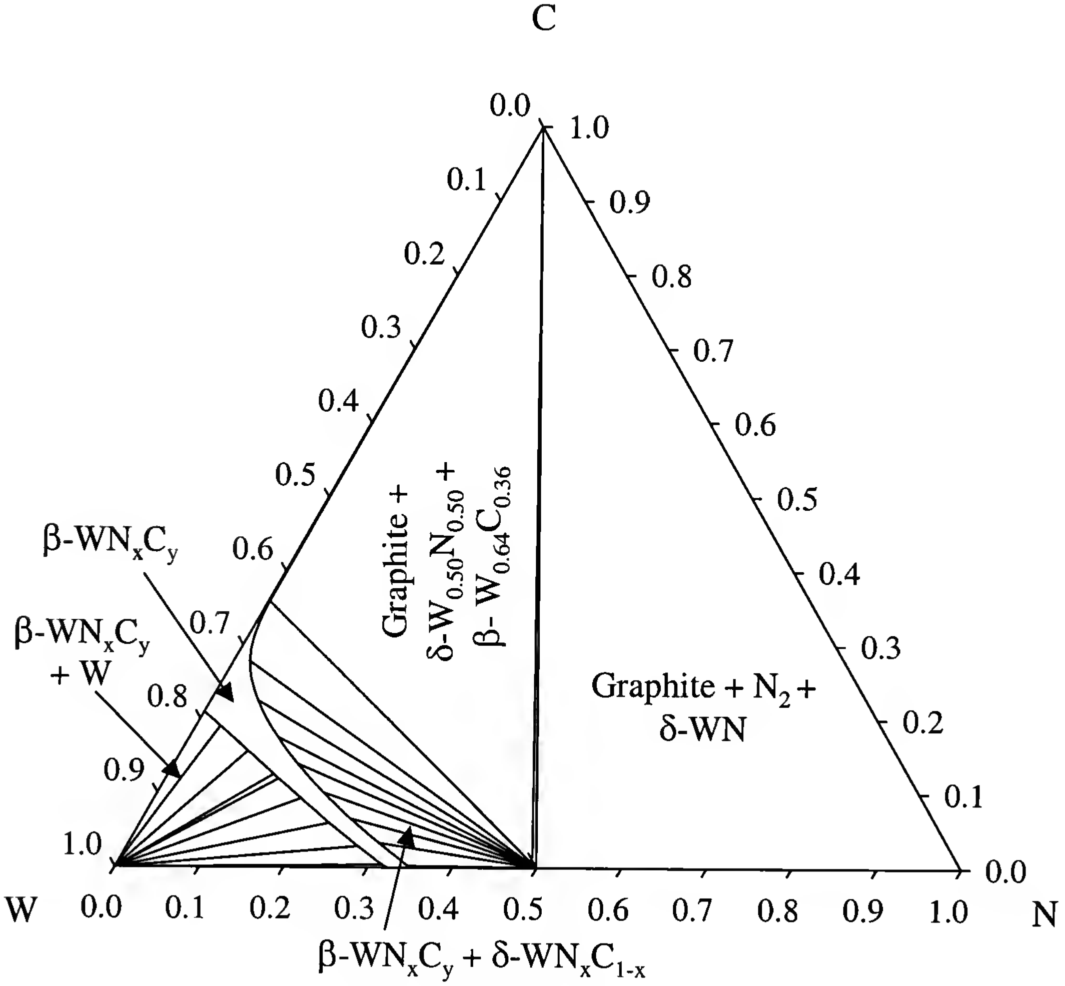
C
0.0
0.1
0.2
0.3
0.4
0.5
0.6
0.7
0.8
0.9
1.0
1.0
0.9
0.8
0.7
0.6
0.5
0.4
0.3
0.2
0.1
0.0
W
N
0.0 0.1 0.2 0.3 0.4 0.5 0.6 0.7 0.8 0.9 1.0
β-WN$_x$C$_y$
β-WN$_x$C$_y$ + W
Graphite + δ-W$_{0.50}$N$_{0.50}$ + β- W$_{0.64}$C$_{0.36}$
Graphite + N$_2$ + δ-WN
β-WN$_x$C$_y$ + δ-WN$_x$C$_{1-x}$

Figure 3–18. Predicted ternary equilibrium phase diagram for the W–C–N system at 573 K and 1×10^5 Pa.

3.14 Predicted β–$WC_{0.5}$ – β–$WN_{0.5}$ Pseudobinary Equilibrium

Since FCC is the desirable structure for barrier film deposition, it is useful to understand how temperature affects the equilibrium composition of FCC β–WN_xC_y. The pseudobinary diagram in Figure 3–19 shows the effect of temperature on the FCC β–WN_xC_y for varying N and C content. The end members of this pseudobinary are the FCC β–$WC_{0.5}$ and FCC β–$WN_{0.5}$ phases. While the C and N content of this phase varies substantially, the end member stoichiometries were fixed to β–$WC_{0.5}$ and β–$WN_{0.5}$ to match the most desired stoichiometry for nitride barriers (β–$WN_{0.5}$ = β–W_2N). As evident from Figure 3–19a, FCC β–WN_xC_y is stable at 1×10^5 Pa for temperatures below 1869 K. The pure nitride begins to decompose above this temperature, leading to formation of gas and FCC β–WN_xC_y. As temperature increases above 1869 K, the N content of FCC β–WN_xC_y decreases (due to formation of N_2 in the gas phase) while C content increases. The trend of decreasing N and increasing C content for the FCC β–WN_xC_y phase with increasing temperature matches the trend for the deposited films. This behavior is consistent with decomposition of the binary nitride phase at higher temperature, rather than melting, which is reported for the binary carbide phase (far left of diagram). An expanded view of the left side of the pseudobinary diagram is shown in Figure 3–19b. On the far left side of the diagram, congruent melting of FCC β–WN_xC_y (with N content below 0.002) is predicted for temperatures at and above 3004 K. A single ternary liquid phase is present above 3004 K in this region of the diagram. A small triangular region from T=3004 to 3012 K, with N content between 0.002 and 0.01, contains FCC + liquid in equilibrium. Above 3012 K for N content above 0.002, liquid exists in equilibrium with a gas phase. Between the FCC + gas and liquid + gas two–phase fields on the diagram is a narrow, three–phase equilibrium region containing FCC + liquid + gas. The temperature at which liquid forms in equilibrium with FCC and gas increases with increasing C content on the interstitial sublattice, reaching a maximum value near 3012 K.

In addition to predicting the ternary W–C–N and pseudobinary β–$WN_{0.5}$–β–$WC_{0.5}$ equilibria, the site fraction of C, N and vacancies on the FCC W interstitial sublattice was also examined. The change in interstitial site occupation with

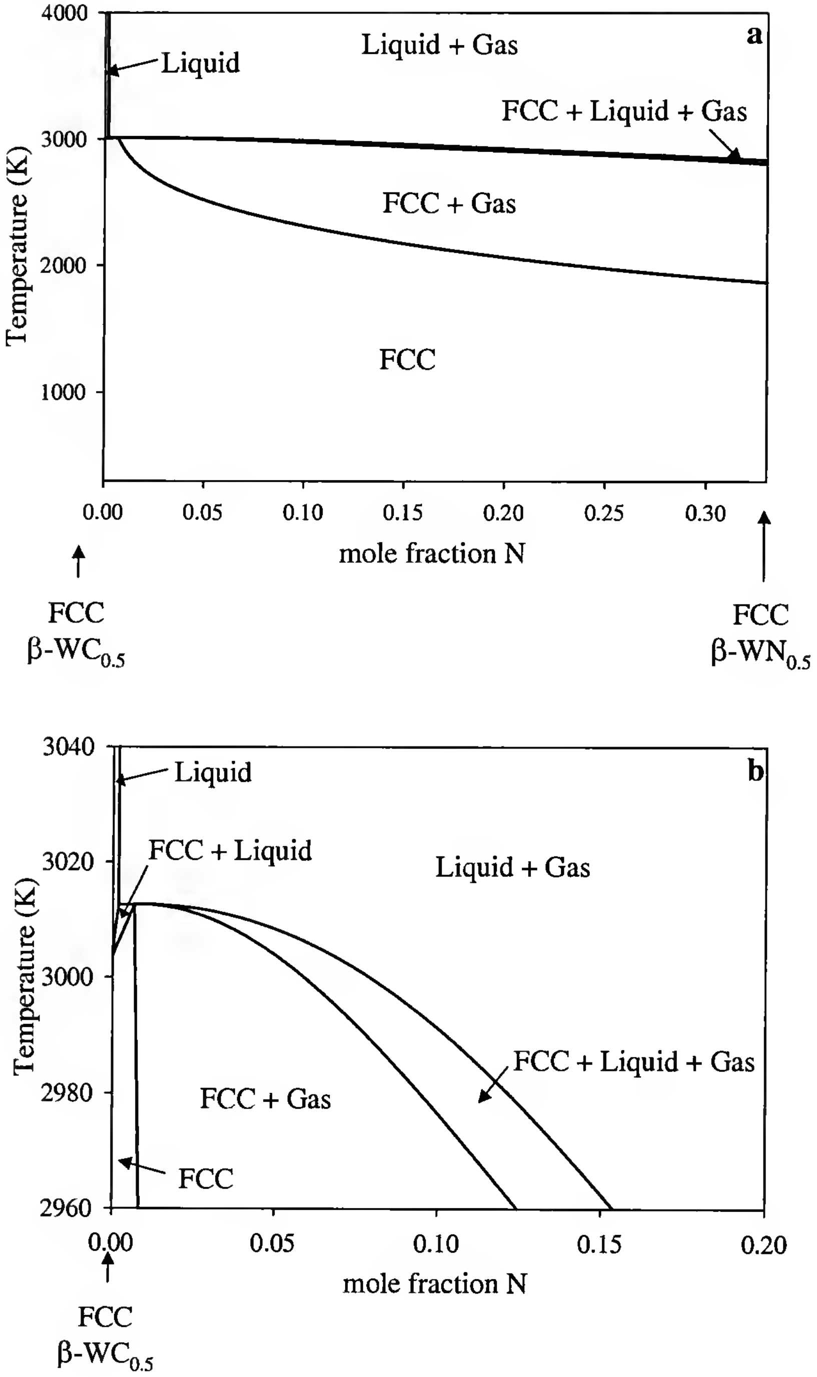

Figure 3–19. FCC β–$WN_{0.5}$ –β–$WC_{0.5}$ solid–liquid–gas pseudobinary diagram at 1×10^5 Pa. a) Full view. b) Zoom view to show three–phase regions.

temperature is shown in Figure 3–20 below. The graph indicates complete occupation of all interstitial sites by N at temperatures below ~680 K, with N occupation decreasing steadily above this temperature. Between 680 and 1100 K, escaping N atoms leave behind vacancies, rather than incorporating C in place of N. At 1100 K, C begins to occupy interstitial sites on the sublattice, and increases to a maximum occupation of 0.66 near 2500 K. Experimentally, C replaces N on the interstitial sublattice at temperatures far below 1100 K, which again may be due to the inability of C to form and/or desorb in a volatile species at our lower deposition temperatures.

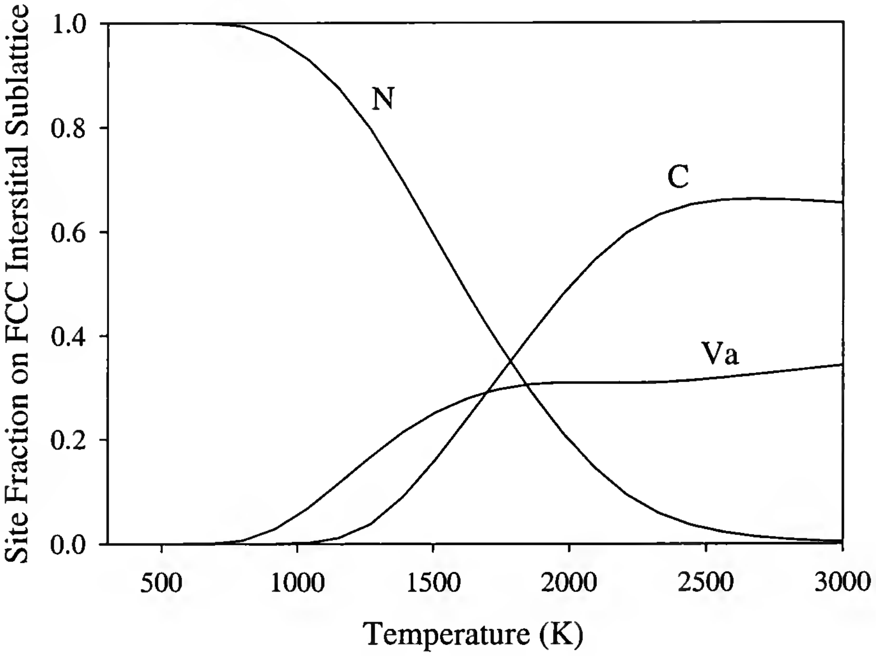

Figure 3–20. Temperature dependence of C, N and Va site fraction on interstitial FCC W sublattice at 350 Torr.

CHAPTER 4
EXPERIMENTAL APPROACH FOR CVD

4.1 Substrate Preparation

The majority of film depositions were done on Si substrates for several reasons. First, Si is inexpensive and readily available. Second, interdiffusion and reaction between Cu and Si is very rapid, even at low temperatures, making Si a very conservative material on which to test a barrier. Third, future metallization schemes will look to extend Cu down to the contact level, meaning that Cu will be in intimate contact with Si. In addition to Si, however, barriers must also be tested on other materials, such as new, potential low–k and high–k dielectric materials. Depositions on these materials will be pursued in the future.

Boron doped (p–type) Si substrates from Wacker–Chemitronic GMBH were used for the WN_x growths. Substrates included both Si (100) and (111) orientations, which were cut from 150 mm wafers. Substrate resistivity ranged from 1 to 2 Ω–cm. Substrate preparation prior to deposition included degreasing and etching steps. Grease remaining from the Si wafer production process must first be removed from the substrates, after which the thin native oxide layer (10 to 20 Å) typically present on the Si surface (due to air exposure) must be removed [Jae88]. To degrease the substrates, they were immersed for three minutes per solvent in warm trichloroethylene (TCE), acetone, and methanol. The substrates were then placed in boiling deionized (DI) water for thirty seconds to remove any remaining solvent, and were then submersed for 2 minutes in buffered oxide etch (BOE) solution (6:1 NH_4F:HF in water) to remove the native oxide layer. After etching, the substrates were wiped off with acetone, blown dry and placed onto the susceptor. The susceptor (with substrates) was loaded into the reactor before each run through a pneumatically controlled gate valve on the reactor head.

4.2 Solvent Tests

After synthesis (details of which are given in Chapters 5, 6 and 7), the solid precursor was dissolved in solvent and loaded into a Hamilton Samplelock 14.57 mm ID syringe. Syringes were normally filled to 10 mL. Due to the light sensitivity of the precursor/solvent mixture, syringes were covered with aluminum foil after being filled. Solvents tested included acetonitrile (MeCN), N–methylpyrrolidinone (NMP), dimethylacetamide (DMA), dimethylformamide (DMF), benzonitrile (PhCN) and *o*–dichlorobenzene (1,2–DCB). The structures of these solvents are shown in Figure 4-1.

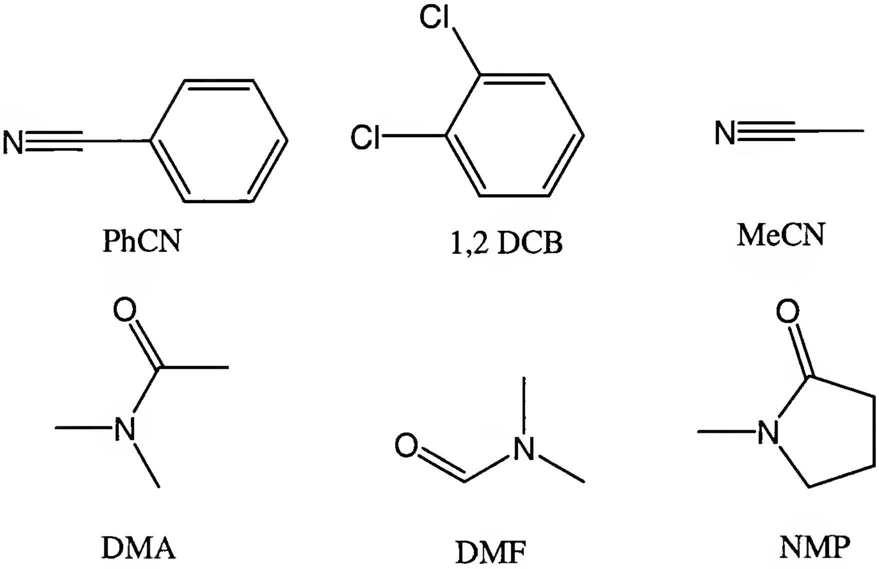

PhCN 1,2 DCB MeCN

DMA DMF NMP

Figure 4-1. Solvents tested for dissolution of the precursor

4.3 Description of CVD System Components

Film growths were conducted in a custom built chemical vapor deposition (CVD) reactor system (detailed PFDs are in Appendix A). The CVD system contains a 63 mm ID quartz tube reactor, capped on each end by stainless steel flanges. These flanges contain metal collars, which compress viton o–rings onto the quartz tube to vacuum seal the reactor system. To prevent overheating of these o–rings, the stainless steel flanges are encased in water–cooled jackets.

The system was maintained at vacuum by a Fisher Scientific Maxima C roughing pump. A Pyrex cold trap upstream of the roughing pump was used to remove particulates from the effluent stream and prevent damage to the roughing pump. System pressures above 1 Torr were measured by an MKS Baratron Type 221A pressure gauge, while pressures below 1 Torr were measured with a Sensavac Series 315 Pirani gauge.

An MKS 253A throttle valve between the reactor and the cold trap was used to control operating pressure in the system. Depositions were conducted at pressures ranging from 150–760 Torr. Carrier and reacting gases, supplied from cylinders, were metered into the system via MKS 1159B Mass Flow Controllers. Gases available to the system included boron trichloride (BCl_3), diborane (B_2H_6), nitrogen (N_2), hydrogen (H_2), ammonia (NH_3) and helium (He). Lines were traced with heat tape when required. Heat tape temperature was controlled with Staco Energy Variable Autotransformers.

A 32 mm OD cylindrical graphite pedestal–type susceptor was used to heat the substrates during deposition. The susceptor rests on an alumina encased type–S thermocouple (Pt–Rh), which gives a continuous temperature measurement. The susceptor has a small bore hole through its center, which extends from the bottom of the susceptor up to a point roughly 2 mm below its surface. The thermocouple was inserted into this hole, so that its top was very close to the susceptor surface for accurate temperature measurement. The thermocouple/susceptor assembly is shown in Figure 4-2. The susceptor is inductively heated by radio frequency (RF) coils, which are powered by a Westinghouse 7.5 KW RF Generator. Susceptor temperature is controlled manually by adjusting the power control knob on the RF Generator.

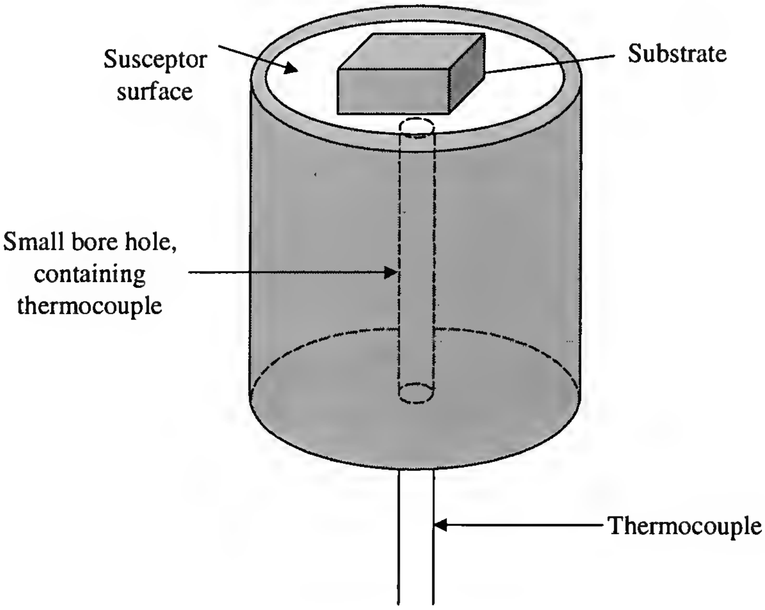

Figure 4-2. Graphite susceptor / alumina encased thermocouple assembly.

A Cole–Parmer 74900–00 Syringe Pump was used to meter the precursor/solvent mixture to the nebulizer unit. A Swagelok 25 PSI poppet valve (SS–2C–KZ–25) was used to prevent the syringe contents from evaporating into the system's vacuum. A Cetac Technologies nebulizer unit was used to generate a droplet mist from the liquid precursor/solvent mixture. The nebulizer contains a piezoelectric quartz plate, which vibrates continuously at a frequency of 1.44 MHz due to the application of an electrical potential. This rapid vibration causes liquid droplets contacting the plate to be vaporized into a mist. The diameter of liquid droplets in the mist formed by the nebulizer can be estimated with Equation 4–1, proposed by Lang [1962]:

$$D = 0.34\left(\frac{8\pi T}{\rho F^2}\right)^{\frac{1}{3}} \tag{4–1}$$

where D is mean particle diameter (cm), T is the surface tension (dynes/cm), ρ is the liquid density (g/cm³) and F is the excitation sound frequency (s^{-1}). If one assumes the liquid/precursor mixture to have essentially the same physical properties as benzonitrile solvent at 25°C, for example, the median droplet diameter produced by the nebulizer is ~2.4 μm.

After nebulization, the mist is conveyed by carrier gas, which is introduced through the side of the nebulizer chamber, to a heated double tube impinging jet. The jet contained an inner tube, which conveyed the reactant/carrier gas mixture, and an outer tube, which was sealed by an o–ring against the reactor head. The annular space between the tubes contained heating tape, whose temperature was adjusted with an Autotransformer. The heating tape for the impinging jet and the nebulizer discharge line was typically kept at 50°C. A schematic of the impinging jet is shown in Figure 4-3. A schematic of the nebulizer and reactor is shown in Figure 4-4.

An Inficon Transpector 2 residual gas analyzer (RGA) was used during some experiments to determine composition in the gas phase. The device contains a quadrupole mass spectrometer, and is connected to the system by a 1/16” stainless steel capillary tube, which pulled a gas sample from very near the surface of the substrates inside the reactor. The RGA sensor required high vacuum for operation, and hence a turbo and roughing pump in series were connected to the sensor for this purpose.

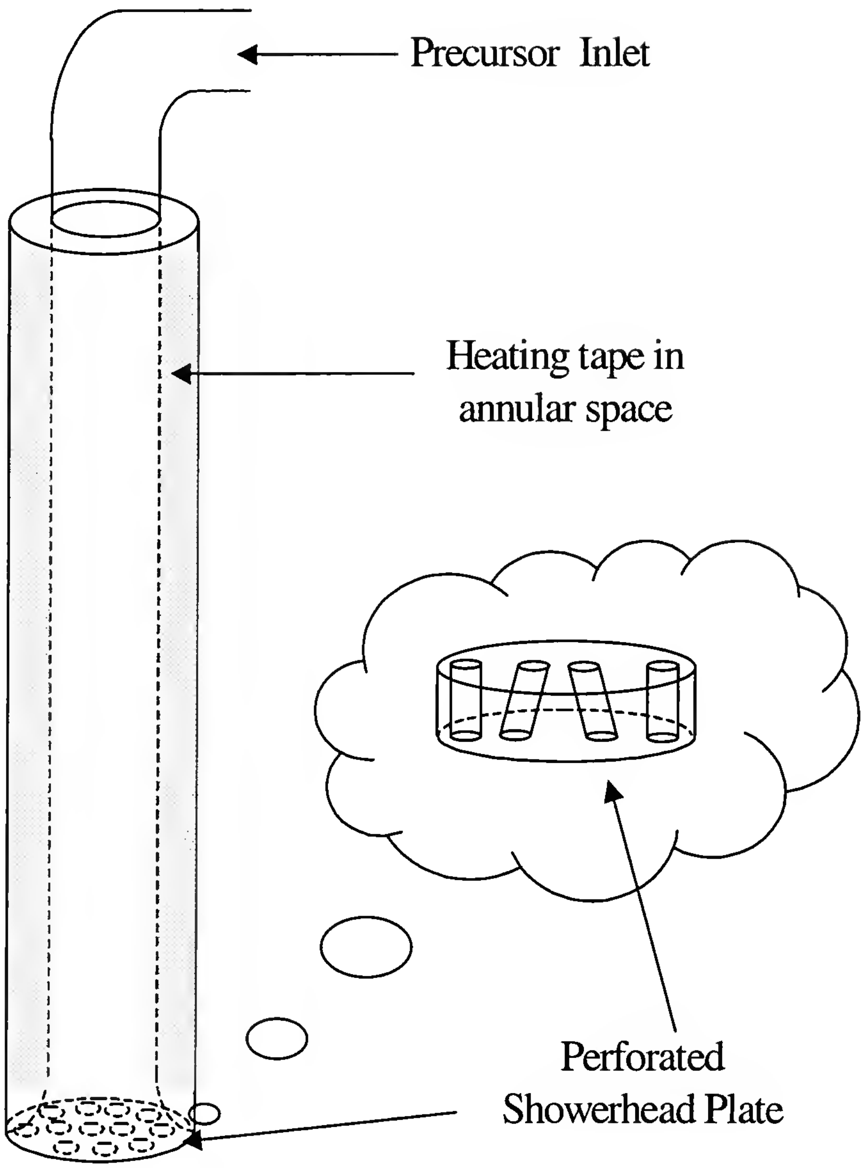
Precursor Inlet
Heating tape in annular space
Perforated Showerhead Plate

Figure 4-3. Schematic of the double tube impinging jet with detailed inlay of the perforated showerhead plate.

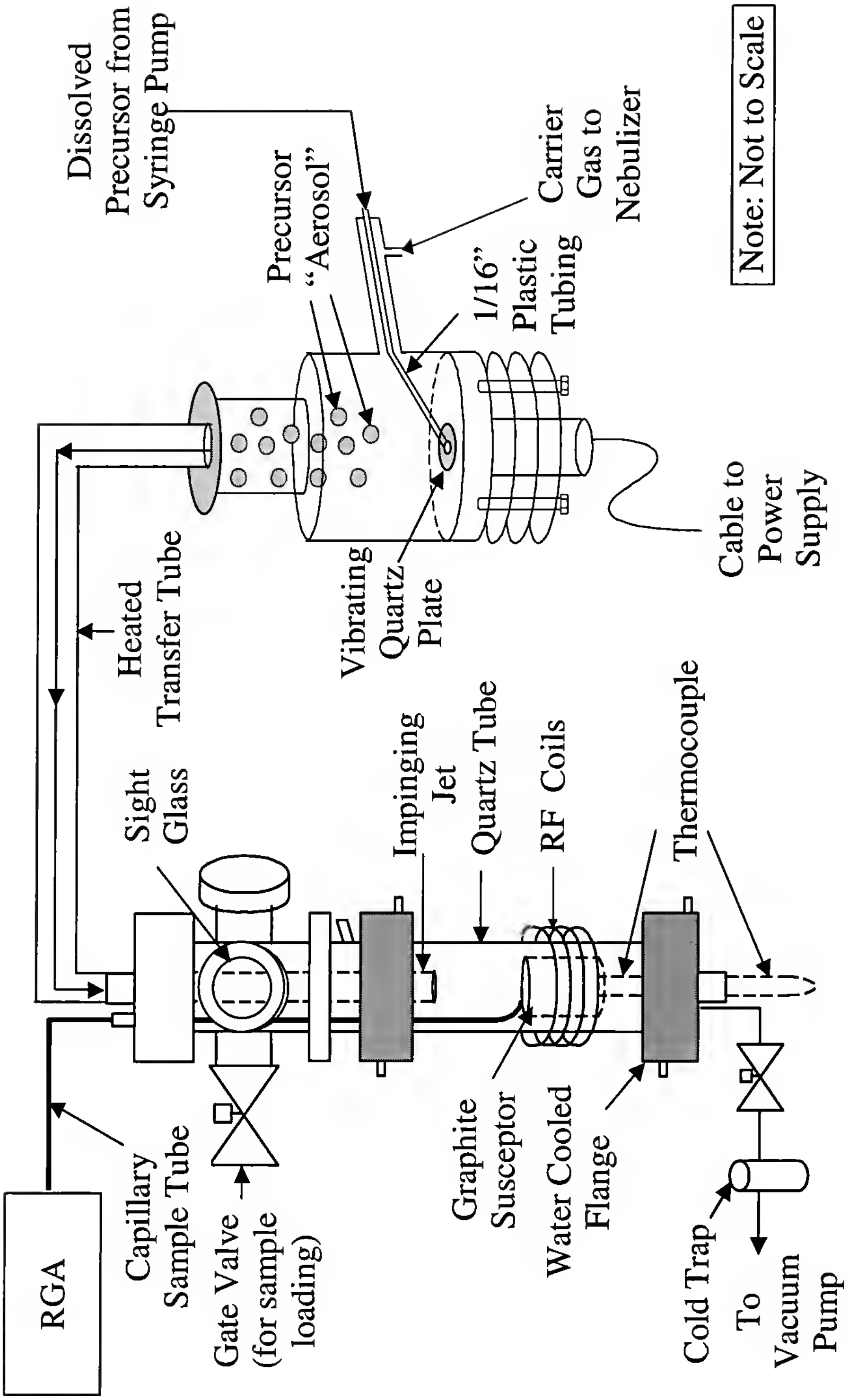
Dissolved Precursor from Syringe Pump
Precursor "Aerosol"
Carrier Gas to Nebulizer
1/16" Plastic Tubing
Note: Not to Scale
Heated Transfer Tube
Vibrating Quartz Plate
Cable to Power Supply
Sight Glass
Impinging Jet
Quartz Tube
RF Coils
Thermocouple
RGA
Capillary Sample Tube
Gate Valve (for sample loading)
Graphite Susceptor
Water Cooled Flange
Cold Trap
To Vacuum Pump

Figure 4-4. Schematic of the nebulizer and reactor.

4.4 Start–Up

The time lag between substrate removal from the etch solution and achievement of reactor vacuum was minimized (<5 minutes) to limit the thickness of the native oxide (SiO_2) layer reforming on the substrates, which was estimated to range from 1–8 Å for exposures less than 10 minutes [Gan92, Phi92]. Once the substrates were loaded, the reactor was sealed and brought to ultimate vacuum (usually 600–900 mTorr). Vacuum was pulled on the system for 5 minutes, and inert gas was then introduced to bring the system up to its operating pressure. Once at the operating pressure, the substrates were typically reduced in a H_2 atmosphere at 1000°C for 10 minutes ("H_2 bake") to remove any remaining surface oxides. Upon completion of the H_2 bake, the system was brought to the reaction temperature. Once reaction temperature and pressure were stabilized, the syringe pump and nebulizer were started. Deposition time ranged from 0.5 to 2.5 hours, with syringe pump flowrate set to 4.0 mL/hr. The goal of the depositions was to thermally decompose the precursor molecule in a manner that cleaved off all leaving groups in a clean fashion, leaving behind only W and N in the film.

4.5 Copper Deposition

The two means of Cu deposition available to us were ECD and sputtering. A prior study was used as the framework for our Cu ECD setup [Sha01]. The ECD solution contained copper sulfate pentahydrate [$CuSO_4 \cdot 5H_2O$], ammonium citrate ($(NH_4)_2HC_6H_5O_7$), and aqueous ammonia [$NH_3(aq)$], all of which were purchased from Fisher Scientific. The molar concentration of these species in the bath was 0.08 M $CuSO_4 \cdot 5H_2O$, 0.08 M $(NH_4)_2HC_6H_5O_7$, and 0.175 M $NH_3(aq)$, per a published ECD procedure [Sha01]. The beaker of ECD solution, which contained a magnetic stirring bar, was placed on a stirring plate to get good mixing during the plating process. Good mixing ensured intimate contact between the film surface and fresh electroplating solution. Gator clips were clamped on the substrates, and a Gelman Instrument Company constant voltage power supply was used to provide power to the conductive surface of the substrates.

Barrier film samples were also coated with Cu by RF magnetron sputtering at 5 mTorr pressure in Ar. Michael Jones in Dr. Norton's group ran the depositions. The sputter deposited Cu film thickness was ~100 nm. Annealing of some samples with sputtered Cu was done in–situ in the sputter chamber.

4.6 Analysis Techniques

The following is a brief description of the different characterization techniques used to analyze the films in this study.

AES

Auger electron spectroscopy (AES) is a three–electron process, which can be used to determine sample composition. An electron beam is used to eject a core electron from an atom, forming a hole in the subshell from which ejection occurred. This hole is then filled by an electron from a higher energy (outer) shell. The higher energy electron must release energy as it drops to fill the lower energy hole. The energy may be released either as an x–ray or by ejected a third electron from one of the outer electron shells in the atom. The energy of this third electron, called the Auger electron, is very specific to the atom and energy level from which it originated. By comparing Auger electron energies for a given sample against standards, the element and percent composition can be determined.

Film composition was checked by Auger electron spectroscopy (AES) using a Perkin–Elmer PHI 660 Scanning Auger Multiprobe. The AES system had a nominal sputter rate of 100 Å/min. It is important to note that calculation of film concentrations using AES involves taking the ratio an element's peak height in the experimentally measured film to its peak height for the pure element standard. This is shown mathematically in Equation 4–2 [Bri90, Fit95]:

$$\frac{x_A}{x_B} = F_{AB}\left(\frac{I_A / I_A^{Std}}{I_B / I_B^{Std}}\right) \tag{4–2}$$

where x_A is the concentration of element A in the film, I_A is the measured intensity of the Auger electron from component A in the film matrix, I_A^{Std} is the intensity for A's pure element standard, and F_{AB} is a matrix dependent factor, which would take into consideration interactions between the elements in the film matrix, and adjust the measured intensities accordingly. If this F_{AB} is unknown, as is the case for our films, it is not possible to get highly quantitative values for elemental concentrations in the films. The value in using AES for multi element films where values for F_{AB} are unavailable is therefore to compare elemental trends in films with similar properties, which should have similar values for F_{AB}. Trends in film content vs. deposition temperature, for example, can give insight into the impact of experimental conditions on film compositions, without giving exact compositions. Thus, the concentration measurements do not take into account any shifts in sensitivity factor due to matrix effects.

In addition to determination of film composition, the AES system was used for some depth profiling studies. The three–point AES depth profiling method was used to determine the change in elemental content with depth into the films.

AFM

Film roughness was analyzed by atomic force microscopy (AFM) using a Digital Instruments Nanoscope III in tapping mode. Kee–Chan Kim assisted with some AFM measurements.

CS–SEM

Samples were cleaved to expose the film's cross section at the middle of the substrate, and were then mounted vertically onto modified SEM stub pieces. Conductive carbon paint was used to mount the samples, and to close the electrical connection between the stub piece and the film surface. Film thickness was estimated by cross–sectional scanning electron microscopy (CS–SEM) on a JEOL JSM–6400, with growth rate calculated by dividing film thickness by deposition time.

Four–Point Probe

Four point probe was used to determine the resistivity of our sample films. The 4–point probe sensor head has 4 metal contacts (points), where the two outside tips pass a current and the two inner tips measure the voltage between them. Once measurements were taken, the sheet resistance was determined by Equation 4–3:

$$R_s = 4.532 * \left(\frac{V}{I}\right) \tag{4–3}$$

where R_s is sheet resistance (Ω / square), V is voltage (Ω), and I is current (Amperes). Film resistivity is determined by multiplying sheet resistance by film thickness (Equation 4–4):

$$\rho = R_s * t \tag{4–4}$$

where ρ is film resistivity (Ω*cm) and t is film thickness (cm). Film resistivity was measured with an Alessi Industries four–point probe.

SIMS

Secondary ion mass spectrometry (SIMS) depth profiles were acquired with a Perkin–Elmer PHI 6600 SIMS system using a 5keV Cesium primary ion beam and negative secondary acquisition. Dr. Margarida Lambers operated the SIMS system and provided the depth profile data to us. After the films were sputtered by the Cs beam, the crater depths were measured with an Alpha–Step 500 stylus profilometer.

TEM

Young–Woo Heo from Dr. Norton's group prepared samples for transmission electron microscopy (TEM) using an FEI Strata DB235 Focused Ion Beam (FIB) system. After the samples were prepared, he used a JEOL 2010F TEM to collect diffraction patterns and micrograph images.

XPS

X–ray photoelectron spectroscopy (XPS) uses monoenergetic soft X–rays to eject electrons from the various electron shells of the atoms under examination. The kinetic energy (KE) of the ejected electron (called a photoelectron) is directly dependent on the x–ray excitation energy and the binding energy (BE), which holds the electron to the atom, per Equation 4–5:

$$BE = h\nu - KE - \phi_{SP} \qquad (4\text{–}5)$$

where hν is the energy of the incoming x–ray (h is Planck's constant, 41.3×10^{-16} eVs, and ν is frequency in s^{-1}), and ϕ_{SP} is the work function of the spectrometer [Mou95, Dia73, Ole97, Bar94]. The kinetic energy of ejected photoelectrons is measured with the spectrometer, so for known values of hν and ϕ_{SP}, the BE can be calculated. A Mg anode x–ray source with hν =1253.6 eV was used for this analysis. Photoelectron BE is very specific to the parent atom and subshell from which the ejected electron emanates. While the magnitude of the BE can be used to determine the atom and subshell from which the photoelectron emanates, small shifts in the BE can be used to determine the bonding state of the parent atom. Bonding states for the parent atoms can be deduced by comparison of BE values to those published in the literature. Determination of bonding states from BE shifts must be reconciled with sample charging, which occurs when there is an imbalance between the number of photoelectrons ejected from the sample and the number of electrons introduced to the sample by conduction. Positive charging of the sample retards outgoing electrons and causes peaks to shift to higher binding energy, while negative charging causes peaks to shift to lower binding energy [Mou95]. Photoelectron lines are typically 0.5 eV wider for insulators than for conductors, since line width depends on the lifetime of holes generated by the photoionization process [Mou95]. The conductor is able to fill holes much more quickly and therefore has a narrower linewidth. This is true in the case of WN_x vs WO_3, where WN_x (a conductor) has a narrower peak relative to WO_3 (a semiconductor). A more detailed description of XPS fundamentals is available elsewhere [Bar94, Mou95, Ole97].

Bonding in the films was examined by X–ray photoelectron spectroscopy (XPS) using a Perkin–Elmer PHI 5100 ESCA System with a Mg anode ($h\nu=1253.6$ eV). The XPS system had a nominal sputter rate of 20 Å/min. Deconvolution of XPS spectra was done using RBD Analysis Suite software.

XRD

After growth, film structure was examined by room temperature X–ray diffraction (XRD) on a Philips APD 3720 diffractometer operating from 5–85 2θ degrees with Cu Kα radiation. The term diffractometer refers to an instrument used to study crystalline (and non–crystalline) materials by measuring the way they diffract x–rays of known wavelength [Cul01]. The XRD unit used for analysis used the Bragg–Brentano θ–2θ method to collect spectra. The governing equation used for XRD is Bragg's Law (Equation 4–6):

$$n\lambda = 2d\sin\theta \tag{4–6}$$

where n is the number of whole wavelengths, λ is the x–ray wavelength (1.5406 Å for Cu Kα), d is the interplanar spacing (Å) and θ is the Bragg angle (degrees).

Several potential sources of error are associated with this method of XRD, including the flat substrate error, the specimen transparency error, and specimen displacement error [Jen96]. To limit the effects of these error sources on the location of peak maxima, all peaks from the deposited film were calibrated to the Si(400) peak position, which was shifted (when necessary) to its standard value ($2\theta = 69.13$). XRD spectra were used to estimate lattice parameter, calculate grain size, and to observe texturing. Since the (111) orientation of β–WN_x (or β–WN_xC_y) is typically the dominant peak in the film's spectrum, it was used to estimate grain size and lattice parameter in the films. The lattice parameter of a cubic phase is shown in Equation 4–7:

$$a = d\sqrt{h^2 + k^2 + l^2} \tag{4–7}$$

where a is the lattice parameter (Å) and h, k, and l are the plane indices [Cul78]. The Scherrer equation (Equation 4–8) may be used to estimate the average crystallite size (t, Å) [Cul78, Nag00]:

$$t = \frac{0.9\lambda}{(B\cos\theta)} \tag{4–8}$$

where B is the full width at half maximum (FWHM) for the selected diffraction peak.

XRR

X–ray reflectivity measurements were taken to estimate density in some film samples. XRR data were collected and analyzed by Dr. Valentin Craciun, using a Philips MRD X'Pert system.

4.7 Precursor Screening Procedure

After synthesis of a new precursor by Dr. McElwee–White's group, the candidates were screened by a two–part procedure. This procedure involved precursor composition and mass spectrometry testing by the chemistry group and CVD testing of these precursors by our group. The stepwise screening procedure is outlined below.

Part I –Feasibility Study

- Synthesize precursor.
- Collect mass spectral data (both positive ion EI and negative ion CI).
- Analyze spectral data to determine if precursor molecule may cleave in a manner consistent with objectives.

- If promising, run solvation tests to see which solvent may be used for delivery to the nebulizer, and to see if adequate transport from nebulizer to reactor occurs.
- Use dissolved precursor to grow film at mid–range growth temperature (~600°C).
- Check film crystallinity (or lack thereof) with XRD.
- If XRD indicates possible presence of WN_x film, run AES.
- If AES results reinforce that W and N are present, continue to deposition and analysis section

Part II – Film Deposition and Analysis

- Vary film growth temperatures to minimize carbon and oxygen contamination, optimize nitrogen concentration and grow amorphous films.
- Analyze films for crystallinity with XRD.
- Analyze films with AES for compositions.
- Using AES data, determine nitrogen, carbon and oxygen content of films as a function of deposition temperature.
- Determine film thickness by X–SEM, and calculate growth rate. Determine activation energy for film growth.
- Analyze film resistivities as a function of contaminant concentration and reaction temperature.
- Run SIMS to check for Cl contamination in films.
- Check film conformality by depositions on patterned wafers.
- Test barrier integrity by a Cu deposition and anneal process.

CHAPTER 5
EVALUATION OF $Cl_4(CH_3CN)WN$–*i*–Pr AS A SUITABLE WN_x PRECURSOR

Imido complexes are attractive candidates for MOCVD of tungsten nitride since the W–N multiple bond in the precursor is likely to survive the deposition process and facilitate incorporation of nitrogen into the film. Additionally, the linear geometry of the multiple bond keeps the alkyl or aromatic group of the imido ligand away from the metal, thus deterring any cyclometallation process. Moreover, by changing this group, the N–C homolytic bond strength of the imido moiety is tunable, which should allow for a degree of control over carbon impurities and other film characteristics.

5.1 Synthesis of Isopropyl [$Cl_4(CH_3CN)WN$–*i*–Pr] Precursor

The first precursor examined in detail was $Cl_4(CH_3CN)WN$–*i*–Pr, which contains an isopropyl group singly bound to the imido nitrogen. To prepare the precursor, an orange slurry of tungsten oxychloride ($WOCl_4$, 3.41 g, 10 mmol) and isopropyl isocyanate (*i*–PrNCO, 1.57 mL, 16 mmol) in 60 mL of heptane was heated while stirring at 100°C for 2 days. After this time, a dark red solution containing red crystals was obtained. The solvent was removed *in vacuo* and the solid was redissolved in 20 mL of acetonitrile. After stirring for 2 hours at room temperature, the brown solution was filtered and the solvent evaporated to yield 3.7 g of brown crystals. The yield of the crystals from the solution was 88%. ^1H NMR ($CDCl_3$): δ 1.67 (d, 6H), 2.49 (s, 3H), 7.07 (m, 1H). ^{13}C NMR ($CDCl_3$): δ 3.35, 23.12, 68.52, 118.37. IR (CH_2Cl_2): 2319, 2282, 1462, 1452, 1386, 1366, 1310, 1271, 1154, 1108, 1075 cm^{-1}.

The solid precursor had low vapor pressure, making solid source delivery to the reactor impractical. To overcome this inherently low vapor pressure, the single–source precursor was dissolved in a solvent and the precursor/solvent mixture was subsequently vaporized in a nebulizer for easy delivery to the reactor.

5.2 Solvent Selection

Choice of an appropriate solvent to convey the precursor compound is essential. The solvent's volatility must be adequate for the solvent/precursor mixture to be nebulized. If the solvent's volatility is too high, it evaporates in the nebulizer and leaves the dissolved solid precursor behind. Several solvents, including benzonitrile (PhCN), acetonitrile (MeCN), N–methyl pyrrolidinone (NMP), dimethylformamide (DMF) and dimethyl acetamide (DMA) were tested with the i–Pr precursor. Benzonitrile (PhCN), with a mid–range vapor pressure (~1 Torr at 25°C), was the most commonly used solvent because the other solvents had various drawbacks. Depositions using MeCN, which has a high vapor pressure (~89 Torr at 25°C), resulted in no film deposition, because the solvent and precursor disengaged in the nebulizer. Solid precursor remained in the nebulizer chamber while the MeCN evaporated into the reactor, hence no precursor transport to the substrate surface occurred. Use of N–methyl pyrrolidinone (NMP) solvent (~0.33 Torr at 25°C) at 550°C resulted in the incorporation of iron into the deposited films. The source of the iron was the impinging jet, which appeared to be oxidized after the run was complete. The NMP solvent, either with or without the precursor, reacted with the iron in the steel impinging jet. This iron was then transported to the substrate surface and incorporated into the films. Per AES, the percentage of iron in the films after deposition with NMP solvent ranged from 10 to 17 at.%. Use of dimethyl formamide (DMF) solvent (~3.7 Torr at 25°C) at 550°C also caused iron incorporation in the deposited films, for reasons similar to NMP. These films contained 6 to 7 at.% iron. Films grown from the i–Pr precursor in dimethyl acetamide (DMA) solvent (~1.3 Torr at 25°C) at 550°C yielded high carbon contamination (~50 at. %), believed due to substantial solvent decomposition at this temperature.

5.3 Precursor Mass Spectral Pre–Screen

Because benzonitrile was typically used as the solvent with the $Cl_4(CH_3CN)W(N^iPr)$ precursor, exchange of the acetonitrile ligand with benzonitrile occurs to some extent in the solutions used for MOCVD. For completeness, authentic samples of the $Cl_4(C_6H_5CN)W(N^iPr)$ compound were synthesized for analysis. The synthesis was done by slurrying $WOCl_4$ (1.025 g, 3.00 mmol) in a solution of *i*–PrNCO (0.435 g, 5.11 mmol) in heptane (35 mL) in a sealed pressure vessel. The mixture was heated for two days at 110° C. The solvent was removed from the resulting dark orange–red solution *in vacuo*. The orange residue was dissolved in a minimal amount of C_6H_5CN (approximately 5 mL). The resulting solution was stirred for two hours and then added to stirring pentane in a nitrogen glove box to precipitate the dark orange product. The solid was filtered and washed with 25 mL of additional pentane to afford 0.829 g (58.4 % yield) of the product. The desired isopropyl imido precursor structure and its PhCN derivative are shown in Figure 5-1.

Although the precursor solutions were prepared with $Cl_4(CH_3CN)W(N^iPr)$ (**1**), the CVD process uses benzonitrile as the solvent. We have demonstrated by NMR experiments that exchange of the acetonitrile ligand of **1a** with benzonitrile to yield $Cl_4(PhCN)W(N^iPr)$ (**1b**) occurs to some extent in the solutions used for MOCVD.

Therefore, mass spectrometry (MS) experiments were carried out with both **1a** and **1b**. These experiments yielded information about the fragmentation characteristics of the complexes under gas phase ionization conditions. The utilization of mass spectral data to predict possible mechanisms for CVD processes has been previously established [Int89]. Care must be taken in extrapolating any fragmentation information from mass spectral data to the CVD process, however, since the latter is thermal in nature [Lew94]. Nevertheless, MS data have provided insights into probable fragmentation patterns of the tungsten imido precursors.

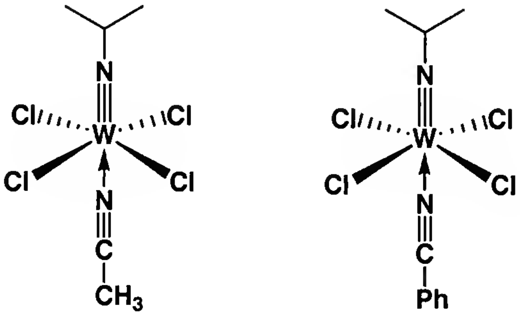

a **b**

Figure 5-1 Schematic of the isopropyl imido precursor. a) With the desired acetonitrile ligand. b) With the benzonitrile ligand.

All mass spectral analyses were performed using a Finnigan MAT95Q hybrid sector mass spectrometer (Thermo Finnigan, San Jose, CA). Electron ionization (EI) was carried out in positive ion mode using electrons of 70 eV potential and a source temperature of 200°C. Negative ion electron capture chemical ionization (NCI) used methane as the bath gas at an indicate pressure of 2×10^{-5} Torr, an electron energy of 100 volts and a source temperature of 120°C. All samples were introduced via a controlled temperature probe with heating and cooling enabling temperature control down to 35°C. The mass resolving power (m/Δm) was 5000 full width–half maximum (FWHM).

Figure 5-2 shows the positive ion electron–impact ionization (EI) and negative ion electron capture chemical ionization (NCI) mass spectra of **1a**. The molecular ion could not be observed in either case. The EI spectrum displays more fragmentation than the CI spectrum, due to the more energetic nature of the EI process relative to the CI process. The base peak in the EI spectrum occurs at *m/z*=348 and is assigned to the $[Cl_3W(N^iPr)]^+$ fragment. The isotopic pattern is consistent with a moiety containing three chlorines. The only organic ion observed in the EI spectrum occurs at *m/z*=41, corresponding to the fragment $[CH_3CN]^+$. Another tungsten fragment at *m/z*=306 demonstrates a high relative abundance (~80%). This ion corresponds to the $[Cl_3W(NH)]^+$ fragment. The only other significant peaks occur at *m/z*=291 and 326. These represent the loss of both the nitrile and imido ligands to form $[Cl_3W]^+$ and $[Cl_4W]^+$, respectively (abundances for both < 30%).

Only two peaks of consequence are observed in the NCI experiment (Figure 5-2b). The first occurs at *m/z*=383 (~42% abundance), and involves the loss of the acetonitrile ligand to form $[Cl_4W(N^iPr)]^-$. The base peak of the NCI spectrum appears at *m/z*=340, corresponding to the formation of $[Cl_4WN]^-$. Thus, the NCI spectrum indicates cleavage of both the nitrile ligand and the isopropyl moiety to afford a tungsten nitrido fragment. This tungsten nitrido fragment is desirable, as it will ostensibly lead to deposition of W and N in the films.

The benzonitrile complex **1b** was also subjected to similar MS analysis. Again, the positive ion EI spectrum contains a base peak at *m/z*=348, corresponding to the $[Cl_3W(N^iPr)]^+$ fragment. All of the other tungsten–containing fragments observed for the acetonitrile complex were also found in the spectrum of **1a**. Interestingly, the NCI experiment again exhibited the base peak at m/z=340 ($[Cl_4WN]^-$); however, only a small amount (~1% relative abundance) of the $[Cl_4W(N^iPr)]^-$ fragment was observed. Table 5-1 summarizes the fragments and the relative abundances observed for **1a** and **1b**.

The mass spectral data collected for the tungsten imido complexes offer some perspectives about these systems as CVD precursors. Most importantly, the cleavage of the isopropyl moiety from the imido group is relevant due to the necessity of this process in forming tungsten nitride films. Furthermore, the absence of a molecular ion in either the EI or CI mass spectra suggests facile loss of the nitrile trans ligand. Observation of the $[WCl_4]^+$ and $[WCl_3]^+$ fragments may be problematic since this indicates loss of the W–N bond; however, similar fragments were not present in the NCI spectrum. Thus, these fragments may be a result of the more energetic EI process. Based on these results and the deposition of tungsten nitride from the imido complexes, there appears to be a correlation between the mass spectral data and behavior under CVD conditions.

Table 5-1. Summary of Relative Abundances for Positive Ion EI and Negative Ion NCI Mass Spectra of Tungsten Imido Precursors **1a** and **1b**.[a]

EI Fragments	*m/z*	**1a**	**1b**
$[Cl_3W(N^iPr)]^+$	348	100	100
$[Cl_4W]^+$	326	26	41
$[Cl_3W(NH)]^+$	306	78	90
$[Cl_3W]^+$	291	30	52
$[C_6H_5CN]^+$	103	n/a	97
$[CH_3CN]^+$	41	24	n/a
CI Fragments	*m/z*	**1a**	**1b**
$[Cl_4W(N^iPr)]^-$	383	42	1
$[Cl_4WN]^-$	340	100	100

[a] Relative abundances were adjusted by summing the observed intensities for the predicted peaks of each mass envelope and normalizing the largest sum to 100%.

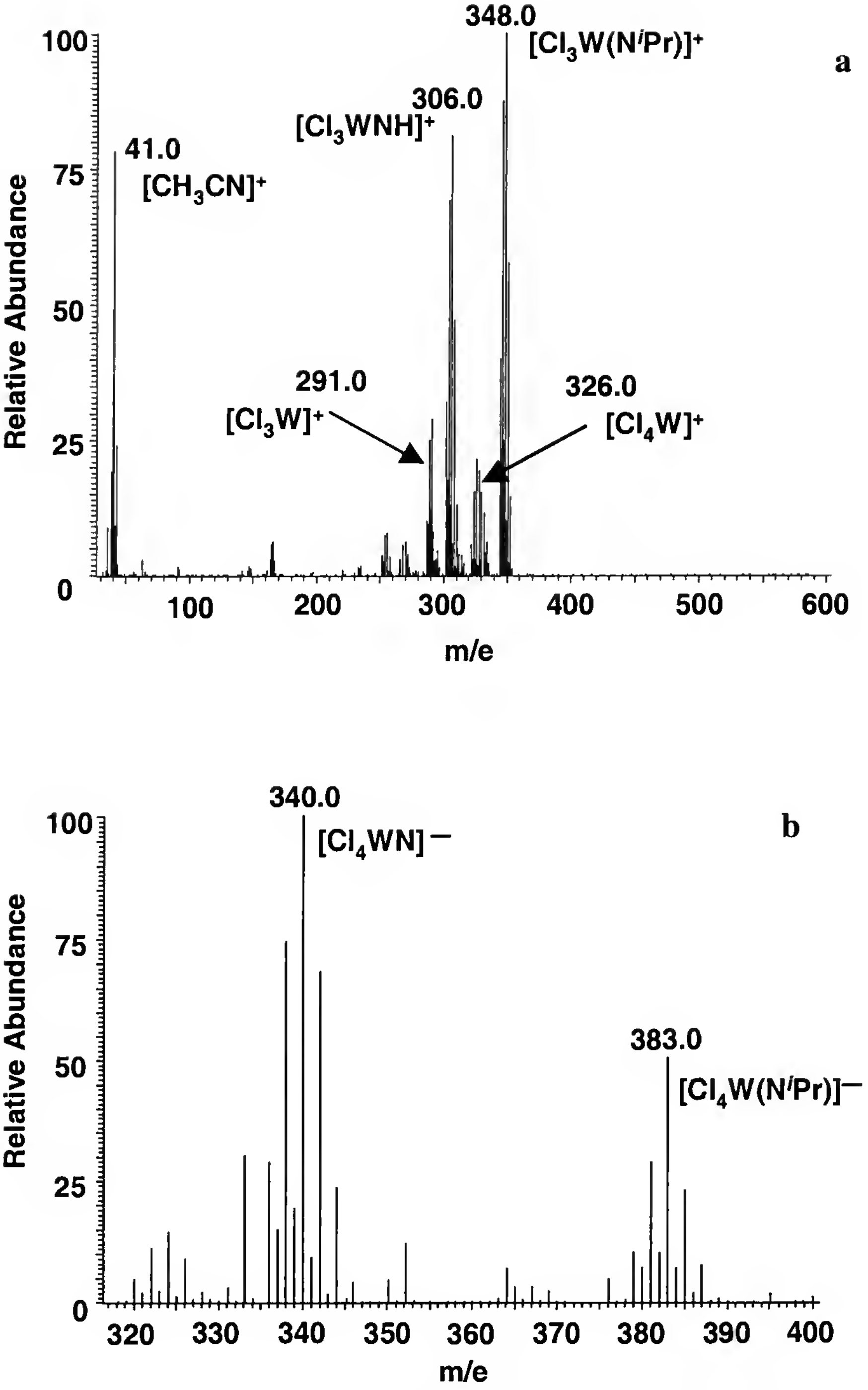

Figure 5-2 Mass spectra of $Cl_4(CH_3CN)W(N^iPr)$. a) Positive ion electron–impact ionization (EI). (b) Negative ion electron capture chemical ionization (NCI)

5.4 Film Structure

5.4.1 XRD Results

The XRD plot in Figure 5-3a indicates amorphous film deposition at 450°C, evidenced by a flat profile without any characteristic FCC $\beta-WN_x$ peaks. Figure 5-3b depicts polycrystalline film deposition at 700°C. Four characteristic peaks are evident, with relative peak intensities indicating that no preferred crystal orientation exists. Although the relative peak intensities in Figure 5-3b are consistent with the pattern for polycrystalline $\beta-WN_{0.5}$, the 2θ peak positions lie between the standard values for $\beta-WN_{0.5}$ and $\beta-WC_{0.6}$, which are shown in Figure 5-3c. Peak positions between these standard values suggest that carbon is mixing with nitrogen and vacancies on tungsten's interstitial sublattice to form $\beta-WN_xC_y$ polycrystals. For the spectrum in Figure 5-3b, primary reflections at 37.42 and 43.12 2θ degrees are consistent with (111) and (200) $\beta-WN_xC_y$ growth planes, while additional reflections at 62.52 and 75.22 2θ degrees indicate (220) and (311) planes, respectively. No peaks consistent with the hexagonal WN or WC (or WN_xC_{1-x}) phases or the BCC W phase were evident for any of the films.

Figure 5-4 shows the evolution of film crystallinity with deposition temperature. At the two lowest deposition temperatures (450°C and 475°C), the characteristic $\beta-WN_x$ peaks are not observed. At 500°C, a broad peak appears near 37.94 2θ degrees, indicating polycrystalline $\beta-WN_xC_y$ (111) growth. This is similar to a previous report that amorphous WN_x films transform into polycrystalline $\beta-W_2N$ between 450 and 500°C [Gal97]. As the deposition temperature increases to 550°C, this peak sharpens and a broad peak at 44.42 2θ degrees appears, indicating $\beta-WN_xC_y$ (200) growth. Films deposited between 475 and 600°C displayed two additional peaks at 33.03 and 61.67 2θ degrees, representing Si (200) Kα and Si (400) Kβ radiation, respectively. Broad peaks emerge at 63.00 and 75.82 2θ degrees for growth at 650°C, indicating β–WN_xC_y (220) and (311) growth. The peaks sharpen further as the temperature approaches 700°C, indicating polycrystalline grain growth. The formation of polycrystalline films is highly undesirable, since grain boundaries are facile paths through which Cu can diffuse to the underlying Si. Hence, deposition below 500°C with this precursor is required to grow an amorphous film.

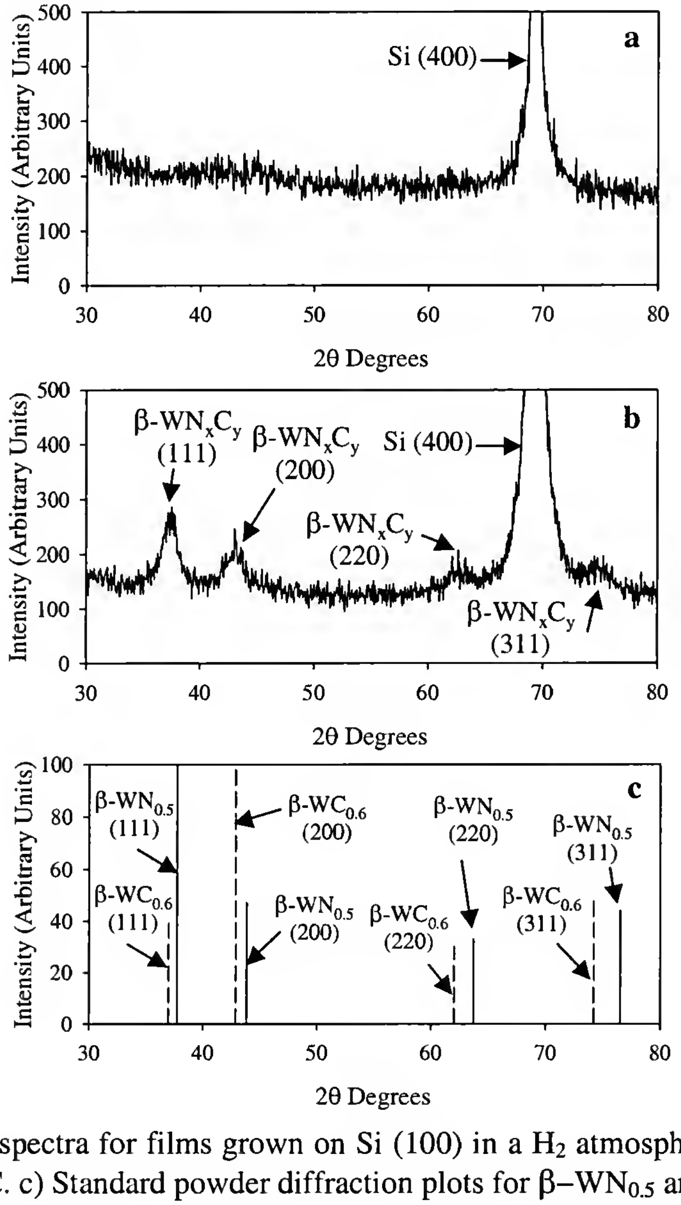

Figure 5-3 XRD spectra for films grown on Si (100) in a H_2 atmosphere. a) 450°C. b) 700°C. c) Standard powder diffraction plots for β–$WN_{0.5}$ and β–$WC_{0.6}$.

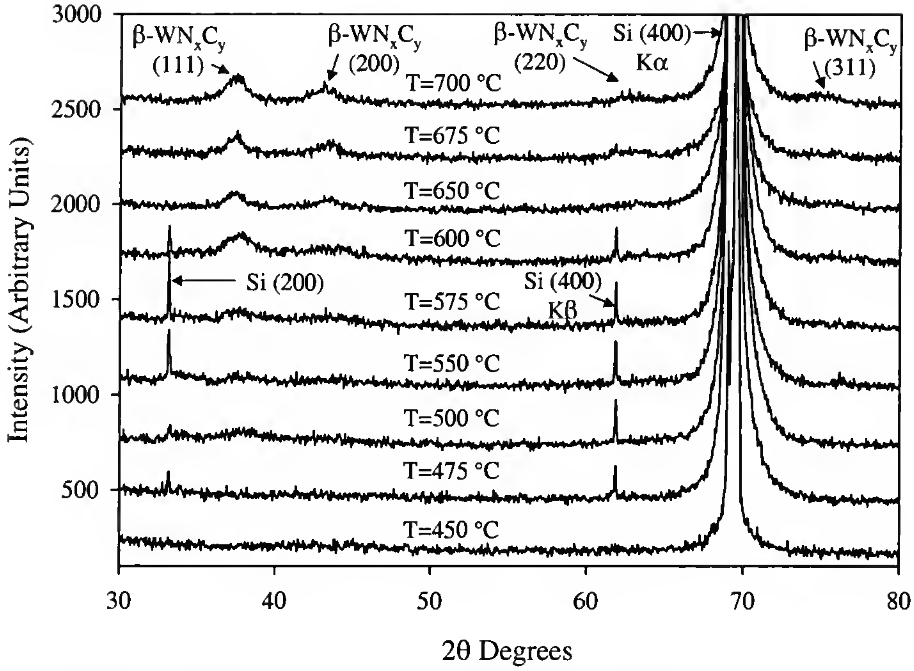

Figure 5-4 Change in XRD pattern with deposition temperature for films grown with **1b** on Si (100) in a H_2 atmosphere.

5.4.1.1 Lattice Parameter

The dependence of lattice parameter on deposition temperature was determined by XRD using the 2θ position of the β–WN_xC_y (111) diffraction peak, with peak position calibrated to the Si (100) diffraction peak. Figure 5-5 shows the change in lattice parameter with deposition temperature. The dashed line at 4.126 Å represents the standard lattice parameter value for β–$WN_{0.5}$, while that at 4.236 Å is for β–$WC_{0.6}$. Error bars indicate uncertainty in lattice parameter (± 0.002 Å) due to X–ray Kα line broadening [JCP88]. Figure 5-5 shows the lattice parameter increasing from 4.11 to 4.17 Å as deposition temperature increases from 500 to 650°C, and then decreasing to 4.16 Å at 700°C. Shifts in the lattice parameter reflect either a composition change in the polycrystals or a change in the residual film stress. Since AES gives bulk film concentrations, compositions in the bulk polycrystals and at the grain boundaries cannot be resolved. Shifts in lattice parameter cannot therefore be attributed solely to film composition without considering the possible influence of residual film stress. But, if we assume compositional variation dominates the shift in lattice parameter, the likely cause for lattice expansion between 500 and 650°C would be incorporation of additional C into the polycrystals. Lattice dilation for W–C mixtures relative to pure W has been reported, with lattice parameter increasing by more than 3 % with C content of 22.5% [Pau92].

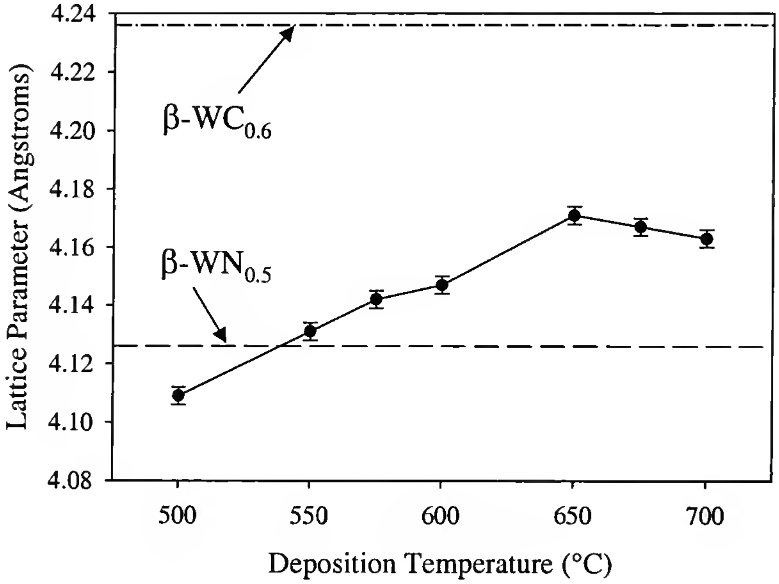

Figure 5-5 Lattice parameters for films grown from **1b** based on β–WN_xC_y (111) diffraction peak.

As shown in Figure 5-10, only the C content increases continuously with temperature in this range. The existence of a continuous FCC β–WN_xC_y solid solution has been predicted [Jon93], hence as x decreases, the lattice parameter of β–WN_xC_y polycrystals would increase from a = 4.126 Å at x = 0.5 (β–$WN_{0.5}$) to a = 4.236 Å at x = 0 (β–$WC_{0.6}$). Above 650°C, the lattice parameter decreases. Again, this may indicate a change in film stress or a change in film composition. If we again assume that compositional variation dominates, we note that N and O levels are essentially unchanged in this temperature range, while C levels continue to increase with temperature. Lattice parameter decrease may indicate a solubility limit for C in the β–WN_xC_y polycrystals at 650°C, with additional C incorporated above 650°C preferring to reside in grain boundaries rather than bulk polycrystals.

5.4.1.2 Average Grain Size

Two main causes of peak broadening in XRD thin film spectra have been reported: non–uniform film stress and the presence of small crystal grains. If the film stress is determined to be uniform, peak broadening may be attributed simply to the presence of small crystal grains. Likewise, if the presence of small crystal grains is ruled out, peak broadening may be attributed simply to non–uniform film stress. If we assume only uniform film stress, the average crystallite size (t) may be estimated using the Scherrer equation (Equation 5–1) [Cul78, Nag00]:

$$t = \frac{0.9\lambda}{(B\cos\theta)} \tag{5–1}$$

where λ is the X–ray wavelength (1.5406 Å for Cu Kα), B is the full width at half maximum (FWHM) for the selected diffraction peak and θ is the Bragg angle for that peak. The dominant diffraction peak for the films, β–WN_XC_y (111), was used as the reference peak for FWHM determination. As depicted in Figure 5-6, grain size increased with deposition temperature, varying from 32 to 67 Å over the 500–700°C temperature range. Below 500°C, the films were X–ray amorphous, inferring that amorphous films had a maximum grain size near 30 Å. In comparison, Leedy et al. [2000b] reported grain sizes of 50 to 100 Å for sputter–deposited WN_x films, while Jun [1996] reported an average grain size of 30 Å for TaC_xN_y films deposited by MOCVD at

350°C. The incorporation of C into W barrier films results in much smaller grain sizes relative to films containing pure W metal [Wan01b]. The presence of N and O has also been reported to hinder grain growth, resulting in smaller grain sizes [She00b]. The levels of N and O drop off with deposition temperature, though, and C becomes the dominant contaminant in films deposited at and above 500°C. Thus, as deposition temperatures increase, a competition between increased grain growth due to higher surface diffusivity and decreased grain growth due to increased C content occurs. At lower growth temperatures, enhanced surface diffusivity due to temperature dominates the grain growth process, causing grains to increase with deposition temperature. Above 675°C, though, grain size levels off, indicating that large scale C contamination is retarding the grain growth that would normally occur with increased temperature.

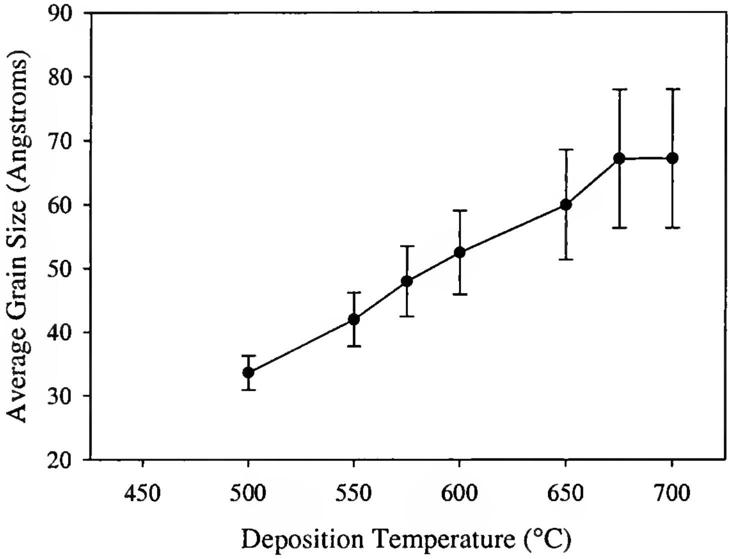

Figure 5-6 Average grain size for polycrystalline films based on the β–WN_xC_y (111) diffraction peak. Error bars reflect uncertainty of ± 0.1 2θ degrees in FWHM measurements.

5.4.2 TEM

Transmission electron microscopy (TEM) may be used to determine the presence and size of crystallites in the film. The transmission electron diffraction (TED) image in Figure 5-7a shows that a film deposited with **1b** at 450°C on Si (100) had an amorphous structure, as evidenced by the blurred pattern without rings or spots, which is consistent with XRD measurements. In contrast, Figure 5-7b shows diffuse rings for the film deposited at 700°C, indicating that this film had some degree of crystallinity, in agreement with XRD measurements.

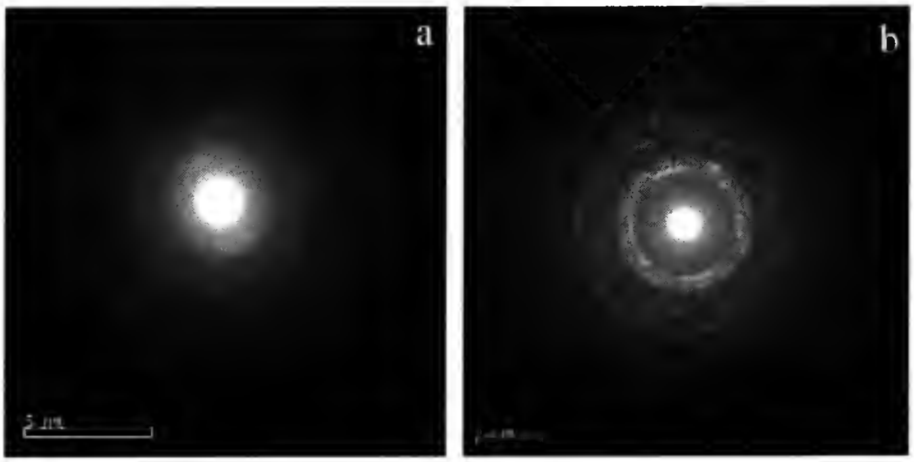

Figure 5-7 TED patterns for films deposited with i–Pr on Si (100). a) 450°C. b) 700°C.

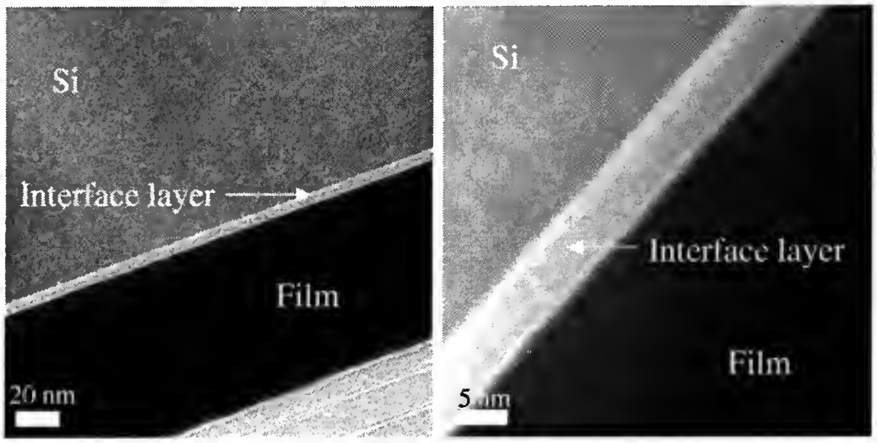

Figure 5-8 TEM micrographs for film deposited on Si (100) with **1b** at 450°C.

TEM micrographs for the film deposited at 450°C are shown in Figure 5-8. These images indicate a ~60 Å bright interface layer between the Si (100) substrate and the deposited film. This interface contained a mixture of WSi_2, WO_3, SiO_2 and SiO, which is discussed further in the XPS analysis section below.

TEM micrographs for the film deposited at 700°C are shown in Figure 5-9. Polycrystal grains are evident in the micrograph on the left, in agreement with XRD results, along with some roughness at the top of the film. These images also indicate a bright interface layer (~50 Å thick) between the Si (100) substrate and the deposited film. The edges of this interface layer are not as sharply defined as for the 450°C film, which may point to increased interface roughness for the higher deposition temperature. This agrees with SIMS depth profile results (Figure 5-21 and Figure 5-22), which indicate a longer overlap time for the W and Si signals in the 700°C film relative to the 450°C one.

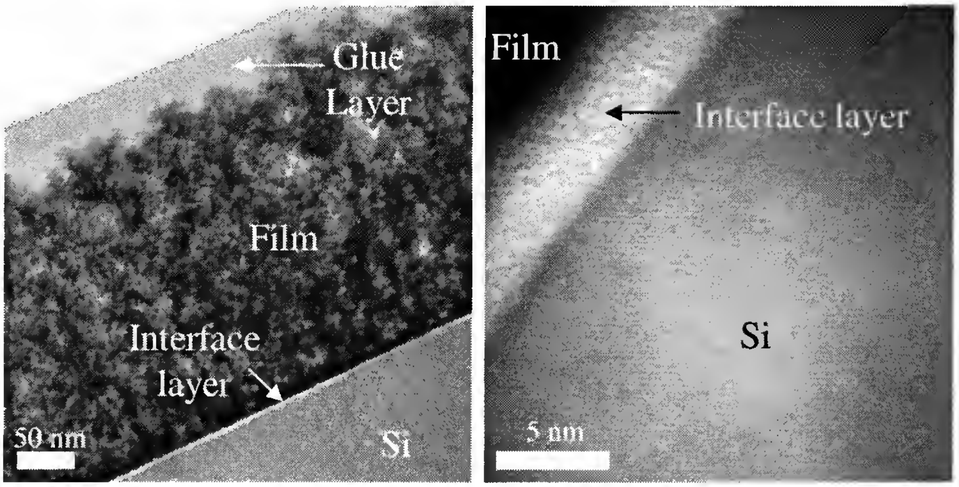

Figure 5-9 TEM micrographs for film deposited on Si (100) with **1b** at 700°C.

5.5 Film Composition

5.5.1 AES

Auger results in Figure 5-10 indicate that W, N, C and O were present in the deposited films, while Cl was not detected. Between 450°C and 500°C, the C level is fairly constant at ~12 at. %. Between 500 and 650°C, C content increases steadily from 12 to 43 at. %, and then increases mildly to 49 at. % at 700°C. The overall trend reflects the increasing tendency of the hydrocarbon groups present in the precursor ligands and the solvent to decompose with increasing deposition temperature. Fragmentation of ligands and solvent leaves carbon–containing moieties at the film surface, resulting in C incorporation into the growing film.

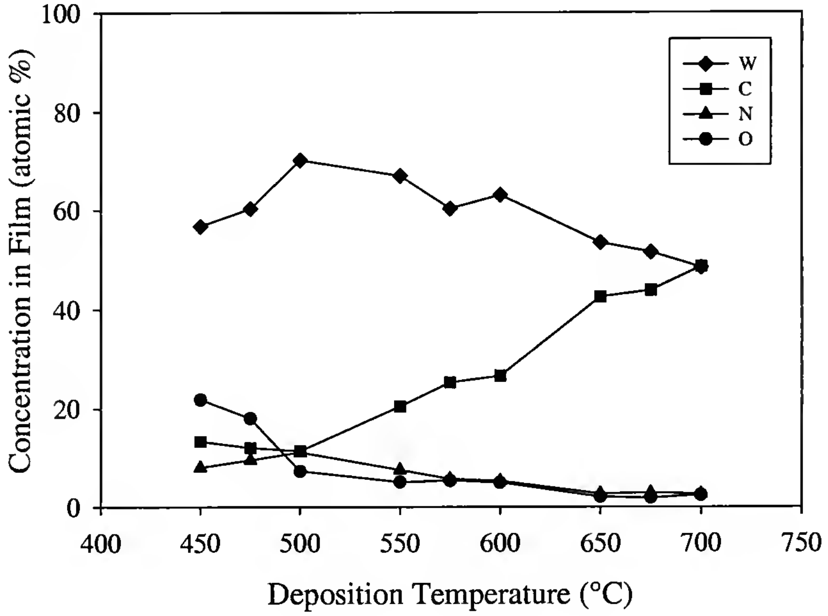

Figure 5-10 Variation of W, N, C and O content in films from **1b** with deposition temperature. Data are from AES after 2.0 minutes sputter.

The N content in films grown at 450°C was 8 at.%, and this rose slightly to 11 at.% at 500°C. Above 500°C, the N levels decrease, dipping to ~3 at.% at 700°C. The higher N levels at and below 500°C reflect the stability of the W–N multiple bond in the precursor molecule, which likely endures at deposition temperatures up to 500°C, inhibiting release of N into the gas phase during deposition. The drop in N above 500°C may indicate decomposition of the W–N multiple bond in the gas phase and/or increased N desorption from the film (to form N_2 gas) at higher temperature. Substantial N release from WN_x films at higher temperature (~700°C) has been reported [Kat85], consistent with AES results in this range.

Lack of a load–lock and vacuum transfer system necessitated a vacuum break after barrier film deposition. Oxygen contamination resulted from post–growth exposure of the film samples to air. Incremental AES sputtering showed a steady decrease in O levels with increasing depth into the WN_x films. The O concentration was highest at 450°C, reaching 22 at. %, and decreased slightly to 18 at. % at 475°C. The amorphous films deposited below 500°C had low density and high porosity, allowing substantial amounts of oxygen to penetrate into the film lattice. X–ray reflectivity (XRR) indicated that the film deposited at 450°C, for example, had a density of 8.6 g/cm³. High oxygen concentrations (~20%) attributed to air exposure have also been reported for porous TiN, TiC and TiCN barriers [Eiz94a, Par96, Wan01a]. As the deposition temperature was increased from 475 to 500°C, the O content drops sharply down to 7 at. %, while the C and N levels are fairly steady. This indicates crystallization of the film in this temperature range. As the film crystallizes, its microstructure densifies, thereby inhibiting post–growth oxygen diffusion into the lattice [Jos02, Pok91]. XPS results for oxygen in the films are consistent with WO_3, which has considerably higher thermodynamic stability than β–WN_x or β–WC_x. For example, reported values of the Gibbs energy of formation (ΔG°_f) at 700°C for the WO_3, β–$WN_{0.5}$ and β–$WC_{0.6}$ phases are –592 kJ/mol, +17 kJ/mol, and –11 kJ/mol, respectively [Lid85, Lak79, Gus86]. The experimental observation of lower levels of oxygen at higher deposition temperatures is consistent with post–growth oxygen contamination. As deposition temperature increases above 500°C, the O concentration drops further, falling to 2 at. % at 700°C. This results from film densification (by polycrystal grain growth) and increased C levels at higher deposition temperature, which stuffs the grain boundaries and blocks O in–diffusion. Porosity of amorphous films grown below 500°C may be problematic, as defects in the film can degrade the barrier's resistance to Cu diffusion. A previous report, however, indicates that diffusion barrier performance depends more strongly on film microstructure than film density [Kim99c].

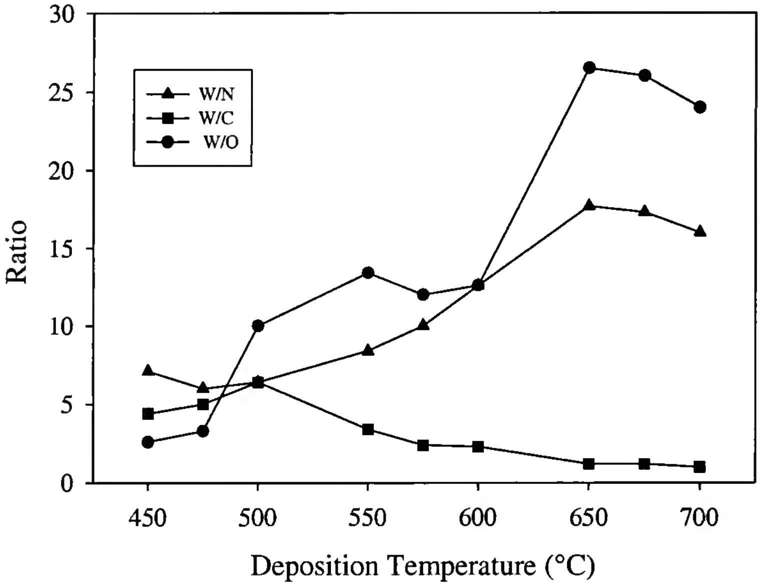

Figure 5-11 Variation of tungsten to nitrogen (W/N), tungsten to carbon (W/C) and tungsten to oxygen (W/O) ratios with deposition temperature for films from **1b**. Data are from AES after 2.0 minutes sputter.

Figure 5-11 shows the ratios of W to C, N and O in the deposited films. The W/N ratio was quite high, ranging from 6 to 18, which is much higher than the desired ratio of

2 for $\beta-W_2N$. The trend followed by the W/N ratio is expected, since higher deposition temperature enhances N desorption from the films to form N_2 gas, causing W/N to increase. Although the general trend of N content with deposition temperature is discernible from the AES data, exact measurement of the N level is difficult. Preferential incorporation of C and removal of N by Ar^+ sputtering during AES analysis has been reported to cause artificially high C and low N concentration readings [Ing82]. Since the AES data were collected after 2.0 minutes of sputter, N atoms were likely sputtered and replaced by C atoms, causing the W/N and W/C ratios to be artificially high and low, respectively. Moreover, Lee et. al [1994a] reported $\beta-W_2N$ growth per XRD while their AES results showed only 12 at. % N. This was attributed to a shift in the sensitivity factor for N in the WN_x films away from the value for pure elemental N. In addition, Alay et al. [1991] studied the N content of sputter deposited amorphous WN_x films with a variety of characterization techniques. For a given WN_x film, the N content (per AES) was ~13%, while Rutherford backscattering spectrometry (RBS) indicated ~33%. Since RBS does not require an elemental standard for calibration and is considered accurate to ~1 at. % [Ohr92], these results may indicate that our actual N levels, especially at lower deposition temperature, are considerably higher than indicated by AES.

The decrease in W/C with increasing deposition temperature reflects the enhanced decomposition of hydrocarbon moieties from the precursor and solvent with temperature. The W/C ratio drops to 1 at 700°C due to large–scale alkyl decomposition. The W/O ratio increases from 3 to 10 between 450 and 500°C, due to the aforementioned film crystallization, and then rises from 10 to 27 between 500 and 650°C. This increase is related to the jump in C content in this temperature range (Figure 5-10), where C further stuffs the grain boundaries, physically blocking oxygen in–diffusion. The W/N and W/O ratios reached their maximum values at 650°C, and decreased above this temperature. The decrease in these ratios above 650°C does not reflect an increase in C and O content in the films, but rather a decrease in the W content of the film, due to massive C contamination.

5.5.2 AES Depth Profiling

The three–point AES depth profiling method was used to determine the change in elemental content with depth into the films. As evident in Figure 5-12, films deposited at 450°C contained significant levels of O, due to high film porosity enabling substantial O in–diffusion after air exposure. Note that due to use of the three–point depth profiling method, the y–axis in Figure 5-12 is not concentration in film, but is proportional to the area under the curve for the elemental signal. The oxygen level initially dropped with increasing sputter depth, but increased at the barrier–Si interface. This suggests that the barrier film near the interface is very porous and defective, which may be a consequence of film growth dynamics during the nucleation process on Si. HCl, formed by reaction of H_2 carrier gas (or H on the precursor ligands) with Cl from the precursor, may etch and roughen the Si interface before and during the nucleation process. Moreover, steric effects may inhibit the ability of the precursor to uniformally cover the Si surface, all of which can lead to voids and stresses at the interface. The defects would leave substantial amounts of exposed W with dangling bonds, which readily reacts with O diffusing in from the film surface. The makeup of this interface layer is discussed in more detail in the XPS film analysis section below. After the nucleation stage, the films are growing on WN_x (or WN_xC_y) that has already deposited, and this decreases the concentration of defects (porosity), leading to lower O levels in the middle of the film. The O level is highest at the film surface due to direct contact with air. Apart from O, a high level of C was evident on the film surface, indicating the presence of both deposited C and adventitious C. After sputtering off the initial film layers, the C level dropped to a steady level, with magnitude similar to that for N. The W level is initially steady, and drops gradually at the approach to the Si interface, due to increasing O levels. The O and Si signals overlapped briefly, but the W and Si signals overlapped some additional time. This suggests that the barrier–Si interface may be rough, which could be caused by HCl etching during deposition. In addition, the W–Si overlap may indicate that some amount of WSi_x may be present at the interface.

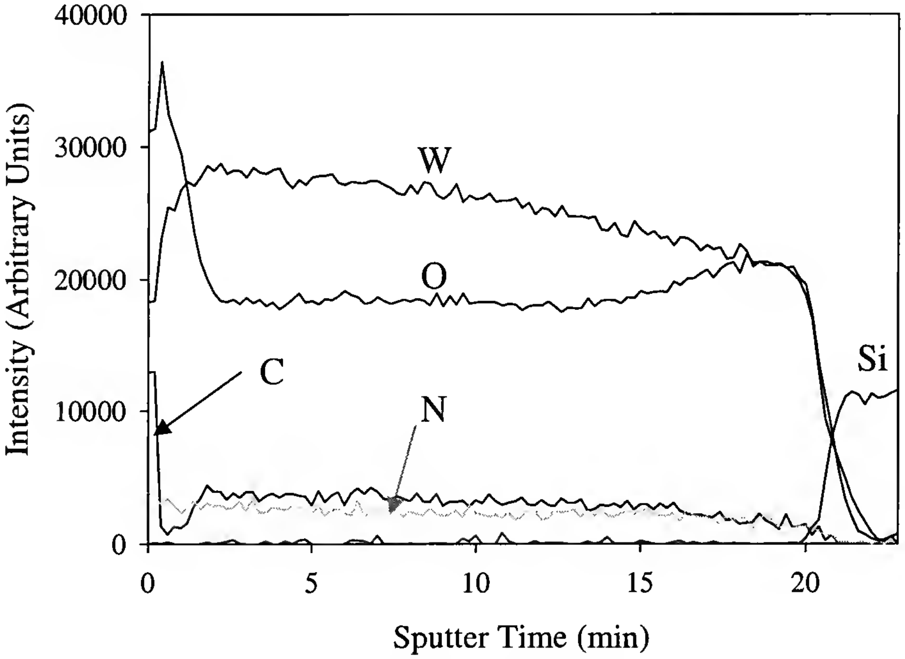

Figure 5-12 Three–point AES depth profile for film deposited from **1b** at 450°C. Nominal AES sputter rate was 100 Å/min.

Figure 5-13 shows the depth profile for a film deposited at 500°C. As expected, the O level decreases relative to the 450°C film, due to crystallization (and densification) of the film at 500°C, which decreases the degree of O in–diffusion. The O level still increases near the barrier–Si interface, however, for reasons discussed above, but the O "bump" near the interface is narrower, indicating that the defect–laden layer at the interface thins with increasing deposition temperature. Increased deposition temperature improves surface diffusion of depositing species, which would cause defect (and void) density to decrease. The C signal increases slightly relative to the 450°C film, due to increased C contamination at higher temperature. Overlap of the W and Si signals occurs for longer sputter time relative to the 450°C sample, and may indicate increased roughening of the Si surface (due to HCl etching) and/or increased WSi_x formation with higher temperature. The increased sputter time relative to the 450°C sample reflects increased film thickness and higher film density for the 500°C sample.

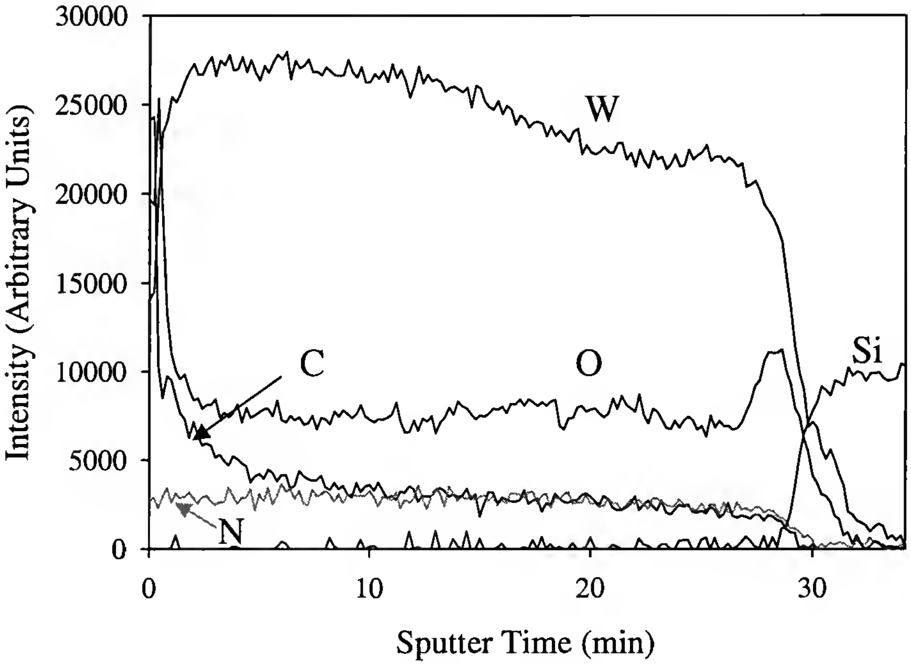

Figure 5-13 Three–point AES depth profile for film deposited from **1b** at 500°C. Nominal AES sputter rate was 100 Å/min.

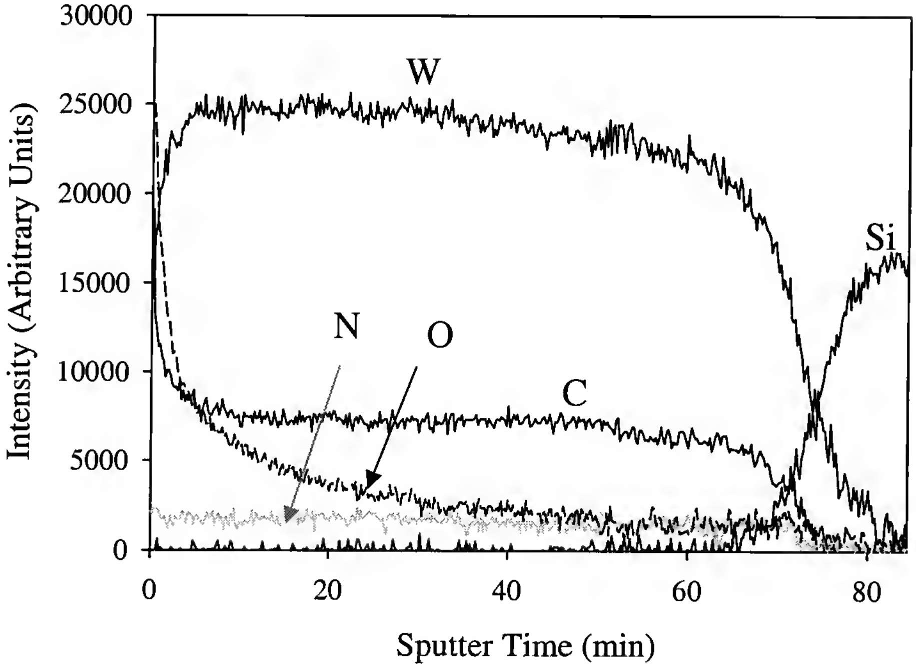

Figure 5-14 Three–point AES depth profile for film deposited from **1b** at 700°C. Nominal AES sputter rate was 100 Å/min.

Figure 5-14 shows the depth profile for a film deposited at 700°C. Oxygen levels through the film are decreased relative to the two lower temperatures, due to densification by polycrystal grain growth and plugging of voids/grain boundaries by additional C in the films. A very small O "bump" at the barrier–Si interface is visible, indicative both of a thinner defective region and decreased O in–diffusion. The N level is steady, but decreased relative to the 450 and 500°C films, due to increased N desorption at higher deposition temperature. Carbon levels are higher relative to the lower temperature films, which again reflect the increased ability of the ligands and solvent to decompose at higher temperature. Overlap of the W and Si signals occurs for longer sputter time relative to the lower temperature samples, which again may indicate increased roughening of the Si surface due to HCl etching and/or increased WSi_x formation with higher temperature. The increased sputter time relative to the lower temperature films again reflects increased film thickness and possibly higher film density for the 700°C sample.

5.5.3 XPS

Standard binding energies for elements present in the films from this study are shown in Table 5-2 below. The sensitivity factor relates to an atom's ability to emit a photoelectron when exposed to X–ray radiation, and is relative to the F1s line, which is 1.0 eV.

Table 5-2. Standard Elemental XPS Values for Film Components*

Element	Binding Energy (eV)	Sensitivity Factor (S)
W4f	31.32	2.75
C1s	284.5 (C in Graphite)	0.25
N1s	398.5 (N in BN)	0.42
O1s	531.0 (O in Al_2O_3)	0.66

*References: [Wag90, Cri00]

5.5.3.1 XPS Literature Data

XPS survey spectra for W typically show peaks at many binding energies, with each representing photoelectrons from a specific energy level in the W atom. The W4f photoelectron line has two peaks ($W4f_{7/2}$ and $W4f_{5/2}$), while the N1s, C1s and O1s lines each have one. Binding energy ranges for the f and d subshells of some potential W compounds present in our films are shown in Table 5-3.

As seen in Table 5-3 , reported $W4f_{7/2}$ binding energies for metallic W range from 30.9 to 32.7 eV, while $W4f_{5/2}$ binding energies range from 33.2 to 34.8 eV. XPS data for two forms of tungsten nitride, the FCC β–WN_x and SHP WN forms, have been reported. $W4f_{7/2}$ and $W4f_{5/2}$ values for β–WN_x, the desired phase, range from 30.7 to 33.6 and 33.3 to 35.8 eV, respectively. Binding energies for the analagous tungsten carbide phases (FCC and SHP) have also been reported, with SHP WC having a $W4f_{7/2}$ ranging from

31.4 to 32.8 eV. FCC WC_{1-x} has been reported with $W4f_{7/2}$ BE values ranging from 31.2 to 31.9 eV [Ji01, Pau92], which are close to the value for metallic W, since W and C do not have a strong covalent or ionic bond in this phase [Nak87]. The addition of O to WC films has been reported to increase the W4f binding energies, due to formation of a WO_xC_y compound [Chi97, Ji01]. Katrib [1994] reported a $W4f_{7/2}$ BE value for WO_xC_y of 31.5 eV. Bonding between W and O in tungsten oxide compounds exhibits substantial electron transfer from metal to nonmetal, similar to the bonding in tungsten nitrides [Col76]. This electron transfer causes an increase in binding energy for W in oxides

Table 5-3. Literature Binding Energy Data for Electron Subshells in W Compounds

	Binding Energy (eV) for Subshell				
Compound	$W4f_{7/2}$	$W4f_{5/2}$	$W4d_{3/2}$	$W4d_{5/2}$	References
Metallic W	30.9–32.7	33.2–34.8	255.6	242.6–244.2	[Ala91, Cha97b, Cha99, Col76, Cri00, Gir00, Gru87, Ji01, Kak99, Kat95, Lut01, McG73, Meu98, Mou95, Nag00, Nak87, Pau92, She00c–f, Wag90, Yeh96, Zha99]
WN_x	30.7–33.6	33.3–35.8	–	244.9	[Ala91, Chi93, Col76, Lee93, Meu98, Nag00, Nak87, She00b–d, Tak97a, Zha97, Zha99]
FCC β–WC_x	31.2–31.9	–	–	–	[Ji01, Kou02, Pau92]
WO_4	–	37.6	–	–	[Col76]
WO_3[a]	34.9–38.0	35.2–38.7	259.9–260.0	247.4–248.4	[Bla86, Cha88, Cha97b, Cha97c, Cho02, Col76, Cri00, Gir00, Gog00, Gru87, Kat95, Lec96, Lee98b, Lut01, McG73, Nag00, Nak87, Rus99, Sar80, She00d–f, Wag90, Zha99]
W_2O_5[b]	34.5–35.7	36.7–37.8	–	–	[Kat95, Ji01, Nag00]
WO_2[c]	31.1–34.8	33.1–36.9	256.1	243.2	[Cha88, Col76, Ji01, Kat95, Lut01, Mon99, Nag00, Rus99, Sar80, Wag90]
WO[d]	32.9	35	–	–	[Nag00]
WO_xC_y	31.5	–	–	–	[Kat94]
WCl_6	37.1	–	–	248.5	[McG73]
$WOCl_4$	37.4	–	–	–	[McG73]
WSi_2	31.5	33.5	–	–	[Cho02]

[a] Note, this includes references to "surface tungsten oxide," which are taken to mean WO_3

[b] Note, this includes references to "W^{5+}," which are taken to mean $WO_{2.5}$ or W_2O_5

[c] Note, this includes references to "W^{4+}," which are taken to mean WO_2

[d] Note, this includes reference to "W^{2+}," which is taken to mean WO

relative to the metallic state, with the increase frequently on the order of 1 eV per unit change in oxidation state [Rig75]. Several WO_x compounds, with x ranging from 1 to 4, have been reported in the literature, as indicated in Table 5-3.

Binding energy for N atoms is strongly dependent on their environment in the WN_x film. Care must be taken when determining WN_x film compositions from XPS data, as large shifts in sensitivity factor for N in compound materials have been reported [Lee93]. Nitrogen atoms are typically found either at octahedral interstitial sites within the WN_x crystal lattice or at the grain boundaries.

Table 5-4. Literature Binding Energy Data for Electron Subshells in N Compounds.

Nitrogen Bonding Environment	N1s Binding Energy Range (eV)	References
Interstitial N in β–WN_x	396.7–398.3	[Cha97b–c, Cha99, Chi93, Col76, Hon00, Kak99, Lee90, Lee93, Lee00b, Meu98, Mou95, Nag93, Nak87, She00b–c, Yeh96, Zha97, Zha99]
Interstitial N in SHP WN	398.2	[Zha97]
$W(O,N)_x$	398.1–399.3	[Zha99]
N in β–C_3N_4	398.5	[Wei99]
N in N–sp^3C	398.5–398.8	[Jel00, Nin02]
Free N (grain boundary N)	399.2–400.1	[Cha97b–c, Cha99, Nag93, Nak87]
N in N–sp^2C	400.0–400.9	[Jel00, Nin02]
N in Al(N,O) Oxynitride	400.1	[Sim94]
N in CN_x	400.2	[Wei99]
N in $TiAl_x$ Oxynitride	400.3	[Sim94]
N in an N–O/N–N surface species	402.0–402.9	[Cri00, Lee00b, Wei99]
"Dissolved" N	403.3–404.5	[Sim94]

For WN_x films, N1s binding energies ranging from 396.7 to 398.3 eV, which are below the standard N1s value (398.5 eV), are typically reported as interstitial N (N bound to W). The drop in BE is caused by electron transfer from W to N, due to the $W^{\delta+}$–$N^{\delta-}$

bond having some ionic character [She00b]. Shifting of the N peak to BE values above the N1s standard value may be due to several different phenomena. N present at grain boundaries in the film would have higher BE because electron transfer from W to N at the grain boundary does not occur. A lack of electron transfer means that N1s core electrons (for N at the grain boundary) do not decrease in binding energy [Cha97b–c, Cha99, Nag93, Nak87]. Another cause may be the reaction of O (after air exposure) with the WN_x lattice to form a complex bivalent oxynitride such as $W(N,O)_x$ [Lai98b, Sim94, Zha99]. Oxygen atoms are more electronegative than N atoms, withdrawing electrons more readily from the metal. This causes increased ionicity of the metal–oxide bond relative to the metal–nitride bond [Gub94]. The addition of O to WN_x films causes electrons to be withdrawn more strongly from W by O, decreasing the net electron transfer from W to N and thereby increasing the N1s binding energy. One report from Prieto et al. [1995] suggests that N1s BE values are lower for oxynitrides relative to nitrides, but this conflicts with many other reports describing higher oxynitride BE values relative to nitrides [Lai98b, Sim94, Zha99]. Several lines in the standard XRD powder diffraction spectra for β–$WN_{0.5}$ and the oxynitride $W(N,O)_{1.33}$ overlap exactly due to similarities in their lattice structures, with O and N atoms sitting on interstitial sites in the FCC W lattice [JCP88, Sel95]. Hence, the presence of the oxynitride typically cannot be ruled out if some amount of O is present in the film and an N1s peak is present at higher BE. XRD spectra rule out the presence of another oxynitride ($W(O,N)_{1.61}$), however, which has a hexagonal structure [Che97, JCP88]. A third cause for increased N1s binding energy is the reaction of N with O near the film surface [Cri00, Lee00b, Wei99]. N1s BE values of 401.4 eV and 402 eV, respectively, have been reported for N that has reacted with O at the film surface [Cri00, Lee00b], while another report assigned a BE of 402.88 eV to surface N–O/N–N species [Wei99]. A fourth cause may be expansion of the WN_x lattice due to C addition to form WN_xC_y. As discussed earlier, substitution of C for some N on the interstitial sublattice increases the film's lattice parameter relative to that for the nitride. This lattice expansion would strain the $W^{\delta+}$–$N^{\delta-}$ bond, decreasing the metal to nonmetal electron transfer. The decreased electron transfer would cause the N1s binding energy to increase relative to its value in pure FCC β–WN_x.

Yet another possibility to account for increased BE is the formation of N–C bonds in the film. Ning et al. [2002] reported that N1s peaks at 398.6 and 400.0 eV were consistent with formation of N–sp^3C and N–sp^2C, respectively. Another report suggested that 1s peaks at 398.5 and 398.8 were for N–sp^3C bonding, while peaks at 400 and 400.9 eV were for N–sp^2C bonding and a peak at 399.9 eV was for N bound to H [Jel00]. The presence of β–C_3N_4, which has a hexagonal structure homologous to Si_3N_4, was suggested, as this phase is considered to have a mixture of sp^3 and sp^2 C–N bonds [Jel00]. Wei [1999] reported that C1s and N1s binding energies of 285.96 and 400.17 eV, respectively, indicated the presence of CN_x. In addition, C1s and N1s binding energies at 287.32 and 398.46 eV, respectively, represented β–C_3N_4.

XPS values for a variety of potential C–containing compounds in our films are listed in Table 5-5. While graphite and amorphous ("free") C have similar BE ranges, the presence or absence of graphite can be confirmed by XRD. If graphitic peaks do not appear on XRD, the C is present in amorphous ("free") form. Diamond–like C, like graphite, is discernible from XRD analysis. Other potential bonding states include C bound to H, O, or N, and C in the oxycarbide WO_xC_y.

XPS values for a variety of potential O–containing compounds in our films are listed in Table 5-6. O bound to W has been reported in oxides (WO_x) of varying stoichiometry, oxynitrides ($W(N,O)_x$), oxycarbides (WO_xC_y), and in compounds containing C or H. A BE value for O in WO_xC_y was not reported [Kat94], however.

Table 5-5. Literature Binding Energy Data for Electron Subshells in C Compounds

Carbon Bonding Environment	C1s Binding Energy (eV)	References
C in SHP WC or FCC WC_{1-x}	282.6–283.8	[Bon80, Col76, Gir00, Kat94, Kou02, Lai98b, Lec96, Lut01, Mon99, Pau92, Sun01b, Wan01b, Xue98]
C in WO_xC_y	283.2	[Kat94]
Graphitic C	284.2–285.0	[Ala91, Bon80, Kat94, Kou02, Lut01, Mou95, Pau92, Wag90, Xue98]
Free (amorphous, adventitious) C	284.5–285.2	[Bla86, Cri00, Gir00, Gog00, Kat94, Kou02, Lec96, Lut01, Pau92, Wei99]
C in C=C	284.5	[Nin02]
C in C–H	284.8–285.1	[Bou91, Pau92]
"Diamond–like" C	285.5–286.8	[Mon99]
C bound to O	285.3–291.9	[Bon80, Bou91, Chi93, Gog00, Jam92, Lec96, Wag90, Wei99]
C in CN_x	286.0	[Wei99]
C in sp^2C–N	286.1	[Nin02]
C in β–C_3N_4	287.3	[Wei99]
C in sp^3C–N	287.5	[Nin02]

Table 5-6. Literature Binding Energy Data for Electron Subshells in O Compounds

Oxygen Bonding Environment	O1s Binding Energy (eV)	References
O in WO_3	530.1–531.6	[Chi93, Col76, Cri00, Gir00, Gog00, Gru87, Kat94, Lec96, Lut01, Sar80, Zha99]
O in WO_2	530.2–530.5	[Col76, Sar80]
O bound to C	531.3–534.9	[Bou91, Jam92, Lec96]
“Free” O	531.6–531.7	[Ala91, Cri00]
O in oxynitride	531.7	[Pri95]
O in OH group	532.6	[Lec96]
O in H_2O	532.6–533	[Bla86, Gar90, Lec96, Wag90]
O in WO_x	532.9	[Zha99]
O in SiO_2	532.5–533.0	[Mou95, Wag90]

5.5.3.2 XPS Film Analysis

Deconvolution of XPS spectra was performed with combined Gaussian and Lorentzian curve fitting (90%–10%) and Shirley background subtraction using the RBD

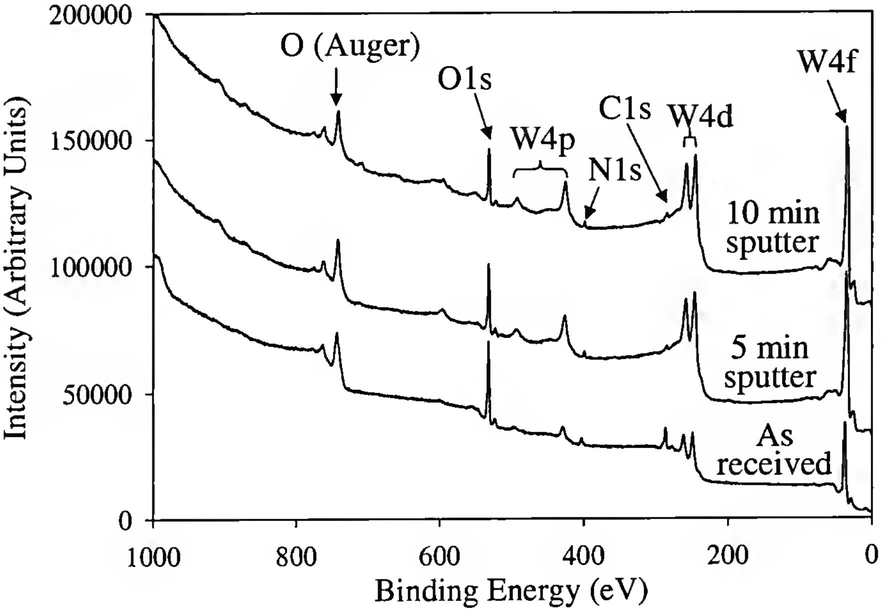

Figure 5-15 XPS survey spectra for films deposited at 450°C. a) As received. b) After 5 minutes sputter. c) After 10 minutes sputter.

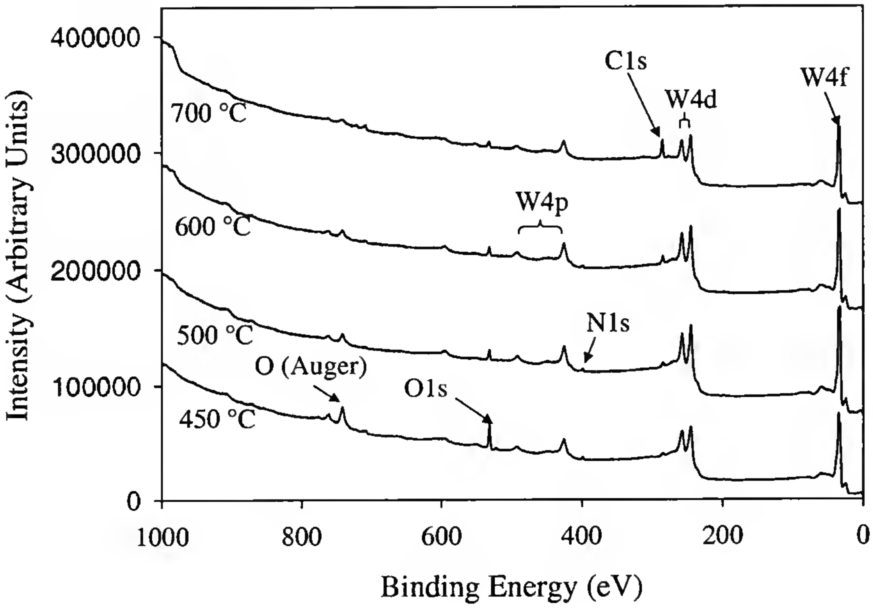

Figure 5-16 XPS survey spectra after 10 min sputter for films deposited at 450 to 700°C.

Analysis Suite software. Due to the presence of C both at the film surface and in the film bulk, quantification of charging to an exact value of BE shift was difficult. XPS survey spectra for films deposited at 450°C are shown in Figure 5-15. These spectra indicate the presence of W, N, C and O in the films, while a peak for Cl is not present. Some amount of adventitious C is evident on the as–received spectra, as the C1s peak decreases in height after sputtering. The O1s peak endures after sputtering, however, due to the porosity of these films. The W4d$_{5/2}$ and W4d$_{3/2}$ BE values in the as received film were 248 and 260.5 eV, respectively, which are consistent with WO_3 (Table 5-3). The W4d$_{5/2}$ and W4d$_{3/2}$ BE values after 5 and 10 min sputter were 245 and 257 eV, respectively, which is indicative of WN_x deposition. Figure 5-16 shows survey spectra after 10 min sputter for films deposited at 450 to 700°C. The N1s and O1s peaks decrease with increasing deposition temperature, while the C1s peak increases with deposition temperature, for reasons discussed above. The W4d$_{5/2}$ and W4d$_{3/2}$ BE values are similar for all temperatures after sputtering, near 245 and 257 eV, respectively, which indicates the presence of WN_x at all of the temperatures.

To view the most intense elemental peaks more closely, multiplexes were taken for the W4f, N1s, C1s and O1s lines. XPS multiplex spectra for films deposited at 450°C are shown in Figure 5-17. Focusing first on the sputtered films, we see that the elemental peaks have similar positions after 5 and 10 minutes of sputtering. The spectra in Figure 5-17a taken after 10 minutes sputter shows two sets of overlapping W4f binding energy curves, which indicate W in two different bonding states. The W4f$_{7/2}$ and W4f$_{5/2}$ peaks at 35.7 and 37.8 eV fall into the range for WO_3 (Table 5-3), with the 1.9 eV spin orbit splitting for these peaks being close to 2.0 eV reported previously for WO_3 [Sar80]. This is supported by an O1s peak at 531.4 eV, which is consistent with WO_3 (Table 5-3). As

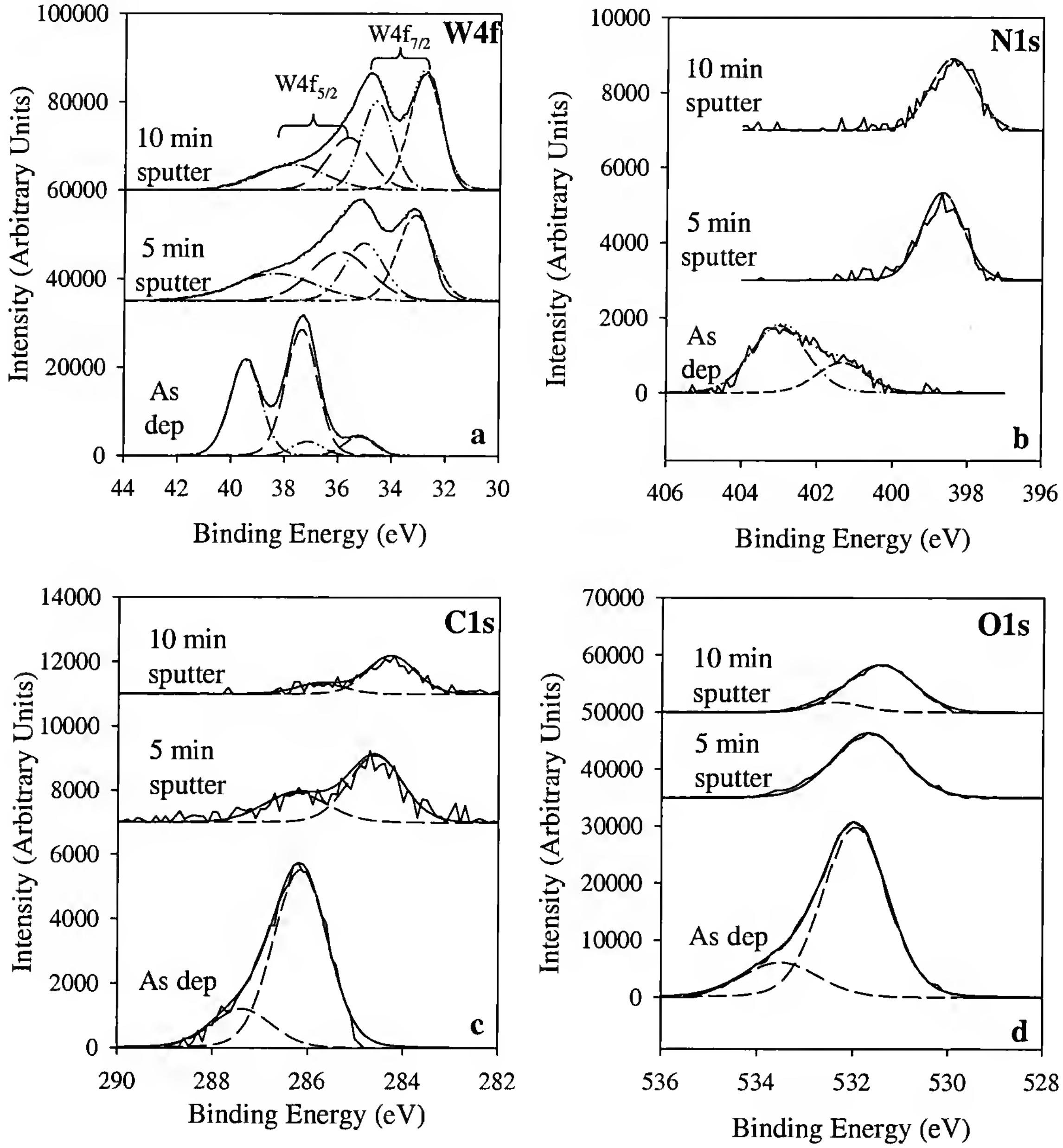

Figure 5-17 XPS spectra for films deposited from **1b** at 450°C for the a) W4f b) N1s c) C1s d) O1s BE lines. Dashed lines are deconvoluted peaks.

mentioned earlier, O in the films is due to post–growth air exposure, where O diffuses into the film and oxidizes unsaturated W atoms. Oxygen is reportedly mobile enough at ambient conditions to diffuse into surface or near–surface region of tungsten oxynitride, with chemisorption of oxygen to this surface causing continuous formation of WO_3 [Cho00]. The behavior of our films in air is likely similar to the oxynitride films.

As seen for the sputtered films in Figure 5-17a, the $W4f_{7/2}$ and $W4f_{5/2}$ peaks at 32.8 and 34.6 eV fall into the range for β–WN_x, but are believed to actually represent β–WN_xC_y. BE values for β–WN_xC_y have not been reported in the literature, but several things point to this possibility. First, the single N1s peak at 398.4 eV is shifted above the standard values for β–WN_x to a value similar to that for N–C bonding (Table 5-4). Second, a C1s BE value at 285.8 eV supports the presence of C–N bonding (Table 5-5), and is considerably higher than reported values for carbidic C. Third, the upward shift for W4f BE away from metallic or carbidic W (Table 5-3), coupled with nitridic peak positions for W4d, suggest W–N bonding. Since no metallic or carbidic W peaks were observed, the presence of metallic W or β–WC_x clusters in the film is unlikely [Mon99]. These items therefore point toward formation of β–WN_xC_y, which is also supported by our XRD lattice parameter data for films deposited at higher temperature. Moreover, the upward shift in N1s and C1s binding energy in β–WN_xC_y suggests that these elements have an attractive interaction on the FCC W interstitial sublattice. In an analogous case, attractive N–C interactions were reported on the FCC Nb and FCC Ti interstitial sublattices [Lee01a]. The large FWHM value for BE of N1s electrons suggests a disordered or defective structure, which is consistent with amorphous (or nanocrystalline) films [Pri95]. The lack of a second N1s peak above 399 eV suggests that all N is bound to W, with none present in its "free" form.

The additional C1s peak at 284.6 eV falls into the range for either graphitic or free (amorphous) C (Table 5-5). Since XRD results do not indicate the presence of graphite in the films, this C1s value represents free (amorphous) C. A small, additional O1s peak at 532.4 eV is likely due to the presence of a suboxide (WO_x). While the suboxide W4f peaks are convoluted with the WO_3 and β–WN_xC_y peaks, their exact location is unknown due to lack of an additional shoulder for them in the W4f spectra.

When compared to the sputtered films, the as received films in Figure 5-17 have significant BE shifts and additional peaks. The surface region of the as–received films contain significant amounts of WO_3, evidenced by the large $W4f_{7/2}$ and $W4f_{5/2}$ peaks at 37.4 and 39.4 eV, respectively, which corroborate the W4d BE values in the as–received survey spectrum (Figure 5-15). An O1s peak at 531.9 eV also supports the presence of WO_3. A significant amount of non–conductive WO_3 at the film surface leads to sample charging, which causes the shift in BE to higher values [Gru87, Nag00]. The $W4f_{7/2}$ BE, in particular, increases by 1.7 eV from 35.7 eV after 10 minutes sputter to 37.4 eV at the surface. The area under the WO_3 peak decreases after sputtering, but does not disappear completely, which is consistent with a previous report on ambient air oxidation of a tungsten oxynitride surface [Cho00].

Decreasing the as–received BE values for W, C and O by 1.7 eV leads to a close match to peak positions after 5 min and 10 min sputter. With this in mind, the $W4f_{7/2}$ and $W4f_{5/2}$ peaks at 35.2 and 37.1 eV would suggest β–WN_xC_y that has been shifted upward by 1.7 eV. The corresponding N1s value for nitridic N at 401.3 eV would be 399.6 eV after a downward shift of 1.7 eV, however, which is still higher than that for N1s in β–WN_xC_y. This suggests that a tungsten oxynitride ($W(O,N)_x$) or oxycarbonitride

($W(O,C,N)_x$) is present at the surface before sputtering. This is supported by an O1s peak at 533.5 eV, which would be 531.8 eV after a downward shift of 1.7 eV, consistent with O in oxynitride (or possibly oxycarbonitride). A second N1s peak at 403.0 eV, which would be 401.3 eV after a 1.7 eV shift, is close to the value of 402.0 eV reported for N in a surface N–O/N–N compound [Wei99]. The two C1s peaks at 286.2 and 287.4 eV, when shifted down by 1.7 eV, are 284.5 and 285.7 eV, consistent with free C and C in β–WN_xC_y, respectively.

Table 5-7 summarizes the BE values for the elemental peaks shown in Figure 5-17 and the compounds to which these BE values correspond (based on comparison of these values to Table 5-3 through Table 5-6). Question marks in Table 5-7 indicate that exact location of the corresponding W4f peaks for the WO_x suboxide is unknown, due to lack of additional shoulders in the W4f spectra.

Table 5-7. Compounds in Films Deposited from **1b** at 450°C

Sputter Time (min)	$W4f_{7/2}$ (eV)	$W4f_{5/2}$ (eV)	N1s (eV)	O1s (eV)	C1s (eV)	Compound
0	37.4	39.4	–	531.9	–	WO_3
0	35.2	37.1	401.3	533.5	287.4	β–$W(N,C,O)_x$
0	–	–	403.0	–	–	N–O/N–N surface species
0	–	–	–	–	286.2	Free C
5	33.1	35.0	398.7	–	286.3	β–WN_xC_y
5	36.0	38.4	–	531.7	–	WO_3
5	–	–	–	–	284.6	Free C
10	32.8	34.6	398.4	–	285.8	β–WN_xC_y
10	35.7	37.8	–	531.4	–	WO_3
10	?	?	–	532.4	–	WO_x
10	–	–	–	–	284.6	Free C

The interface layer evident in the TEM and AES Depth Profiling sections was also examined with XPS to determine the bonding states in this layer. The film was sputtered until the interface layer was exposed, and the multiplex was then collected. XPS spectra in Figure 5-18 indicate the presence of W, Si and O in the interface layer,

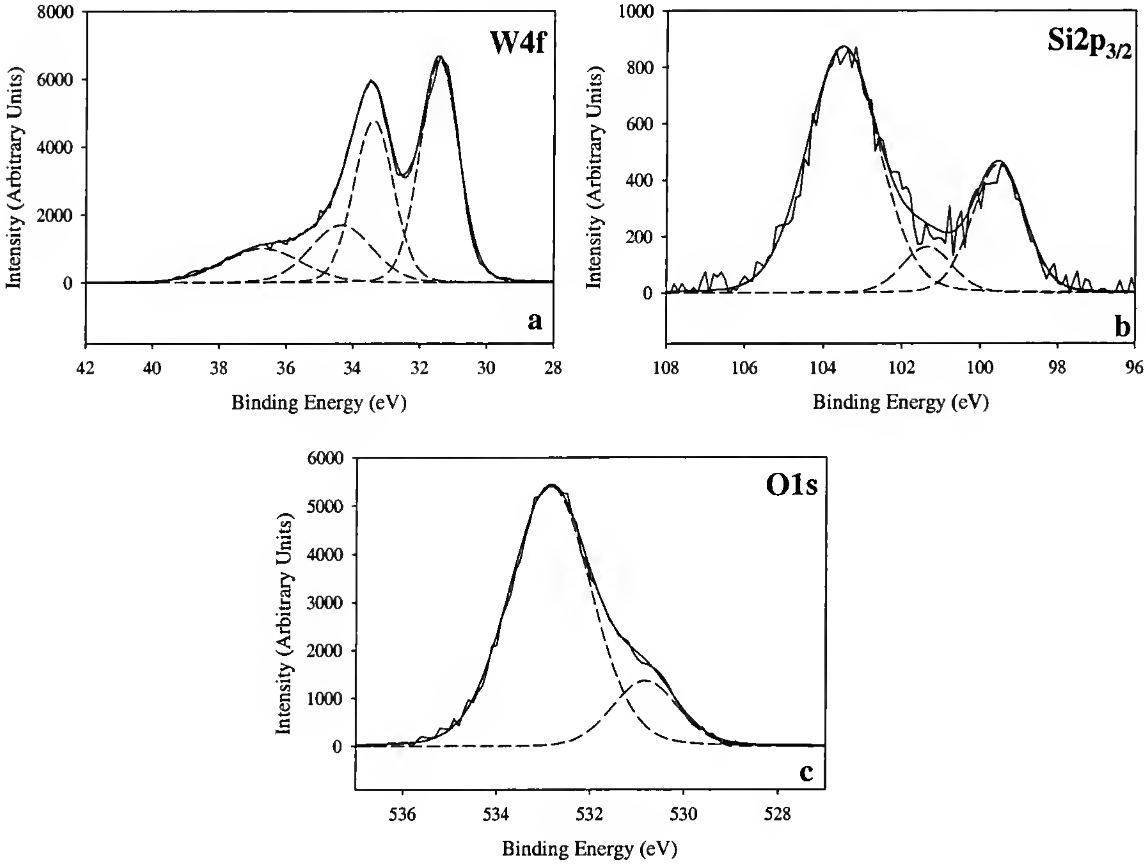

Figure 5-18 XPS spectra for the film–Si subsrate interfacelayer for film deposited from **1b** at 450°C. a) W4f b) Si2p$_{3/2}$ c) O1s BE lines. Dashed lines are deconvoluted peaks.

while the C1s and N1s BE lines were absent. The W4f$_{7/2}$ and W4f$_{5/2}$ BE values at 34.4 and 36.7 eV, coupled with an O1s BE at 530.8, are consistent with WO_3 (Table 5-3 and Table 5-6). The Si 2p$_{3/2}$ and O1s BE values at 103.5 and 532.9 eV, respectively, indicate SiO_2 (Table 5-6). W4f$_{7/2}$ and W4f$_{5/2}$ BE values at 31.5 and 33.5, coupled with the Si 2p$_{3/2}$ peak at 99.5 eV, suggests WSi_2, where the Si 2p$_{3/2}$ BE value is consistent with silicide bonding [Mou95]. This indicates that some W reacts with the Si substrate. A mixture of WSi_2 and metallic W is also possible, however, as their W4f peaks overlap. The small peak at 101.4 eV is close to a reported BE of 101.7 eV for SiO [Ngu89], which may form due to the reduction of SiO_2 at the interface by the XPS Ar^+ sputter beam. The corresponding O1s BE peak for SiO is likely convoluted under the two larger O1s peaks in Figure 5-18.

Table 5-8 summarizes the BE values for the elemental peaks shown in Figure 5-18 and the compounds to which these BE values correspond (based on comparison of these values to Table 5-3–Table 5-6). The question mark in Table 5-8 indicates that exact location of the corresponding O1s peaks for the SiO suboxide is unknown, due to the likely convolution of this peak under the two larger O1s peaks for SiO_2 and WO_3.

Table 5-8. Compounds at Film–Si substrate interface for Deposition with **1b** at 450°C

$W4f_{7/2}$ (eV)	$W4f_{5/2}$ (eV)	$Si2p_{3/2}$ (eV)	O1s (eV)	Compound
31.4	33.4	99.5	–	WSi_2
34.4	36.7	–	530.8	WO_3
–	–	101.4	?	SiO
–	–	103.5	532.9	SiO_2

The bulk of the O in the films appears to be from post–growth in–diffusion, as evidenced by the decrease in O content with increased crystallinity and C content. The presence of SiO_2 at the interface suggests, however, that a small amount of background oxygen (from O_2 or H_2O) in the reactor may be causing reformation of the SiO_2 layer before film deposition. The source of the background O is unclear, but may be from an impure N_2 gas source (used during the reactor heating cycle before the H_2 bake) or from a small air leak in the system. This background level is believed to be small, however, because the presence of considerable amounts of O during reaction will favor WO_3 formation, especially at higher deposition temperature. Deposition of WO_3 films in our system, evidenced by high intensity WO_3 XRD peaks, has occurred on several occasions due to large–scale air leaks during deposition at a variety of temperatures.

The interface layer thickness was similar for deposition at 450 and 700°C, but the content of the layer changes with increasing deposition temperature, as indicated in the AES depth profiles. The decrease in O level at the interface for deposition at 700°C (Figure 5-14) may be due to higher temperature shrinking incubation time, which leaves less time for background O to react with the Si substrate before film deposition begins. Lower O content at the interface for the 700°C film also suggests that the relative amount of WSi_2 is higher for this interface compared to that deposited at 450°C. This is supported by a larger overlap region for the W and Si signals in the SIMS spectra for the 700°C film relative to the 450°C one (Figure 5-21 and Figure 5-22).

Nucleation of the films presumably occurs on SiO_2, with initial deposition of W on the oxide leading to formation of both WSi_2 and WO_3. After nucleation of the initial interface layer is complete, deposition of the WN_xC_y films begins. One report of sputtered WN_x films on Si (100) found an interface layer with a multilayered structure consisting of SiO_2/SiO_xN_y/nano–WSi_2 [Cho02]. An oxynitride layer is not evident in our interface layer, however, as N is not present.

Figure 5-19 shows multiplex spectra for films after 10 min sputter. The peak assignments are similar to those for the 450°C film after 10 minutes sputter, and are summarized in Table 5-9. Again, question marks in Table 5-9 indicate that exact location of the corresponding W4f peaks for the WO_x suboxide is unknown, due to lack of additional shoulders in the W4f spectra. Trends indicate that O and N levels generally decrease with increasing temperature. The N1s peak intensity increases from 450 to

500°C, however, which is consistent with AES results indicating higher N levels at 500°C. The N1s peak intensity drops at 600°C, and then disappears into the background noise at 700°C, although the β–WN_xC_y peak is still evident. The disappearance of this peak contrasts with AES results, which indicate that a small amount of N (~3 at.%) remains in the films at 700°C. This discrepancy may be due to large shifts in XPS sensitivity for N in compound materials, as has been reported [Lee93]. XRD results for higher temperature films indicate β–WN_xC_y formation. While films at 450°C are x–ray amorphous, they likely contain FCC β–WN_xC_y in unit cell form, because the W4f BE values for β–WN_xC_y have minimal shift when going from an amorphous film (below 500°C) to a polycrystalline film (at and above 500°C). This infers that the bonding state doesn't change for β–WN_xC_y with increasing temperature, but rather that the unit cells grow with increasing temperature until they are large enough (at 500°C) to diffract x–rays. In contrast, the C content increases with temperature, with the peak for free C growing significantly when going from 600 to 700°C. In addition, the C1s peaks shift to slightly higher BE at 700°C, which may be due to some charging, as film resistivity jumps at 700°C. Interestingly, no W4f or C1s peaks consistent with carbide compounds were evident for any of the films, even at the highest temperature (Table 5-3 and Table 5-5). This may be due to the presence of some N in the films at all deposition temperatures, which may alter the electron distribution around the W atoms enough to force an upward shift in BE, irrespective of the interstitial site fraction of C.

Figure 5-20 shows the area under the $W4f_{7/2}$ XPS curve for films deposited from 450 to 700°C. The area under the $W4f_{7/2}$ curve for β–WN_xC_y increases from 450 to 500°C, and then drops above this. As mentioned above, the film crystallizes at 500°C, which densifies the film and decreases oxygen's ability to in–diffuse and form WO_3 on the surface of β–WN_xC_y nano– or polycrystals. This is reflected by the increase in area

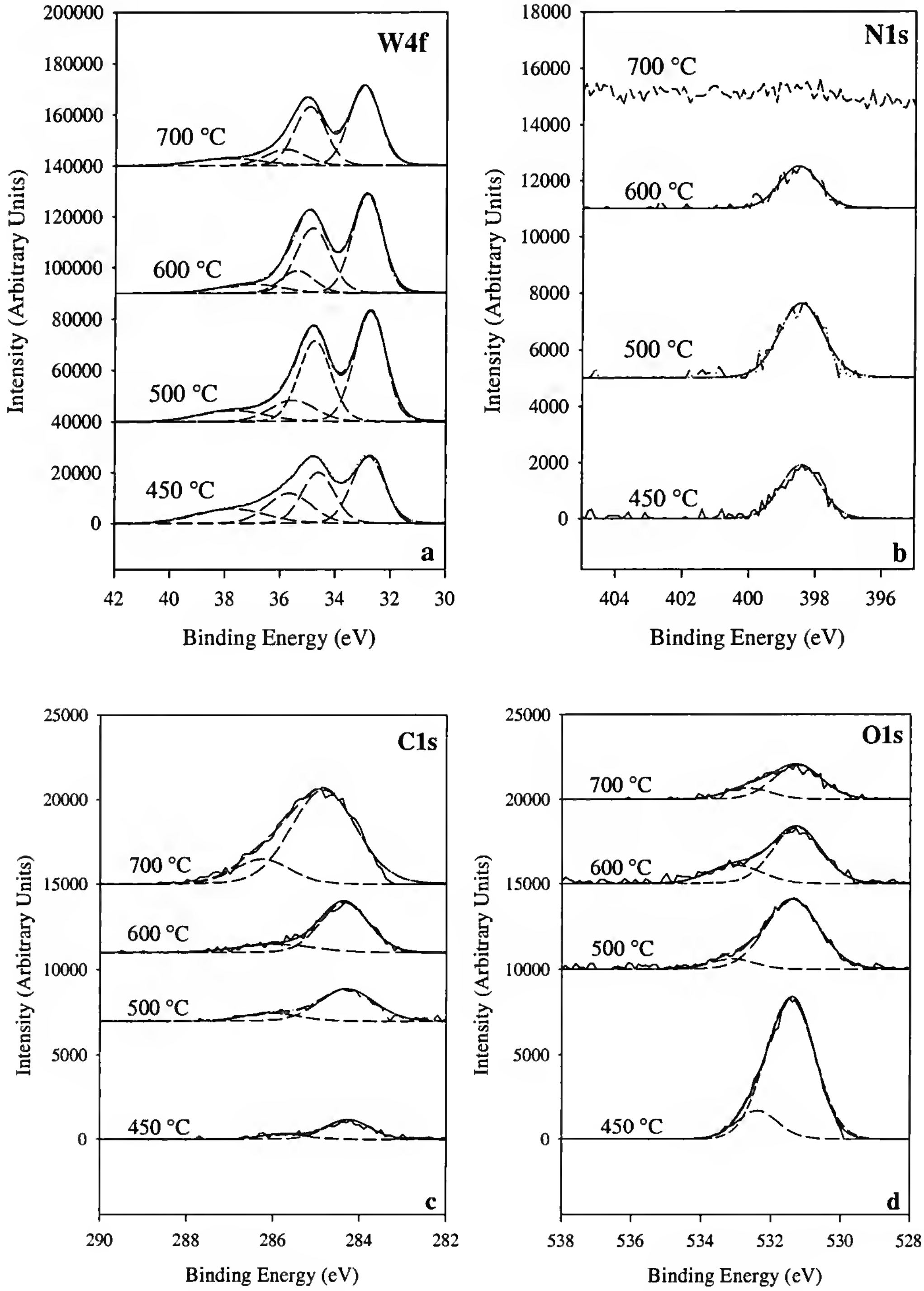

Figure 5-19 XPS spectra for films deposited from **1b** at 450 to 700°C after 10 min sputter. a) W4f b) N1s c) C1s and d) O1s BE lines. Dashed lines are deconvoluted peaks.

under the β–WN_xC_y curve at 500°C. The drop in β–WN_xC_y area above 500°C follows the trend of decreasing N content with increasing temperature. Decreasing levels of N decrease the ability to form β–WN_xC_y at higher temperature.

The area under the curve for WO_3 decreases steadily with increasing temperature. This may indicate a shift in film composition with increasing depth into the film, or it may reflect a change in film structure due to sputtering by Ar^+ ions. Katrib et al. [1995] reported that Ar^+ sputtering of a mixture of WO_2+WO_3 caused formation of metallic W. Although metallic W is not formed in our films, the drop in WO_3 content may indicate preferential sputtering of O atoms from WO_3 in the film. Sputtering of O atoms from WO_3 would lead to an apparent decrease in WO_3 content and possibly an increase in WO_x content. Since the pattern for WO_3 is not evident on the XRD spectra, any WO_3 present in the film is likely to be highly disordered (e.g., nanocrystallites), rather than existing as large crystallites.

Table 5-9. Compounds in Films from **1b** After 10 Minutes Sputter

Deposition Temp. (°C)	$W4f_{7/2}$ (eV)	$W4f_{5/2}$ (eV)	N1s (eV)	O1s (eV)	C1s (eV)	Compound
450	32.8	34.6	398.4	–	285.8	β–WN_xC_y
450	35.7	37.8	–	531.4	–	WO_3
450	?	?	–	532.4	–	WO_x
450	–	–	–	–	284.6	Free C
500	32.7	34.8	398.4	–	286.0	β–WN_xC_y
500	35.6	37.7		531.4	–	WO_3
500	?	?	–	533.1	–	WO_x
500	–	–	–	–	284.3	Free C
600	32.9	34.8	398.5	–	286.0	β–WN_xC_y
600	35.4	37.1	–	531.3	–	WO_3
600	?	?	–	533.0	–	WO_x
600	–	–	–	–	284.4	Free C
700	33.0	35.0	–	–	286.3	β–WN_xC_y
700	35.9	37.9	–	531.3	–	WO_3
700	?	?	–	532.7	–	WO_x
700	–	–	–	–	284.8	Free C

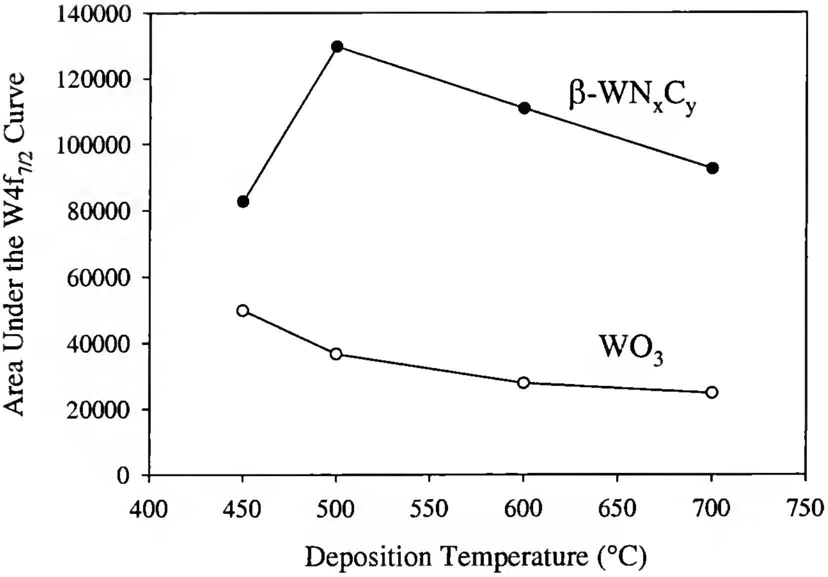

Figure 5-20 Area under the $W4f_{7/2}$ peak for films after 10 minutes sputter.

The formation of oxide is believed to be due to post–growth reaction of the films with ambient air. Potential oxygen sources in air include water and O_2. Vu et al. [1990] reported values for activation energy and pre–exponential factor for the oxidation of $W_{0.80}N_{0.20}$ in wet and dry air over a temperature range of 450 to 575°C. The rate constant for oxide formation was slightly higher in wet air than dry air, indicating that water is the more favorable oxygen source in this temperature range. Oxide formation still occurred in dry air, however, suggesting that both O_2 and H_2O participate in the oxidation process with ambient air. Extrapolating Vu's kinetic data down to room temperature (25°C) gives a negligibly small value for oxide thickness. Since our low temperature amorphous films are very porous, significant O was able to diffuse down into the bulk of the films. A thin, amorphous WO_3 layer (which is invisible to XRD), consistent with Vu's extrapolated data, may have formed by in–diffused O oxidizing the surface of β–WN_xC_y nanocrystals in the film. This is consistent with a previous report, which indicated that oxidic phases formed by exposure of tungsten–containing films to air were amorphous [Cho00]. AES analysis after 1 minute of sputter indicates substantial drop in oxygen content for all deposited films, further supporting this assertion.

Overall results indicate that W bonding in the bulk films may be a mixture of WN_xC_y, WO_3 and WO_x. The presence of some oxynitride in the film cannot be ruled out by XRD due to exact overlap of β–WN_x and $W_{0.75}(N,O)$ spectra [JCP88]. XPS results, however, exclude this possibility, as no additional W and N peaks consistent with oxynitride in the bulk films are present. Carbon is typically present in two bonding states, as amorphous (free) C and as C bound to W (and possibly to N) in β–WN_xC_y form. While the formation of CN_x at the grain boundaries is possible, the single N1s peak and upward shift for W4f BE away from carbidic W suggest that all N is preferentially located at the polycrystal's interstitial sublattice, along with some C, which causes the upward shift in N1s BE. Although the lattice parameter for the films increases up to 675°C, it levels off above this temperature. This may indicate a solubility limit for C in the β–WN_xC_y polycrystals. Above 675°C, additional C contamination goes to the grain boundaries, which is confirmed by a sharp increase in film resistivity and the C1s peak for free C at 700°C. As mentioned previously, β–WC_x films with interstitial C tend to have low resistivity due to little covalency or ionicity in the W–C bonds. In contrast, when W films contain substantial free C rather than interstitial C, the free C regions scatter electrons, increasing film resistivity. As the amount of free C in the grain boundaries increases, the resistivity of the films also increases. While the W4f peak representing β–WN_xC_y remains for the 700°C films, the corresponding N1s peak disappears. AES results contrast with XPS, though, showing that some N remains in the films at 700°C, supporting the possibility of β–WN_xC_y remaining in the film at this temperature. This suggests, however, that β–WN_xC_y present in the films at higher temperature is N deficient, with values of x being well below 0.33.

5.5.4 SIMS Depth Profiling

SIMS depth profile results are shown in Figure 5-21 and Figure 5-22. Since β–WN_x and β–WN_xC_y film standards were unavailable for calibration, the SIMS data are not quantitative in nature, as the sputter rates and ionization probabilities are matrix dependent. The change in the SIMS profiles with depth into the film, along with the change in profiles with film deposition temperature, can still give us some perspective, however. Figure 5-21 indicates a SIMS depth profile for a film deposited at 450°C. These results reinforce XPS data suggesting W–O and W–N bonding in the films, because WO and WN fragments were sputtered from the films during SIMS analysis. In addition to the presence of W, N, C and O, SIMS analysis also shows significant amounts of H, which cannot be detected by AES or XPS, and Cl, which can be detected by AES and XPS if present in sufficient quantity (~1 at.%). This suggests that some amount of Cl from the precursor is depositing in the films, although the amount is less than 1 at.%. This small amount of Cl may still be troublesome for device applications, as Cl can etch substrates and corrode subsequent metal layers. H in the films originated either from the precursor ligands, the solvent, or the H_2 carrier gas. At low temperature, the ability to form volatile HCl is lower, meaning that more Cl may remain at the film surface without desorbing. At higher temperature, volatile HCl forms more readily, and this is reflected by decreased Cl content at the higher deposition temperature. Another difference between the films at 450 and 700°C involves the Si levels. The Si signal increases

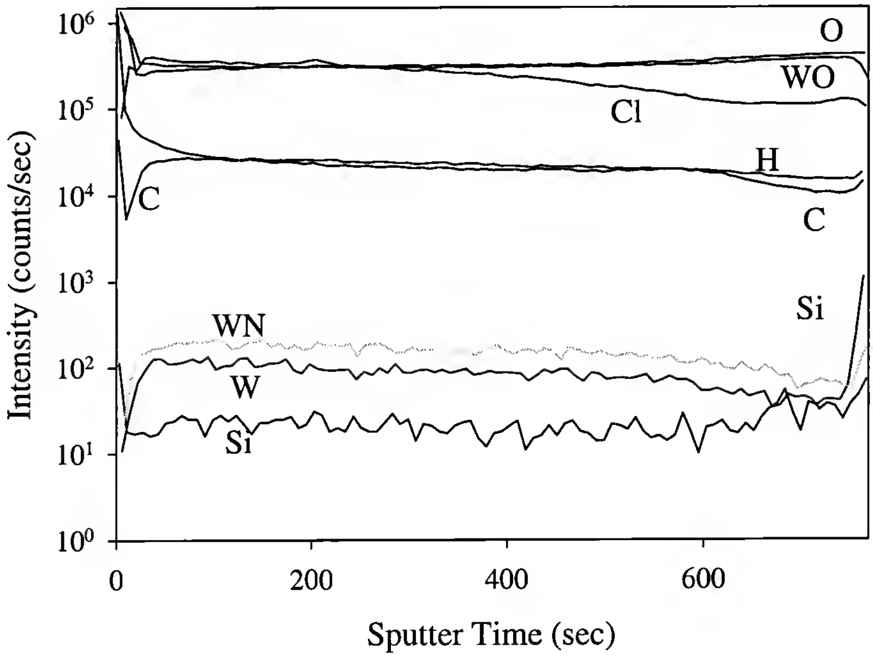

Figure 5-21 SIMS depth profile for film deposited with **1b** at 450°C.

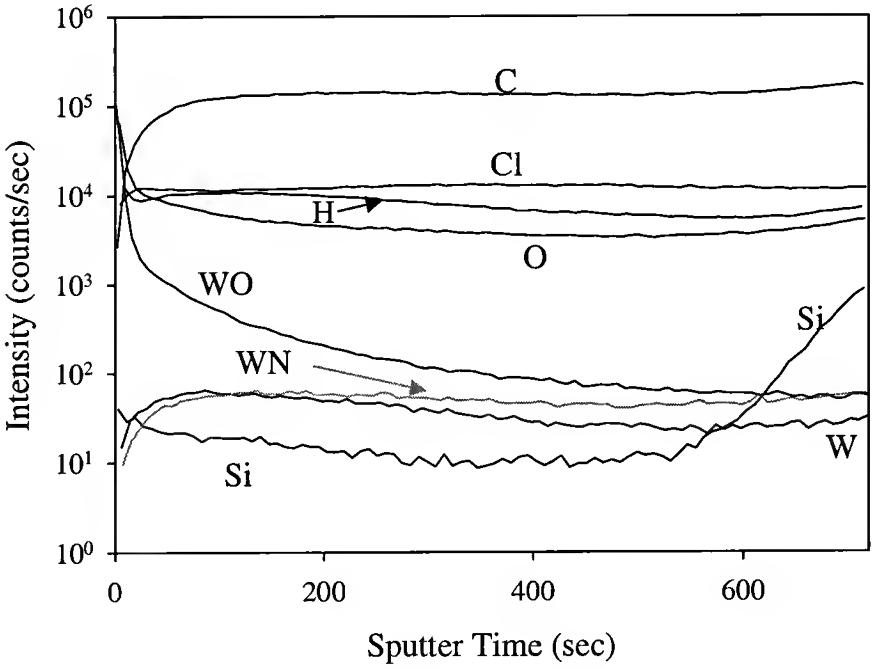

Figure 5-22 SIMS depth profile for film deposited with **1b** at 700°C.

sharply at the barrier–Si interface in the 450°C film, while it increases much more gradually in the 700°C film. This suggests either substantial Si roughness at the interface and/or silicide (WSi_x) formation at the higher temperature, consistent with AES depth profile results. The levels of O and WO are significantly higher in the low temperature film, consistent with increased O in–diffusion into these porous films. In addition, the C level is higher in the 700°C film, consistent with increased ligand and solvent decomposition at the higher temperature.

5.6 Film Growth Rate (XSEM)

Growth rates were estimated by dividing the total film thickness (from X–SEM) by deposition time. Figure 5-23 gives two sample X–SEM photos. The surface of the deposited films appeared to be fairly smooth, and film thickness varied from ~1500 Å for the deposition at 450°C up to ~4000 Å for deposition at 700°C.

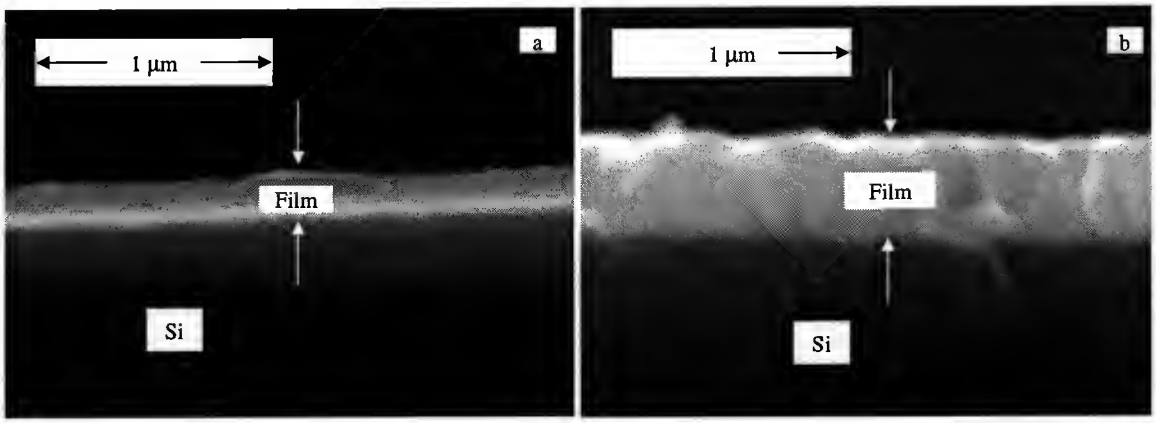

Figure 5-23 Cross–section SEM photo depicting film thickness for growth from **1b** for 150 minutes on a Si (100) substrate. a) Deposition at 450°C. b) Deposition at 700°C.

These film thicknesses correspond to deposition rates ranging from 10–27 Å/min. The growth rate of the films (as determined by X–SEM) varied with temperature, as shown in Figure 5-24.

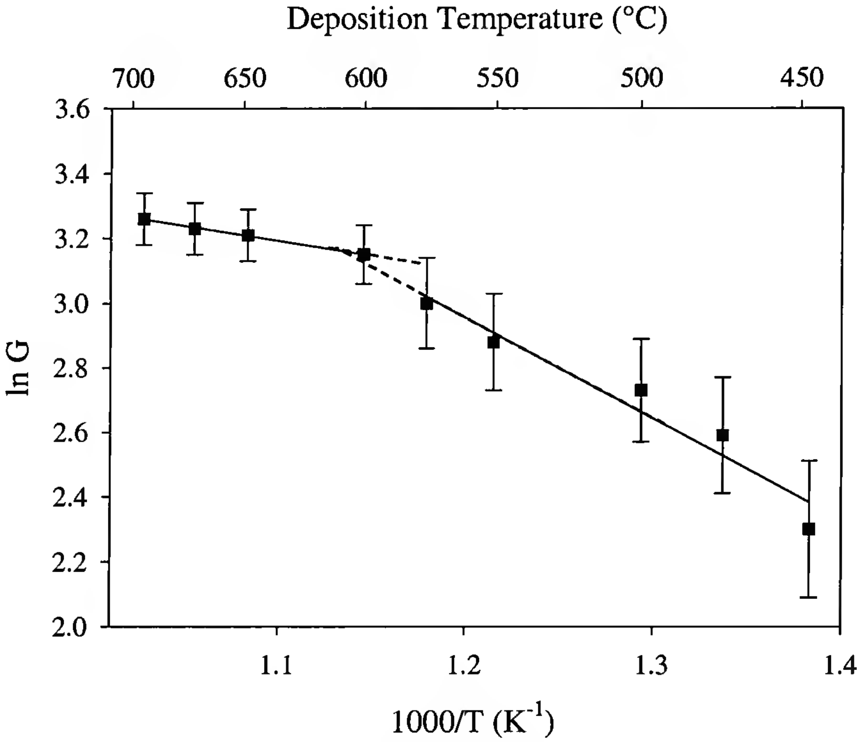

Figure 5-24 Plot of film growth rate on Si (100) vs. inverse temperature. Error bars indicate uncertainty due to deposition temperature variation (+/– 10°C) and thickness measurement from XSEM photos.

From this figure, two growth regimes are apparent. The region with shallow slope shows a weak dependence on temperature that is indicative of the mass transfer controlled regime. Mass transport to the surface is the rate–determining step in this regime, where high substrate temperature enables immediate reaction of species arriving at the surface. The region with a steep slope indicates that growth rate increases exponentially with temperature, which is indicative of the kinetically controlled regime. In this regime, the rate–determining step for film growth is reaction on the substrate surface. Ample reactants are available at the substrate surface, and growth rate is determined by the reaction rate. Growth rate in the kinetically controlled regime can be estimated by the Arrhenius expression for growth rate (Equation 5–2):

$$G = Ae^{-E_a/RT} \qquad (5\text{–}2)$$

where G is growth rate (Å/s) and E_a is the apparent activation energy (eV). From this expression, we can calculate E_a for the precursor molecule by plotting ln G vs. 1/T according to Equation 5–3:

$$\ln G = -\left(\frac{E_a}{R}\right)\left(\frac{1}{T}\right) + \ln A \qquad (5\text{–}3)$$

where A is a constant, E_a/R is the slope of the line in the kinetically controlled regime, and E_a is the apparent activation energy for film growth. The calculated E_a for film growth from the **1b** precursor was 0.84 eV in the kinetically controlled regime, compared to 0.9 eV reported for bis(*tert*–butylimido)bis(*tert*–butylamido)tungsten [Tsa96]. This value falls within the typical activation energy range for CVD growth in the kinetic regime, which ranges from 0.5 to 1 eV [Raa93]. In the kinetically controlled regime, a change in temperature of 1% yielded a 10% change in growth rate. The kinetically controlled regime appears to have an upper temperature limit near 600°C. Above 600°C, the region's shallower slope indicates mass transfer controlled growth. Depositions at 400 and 750°C were done to establish the temperature boundaries for film growth with the precursor. Although the results of these growths were not included in Figure 5-24, they do provide some useful information. Films deposited at 400°C were not visible by X–SEM, but AES depth profiling indicated a nominal film thickness of ~100 Å. This thickness value was used to estimate E_a for the kinetic regime. The growth rate at 750°C dropped to 10 Å /min, with black particulates visible on the substrates after deposition. Particulate formation and reduced growth rate result from gas phase decomposition of the precursor. At this high temperature, upstream heating caused precursor decomposition and reaction in the gas phase. Particulates on the substrates confirmed a gas phase reaction, while the drop in film deposition rate is consistent with reactant depletion.

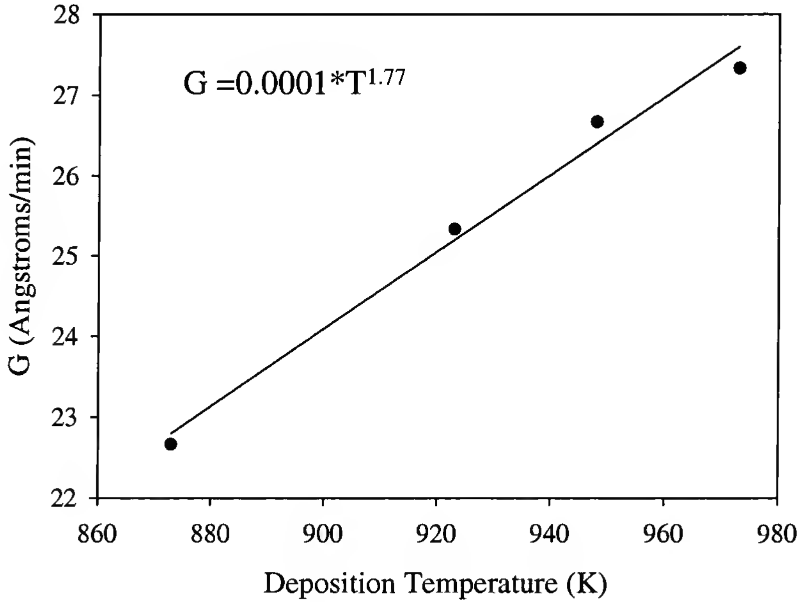

Figure 5-25 Temperature dependence of film growth rate on Si (100) in the diffusion controlled regime.

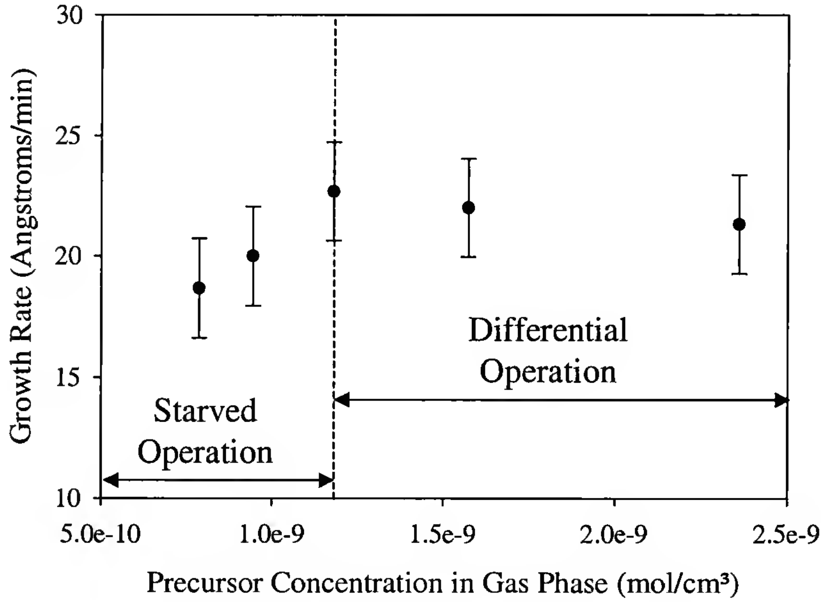

Figure 5-26 Plot of film growth rate on Si (100) vs. precursor concentration in the gas phase. Error bars indicate uncertainty due to deposition temperature variation (+/– 10°C) and thickness measurement from XSEM photos.

Figure 5-25 shows a plot of deposition temperature vs. film growth rate in the mass transfer controlled regime. Experiments indicated growth rate in the mass transfer controlled regime had a temperature dependence of $T^{1.78}$. This is similar to a reported value of $T^{1.7}$ for diffusion controlled film growth in an impinging flow reactor [Hua03].

Figure 5-26 indicates dependence of film growth rate on the concentration of i–Pr precursor in the gas phase. Below ~ 1.2×10^{-9} mol/cm³, the growth rate appeared to have a linear dependence on concentration, indicative of operation in the starved regime (Chapter 1). Above this concentration, the growth rate was steady, which indicates operation in the differential regime.

5.7 Film Incubation Time and Morphology

The orientation of the underlying Si substrate also affected film deposition rate. Growth from the i–Pr precursor at 650°C on Si (100) yielded an incubation time of ~50 minutes, while an incubation time of ~30 minutes was evident for growth on Si (111) with a 4 ° miscut. Initial nucleation for the deposited films is therefore slower on Si (100) than on miscut Si (111), which is caused by a difference in surface energy between the Si (100) and miscut Si (111) surfaces. Several factors give rise to this difference in surface energy, including the number of dangling bonds, the density of surface sites, and the number of surface features (such as steps, kinks and ledges) [Vos78]. The number of dangling bonds on the surface, for example, is proportional to that surface's energy, where more dangling bonds mean higher surface energy. Si crystals have a diamond cubic structure, with each Si atom tetrahedrally bonded to four other Si atoms. When cleaved along the (100) plane, each Si atom on the substrate surface retains two of the four bonds to other Si atoms, while two of the bonds are left dangling (unbonded). When cleaved along the (111) plane, each Si atom retains three bonds to neighboring Si atoms, while one bond is left dangling. Since Si (100) has 2 dangling bonds per surface atom, it has a higher surface energy than the Si (111) face. But, when Si(111) is miscut, the number of dangling bonds, along with steps, kinks and ledges, increases, due to the formation of vicinal surfaces. Hence, the 4 ° miscut Si (111) has higher surface energy than Si (100).

The substrate's surface energy plays a large role in nucleation and film growth, and takes part in two of the three interface energies, which together determine the feasibility of film deposition. The three energies are γ_{sv} (substrate–vapor interface energy), γ_{sf} (substrate–film interface energy) and γ_{fv} (film–vapor interface energy). The necessary criterion between these three energies for film deposition to occur is shown in Equation 5–4:

$$\gamma_{sv} > \gamma_{sf} + \gamma_{fv} \tag{5–4}$$

Film deposition will not occur unless this criterion is met; hence deposition is more likely for a system with a larger value of γ_{SV}. The relationship between the two terms on the right side of Equation 5–4 determines how the film will nucleate on the substrate surface (i.e., island formation vs. film wetting). Since Si (100) has lower surface energy (γ_{sv}) than 4 ° miscut Si (111), nucleation should occur more readily on miscut Si (111). This is consistent with growth data, which indicate lower incubation time (~30 minutes) on miscut Si (111) compared to the incubation time (~50 minutes) for deposition on Si (100) as shown in Figure 5-27. Once a layer of film has deposited on the Si substrate, the film continues to grow on itself at essentially the same rate regardless of substrate orientation, evidenced by similar slopes for the film thickness vs. deposition time lines in Figure 5-27.

The variation in film roughness with deposition time at 650°C on Si (100) is also shown in Figure 5-27. RMS roughness was highest (470 Å) for the 30 min deposition, indicating that some deposition and/or etching had occurred by this time. After 45 min of deposition, RMS roughness dropped substantially to a local minimum (100 Å), suggesting that nucleation of the interface layer was near completion, which supports an incubation time of ~50 min. At the 60 min point, film roughness increased to 190 Å, suggesting a Stranski–Kranstanov (S–K) growth mechanism [Ohr92], which may be caused by strain energy associated with defects and pores in the interface layer. As growth continued to 120 minutes, the RMS roughness dropped slightly to 170 Å, suggesting that S–K growth continued through this time. Between 120 and 150 minutes, roughness dropped considerably to 40 Å, which may indicate a shift toward layer–by–layer growth when film thickness increases above 2000 Å. AFM micrographs supporting the roughness results are shown in Figure 5-28.

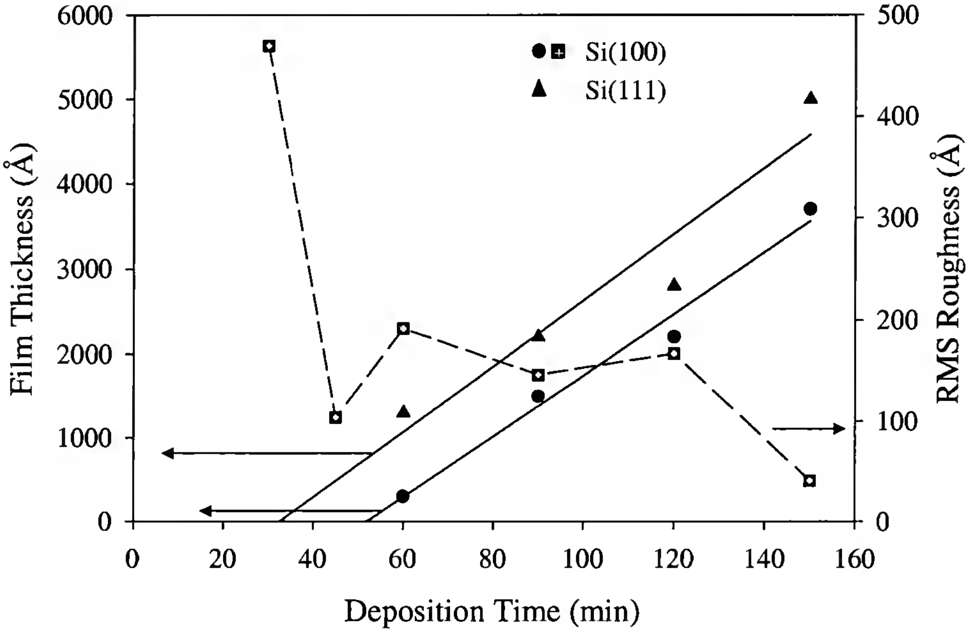

Figure 5-27 Film thickness vs. deposition time for growth at 650°C on Si (100) and Si(111) substrates; RMS roughness is shown for growth on Si (100)

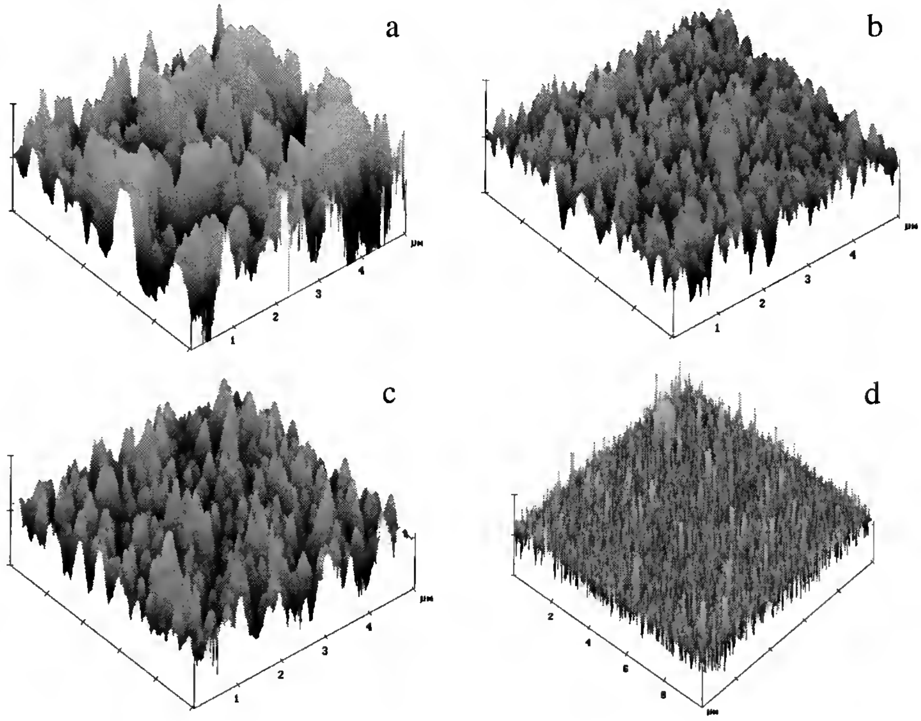

Figure 5-28 AFM micrographs of film surface for growth at 650°C on Si (100). a) 30 min growth. b) 45 min growth. c) 60 min growth. d) 150 min growth.

AFM roughness measurements are supported by SEM micrographs of the films at different times during the growth cycle. Figure 5-29 shows films deposited at times varying from 30 to 150 minutes. For the 30 minute sample, a very disordered nucleation pattern is evident on the underlying Si (100) substrate, which may be the initial stages of interface layer deposition. As deposition time increases to 45 minutes (near the incubation time), the film is still very disordered, but its coverage of the Si substrate has increased substantially. After 60 minutes, islands appear to have formed on the underlying nucleation layer of the film, in a manner consistent with S–K growth. As growth time increases to 90 and 120 minutes, the average size of the islands increases, indicating that the island/film interface energy is decreasing, which leads to islands with less curvature. Finally, after 150 minutes, a shift to layer growth is apparent, as the islands have disappeared in favor of a very smooth surface.

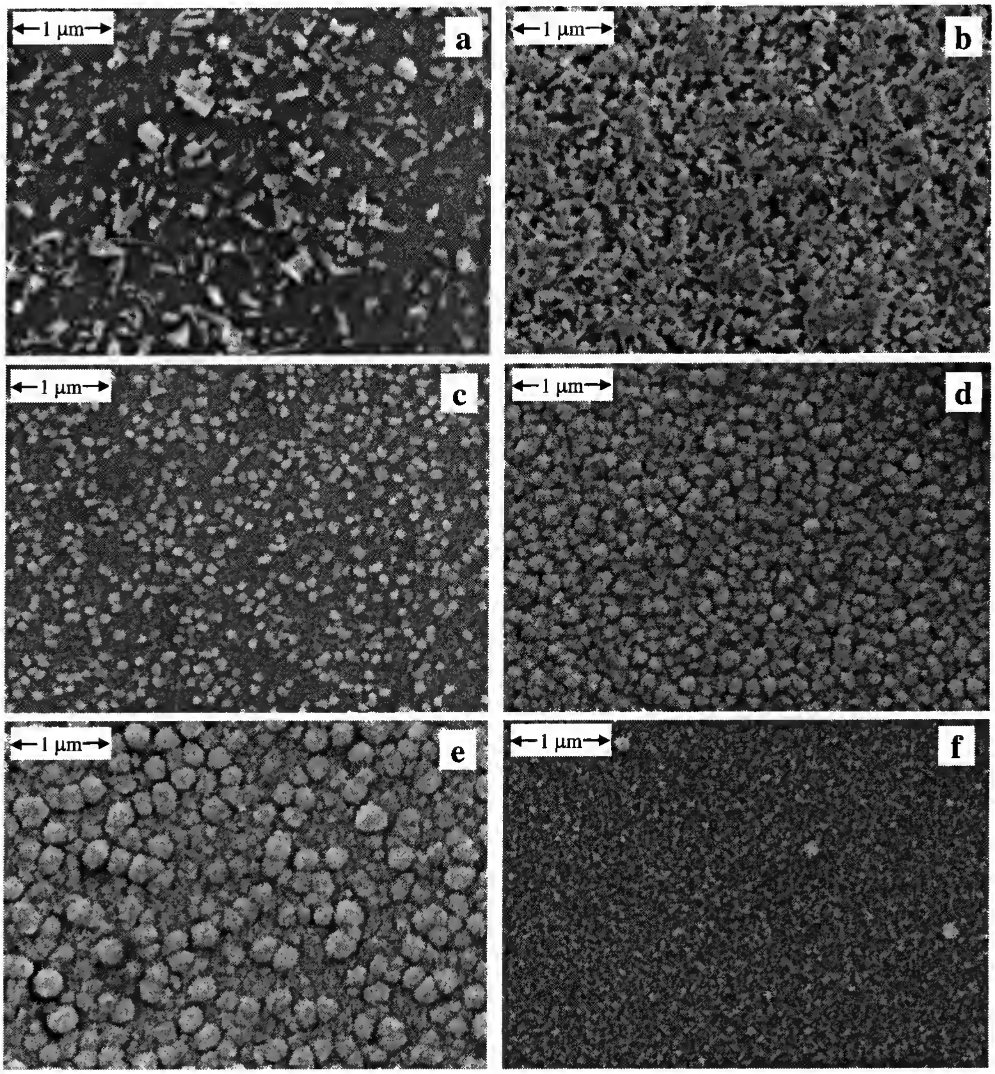

Figure 5-29 Morphology of films deposited at 650°C. a) 30 min growth. b) 45 min growth. c) 60 min growth. d) 90 min growth. e) 120 min growth. f) 150 min growth.

Cross–section SEM micrographs in Figure 5-30 below further underscore the change in film growth with deposition time. Film thickness is minimal after 60 minutes, and increases substantially for 90 minutes of deposition. The thickness continues to increase with deposition time, and the film thickness and roughness are highest and lowest, respectively, after deposition for 150 minutes.

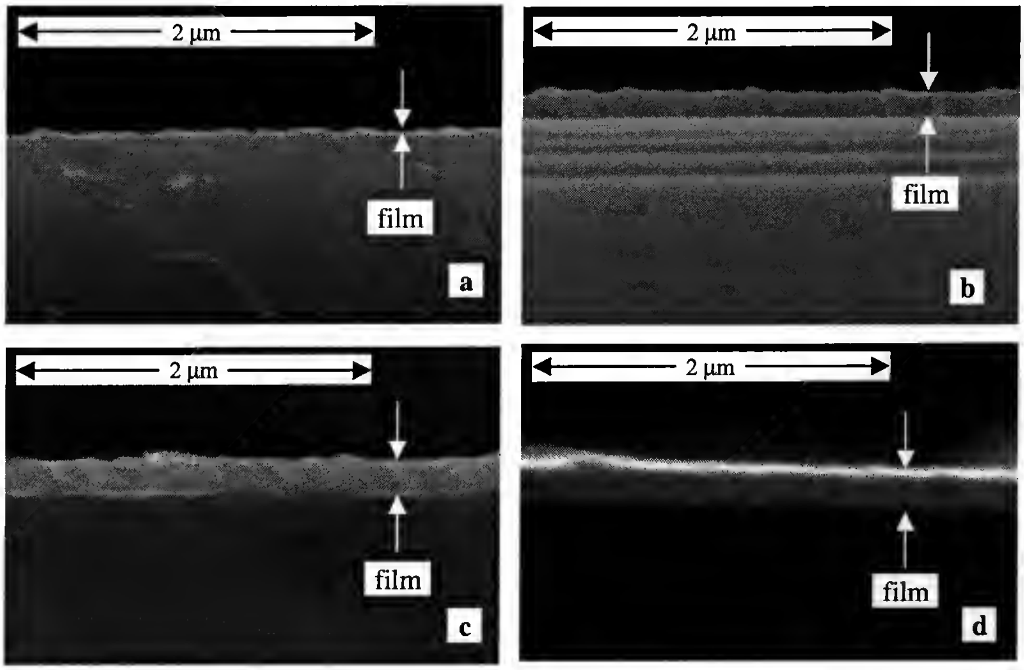

Figure 5-30 XSEM pictures of films deposited with **1b** at 650 °C on Si (100) substrates. a) 60 min growth. b) 90 min growth. c) 120 min growth. d) 150 min growth.

5.8 Film Electrical Properties

Film resistivity was calculated using Equation 5–5:

$$\rho = R_s t \qquad (5\text{–}5)$$

where ρ is resistivity (Ω–cm), R_s is sheet resistance (Ω/□) from 4–point probe, and t is film thickness (cm) from X–SEM. Sheet resistance of the films was checked with 4–point probe. The variation of film resistivity with deposition temperature is shown in Figure 5-31.

Deposition at 450°C produced films with the lowest resistivity value, 750 μΩ–cm, despite C and O contamination levels of 13 and 22 at.%, respectively. This is slightly higher than 620 μΩ–cm reported for film growth from the single–source precursor bis(*tert*–butylimido)bis(*tert*–butylamido)tungsten at 650°C [Tsa96].

Resistivity climbs steadily from 750 μΩ–cm to 4800 μΩ–cm as deposition temperature increases from 450–550°C. The jump in resistivity is most likely due to the combined effects of increasing C levels and polycrystal formation. Contamination by free C increases film resistivity by scattering electrons as they travel through the film, and C levels increased from 13 to 20 at.% over this temperature range. In addition, transitioning from an amorphous to polycrystalline film structure causes formation of grain boundaries, which scatter electrons and increase film resistivity. Once polycrystal grains have formed, the film resistivity is typically lowered by grain growth, which decreases the number of grain boundaries. Between 550 and 675°C, the resistivity increases gradually from 4800 to 5500 μΩ–cm, despite grain growth in this temperature range, evident in Figure 5-4. This can be attributed to increasing C contamination through this temperature range, which is shown in Figure 5-10. In this range, interplay between grain growth, which decreases

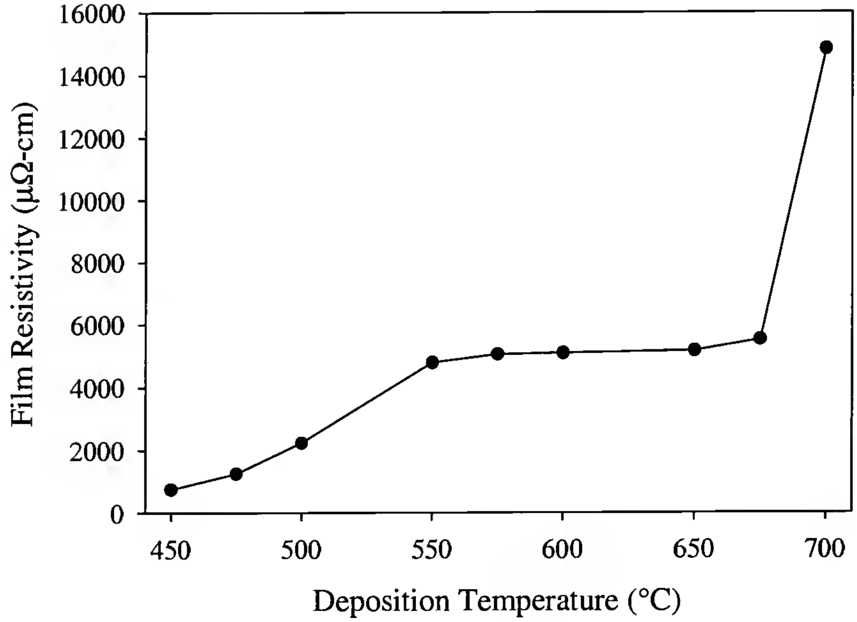

Figure 5-31 Variation of film resistivity with deposition temperature.

resistivity, and increasing free C content, which increases resistivity, led to the gradual increase in film resistivity. Between 675 and 700°C, film resistivity jumps to 15000 μΩ–cm, and is due to massive C concentration, which overtakes the W concentration near 700°C. In Figure 5-6, the grain size levels off between 675 and 700°C, which is the same temperature range where the film resistivity increases greatly. Figure 5-10 indicates that C content continues to rise in this temperature range. This may indicate that the additional free carbon is depositing in the grain boundaries, making it difficult for current to pass between the polycrystal grains. Decreasing the deposition temperature decreases the amount of C present in the film and therefore should decrease the film resistivity. This trend is additional incentive to move to lower deposition temperatures.

Film resistivities calculated with Equation 5–5 depend on both the sheet resistance and thickness of the analyzed films. As deposition temperature increases, both the film resistivity and the film thickness increase. To decouple the impact of film thickness from carbon contamination on the film's electrical properties, the sheet resistance was plotted as a function of deposition temperature in Figure 5-32. The sheet resistance increases with deposition temperature from 47 Ω/□ at 450°C to 184 Ω/□ at 500°C, decreases to 145 Ω/□ at 675°C, and increases sharply to 371 Ω/□ at 700°C. The increase in sheet resistance up to 550°C is attributed to polycrystal formation and increased C contamination. Between 550 and 675°C, the decrease in sheet resistance is due to grain growth, which overcomes any increase caused by additional C contamination. At 700°C, overwhelming C contamination dominates the sheet resistance, driving it up sharply.

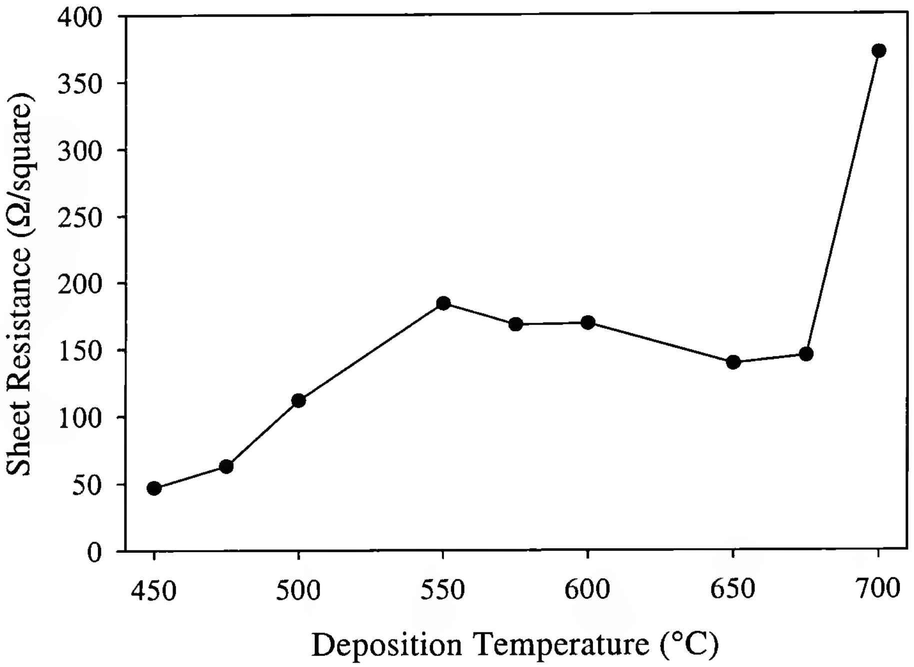

Figure 5-32 Variation of film sheet resistance with deposition temperature.

5.9 Effect of NH_3 and N_2 Addition to Film Growth

The effect of NH_3 addition to the reactor during deposition from **1b** was also examined. The total carrier gas flowrate to the reactor was fixed at 1000 sccm, with a H_2/NH_3 flowrate ratio of 999/1. The deposition temperature ranged from 450 to 700°C, and the pressure was again fixed at 350 Torr.

5.9.1 Film Structure

5.9.1.1 XRD Results

Figure 5-33a illustrates the effect of deposition temperature on crystallinity for films deposited from **1b**. The absence of WN_x peaks in the XRD spectra at 450°C suggests that films were X–ray amorphous. Crystallinity appeared in the films deposited above ~500°C, with the first peak emerging at 37.94 2θ degrees, consistent with polycrystalline β–WN_x (111) growth. This is in accord with a previous report that amorphous WN_x films transform into polycrystalline β–W_2N between 450 and 500°C [Gal97]. As the deposition temperature increases to 600°C, the (111) peak sharpens and shifts to a lower 2θ value, consistent with β–WN_xC_y formation, in which N and C intermix on the FCC W interstitial sublattice [Bch03c]. The (111) peak positions for the

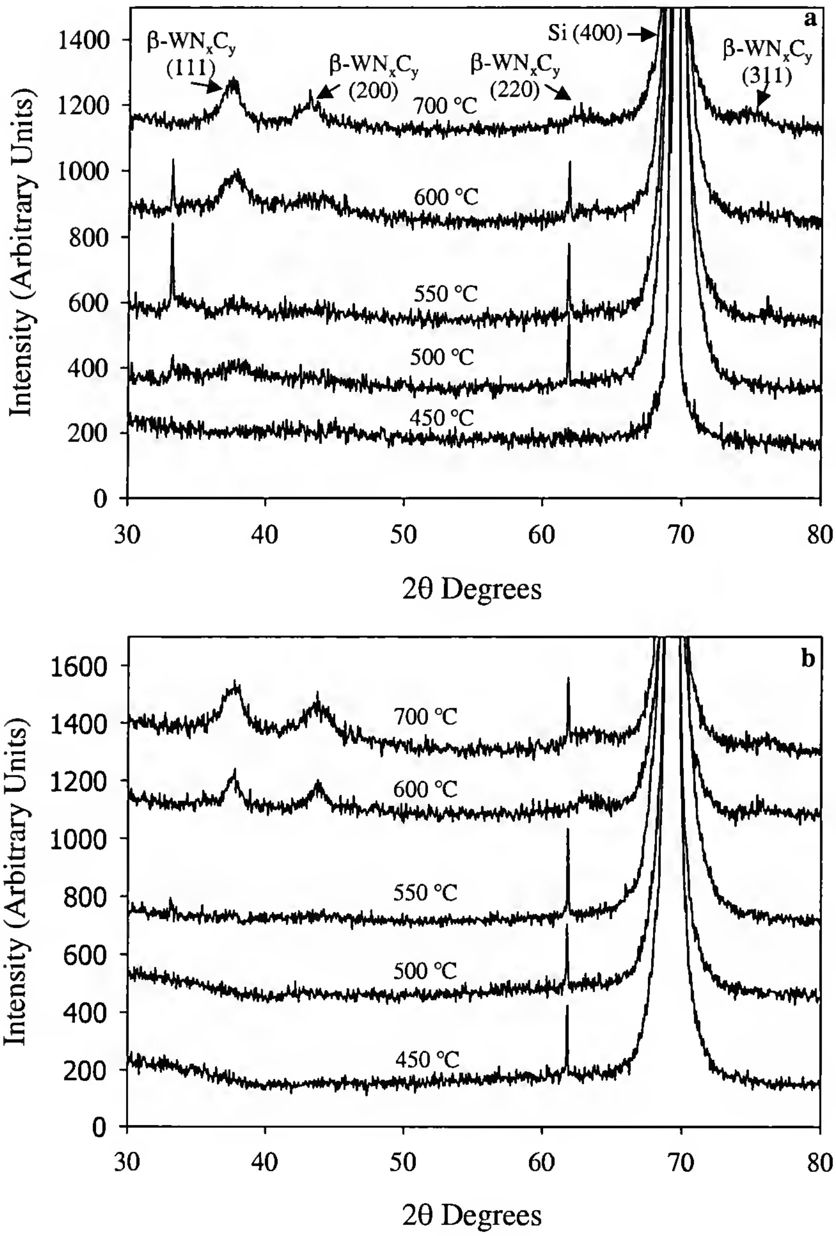

Figure 5-33 XRD spectra for films grown on Si (100) in a H_2 atmosphere. a) Without NH_3. b) With NH_3.

binary β–$WN_{0.5}$ and β–$WC_{0.6}$ phases are 37.74 and 36.98 2θ degrees, respectively, hence a peak location between them suggests a ternary β–WN_xC_y phase [JCP88]. Another broad peak at 44.42 2θ degrees also appears at this temperature, suggesting β–WN_xC_y (200) formation. Films deposited at 500 and 600°C displayed two additional peaks at 33.03 and 61.67 2θ degrees, representing Si (200) $K\alpha$ and Si (400) $K\beta$ radiation, respectively. Increasing the deposition temperature to 700°C results in further sharpening of the β–WN_xC_y (111) and (200) peaks; a shift to lower 2θ value for these peaks is consistent with decreasing x and increasing y in the β–WN_xC_y polycrystals. The emergence of two broad peaks at 63.00 and 75.82 2θ degrees at this temperature indicate β–WN_xC_y (220) and (311) formation. No XRD peaks consistent with graphite, metallic W or WO_3 polycrystals were present in the spectra.

Deposition with NH_3 at 450°C resulted in deposition of an X–ray amorphous film, as had been observed without NH_3. Material grown with NH_3 at 500°C was also amorphous, in contrast to polycrystalline films grown without NH_3 at 500°C. This phenomenon may be due to surface site blocking and insufficient surface diffusion of NH_3 at lower deposition temperature. Addition of NH_3 resulted in similar spectra for films grown at 600 and 700°C, but with sharpened peaks (Figure 5-33b) indicating enhanced grain growth relative to deposition without NH_3. In addition, the peaks at 63.00 and 75.82 2θ degrees appear for the 600°C deposition with NH_3, while they do not appear until 700°C for films deposited without NH_3. Carbon is reported to decrease grain size when added to refractory metal films [Wan01b]. Thus, the increase in polycrystal grain size is likely due to the decrease in C content (Figure 5-34c) accompanying NH_3 addition at these higher temperatures.

5.9.2 Film Composition

5.9.2.1 AES Results

Figure 5-34 depicts the impact of NH_3 addition on the concentration of W, N, C and O in the films. Addition of NH_3 dramatically increased the N levels over the entire deposition temperature range, as depicted in Figure 5-34b. The concomitant decrease in W is attributed to the increased concentration of N in the films. The addition of NH_3 increased the N content from 8 to 24 at. % for deposition at 450°C, and levels increased from 11 to 29 at. % at 500°C. As the deposition temperature increases to 600 and 700°C, N levels drop off. Metal nitride barriers typically show a decrease in N content with increasing deposition temperature, because higher temperatures impart more energy to the film lattice, inducing N to desorb as N_2 gas. Nitrogen loss from WN_x films has been reported at temperatures above 700°C [Kat85], consistent with AES results in this range. Similar experiments replacing NH_3 with N_2, an inert species at these temperatures, yielded poor film coverage and lower nitrogen levels than films deposited without a co–reactant.

Figure 5-34c depicts the change in C concentration with deposition temperature for films deposited with and without NH_3. Addition of NH_3 appears to have little impact on C content at the two lower deposition temperatures. This may reflect a change in the reaction kinetics of C removal processes between low and high temperature. Enhanced NH_3 decomposition at increased temperatures may improve production of gaseous carbon species (such as CH_4), which scavenge C from the film.

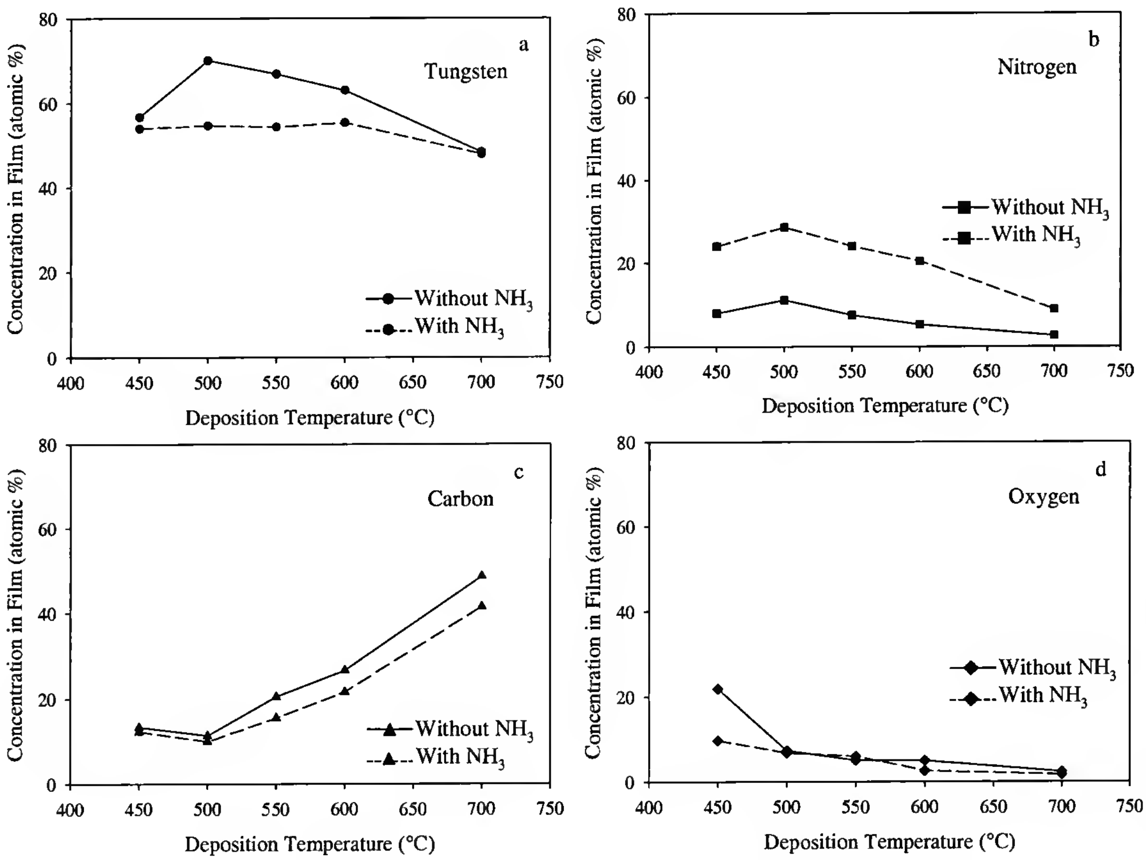

Figure 5-34 Variation of content in the films with deposition temperature. a) W b) N c) C and d) O. Data are estimated from AES spectra taken after 2 min sputter time.

Figure 5-34d depicts the change in O concentration with deposition temperature for films deposited with and without NH_3. Oxygen contamination results from post–growth exposure of the films to air, and high O levels at low deposition temperatures are likely due to film porosity [Bch03a]. Oxygen content drops substantially for deposition without NH_3 between 450 and 500°C. Film crystallization at higher deposition temperature causes an increase in film density, which inhibits diffusion of O into the films upon exposure to air. The ~12% drop in O concentration for films deposited with NH_3 at 450°C relative to those without might suggest that addition of NH_3 leads to a denser amorphous film structure, which allows less O in–diffusion. However, this possibility was ruled out by density measurements (per XRR) of 8.3 and 8.6 g/cm³, respectively, for films deposited at 450°C with and without NH_3. While these values are similar to those obtained for WN_x deposited with WF_6 and NH_3 at 450°C [Mar93], they indicate that film density actually decreases with NH_3 addition. Oxygen content was lower in these films, however, despite their lower density, suggesting that microstructure has greater impact than density on the film's resistance to post–growth oxygen incorporation. This is consistent with a previous report, which indicates that diffusion barrier performance depends more strongly on film microstructure than film density [Kim99c]. As the deposition temperature increases above 500°C, the O levels in both films decrease, becoming roughly equal near 2 at. % for deposition at 700°C. Similar O concentrations at 700°C reflect the impact of polycrystal size and C contamination on O diffusion. Films deposited without NH_3 have higher C content at 700°C, and this C is expected to stuff grain boundaries, preventing O diffusion into the film. Films deposited with NH_3 have lower C contamination, but larger polycrystals, which resist O migration.

Figure 5-35 shows an AES depth profile for a film deposited at 450°C with NH_3. The N level is elevated and the O level is reduced in this film compared to that deposited without NH_3 (Figure 5-12). The O level still rises at the barrier–Si interface, however, indicating that NH_3 addition does not eliminate the formation of a porous/defective layer at the interface. This layer may be thinner when NH_3 is added, however, which is evidenced by the narrower O bump at the interface. The C level is somewhat reduced throughout the film when NH_3 is added. As in the film deposited without NH_3, the W and O signals overlap with the Si signal for a similar amount of time.

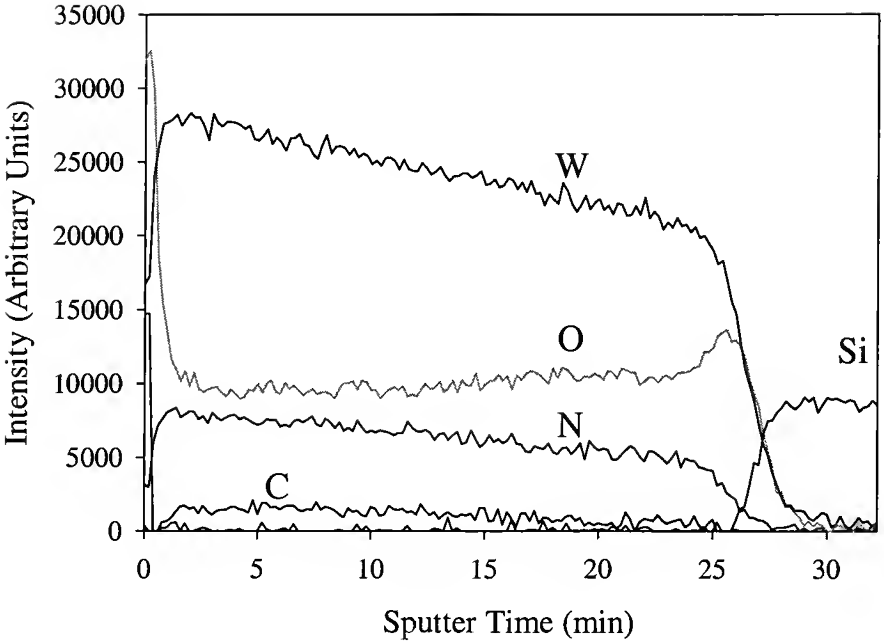

Figure 5-35 Three–point depth profile for film deposited with NH_3 at 450°C. Nominal AES sputter rate was 100 Å/min

5.9.2.2 XPS Results

The W4f, N1s, C1s and O1s photoelectron lines were also used to examine the bonding states in films deposited with NH_3. Again, literature BE values for potential compounds in the films are listed in Table 5-3 through Table 5-6. XPS results for films deposited at 4 different temperatures without NH_3 after 10 minutes sputter were discussed above. Figure 5-19, along with Table 5-9, summarize those results.

Figure 5-36 shows the effect of NH_3 addition on the W4f and N1s binding energies. The principal $W4f_{7/2}$ and $W4f_{5/2}$ peaks for 450°C are at 33.6 and 35.6 eV, respectively, corresponding to the upper limit for WN_x (Table 5-3). Again, this upward shift may be due in part to an attractive N–C interaction on the interstitial sublattice of W in the β–WN_xC_y bonding state. Although these BE values are stable over the entire temperature range, they are shifted to ~1 eV higher relative to films deposited without

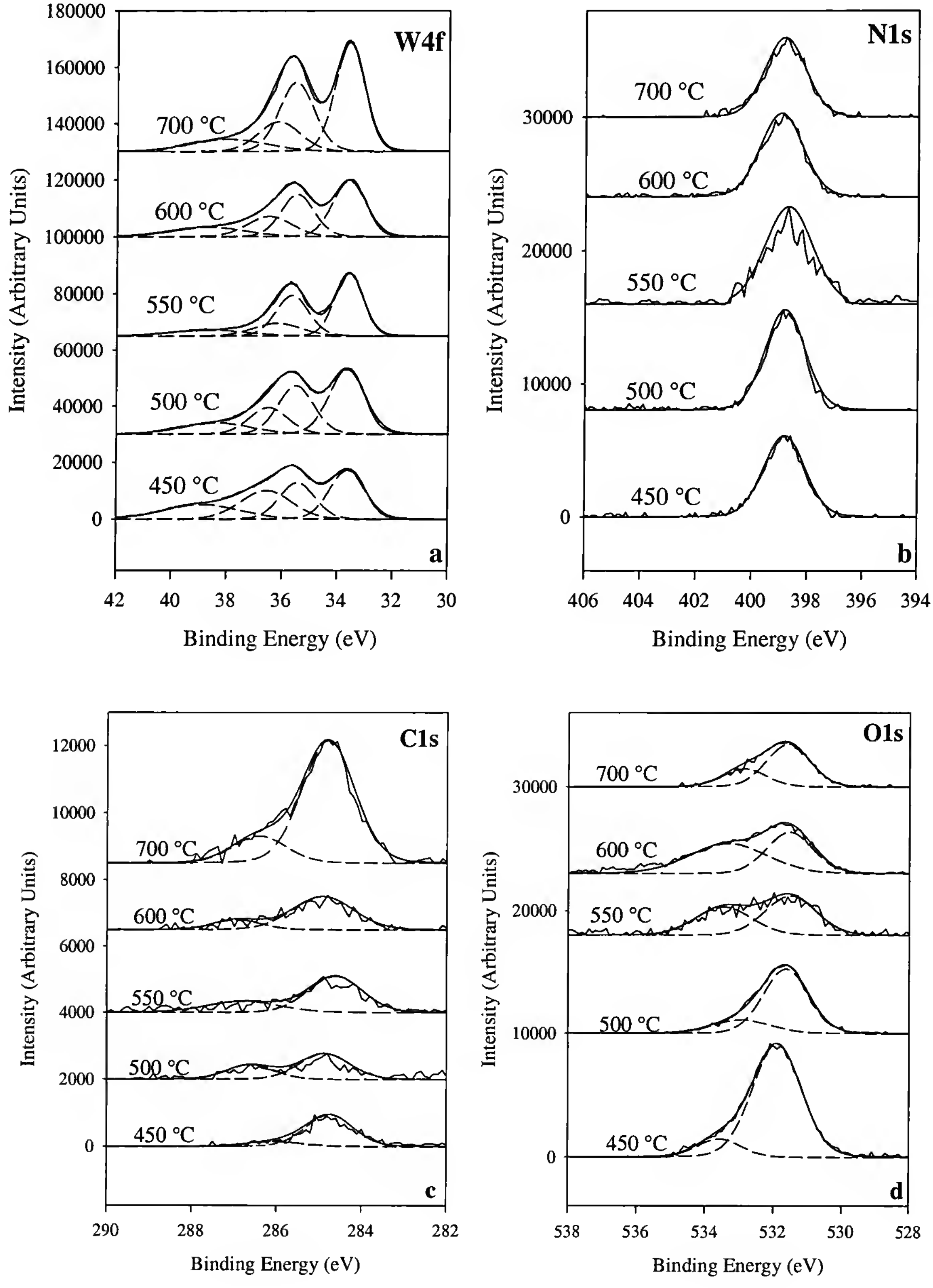

Figure 5-36 Variation of binding energies with deposition temperature for films deposited with **1b** + NH_3. a) W4f b) N1s c) C1s and d) O1s. Data are from XPS after 10 min sputter. Dashed lines are deconvoluted peaks.

NH_3. This shift is due in part to increased nitrogen content in the films, which suggests greater occupancy of N sites relative to films deposited without NH_3 (Figure 5-17a), and therefore more complete W–N bonding. Higher numbers of W–N bonds raise the partial positive charge at W and thereby increase the W4f BE. In addition, some sample charging may occur, which would also cause an increase in BE. Like the films deposited without NH_3, a W4f shoulder was observed for films deposited at lower temperatures, indicating the presence of WO_3.

The N1s BE values are steady over the entire temperature range, and are centered around 398.8 eV, above the reported range for WN_x values (Table 5-4). Again, the lack of a second N1s peak above 399 eV suggests that all N is bound to W, with none present in its "free" form. This increase in N1s BE is unusual, considering the increased W–N bonding that should occur for higher N content, and may be attributed to sample charging. Again, the upward shift in N1s BE may also be due in part to an attractive N–C interaction on the interstitial sublattice of W in the β–WN_xC_y bonding state. In addition to BE, we note that the N1s peaks endure through the entire temperature range for films deposited with NH_3. Although N content does drop for these films above 500°C, AES results in Figure 5-34b indicate a substantial increase in N for these films relative to those grown without NH_3. This is consistent with competition between increased rates of nitrogen release from the film into the gas phase and higher reactivity of NH_3 with the growing film at higher temperature. Again, while films deposited with NH_3 at 450°C are x–ray amorphous, they likely contain β–WN_xC_y in unit cell form, because the W4f BE values for β–WN_xC_y have minimal shift when going from an amorphous film (below 600°C) to a polycrystalline film (at and above 600°C).

Comparing Figure 5-36c to Figure 5-19c shows that the C1s peaks have lower intensity for films deposited with NH_3, consistent with the lower C content shown in Figure 5-34c. For the film deposited at 450°C, the C1s peak at higher BE is very small, suggesting that the interstitial sites are almost completely filled by N, leaving little room for C to intermix. In addition, the convoluted peak at 700°C is narrower than that from films without NH_3, with a small peak at lower BE and a small shoulder at higher BE. This suggests that NH_3 addition not only lowers the C content at higher temperature, but the additional N displaces C into the grain boundary region, leaving a smaller amount present in the $\beta\text{–}WN_xC_y$ bonding state (higher BE). The additional, displaced C at the boundaries of the $\beta\text{–}WN_xC_y$ unit cells (or nanocrystals) in the amorphous film deposited at 450°C could help to plug these regions, inhibiting O in–diffusion. Hence, although films deposited at 450°C with NH_3 have lower density, their microstructure may enhance resistance to O intrusion in the films.

Comparing O1s lines in Figure 5-36d and Figure 5-19d indicates that O levels are highest in the low temperature films, and decrease with increasing deposition temperature due to film crystallization (which increases density) and additional C incorporation (which stuffs grain boundaries). The O peaks for deposition without NH_3 were centered near 531.3 eV, consistent with WO_3 formation (Table 5-6). The peaks were broad, with small shoulders near 533 eV caused by WO_x [Zha99], which forms during Ar^+ ion sputtering of WO_3 in the XPS chamber. Similar behavior, with lower intensity, was evident for films deposited with NH_3, although the peaks are shifted to slightly higher BE (~531.6 and ~533.3 eV, respectively), which may be due to charging effects. For deposition at 450°C, the peak intensity is noticeably lower for deposition with NH_3 than without, and is attributed to free C, which is displaced from interstitial sites by additional N, stuffing pores in the film.

Table 5-10. Compounds in Films Grown with NH_3 After 10 Minutes Sputter

Deposition Temp. (°C)	$W4f_{7/2}$ (eV)	$W4f_{5/2}$ (eV)	N1s (eV)	O1s (eV)	C1s (eV)	Compound
450	33.6	35.4	398.8	–	286.0	β–WN_xC_y
450	36.6	38.9	–	531.9	–	WO_3
450	?	?	–	533.6	–	WO_x
450	–	–	–	–	284.8	Free C
500	33.6	35.5	398.8	–	286.6	β–WN_xC_y
500	36.5	38.4		531.6	–	WO_3
500	?	?	–	532.9	–	WO_x
500	–	–	–	–	284.8	Free C
550	33.6	35.7	398.7	–	286.8	β–WN_xC_y
550	36.2	38.7		531.5	–	WO_3
550	?	?	–	533.5	–	WO_x
550	–	–	–	–	284.6	Free C
600	33.5	35.4	398.8	–	286.9	β–WN_xC_y
600	36.4	38.6	–	531.6	–	WO_3
600	?	?	–	533.3	–	WO_x
600	–	–	–	–	284.9	Free C
700	33.6	35.5	398.9	–	286.4	β–WN_xC_y
700	36.2	38.0	–	531.6	–	WO_3
700	?	?	–	532.9	–	WO_x
700	–	–	–	–	284.8	Free C

The peak assignments are summarized in Table 5-10. Question marks in Table 5-10 indicate that exact location of the corresponding W4f peaks for the WO_x suboxide is unknown, due to lack of additional shoulders in the W4f spectra.

5.9.3 Growth Rate

Growth rates were estimated by dividing the total film thickness (as measured X–SEM) by deposition time. Figure 5-37 depicts two sample X–SEM photos. The surface of the films was smoother for those deposited with NH_3 than those without, with AFM indicating a root mean square (RMS) roughness of 3.8 and 7.1 nm for films deposited at 450°C with and without NH_3, respectively. Film thickness for depositions with NH_3 varied from 2600 Å for the deposition at 450°C up to 3400 Å for deposition at

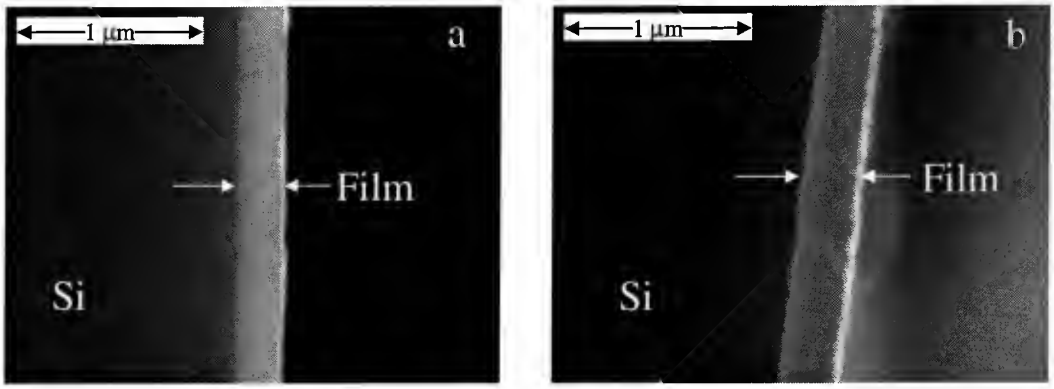

Figure 5-37 Cross–section XSEM photo of films deposited with NH_3. a) 450°C. b) 700°C.

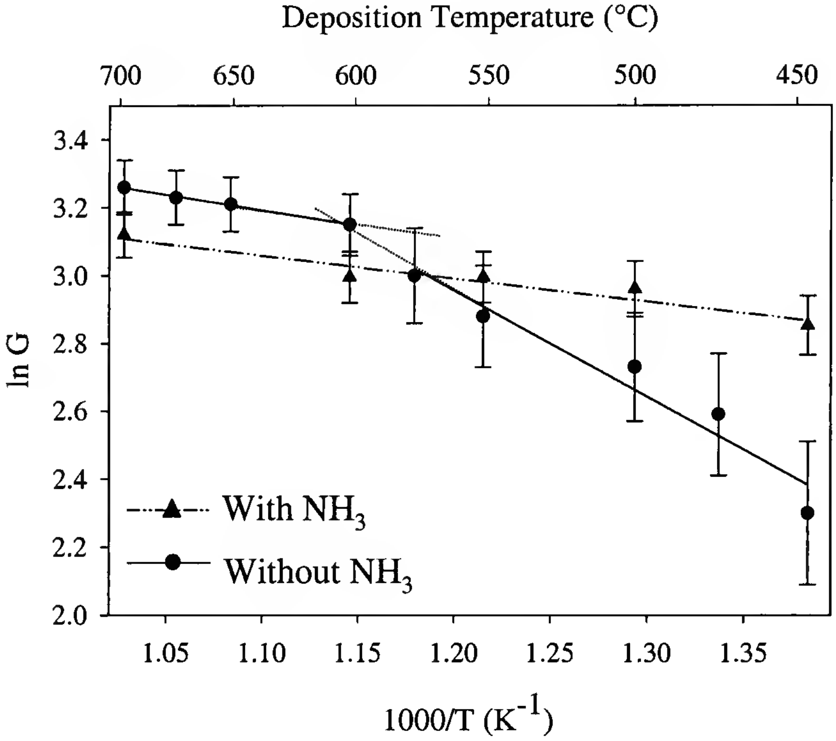

Figure 5-38 Dependence of film growth rate (G) on temperature for films deposited with and without NH_3. Error bars indicate uncertainty due to deposition temperature variation (+/– 10°C) and thickness measurement from X–SEM photos.

700°C. These film thicknesses correspond to deposition rates ranging from 17–23 Å/min, compared to rates of 10–27 Å/min for depositions without NH_3 [Bch03a]. The growth rate of the films (as determined by X–SEM) varied with temperature, as shown in Figure 5-38.

Interestingly, the deposition rate with NH_3 was enhanced at lower temperature and reduced at higher temperature relative to deposition without NH_3. In addition, deposition with NH_3 was mass–transfer controlled across the entire temperature range, while deposition without NH_3 had a kinetic to diffusion control transition point near 600°C. This indicates a shift in deposition mechanism with the addition of NH_3 as a co–reactant.

5.9.4 Film Resistivity

Film resistivity was again calculated using Equation 5–5 above. The variation of film resistivity with deposition temperature is shown in Figure 5-39, which indicates that resistivity with NH_3 goes through a maximum value of 55,000 $\mu\Omega$–cm at 500°C. The temperature dependence of resistivity for films deposited with NH_3 followed a trend consistent with N content, shown in Figure 5-34b. Additional N in the amorphous films would increase film resistivity in two ways. First, the added N would increase resistivity in the β–WN_xC_y nanocrystals, since the resistivity is higher for β–WN_x relative to β–WC_x. Second, additional N would displace C from the nanocrystals into the “free” state. Increased free C increases electron scattering, thereby raising film resistivity. As the deposition temperature increases from 500 to 600°C, the resistivity drops sharply, caused by a decrease in N content along with film crystallization in this temperature range. A resistivity decrease is expected with decreasing N content in WN_x films

[Lee93]. At the highest temperature, resistivity for films deposited with NH_3 dropped below that for films grown without NH_3. This is due to lower C content, larger polycrystal grain size (not shown), and decreased thickness for films grown with NH_3.

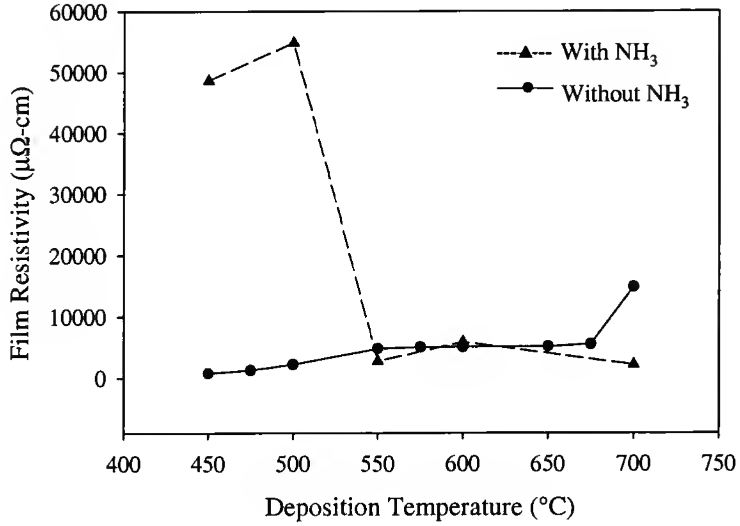

Figure 5-39 Film resistivity for samples grown with and without NH_3.

5.9.5 Sheet Resistance

To decouple the impact of film thickness from the electrical properties, the sheet

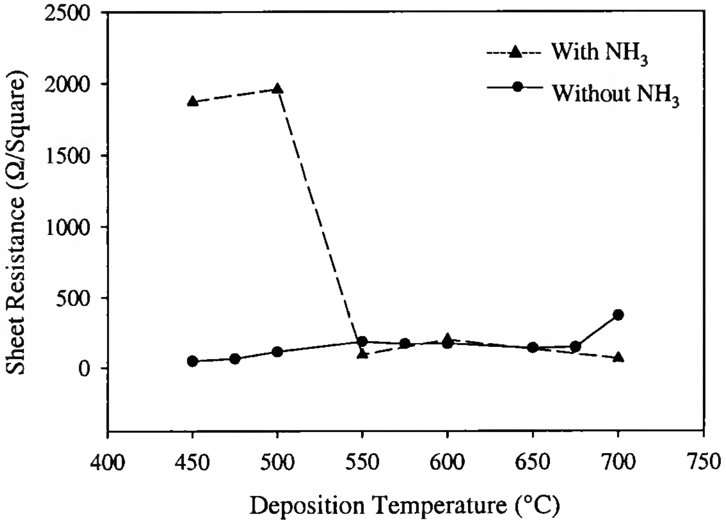

Figure 5-40 Sheet resistance for samples grown with and without NH_3.

resistance as a function of temperature is plotted in Figure 5-40. The trend is similar to that for film resistivity, for similar reasons. A difference in R_s at 700°C is evident, confirming that the electrical properties of the two types of films differ at this temperature. Again, the lower R_s value for the film deposited with NH_3 at 700°C is due to lower C content and larger polycrystal grain size.

5.10 Conclusions for Use of NH_3 and N_2 with i–Pr

Deposition of WN_x (or WN_xC_y) thin films from $Cl_4(CH_3CN)W(N^iPr)$ in the presence and absence of an NH_3 co–reactant was demonstrated. AES results indicated that films grown with NH_3 had significantly higher levels of N (especially for low deposition temperatures), along with decreased levels of C and O as compared to films grown without NH_3.

XRD and AES results suggest that increased crystallinity for films deposited at 600 and 700°C with NH_3 was due to decreased C content. XPS W4f binding energies suggested the presence of W in both the β–WN_xC_y and WO_3 environments, with O incorporation occurring post–growth. Moreover, due to the presence of O in the films, the possibility that some $W(N,O)_x$ exists in the films cannot be ruled out, as the N1s binding energies and XRD pattern for the oxynitride are very close to those for WN_x. While XPS indicates the presence of WO_3, XRD results do not show any WO_3 peaks. Hence, any WO_3 present in the film is likely in the form of nanocrystallites, which are not detectable by XRD. The overall film structure is amorphous at lower temperatures, and the polycrystalline films deposited at higher temperatures likely contain small WO_3 nanocrystallites embedded between larger WN_xC_y polycrystals. XPS also indicated a lack of grain boundary N in films regardless of NH_3 addition. Although some evidence of charging was apparent from the XPS results, quantification of charging through indexing of the adventitious C peak is difficult because the films contain C throughout their bulk. Adding NH_3 as a co–reactant changed the mechanism for film deposition, as is reflected by the mass transfer controlled nature of film growth over the entire temperature range. Film resistivity at lower temperature was significantly higher for films deposited with NH_3, and this was attributed to additional N in β–WN_xC_y and additional C at the grain boundary.

Addition of N_2 to **1b** during deposition prevented film deposition from occurring. This was likely due to N_2 site blocking on the substrate surface, as N_2 is inert over our experimental temperature range, and would not take part in the reaction.

5.11 Effect of Solvent Change on Carbon Content

Potential sources of the C contamination in the films grown from $Cl_4(CH_3CN)W(N^iPr)$ (**1a**) (Figure 5-1) are the alkyl moieties in the precursor itself and the benzonitrile (PhCN) solvent. Use of an alternative solvent in the volatilization process, then, could provide a means to differentiate these possibilities. If the C incorporation is dominated by decomposition of **1a**, the amount of C will be insensitive to the nature of the solvent. If the C derives from the solvent instead, the level of contamination will depend on the solvent. To address this question, films were deposited from solutions of **1a** in 1,2–dichlorobenzene (1,2–DCB) for comparison to films derived from **1b** in PhCN. 1,2–DCB was chosen because it has a similar vapor pressure to PhCN and is unable to engage in substitution chemistry with the acetonitrile ligand of precursor **1a**. During the depositions, the composition of the gas near the substrate surface was measured using an Inficon Transpector 2 residual gas analyzer (RGA). N_2 was used as the carrier gas for RGA analyses, and total pressure in the RGA was ~6.5×10^{-6} Torr.

Table 5-11. Potential solvent–derived species in the reactor and their decomposition products.

Molecule (source)	Decomposition Type	Major Decomposition Products	Reported Decomposition Temperature (°C)	Reference
PhCN (solvent)	Homogeneous	HCN, C_6H_6, C_4H_2, C_2H_2	550–1477°C	[Ete93, Lif96]
1,2–$C_6H_4Cl_2$ (solvent)	Homogeneous	C_6H_5Cl, HCl	750 – 1020°C	[Klu91, You89]
	Heterogeneous on Ni/CrO_3 with H_2	C_6H_5Cl, C_6H_6	127 – 327°C	[Ser01]
C_6H_5Cl (dec.[a])	Homogeneous	C_6H_6, HCl	560 – 1002°C	[Rit90]
	Heterogeneous on Ni/CrO_3 with H_2	C_6H_6	127 – 327°C	[Ser01]
C_6H_6 (dec.)	Homogeneous	C_2H_2, C_4H_2, C_2H_4, CH_4, H_2	>763°C	[Bro79, Sly61]
	Heterogeneous on W(100)	C_2H_2, C(ads)	27 – 177°C	[Bha80]
C_4H_2 (dec.)	Homogeneous	C_2H_4, C_2H_2, CH_4, H_2	700–1000°C	[Sly61, Hom86, Hou65]
CH_3CN (dec.)	Homogeneous	HCN, CH_4	880 – 960°C	[Asm69]
	Heterogeneous on W(100)	HCN, CH_4, H_2	177 – 727°C	[Pea86b]
C_2H_2, C_2H_4, CH_4 (dec.)	Heterogeneous on W wire	C(ads)	27–347°C	[Rye69]
C_2H_4 (dec.)	Heterogeneous on W (100), (110), (112), (111)	C_2H_6 (1.5 %), H_2+C(ads) (98.5%)	>–73°C	[Car74]
HCN (dec.)	Homogeneous	H, CN	2427–3327°C	[Sze84]
	Heterogeneous on W(100)	N_2, H_2, C(ads), N(ads), WC	27–1127°C	[Cai70, Pea86a]

[a] dec = derived from primary or secondary decomposition of one or both solvents.

In the deposition temperature range of this study (450 to 700°C), the solvent molecules likely undergo some degree of homogeneous decomposition before reaching the substrate surface, so homogeneous and heterogeneous C deposition processes must be considered. Species that are potentially present in the reactor (including previously reported primary and secondary solvent decomposition products) are listed in Table 5-11. Data on heterogeneous decomposition for PhCN and 1,2–DCB are not available.

Table 5-11 indicates that several primary and secondary gas–phase decomposition products from each solvent may be present in the reactor, along with the solvents themselves. Each of these species is potentially capable of depositing C. Furthermore, all of the decomposition products, with the exception of HCN and HCl, are common to both PhCN and 1,2–DCB. Low concentrations of HCN and HCl that derive from **1a**, however, are presumably present in the reactor regardless of the solvent. This is due to reaction of the CH_3CN ligand or the four chlorines, respectively, with the H_2 carrier gas. A study of C deposition dependence on solvent should therefore focus on the concentration of the various carbon–containing species near the substrate surface, as measured by RGA, to identify which species are the most likely sources of C deposition.

5.11.1 Film Structure

5.11.1.1 XRD Results

XRD spectra for films deposited with PhCN (Figure 5-4) and 1,2–DCB (Figure 5-41) indicate β–WN_xC_y polycrystal formation down to 500 and 525°C, respectively. Below 500°C, films grown with PhCN were amorphous, while those grown with 1,2–DCB at and below 500°C were consistent with tungsten oxide formation. Lower levels of N and C make these films less resistant to O in–diffusion, enabling oxide formation to occur. Above 500°C, films from 1,2–DCB solutions were polycrystalline and contained substantial C, which enabled them to resist O in–diffusion and prevented oxide formation.

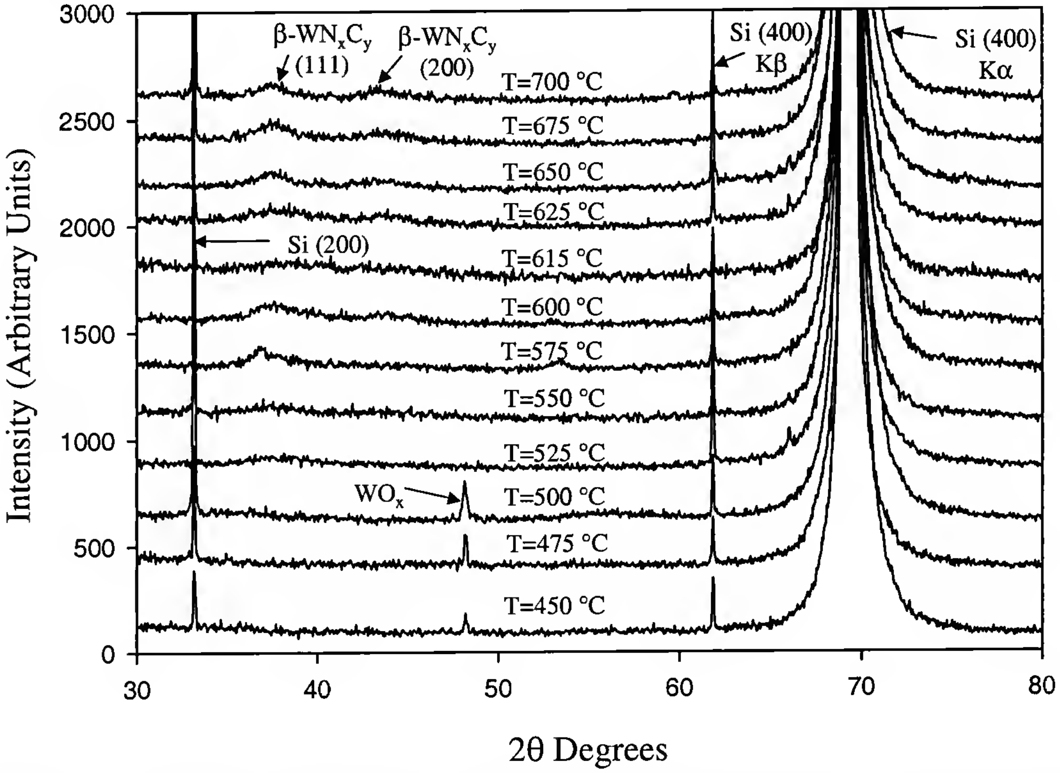

Figure 5-41 Change in XRD pattern with deposition temperature for films grown with **1a** + 1,2–DCB on Si (100) in a H_2 atmosphere.

5.11.1.2 Lattice Parameter and Grain Size

Lattice parameter and grain size were determined using the 2θ position and full width half maximum (FWHM) of the β–WN$_x$C$_y$ (111) diffraction peak, as described previously [Bch03c]. The values of the lattice parameter in films deposited at higher temperature (i.e., ≥ 650°C) were similar regardless of the solvent used, as shown in Figure 5-42a. A noticeable deviation occurred at 550 and 575°C, with films from 1,2–DCB solutions having a higher lattice parameter at these temperatures. Although films from 1,2–DCB solutions had lower N content than those from PhCN solutions at these temperatures, they had substantially higher C content. Decreasing x and increasing y in the β–WN$_x$C$_y$ polycrystals causes lattice expansion, since β–WN$_{0.5}$ and β–WC$_{0.6}$ have lattice parameters of 4.126 and 4.236 Å, respectively. Some of the additional carbon was incorporated into the polycrystals of films grown from solutions of 1,2–DCB, causing lattice expansion, while the remainder presumably deposited at the grain boundary. The drop in lattice parameter at 615°C, which accompanies a drop in C content (Figure 5-43), indicates decreased C incorporation into the β–WN_xC_y polycrystals at this temperature. The discontinuity in the C incorporation process suggests a change in the C deposition mechanism near this temperature.

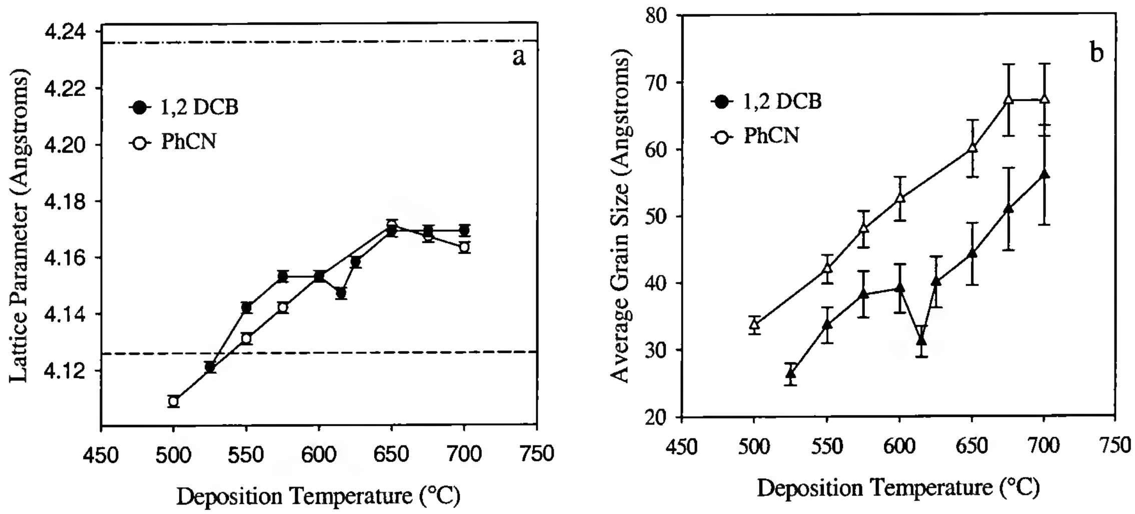

Figure 5-42 Dependence of (a) lattice parameter and (b) grain size on deposition temperature. Dashed line in (a) is lattice parameter for β–$WN_{0.5}$; dot–dash is for β–$WC_{0.6}$.

The grain size was estimated using the Scherrer equation [Cul78]. Figure 5-42b shows that grain size generally increases with temperature for films grown from both PhCN and 1,2–DCB solutions, with films from PhCN solutions having larger grain size relative to those grown from 1,2–DCB across the entire temperature range. This effect is due to enhanced C deposition in the films from 1,2–DCB solutions, as C is reported to decrease grain size when added to polycrystalline tungsten films [Wan01b]. The drop in grain size at 615°C indicates increased disorder in the film, which again is likely caused by a transition between C deposition processes.

5.11.2 Film Composition

5.11.2.1 AES Results

Elemental compositions of films deposited with PhCN and 1,2–DCB as determined by AES are shown in Figure 5-43. Since standard film samples for calibration of our elemental concentrations are unavailable, the error bars on the AES compositions are several atomic percent. Despite the uncertainty in the concentration values, the AES data serve to identify trends in film composition with deposition temperature. The change in C content with deposition temperature was significantly different for the two solvents. The C levels were independent of temperature below 500°C, with films from PhCN and 1,2–DCB solutions containing ~12 and ~5 at.% C, respectively. For films grown from both solvents, an increase in C content above 500°C coincided with the onset of film crystallization, which suggests that polycrystals and/or grain boundaries may promote C deposition. Above 500°C, the C content increased steadily for films from PhCN solutions. For films from 1,2–DCB solutions, C levels increased between 500 and 600°C, and then dropped, reaching a constant value near 50 at.% up to 700°C. The decreased C level above 600°C reflects a change in C deposition behavior, but the cause of the change is unclear. This effect may be due to a side reaction in the gas phase and/or on the reactor walls in this temperature range, or due to a competing reaction on the film surface.

Although trends in N content are evident, exact measurement of the N level by AES is problematic, due to preferential incorporation of C and removal of N by Ar^+ sputtering [Ing82]. The films from 1,2–DCB solutions had lower N content than those from PhCN, especially at lower temperature, with maximum levels of 4 and 11 at. %, respectively, at 500°C. This suggests that the CN group, produced by PhCN decomposition, is deposited on the film surface, leaving adsorbed C and some N. Direct decomposition could occur via η^1 bonding (through the N σ lone pair) of PhCN to the film surface [Mro01], with subsequent cleavage of the C–Ph bond. An alternative is a stepwise process that would entail homogeneous decomposition of PhCN to HCN, which then adsorbs onto the film surface. Since homogeneous decomposition of HCN requires temperatures well above our experimental range [Sze84], HCN decomposition in this system would be heterogeneous.

If the CN moiety contributes to N levels in films from PhCN solutions, decreased N levels would be expected for films from 1,2–DCB solutions, in which the solvent contains no N. An alternative explanation involves selective N etching by additional HCl produced by 1,2–DCB decomposition. The N level in the films from 1,2–DCB solutions is relatively constant (~2 at. %) at and above 650°C, however, which makes HCl etching (which should accelerate with temperature) unlikely. Moreover, HCl etching of WN_x has not been reported. Chemical etchants for tungsten nitride typically involve the use of H_2O_2 [Iva99] and are not selective for N. The N content for films grown from both PhCN and 1,2–DCB solutions is similar at the highest deposition temperature. While low temperature deposition may enable N addition to the films from PhCN solutions, increasing deposition temperature enhances desorption of this N as N_2. At the highest temperature, most of this N in the films grown from PhCN solutions has desorbed, leading to similar N levels as the films deposited from 1,2–DCB solutions, whose N is derived entirely from the precursor.

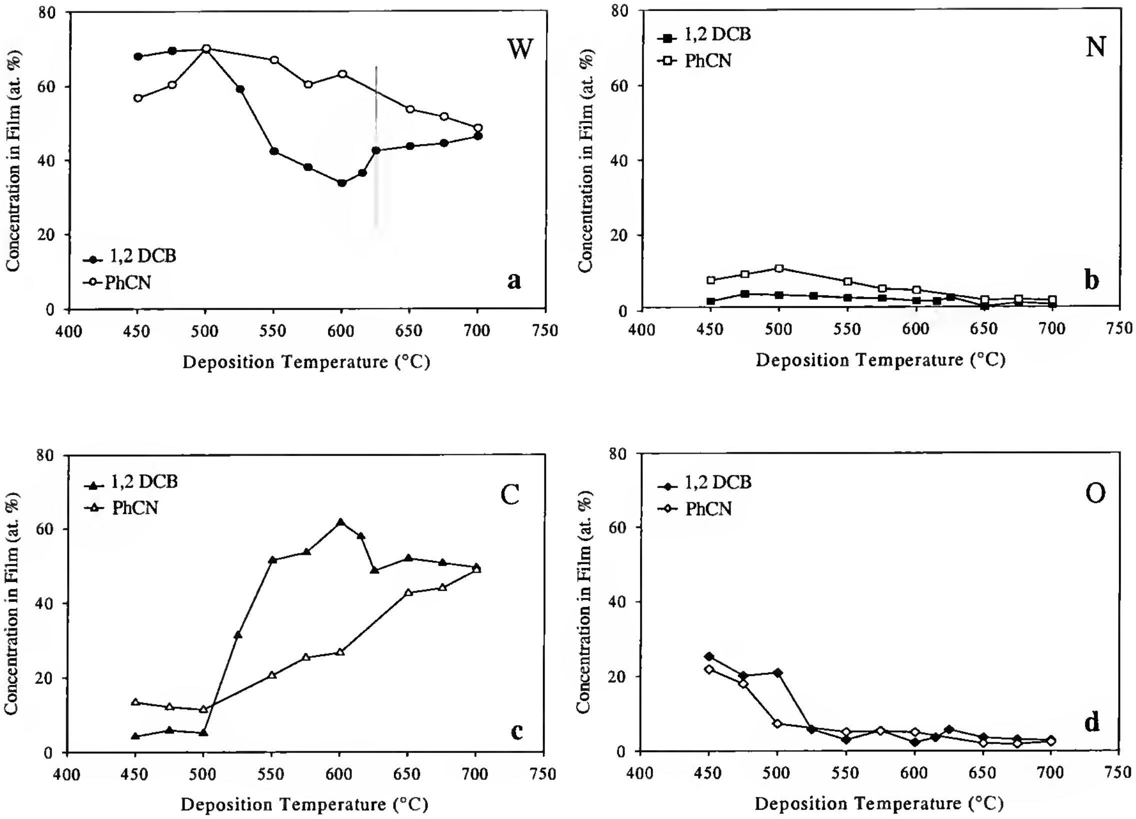

Figure 5-43 Variation of film content with deposition temperature and solvent. a) W b) N c) C d) O. Data are from AES after 2.0 minutes sputter.

Oxygen in the films originated from post–growth exposure to air. Substantial levels of C and N, which help the film's polycrystals to resist post–growth O in–diffusion, were deposited with PhCN solutions, even at the lowest temperature. Films from 1,2–DCB solutions deposited at lower temperature contained lower C and N levels, leaving a significant amount of bare W, which is susceptible to oxidation. The O level in the films from 1,2–DCB solutions was significantly lower above 500°C, due to film crystallization and increased C levels, which make the film denser and enable it to resist O in–diffusion.

Chlorine was not detected in the films by AES for either solvent, placing an upper limit of ~1 at. % on the Cl content. Although use of 1,2–DCB increases the amount of Cl in the reactor, the decomposition of chlorinated aromatics reportedly accelerates in a H_2 atmosphere relative to an inert one [Ser01], producing gaseous HCl as the principal chlorine–containing product. This likely occurs in the reactor under deposition conditions, causing minimal Cl incorporation into the films.

5.11.2.2 XPS Results

XPS analysis indicated that polycrystalline films deposited from PhCN solutions

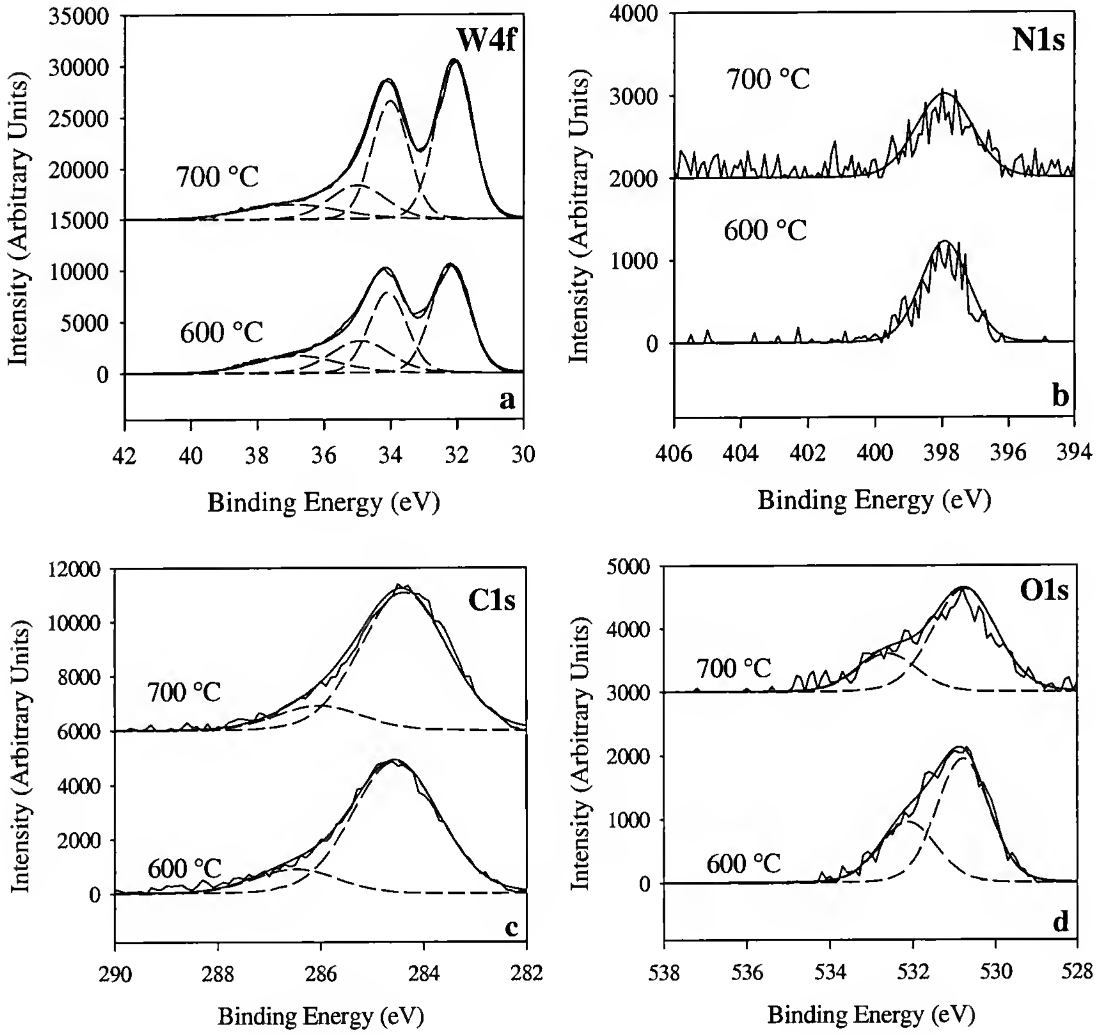

Figure 5-44 XPS spectra for films deposited at 600 and 700°C with 1,2–DCB after 10 min sputter. a) W4f b) N1s c) C1s and d) O1s BE lines. Dashed lines are deconvoluted peaks.

contained W in the nitride/carbonitride (β–WN_xC_y) bonding state, as well as a small amount of oxide (WO_3) [Bch03b]. Carbon was present at interstitial lattice sites in the β–WN_xC_y polycrystals and also in amorphous form at the polycrystal (or nanocrystal) boundaries, while N preferentially occupied interstitial sites in the β–WN_xC_y poly–(or nanocrystals). Oxygen was present in the WO_3 bonding state. Films from 1,2–DCB solutions had similar XPS results, as shown in Figure 5-44. The results are summarized in Table 5-12. Question marks in Table 5-12 indicate that exact location of the corresponding W4f peaks for the WO_x suboxide is unknown, due to lack of additional shoulders in the W4f spectra.

Table 5-12. Compounds in Films Grown with i–Pr in 1,2–DCB After 10 Minutes Sputter

Deposition Temp. (°C)	$W4f_{7/2}$ (eV)	$W4f_{5/2}$ (eV)	N1s (eV)	O1s (eV)	C1s (eV)	Compound
600	32.2	34.1	397.9	–	286.5	β–WN_xC_y
600	34.9	36.8	–	530.8	–	WO_3
600	?	?	–	532.1	–	WO_x
600	–	–	–	–	284.6	Free C
700	32.1	34.0	397.9	–	286.0	β–WN_xC_y
700	35.0	37.0	–	530.8	–	WO_3
700	?	?	–	532.6	–	WO_x
700	–	–	–	–	284.4	Free C

5.11.3 Carbon Deposition Rate

To determine the C deposition rate, the number of atoms deposited in each film was first estimated using an atom balance approach, with W, N, C and O atoms situated in the film based on XPS results. The analysis was restricted to polycrystalline films, which contain both polycrystals and grain boundary regions, because they have relatively low porosity and steady oxygen levels. Using a basis of 100 atoms, for example, the number of W atoms can be calculated from the AES fraction. From XPS data, the location of W would be either in β–WN_xC_y polycrystals or in WO_3. The number of W atoms bonded in WO_3, assumed to be 1/3 the number of oxygen atoms, was subtracted to give the number of W atoms in the β–WN_xC_y polycrystals. The $(W)_1(N,C,Va)_1$ two–sublattice model [Hua97, Sau98], with N, C and vacancies (Va) intermixing on the interstitial FCC W sublattice, was coupled with Vegard's law [Kos93] and lattice parameter data [Bch03c] to approximate the C content and density of the polycrystals. The grain boundaries were assumed to contain any remaining C in amorphous form [Bch03b], with an assumed density of 3 g/cm³ [Koh95], along with a small amount of amorphous WO_3, with an assumed density of 6.4 g/cm³ [Sch87]. The volume of the 100 atom basis set was calculated by summing the volume contributions from the β–WN_xC_y polycrystals, the amorphous WO_3 and the amorphous carbon. The density of W atoms in this basis set, $\rho_{W,basis}$ (W atoms/cm³), was calculated by dividing the number of W atoms in the 100 atom basis by the volume of the basis set. The total number of W atoms (W_T) deposited was then estimated with Equation 5–6:

$$W_T = (a * t) * (1 - VF) * \rho_{W,basis} \qquad (5\text{–}6)$$

where a is the area of the film (cm²) and t is film thickness (cm). The area of the film was assumed to be 2 cm², which is the typical total cross sectional substrate area input to the reactor, and t was determined by XSEM. A film void fraction (VF) of 0.10, per a previous report, was included to account for any defects/pores in the film structure [She00c].

The total number of carbon atoms (C_T) in each film was estimated with Equation 5–7 below:

$$C_T = \left(\frac{W_T}{\%W}\right) * \%C \qquad (5\text{–}7)$$

where % W and % C are the atomic % of W and C, respectively, as determined by AES. The area–averaged nature of AES ensures that W and C contents are measured regardless of location in the film's microstructure. Dividing C_T by deposition time gives the C deposition rate, which can be estimated by an Arrhenius expression in the kinetically controlled regime (Equation 5–8):

$$D = Ae^{-E_a/RT} \qquad (5\text{–}8)$$

where D is C deposition rate (atoms/min), E_a is the apparent activation energy (eV) for C deposition, and A is a constant. Figure 5-45 shows a plot of ln D vs. 1/T for films deposited with PhCN and 1,2–DCB. A line with a steep slope indicates a kinetically controlled regime (slope = $-E_a/R$), whereas a line with small slope indicates mass transfer control. If the rate of carbon deposition shows an exponential dependence, the process is kinetically controlled. If the rate does not show this dependence, the carbon deposition process is assumed to be mass–transfer controlled.

Error bars on Figure 5-45 address several sources of uncertainty in the calculation of carbon deposition rate. Uncertainty in film thickness was due to error in thickness measurement from X–SEM photos (± 0.02 μm), roughness on the film surface (± 0.01 μm), as determined by AFM, and fluctuations in film growth rate due to experimental temperature variation (± 10°C). Uncertainty in film density was due to lattice parameter shifts from X–ray line broadening (± 0.002 Å). Uncertainty in C deposition rate was due to uncertainty in the number of W and C atoms from AES (± 5 at. % each).

Figure 5-45 indicates C deposition rate to be kinetically controlled over the entire temperature range for PhCN, suggesting that a single process dominates C deposition at the surface of these films. The apparent activation energy for C deposition from PhCN was 0.70 ± 0.10 eV.

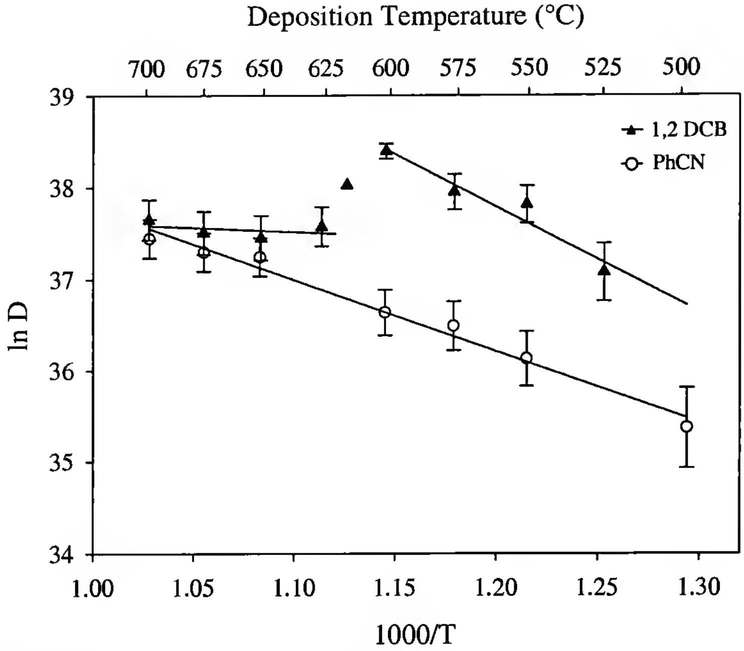

Figure 5-45 Dependence of carbon deposition rate on growth temperature for polycrystalline films grown with PhCN and 1,2–DCB solvent.

Figure 5-45 indicates kinetically controlled C deposition at and below 600°C for films from 1,2–DCB solutions, with an apparent activation energy for C deposition of 1.0 ± 0.14 eV. The drop in C level for films from 1,2–DCB solutions above 600°C was accompanied by a drop in film thickness, as measured by XSEM. The region between 600 and 625°C appears to be a transition zone between different C deposition processes, but the mechanisms for these processes are unclear. The film growth rate from 1,2–DCB solutions at and below 600°C was exponentially dependent on temperature, reaching a maximum of 43 Å/min at 600°C. The growth rate dropped to 22 Å/min at 650°C. This behavior contrasts with that for films deposited from PhCN solutions, whose thickness increased steadily from low to high temperature.

Above 625°C, film growth and C deposition rates for films from 1,2–DCB solutions appear to be mass transfer controlled, with both increasing slightly up to 700°C. Kinetically controlled C deposition for films from 1,2–DCB solutions has a higher apparent activation energy than the value obtained for films deposited from PhCN solutions. This difference is consistent with a change in the C deposition process between the two solvents, which is expected, assuming that the nitrile carbon group (which is present in PhCN but absent in 1,2–DCB) controls C deposition in films from solutions of the former.

Residual gas analysis indicated the presence of PhCN and 1,2–DCB molecular ions, as well as various fragments associated with solvent decomposition. While a full analysis of the fragmentation pathways is beyond the scope of this dissertation, Figure 5-46 shows partial pressures for several products whose *m/z* ratios correspond to known solvent decomposition products. The measured partial pressures of the various fragments were adjusted to compensate for contributions from electron impact (EI) fragmentation in the RGA [NIS03]. The RGA data are included to show which species were present in the gas phase for depositions with the two solvents. The species concentrations are generally insensitive to temperature, however, which reflects the large excess of gas phase carbon–containing species relative to the amount of any particular specie(s) removed from the gas by deposition on the substrate.

For deposition with PhCN, partial pressure readings at $m/z = 2, 26, 27, 36$ and 76 are consistent with formation of H_2, C_2H_2, HCN, HCl and C_6H_4, respectively [Las96, NIS03]. Significant quantities of HCN ($m/z = 27$), the principal carbon–containing fragment, along with C_6H_4 ($m/z = 76$), are consistent with PhCN decomposition in the reactor. The other carbon–containing product, C_2H_2 (m/z = 26), is also a potential C source. The formation of C_6H_4 and H_2 by benzene (C_6H_6) adsorption on Ir(100) [Joh01] and Mo(110) [Liu88] has been reported, and may explain why C_6H_6 was not observed with the RGA.

For deposition with 1,2–DCB, peaks are again observed at m/z 2, 26 and 36 along with readings at m/z = 50 and 75, which are consistent with formation of C_4H_2 and C_6H_3, respectively [NIS03, Sch01]. Figure 5-46 also indicates high partial pressures of H_2, which are produced by solvent and ligand decomposition. 1,2–DCB solutions also give rise to a partial pressure of C_6H_3, the principal carbon–containing fragment, which is almost an order of magnitude higher than its PhCN counterpart, C_6H_4. Another carbon–containing fragment, C_4H_2, also has relatively high partial pressure. These fragments are likely contributors to C deposition from 1,2–DCB. Similar levels of C_2H_2 are present for 1,2–DCB and PhCN solutions.

Surprisingly, the HCl level with 1,2–DCB was just slightly higher than for films from PhCN solutions; however, this may not be the case for depositions utilizing H_2 as the carrier gas, which should facilitate HCl formation. The H_2 level initially decreases with increasing temperature, reaching a minimum at 600°C, and then increases above this temperature. The increase in H_2 above 600°C suggests a change in reaction mechanism at higher temperature. Results for RGA runs with neat PhCN and 1,2–DCB were similar to those containing precursor **1**, except that in both cases, the concentration of the principal decomposition product (HCN and C_6H_3, respectively) was higher than the molecular solvent ion. This suggests that the primary decomposition products may interact with the growing films and deposit C, causing their concentration to drop relative to that for neat solvent.

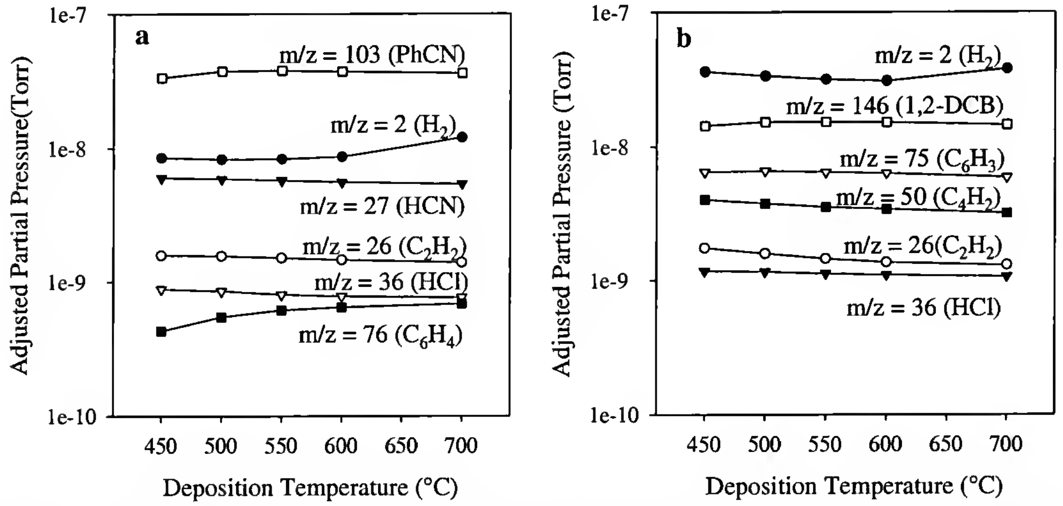

Figure 5-46 Dependence of adjusted partial pressure on temperature for selected gas phase species. a) Deposition with PhCN. b) Deposition with 1,2–DCB.

5.11.4 Conclusions On Effect of Solvent Change

Carbon and nitrogen levels in the deposited films were highly dependent on the nature of the solvent used. The activation energy for C deposition in WN_x films grown from **1a** in PhCN solutions was 0.70 ± 0.10 eV, while that for 1,2–DCB solutions was 1.0 ± 0.14 eV. This shift in activation energy for C deposition upon changing the solvent is evidence for an alteration in the C deposition process. Higher N content for films deposited with **1a** in PhCN solution relative to those from 1,2–DCB solutions suggests that CN moieties derived from the solvent decompose on the film surface, leaving adsorbed C and N. RGA results indicated substantial levels of HCN, along with some C_6H_4, consistent with decomposition of the PhCN solvent in the reactor. The C deposition source for films from 1,2–DCB solutions is unclear, although deposition behavior suggests a kinetically controlled surface process at and below 600°C. Films deposited from 1,2–DCB solutions above 600°C had decreased growth rate and C levels, which may be due to a change in C deposition process at the higher temperatures.

5.12 Conformality Tests

Figure 5-47 indicates that for deposition with **1b** at 450°C on Si (100) with 2 µm diameter features and AR= 2.75, sidewall and bottom conformality were 90 and 50%, respectively. Deposition at 500°C resulted in sidewall and bottom conformalities of 45 and 25%, respectively. As expected, film conformality improves at lower deposition temperature, for reasons discussed in Chapter 1. The conformality values at 450°C, while better than those at 500°C, are inadequate for industrial applications, however, especially considering that the tested feature diameter (2 µm) was much larger than the current feature diameter used in IC production (0.1 µm). In addition, film roughness in and around the feature is larger than that for deposition on flat Si (100) substrates. The reason for this is unclear.

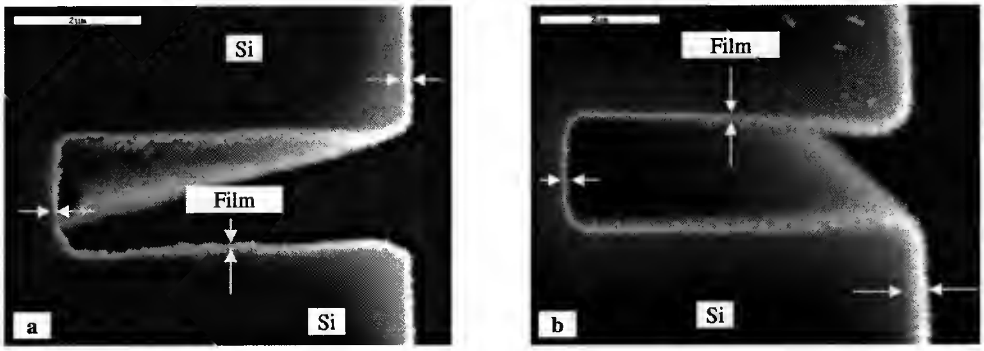

Figure 5-47 Conformality for films deposited with i–Pr on patterned Si (100) substrates. a) 450°C. b) 500°C.

5.13 Adhesion Tests

Adhesion to Si (100) substrates for films deposited with and without NH_3 was tested using the Scotch tape method. In this method, a small grid is scribed onto the film surface, and Scotch tape is then pressed directly onto the film. The tape is then pulled off of the film, and is inspected to determine if the film delaminated and stuck to the tape. Although this method does not give quantitative data on the strength of a film's adhesion to the underlying substrate, it is a quick way to determine if the films are prone to easy delamination. All of the films tested in this manner, which were deposited with and without NH_3, passed this test, as summarized in Table 5-13 below. This indicates that all of the films had good adhesion to the underlying substrate, with the film–substrate adhesion strength being higher than the film–Scotch tape adhesion strength.

Table 5-13. Scotch tape test results for films deposited with and without NH_3 on Si (100) substrates

Deposition Chemistry	Deposition Temperature (°C)	Scotch Tape Test Results
1b + PhCN + H_2	450	Passed
	500	Passed
	550	Passed
	600	Passed
	700	Passed
1b + PhCN + H_2 + NH_3	450	Passed
	500	Passed
	550	Passed
	600	Passed
	700	Passed

5.14 Conclusions on Use of $Cl_4(CH_3CN)WN$–*i*–Pr to Deposit WN_x

Repeatable deposition of films using the i–Pr precursor with and without NH_3 was achieved. Use of 1,2–DCB in place of PhCN solvent resulted in significantly different C incorporation behavior. The PhCN solvent appears to contribute both C and N to the films, which typically contain FCC β–WN_xC_y and amorphous C, with some amount of WO_3 depending on deposition temperature. All of the films had good adhesion to the Si (100) substrates, which is vital to ensure good device lifetime.

The minimum film deposition temperature with **1b** was 450°C, which is higher than the current temperature ceiling for IC production (< 400°C). Films deposited with the i–Pr precursor at the lowest achievable temperature were very porous, enabling them to absorb significant amounts of O from the air. While addition of NH_3 at low temperature decreased the O content, these films were also too porous, and had very high resistivity. Chlorine present in the films (per SIMS) is also a concern, as it can corrode subsequent metallization layers and etch Si substrates. In addition, a ~60 Å thick interface layer containing a mixture of WSi_2, WO_3, SiO_2 and SiO was present between the film and the Si substrate. This layer alone is almost as thick as the current required barrier thickness (100 Å), and its presence makes the deposition of ultra–thin (100 Å), high quality WN_x films by MOCVD using **1b** in our reactor unlikely. The overall film thickness was ~1500 Å, which is much larger than the currently required barrier thickness. While decreasing deposition time would decrease the film thickness, it would not result in a barrier film with appropriate properties, because the properties of the bulk film and the interface layer are not the same. Moreover, a significant incubation time on the Si substrates would make it difficult to rapidly deposit a barrier film with appropriate thickness in a reasonable amount of time.

Lastly, conformality of films deposited at 450°C on large diameter features was mediocre, suggesting that deposition on state–of–the–art feature sizes would be poor. While we do have state–of–the–art substrates with 100 nm features (provided by Intel), the recommended temperature ceiling for these substrates is ~400°C due to the presence of a low–k dielectric material on the substrate surface. A minimum deposition temperature of 450°C was required for deposition with the i–Pr precursor, hence the use of these substrates will be deferred to future ALD studies.

ALD using this precursor may be a promising way to deposit denser films at low temperature. The increase in N content due to NH_3 addition during CVD suggests that a stepwise i–Pr/NH_3 pulse scheme may enable ALD deposition. ALD should improve smoothness and conformality of the films, and enable ultra–thin film deposition. The Cl content of the precursor would still be an issue during ALD, however. Modification of this precursor to eliminate Cl, as well as boosting its N content, would be preferable. Finally, further investigation of solvent schemes should be carried out, to determine if another solvent with higher thermal stability than PhCN could be used to limit the solvent's participation in the deposition process.

CHAPTER 6

EVALUATION OF $Cl_4(PhCN)W(NPh)$ AS A SUITABLE WN_x PRECURSOR

MOCVD of thin WN_xC_y films from benzonitrile solutions of the single–source imido precursor $Cl_4(CH_3CN)W(N^iPr)$ (**1a**) as a mixture with its benzonitrile derivative **1b** was discussed in Chapter 5. The simple synthesis of **1a,b** was adapted to produce a series of related complexes containing different alkyl or aryl substituents on the imido ligand. This feature allowed variation of the N–C bond dissociation energy, which is important since this bond must be cleaved during the CVD process. The N–C (imido N to 2° alkyl) bond of **1a,b** will be relatively weak, compared to the N–aryl bond of the phenylimido complex $Cl_4(PhCN)W(NPh)$ (**2b**). These precursors are shown schematically in Figure 6-1. WN_x (and WN_xC_y) films were deposited from **2b**, and a comparison of material deposited from **1a,b** and **2b** was performed to determine if the imido N–C bond strength has an effect on the MOCVD process.

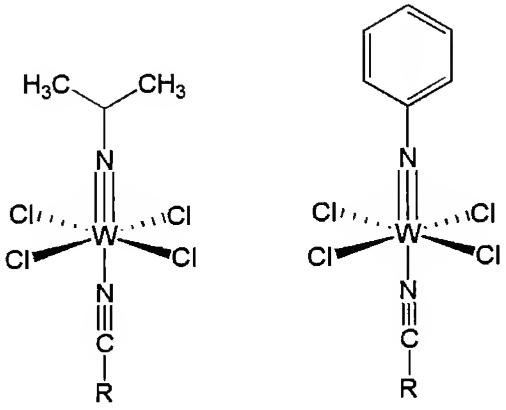
1a R = CH_3
1b R = Ph

2a R = CH_3
2b R = Ph

Figure 6-1. Structures of the $Cl_4(RCN)W(N^iPr)$ and $Cl_4(RCN)W(NPh)$ precursors.

6.1 Film Growth Studies

Experiments were conducted in the CVD reactor system described in Chapter 4. P–type boron doped Si (100) substrates with resistivity of 1–2 Ω–cm were used for the film growths. Growths were conducted for a fixed time of 150 minutes at temperatures ranging from 450–800°C. The system was maintained at vacuum by a mechanical roughing pump, with the operating pressure fixed at 350 Torr. Hydrogen (H_2) carrier gas was used for the depositions.

6.2 Synthesis of $Cl_4(PhCN)WNPh$

The complex $Cl_4(OEt_2)W(NPh)$ (**3**) was synthesized as previously described by Schrock *et al.* [Ped82]. The benzonitrile complex $Cl_4(PhCN)W(NPh)$ (**2b**) was not isolated, but was produced *in situ* by the substitution of the ether ligand of **3** with benzonitrile following solvation in the 10:1 $PhCN/Et_2O$ co–solvent utilized for the deposition experiments. The acetonitrile complex $Cl_4(CH_3CN)W(NPh)$ (**2a**) was prepared as previously reported [Nie83].

6.3 Solvent Selection

Deposition of thin films by MOCVD requires transport of the solid phenylimido precursor **2b** to the reactor in the vapor phase. Previous tests with similar complexes in a solid source delivery system resulted in minimal precursor transport, due to the low vapor pressure of the compounds. Transport difficulties were overcome by using a nebulizer to generate an aerosol of the precursor/solvent mixture, which is conveyed by carrier gas to the reactor. Although benzonitrile is an appropriate solvent for deposition from isopropylimido complexes **1a,b**, poor solubility of the phenylimido complexes in benzonitrile necessitated a co–solvent mixture of 10:1 benzonitrile:ether to achieve the same precursor concentration (7.5 mg/mL) previously used with **1a,b**. To determine the impact, if any, of the co–solvent on film composition, acetonitrile was tested in place of ether. AES results indicated similar film compositions regardless of the co–solvent used.

6.4 Precursor Mass Spectral Pre–Screen

All mass spectral analyses were again performed using a Finnigan MAT95Q hybrid sector mass spectrometer (Thermo Finnigan, San Jose, CA). Electron ionization (EI) was carried out in positive ion mode using electrons of 70 eV potential and a source temperature of 200°C. Negative ion electron capture chemical ionization (NCI) used methane as the bath gas at an indicate pressure of 2×10^{-5} Torr, an electron energy of 100 volts and a source temperature of 120°C. All samples were introduced via a controlled temperature probe with heating and cooling enabling temperature control down to 35°C. The mass resolving power ($m/\Delta m$) was 5000 full width–half maximum (FWHM).

As noted before, care must be taken in using mass spectral data to predict CVD behavior since the latter is thermal in nature [Lew94]. Nevertheless, mass spectrometry does provide insights into the relative fragmentation characteristics of various precursors [Int89]. In order to provide a direct comparison of mass spectral data for a phenylimido complex and its isopropyl analogue, the acetonitrile adduct $Cl_4(CH_3CN)W(NPh)$ (**2a**) was prepared as a model for **2b**. Precedent for the modeling of **2a** by **2b** is provided by the virtually identical ion fragmentation patterns for the isopropyl imido complexes **1a** and **1b** [Bch03a]. Mass spectrometry results for **2a** could then be compared to our previously reported data for the isopropyl imido complex $Cl_4(CH_3CN)W(N^iPr)$ (**1a**) [Bch03a]. Accordingly, **2a** was analyzed using both positive ion electron–impact (EI) and negative ion electron–capture chemical ionization (NCI) methods.

The EI and NCI mass spectra of **2a** are depicted in Figure 6-2, and the relative abundances of the observed peaks of the phenylimido and isopropylimido complexes **2a** and **1a** are summarized in Table 6-1. As observed in the mass spectra of the isopropyl precursor, no molecular ion was detected for **2a** using either ionization method. The base peak in the EI spectrum occurs at *m/z*=382, and corresponds to the fragment $[Cl_3W(NPh)]^+$. The highest mass peak observed in the EI spectrum was $[Cl_4W(NPh)]^+$ at *m/z*=417 (9% abundance). Interestingly, although the high mass envelopes correspond to fragments in which acetonitrile is lost, only a small amount (~1% abundance) of the $[CH_3CN]^+$ ion was detected at *m/z*=41 in the EI spectrum of **2a**. The presence of the $[Cl_4W]^+$ and $[Cl_3W]^+$ fragments suggests cleavage of the W–N bond occurs in the gas phase. Furthermore, observation of the $[Ph]^+$ fragment (*m/z*=77) indicates that the critical N–Ph bond is broken to some extent under EI conditions; however, there is no evidence of a metal nitrido fragment in the resulting spectrum. Moreover, the base peak in the NCI spectrum corresponds to $[Cl_4W(NPh)]^-$ (*m/z*=417) while the mass envelope of the nitride fragment $[Cl_4WN]^-$ (*m/z*=340) has a relative abundance of 4%. The presence of the fragment $[Cl_5W(NPh)]^-$ suggests that the nitrile ligand of **2a** is removed during the process of heating the condensed phase sample to afford $[W(NPh)Cl_4]_2$ prior to ionization.

The mass spectral data for phenylimido complex **2a** and isopropylimido complex **1a** show some similarities. For both, the most prevalent ion on the high mass end of the EI spectrum corresponds to $[Cl_3W(NR)]^+$, although **2a** does also exhibit lower abundance peaks from $[Cl_4W(NPh)]^+$. This, coupled with the lack of molecular ion signals, is consistent with high lability of the nitrile ligand in both complexes. Moreover, the presence of the $[Cl_5W(NPh)]^-$ fragment in the NCI spectrum suggests that the lability of the nitrile ligand results in partial conversion of **2a** to the dimer $[W(NPh)Cl_4]_2$ prior to ionizations. The observation of this chloride transfer process in **2a**, but not **1a**, is consistent with the greater electron withdrawing nature of the phenyl substituent, as compared to isopropyl.

Table 6-1. Summary of relative abundances for positive ion EI and negative ion NCI mass spectra of tungsten imido complexes $Cl_4(CH_3CN)W(NPh)$ (**2a**) and $Cl_4(CH_3CN)W(N^iPr)$ (**1a**).

Complex	EI Fragments	NCI Fragments	*m/z*	Abundance[a,b]
	$[Cl_4W(NPh)]^+$		417	9
	$[Cl_3W(NPh)]^+$		382	100
	$[Cl_4W]^+$		326	7
	$[Cl_3W]^+$		291	15
	$[PhN]^+$		91	<1
	$[Ph]^+$		77	22
	$[C_5H_4]^+$		64	1
$Cl_4(CH_3CN)W(NPh)$ (**2a**)	$[C_4H_3]^+$		51	10
	$[CH_3CN]^+$		41	1
	$[C_3H_2]^+$		38	1
		$[Cl_5W(NPh)]^-$	452	23
		$[Cl_4W(NPh)]^-$	417	100
		$[Cl_4WN]^-$	340	4
	$[Cl_3W(N^iPr)]^+$		348	100
	$[Cl_4W]^+$		326	26
	$[Cl_3WNH]^+$		306	78
	$[Cl_3W]^+$		291	30
$Cl_4(CH_3CN)W(N^iPr)$ (**1a**)	$[CH_3CN]^+$		41	24
		$[Cl_4W(N^iPr)]^-$	383	42
		$[Cl_4WN]^-$	340	100

[a] Relative abundances were adjusted by summing the observed intensities for the predicted peaks of each mass envelope and normalizing the largest sum to 100%.
[b] Values for **1a** are from Chapter 5.

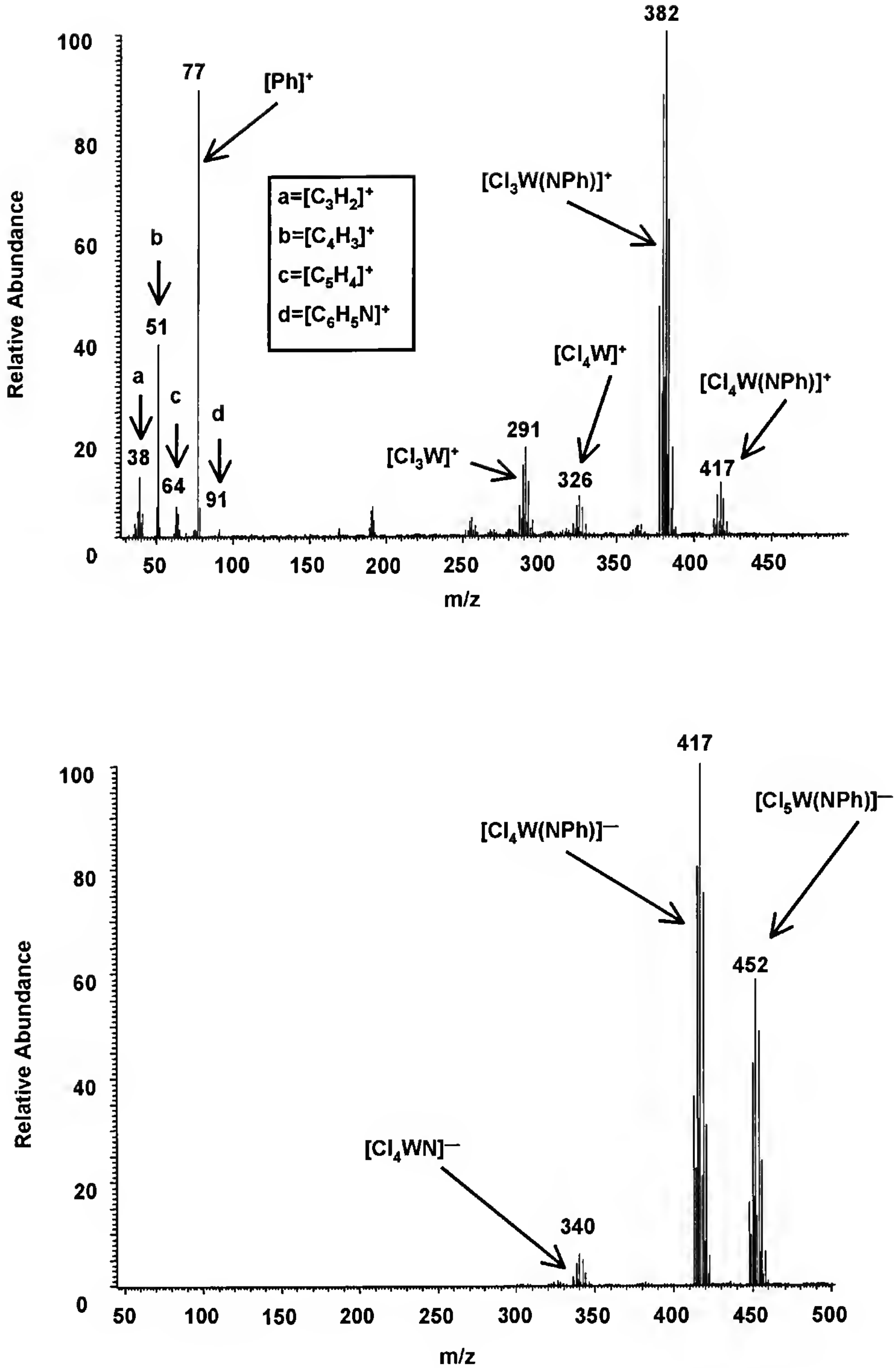

Figure 6-2. Positive ion electron–impact ionization (EI) and negative ion electron capture chemical ionization (CI) mass spectra of **2a**.

The most notable difference in the spectra of **2a** and **1a** concerns the fragments $[Cl_3WNH]^+$ and $[Cl_4WN]^-$. Since these ions are derived from cleavage of the N–R bond of the imido moiety, they are critical to the CVD process. As shown in Table 6-1, $[Cl_3WNH]^+$ appears in the EI spectrum of **1a** with a relative abundance of 78%; however, this fragment is not present in the spectrum of the phenylimido complex **2a**. Nevertheless, the presence of $[Ph]^+$ indicates the N–Ph bond is broken to a certain extent under EI conditions. The ion $[PhN]^+$ (m/z=91) was observed in very small relative abundance (<1%), and its subsequent fragmentation may be responsible for the small clusters of peaks centered at m/z=64, 51 and 37 [Cro67]. Even more striking is the fact that the $[Cl_4WN]^-$ fragment is the base peak in the NCI spectrum of **1a**, but only accounts for 4% relative abundance in the phenylimido complex **2a**.

In relation to the use of $Cl_4(PhCN)W(NPh)$ (**2b**) as a precursor for tungsten nitride deposition, the mass spectral data of **2a** and **1a** suggest that the N–Ph bond is more difficult to break than the N–^{i}Pr bond. This is consistent with the homolytic bond strength of the two N–R moieties [Ben76]. If N–Ph bond cleavage were involved in the rate determining step, **2b** would be expected to require higher deposition temperatures relative to the isopropyl system. The stronger N–Ph bond may also affect growth rate and composition of the deposited films. Additionally, these data suggest that replacing the phenyl moiety with a group that will cleave more readily (*e.g.*, allyl) could decrease the deposition temperature and improve the compositional characteristics of the WN_x films.

6.5 Film Structure

6.5.1 XRD

The films typically had a smooth, shiny metallic appearance with color varying from black to gold, depending on the deposition conditions. The desired WN_x film structure and stoichiometry is face centered cubic (FCC) β–W_2N (β–$WN_{0.5}$), since this phase has the lowest resistivity. The X–ray diffraction (XRD) spectrum in Figure 6-3a is consistent with amorphous film deposition from **2b** at 475°C, as evidenced by a flat profile with no characteristic β–WN_x peaks. In contrast, the XRD spectrum shown in Figure 6-3b indicates polycrystalline film deposition at 750°C. Four characteristic peaks are evident, with relative peak intensities indicating that no preferred crystal orientation exists. Although the relative peak intensities in Figure 6-3b are consistent with the pattern for polycrystalline β–$WN_{0.5}$, the 2θ peak positions lie between the standard values for β–$WN_{0.5}$ and β–$WC_{0.6}$, which are shown in Figure 6-3c.

Peak positions between these standard values suggest that C is mixing with N and vacancies on tungsten's interstitial sublattice to form β–WN_xC_y polycrystals. For the spectrum in Figure 6-3b, primary reflections at 37.13 and 43.08 2θ degrees are consistent with (111) and (200) β–WN_xC_y growth planes, while additional reflections at 62.73 and 74.98 2θ degrees indicate (220) and (311) planes, respectively. No peaks arising from the hexagonal WN or WC phases, or the body centered cubic (BCC) α–W phase were evident for any of the films.

Figure 6-4 illustrates the evolution of film crystallinity with deposition temperature for growth from **2b**. The trend of increasing crystallinity with deposition temperature is similar to that observed for the isopropyl imido precursor **1b** [Bch03a]. At the lowest deposition temperature (475°C), the characteristic β–WN_x peaks are not observed, indicating that the film is amorphous.

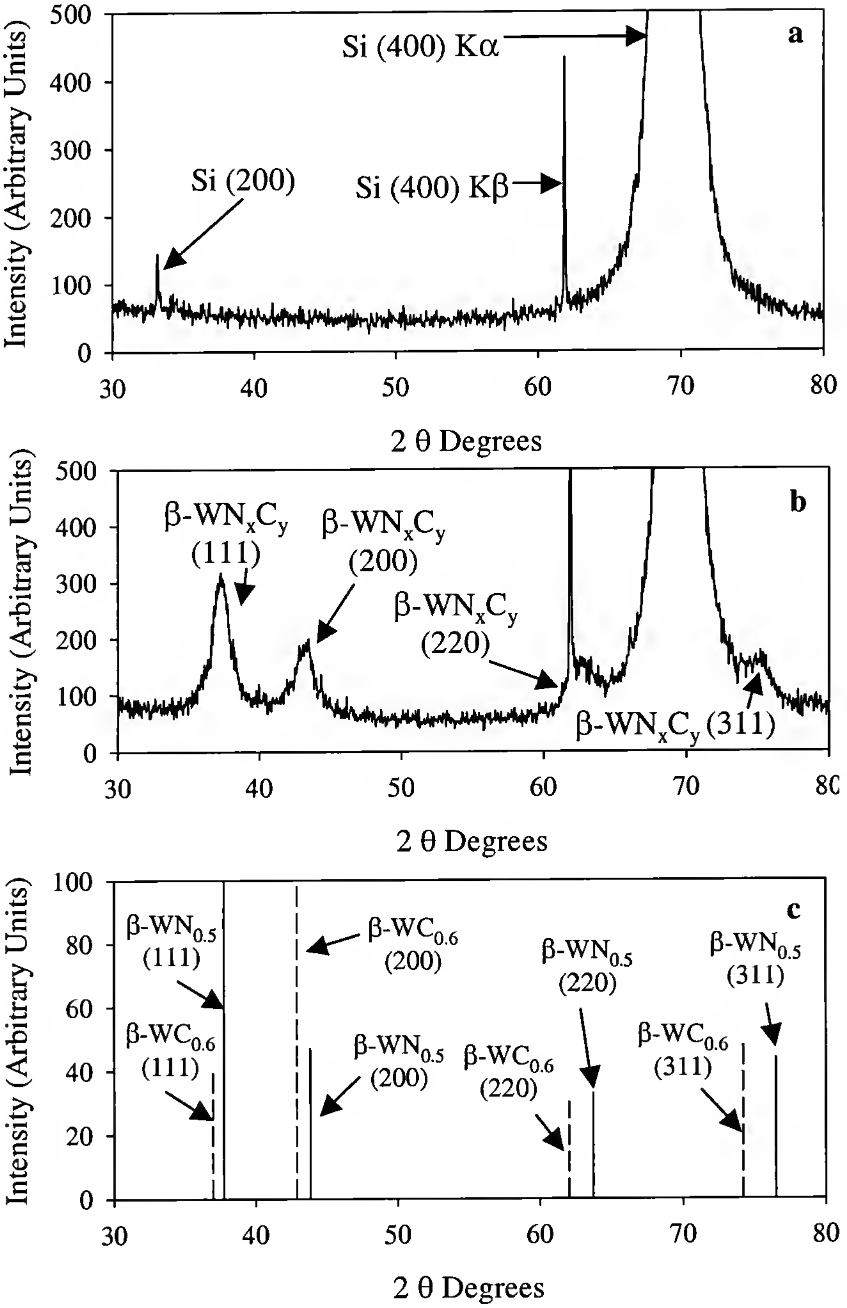

Figure 6-3. XRD spectra of films grown from **2b** on Si (100) in a H_2 atmosphere. a) 475°C. b) 750°C. c) Standard powder diffraction plot for β–$WN_{0.5}$ (solid lines) and β–$WC_{0.6}$ (dashed lines).

As the temperature increases to 500°C, peaks appear at 23.48 (not shown) and 47.98 2θ degrees, consistent with formation of tungsten oxide (WO_x, $x \approx 3$). Repeated attempts to deposit films at 500°C resulted in formation of tungsten oxide, while peaks consistent with WN_x (or WN_xC_y) are seen at all deposition temperatures above this. Reproducible deposition of tungsten oxide at a single temperature suggests that an air leak in the reactor system is unlikely to be the source of O. Microstructure dependent, post–growth O incorporation is a likely cause of oxide formation, especially for low temperature, "clean" tungsten films with low C and N levels. This is due to lower contamination levels, which make these films less resistant to O in–diffusion and reaction. The existence of a second O incorporation pathway involving the Et_2O co–solvent, however, cannot be ruled out. Diethyl ether is known to undergo both homogeneous and heterogeneous decomposition at temperatures near 500°C [Fle36, Fou79]. Although oxide formation still occurs for films grown at 500°C from $Cl_4(PhCN)W(NPh)$ (**2b**) in a benzonitrile/acetonitrile mixture (no Et_2O present), the size of the oxide crystallites is larger when the ether complex $Cl_4(Et_2O)W(NPh)$ (**3**) is used to generate precursor or when Et_2O is the co–solvent. Even though the film is amorphous at 475°C, indicating that inadequate thermal energy is available to produce oxide polycrystals, the possibility of O incorporation similar to that at 500°C cannot be ruled out. High levels of O in the amorphous film, as demonstrated by AES data, support this possibility.

A broad peak near 38.03 2θ degrees, which is above the standard peak position for β–$WN_{0.5}$ (111), appears for deposition at 525°C, and indicates the presence of N–deficient polycrystalline β–WN_x (111). A broad peak at 44.03 2θ degrees for deposition at 550°C indicates the first appearance of β–WN_x (200). As the temperature increases to 600°C, film peak positions shift below the standard β–$WN_{0.5}$ positions, indicating that β–WN_xC_y deposition is occurring. Broad peaks emerge at 62.93 and

75.58 2θ degrees for deposition at 700°C, indicating β–WN_xC_y (220) and (311) growth. The peaks sharpen further as the temperature increases to 750°C, due to polycrystalline grain growth. Peak sharpness decreased somewhat for the film deposited at 800 °C (not shown), which is likely due to a decrease in film thickness as measured by XSEM. Decreased film thickness may be caused by rapid desorption of reactants from the film surface due to high temperatures or by gas phase reactions, which deplete the amount of reactant available at the film surface. Some films deposited between 475 and 600°C displayed additional peaks at 32.98 and/or 61.68 2θ degrees, representing reflections from the underlying Si consistent with Si (200) Kα and Si (400) Kβ radiation, respectively.

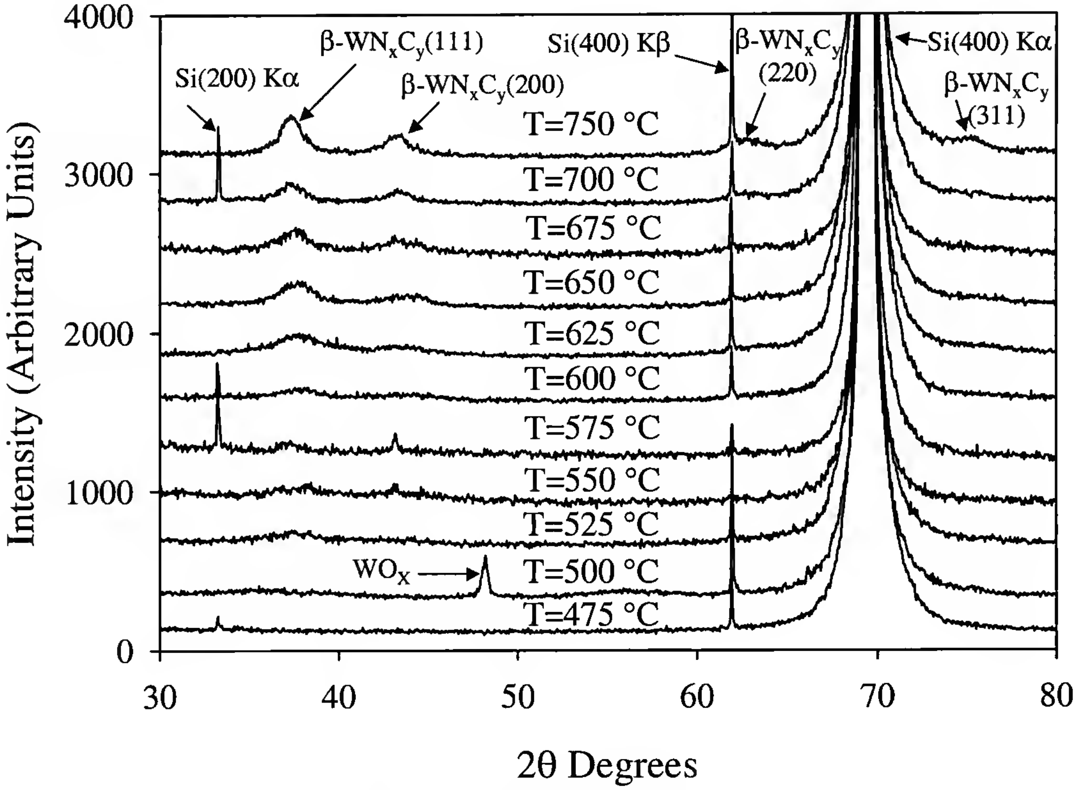

Figure 6-4. Change in XRD pattern with deposition temperature for WN_xC_y grown from **2b** on Si (100) in a H_2 atmosphere.

At the highest deposition temperature, minimal N and high C levels suggest that the stoichiometry of the β–WN_xC_y polycrystals may be approaching β–WC_y deposition. A shift in the position of the peaks toward β–$WC_{0.6}$ at higher deposition temperature provides evidence of this trend.

6.5.2 Lattice Parameter

The dependence of lattice parameter on deposition temperature in Figure 6-5 was determined by XRD using the 2θ position of the (111) β–WN_xC_y diffraction peak, with peak position calibrated to the Si (400) diffraction peak. The standard β–$WN_{0.5}$ (111) and β–$WC_{0.6}$ (111) peak positions are 37.735 and 36.977 2θ degrees (Figure 6-3c), respectively, and correspond to standard lattice parameter values of 4.126 and 4.236 Å. The position of the (111) reflection peak can vary as a result of a change in composition or a change in the film's residual stress.

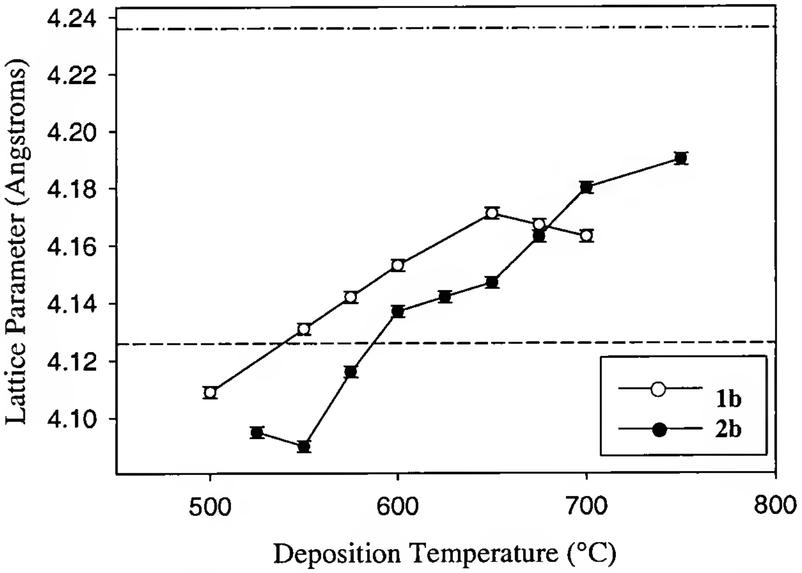

Figure 6-5. Lattice parameters for films grown from **1b** and **2b**, based on the β–WN_xC_y (111) diffraction peak. The dashed line at 4.126 Å represents the standard lattice parameter value for β–$WN_{0.5}$, while the dash–dot line at 4.236 Å is that for β–$WC_{0.6}$. Error bars indicate uncertainty in lattice parameter (± 0.002 Å) due to X–ray Kα line broadening.

Assuming that compositional variation is responsible for the peak shift and, thus, lattice parameter change, trends in the relative concentrations of N, C, and Va on the interstitial sublattice can be suggested by coupling the peak shift with the compositions measured by AES (Figure 6-7). If the (111) peak position is higher than 37.735 2θ degrees, corresponding to a lattice parameter below 4.126 Å, then minimal C, a deficiency of N, and an excess number of vacancies exist in the polycrystals. This is the case for depositions between 525 and 575°C. A peak position between 37.735 and 36.977 2θ degrees, which corresponds to a lattice parameter between 4.126 and 4.236 Å, suggests mixing of N, C and Va on the interstitial sublattice. This is the case for depositions at and above 600°C. As mentioned above, however, β–WN_xC_y polycrystals may be forming even at the lower temperatures, with C playing a role in the lattice parameter increase at lower temperatures. While an explicit relationship between x and y in β–WN_xC_y cannot be determined from XRD and AES data without some assumptions (e.g., use of Vegard's law), insight into the relation between C and Va on the interstitial sublattice is possible. Nitrogen prefers to occupy interstitial lattice sites in the polycrystals, and only resides at the grain boundary when its concentration in the film exceeds the β–$WN_{0.5}$ stoichiometry. Low N levels in the **2b** films imply that all N resides at interstitial sites. Essentially constant, low N levels (Figure 4) indicate that changes in lattice parameter will likely depend on the ratio of C to vacancies on the interstitial sublattice.

Values for lattice parameter in the films from **2b** tend to follow C content over the entire deposition temperature range. This likely reflects an increase in the ratio of C to vacancies on the interstitial sublattice with deposition temperature. The lattice parameter for the films from **2b** is 4.10 Å for 525°C deposition, drops to 4.09 Å for 550°C, and then increases to 4.14 Å for 600°C. The C content follows the same trend (Figure 6-7), decreasing from 525 to 550°C, and then increasing up to 600°C. The lattice parameter increases only slightly from a value of 4.14 Å at 600°C to 4.15 Å at 650°C, consistent with a small increase in C levels as measured by AES. This behavior is consistent with a decrease in compressive film stress, coupled with grain growth. Above 650°C, the lattice parameter again increases with C content, reaching 4.19 Å at 750°C.

6.5.3 Polycrystal Grain Size

Grain size (t) was estimated using the Scherrer equation (Equation 6–1) [Cul78, Nag00]. The two main causes of peak broadening in XRD thin film spectra are non–uniform film stress and the presence of small crystal grains. If we assume uniform film stress, the average crystallite size (t) may be estimated using the Scherrer equation:

$$t = \frac{0.9\lambda}{(B\cos\theta)} \qquad (6\text{–}1)$$

where λ is the X–ray wavelength (1.5406 Å for Cu Kα), B is the full width at half maximum (FWHM) for the selected diffraction peak and θ is the Bragg angle for that peak.

The dominant (111) diffraction peak for the films was used as the reference peak for FWHM determination. As depicted in Figure 6-6, grain size for the films from **2b** increased with deposition temperature, varying from 35 to 67 Å over the 525 to 750°C temperature range. Below 525°C, the films were X–ray amorphous, hence the maximum grain size for amorphous films was below 35 Å. Interestingly, the grain size is essentially constant between 550 and 600°C, which coincides with the transition region between kinetic and diffusion controlled growth. As the deposition temperature increases, a competition likely exists between increased grain growth due to higher surface diffusivity and decreased grain growth due to increasing C concentration on the film surface, which inhibits surface diffusion. Interplay between these phenomena cause grain growth in regions with small shifts in C content and leveling off of grain size in regions with larger shifts in C content.

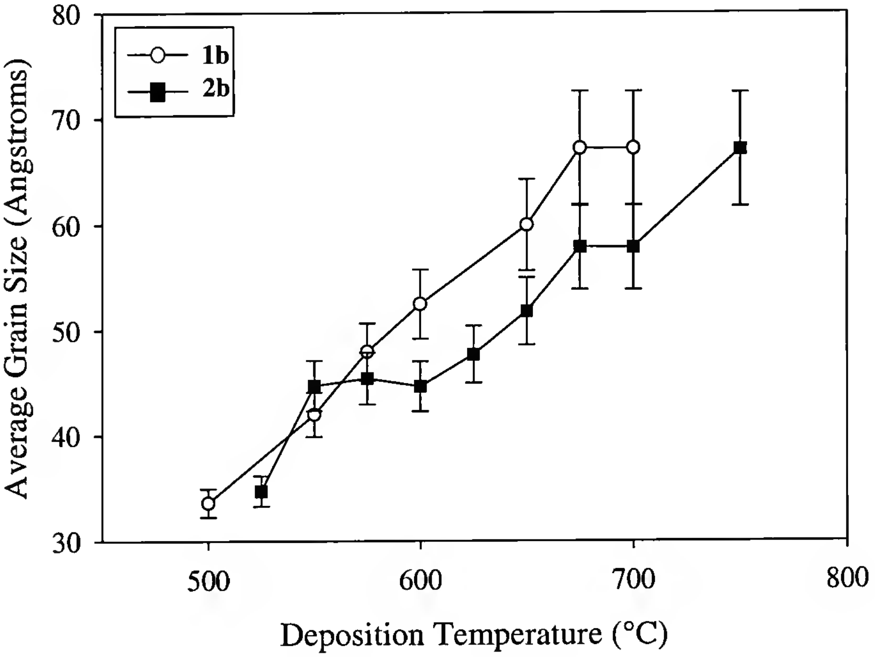

Figure 6-6. Change in average grain size with deposition temperature for polycrystalline films grown from **1b** and **2b** based on the FWHM of the β– $WN_xC_y(111)$ diffraction peak. Error bars reflect uncertainty in FWHM measurements.

6.6 Film Composition

6.6.1 AES

AES results for films deposited from the phenylimido complex **2b** indicate the presence of W, N, C and O (Figure 6-7). No chlorine was detected in the films by AES or XPS, placing an upper limit of ~1 at. % on Cl content. HCl is the thermodynamically favored gas phase chlorine–containing species, and was observed by residual gas analysis during deposition from **1b.** It is assumed that HCl is the dominant gas phase chlorine–containing species for deposition from **2b** as well. Neither Cl_2 nor chlorinated hydrocarbons were detected in the reactor effluent, leading to the conclusion that Cl is lost from the precursor as HCl. From 475 to 500°C, the C level is constant at approximately 3 to 5 at. %. The C content jumps from 5 to 14 at. % between 500 and 525°C. Although XRD indicates β– WN_x polycrystalline deposition at 525°C, results for growth rate and sheet resistance at this temperature show strong deviation from the trends evident between 550 to 750°C. Given the proximity in deposition temperature of the C spike (525°C) to the anomalous tungsten oxide formation seen in the XRD (500°C), the two phenomena may be related. Above 550°C, the C content rises steadily from 9 to 22 at. % at 750°C. The increase in C content from lowest to highest deposition temperature reflects the increasing tendency of the hydrocarbon groups present in the precursor ligands and the solvent to deposit in the films at higher growth temperature.

The initial N content of films grown at 475°C was 1 at. %. The N content increased to a maximum value of 3 at. % at 525°C, and then decreased with increasing temperature, dropping below 1 at. % above 700°C. Although metal nitride barriers typically exhibit low N content at higher deposition temperatures (due to desorption of N_2 gas), the films deposited from **2b** were N–deficient throughout the temperature range studied. This N deficiency in the films contrasts with XRD results in Figure 3, which indicate β–WN_x polycrystal growth at lower temperatures. This may indicate that β–WN_xC_y polycrystal formation begins at temperatures below 600°C, with C filling the excess vacancies present in the polycrystals due to N deficiency.

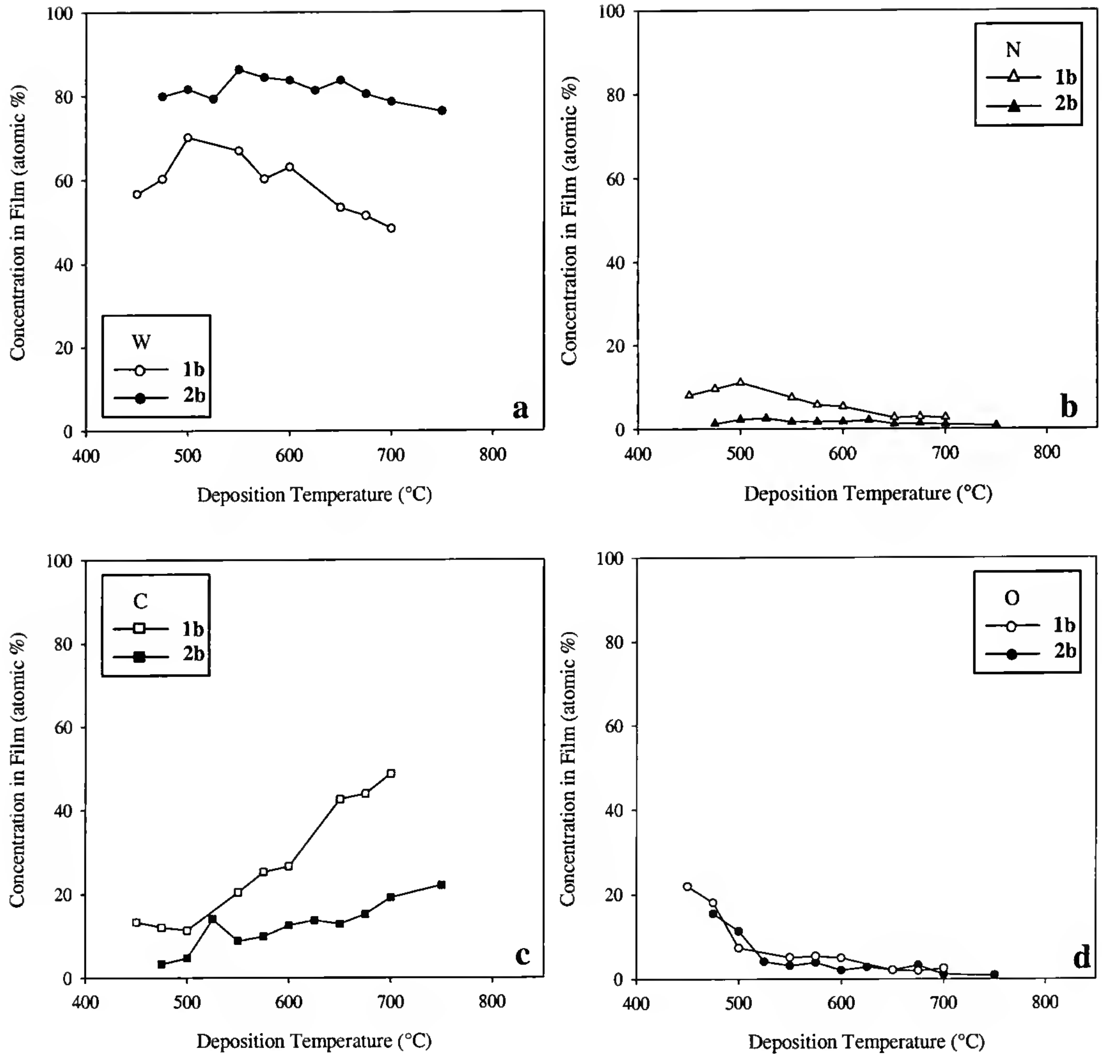

Figure 6-7. Comparison of film content for growths from the **1b** and **2b** compounds. a)W b)N c)C d)O. Data are from AES measurements after 2.0 minutes sputter.

Although the value of y in $\beta\text{–}WN_xC_y$ should be relatively small at the lower deposition temperatures, it may be sufficiently large to shift the XRD peak position to lower values of 2θ (and concomitantly increase the lattice parameter), even at the lower temperatures. It should also be noted that preferential incorporation of C and removal of N by Ar^+ sputtering during AES analysis has been reported to cause artificially high C and low N concentration readings [Ing82]. Since the AES data were collected after 2.0

minutes of sputter, artificially high C and low N compositions may have been observed. In addition, the lack of a standard film sample for calibration of elemental concentrations means that AES data may vary up to several atom percent from the actual values. Despite the error bars on the concentrations, the AES data serve to identify trends in film composition with deposition temperature.

The slight O contamination in the film samples deposited at higher temperatures likely resulted from post–growth exposure of the film samples to air. The higher O levels in films deposited at and below 500°C may be influenced by the presence of the Et_2O co–solvent during growth and exposure of the films to air after growth. Incremental AES sputtering showed a steady decrease in O levels with increasing depth into the WN_x films. The O concentration was highest at 475°C, reaching 15 at. %, and then decreased slightly to 11 at. % at 500°C. This behavior is consistent with low density and high porosity in the amorphous films deposited below 525°C, which allow substantial amounts of O to penetrate into the film lattice. High O concentrations (~20%) attributed to air exposure have been reported for porous TiN, TiC and TiCN barriers [Eiz94a, Par96, Wan01a]. XPS results for O in the films are consistent with WO_3, which has considerably higher thermodynamic stability than β–WN_x or β–WC_x. For example, values of the Gibbs energy of formation (ΔG°_f) at 750°C for the WO_3, β–$WN_{0.5}$ and β–$WC_{0.5}$ phases are –579 kJ/mol, +21 kJ/mol, and –8.5 kJ/mol, respectively [Gus86, Lak79, Lid85]. The experimental observation of lower levels of O at higher deposition temperatures is consistent with post–growth O contamination, as oxide formation is thermodynamically favored to occur if an O leak into the reactor occurred during growth. As the deposition temperature rises from 500 to 525°C, the O content drops sharply to 4 at. %, while the C and N levels are moderately steady. This behavior is consistent with the change in crystallinity observed by XRD. As the film crystallizes, it becomes more dense [Pok91], thereby inhibiting post–growth O diffusion into the lattice and decreasing the density of adsorption sites. As deposition temperature increases above 525°C, the O concentration drops further, falling below 1 at. % above 700°C. This drop in O levels likely results from film densification (by polycrystal grain growth) and increased C levels at higher deposition temperature stuffing the grain boundaries. Porosity of amorphous films grown below 525°C may be problematic for diffusion barrier applications, since defects in the film may degrade the barrier's resistance to Cu diffusion. A previous report, however, indicates that diffusion barrier performance depends more strongly on film microstructure than film density [Kim99c]. In addition, impurities such as O, N and C have been reported to enhance the stability of diffusion barrier films [Cha99].

6.6.2 Film Growth Rate (XSEM)

Growth rates were estimated by dividing the total film thickness (from X–SEM or AES sputter profile for the sample grown at 425°C) by deposition time. Figure 6-8 depicts X–SEM photos for films grown at the lowest and highest growth temperature, corresponding to deposition rates of 2 and 21 Å/min. An Arrhenius plot using the measured growth rates (Figure 6-9) clearly delineates two growth regimes. The region with the shallow slope above 550°C exhibits a weak dependence on temperature that is indicative of mass transfer controlled growth. The region with a steep slope below 550°C suggests that growth is controlled by a kinetic process. In this regime, the rate–determining step for film growth is presumably reaction on the substrate surface. As observed in the XRD and AES studies, the growth rates for films grown at 500 and

525°C appear to be anomalous. This may be due to a decrease in the film density causing the measured thickness change to overestimate the reaction rate. Excluding the data points at 500 and 525°C, a fit of the data gives an apparent activation energy for growth of films from **2b** in the kinetic regime as 1.41 ± 0.58 eV.

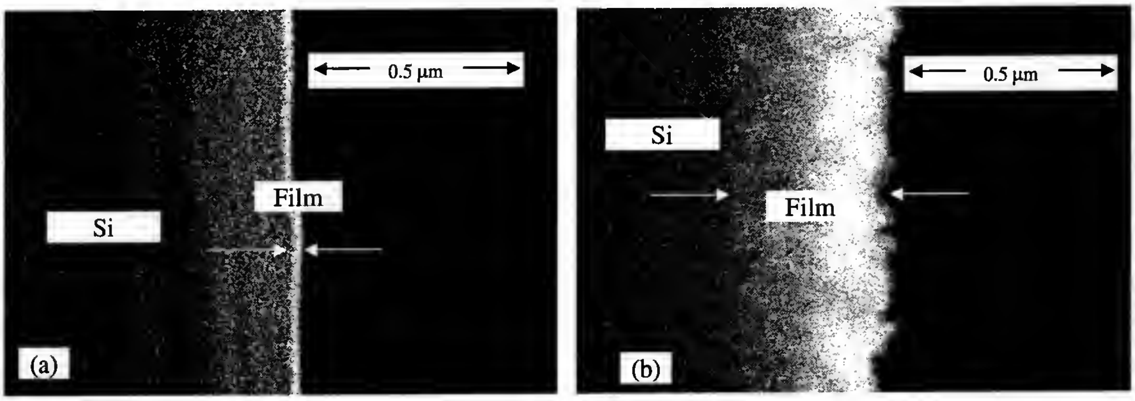

Figure 6-8. Cross–sectional SEM photo depicting thickness of films grown from **2b** on a Si (100) substrate. a) 475°C. b) 750°C.

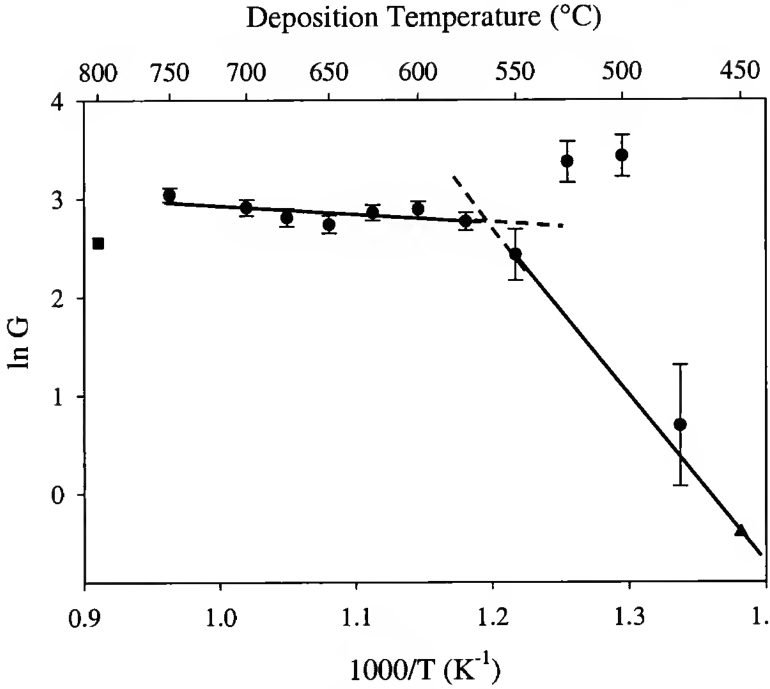

Figure 6-9. Plot of film growth rate (G, Å/min) from **2b** on Si(100) vs. inverse temperature. Error bars indicate uncertainty due to deposition temperature variation (+/– 10°C) and thickness measurement from X–SEM photos. The line fit for the kinetic regime includes data points for 450, 475 and 550°C, and excludes points at 500 and 525°C.

Depositions at 450 and 800°C were done to establish the temperature boundaries for film growth from the phenylimido complex **2b**. Films deposited at 450°C were not visible by X–SEM, but AES depth profiling indicated a nominal film thickness of ~100 Å. This thickness value (triangular symbol in Figure 6-9) was used to estimate the value of the apparent activation energy for film growth in the kinetic regime. The growth rate at 800°C dropped to 13 Å/min (square symbol in Figure 6-9), with a high degree of surface roughness visible on the substrates after deposition. These results may be explained by either premature gas phase decomposition of the precursor, due to upstream heating at the higher temperature or by high desorption rate for a reactant species.

6.7 Film Electrical Properties

6.7.1 Film Resistivity

Film resistivity was calculated with Equation 5–5, as discussed in Chapter 5. Sheet resistance measurements were collected using 4–point probe, and film thickness measurements were taken from X–SEM images. The variation of film resistivity with deposition temperature is shown in Figure 6-10. A deposition at 475°C produced films with the lowest resistivity value (225 μΩ–cm) despite C and O contamination levels of 3 and 15 at.%, respectively. This is lower than the 620 μΩ–cm reported for films grown from $(^{t}BuNH)_2W(N^{t}Bu)_2$ at 650°C [Chi93, Tsa96], and also lower than the 750 μΩ–cm value observed for films grown from **1b**.

In the temperature range where anomalous growth was observed, 500 to 525°C, the resistivity sharply increases, e.g., 73,000 μΩ–cm at 500°C. This dramatic rise is consistent with deposition of tungsten oxide at 500°C. Interestingly, the resistivity

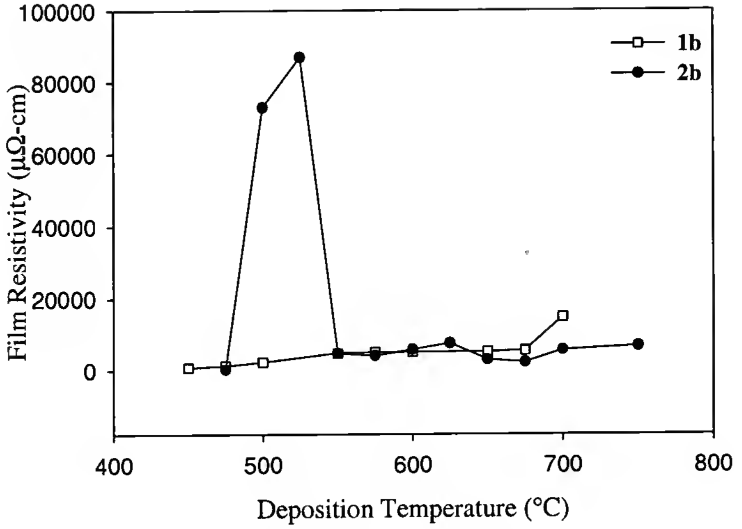

Figure 6-10. Variation of film resistivity with deposition temperature for films deposited with **1b** and **2b**.

climbs even higher to 87,000 μΩ–cm for deposition at 525°C, despite XRD data consistent with polycrystalline β–WN_x. Moving to 550°C, the film resistivity drops to 4,750 μΩ–cm, then fluctuates somewhat with increasing growth temperature. Changes in the film resistivity above 550°C occur due to the interplay of polycrystal grain growth, C content and film thickness. Increased grain growth generally causes a resistivity decrease, while increased free C content and film thickness are associated with increased resistivity.

6.7.2 Film Sheet Resistance

Film resistivities calculated with Equation 5–5 depend on both the sheet resistance and thickness of the analyzed films. As deposition temperature increases above 550°C, the film thickness also increases. To decouple the impact of film thickness from the film's electrical properties, the sheet resistance was plotted as a function of deposition temperature (Figure 6-11). The sheet resistance increases sharply with deposition temperature from 75 Ω/□ at 475 °C to 1600 Ω/□ at 500 °C, then rises further to

2000 Ω/□ at 525 °C. This increase in sheet resistance for the less conductive films grown at 500 and 525°C indicates that these higher resistivity values (Figure 6-10) are not due solely to higher film thickness and is consistent with oxide formation and the spike in C content determined by AES (Figure 6-7). As the deposition temperature is increased to 550 °C, the sheet resistance decreases to 279 Ω/□, concomitant with lower O and C content. The sheet resistance, like the resistivity, fluctuates somewhat for deposition temperature above 550°C, but eventually reaches a constant value near 210 Ω/□ at 750°C.

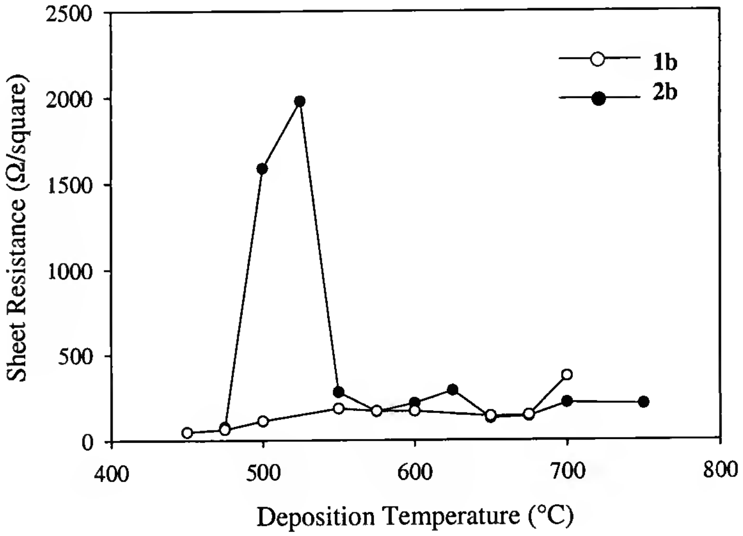

Figure 6-11. Variation of film sheet resistance with deposition temperature for films deposited from **1b** and **2b**.

6.8 Conclusions on Use of $Cl_4(CH_3CN)WNPh$ to Deposit WN_x

In terms of their decomposition chemistry, the most significant difference between isopropylimido complex **1b** and phenylimido complex **2b** is the dissociation energy of the N–C bond in the imido ligand. Based on data from organic model compounds, the N–C bond of isopropylimido complex **1b** is expected to be approximately 20 kcal/mol weaker than the analogous bond in **2b** [Ben76]. Since cleavage of this bond is necessary for deposition of WN_x, one would expect there to be differences in film structure, film composition, and lattice parameter between films grown from the two precursors.

Amorphous film growth occurs below 500°C for **1b** and **2b**. At 500°C, a broad β–W_2N (111) polycrystalline peak appears for films from **1b**, while polycrystalline oxide peaks appear for the material from **2b**. Evidence of polycrystalline WN_x deposition from **2b** first appears at 525°C. The anomalous film characteristics of material grown from **2b** at 500°C appear to be linked to the presence of the Et_2O co–solvent (necessary because the solubilities of **1b** and **2b** differ). The maximum deposition temperature for films deposited from the isopropyl complex was 700 °C. Above this temperature, black particles were deposited on the substrate and susceptor, which subsequently compromised film quality. In contrast, deposition from phenylimido complex **2b** was possible up to 750 °C. The higher temperature limit for **2b** could be due to the enhanced N–C bond strength in its imido ligand.

Carbon levels in the films from **2b** were considerably lower than those from **1b** throughout the temperature range (Figure 6-7). From 550 to 750°C, films from both precursors exhibited a gradual rise in C content, with the isopropyl imido complex **1b** affording a steeper rise in C as growth temperature increased. Maximum N content for films from the two precursors occurred near their respective crystallization temperatures (500°C for **1b** and 525°C for **2b**). Throughout the temperature range studied, the N content in films deposited from **2b** was significantly lower than those grown from **1b**. The fact that films from phenylimido complex **2b** contained lower levels of both N and C than those from isopropylimido complex **1b** suggests that the phenylimido moiety is more likely to dissociate intact than the isopropylimido ligand. This is consistent with the higher N–C bond strength in the phenylimido group.

Corroborating evidence for this effect can be found in the mass spectra of **1a** and **2a**. Facile dissociation of the isopropyl group from **1a** is indicated by the observation of $[Cl_3WNH]^+$ at 78% abundance in the EI spectrum and detection of $[Cl_4WN]^-$ as the base peak in the NCI trace. Loss of the phenyl moiety from **2a** to yield the same ions does not occur under EI conditions and the NCI spectrum contains $[Cl_4WN]^-$ at only 4% abundance. Moderate amounts of $[Cl_4W]^+$ and $[Cl_3W]^+$ were detected in the mass spectra of **2b** under EI conditions, as well as fragments a–d (Figure 6-2), which are consistent with what has previously been observed upon generation of NPh^+ from phenyl azide [Cro67]. Although the mass spectral evidence for NPh loss consists of low intensity mass envelopes, their presence is significant. Because of the difference in conditions between mass spectrometry (ion chemistry) and MOCVD (thermal decomposition), the data in Figure 6-2 and Table 6-1 do not rule out loss of NPh as a major heterogeneous process during deposition. Ideally, cleavage of the N–C bond in **2b** to release a phenyl group should occur during CVD of WN_x films. However, the high N–C dissociation energy would slow this process, allowing cleavage of the W–N bond to compete. Isopropylimido complex **1b**, with its weaker N–C bond, would be more likely to release the isopropyl moiety and leave the imido N in the growing film.

For both precursors, O levels were highest for films deposited at the lower end of the temperature range (≤ 500°C). AES indicated a decrease in O content with increasing sputter depth into the films; hence, high O levels were attributed to post–growth exposure of the films to air. The low density and high porosity of the amorphous structures grown at lower temperatures allow more rapid diffusion of O from the air into the films and provide a large surface to volume ratio for adsorption. High O levels in the films from **2b**, however, may be due to a combination of post–growth exposure to air and the presence of Et_2O during deposition. Increased C content in the films grown at higher temperatures is believed to inhibit post–growth oxidation of the films by stuffing grain boundaries.

Lattice parameter shifts were also dependent on the precursor. Figure 6-5 shows the lattice parameter increasing with temperature for films from both **1b** and **2b** at temperatures up to 650°C, with films from **1b** having higher lattice parameter values throughout this range. This is expected, due to higher C content in films from the isopropylimido complex **1b**. Just above 675°C, though, the lattice parameter in the films from **2b** becomes larger than that of the films from **1b**. Polycrystalline films deposited by **1b** have adequate N, even at high temperatures, to be considered primarily β–WN_x into which C is incorporated to form β–WN_xC_y. This β–WN_xC_y, although N–deficient at higher temperatures, contains sufficient N to prevent a shift from formation of β–WN_xC_y toward β–WC_y, and leads to an upper limit in lattice parameter for films from **1b** near 4.16 Å. Thus, the decrease in lattice parameter in films from **1b** deposited above 650°C was attributed to a solubility limit for C in β–WN_xC_y polycrystals with excess C residing at the grain boundaries above 675°C.

The films from **2b**, however, contain so little N that W is effectively left "bare" during deposition, enabling formation of carbide by reaction with depositing C at high temperature. Minimal N coupled with ~20 at. % C above 675°C may mean that a shift away from deposition of β–WN_xC_y toward β–WC_y is occurring at high temperature with the **2b** precursor. The lattice parameter of 4.19 Å for films grown from **2b** at 750°C indicates that the composition of the β–WN_xC_y polycrystals is nearing β–$WC_{0.6}$ (i.e., x is approaching zero and y is approaching 0.6), which has a lattice parameter of 4.236 Å.

Although β–WN_x films are reported to outperform β–WC_y for diffusion barrier applications, recent reports indicate interest in β–WN_xC_y as a potential barrier material. Thin films (~250 Å) of β–WN_xC_y have been deposited by ALD onto various substrates (*e.g.,* SiO_2, Cu, SiC and SiLK) by sequential reaction of WF_6, NH_3 and BEt_3 [Li02, Smi02]. Addition of C to β–WN_x was reported to lower film resistivity. In addition, β–WN_xC_y with a composition ratio W:N:C ≈ 55:15:30 exhibited excellent adhesion to Cu. Hence, although films deposited from **2b** have low N content (compared to typical WN_x films), this precursor may be of interest for β–WN_xC_y deposition. While we have demonstrated the ability of an NH_3 co–reactant to dramatically increase the N content for films deposited from **1b**, as discussed in Chapter 5, a similar approach with **2b** did not result in increased N content in the deposited film.

Nitrogen levels in the films from **2b** are much lower than films from **1b** at all temperatures. This trend in the films grown from the phenylimido precursor can again be attributed to the high N–C bond dissociation energy in the imido ligand of **2b**, which causes less N incorporation into the films, leaving open the possibility of β–WC_y formation. The XPS binding energy values for C1s and $W4f_{7/2}$ energy levels for films deposited from **2b** at 650°C were 284.6 and 33.0 eV, respectively, while those for deposition at 750°C, were 283.6 and 32.1 eV. These data are consistent with a shift toward formation of the β–WC_y phase for the film deposited from **2b** at 750°C [Kou02]. The XPS results for films from **1b** did not indicate this shift. This suggests that adequate

N remained in the polycrystals to prevent a shift to carbide formation, forcing additional C to deposit at the grain boundaries.

Grain growth behavior was similar for the two precursors. Grain sizes for films grown from **1b** and **2b** increased from lowest to highest deposition temperature, with those from **2b** generally having smaller size grains than those from **1b**. Above 600°C, where both precursors are operating in the diffusion controlled regime, the films from **2b** required a ~50°C higher temperature to deposit grains of similar size to their **1b** counterparts. This observation can again be traced to the difference in the strengths of imido N–C bonds in the precursors, with the weaker isopropyl imido bond affording higher growth rate and grain size for a given deposition temperature.

Deposition rates from the phenylimido complex **2b** films were lower than those from the isopropylimido complex **1b**. Film deposition rates ranged from 10 to 27 Å/min for films from **1b**, while the range was 2 to 21 Å/min for films from **2b**. The calculated E_a for film growth from **2b** in the kinetically controlled regime was 1.41 ± 0.58 eV, as compared to 0.84 eV for **1b** and 0.9 eV for $(^tBuNH)_2W(N^tBu)_2$ [Chi93, Tsa96]. The higher activation energy for **2b** is consistent with cleavage of the stronger imido N–C bond before or during the rate–determining step of the deposition process. Interestingly, the E_a for **2b** is above the typical activation energy range for CVD growth in the kinetic regime, which is 0.5 to 1 eV [Raa93].

With the exception of the anomalous results for growth at 500 and 525°C, comparison of the sheet resistances, which negate the impact of film thickness on electrical properties, shows that the films from **1b** and **2b** have similar electrical properties when deposited at or below 675°C. Above 675°C, **1b** films have higher sheet resistance than **2b** films, consistent with the high C levels in the **1b** films, which scatter electrons flowing through the material.

The tungsten imido complex $Cl_4(CH_3CN)W(NPh)$ **2b** was tested to determine its suitability as a single–source precursor for low temperature growth of β–WN_x thin films. Comparison of the film growth properties of **2b** to those of its isopropylimido analogue **1b** allowed evaluation of the effect of the imido N–C bond dissociation energy on film growth and properties. Films deposited from **2b** were deficient in N compared to those from **1b**, consistent with a tendency of the stronger imido N–C bond of **2b** to result in dissociation of intact NPh fragments during deposition. Since its films contain more N and have lower amorphous deposition temperatures and sheet resistances, the isopropyl imido precursor **1b** is superior to **2b** for barrier deposition.

CHAPTER 7
EVALUATION OF $Cl_4(CH_3CN)WNCH_2CH{=}CH_2$ AS A SUITABLE WN_x PRECURSOR

MOCVD of thin WN_xC_y films from benzonitrile solutions of the single–source imido precursors $Cl_4(CH_3CN)W(N^iPr)$ (**1a,** as a mixture with its benzonitrile derivative **1b)** and $Cl_4(PhCN)W(NPh)$ (**2b**) were discussed in Chapters 5 and 6, respectively. Based on mass spectral data of the precursors and film properties from material grown with the isopropyl imido and phenyl imido complexes, the isopropyl imido precursor **1a,b** enables increased N incorporation relative to the phenyl imido precursor **2b**, presumably due to the weaker N–C imido bond of the former (Chapter 5 and 6 have more detail). By this reasoning, a more promising precursor should contain a weaker N–C imido bond than that in either of the previously discussed complexes. Deposition tests were therefore undertaken with the allyl imido precursor $Cl_4(RCN)W(NCH_2CH{=}CH_2)$ (**3a**, $R{=}CH_3$ and **3b**, R=Ph).

7.1 Film Growth Studies

Experiments were conducted in the CVD reactor system described in Chapter 4. P–type boron doped Si (100) substrates with resistivity of 1–2 Ω–cm were used for the film growths. Growths were conducted for a fixed time of 150 minutes at temperatures ranging from 425 to 675°C. The system was maintained at vacuum by a mechanical roughing pump, with the operating pressure fixed at 350 Torr. Hydrogen (H_2) carrier gas was used for the depositions.

All mass spectral analyses were again performed using a Finnigan MAT95Q hybrid sector mass spectrometer (Thermo Finnigan, San Jose, CA). Electron ionization (EI) was carried out in positive ion mode using electrons of 70 eV potential and a source temperature of 200°C. Negative ion electron capture chemical ionization (NCI) used methane as the bath gas at an indicate pressure of 2×10^{-5} Torr, an electron energy of 100 volts and a source temperature of 120 °C. All samples were introduced via a controlled temperature probe with heating and cooling enabling temperature control down to 35 °C. The mass resolving power (m/Δm) was 5000 full width–half maximum (FWHM).

7.2 Synthesis of Allyl $Cl_4(CH_3CN)WNCH_2CH{=}CH_2$ Precursor

Standard Schlenk and glovebox techniques were employed in the synthesis of $Cl_4(CH_3CN)W(NCH_2CH{=}CH_2)$ (**3a**). Tungsten oxychloride was prepared by a slightly modified literature method [Ped82]. Complex **3a** was prepared in an analogous fashion to other previously reported tungsten imido precursors [Bch03a]. The benzonitrile complex $Cl_4(PhCN)W(NCH_2CH{=}CH_2)$ (**3b**) was not isolated, but was produced *in situ* by the substitution of the acetonitrile ligand of **3a** with benzonitrile, which was utilized as the solvent for the deposition experiments. Tungsten(VI) chloride was purchased from Strem Chemical Company. Allyl isocyanate and anhydrous heptane were used as purchased from Aldrich Chemical Company. Toluene and hexane were purged with N_2 and dried by passing the degassed solvent through a column packed with activated Al_2O_3 [Pan96]. Robertson Microlit in Madison, NJ performed the elemental analyses.

To prepare $Cl_4(CH_3CN)W(NCH_2CH{=}CH_2)$ (**3a**), tungsten oxychloride (2.047 g, 5.99 mmol) was slurried in a solution of allyl isocyanate (0.513 g, 6.17 mmol) in heptane (60 mL) in a sealed pressure vessel. The mixture was heated for 18 h at 110° C. The solvent was removed from the resulting dark red solution *in vacuo*. The reddish brown residue was dissolved in a minimal amount of CH_3CN (approximately 10 mL). The resulting solution was stirred for two hours and the solvent removed under reduced pressure. The resulting brown residue was washed with 5x10 mL of toluene and the extracts concentrated to approximately 5 mL. Hexane was added to precipitate the product. The orange–brown solid was filtered and washed with pentane to afford 1.59 g (63 % yield) of the imido complex. ^1H NMR ($CDCl_3$, δ): 7.57 (d, *J* = 5.6 Hz, 2H, NCH_2CHCH_2); 6.07 (dddd, *J* = 5.6, 10.2, 16.9 Hz, 1H, NCH_2CHCH_2); 5.73 (d, *J* = 16.9, 1H, NCH_2CHCHH); 5.60 (d, *J* = 10.2 Hz, 1H, NCH_2CHCHH); 2.50 (s, 3H, CH_3CN). ^{13}C NMR ($CDCl_3$, δ): 129.8, 121.9 (CH_2CHCH_2N); 118.9 (CH_3CN); 68.3 (CH_2CHCH_2N); 3.5 (CH_3CN). Anal. Calculated for $WC_5H_8N_2Cl_4$: C, 14.24%, H, 1.91%, N, 6.64%. Found: C, 14.51%, H, 1.86%, N, 6.43%.

7.3 Solvent Selection

For the isopropyl imido system, **1b** was generated *in situ* following solvation of **1a** in the benzonitrile used as the solvent for the CVD process. In the case of the phenyl imido compound, the solid precursor employed was the ether adduct $Cl_4(OEt_2)W(NPh)$ (**4**); however, the limited solubility of this (and other phenyl imido precursors) in benzonitrile necessitated the use of a 10:1 benzonitrile/ether co–solvent mixture. Accordingly, compound **4** was converted to the benzonitrile adduct $Cl_4(PhCN)W(NPh)$ (**2b**) in situ prior to deposition. Much like the isopropyl imido precursor **1a**, the allyl complex **3a** is soluble in PhCN allowing this solvent to be used for deposition experiments.

7.4 Precursor Mass Spectral Pre–Screen

We have previously shown that mass spectrometry of the tungsten imido precursors $Cl_4(CH_3CN)W(N^iPr)$ (**1a**) and $Cl_4(CH_3CN)W(NPh)$ (**2a**) affords insights into possible fragmentation patterns which arise during the CVD process [Bch03a, Bch03c]. Nevertheless, since mass spectrometry is an ionic process, care must be taken in applying the fragmentation patterns observed to a thermal process such as CVD [Lew94]. As in previous studies, we subjected the allyl imido precursor **3a** to both positive ion electron–impact (EI) and negative ion electron–capture chemical ionization (NCI) processes.

Table 7-1 summarizes the major fragments observed in the EI and NCI spectra of precursor **3a**. As with the isopropyl and phenyl imido complexes **1a** and **2a**, neither method detected a molecular ion. Instead the highest mass envelopes in the EI and NCI spectra occurred at *m/z*=346 and 381, corresponding to $[Cl_3W(NC_3H_5)]^+$ and $[Cl_4W(NC_3H_5)]^-$ respectively. The $[Cl_3W(NC_3H_5)]^+$ fragment was also the base peak of the EI spectrum. A high abundance (95%) peak at *m/z*=41 corresponds to both the acetonitrile fragment $[CH_3CN]^+$ and the allyl fragment $[C_3H_5]^+$ from the imido moiety.

Importantly, the base peak of the NCI spectrum corresponds to the mass envelope of the nitride fragment $[Cl_4WN]^-$ (*m/z*=340). A small amount of the protonated nitrido complex fragment $[Cl_3WNH]^+$ was detected in the EI spectrum, but at low relative abundance (~12%). As observed with precursors **1a** and **2a**, the EI spectrum of the allyl imido complex **3a** also exhibited fragments corresponding to loss of the imido N. Accordingly, mass envelopes at *m/z*=256 (27% abundance) and 291 (58% abundance) are assigned to the fragments $[Cl_2W]^+$ and $[Cl_3W]^+$ respectively.

Cleavage of the W–N multiple bond to afford the tungsten chloride fragments $[Cl_2W]^+$ and $[Cl_3W]^+$ seems problematic in regards to CVD of tungsten nitride; however, the high–energy nature of EI mass spectrometry most likely accounts for this observation. The lack of any molecular ion in either mass spectrum is consistent with lability of the nitrile ligand. More importantly, the observation of the nitride fragments $[Cl_3WNH]^+$ and $[Cl_4WN]^-$ indicates that the critical imido N–C bond is broken under the ionization conditions.

Relative to the isopropyl and phenyl imido precursors **1a** and **2a**, the allyl complex **3a** shows some similarities and important differences. In each case, the base peak of the EI spectrum corresponds to the loss of CH_3CN and one chloride ligand (*i.e.*, $[Cl_3W(NR)]^+$). The abundance of the protonated nitrido fragment $[Cl_3WNH]^+$ in the EI spectrum of the allyl imido complex **3a** was only about 12% as compared to the 78% relative abundance of the same mass envelope in the spectrum of the isopropyl imido precursor **1a**. Strikingly, this fragment is not observed at all in the EI spectrum of the phenyl precursor. Additionally, the fragment corresponding to the loss of the nitrile ligand (i.e., $[Cl_4W(NR)]^-$) was observed in the NCI spectra of all three precursors The relative abundance of this fragment is consistent with the relative strength of the N–C imido bond for the three precursors. Interestingly, this fragment was the base peak for the NCI spectrum of the phenyl precursor **2a**, while its relative abundance was lowest for **3a** (5%) and in–between (42%) for **1a**. In contrast, the nitrido fragment $[Cl_4WN]^-$ was the base peak in the NCI spectra of the isopropyl and allyl complexes **1a** and **3a**, while this mass envelope only accounted for 4% relative abundance in the spectrum of **2a**.

The greater abundance of the nitrido fragment $[Cl_4WN]^-$ in the NCI spectra of **1a** and **3a** relative to **2a** indicates that the N–C bond of the imido ligand is more easily broken for the allyl and isopropyl imido precursors than for their phenyl imido analogue. This conclusion is supported by the absence of $[Cl_3WNH]^+$ in the EI spectrum of **2a** and its presence in the spectra of **1a** and **3a**. These data correlate well with the homolytic C–N bond dissociation energies reported for the corresponding amines ($C_3H_5NH_2$=73 kcal/mol, $^iPrNH_2$=84 kcal/mol, and $PhNH_2$=105 kcal/mol) [Ben76, Luo94]. The smaller relative abundance of $[Cl_3WNH]^+$ observed for allyl imido complex **3a** versus the isopropyl imido complex **1a** cannot be easily explained within the context of C–N bond strengths.

Table 7-1. Summary of relative abundances for positive ion EI and negative ion NCI mass spectra of tungsten imido complexes $Cl_4(CH_3CN)W(NCH_2CH{=}CH_2)$ **(3a)**

EI Fragments	NCI Fragments	*m/z*	Abundance[a]
$[Cl_3W(NC_3H_5)]^+$		346	100
$[Cl_4W]^+$		326	34
$[Cl_3WNH]^+$		306	12
$[Cl_3W]^+$		291	58
$[Cl_2W]^+$		256	27
$[CH_3CN]^+$ or $[C_3H_5]^+$		41	95
	$[Cl_4W(NC_3H_5)]^-$	381	5
	$[Cl_4WN]^-$	340	100

[a]Relative abundances were adjusted by summing the observed intensities for the predicted peaks of each mass envelope and normalizing the largest sum to 100%

7.5 Film Structure

7.5.1 XRD

The X-ray diffraction (XRD) spectra in Figure 7-1 indicate amorphous and polycrystalline film deposition at 450 and 650°C, respectively, from the **3b** complex. The polycrystalline film has peak locations consistent with polycrystalline $\beta-WN_xC_y$.

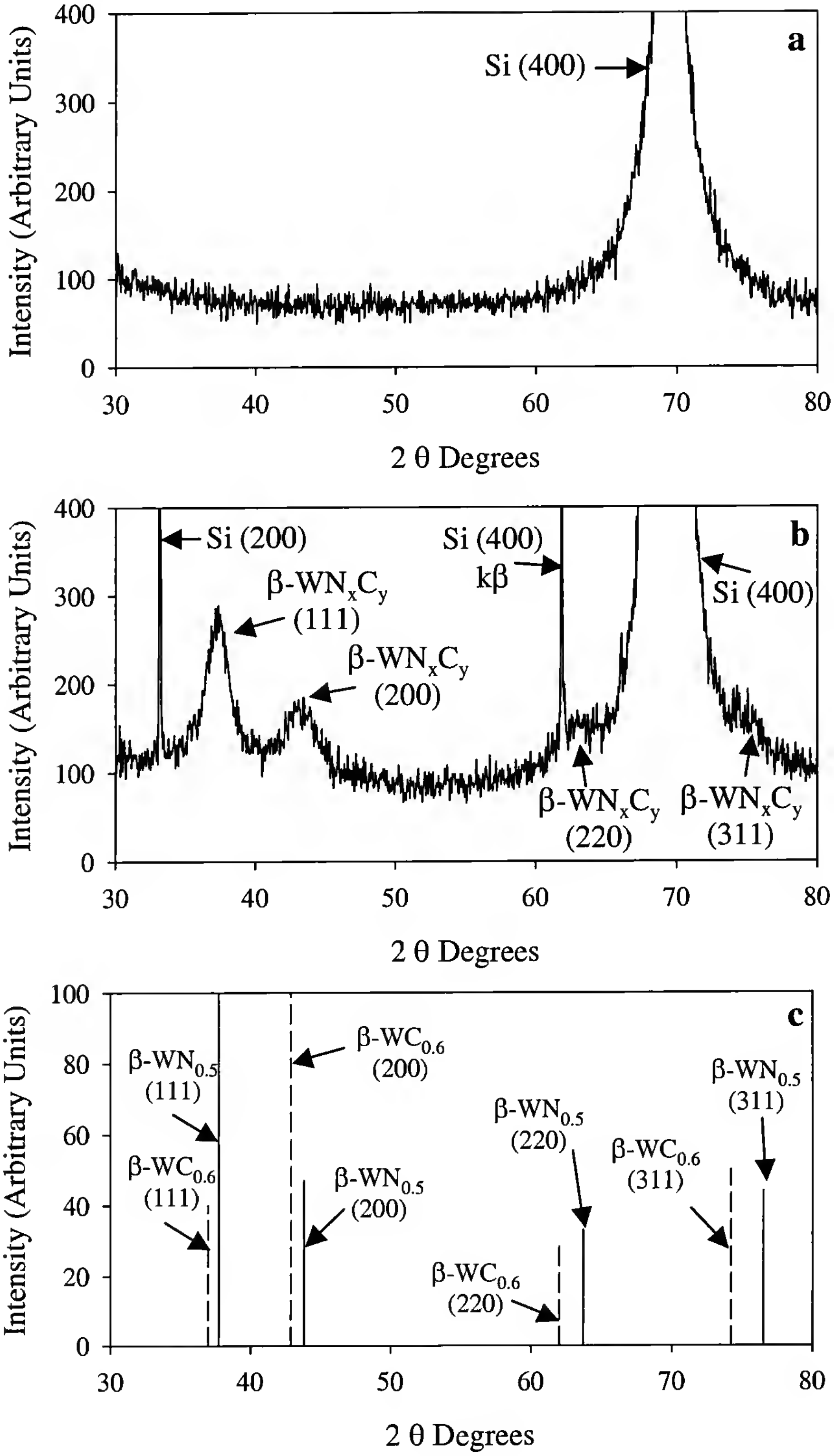

Figure 7-1. XRD spectra for films grown with **3b** on Si (100) in a H_2 atmosphere. a) 450°C. b) 650°C. c) Standard powder diffraction plots for β–$WN_{0.5}$ and β–$WC_{0.6}$.

Four characteristic peaks are evident, indicating that no preferred crystal orientation was present in the films. Primary reflections at 37.18 and 43.33 2θ degrees are consistent with (111) and (200) β –WN_xC_y growth planes, while additional reflections at 62.88 and 74.88 2θ degrees indicate (220) and (311) planes, respectively.

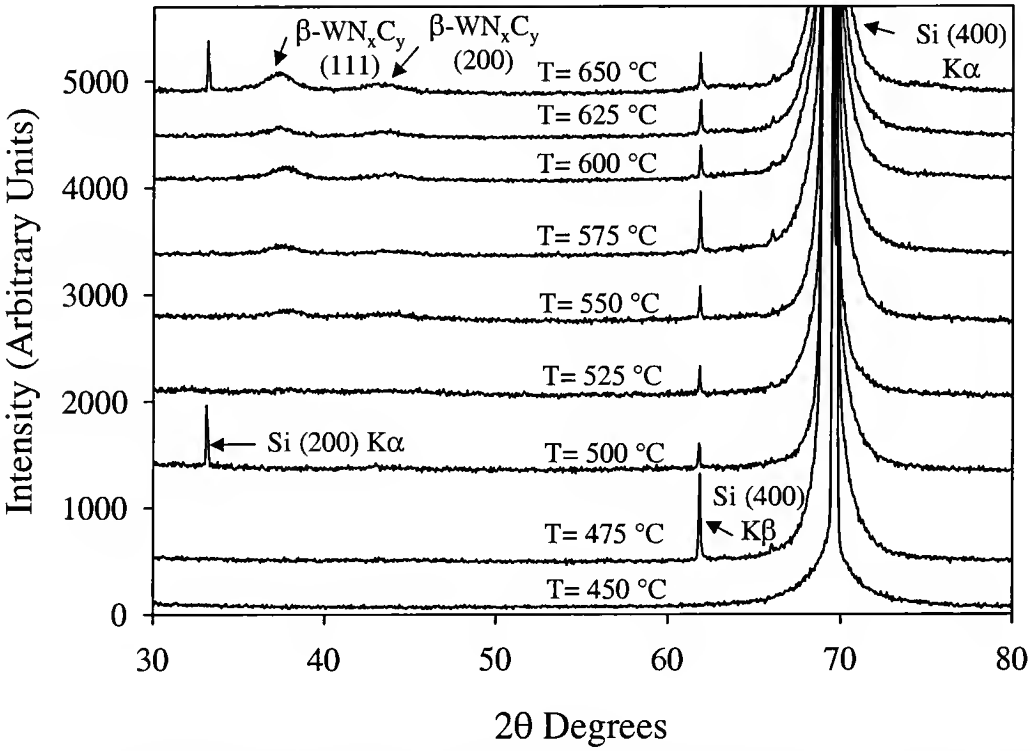

Figure 7-2. Change in XRD pattern with deposition temperature for films grown with **3b** on Si (100) in a H_2 atmosphere.

Figure 7-2 shows the evolution of film crystallinity with deposition temperature. For deposition at and below 525°C, the characteristic β –WN_x peaks are not observed. At 550°C, a broad peak appears near 37.63 2θ degrees, indicating polycrystalline β –WN_xC_y (111) growth. As the deposition temperature increases to 575°C, this peak sharpens and a broad peak at 44.08 2θ degrees appears, indicating β –WN_xC_y (200) growth. The peaks sharpen further as the temperature approaches 650°C, indicating polycrystalline grain growth. Some of the films displayed two additional peaks at 32.98

and 61.63 2θ degrees, representing Si (200) Kα and Si (400) Kβ radiation, respectively. Broad peaks emerge at 63.33 and 75.43 2θ degrees for growth at 650°C, indicating β $-WN_xC_y$ (220) and (311) growth. Since the formation of polycrystalline films is highly undesirable, deposition below 550°C with this precursor is required to grow an amorphous film.

7.5.2 Lattice Parameter

The dependence of lattice parameter on deposition temperature in Figure 7-3 was determined by XRD using the 2θ position of the (111) $\beta-WN_xC_y$ diffraction peak, with peak position calibrated to the Si (400) diffraction peak. The standard $\beta-WN_{0.5}$ (111) and $\beta-WC_{0.6}$ (111) peak positions are 37.735 and 36.977 2θ degrees (Figure 7-1c), respectively, and correspond to standard lattice parameter values of 4.126 and 4.236 Å. The position of the (111) reflection peak can vary as a result of a change in composition or a change in the film's residual stress. Assuming that compositional variation is responsible for the peak shift and, thus, lattice parameter change, trends in the relative concentrations of N, C, and Va on the interstitial sublattice can be suggested by coupling the peak shift with the compositions measured by AES (Figure 7-5), as discussed in Chapter 6. If the (111) peak position is higher than 37.735 2θ degrees, corresponding to a lattice parameter below 4.126 Å, then minimal C, a deficiency of N, and an excess number of Va exist in the polycrystals. This is true for deposition with **1b** at 500°C. A peak position between 37.735 and 36.977 2θ degrees, which corresponds to a lattice parameter between 4.126 and 4.236 Å, suggests mixing of N, C, and Va on the interstitial sublattice. This is the case for all polycrystalline films deposited from **3b**, and for films deposited at and above 550°C with **1b**. As mentioned in Chapter 6, however, $\beta-WN_xC_y$

polycrystals may be forming even at the lower temperatures, with C playing a role in the lattice parameter increase at lower temperatures.

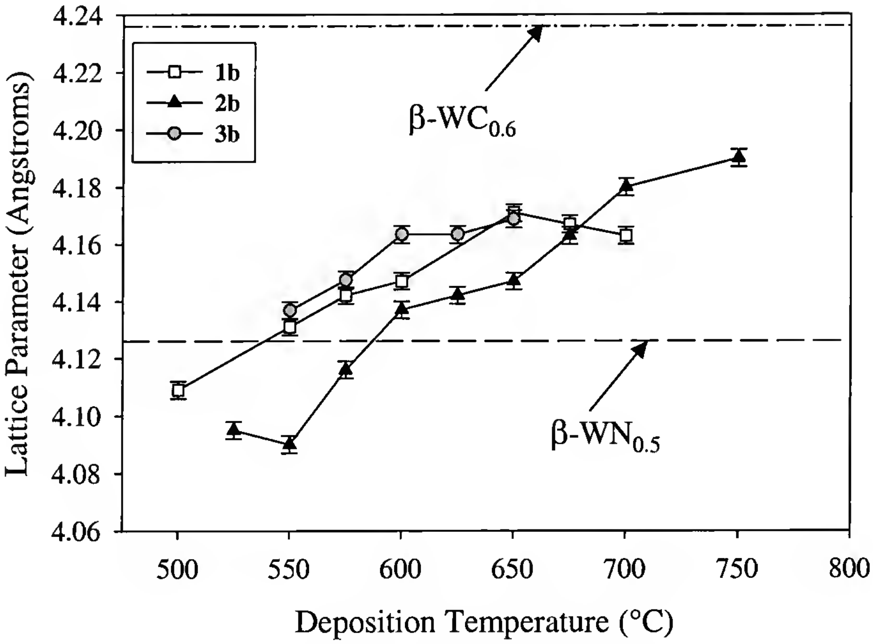

Figure 7-3. Lattice parameters for films grown from **1b**, **2b** and **3b**, based on the β–WN_xC_y (111) diffraction peak. The dashed line at 4.126 Å represents the standard lattice parameter value for β–$WN_{0.5}$, while the dash–dot line at 4.236 Å is that for β–$WC_{0.6}$. Error bars indicate uncertainty in lattice parameter (± 0.002 Å) due to X–ray Kα line broadening.

Values for lattice parameter in the films from **3b** increase with deposition temperature. Between 550 and 600°C, the lattice parameter increases from 4.14 to 4.16 Å. While N content decreases from 10 to 8 at.% through this temperature range, C content increases from 15 to 34 at.% (Figure 7-5). An increase in lattice parameter coupled with constant or decreasing N levels, as occurs for films deposited above 550°C, suggests that the amount of C incorporated into the interstitial sublattice is increasing in this region, causing expansion of the lattice. Increasing deposition temperature to 625°C does not cause a change in lattice parameter, but it increases slightly for deposition at

650°C to a maximum of 4.17 Å. This lattice parameter value coincides with the maximum lattice parameter for films deposited from **1b**, which also occurs at 650°C.

7.5.3 Polycrystal Grain Size

Grain size (t) was estimated using the Scherrer equation, as discussed in Chapter 6. The dominant (111) diffraction peak for the films was used as the reference peak for FWHM determination. As depicted in Figure 7-4, grain size for the films from **3b** increased with deposition temperature, varying from 34 to 48 Å over the 550 to 650°C temperature range. Below 550°C, the films were X–ray amorphous, hence the maximum grain size for these films was below 34 Å. The grain size increases most rapidly between 550 and 575°C, with grain growth slowing above this temperature. As mentioned in Chapter 5, increasing deposition temperature causes a competition between increased grain growth due to higher surface diffusivity and decreased grain growth due to

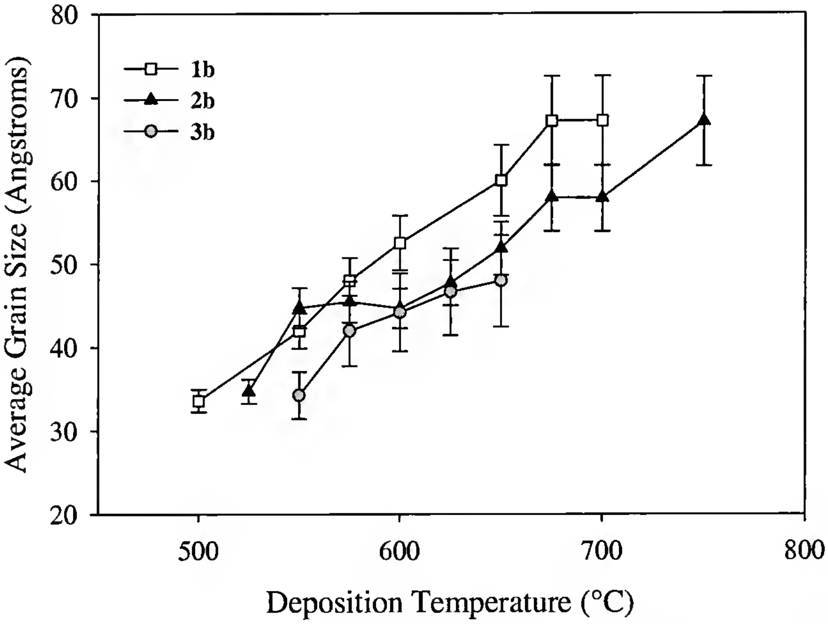

Figure 7-4. Change in average grain size with deposition temperature for polycrystalline films grown from **1b**, **2b** and **3b** based on the FWHM of the β–WN_xC_y(111) diffraction peak. Error bars reflect uncertainty in FWHM measurements.

increasing C concentration on the film surface, which inhibits surface diffusion. Interplay between these phenomena cause grain growth in regions with small shifts in carbon content and leveling off of grain size in regions with larger shifts in carbon content.

7.6 Film Composition

Auger results in Figure 7-5 indicate that W, N, C and O were present in the films deposited from **3b**, while Cl was not detected. The lowest C level, 6 at. %, occurs at the lowest deposition temperature, 450°C. Carbon content increases with deposition temperature from 6 to 38 at. % between 450 and 600°C. Above 600°C, C content levels off near 40 at. %. As in the case for the **1b** and **2b** precursors, the overall trend in C content for **3b** reflects the increasing tendency of the hydrocarbon groups present in the precursor ligands and the solvent to decompose with increasing deposition temperature.

The N content in films grown at 450°C was 4 at.%, and this rose to a maximum of 11 at. % for deposition at 500°C. Above 500°C, the N levels decrease, dipping to 2 at. % at 650°C. The higher N levels at lower temperature reflect the stability of the W–N multiple bond in the precursor molecule, which likely endures at deposition temperatures up to 500°C, inhibiting release of N into the gas phase during deposition. The drop in N above 500°C may indicate decomposition of the W–N multiple bond in the gas phase and/or increased N desorption from the film (to form N_2 gas) at higher temperature.

Again, O contamination resulted from post–growth exposure of the film samples to air. Incremental AES sputtering showed a steady decrease in O levels with increasing depth into the films. The O concentration was highest at 450°C, reaching 16 at. %, and decreased slightly to 11 at. % at 525°C. Amorphous films deposited below 550°C had low density and high porosity, which allowed substantial amounts of oxygen to penetrate into the film lattice. As the deposition temperature was increased to 550°C, the O content dropped sharply to 4 at. %. This was consistent with crystallization of the film in this

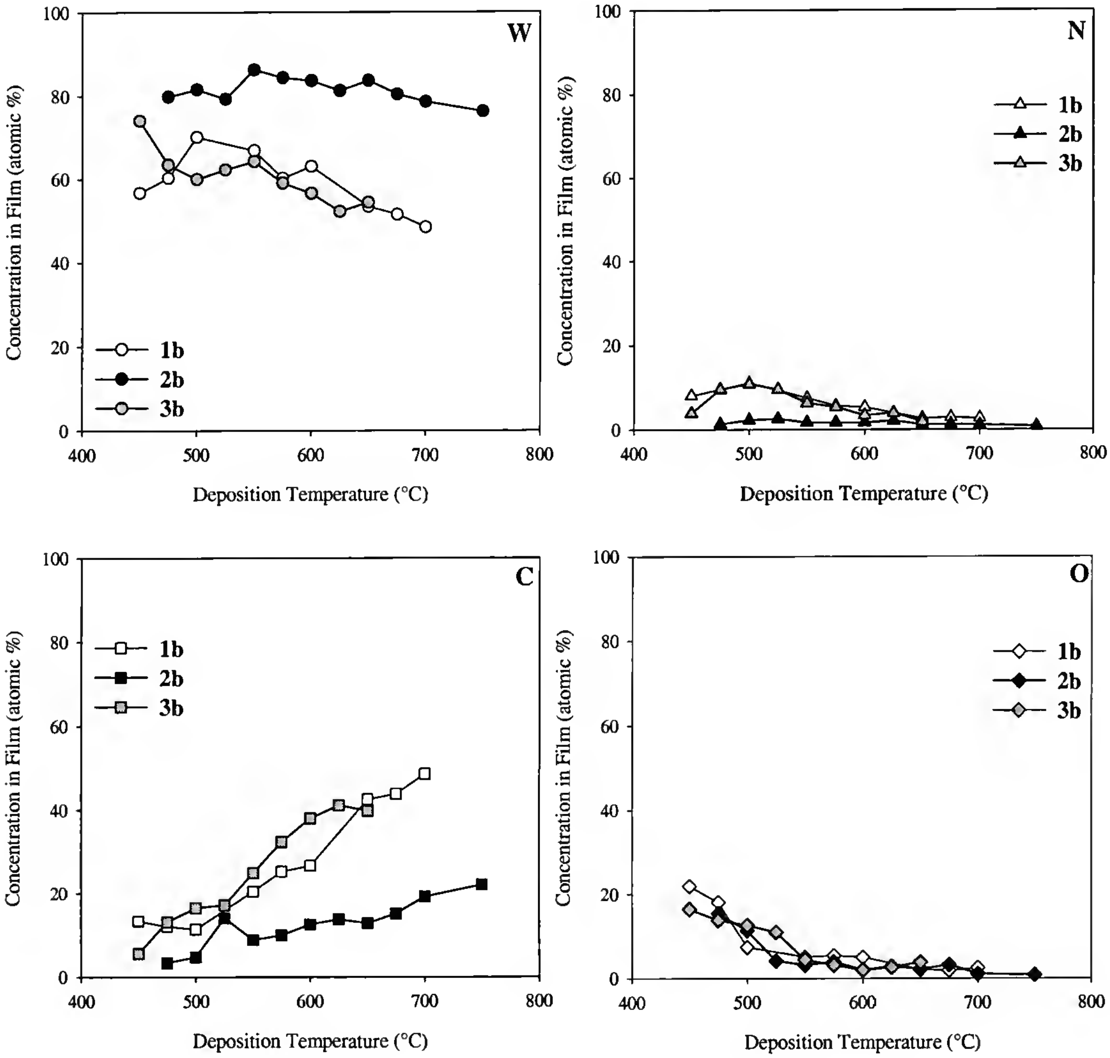

Figure 7-5. Comparison of W, N, C and O content in the films grown from **1b**, **2b** and **3b**. Data are from AES measurements after 2.0 minutes sputter.

temperature range. As the film crystallized, its microstructure densified, thereby inhibiting post–growth oxygen diffusion into the lattice [Pok91, Jos02]. As deposition temperature increased above 550°C, the O concentration dropped further, steadying out near 3 at. % at the highest deposition temperatures. This resulted from further film densification (by polycrystal grain growth) and increased C levels at higher deposition temperature, which stuffed the grain boundaries and blocked O in–diffusion. Again, porosity of amorphous films may be problematic, as defects in the film can degrade the barrier's resistance to Cu diffusion.

7.7 Film Growth Rate (XSEM)

Growth rates were estimated by dividing total film thickness (from X–SEM) by deposition time. Figure 7-6 depicts X–SEM photos for films grown at the lowest and highest growth temperatures, 450 and 650°C, respectively, which have corresponding deposition rates of 5 and 10 Å/min. An Arrhenius plot using the measured growth rates (Figure 7-7) indicates one growth regime, evidenced by a single line without any break points. The apparent activation energy (E_a) for deposition with **3b** was 0.15 eV, which is substantially lower than the typical activation energy range for CVD growth in the kinetic regime (0.5 to 1.0 eV) [Raa93].

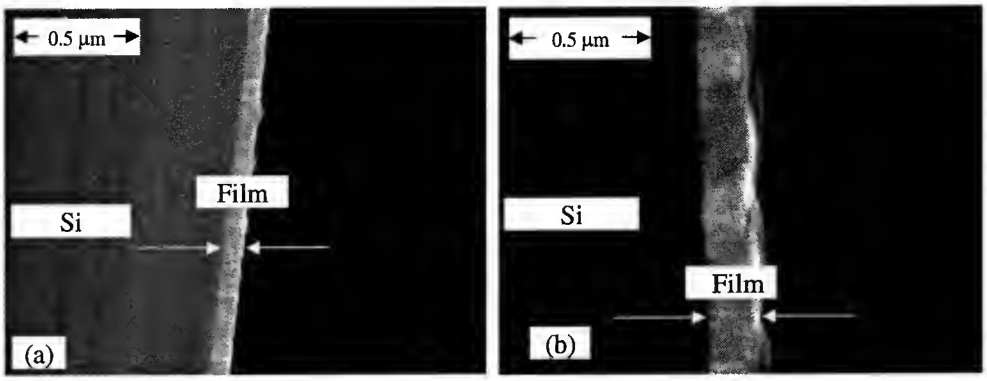

Figure 7-6. Cross–sectional SEM photo depicting thickness of films grown from **3b** on a Si (100) substrate. a) 450°C. b) 650°C.

Deposition with **3b** at temperatures below 450°C did not result in significant film growth. This suggests that while cleavage of the N–C bond in the imido moiety may be the rate–determining step for deposition from this family of precursors, another gas–phase or surface process dictates the minimum temperature required to initiate deposition. Deposition at 675°C resulted in deposition of black particles on the substrate and susceptor surface, indicating that gas–phase nucleation was occurring. For this reason, 650°C was deemed to be the upper temperature limit for deposition from this precursor.

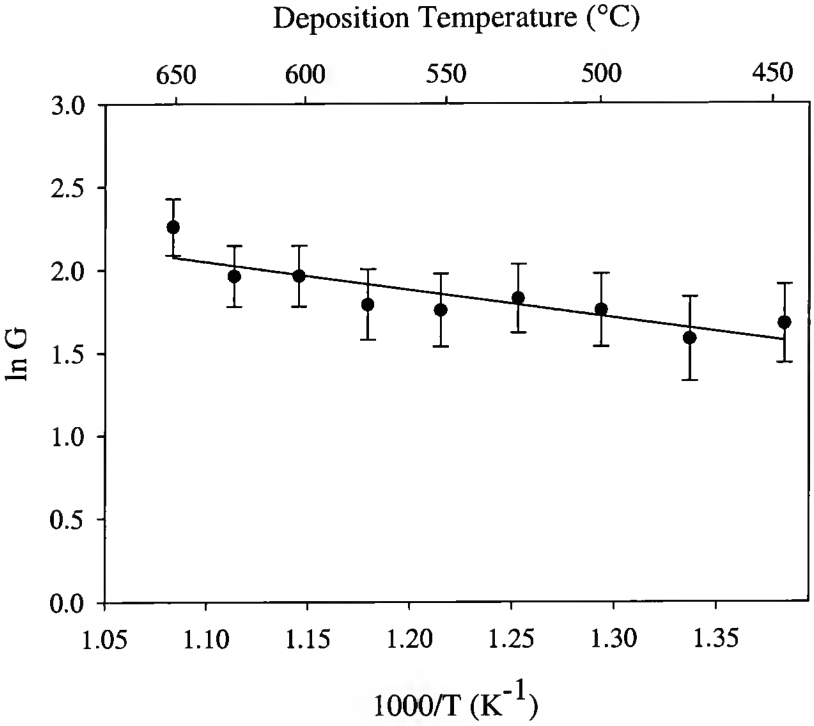

Figure 7-7. Plot of film growth rate on Si (100) vs. inverse temperature for deposition from **3b**. Error bars indicate uncertainty due to deposition temperature variation (+/– 10°C) and thickness measurement from XSEM photos.

7.8 Film Electrical Properties

7.8.1 Film Resistivity

Film resistivity was calculated with Equation 5–5, as discussed in Chapter 5. Sheet resistance measurements were collected using 4–point probe, and film thickness measurements were taken from X–SEM images. The variation of film resistivity with deposition temperature is shown in Figure 7-8. Deposition at 450°C produced films with the lowest resistivity value (287 μΩ–cm) despite C and O contamination levels of 6 and

16 at.%, respectively. This is slightly higher than the 225 μΩ–cm value for a film deposited at 475°C with **2b**, and lower than the 750 μΩ–cm value observed for films grown at 450°C from **1b**. The lower resistivity for films deposited at 450 °C from **3b** relative to **1b** was likely due to decreased N content in films from **3b**.

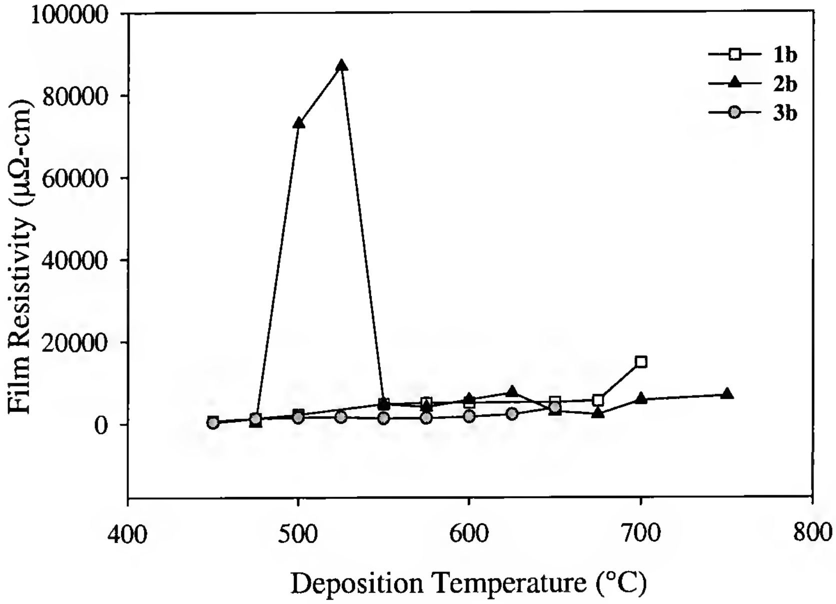

Figure 7-8. Variation of film resistivity with deposition temperature for films deposited with **1b**, **2b** and **3b**.

Film resistivity increases to 1260 μΩ–cm for deposition with **3b** at 475°C, likely due to increases in both N and C levels, which can increase film resistivity. The interplay of grain growth, C content and film thickness causes the resistivity to be fairly steady up to 600°C. Above this temperature, resistivity increases slightly, which is likely related to increased C content at higher temperature.

7.8.2 Film Sheet Resistance

To decouple the impact of film thickness from the film's electrical properties, the sheet resistance was plotted as a function of deposition temperature (Figure 7-9). The sheet resistance results follow a similar trend as the film resistivity. Sheet resistance increases with deposition temperature from 36 Ω/□ at 450 °C to 172 Ω/□ at 475 °C, and is fairly steady to 600°C. Above 600°C, the sheet resistance increases again, reaching a maximum value of 274 Ω/□ at 650 °C.

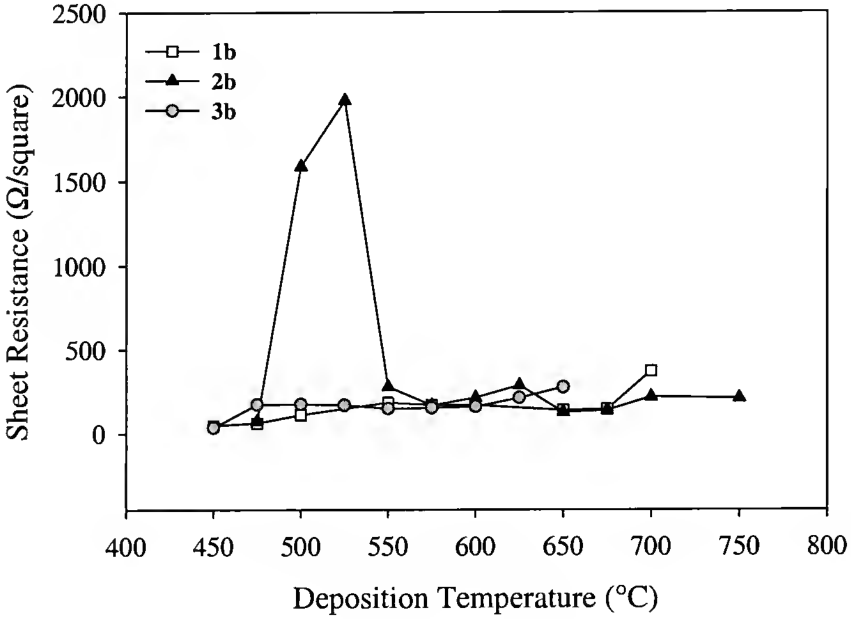

Figure 7-9. Variation of sheet resistance with deposition temperature for films deposited from **1b**, **2b** and **3b**.

7.9 Conclusions on Use of $Cl_4(CH_3CN)WNCH_2CH=CH_2$ to Deposit WN_x

In terms of their decomposition chemistry, the most significant difference between the isopropylimido complex **1b**, the phenylimido complex **2b**, and the allylimido complex **3b** are the respective dissociation energies of the N–C bond in the imido ligand. Using the corresponding primary amines as organic model compounds, the N–C bond of complex **3b** is expected to be approximately 11 kcal/mol weaker than the analogous bond in **1b** and 32 kcal/mol weaker than that in **2b** [Ben76]. Since cleavage of this bond is necessary for deposition of WN_x, one would expect there to be differences in film properties and deposition behavior for the three precursors. Table 7-2 summarizes some of the main differences in deposition behavior for the three precursors.

Table 7-2. Comparison of Deposition Behavior for the Three Precursors

Precursor	Deposition Temp. Range (°C)	Deposition Rate (Å/min)	Approx. Film Crystallization Temperature (°C)	E_a (eV)
$Cl_4(PhCN)W(NCH_2CH{=}CH_2)$, **3b**	450–650	5–10	550	0.15
$Cl_4(PhCN)W(N^iPr)$, **1b**	450–700	10–27	500	0.84
$Cl_4(PhCN)W(NPh)$, **2b**	475–750	2–21	525	1.41

The E_a for film deposition varied significantly for the three precursors, following a trend consistent with the strength of the N–C bond in the imido moiety of the precursor. Film deposition from **2b**, with the strongest N–C bond, yielded the highest value for E_a (1.41 eV), while that from **1b** yielded an intermediate value (0.84 eV). Deposition from **3b**, which presumably has the weakest N–C bond, yielded the lowest E_a (0.15 eV), which is well below the typical activation energy range for CVD growth in the kinetic regime (0.5 to 1 eV) [Raa93]. A plot of the E_a values for deposition with the three precursors against the N–C imido bond strengths for the analogous amines is linear (Figure 7-10), with a goodness of fit (R^2) of 0.96. The linear relationship suggests that cleavage of the N–C imido bond is the rate-determining step in film growth from the **1b**, **2b** and **3b** complexes. The strength of the bond in **3b** is so low, though, that film growth borders on being mass-transfer controlled. While the typical film growth temperature dependence in the mass-transfer controlled region is $\sim T^{1.7-1.8}$ (Chapter 5), the temperature dependence for film growth from **3b** was slightly higher ($\sim T^{2.1}$), indicating that the rate-determining step for film growth from **3b** has a very weak kinetic barrier. Changing the imido ligand from the isopropyl to the allyl complex may lower the N–C imido bond energy to where loss of the imido alkyl is no longer the rate–determining step at the surface. Weakening this bond any further would likely eliminate the kinetic barrier posed by this bond, causing a shift to mass–transfer controlled growth over the entire deposition temperature range. Imido moieties with higher N–C bond energies, such as those in **1b** and **2b**, present a substantial kinetic constraint on film growth at lower temperature.

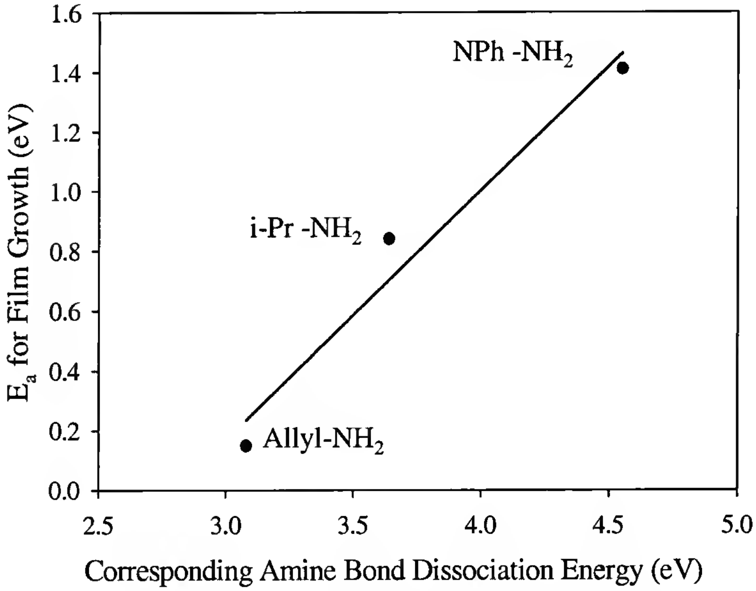

Figure 7-10. Variation of apparent film growth activation energy (E_a) with predicted N–C imido bond energies for the **1b** (i-Pr), **2b** (NPh) and **3b** (Allyl) precursors.

Overall, deposition with **3b** resulted in a substantially lower maximum growth rate than for deposition with **1b** or **2b**. Deposition rates ranged from 10 to 27 Å/min for films from **1b**, while the range was 2 to 21 Å/min for films from **2b** and 5 to 10 Å/min for films from **3b**. At 450°C, the deposition rate with **3b** (5 Å/min) was half of the value for deposition with **1b** (10 Å/min).

The shelf life of the **3b** precursor was poor relative to **1b** and **2b**, as evidenced by a discoloration of the precursor/solvent mixture after sitting in the syringe for more than 1 to 2 days. This color change was accompanied by a negligible growth rate and/or a shift in film composition away from the general trend. The decrease in deposition rate for films from **3b** may be due to a lower concentration of precursor available, due to decreased stability of the **3b** precursor. Alternatively, cleavage of the N–C imido bond may occur to a substantial degree in the gas phase for **3b**, in contrast to **1b** and **2b**, leading to oligomerization or some other gas phase process that consumes the remaining W–based moiety. The small kinetic barrier posed by the N-C imido bond in **3b**, whose deposition behavior borders on being mass–transfer controlled, means that adequate energy may be available in the gas phase to cleave this bond prior to the precursor's arrival at the deposition surface.

Film crystallization occurs for growth at 550°C with **3b**, compared to 500 and 525°C for **1b** and **2b**, respectively. This may be due to higher C levels in the films from **3b** relative to those from **1b** and **2b**. Higher C content at a given deposition temperature decreases surface diffusivity, thereby suppressing crystallization in the film. The maximum deposition temperature for films deposited from **3b** was 650 °C, as compared to 700 and 750°C for **1b** and **2b**, respectively. For all three precursors, deposition above the respective maximum growth temperature resulted in formation of black particles on the substrate and susceptor, which subsequently compromised film quality. The magnitude of the maximum deposition temperatures for the three precursors reflects the stability of the N–C bond in the imido group for each precursor. The precursor containing the weakest bond, **3b**, has the lowest maximum deposition temperature, while the precursor with the strongest bond, **2b**, has the highest, with the **1b** precursor falling in between. As mentioned above, the weaker N–C imido bond in **3b** did not lead to a decrease in the minimum deposition temperature relative to growth with **1b**.

The strength of the N–C imido bond has a strong effect on the amount of N incorporated into the film. If the N–C imido bond strength is relatively high, as with **2b**, the imido–N group stays intact, causing cleavage of the W–N bond, which leaves the films deficient in N. If the bond strength is relatively low, as with **1b** and **3b**, the alkyl group cleaves from the N more easily, leading to substantial N in the film. The amount of N incorporated into films from **1b** and **3b** is similar at all temperatures except the lowest one (450°C). The value for N content at 450°C is lower for **3b** (4 at.%) than for **1b** (8 at.%). The reason for this is unclear, as one might expect the weaker N–C bond in the allylimido ligand to enhance N incorporation by decreasing the likelihood for the entire imido ligand to desorb intact from the reaction surface. If cleavage of the imido N–C bond occurs in the gas phase, however, some of the resulting nitrido complexes may be consumed in other processes before the W–containing moiety reaches the deposition surface. EI mass spectral data indicate 78% and 12% relative abundance for the $[Cl_3WNH]^+$ fragment from **1a** (Chapter 5, Table 5–1) and **3a** (Table 7-1), respectively, while this fragment did not appear for **2a** (Chapter 6, Table 6–1). A lower relative abundance for $[Cl_3WNH]^+$, coupled with higher relative abundances for the $[Cl_4W]^+$ and $[Cl_3W]^+$ fragments and the presence of a $[Cl_2W]^+$ fragment for **3a** (Table 7-1), are further evidence that loss of imido N is more likely for **3a** than for **1a**. This would lead to lower N levels in films from **3b** relative to **1b**. These results suggest that an optimal window for N–C imido bond energy exists in these precursors, with high and low bond energy values detrimentally affecting N content.

Maximum N content for films from **1b** and **3b** occurred near 500°C, while that for **2b** occurred near 525°C. Throughout the temperature range studied, the N content in films deposited from **2b** was significantly lower than those grown from **1b** and **3b.** The fact that films from **2b** contained lower levels of both N and C than those from **1b** or **3b** suggests that the phenylimido moiety is more likely to dissociate intact than the isopropylimido or allylimido ones. This is consistent with the higher N–C bond strength in the phenylimido group relative to the others. Similar N levels for growth with **1b** and **3b** at and above 475°C suggest that N derived from PhCN decomposition may supplant the precursor as the principal N source for the films deposited above 450°C. While deposition from **1b** in 1,2–DCB rather than PhCN solvent resulted in reduced N levels, N was still deposited in those films, indicating that the imido N was retained in the films to some degree. Testing the **3b** precursor with a N–free solvent, such as 1,2–DCB, would be useful to determine if the allyl imido ligand causes a change in precursor–derived N content compared to films deposited from **1b** in 1,2–DCB.

Carbon levels in the films from **3b** were slightly higher than those from **1b** for most deposition temperatures, and significantly higher than those from **2b** (Figure 7-5). Above 500°C, films from the three precursors typically exhibited a gradual rise in C content, with **1b** and **3b** affording a steeper rise in C with increasing growth temperature compared to **2b**. The fact that films from **2b** contained lower levels of both N and C than those from **1b** or **3b** suggests that the phenylimido moiety is more likely to dissociate intact than the isopropylimido or allylimido ones, consistent with the higher N–C bond strength in the phenylimido group. Higher C levels for **3b** compared to **1b** were probably caused by the decreased stability of the allylimido ligand relative to the isopropylimido one.

Oxygen content for films deposited with all three precursors was essentially similar. For all three precursors, O levels were highest for amorphous films, which were deposited at the lower end of the temperature range. AES indicated a decrease in O content with increasing sputter depth into the films; hence, high O levels were attributed to post–growth exposure of the films to air. The low density and high porosity of the amorphous structures grown at lower temperatures allow more rapid diffusion of O from the air into the films and provide a large surface to volume ratio for adsorption. Oxygen content drops considerably for films from each of the three precursors above their respective crystallization temperatures, due to film densification upon crystallization. In addition to crystallization at higher deposition temperature, increased C content in the films grown at higher temperature is believed to further inhibit post–growth oxygenation of the films by stuffing grain boundaries.

Lattice parameter shifts were also dependent on the precursor. Figure 7-3 shows lattice parameter generally increasing with temperature for films from **1b**, **2b** and **3b**. Lattice parameter was slightly higher for films deposited with **3b** relative to **1b**, and significantly higher than for **2b** at deposition temperatures ≤ 650°C. Higher C content in films from **1b** and **3b** compared to **2b** is consistent with lower lattice parameter for films from **2b**, as less C is available to expand the polycrystalline lattice in films from **2b**. Since N levels are similar for polycrystalline films from **1b** and **3b**, differences in lattice parameter are likely caused by differing C content on the interstitial sublattice. Films from **3b** have slightly higher C content than those from **1b**, which may explain the slightly higher lattice parameter in films from **3b**. Interestingly, the lattice parameter for films deposited with both **1b** and **3b** is 4.17 Å at 650°C. Polycrystalline films deposited by **1b** and **3b**, then, have adequate N, even at high temperatures, to be considered primarily β–WN_x into which carbon is incorporated to form β–WN_xC_y. The β–WN_xC_y polycrystals deposited with **1b** and **3b**, although N–deficient at higher temperatures, contain sufficient N to prevent a shift from formation of β–WN_xC_y toward β–WC_y. This is not the case for films from **2b**, however, which experience a shift toward β–WC_y for deposition at temperatures above 675°C, as discussed in Chapter 6. The difference in lattice parameter for films from **1b** and **3b** at 450°C suggests that the imido ligand takes part in the deposition of C into the β–WN_xC_y polycrystals, potentially by interacting with the W atom during deposition.

Grain growth behavior was similar for the three precursors, with grain size increasing from lowest to highest deposition temperature. The smaller grain size for films from **2b** relative to **1b** was attributed to the difference in the strengths of imido N–C bonds in the precursors, where the weaker bond in **1b** afforded higher growth rate and grain size for a given deposition temperature. While the same bond is presumably weakest in **3b**, the estimated grain size was surprisingly lower than that for films deposited with **1b** and **2b**. The reason for this is unclear, but may be related to differences in the decomposition mechanism of **3b** relative to **1b** and **2b**, which cause a decreased growth rate for films from **3b**.

As mentioned in Chapter 2, recent reports indicate interest in β–WN_xC_y as a potential barrier material. Although films deposited from **3b** had relatively low N content (compared to typical WN_x films), this precursor may be of interest for β–WN_xC_y deposition. We have demonstrated the ability of an NH_3 co–reactant to dramatically increase the N content for films deposited from **1b**, as discussed in Chapter 5, and a similar approach with **3b** may be possible. A similar approach with **2b** did not result in increased N content in the deposited film, and may be due to the stronger N–C bond in the imido group of **2b** inhibiting reaction with NH_3. If this is the case, the decreased energy of the N–C bond in the imido group of **3b** relative to **1b** may make **3b** even more reactive with NH_3 than its **1b** analogue.

With the exception of the anomalous results for growth at 500 and 525°C with **2b**, a comparison of the sheet resistance, which negates the impact of film thickness on electrical properties, shows that films from **1b**, **2b** and **3b** have similar electrical properties when deposited at or below 625°C. The sheet resistances for films from **1b** and **3b** are 47 and 36 Ω/□, respectively, for deposition at 450°C, rising above these values for increasing deposition temperature. The sheet resistance for films from **3b** at 650°C is 274 Ω/□, compared to 139 and 127 Ω/□ for films from **1b** and **2b**, respectively. The higher value for films from **3b** is related both to elevated C content and smaller average grain size at 650°C compared to films from the other precursors. Films from **1b** have similar C content (43 at.%) to those from **3b** (40 at.%) at 650°C, but have a larger average grain size (60 Å) compared to films from **3b** (48 Å), which tends to lower sheet resistance. Films from **2b** have a slightly larger grain size (52 Å) than those from **3b**, and also substantially lower C content (13 at.%), both of which tend to decrease sheet resistance.

Comparison of the film growth properties of **3b** to those of **1b** and **2b** allowed evaluation of the effect of the imido N–C bond dissociation energy on film growth and properties. Films deposited from **2b** were deficient in N compared to those from **1b** and **3b**, consistent with a tendency of the stronger imido N–C bond of **2b** to result in dissociation of intact NPh fragments during deposition. As mentioned above, an optimal window for N–C imido bond energy appears to exist in these precursors. If the energy of this bond is too high (as in **2b**), the W–N bond cleaves, leaving the films very deficient in N. If the bond energy is too low (as in **3b**), N–C bond cleavage may occur in the gas phase, leading to processes that cause loss of imido N before final reaction at the substrate surface. A moderate N–C imido bond energy (as in **1b**) combines better N retention in the films with a substantial growth rate, due to enhanced precursor stability (relative to **3b**) coupled with greater likelihood of N–C imido bond cleavage (relative to **2b**).

As discussed in Chapter 6, films from the isopropylimido precursor **1b** are superior to those from the phenylimido precursor **2b** for barrier applications because they can be deposited at a lower minimum temperature (450°C), contain more N, and have lower sheet resistance. Moreover, the isopropylimido precursor **1b** appears to be superior to the allylimido precursor **3b**, due to higher growth rate and N content at their mutual lowest deposition temperature (450°C). A variety of other precursors, listed in Appendix B, have also been tested for MOCVD of WN_x. These precursors, however, did not prove to be promising.

CHAPTER 8
COPPER BARRIER TESTS

8.1 Copper Deposition Results

Barrier films deposited from the i–Pr complex **1b** in PhCN solvent at the lowest temperature (450°C) were used for Cu barrier testing. ECD and sputtering, the details of which are discussed in Chapter 4, were used to deposit Cu on the barrier films. Vacuum had to be broken after barrier film deposition and prior to Cu deposition, due to the nature of our CVD reactor set–up. This vacuum break enables large scale O in–diffusion into our barrier films, especially for the highly porous films deposited at low temperature. ECD Cu deposited by the bath chemistry detailed in Chapter 4 is reported to enhance the removal of surface oxides from the barrier layer, which form due to exposure of the barrier films to air [Sha01]. While some preliminary ECD Cu results are shown below, the properties of these films during the Cu removal process (discussed below) made them unusable for barrier integrity analyses. Moreover, due to difficulties with Cu oxidation during anneals in sweeping N_2 flow, only the sputtered Cu/barrier/Si stack samples which had been annealed in–vacuo after Cu sputter deposition were examined in detail.

8.2 Electrical Measurements

Sheet resistance of the deposited Cu films was measured by 4–point probe. Measurements indicated that as–deposited ECD Cu had a sheet resistance of 0.29 $\Omega/\square$, while as–deposited sputtered Cu had a sheet resistance of 0.54 $\Omega/\square$. The difference in sheet resistance was likely due to film stress and voids in the sputtered Cu, which can increase resistivity. Sputtered Cu films deposited at room temperature suffer from film stress and voids due to the inability of Cu atoms on the film surface to diffuse at low temperature. The film resistivity can be lowered by sputtering at elevated substrate temperature or by annealing the film stack. As discussed in Section 8.4.2, sheet resistance for sputtered Cu films decreased to a value of 0.24 Ω/□ after annealing the film stack in–vacuo at 500°C.

8.3 Scotch Tape Tests

Scotch tape tests were conducted on as–deposited ECD and sputtered Cu/barrier stacks. The sputtered Cu had poor adhesion to the barrier layer, and came off completely onto the Scotch tape, leaving the barrier intact on the Si (100) substrate. This reflects poor adhesion at the sputtered Cu/barrier interface, likely caused by a significant quantity of oxide at this interface. The ECD Cu had strong adhesion to the barrier, however, which may reflect the ability of the electrochemical bath to reduce/remove the oxide at the barrier surface before Cu deposition begins. While the ECD Cu had good adhesion to the barrier, the ECD Cu and barrier layers came off onto the Scotch tape together. This indicates that the barrier/Si adhesion strength was lower than the ECD Cu/barrier adhesion strength. This contrasts with Scotch tape tests indicating good barrier/Si adhesion strength (discussed in Chapter 5), and suggests that the electrochemical bath deposition process weakens the barrier/Si interface. The weakening of this interface may be due to removal of oxygen from the bulk of the barrier film (due to the barrier's porosity), rather than just the removal of surface oxides.

8.4 Barrier Integrity Tests

After Cu deposition, the samples were annealed at various temperatures for 30 minutes to determine the maximum temperature at which the barrier could repel Cu from diffusing into the Si substrate. Annealing of the samples was first attempted in a Bio–Rad SKZ–1 Seiwa Optical microscope with a built–in bell jar chamber and heater assembly. N_2 gas was flowed through the chamber during annealing to minimize the amount of oxygen in the chamber and to sweep out any Cu present in the vapor above the sample. Significant oxidation of the Cu during annealing in the bell jar, however, necessitated an in–vacuo anneal of the sputtered Cu/barrier/Si stack samples in the sputter chamber after Cu deposition. Unlike sputtered Cu, which is deposited in a vacuum chamber, ECD Cu was deposited in ambient air, making an in–situ vacuum anneal of the ECD Cu/barrier/Si stacks impossible. Moreover, attempts to etch ECD Cu from the stack prior to SIMS depth profiling resulted in dissolution of both the Cu and the barrier layers into the etchant solution. For this reason, sample stacks containing ECD Cu were not useful for SIMS depth profiling analyses. The barrier integrity study was therefore focused on the sputtered Cu/barrier/Si stack samples that were annealed in–vacuo, as only Cu dissolved into the etchant from these samples.

8.4.1 XRD

XRD was done as a quick first check to determine if massive barrier failure had occurred. The presence of $CuSi_x$ compounds on the XRD spectra would indicate large–scale Cu penetration into the Si substrate, meaning that the barrier layer failed to prevent diffusion. Figure 8-1 shows XRD spectra for ECD Cu/barrier/Si stacks, while Figure 8-2 shows spectra for sputtered Cu/barrier/Si stacks. Note that the Si (400) peak in the as–received spectrum of Figure 8-1 is not visible, due to higher ECD Cu film thickness relative to the sputtered Cu layer shown in the as–received spectrum in Figure 8-2. The spectrum for the as–received ECD stack (Figure 8-1) shows three Cu orientations deposited by ECD, indicating polycrystalline Cu deposition.

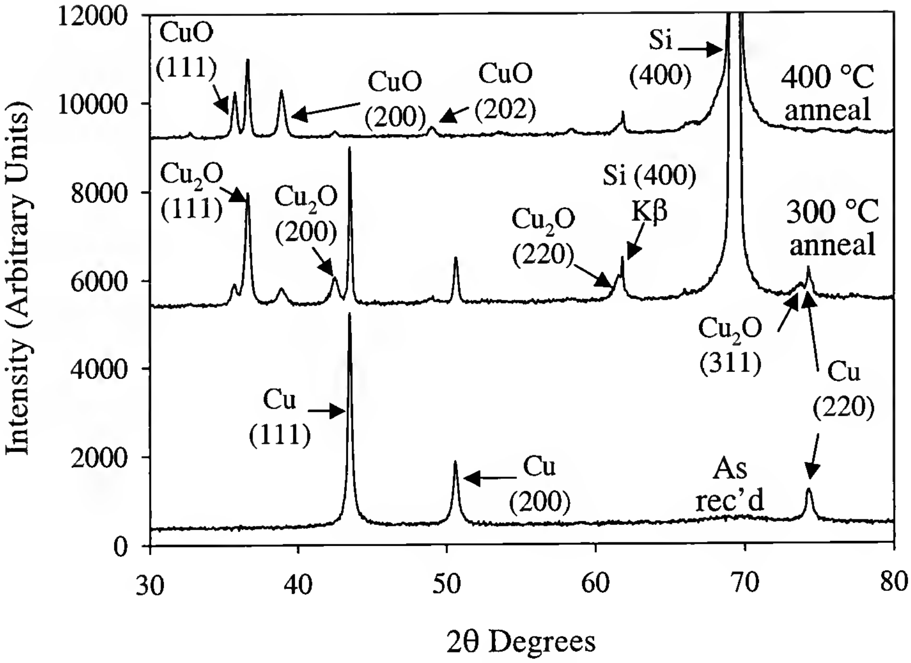

Figure 8-1. XRD spectra for ECD Cu, before and after annealing in sweeping N_2 flow. The most intense peak is for Cu (111) at 43.50 2θ degrees, which is the desired phase from an electromigration and resistivity standpoint, but other peaks for Cu (200) and (220) at 50.65 and 74.50 are also present. The as–received spectrum in Figure 8-2 for sputtered Cu indicates only two peaks at 43.50 and 50.70 2θ degrees, consistent with the Cu (111) and (200) orientations. While the Cu (111) and Cu (200) typically appear together in deposited Cu films, maximizing the intensity ratio of Cu (111) to Cu (200) is desirable. The intensity ratio in the as–received ECD Cu film is ~2.8, while that for the as–received sputtered Cu was ~2.2 (Figure 8-2), suggesting that ECD is superior to sputtering for preferential deposition of Cu (111) on our barrier films.

The spectra in Figure 8-1 for samples after annealing do not indicate the presence of any peaks consistent with $CuSi_x$ compounds, hence massive ECD Cu in–diffusion into the underlying Si after annealing up to 400°C is unlikely. While silicides are not present, spectra for the annealed stacks do indicate the presence of several Cu and CuO_x peaks.

The ECD Cu stack sample annealed at 300°C still shows the Cu (111), (200) and (220) peaks, but contains oxide peaks as well. Peaks at 35.75 and 39.25 2θ degrees are consistent with the (111) and (200) growth planes of CuO, respectively, while peaks at 36.65, 42.55, 61.60 and 74.30 2θ degrees are consistent with the (111), (200), (220) and (311) growth planes of Cu_2O, respectively. The ECD Cu stack sample annealed at 400°C does not contain any peaks consistent with pure Cu. This stack still contains the Cu_2O (111) and (220) orientations, but the other Cu_2O peaks have disappeared in favor of CuO. One new CuO peak appears at 49.10 2θ degrees, consistent with the (202) orientation. While the annealed ECD Cu spectra contain peaks consistent with Cu, CuO and Cu_2O, the annealed sputtered Cu spectra indicate the presence of only CuO and Cu_2O polycrystals. The sputtered Cu sample annealed at 300°C has one peak at 36.65 2θ degrees, which indicates the Cu_2O (111) growth plane. The sputtered Cu sample annealed at 400°C has peaks at 35.75 and 39.05 2θ degrees, which indicate the CuO (111) and (200) growth planes. Several of the ECD and sputtered Cu spectra display additional peaks at 32.70 and 61.85 2θ degrees, representing reflections from the underlying Si consistent with Si (200) $K\alpha$ and Si (400) $K\beta$ radiation, respectively.

The increase in CuO intensity and concomitant decrease in Cu_2O intensity when increasing annealing temperature from 300 to 400°C indicates the increased stability of CuO relative to Cu_2O, assuming that adequate O is available to make a 1:1 stoichiometric oxide. The presence of Cu peaks on the ECD Cu samples after annealing at 300°C, but not on the sputtered Cu samples annealed at the same temperature, was due to increased thickness of ECD Cu relative to the sputtered Cu layer. The thicker ECD Cu layer was not consumed by oxide formation as quickly as the thinner sputtered Cu layer.

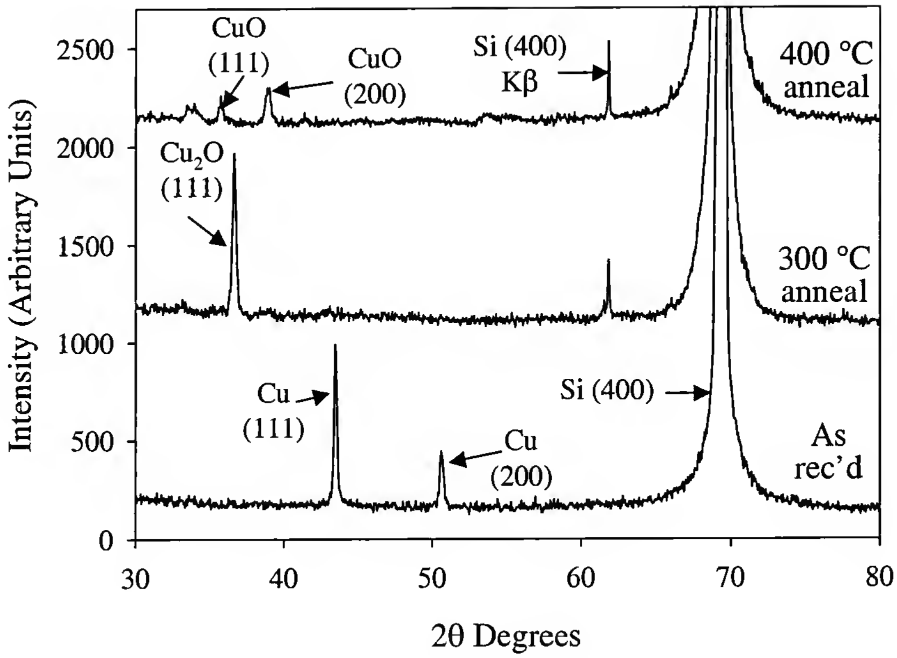

Figure 8-2. XRD spectra for sputter deposited Cu, before and after annealing in sweeping N_2 flow

ECD and sputtered Cu stack samples were observed using a SKZ–1 microscope during annealing in the bell jar assembly. A change in the properties of the Cu layer was visually apparent, indicated by an abrupt color shift from shiny, metallic Cu to a dull gray CuO_x at approximately 100 °C. For the samples annealed at 500 °C, the Cu layer was observed to peel away from the barrier at approximately 475 °C.

Figure 8-3 shows XRD spectra for sputtered Cu/barrier/Si sample stacks before and after annealing in–vacuo in the sputter chamber. Sputtered Cu/barrier/Si stacks annealed in–vacuo in the sputter chamber did not undergo a color shift during annealing, as the sputtered Cu maintained the same shiny luster as that for the as–deposited film, even after an in–situ anneal at 500°C. This indicated that the source of O leading to oxidation of the top surface of the sputtered and ECD Cu during the bell jar anneals was atmospheric O rather than O diffusing from the Cu–barrier interface to the surface of the Cu. Annealing *in vacuo* would appear to be a more conservative test than annealing in the bell jar, because Cu is not consumed by reaction with atmospheric oxygen in this case, leaving more Cu available to potentially diffuse into the barrier. None of the spectra indicate the presence of any peaks consistent with $CuSi_x$ compounds, even after annealing at 500°C, hence massive in–diffusion of Cu into the underlying Si after annealing *in vacuo* is unlikely. The spectra do indicate the presence of polycrystalline Cu, without any oxide peaks being present. Grain growth occurred for the Cu films after annealing *in vacuo*, as is evident by an increase in intensity and sharpness of the Cu (111) peak when comparing spectra for the as–received films to the annealed ones. The difference between XRD spectra for films annealed *in vacuo* and in atmosphere highlights the importance of annealing *in vacuo* to prevent degradation and atmospheric oxidation of the Cu layer during annealing. The presence of O in the barrier and/or Cu layers can be eliminated by depositing the Cu on the barrier layer without a vacuum

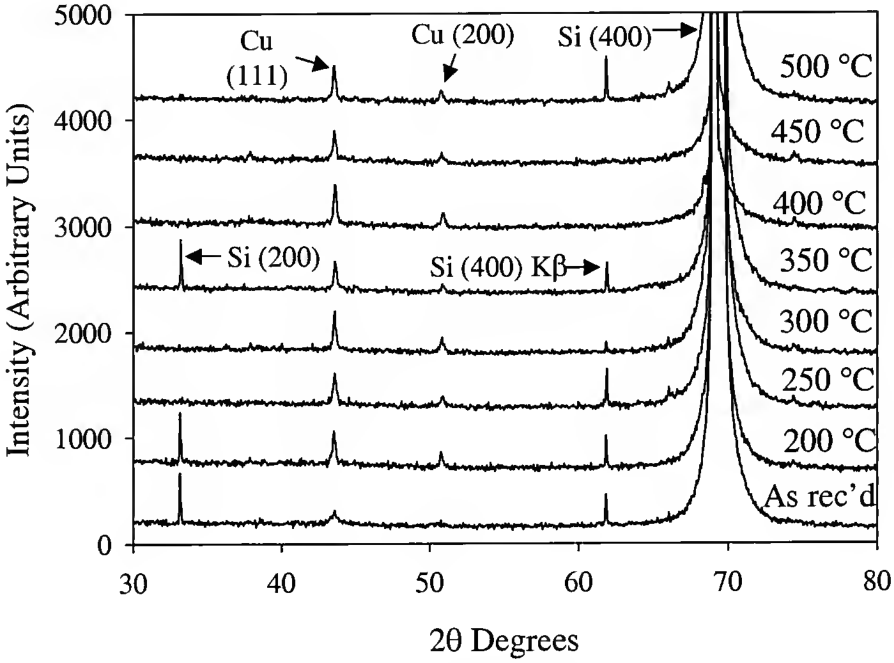

Figure 8-3. XRD spectra for as–received and annealed sputtered Cu/barrier/Si stacks, with annealing temperatures listed on the right side of the diagram. Annealing was performed *in vacuo* in the sputter chamber.

break (discussed further in Chapter 9), followed by subsequent annealing of the stack in–vacuo. Eliminating O from the barrier and Cu layers would give the most robust test of a barrier's ability to resist Cu diffusion.

8.4.2 Electrical Measurements

Four–point probe measurements were attempted on the samples that were annealed in the bell jar, but the film surface, which was presumably copper oxide, was too resistive to give a sheet resistance measurement. Measurements were obtained for sample stacks containing sputtered Cu that were annealed *in vacuo*, however. The results are shown in Figure 8-4. The results indicate that the sheet resistance of the as–deposited sputtered Cu film drops after the *in vacuo* anneal. This is consistent with XRD spectra, which indicate grain growth in the Cu film after annealing. Increasing grain size in the Cu films tends to decrease the resistance to current flow, which is indicated by the drop in sheet resistance for annealed films relative to the as–deposited one. Some variation in

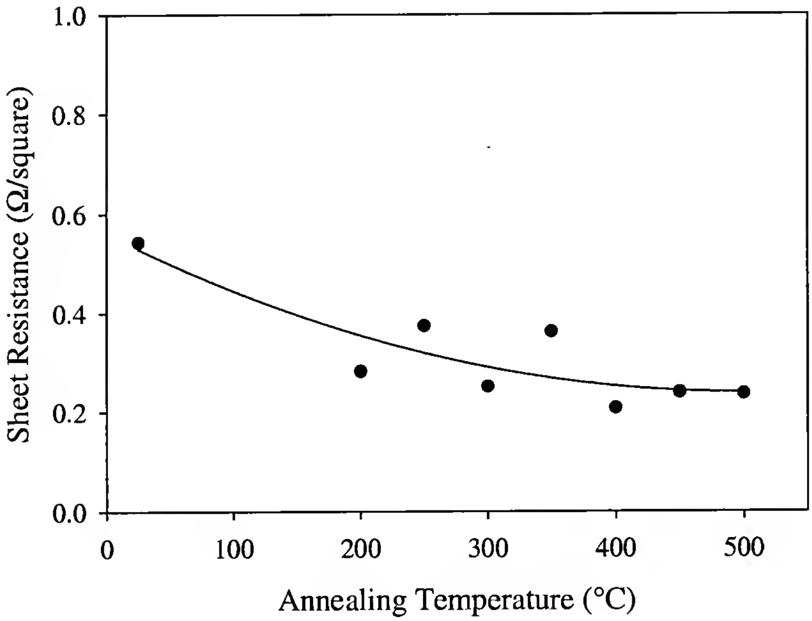

Figure 8-4. Variation of Cu sheet resistance with annealing temperature for a sputtered Cu/barrier/Si stack annealed *in vacuo*. As–deposited Cu sample shown with annealing temperature of 25°C.

sheet resistance for the annealed samples is evident in the plot, but the general trend indicates a decrease in sheet resistance with higher annealing temperature. If large–scale Cu penetration through the barrier was occurring, one would expect an increase in sheet resistance as the Cu moves into the barrier and Si substrate.

8.4.3 Depth Profiling Analysis

AES depth profiling was done as a first pass to determine if the barrier prevents large–scale Cu diffusion. Figure 8-5 shows a depth profile of a Cu/barrier/stack annealed at 300°C in the bell jar assembly. After nearly 40 minutes of sputtering, the Cu signal disappears to the noise level. The Si signal rises above the noise level after slightly more than 40 minutes of sputtering, suggesting that the barrier prevented Cu from intermixing with Si during the 300°C anneal. Significant O contamination is evident in the Cu and barrier layers, with the Cu layer's O contamination coming from ambient oxygen during the anneal. Since the consumption of Cu by oxide formation could presumably slow the advance of Cu through the barrier, samples which were annealed *in vacuo* need to be checked by depth profiling.

In addition to testing of samples annealed *in vacuo*, depth profiling by SIMS should be done to get a more conservative analysis of the barrier's ability (or lack thereof) to prevent Cu diffusion, since the elemental detection limits for SIMS are much lower than those for AES. To prevent knock–in effects from ion bombardment during SIMS, any Cu on the samples after annealing must be stripped off prior to SIMS depth profiling [Wan01b, Bai90]. A variety of etchant recipes for the removal of Cu deposited on WN_x barrier layers have been reported in the literature. One report suggested a Cu etchant containing H_3PO_4:HNO_3:CH_3COOH:H_2O with a ratio of 80:5:5:10 [Lee98c], while other reports suggested 10% nitric acid (HNO_3) [Iva99] or "diluted" HNO_3 in water [Vij99]. Due to its simplicity, the 10% HNO_3 in water formulation was used.

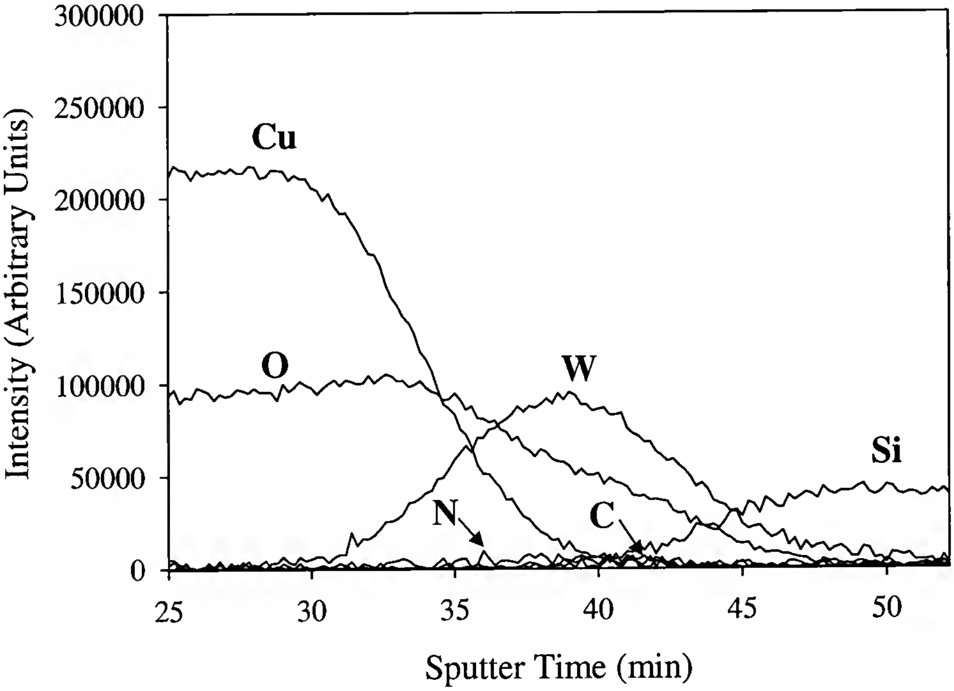

Figure 8-5. AES depth profile for sputtered Cu/barrier/Si stack after annealing in sweeping N_2 at 300°C for 30 minutes

SIMS depth profiles are required both to test barrier integrity and to determine the apparent diffusivity and the apparent activation energy for diffusion in the films. Due to the current inoperability of the SIMS system, however, these measurements must be deferred to future work.

8.5 Conclusions Regarding Cu Testing of Deposited Barrier Layers

ECD Cu had superior adhesion to the barrier layer compared to sputtered Cu, and may have been due to reduction of oxides on the barrier surface before ECD deposition initiated. The as–deposited ECD Cu layer also had lower sheet resistance than as–deposited sputtered Cu. Annealing of ECD samples had to be done in the bell jar, as the ECD process is done at ambient conditions, making a post Cu deposition *in vacuo* anneal of ECD Cu impossible. Annealing in the bell jar did not cause any Cu silicide peaks to appear on the XRD spectra, but did cause large–scale oxidation of the ECD and sputtered Cu samples, making this annealing process impractical if further barrier integrity testing with 4–point probe is desired. To prevent oxidation of Cu by ambient oxygen during annealing, some sputtered Cu/barrier/Si stacks were annealed *in vacuo.* For the sputtered Cu/barrier/Si sample stacks annealed *in vacuo*, neither XRD nor 4–point probe measurements were consistent with large–scale Cu diffusion through the barrier to the underlying Si, even after a 30 minute anneal at 500°C.

Due to the possibility of knock–in effects during SIMS analysis, the Cu layer should be etched off of the barrier before a SIMS depth profile is collected. Since the ECD Cu and barrier came off together during the etch step, a study of ECD Cu/barrier integrity (or lack thereof) by SIMS depth profile analysis was impractical. Future SIMS depth profiles are still required, however, and await repairs to the SIMS system.

Due to the high porosity and high O content in the films deposited from **1b** at 450°C, further work to deposit dense, amorphous barrier films is necessary, as O may have enhanced the ability of these barrier films to resist Cu diffusion. As discussed further in Chapter 9, *in situ* Cu deposition and annealing capability will eliminate the occurrence of barrier oxidation prior to Cu deposition tests, giving a truer test of the barrier's integrity.

CHAPTER 9
RECOMMENDATIONS FOR FUTURE WORK

In this study, we have shown a correlation between precursor structure and deposited film properties, and how modifications to the precursor structure can lead to desirable (or undesirable) shifts in these properties. Overall results for the three precursors studied in depth, however, indicate that these precursors, deposited by solvent/nebulizer based MOCVD, are unable to deposit clean, dense, low resistivity, highly conformal barrier films with excellent barrier integrity at low temperature (<400°C). Continued synthesis and testing of novel precursors, which lead to industrially applicable diffusion barrier materials, will require significant future research and development. Several different avenues of precursor optimization and barrier research that should be pursued, and these are discussed in some detail below.

9.1 Control Film Composition

Contamination levels in the deposited films must be reduced in order for the deposited films to be industrially applicable. Contamination by O, Cl and free C can have detrimental effects on film properties, such as increased film resistivity, poor inter–layer adhesion, and corrosion of the metallization layers. In addition, the amount of N (and C) in β–WN_x (or β–WN_xC_y) must be controlled to ensure good film resistivity coupled with excellent resistance to Cu in–diffusion.

To decrease contaminant levels, the precursor's molecular structure must be modified. The precursor structure should continue to exclude oxygen, and its R–groups should resist homogeneous and heterogeneous decomposition at the reaction conditions. If the R–groups separate from the W–N fragment and remain intact in the gas phase, the amount of free C from the R–groups depositing into the growing film decreases. If these R–groups decompose during the reaction, though, the amount of free C deposited into the film will be significant. In addition, Cl should be eliminated from the precursor, as the Cl ligands can cause significant Cl incorporation into the barrier films, which can corrode subsequent metallization layers deposited on the barrier. Other N bearing ligands should be used to replace the Cl atoms, if possible, both to eliminate Cl and to boost N levels in the film. The addition of N–bearing co–reactants (such as NH_3) to the reactor should also be pursued with any new precursors, as this showed promise in boosting N levels for films deposited with the isopropyl imido (**1b**) precursor.

Apart from the precursor's structure, the solvent selection issue should be revisited, as benzonitrile has been shown to cause significant amounts of unintentional C and N incorporation into the films. Another solvent, which has desirable vapor pressure properties coupled with minimal operator exposure concerns, should be selected so as to minimize C incorporation. We have discussed the use of mesitylene [1,3,5–trimethylbenzene] as a possible solvent, and this should be pursued experimentally.

If intentional deposition of WN_xC_y films is desired in the future, the amount and location of C in the film must be controlled. A thorough study of C deposition and positioning in WN_xC_y films has yet to be done, however. To deposit C into the film in a controlled manner, a study using C_2H_4 as a co–reactant may be done. This C_2H_4 co–reactant would enable us to independently control the C level in film, so that the effect of varying C content (at a given deposition temperature) on film structure, resistivity, and barrier integrity may be observed. These films should be examined with XRD, AES, RBS (if available) and XPS to determine their structure, content and elemental bonding states.

To limit contamination in the films caused by background contaminants during the reaction, a load–lock chamber should be added to the reactor. After loading the substrate and susceptor into this chamber, the loading door would be closed and vacuum would be pulled on the chamber. Then, the gate valve on the reactor would be opened, and a magnetically coupled loading arm would be used to move the susceptor into the reactor, which would be maintained at vacuum and never exposed to atmosphere (except during cleanout). A glove box would be required around the thermocouple port on the reactor to prevent any air leaks during vertical adjustment of the thermocouple. By maintaining the reactor at vacuum between runs, the background contaminant levels (especially O) in the reactor during deposition will be minimized, thereby improving properties of the deposited film. This should minimize or eliminate the interface layer between the barrier film and the Si substrate, which was discussed in Chapter 5.

After deposition, barrier integrity must be tested by deposition of a Cu layer, followed by subsequent annealing of the Cu/barrier/substrate stack. While a load–lock chamber would minimize contamination of the barrier film during deposition, exposure of the barrier layer to atmosphere after deposition can cause undesirable oxidation of the surface (and potentially bulk) of the film. To prevent oxidation of the barrier film prior to Cu deposition, the vacuum break step should be eliminated. Adding a Cu deposition reactor, with a transfer chamber connected *in vacuo* to the barrier deposition system, should make this possible. After Cu deposition, annealing of the Cu/barrier/substrate stack could be done in the Cu reactor before exposing the sample to air for *ex situ* characterization.

9.2 Decrease Deposition Temperature

The deposition temperature for the MOCVD precursor should be decreased below 400°C, as discussed in Chapter 1. To enable a lower deposition temperature, modifications to the precursor's structure, coupled with the possibility of co–reactant addition (especially for ALD), should be examined. The precursor structure should be altered to contain halide–free ligands that can dissociate at low temperature (<400°C). NH_3 is the obvious choice for a N–containing co–reactant, and is typically used for co–reactant CVD and ALD of WN_x (and WN_xC_y) films. Reactivity of NH_3 drops significantly at lower temperature, hence an alternative low–temperature N source should be investigated. Plasma cracking of an NH_3 or N_2 co–reactant, for example, before they are introduced to the reactor, may help to drop deposition temperature. Alternatively, other less stable N bearing co–reactants, such as hydrazine (N_2H_4), for example, may also be promising as a low–temperature N source, and should be tested with the novel CVD and ALD precursors generated by further study. Lab safety concerns have prevented us from testing N_2H_4 as a co–reactant with existing precursors, so collaborating with a group that has N_2H_4–based CVD (or ALD) capability may be useful.

9.3 Decrease Barrier Thickness

The current industry goal is to deposit a stable diffusion barrier layer with a thickness of 50 Å. Deposition rates and precursor chemistry must be controlled to grow thin, conformal films that adequately prevent Cu–substrate intermixing. If a good, conformal barrier with 50 Å thickness is achieved, this should be valuable for several generations of device feature sizes. The use of ALD should enable deposition of ultra–thin barrier films to meet the needs of future device generations. Moreover, monolayer by monolayer growth that is characteristic of ALD should enhance barrier film density, decreasing the number of voids or pores through which Cu may diffuse. This would also enhance the ability of the barrier to resist O in–diffusion, if a vacuum break is necessary before Cu deposition.

To ensure barrier deposition by ALD, precursor modifications will be necessary so that film growth is stepwise and self–limiting. We have considered the use of an N–chloro tungsten imido precursor $Cl_4(CH_3CN)WNCl$ for ALD, but moving toward an alkyl ligand based chemistry would be preferable to prevent Cl incorporation.

9.4 Further Conformality Testing

Although conformality tests have been performed on 2 μm diameter trench features with an AR of 2.75, the conformality of films grown by MOCVD precursors should be tested on state–of–the–art device feature sizes (diameter $\leq$ 0.10 μm). While we do have test wafers with 0.10 μm diameter features in hand, these wafers contain low–k dielectric material and shallow doped junctions, which must be processed below 400°C to prevent damage to these components. The deposition temperature must be lowered (by precursor modification, use of ALD, etc.) before these test wafers may be used in our reactor.

9.5 Further Adhesion Tests

Good adhesion is essential so that gaps between the barrier and substrate (where electromigration or diffusion may easily occur) do not form. Scotch tape tests were conducted to determine if the barriers adhered better to the Si substrates than to the tape, but this is simply a qualitative test. A nanoindentation or scratch test should be done to get a quantitative idea of adhesion strength between the barrier and the substrate layers.

9.6 Further Barrier Integrity Analyses

To enhance sensitivity of the barrier integrity tests, SIMS depth profiling of the barrier films after annealing with Cu in–vacuo should be performed. Another sensitive test involves deposition of the barrier films on pre–formed p–n junctions on Si substrates, which may be provided by Dr. Norton's group. After barrier deposition, the Cu would be deposited, and the Cu/barrier/p–n junction stack would be annealed to a target temperature. After annealing, the Cu and barrier would be stripped, and leakage current across the p–n junction should be measured. Cu that has penetrated to the Si will cause a significant leakage current, making this a very sensitive electrical technique for detecting barrier failure.

While this technique is very sensitive test of Cu diffusion, it is qualitative in nature, where the barrier film's ability to resist Cu in–diffusion is judged on a pass/fail basis. Typically, the appearance of Cu in the underlying substrate is interpreted as barrier failure. Quantitative measurements of copper flux through the diffusion barrier are lacking. By measuring the flux of Cu through a barrier layer and the Cu concentration at the barrier–substrate interface, Fick's first law may be solved for the true apparent diffusivity of the barrier film. This would enable quantitative comparisons of various barrier materials, and allow determination of the impact of chemical and microstructural differences on barrier behavior. To measure Cu flux through the barrier, the diffusing Cu must be "captured" in a medium that will allow easy composition analysis. In addition to easy compositional analysis, the capture medium should readily absorb Cu and be well mixed, so that the Cu concentration in this medium can be assumed constant. A solid capture medium presumably would contain concentration gradients, making concentration determination at the barrier–substrate interface difficult. Si, for example, has very low Cu solubility, with Cu preferentially populating defect sites in the Si lattice. This would make measurement of an average Cu concentration in the Si difficult, due to the dependence of Cu concentration on defect concentration.

A new technique to capture copper diffusing through a barrier may be set up, wherein a stack of low melting point metal/barrier/Cu would be deposited inside a capped "crucible" made of an impermeable material (e.g., Si_3N_4). A known quantity of low melting point metal would be the capture medium. During annealing, the metal should liquefy to yield a medium with high Cu diffusivity ($\sim 10^{-5}$ cm^2/s), allowing thorough mixing and uniform impurity (i.e., Cu) concentration in the melt. The Cu concentration at the barrier–metal interface can therefore be approximated as bulk concentration in the metal. After annealing for a set time, the stack would be quenched, and the concentration in the capture medium can be checked by a variety of methods, such as Rutherford backscattering spectrometry (RBS). With the Cu concentration in a known quantity of low melting temperature metal determined, the flux of Cu through the barrier, and the true apparent diffusivity, can be calculated. This work would need to address several potential issues before implementation, including de–wetting of the Cu from the crucible, barrier decomposition or dissolution into the liquid metal, and uniformity of crucible heating.

Quantitative barrier diffusivity studies could be coupled with an in–depth analysis of diffusion behavior through the grain boundaries in polycrystalline WN_x films. Depositing amorphous WN_x films with $x<0.5$ by a clean method (such as sputtering), followed by annealing, typically leads to polycrystal β–WN$_x$ films without N at the grain boundary. Increasing N content above x=0.5 should lead to polycrystalline β–WN$_{0.5}$ films with N at the grain boundaries. Quantitative diffusivity through polycrystalline films with and without N at the grain boundaries could be measured using the stack cell mentioned above. The change in diffusivity with annealing temperature may then be used to determine apparent activation energies for diffusion through grain boundaries with and without N. This should give insight into nitrogen's ability to chemically repel Cu diffusion at the grain boundaries.

XPS may also be used to study Cu–N interaction at the grain boundary. XPS can be used to differentiate between N in the polycrystals and N at the grain boundary. If significant repulsion exists between grain boundary N and Cu, a shift in N1s BE for grain boundary N may occur after the barrier is exposed to Cu. Experimental evidence of this type indicating N–Cu repulsion would be very useful in making a case for the continued use of nitride barriers in future device generations, rather than changing over to elemental metal barriers such as Ru.

9.7 Deposition on Alternate Substrate Materials

Diffusion barrier layers will need to be deposited on a variety of substrates on the IC device. Ideally, one barrier material could be used at all points on the IC where a barrier is required. If this material could be deposited on all necessary surfaces by a single precursor, this would save considerable process time caused by precursor/material changeout. While we have studied deposition from a variety of tungsten imido precursors on Si substrates, the ability of these precursors to deposit on other potential IC substrate materials should be tested. Several potential materials that should be investigated include SiO_2 (inter–level and gate dielectric), Si_3N_4 (etch stop layer), new low–K dielectric materials such as SiCOH, HSQ and polyimide, and new high–K dielectric materials such as $HfSiO_xN_y$. In addition, the ability of these precursors to deposit a barrier layer on Cu should be tested, as this should be the future metallization material at all levels on the IC device.

9.8 Testing of Films for X–ray Absorption Mask Applications

Since WN_x films have been reportedly used as X–ray absorption masks for lithography applications, our deposited films should be tested to determine their applicability for this use. Collaboration with a lithographic mask maker, for example, may enable this type of testing to be done.

9.9 Deposition of Alternate Barrier Materials

Other barrier materials in addition to WN_x should be considered for future studies. Current industrial interest in ALD of TaN and WN_xC_y, coupled with minimal precursor routes to these materials, makes precursor development for these schemes a potentially hot area.

9.10 System Modifications

Several modifications to the existing MOCVD system would be useful to improve its operation. In addition to the load–lock and in–situ Cu deposition chambers discussed above, several more modifications to the MOCVD system should be made to improve operation. First, some valves in the system, such as the H_2, NH_3, and B_2H_6 source valves, should be automated and interlocked to a central control panel. This would enable immediate shutdown of flammable/hazardous process gases in the event of a safety incident (e.g., fire) in the lab. Another safety issue to be resolved is replacement of the H_2 gas alarm in the lab. Since the existing alarm is not functioning, a new one should be purchased and installed to ensure that any H_2 leaks from the system are immediately evident.

Apart from the deposition system, one modification to the residual gas analysis (RGA) cart in the lab is necessary. The roughing and turbo pumps on the RGA cart are unable to adequately pump H_2 carrier gas, leading to an overpressure in the RGA sensor when H_2 is used in the reactor. These pumps should be replaced with higher capacity models that can handle the expected H_2 flowrate from the capillary sample tube to the RGA cart.

Work is currently underway to construct a new ALD system for barrier deposition, which will have in–situ Cu deposition capability. The system will contain separate barrier and Cu deposition reactors, connected by an in–vacuo transfer chamber with associated linear magnetic feedthroughs. The barrier chamber will have ALD capability, but can be easily changed over to CVD operation by leaving all reactant gases flowing simultaneously, rather than having separate pulses isolated by purge and vacuum steps. The Cu reactor will be run in CVD mode, based on existing Cu CVD chemistries, but will have the potential for operation in ALD mode, if future research on Cu ALD is desired.

REFERENCES

[Aal03] Aaltonen, T., P. Alen, M. Ritala and M. Leskela, Chemical Vapor Deposition **9**(1) (2003) 45-49.

[Abe93] Abe, H., T.-K. Cheung and A. T. Bell, Catalysis Letters **21**(1-2) (1993) 11-18.

[Aff85] Affolter, K., H. Kattelus and M.-A. Nicolet, Materials Research Society Symposium Proceedings, Vol.47 (1985) 167-173.

[Ala91] Alay, J. L., H. Bender, G. Brijs, A. Demesmaeker and W. Vandervorst, Surface and Interface Analysis **17**(6) (1991) 373-382.

[And99] Andricacos, P. C., Electrochemical Society Interface (1999) 32-37.

[Ans87] Ansara, I. and B. Sundman (1987). Proceedings of the International CODATA Conference (1987): 10th(Comput. Handl. Dissemination Data), Vol.1986, Ottawa, North Holland**:** 154-158.

[Aoy99] Aoyama, T. and K. Eguchi, Japanese Journal of Applied Physics, Part 2 **38**(10A) (1999) 1134-1136.

[Asm69] Asmus, T. W. and T. J. Houser, Journal of Physical Chemistry **73**(8) (1969) 2555-2558.

[Bai90] Bai, P., G.-R. Yang, L. You, T.-M. Lu and D. B. Knorr, Journal of Materials Research **5**(5) (1990) 989-997.

[Bai96] Bai, G., S. Wittenbrock, V. Ochoa, R. Villasol, C. Chiang, T. Marieb, D. Gardner, C. Mu, D. Fraser and M. Bohr (1996). Materials Research Society Symposium Proceedings, Vol.403**:** 501-506.

[Bai03] Bain, M. F., B. M. Armstrong and H. S. Gamble, Journal of Materials Science: Materials in Electronics **14**(5-7) (2003) 329-332.

[Bak02] Baker, C. C. and S. I. Shah, Journal of Vacuum Science Technology A **20**(5) (2002) 1699-1703.

[Bal75] Balluffi, R. W. and J. M. Blakely, Thin Solid Films **25**(2) (1975) 363-392.

[Ban79] Banik, G., P. Ettmayer, A. Vendl and R. Kieffer, High Temperatures - High Pressures **11** (1979) 349-352.

[Bar94] Barr, T. Modern ESCA: The Principles and Practice of X-Ray Photoelectron Spectroscopy. Boca Raton, CRC Press, Inc., (1994)

[Bau97] Baumann, J., C. Kaufmann, M. Rennau, T. Werner and T. Gessner, Microelectronic Engineering **33** (1997) 283-291.

[Bau98] Baumann, J., J. Kriz, K. Gottfried, J. Brauer, A. Ehrlich, C. Kaufmann and T. Gessner (1998). Advanced Metallization and Interconnect Systems for ULSI Applications in 1997,Vol.ULSI XIII, San Diego, CA, MRS: 117-123.

[Bch03a] Bchir, O. J., S. W. Johnston, A. C. Cuadra, T. J. Anderson, C. G. Ortiz, B. C. Brooks, D. H. Powell and L. McElwee-White, Journal of Crystal Growth **249**(1-2) (2003a) 262-274.

[Bch03b] Bchir, O. J., T. J. Anderson, B. C. Brooks and L. McElwee-White (2003b). Electrochemical Society Conference: Chemical Vapor Deposition XVI (CVD-VXI) and EUROCVD 14,Vol.2003-08, Paris, France, The Electrochemical Society: 424-431.

[Bch03c] Bchir, O. J., K. M. Green, M. S. Hlad, T. J. Anderson, B. C. Brooks, C. B. Wilder, D. H. Powell and L. McElwee-White, Journal of Organometallic Chemistry **684**(1-2) (2003c) 338-350.

[Bec03a] Becker, J. S. and R. G. Gordon, Applied Physics Letters **82**(14) (2003a) 2239-2241.

[Bec03b] Becker, J. S., S. Suh, S. Wang and R. G. Gordon, Chemistry of Materials **15**(15) (2003b) 2969-2976.

[Ben76] Benson, S. W. Thermochemical Kinetics. New York, Wiley-Interscience, (1976)

[Bey02] Beyer, G., A. Satta, J. Schuhmacher, K. Maex, W. Besling, O. Kilpela, H. Sprey and G. Tempel, Microelectronic Engineering **64**(1-4) (2002) 233-245.

[Bha80] Bhattacharya, A. K., Journal of the Chemical Society, Faraday Transactions 1: Physical Chemistry in Condensed Phases **76**(1) (1980) 126-134.

[Bin95] Binder, S., W. Lengauer, P. Ettmayer, J. Bauer, J. Debuigne and M. Bohn, Journal of Alloys and Compounds **217**(1) (1995) 128-136.

[Bla86] Blanchard, L., J. Grimblot and J. P. Bonnelle, Journal of Catalysis **98** (1986) 229-234.

[Bla97] Blanquet, E., A. M. Dutron, V. Ghetta, C. Bernard and R. Madar, Microelectronic Engineering **37/38** (1997) 189-195.

[Boh90] Boher, P., P. Houdy, P. Kaikati and L. J. Van Ijzendoorn, Journal of Vacuum Science Technology A **8**(2) (1990) 846-850.

[Bon80] Bonzel, H. P. and H. J. Krebs, Surface Science **91** (1980) 499-513.

[Bos91] Bosseboeuf, A., A. Fourrier, F. Meyer, A. Benhocine and G. Gautherin, Appl. Surf. Sci. **53** (1991) 353-357.

[Bou91] Bou, M., J. M. Martin, T. Le Mogne and L. Vovelle, Appl. Surf. Sci. **47** (1991) 149-161.

[Bou97] Boukhris, L. and J.-M. Poitevin, Thin Solid Films **310** (1997) 222-227.

[Bri46] Brinkley, S. R., Jr., Journal of Chemical Physics **14** (1946) 563.

[Bri90] Briggs, D. and M. P. Seah. Practical Surface Analysis. New York, John Wiley and Sons, (1990)

[Bro79] Brooks, C. T., S. J. Peacock and B. G. Reuben, Journal of the Chemical Society, Faraday Transactions 1: Physical Chemistry in Condensed Phases **75**(3) (1979) 652-662.

[Cai70] Caillet, M., Y. L. Lagarde and J. Besson, Comptes Rendus des Seances de l'Academie des Sciences, Serie C: Sciences Chimiques **270**(23) (1970) 1867-1869.

[Car74] Cartier, P. G. and R. R. Rye, Journal of Catalysis **32**(1) (1974) 88-98.

[Car89] Carim, A. H., A. F. De Jong and P. Houdy, Thin Solid Films **176** (1989) L177-L182.

[Cha82] Chamberlain, M. B., Thin Solid Films **91**(2) (1982) 155-162.

[Cha88] Chappell, P. J. C., M. H. Kibel and B. G. Baker, Journal of Catalysis **110** (1988) 139-149.

[Cha89] Charai, A., S. E. Hoernstroem, O. Thomas, P. M. Fryer and J. M. E. Harper, J. Vac. Sci. Technol., A **7**(3, Pt. 1) (1989) 784-9.

[Cha97a] Chang, K. M., I. C. Deng, T. H. Yeh, C. W. Shih and S. C. Chien (1997a). Electrochemical Society Conference Proceedings,Vol.97-25: 1559-1565.

[Cha97b] Chang, K. M., T. H. Yeh and I. C. Deng, Journal of Applied Physics **81**(8) (1997b) 3670-3676.

[Cha97c] Chang, K. M., T. H. Yeh, I. C. Deng and C. W. Shih, Journal of Applied Physics **82**(3) (1997c) 1469-1475.

[Cha99] Chang, K. M., I. C. Deng, T. H. Yeh, K. D. Lain and C. M. Fu, Japanese Journal of Applied Physics **38**(Part 1, No. 3A) (1999) 1343-1351.

[Cha04] Chappell, J., PVD Still in for the Long Haul, Electronic News (2004)

[Che97] Chen, F., J. Aitken and S. Parasher (1997). Materials Research Society Proceedings, Vol.453**:** 121-126.

[Che99a] Chen, X., H. L. Frisch, A. E. Kaloyeros, B. Arkles and J. Sullivan, Journal of Vacuum Science Technology B **17**(1) (1999a) 182-185.

[Che99b] Chen, X., G. G. Peterson, C. Goldberg, G. Nuesca, H. L. Frisch, A. E. Kaloyeros, B. Arkles and J. Sullivan, Journal of Materials Research **14**(5) (1999b) 2043-2052.

[Chi92] Chiu, H. T. and S. H. Chuang (1992). Materials Research Society Symposium Proceedings: Chemical Vapor Deposition of Refractory Metals and Ceramics II,Vol.250**:** 317-322.

[Chi93] Chiu, H. T. and S. H. Chuang, Journal of Materials Research **8**(6) (1993) 1353-1360.

[Chi96] Chitica, N., A. Lita, G. Marin, I. N. Mihailescu, M. Popescu, C. Grivas and A. Hatziapostolou, Journal De Physique IV **6**(C4 Rayons X et Matiere) (1996) C4-461 - C4-465.

[Chi97] Chitica, N., E. Gyorgy, A. Lita, G. Marin, I. N. Mihailescu, D. Pantelica, M. Petrascu, A. Hatziapostolou, C. Grivas, N. Broll, A. Cornet, C. Mirica and A. Andrei, Thin Solid Films **301** (1997) 71-76.

[Chi98] Chin, B., P. Ding, B. Sun, T. Chiang, D. Angelo, I. Hashim, Z. Xu, S. Edelstein and F. Chen, Solid State Technology **41**(7) (1998) 141-147.

[Chi01] Chin, B., G. Yao, P. Ding, J. Fu and L. Chen, Semiconductor International **24**(5) (2001) 107.

[Chi02] Chin, Y. L., B. S. Chiou and W. F. Wu, Japanese Journal of Applied Physics, Part 1 **41**(5A) (2002) 3057-3064.

[Cho98] Cho, S.-L., K. B. Kim, S. H. Min and H.-K. Shin (1998). Materials Research Society Conference Proceedings, Vol.514, San Francisco, CA, Materials Research Society: 531-536.

[Cho99] Cho, S. L., K. B. Kim, S. H. Min, H. K. Shin and S. D. Kim, Journal of the Electrochemical Society **146**(10) (1999) 3724-3730.

[Cho00] Cho, D.-H., T.-S. Chang and C.-H. Shin, Catalysis Letters **67**(2-4) (2000) 163-169.

[Cho01] Cho, I. H., J. S. Park, D. K. Sohn and J. H. Ha, Japanese Journal of Applied Physics **40**(8) (2001) 4854-4861.

[Cho02] Choi, I. S., J. C. Park, J. T. Choi, H. J. Kim and S. Y. Lee, Applied Physics Letters **80**(23) (2002) 4339-4341.

[Chy03] Chyan, O., T. N. Arunagiri and T. Ponnuswamy, Journal of the Electrochemical Society **150**(5) (2003) C347-C350.

[Col76] Colton, R. J. and J. W. Rabalais, Inorganic Chemistry **15**(1) (1976) 236-238.

[Coo89] Cooke, M. J. and G. Harris, Journal of Vacuum Science & Technology, A: Vacuum, Surfaces, and Films **7**(6) (1989) 3217-3221.

[Cra01] Crane, E. L., H. T. Chiu and R. G. Nuzzo, Journal of Physical Chemistry B **105** (2001) 3549-3556.

[Cri00] Crist, V. Handbook of Monochromatic XPS Spectra: The Elements and Native Oxides. New York, John Wiley & Sons, Ltd., (2000)

[Cro67] Crow, W. D. and C. Wentrup, Tetrahedron Lett. (44) (1967) 4379-&.

[Cul78] Cullity, B. D. Elements of X-ray Diffraction. Reading, MA, Addison-Wesley Publishing Company, (1978)

[Cul01] Cullity, B. D. and S. R. Stock. Elements of X-ray diffraction: Third Edition. Upper Saddle River, NJ, Prentice Hall, (2001)

[Cur92] Currie, A. L. and K. E. Howard, Journal of Materials Science **27** (1992) 2739-2742.

[Dan02] Dance, B., Semiconductor International **25**(4) (2002) 40.

[deB88] de Boer, F. R., R. Boom, W. C. M. Mattens, A. R. Miedema and A. K. Niessen. Cohesion in Metals: Transition Metal Alloys. Amsterdam, North-Holland Physics Publishing, (1988) [DeH93] DeHoff, R. T. Thermodynamics In Materials Science. New York, McGraw-Hill, Inc., (1993)

[Den89] Deneuville, A., M. Benyahya, M. Brunel, J. C. Oberlin, J. Torres, N. Bourhila, J. Paleau and B. Canut, Appl. Surf. Sci. **38** (1989) 139-147.

[Dia73] Dianis, W. P. and J. E. Lester, Analytical Chemistry **45**(8) (1973) 1416-1420.

[Din91] Dinsdale, A. T., Calphad: Computer Coupling of Phase Diagrams and Thermochemistry **15**(4) (1991) 317-425.

[Du91] Du, H. and M. Hillert, Zeitschrift für Metallkunde **82** (1991) 310-316.

[Eck02] Ecke, R., S. E. Schulz, M. Hecker and T. Gessner, Microelectronic Engineering **64** (2002) 261-268.

[Eck03] Ecke, R., S. E. Schulz, M. Hecker, N. Mattern and T. Gessner, Microelectronic Engineering **70**(2-4) (2003) 346-351.

[Eis00b] Eisenbraun, E., A. Upham, R. Dash, W. Zeng, J. Hoefnagels, S. Lane, D. Anjum, K. Dovidenko, A. E. Kaloyeros, B. Arkles and J. Sullivan, Journal of Vacuum Science & Technology B **18**(4) (2000b) 2011-2015.

[Eiz94a] Eizenberg, M., K. Littau, S. Ghanayem, A. Mak, Y. Maeda, M. Chang and A. K. Sinha, Applied Physics Letters **65**(19) (1994a) 2416-2418.

[Eiz94b] Eizenberg, M., F. Meyer, A. Benhocine and D. Bouchier, Journal of Applied Physics **75**(8) (1994b) 3900-3907.

[Eks01] Ekstrom, B. M., S. Lee, N. Magtoto and J. A. Kelber, Appl. Surf. Sci. **171**(3-4) (2001) 275-282.

[Ela01] Elam, J. W., C. E. Nelson, R. K. Grubbs and S. M. George, Surface Science **479**(1-3) (2001) 121-135.

[Ele02] Elers, K.-E., V. Saanila, P. J. Soininen, W.-M. Li, J. T. Kostamo, S. Haukka and J. Juhanoja, Chemical Vapor Deposition **8**(4) (2002) 149-153.

[Ele03] Elers, K.-E., V. Saanila, W.-M. Li, M. Soininen, J. T. Kostamo, S. Haukka, J. Juhanoja and W. Besling, Thin Solid Films **434**(1-2) (2003) 94-99.

[Ell90] Elliott, S. R. Physics of Amorphous Materials: Second Edition. New York, John Wiley & Sons, (1990)

[Ete93] Etemad-Rad, S. T. and E. Metcalfe, Fire and Materials **17** (1993) 33-37.

[Fal98] Faltermeier, C. G., C. Goldberg, M. Jones, A. Upham, A. Knorr, A. Ivanova, G. Peterson, A. E. Kaloyeros and B. Arkles, Journal of the Electrochemical Society **145**(2) (1998) 676-682.

[Fit95] Fitzgerald, S., USA Microscopy and Analysis (1995) 23-25.

[Fix93] Fix, R., R. G. Gordon and D. M. Hoffman, Chemistry of Materials **5**(5) (1993) 614-619

[Fle36] Fletcher, C. J. M. and G. K. Rollefson, Journal of the American Chemical Society **58** (1936) 2129-2135.

[Fle98] Fleming, J. G., E. Roherty-Osmun, P. M. Smith, J. S. Custer, Y. D. Kim, T. Kacsich, M. A. Nicolet and C. J. Galewski, Thin Solid Films **320**(1) (1998) 10-14.

[Fou79] Foucaut, J. F. M., R., International Journal of Chemical Kinetics **11**(7) (1979) 789-798.

[Fri91] Frisk, K., Calphad: Computer Coupling of Phase Diagrams and Thermochemistry **15**(1) (1991) 79-106.

[Fri96] Frisk, K. and A. F. Guillermet, Journal of Alloys and Compounds **238** (1996) 167-179.

[Fri98] Frisk, K., Journal of Alloys and Compounds **278** (1998) 216-226.

[Fri99a] Friedrich, L. J., S. K. Dew, M. J. Brett and T. Smy, Journal of Vacuum Science Technology B 17(1) (1999) 186-193.

[Fri99b] Frisk, K., Zeitschrift für Metallkunde 90(9) (1999) 704-711.

[Fuk00] Fukiage, N. Semiconductor device and fabrication thereof. 2000 PCT Int. Appl., Japan, EP1170784

[Gal93] Galanin, S. G., G. D. Kuzentsov, A. B. Tolstoguzov and E. Y. Chernyak, Physics and Chemistry of Materials Treatment **27**(5) (1993) 489-493.

[Gal97] Galewski, C. J., P. N. Gadgil, L. D. Matthysse, C. A. Sans and V. S. Dharmadhikari (1997). Materials Research Society ULSI XII**:** 277-282.

[Gal99] Galewski, C. and T. Seidel, European Semiconductor **21**(1) (1999) 31-32.

[Gal00] Galewski, C. J., A. R. Londergan, C. A. Sans, T. E. Seidel, D. Clarke and Q. Zhu, European Semiconductor **22**(Part 2) (2000) 28-33.

[Gan92] Ganem, J.-J., S. Rigo, I. Trimaille and G.-N. Lu, Nuclear Instruments and Methods in Physics Research **B64** (1992) 784-788.

[Gan00] Ganguli, S., L. Chen, T. Levine, B. Zheng and M. Chang, Journal of Vacuum Science Technology B **18** (2000) 237-241.

[Gar90] Garnich, F., P. C. Yu and C. M. Lampert, Solar Energy Materials **20** (1990) 265-275.

[Gat96] Gates, S. M., Chemical Reviews **96**(4) (1996) 1519-1532.

[Geb66] Gebhardt, E., E. Fromm and U. Roy, Zeitschrift für Metallkunde **57**(10) (1966) 732-736.

[Gei86] Geissberger, A. E., R. A. Sadler, F. A. Leyenaar and M. L. Balzan, Journal of Vacuum Science Technology A **4**(6) (1986) 3091-3094.

[Gic83] Gicquel, A., M. P. Bergougnan and J. Amoroux (1983). Electrochemical Society Proceedings of the Symposium on Silicon Nitride Thin Insulating Films,Vol.83-8,,**:** 442-452.

[Gir00] Giraudon, J.-M., P. L. Devassine, J.-F., L. Delannoy, L. Leclercq and G. Leclercq, Journal of Solid State Chemistry **154**(2) (2000) 412-426.

[Gog98] Gogova, D., K. Gesheva and A. Veneva, Materials Letters **35**(5-6) (1998) 351-356.

[Gog00] Gogova, D., K. Gesheva, A. Kakanakova-Georgieva and M. Surtchev, European Physical Journal **11** (2000) 167-174.

[Gok99] Gokce, O. H., S. Amin, N. M. Ravindra, D. J. Szostak, R. J. Paff, J. G. Fleming, C. J. Galewski, J. Shallenberger and R. Eby, Thin Solid Films **353**(1,2) (1999) 149-156.

[Gol63] Goldschmidt, H. J. and J. A. Brand, Journal of the Less-Common Metals **5** (1963) 181-194.

[Gol67] Goldschmidt, H. J. Interstitial Alloys. New York, Plenum Press, (1967)

[Gon02] Gonohe, N., Materials Transactions **43**(7) (2002) 1585-1592.

[Goo86] Goodman, C. H. L. and M. V. Pessa, Journal of Applied Physics **60**(3) (1986) R65-R81.

[Gor00] Gordon, R. G., S. Barry, R. N. R. Broomhall-Dillard, V. A. Wagner and Y. Wang (2000). Mater. Res. Soc. Symp. Proc.,Vol.612**:** D9.12/1-

D9.12/6.

[Gru87] Grunert, W., E. S. Shpiro, R. Feldhaus, K. Anders, G. V. Antoshin and K. M. Minachev, Journal of Catalysis **107** (1987) 522-534.

[Gub94] Gubanov, V. A., A. L. Ivanovsky and V. P. Zhukov. Electronic Structure of Refractory Carbides and Nitrides. Cambridge, Cambridge University Press, (1994)

[Gui93] Guillermet, A. F. and S. Jonsson, Zeitschrift für Metallkunde **84**(2) (1993) 106-117.

[Gui95] Guillermet, A. F., Journal of Alloys and Compounds **217**(1) (1995) 69-89.

[Gup95] Gupta, D., Materials Chemistry and Physics **41**(3) (1995) 199-205.

[Gur89] Gurvich, L. V., I. V. Veyts and C. B. Alcock. Thermodynamic Properties of Individual Substances. New York, Hemisphere Pub. Corp., (1989)

[Gus85] Gustafson, P., International Journal of Thermophysics **6** (1985) 395-409.

[Gus86] Gustafson, P., Materials Science and Technology **2** (1986) 653-658.

[Hag30] Hagg, G., Z. physik. Chem. **7 Abt. B** (1930) 339-362.

[Hag54] Hagg, G. and N. Schonberg, Acta Crystallographica **7** (1954) 351-352.

[Han03] Hand, A., Semiconductor International **26**(5) (2003) 46-51.

[Har01] Hara, T. and K. Sakata, Electrochemical and Solid-State Letters **4**(10) (2001) G77-G79.

[Hau93] Haukka, S., E.-L. Lakomaa and T. Suntola, Thin Solid Films **225**(1-2) (1993) 280-283.

[Hau00] Haukka, S., K.-E. Elers and M. Tuominen (2000). Materials Research Society Symposium Proceedings: Materials, Technology and Reliability for Advanced Interconnects and Low-k Dielectrics,Vol.612: D6.4/1-D6.4/6.

[Hec02] Hecker, M., R. Hubner, R. Ecke, S. Schulz, H.-J. Engelmann, H. Stegmann, V. Hoffmann, N. Mattern, T. Gessner and E. Zschech, Microelectronic Engineering **64**(1-4) (2002) 269-277.

[Hei97] Heiser, T., S. McHugo, H. Heislmair and E. R. Weber, Applied Physics

Letters **70**(26) (1997) 3576-3578.

[Hil00] Hillman, J., J. Hautala and S. Caliendo (2000). Advanced Metallization Conference San Diego, CA, Materials Research Society: 313-319.

[Hir98] Hirata, A., K. Machida, S. Maeyama, Y. Watanabe and H. Kyuragi, Japanese Journal of Applied Physics Part 1 **37**(3B) (1998) 1251-1255.

[Hir99] Hirata, A., K. Machida, N. Awaya, H. Kyuragi and M. Maeda, Japanese Journal of Applied Physics, Part 1 **38**(4B) (1999) 2355-2359.

[Hir01] Hirata, A., T. Maeda, K. Machida, M. Maeda, K. Yasui and H. Kyuragi, Journal of Vacuum Science Technology B **19**(3) (2001) 788-793.

[Ho04] Ho, P., R. Rajagopalan, H. Chong, H. Chung and J. Yu, Semiconductor International **27**(7) (2004)

[Hom86] Homann, K. H. and J. V. Pidoll, Bunsen-Gesellschaft fur Physikalische Chemie **90**(10) (1986) 847-854.

[Hon00] Hones, P., M. Diserens, R. Sanjines and F. Levy, Journal of Vacuum Science Technology B **18**(6) (2000) 2851-2856.

[Hon03] Hones, P., N. Martin, M. Regula and F. Levy, Journal of Physics D: Applied Physics **36** (2003) 1023-1029.

[Hos00] Hoshino, A., S. T., S. Hiiro, H. Machida, A. Ogura and Y. Ohshita (2000). Advanced Metallization Conference San Diego, CA, Materials Research Society: 403-408.

[Hou65] Hou, K. C. and H. B. Palmer, Journal of Physical Chemistry **69**(3) (1965) 858-862.

[Hu98] Hu, C.-K. (1998). Materials Research Society Syposium Proceedings,Vol.511, Materials Research Society: 305-316.

[Hua97] Huang, W., Zeitschrift für Metallkunde **88** (1997) 63-68.

[Hua03] Huang, M., Study of TMGa-NH_3-N_2 systems using in situ Raman spectroscopy, PhD, University of Florida, Gainesville, FL,(2003)

[Hub88] Huber, K. J. and C. R. Aita, Journal of Vacuum Science Technology A **6**(3) (1988) 1717-1721.

[Huo02] Huo, J., R. Solanki and J. McAndrew, Journal of Materials Research **17**(9) (2002) 2394-2398.

[Hym98] Hymes, S., K. S. Kumar, S. P. Murarka, P. J. Ding, W. Wang and W. A.

Lanford, Journal of Applied Physics **83**(8) (1998) 4507-4512.

[IBM97] IBM, IBM Research **35**(4) (1997)

[Iij95] Iijima, T., Y. Shimooka and K. Suguro (1995). Materials Research Society Conference Proceedings,Vol.355,, Materials Research Society: 459-464.

[Ima97] Imahori, J., T. Oku and M. Murakami, Thin Solid Films **301**(1-2) (1997) 142-148.

[Inc90] Incropera, F. P. and D. P. DeWitt. Fundamentals of Heat and Mass Transfer: Third Edition. New York, John Wiley & Sons, (1990)

[Ing82] Ingrey, S., M. B. Johnson, R. W. Streater and G. I. Sproule, J. Vac. Sci. Technol. **20**(4) (1982) 968-970.

[Ino01] Inoue, K., N. Ishikawa, I. Ohnuma, H. Ohtani and K. Ishida, ISIJ International **41**(2) (2001) 175-182.

[Int89] Interrante, L. V., G. A. Sigel, M. Garbauskas, C. Hejna and G. A. Slack, Inorganic Chemistry **28**(2) (1989) 252-257.

[Ist98] Istratov, A. A., C. Flink, H. Hieslmair, E. R. Weber and T. Heiser, Physical Review Letters **81**(6) (1998) 1243-1246.

[Ist00] Istratov, A. A. and E. R. Weber (2000). Electrochemical Society Conference Proceedings, Vol.2000-27: 90-111.

[ITR02] International Technology Roadmap for Semiconductors: Interconnect. Austin, TX, International SEMATECH, 2002.: 1-25.

[Iva99] Ivanova, A. R., C. J. Galewski, C. A. Sans, T. E. Seidel, S. Grunow, K. Kumar and A. E. Kaloyeros (1999). Materials Research Society Symposium Proceedings; Advanced Interconnects and Contacts,Vol.564, San Francisco, CA: 321-326.

[Jae88] Jaeger, R. C. Introduction to Microelectronic Fabrication. Reading, MA, Addison-Wesley Publishing Company, (1988)

[Jai99] Jain, A., O. Adetutu, B. Ekstrom, G. Hamilton, M. Herrick, R. Venkatraman and E. Weitzman (1999). Materials Research Society Symposium Proceedings, Vol.564: 269-280.

[Jam92] Jama, C., O. Dessaux, P. Goudmand, L. Gengembre and J. Grimblot, Surface and Interface Analysis **18** (1992) 751-756.

[JCP88] Powder Diffraction File. JCPDS, International Center for Diffraction

Data, Swarthmore, PA, 1982,1988.

[Jeh80] Jehn, H. and P. Ettmayer, Monatshefte fur Chemie (in German) **111** (1980) 1437-1440.

[Jel00] Jelinek, M., J. Zemek, M. Trchova, V. Vorlicek, J. Lancok, R. Tomov and M. Simeckova, Thin Solid Films **366**(1-2) (2000) 69-76.

[Jel03] Jelenkovic, E. V., K. Y. Tong, W. Y. Cheung and S. P. Wong, Semiconductor Science and Technology **18**(6) (2003) 454-459.

[Jen96] Jenkins, R. and R. Snyder. Introduction to X-ray Powder Diffractometry. New York, John Wiley & Sons, (1996)

[Ji01] Ji, H. X. and C. A. Amato-Wierda, Surface and Coatings Technology **148** (2001) 262-267.

[Jin99] Jin, S., H. Li, H. Bender, I. Heyvaert and K. Maex, Institute of Physics Conference Series **164** (1999) 541-544.

[Joh00a] Johnston, S. W., Chemical Vapor Deposition of Nitrides for Electronic Device Applications, PhD Dissertation, University of Florida, Gainesville,FL (2000a)

[Joh00b] Johnston, S. W., C. G. Ortiz, O. J. Bchir, Y. Zhang, L. McElwee-White and T. J. Anderson, Chemical Vapor Deposition: CVD XV (15th), M. D. Allendorf and T. M. Besmann, Electrochemical Society, Pennington, NJ, 2000b. p. 268-276.

[Joh01] Johnson, K., B. Sauerhammer, S. Titmuss and D. A. King, Journal of Chemical Physics **114**(21) (2001) 9539-9548.

[Jon93] Jonsson, S., Phase Relations in Quaternary Hard Materials, PhD Dissertation, Royal Institute of Technology, Stockholm, Sweden,(1993)

[Jon96a] Jonsson, S., Zeitschrift für Metallkunde **87**(9) (1996a) 713-720.

[Jon96b] Jonsson, S., Zeitschrift für Metallkunde **87**(10) (1996b) 788-795.

[Jos02] Joseph, S., M. Eizenberg, C. Marcadal and L. Chen, Journal of Vacuum Science Technology B **20**(4) (2002) 1471-1475.

[Jos03] Josell, D., D. Wheeler, C. Witt and T. P. Moffat, Electrochemical and Solid-State Letters **6**(10) (2003) C143-C145.

[Jun96] Jun, G.-C., S.-L. Cho, K. B. Kim, H.-K. Shin and D.-H. Kim (1996). Materials Research Society Symposium (Advanced Metallization for

Future ULSI), Vol.427, San Francisco, CA, Materials Research Society: 349-354.

[Jup97] Juppo, M., M. Ritala and M. Leskela, Journal of Vacuum Science & Technology, A: Vacuum, Surfaces, and Films **15**(4) (1997) 2330-2333.

[Kak99] Kakanakova-Georgieva, A., L. Kassamakova, T. Marinova, R. Kakanakov, O. Noblanc, C. Arnodo, S. Cassette and C. Brylinski, Appl. Surf. Sci. **151** (1999) 225-232.

[Kal99] Kaloyeros, A. E., X. Chen, T. Stark, K. Kumar, S.-C. Seo, G. G. Peterson, H. L. Frisch, B. Arkles and J. Sullivan, Journal of the Electrochemical Society **146**(1) (1999) 170-176.

[Kal00] Kaloyeros, A. E. and E. Eisenbraun, Annual Review of Materials Science **30** (2000) 363-385.

[Kan01] Kang, S.-K., J. J. Kim, D.-H. Ko, T. H. Ahn, I. S. Yeo, T. W. Lee and Y. H. Lee (2001). Materials Research Society Symposium Proceedings, Vol.670: K5.9.1-K5.9.6.

[Kan02] Kang, S.-K., J. J. Kim, B. G. Min, D.-H. Ko, H. B. Kang, C. W. Yang, T. H. Ahn, T. W. Lee and Y. H. Lee, Journal of the Korean Physical Society **40**(1) (2002) 184-187.

[Kap02] Kapur, P., J. P. McVittie and K. C. Saraswat, IEEE Transactions on Electron Devices **49**(4) (2002) 590-597.

[Kas94] Kasai, K., Y. Akasaka, K. Nakajima, S. Suehiro, K. Suguro, H. Oyamatsu, M. Kinugawa and M. Kakumu (1994). IEEE Conference Proceedings - IEDM 94,Vol. IEDM 94-497: 19.4.1-19.4.4.

[Kat85] Kattelus, H. P., E. Kolawa, K. Affolter and M. A. Nicolet, J. Vac. Sci. Technol., A **3**(6) (1985) 2246-54.

[Kat94] Katrib, A., F. Hemming, L. Hilaire, P. Wehrer and G. Maire, Journal of Electron Spectroscopy and Related Phenomena **68** (1994) 589-595.

[Kat95] Katrib, A., F. Hemming, P. Wehrer, L. Hilaire and G. Maire, Journal of Electron Spectroscopy and Related Phenomena **76** (1995) 195-200.

[Kat97] Kattner, U. R., JOM: The Journal of the Minerals, Metals and Materials Society **49**(12) (1997) 14-19.

[Kel91] Kelder, E. M., Kinetics and Characterization of CVD-Grown BP, PhD, Technical University of Delft, Delft, Netherlands,(1991)

[Kel99] Kelsey, J. E., C. Goldberg, G. Nuesca, G. Peterson, A. E. Kaloyeros and B. Arkles, Journal of Vacuum Science & Technology B **17**(3) (1999) 1101-1104.

[Khi59] Khitrova, V. I. and Z. G. Pinsker, Kristallografiya **4** (1959) 545-53.

[Kie51] Kiessling, R. and Y. H. Liu, Journal of Metals **3**(Trans.) (1951) 639-642.

[Kil75] Kilbane, F. M. and P. S. Habig, Journal of Vacuum Science Technology **12**(1) (1975) 107-109.

[Kim91] Kim, Y. T. and S. K. Min, Applied Physics Letters **59**(8) (1991) 929-931.

[Kim92] Kim, Y. T., C. W. Lee and S. K. Min, Applied Physics Letters **61**(5) (1992) 537-539.

[Kim93] Kim, Y. T., C. W. Lee and S. K. Min, Jpn. J. Appl. Phys. Part 1 - Regul. Pap. Short Notes Rev. Pap. **32**(12B) (1993) 6126-6131.

[Kim94] Kim, Y. T. and C. W. Lee, Journal of Applied Physics **76**(1) (1994) 542-545.

[Kim97a] Kim, D. J., Y. T. Kim and J.-W. Park, Journal of Applied Physics **82**(10) (1997a) 4847-4851.

[Kim97b] Kim, Y. T., D. J. Kim, C. W. Lee and J.-W. Park (1997b). Proceedings of SPIE-The International Society for Optical Engineering (Multilevel Interconnect Technology), Vol.3214**:** 48-56.

[Kim98a] Kim, D. J., Y. T. Kim and J. W. Park (1998). Advanced Interconnects and Contact Materials and Processes for Future Integrated Circuits,Vol.514, San Francisco, CA, Materials Research Society: 417-422.

[Kim98b] Kim, Y. T., C. W. Lee and D. J. Kim, Applied Physics Letters 72(12) (1998) 1507-1509.

[Kim99a] Kim, D. J., Y. T. Kim and J.-W. Park, Journal of Vacuum Science & Technology B **17**(4) (1999a) 1598-1601.

[Kim99c] Kim, S. H., D. S. Chung, K. C. Park, K. B. Kim and S. H. Min, Journal of the Electrochemical Society **146**(4) (1999c) 1455-1460.

[Kim01] Kim, I. G., N. S. Kim, J. H. Choy, B. H. Lee, Y. G. Sung, J. H. Kim, J.

H. Cho, D. C. Kim, K. S. Kim, J. B. Choi, S. K. Choi, Y. W. Kweon, H. Y. Kwon, D. G. Park, J. S. Park and D. Y. Park (2001). IEEE: 28.5.1-28.5.4.

[Kim02a] Kim, D. J., H. S. Sim, S.-I. Kim, Y. T. Kim and H. Jeon, Journal of Vacuum Science & Technology, A: Vacuum, Surfaces, and Films **20**(1) (2002a) 194-197.

[Kim02b] Kim, H., C. Cabral Jr., C. Lavoie and S. M. Rossnagel, Journal of Vacuum Science Technology B **20**(4) (2002b) 1321-1326.

[Kim03a] Kim, D.-H., Y. J. Kim, Y. S. Song, B.-T. Lee, J. H. Kim, S. Suh and R. G. Gordon (2003a). Electrochemical Society Conference: Chemical Vapor Deposition XVI (CVD-VXI) and EUROCVD 14,Vol.2003-08, Paris, France, The Electrochemical Society: 491-502.

[Kim03b] Kim, H., (2003b) Atomic Layer Deposition of Metal and Nitride Thin Films: Current Research Efforts and Applications for Semiconductor Device Processing. Yorktown Heights, NY, IBM, (2003b) 121.

[Kim03c] Kim, S. H., K. T. Nam, A. Datta, H. M. Kim, K. B. Kim and D. H. Kang, Journal of Vacuum Science Technology B **21**(2) (2003c) 804-813.

[Kim03d] Kim, S.-H., S. S. Oh, K.-B. Kim, D.-H. Kang, W.-M. Li, S. Haukka and M. Tuominen, Applied Physics Letters **82**(25) (2003d) 4486-4488.

[Kla00a] Klaus, J. W., S. J. Ferro and S. M. George, Journal of the Electrochemical Society **147**(3) (2000a) 1175-1181.

[Kla00b] Klaus, J. W., S. J. Ferro and S. M. George, Appl. Surf. Sci. **162-163** (2000b) 479-491.

[Klu91] Kluwe, M., B. Kaimann, K. E. Lorber and H. Meier zu Kocker, Chemosphere **23**(8-10) (1991) 1465-1471.

[Kod94] Kodas, T. T. and M. J. Hampden-Smith, Eds. The Chemistry of Metal CVD,Weinheim, VCH (1994)

[Koh95] Kohler, T., T. Frauenheim and G. Jungnickel, Physical Review B **52**(16) (1995) 11837-11844.

[Kol87] Kolawa, E., F. C. So, J. L. Tandon and M. A. Nicolet, Journal of the Electrochemical Society **134**(7) (1987) 1759-1763.

[Kol91] Kolawa, E., P. J. Pokela, J. S. Reid, J. S. Chen and M. A. Nicolet, Appl. Surf. Sci. **53** (1991) 373-376.

[Kos93] Kostikova, G. P. and Y. P. Kostikov, Inorganic Materials **29**(8) (1993) 1005-1006.

[Kou02] Koutzaki, S. H., J. E. Krzanowski and J. J. Nainaparampil, Metallurgical and Materials Transactions A **33A** (2002) 1579-1588.

[Kri01] Krishnamoorthy, A., K. Chanda, S. P. Murarka, G. Ramanath and J. G. Ryan, Applied Physics Letters **78**(17) (2001) 2467-2469.

[Kwo95] Kwon, C. S., D. J. Kim, C. W. Lee, Y. T. Kim and I.-H. Choi, Mater. Res. Soc. Symp. Proc. **355**(Evolution of Thin Film and Surface Structure and Morphology) (1995) 441-5.

[Lai98a] Lai, K. K., A. W. Mak, T. Wendling, P. Jian and B. Hathcock, Thin Solid Films 332(1-2) (1998) 329-334.

[Lai98b] Laidani, N., C. Dorigoni, A. Miotello, L. Calliari, G. Scarel and M. Sancrotti, Thin Solid Films 317 (1998) 477-480.

[Lak79] Lakhtin, Y. M., Y. D. Kogan, T. M. Borovskaya and G. A. Solodkin, Metally (*in Russian*) **4** (1979) 176-184.

[Lan62] Lang, R. J., Journal of the Acoustical Society of America **34**(1) (1962) 6-8.

[Lan00] Lanckmans, F., S. H. Brongersma, I. Varga, H. Bender, E. Beyne and K. Maex (2000). Materials Research Society Symposium Proceedings, Vol.612**:** D1.4.1-D1.4.6.

[Las96] Laskin, A. and A. Lifshitz (1996). Twenty-Sixth Symposium (International) on Combustion/The Combustion Institute, Vol.1**:** 669-675.

[Lau02] Laurila, T., K. Zeng, J. K. Kivilahti, J. Molarius and I. Suni, Journal of Applied Physics **91**(8) (2002) 5391-5399.

[Lec96] Leclercq, G., M. Kamal, J. M. Giraudon, P. Devassine, L. Feigenbaum, L. Leclercq, A. Frennet, J. M. Bastin, A. Lofberg, S. Decker and M. Dufour, Journal of Catalysis **158** (1996) 142-169.

[Lee90] Lee, J. S., C. S. Park, J. Y. Kang, D. S. Ma and J. Y. Lee, Journal of Vacuum Science Technology B **8**(5) (1990) 1117-1121.

[Lee92] Lee, J. H., C. E. J. Hamrin and B. H. Davis, Catalysis Today **15**(2) (1992) 223-241.

[Lee93] Lee, C. W., Y. T. Kim and S. K. Min, Applied Physics Letters **62**(25) (1993) 3312-3314.

[Lee94a] Lee, C. W., Y. T. Kim, C. Lee, J. Y. Lee, S. K. Min and Y. W. Park, Journal of Vacuum Science & Technology B **12**(1) (1994a) 69-72.

[Lee94b] Lee, C. W., Y. T. Kim and J. Y. Lee, Applied Physics Letters **64**(5) (1994b) 619-621.

[Lee94c] Lee, C. W., Y. T. Kim, S.-K. Min, C. Lee, J. Y. Lee and Y. W. Park, Mater. Res. Soc. Symp. Proc. **318**(Interface Control of Electrical, Chemical, and Mechanical Properties) (1994c) 335-40.

[Lee95] Lee, C. W. and Y. T. Kim, Solid-State Electronics **38**(3) (1995) 679-682.

[Lee97] Lee, D. H., C. K. Park, K. C. Song, Y. S. Jeon, T. H. Lee, C. Y. Jeong and J. Ahn, Japanese Journal of Applied Physics **36**(Part 1, No. 12B) (1997) 7570-7574.

[Lee98a] Lee, C.-Y. H., Tzuen-Hsi; Lu, Shing-Chi, Journal of Materials Science: Materials in Electronics **9**(5) (1998a) 337-346.

[Lee98b] Lee, H. G., S. Y. Lee, H. S. Moon, S. H. Kim, J. H. Sohn and J. Ahn, Japanese Journal of Applied Physics **37** (1998b) 6819-6823.

[Lee98c] Lee, S., D. J. Kim, S.-H. Yang, J. Park, S. Sohn, K. Oh, Y. T. Kim and J.-W. Park (1998c). Materials Research Society Symposium Proceedings, Vol.511**:** 347-352.

[Lee99] Lee, Y.-J., B.-S. Suh, M. S. Kwon and C.-O. Park, Journal of Applied Physics **85**(3) (1999) 1927-1934.

[Lee00a] Lee, J.-H., J.-Y. Kim, S.-W. Rhee, D. Y. Yang, D.-H. Kim, C.-H. Yang, Y.-K. Han and C.-J. Hwang, Journal of Vacuum Science & Technology, A: Vacuum, Surfaces, and Films 18(5) (2000) 2400-2403.

[Lee00b] Leedy, K. D., M. J. O'Keefe, J. G. Wilson, R. Osterday and J. T. Grant (2000). Materials Research Society Conference Proceedings, Vol.612, San Francisco, CA: D9.20.1-D9.20.6.

[Lee01a] Lee, B.-J., Metallurgical and Materials Transactions A **32A**(10) (2001a) 2423-2439.

[Lee01b] Lee, C. W., Y. T. Kim, H. S. Lee, Y. K. Park, T.-H. Lee, Q. Chen and N. V. Richardson, Journal of the Korean Physical Society **39**(6) (2001b) 1019-1022.

[Lee01c] Lee, J. W., C. H. Han, J. S. Park and J. W. Park, Journal of the Electrochemical Society **148**(3) (2001c) G95-G98.

[Lee03] Lee, K. S., Japanese Journal of Applied Physics **42**(Part I, No. 6A) (2003) 3368-3371.

[Les02] Leskela, M. and M. Ritala, Thin Solid Films **409**(1) (2002) 138-146.

[Lev98] Levine, T. E., L. Chen, S. Ganguli, A. Mak, J. Tseng and M. Chang (1998). Advanced Metallization and Interconnect Systems for ULSI Applications in 1997,Vol.ULSI XIII, San Diego, CA, MRS: 95-101.

[Lew94] Lewkebandara, T. S., P. H. Sheridan, M. J. Heeg, A. L. Rheingold and C. H. Winter, Inorganic Chemistry **33**(25) (1994) 5879-5889.

[Li00] Li, H., S. Jin, H. Bender, F. Lanckmans, I. Heyvaert, K. Maex and L. Froyen, Journal of Vacuum Science Technology B **18** (2000) 242-251.

[Li02] Li, W. M., K. Elers, J. Kostamo, S. Kaipio, H. Huotari, M. Soininen, P. J. Soininen, M. Tuominen, S. Haukka, S. Smith and W. Besling (2002). IEEE International Interconnect Technology Conference, 5th Burlingame, CA, United States: 191-193.

[Li03] Li, W.-M., M. Tuominen, S. Haukka, H. Sprey and I. J. Raaijmakers, Solid State Technology **46**(7) (2003) 103-104,106.

[Lid85] Lide, D. R., Ed. JANAF Thermochemical Tables, Third Edition. New York, American Institute of Physics (1985)

[Lif96] Lifshitz, A., Y. Cohen, M. Braun-Unkhoff and P. Frank (1996). Twenty-Sixth Symposium (International) on Combustion, The Combustion Institute: 659-667.

[Lim03] Lim, B. S., A. Rahtu and R. G. Gordon, Nature Materials **2**(11) (2003) 749-754.

[Lin90] Lin, D., B. Yan and W. Yu (1990). Materials Research Society Symposium Proceedings: Thin Film Struct. Phase Stab.,Vol.187: 161-166.

[Lin98a] Lin, J., A. Tsukune, T. Suzuki and M. Yamada (1998a). Advanced Metallization and Interconnect Systems for ULSI Applications in 1997,Vol.ULSI XIII, San Diego, CA, MRS: 693-697.

[Lin98b] Lin, J., A. Tsukune, T. Suzuki and M. Yamada, Journal of Vacuum Science & Technology, A: Vacuum, Surfaces, and Films **16**(2) (1998b) 611-614.

[Lin99] Lin, J., A. Tsukune, T. Suzuki and M. Yamada, Journal of Vacuum Science & Technology, A: Vacuum, Surfaces, and Films **17**(3) (1999) 936-938.

[Lip03] Lipsanen, A., P. Kuivalainen, E. Rauhala, A. Seppala and S. Franssila, Journal of Materials Science: Materials in Electronics **14**(5/6/7) (2003) 315-318.

[Liu88] Liu, A. C. and C. M. Friend, Journal of Chemical Physics **89**(7) (1988) 4396-4405.

[Liu98] Liu, Z. Q., W. J. Wang, T. M. Wang, S. Chao and S. K. Zheng, Thin Solid Films **325** (1998) 55-59.

[Liu00] Liu, P. T., T. C. Chang, J. C. Hu, Y. L. Yang and S. M. Sze, Journal of the Electrochemical Society **147**(1) (2000) 368-372.

[Llo95] Lloyd, J. R. and J. J. Clement, Thin Solid Films **262**(1-2) (1995) 135-141.

[Lu98a] Lu, J. P., W. Y. Hsu, Q. Z. Hong, G. A. Dixit, V. T. Cordasco, E. M. Zielinski, J. D. Luttmer, R. H. Havemann, L. K. Magel and H. L. Tsai (1998a). Materials Research Society Conference Proceedings,Vol.514: 507-512.

[Lu98b] Lu, J. P., W. Y. Hsu, J. D. Luttmer, L. K. Magel and H. L. Tsai, Journal of the Electrochemical Society **145**(2) (1998b) L21-L23.

[Luc96] Lucy, T. E., Synthesis, Characterization and Reactivity of Tungsten Oxynitride, Master's Thesis, Virginia Polytechnic Institute and State University, Blacksburg,(1996)

[Luo94] Luo, Y.-R. and J. L. Holmes, Journal of Physical Chemistry **98**(1) (1994) 303-12.

[Lut01] Luthin, J. and C. Linsmeier, Journal of Nuclear Materials **290-293** (2001) 121-125.

[Mar93] Marcus, S. D. and R. F. Foster, Thin Solid Films **236**(1-2) (1993) 330-333.

[Mar95] Maruyama, T. and T. Morishita, Journal of Applied Physics **78**(6) (1995) 4104-4107.

[Mas96] Masel, R. I. Principles of Adsorption and Reaction on Solid Surfaces. New York, John Wiley & Sons, (1996)

[Mat94] Matsuhashi, H. and S. Nishikawa, Japanese Journal of Applied Physics **33**(3A) (1994) 1293-1297.

[Mat02] Matsui, Y., T. Hiratani, T. Nabatame, Y. Shimamoto and S. Kimura, Electrochemical and Solid-State Letters **5**(1) (2002) C18-C21.

[May90] Mayer, J. W. and S. S. Lau. Electronic Materials Science: For Integrated Circuits in Si and GaAs. New York, Macmillan Publishing Company, (1990)

[McG73] McGuire, G. E., G. K. Schweitzer and T. A. Carlson, Inorganic Chemistry **12**(10) (1973) 2450-2453.

[Mer97] Mercier, M., S. Weber, A. Jacques, H. Hirabayashi, H. Ohkawa and M. Kinoshita, Diffusion and Defect Data--Solid State Data, Pt. A: Defect and Diffusion Forum **143-147**(Pt. 2, Diffusion in Materials, Pt. 2) (1997) 1285-1290.

[Mer01] Merchant, S. M., S. H. Kang, M. Sanganeria, B. van Schravendijk and T. Mountsier,Copper Interconnects for Semiconductor Devices, Novellus (2001), http://www.novellus.com/damascus/tec/tec_24.asp

[Meu98] Meunier, C., C. Monteil, C. Savall, F. Palmino, J. Weber, R. Berjoan and J. Durand, Appl. Surf. Sci. **125** (1998) 313-320.

[Mig01] Migita, T., R. Kamei, T. Tanaka and K. Kawabata, Appl. Surf. Sci. **169-170** (2001) 362-365.

[Min96] Minamihaba, G., T. Iijima, Y. Shimooka, H. Tamura, T. Kawanoue, H. Hirabayashi, N. Sakurai, H. Ohkawa, T. Obara, H. Egawa, T. Idaka, T. Kubota, T. Shimizu, M. Koyama, J. Ooshima and K. Suguro, Japanese Journal of Applied Physics Part 1: Regular Papers, Short Notes & Review Papers **35**(2B) (1996) 1107-1110.

[Min00] Min, J.-S., J.-S. Park, H.-S. Park and S.-W. Kang, Journal of the Electrochemical Society **147**(10) (2000) 3868-3872.

[Mon99] Monteiro, O. R., M. P. Delplancke-Ogletree and I. G. Brown, Thin Solid Films **342** (1999) 100-107.

[Mor98] Mori, H., J. Imahori, T. Oku and M. Murakami (1998). AIP Conference Proceedings, Vol.418 (Stress Induced Phenomena in Metallization): 475-480.

[Mou95] Moulder, J. F., W. F. Stickle, P. E. Sobol and K. D. Bomben. Handbook of X-ray Photoelectron Spectroscopy. Eden Prairie, MN, Physical Electronics, Inc., (1995)

[Mro01] Mrozek, M. F., S. A. Wasileski and M. J. Weaver, Journal of the American Chemical Society **123**(51) (2001) 12817-12825.

[Muk93] Mukerji, J., Chemistry of Advanced Materials: A 'Chemistry for the 21st Century' monograph, C. N. R. Rao, Blackwell Scientific Publications, Oxford, 1993. p. 169-196.

[Mur95] Murarka, S. P. and S. W. Hymes, Crit. Rev. Solid State Mat. Sci. **20**(2) (1995) 87-124.

[Nag93] Nagai, M. and K. Kishida, Appl. Surf. Sci. **70-1** (1993) 759-762.

[Nag94] Nagaoka, M., K. Ishida, T. Matsunaga, K. Nishihori, T. Hashimoto, M. Yoshimura, Y. Tanabe, M. Mihara, Y. Kitaura and N. Uchitomi, Japanese Journal of Applied Physics **33**(Part 1, No. 1B) (1994) 767-770.

[Nag00] Nagai, M., N. Hirano and S. Omi, Japanese Journal of Applied Physics **39**(Part 1, No. 7B) (2000) 4558-4560.

[Nak87] Nakajima, T., K. Watanabe and N. Watanabe, Journal of the Electrochemical Society **134**(12) (1987) 3175-3178.

[Nak97] Nakajima, K., Y. Akasaka, K. Miyano, M. Takahashi, S. Suehiro and K. Suguro, Appl. Surf. Sci. **117/118** (1997) 312-316.

[Neu34] Neumann, B., C. Kroger and H. Kunz, Zeitschrift für anorganische und allgemeine Chemie **218** (1934) 379-401.

[Ngu89] Nguyen, T. P. and S. Lefrant, Journal of Physics: Condensed Matter **1**(31) (1989) 5197-5204.

[Nic78] Nicolet, M. A., Thin Solid Films **52**(3) (1978) 415-443.

[Nic95] Nicolet, M.-A., Appl. Surf. Sci. **91**(1-4) (1995) 269-276.

[Nie83] Nielson, A. J. and J. M. Waters, Aust. J. Chem. **36**(2) (1983) 243-251.

[Nin02] Ning, J., S. Xu, J. W. Chai, L. K. Chen, A. See and J. Ahn, International Journal of Modern Physics B **16**(6&7) (2002) 1127-1131.

[NIS03] NIST Chemistry Webbook: Standard Reference Database Number 69, (2003), http://webbook.nist.gov/chemistry

[Nor01] Norman, J. A. T., Journal de Physique IV: Proceedings **11**(Pr3, Thirteenth European Conference on Chemical Vapor Deposition, 2001) (2001) Pr3/497-Pr3/503.

[Nov00] Novellus, I.,Benefits of Copper :Copper Technology is Here Today in Working Devices, Novellus, Inc. (2000), http://www.novellus.com/damascus/boc/boc.asp

[Nug80] Nugent, W. A. and R. L. Harlow, Inorganic Chemistry **19**(3) (1980) 777-779.

[Ohr92] Ohring, M. The Materials Science of Thin Films. Boston, Academic Press, Inc., (1992)

[Ole97] Olefjord, I., Surface Characterization: A User's Sourcebook, D. Brune, R. Hellborg, H. J. Whitlow and O. Hunderi, Wiley-VCH, Weinheim, 1997. p. 291-319.

[Pac91] Paccagnella, A., A. Callegari, A. Carnera, M. Gasser, E. Latta, M. Murakami and M. Norcott, Journal of Applied Physics **69**(4) (1991) 2356-2364.

[Pan96] Pangborn, A. B., M. A. Giardello, R. H. Grubbs, R. K. Rosen and F. J. Timmers, Organometallics **15**(5) (1996) 1518-1520.

[Par95a] Park, K. C. and K. B. Kim (1995). Materials Research Society Symposium Proceedings, Vol.391, Materials Research Society: 211-216.

[Par95b] Paranjpe, A. and M. IslamRaja, Journal of Vacuum Science Technology B 13(5) (1995) 2105-2114.

[Par96] Park, K. C., K. B. Kim, I. J. Raaijmakers and K. Ngan, Journal of Applied Physics **80**(10) (1996) 5674-5681.

[Par97a] Park, B. L., J. M. Ha, D. H. Ko, B. Y. Yoo, S. I. Lee, H. D. Lee, M. B. Lee, U. I. Chung, Y. B. Koh and M. Y. Lee (1997a). Materials Research Society ULSI XII: 283-288.

[Par97b] Park, B. L., D. H. Ko, Y. S. Kim, J. M. Ha, Y. W. Park, S. I. Lee, H. D. Lee, M. B. Lee, U. I. Chung, Y. B. Koh and M. Y. Lee, Journal of Electronic Materials **26**(2) (1997b) L1-L5.

[Par98a] Park, B. L., M. B. Lee, K. J. Moon, H. D. Lee, H. K. Kang and M. Y. Lee (1998a). Advanced Metallization and Interconnect Systems for ULSI Applications in 1997,Vol.ULSI XIII, San Diego, CA, MRS: 163-167.

[Par98b] Park, S. H., I. H. Kim, T. W. Lee and M. P. Park (1998b). IEEE,Vol. 156, Institute of Physics, Great Britain, Adam Hilger, Ltd: 459-462.

[Par00] Park, Y. K., S.-I. Kim, Y. T. Kim and C. W. Lee, Journal of the Korean Physical Society **37**(3) (2000) 324-327.

[Pau87] Pauleau, Y., Solid State Technology (February 1987) (1987) 61-67.

[Pau92] Pauleau, Y. and P. Gouy-Pailler, Journal of Materials Research **7**(8) (1992) 2070-2079.

[Pea67] Pearson, W. B. A Handbook of Lattice Spacings and Structures of Metals and Alloys. Oxford, Pergamon Press, (1967)

[Pea86a] Pearlstein, K. A. and C. M. Friend, Journal of Physical Chemistry **90**(18) (1986a) 4341-4343.

[Pea86b] Pearlstein, K. A. and C. M. Friend, Journal of Physical Chemistry **90**(18) (1986b) 4344-4347.

[Pec97] Pecz, B., A. Sulyok, G. Radnoczi, O. Noblanc, C. Arnodo, S. Cassette and C. Brylinski (1997). Microscale Semiconductor Materials Conference, Vol.157, Oxford, England, IOP Publishing: 519-522.

[Ped82] Pederson, S. F. and R. R. Schrock, Journal of the American Chemical Society **104** (1982) 7483-7491.

[Pet02] Peters, L., Semiconductor International **25**(9) (2002) 17.

[Pet03] Peters, L., Semiconductor International **26**(3) (2003) 50-52,54.

[Phi92] Philipossian, A., Journal of the Electrochemical Society **139**(10) (1992) 2956-2961.

[Pie96] Pierson, H. O. Handbook of Refractory Carbides and Nitrides: Properties, Characteristics, Processing and Applications. Westwood, NJ, Noyes Publications, (1996) [Pok91] Pokela, P. J., C. K. Kwok, E. Kolawa, S. Raud and M. A. Nicolet, Appl. Surf. Sci **53** (1991) 364-72.

[Pri95] Prieto, P. and R. E. Kirby, Journal of Vacuum Science Technology A **13**(6) (1995) 2819-2826.

[Qin98] Qin, W., W. Shih, J. Li, W. James, H. Siriwardane and P. Fraundorf (1998). Materials Research Society Symposium Proceedings: Nanostructured Powders and Their Industrial Applications,Vol.520,, Materials Research Society: 217-222.

[Raa93] Raaijmakers, I. J. and J. Yang, Appl. Surf. Sci. **73** (1993) 31-41.

[Ram00] Ramberg, C. E., E. Blanquet, M. Pons, C. Bernard and R. Madar, Microelectronic Engineering **50** (2000) 357-368.

[Raz95] Razeghi, M. The MOCVD Challenge. Volume 2: A survey of GaInAsP-GaAs for photonic and electronic device applications. Bristol, Institute of Physics Publishing, (1995)

[Rei75] Reichelt, K. and G. Bergmann, Journal of Applied Physics **46**(6) (1975) 2747-2751.

[Rei92] Reid, J. S., E. Kolawa and M.-A. Nicolet, Journal of Materials Research **7**(9) (1992) 2424-2428.

[Rei94] Reid, J. S., X. Sun, E. Kolawa and M.-A. Nicolet, IEEE Electron Device Letters **15**(8) (1994) 298-300.

[Rei95] Reid, J. S., R. Y. Liu, P. M. Smith, R. P. Ruiz and M. A. Nicolet, Thin Solid Films **262**(1-2) (1995) 218-223.

[Rei00] Reid, J. D.,Fundamentals of Copper:Fundamentals of Electroplating, Novellus Systems (2000), http://www.novellus.com/damascus/foc/foc_e.asp

[Ren96] Reniers, F., E. Silberberg, N. Roose and J. Vereecken, Appl. Surf. Sci. **99**(4) (1996) 379-392.

[Rey02] Reyes-Betanzo, C., S. A. Moshkalyov, A. C. Ramos, J. A. Diniz and J. W. Swart, Journal of the Electrochemical Society **149**(3) (2002) G179-G183.

[Rig75] Riggs, W. M. and M. J. Parker, Methods and Phenomena: Their Applications in Science and Technology **1**(Methods Surf. Anal.) (1975) 103-158.

[Rit90] Ritter, E. and J. W. Bozzelli, Hazardous Waste & Hazardous Materials **7**(1) (1990) 103-115.

[Rit03] Ritala, M. and M. Leskela (2003). Electrochemical Society Conference: Chemical Vapor Deposition XVI (CVD-VXI) and EUROCVD 14,Vol.2003-08, Paris, France: 479-490.

[Ros01] Rossnagel, S. M. and H. Kim, IEEE (2001) 3-5.

[Rud67] Rudy, V. E. and J. R. Hoffman, Planseeberichte fuer Pulvermetallurgie **15**(3) (1967) 174-178.

[Rus99] Rusli, S. F. Yoon, H. Yang, J. Ahn, Q. F. Huang, Q. Zhang, Y. P. Guo, C. Y. Yang, E. J. Teo, A. T. S. Wee and A. C. H. Huan, Thin Solid Films **355-356** (1999) 174-178.

[Rye69] Rye, R. R. and R. S. Hansen, Journal of Chemical Physics **50**(8) (1969) 3585-3595.

[Sak96] Sakata, Y., A. Muto, M. A. Uddin and K. Harino, Journal of Materials Chemistry **6**(7) (1996) 1241-1243.

[Sam80] Samsonov, G. V. and I. M. Vinitskii. Handbook of Refractory Compounds. New York, IFI/Plenum Data Company, (1980)

[Sar65] Sara, R. V., Journal of the American Ceramic Society **48**(5) (1965) 251-257.

[Sar80] Sarma, D. D. and C. N. R. Rao, Journal of Electron Spectroscopy and Related Phenomena **20** (1980) 25-45.

[Sau98] Saunders, N. and A. P. Miodownik. Calphad (Calculation of Phase Diagrams): A Comprehensive Guide. Oxford, Pergamon Press, (1998)

[Sch54] Schonberg, N., Acta Chemica Scandinavica **8**(2) (1954) 204-207.

[Sch87] Schlotter, P., Solar Energy Materials **16**(1-3) (1987) 39-46.

[Sch01] Scheuermann, F., E. Salzborn, F. Hagelberg and P. Scheier, Journal of Chemical Physics **114**(22) (2001) 9875-9881.

[Sel95] Sellem, S., C. Potvin, J. M. Manoli, R. Contant and G. Djega-Mariadassou, Journal of the Chemical Society, Chemical Communications **3** (1995) 359-360.

[Ser01] Serguchev, Y. A. and Y. V. Belokopytov, Kinetics and Catalysis **42**(2) (2001) 174-181.

[Sha89] Shamir, N., J. C. Lin and R. Gomer, Surface Science **214** (1989) 74-84.

[Sha95] Shacham-Diamand, Y., V. Dubin and M. Angyal, Thin Solid Films **262** (1995) 93-103.

[Sha96] Shackleford, J. F. Introduction to Materials Science for Engineers. Upper Saddle River, Prentice-Hall, (1996)

[Sha97] Shacham-Diamand, Y. and V. Dubin, Microelectronic Engineering **33** (1997) 47-58.

[Sha01] Shaw, M. J., S. Grunow and D. J. Duquette, Journal of Electronic Materials **30**(12) (2001) 1602-1608.

[She00a] Shen, Y. G. and Y. W. Mai, Appl. Surf. Sci. **167** (2000a) 59-68.

[She00b] Shen, Y. G. and Y. W. Mai, Materials Science and Engineering **A288** (2000b) 47-53.

[She00c] Shen, Y. G. and Y. W. Mai, Surface and Coatings Technology **127** (2000c) 239-246.

[She00d] Shen, Y. G., Y. W. Mai, W. E. McBride, Q. C. Zhang and D. R. McKenzie, Thin Solid Films (372) (2000d) 257-264.

[She00e] Shen, Y. G., Y. W. Mai, D. R. McKenzie, Q. C. Zhang, W. D. McFall and W. E. McBride, Journal of Applied Physics **88**(3) (2000e) 1380-1388.

[She00f] Shen, Y. G., Y. W. Mai, Q. C. Zhang, D. R. McKenzie, W. D. McFall and W. E. McBride, Journal of Applied Physics **87**(1) (2000f) 177-187.

[Shi97] Shimooka, Y., T. Iijima, S. Nakamura and K. Suguro, Japanese Journal of Applied Physics, Part 1: Regular Papers, Short Notes & Review Papers **36**(3B) (1997) 1589-1592.

[Sim94] Simson, S., N. Heide and J. W. Schultze, Surface and Interface Analysis **22** (1994) 431-435.

[Sim03] Sim, H. S., S.-I. Kim and Y. T. Kim, Journal of Vacuum Science Technology B **21**(4) (2003) 1411-1414.

[Sin02a] Singer, P., Semiconductor International **25**(5) (2002a) 46-53.

[Sin02b] Singer, P., Semiconductor International **25**(6) (2002b) 48-52.

[Siv95] Sivaram, S. C. V. D. T. a. P. D. o. E. M., 119, (1995). Chemical Vapor Deposition: Thermal and Plasma Deposition of Electronic Materials. New York, Van Nostrand Reinhold International Thomson Publishing, (1995)

[Slo99] Sloan, D. W., P. M. Blass and J. M. White, Appl. Surf. Sci. **143** (1999) 142-152.

[Sly61] Slysh, R. S. and C. R. Kinney, Journal of Physical Chemistry **65** (1961) 1044-1045.

[Smi82] Smith, W. R. and R. W. Missen. Chemical Reaction Equilibrium Analysis: Theory and Algorithms. New York, John Wiley & Sons, (1982)

[Smi02] Smith, S., W.-M. Li, K.-E. Elers and K. Pfeifer, Microelectronic Engineering **64**(1) (2002) 247-253.

[So88] So, F. C. T., E. Kolawa, X. A. Zhao, E. T. S. Pan and M. A. Nicolet, J. Appl. Phys. **64**(5) (1988) 2787-9.

[Som97] Somatri-Bouamrane, R., N. Chevarier, A. Chevarier, A. M. Dutron, E. Blanquet and R. Madar (1997). Proceedings of the Electrochemical Society, Vol.97-25 (Chemical Vapor Deposition),, The Electrochemical Society**:** 741-748.

[Sot03] Soto, G., W. de la Cruz, F. F. Castillon, J. A. Diaz, R. Machorro and M. H. Farias, Appl. Surf. Sci. **214**(1-4) (2003) 58-67.

[Sri84] Srivastava, P. K., T. V. Rao, V. D. Vankar and K. L. Chopra, Journal of Vacuum Science Technology A **2**(3) (1984) 1261-1265.

[Suh99] Suh, B. S., Y. J. Lee, J. S. Hwang and C. O. Park, Thin Solid Films **348** (1999) 299-303.

[Suh01] Suh, B. S., H. K. Cho, Y. J. Lee, L. W.J. and C. O. Park, Journal of Applied Physics **89**(7) (2001) 4128-4133.

[Sun92] Suntola, T., Thin Solid Films **216**(1) (1992) 84-89.

[Sun93] Suntola, T., Thin Solid Films **225** (1993) 96-98.

[Sun95] Sundman, B., (1995) Thermo-Calc: User's Guide. Stockholm, Department of Materials Science and Engineering, Royal Institute of Technology, (1995) 300.

[Sun98a] Sun, B., T. Chiang, P. Ding and B. Chin (1998a). Advanced Metallization and Interconnect Systems for ULSI Applications in 1997,Vol.ULSI XIII, San Diego, CA, MRS: 137-141.

[Sun98b] Sun, S. C. (1998b). AIP Conference Proceedings, 418 (Stress Induced Phenomena in Metallization) Tokyo, Japan, The American Institute of Physics: 451-456.

[Sun01a] Sun, S. C., H. Y. Tsai and J. Wang (2001a). Advanced Metallization Conference Montreal, Canada, Materials Research Society: 587-591.

[Sun01b] Sun, Y. M., S. Y. Lee, A. M. Lemonds, E. R. Engbrecht, S. Veldman, J. Lozano, J. M. White, J. G. Ekerdt, I. Emesh and K. Pfeifer, Thin Solid Films **397** (2001b) 109-115.

[Suz98] Suzuki, T., A. Tsukune, O. Tsuboi and M. Yamada (1998). Advanced Metallization and Interconnect Systems for ULSI Applications in 1997,Vol.ULSI XIII, San Diego, CA, MRS: 49-55.

[Swa72] Swalin, R. A. Thermodynamics of Solids. New York, John Wiley & Sons, (1972)

[Sze84] Szekely, A., R. K. Hanson and C. T. Bowman, Journal of Physical Chemistry **88**(4) (1984) 666-668.

[Tak96] Takagi, M. T., K. Miyashita, H. Koyama, K. Nakajima, K. Miyano, Y. Akasaka, Y. Hiura, S. Inaba, A. Azuma, H. Koike, M. Yoshimura, K. Suguro and H. Ishiuchi (1996). Technical Digest - International Electron Devices Meeting: 455-458.

[Tak97a] Takeyama, M. and A. Noya, Japanese Journal of Applied Physics **36**(4A) (1997a) 2261-2266.

[Tak97b] Takeyama, M., A. Noya and T. Fukuda, Journal of Vacuum Science & Technology, A: Vacuum, Surfaces, and Films **15**(2) (1997b) 415-420.

[Tak02] Takahashi, S., K. Tai, H. Ohtorii, N. Komai, Y. Segawa, H. Horikoshi, Z. Yasuda, H. Yamada, M. Ishihara and T. Nogami (2002). Digest of Technical Papers: 2002 Symposium on VLSI Technology Honolulu, HI: 32-33.

[Tim01] Time Domain CVD,Fundamentals of Chemical Vapor Deposition, Time Domain CVD Inc. (2001), www.timedomaincvd.com

[Tot71] Toth, L. E. Transition Metal Carbides and Nitrides. New York, Academic Press, (1971) [Tra03] Traving, M., G. Schindler, G. Steinlesberger, W. Steinhogl and M. Engelhardt, Semiconductor International **26**(8) (2003) 73-78.

[Tsa86] Tsai, C. C., J. C. Knights, G. Chang and B. Wacker, Journal of Applied Physics **59**(8) (1986) 2998-3001.

[Tsa95] Tsai, M. H., S. C. Sun, C. P. Lee, H. T. Chiu, C. E. Tsai, S. H. Chuang and S. C. Wu, Thin Solid Films **270**(1-2) (1995) 531-536.

[Tsa96] Tsai, M. H., S. C. Sun, H. T. Chiu and S. H. Chuang, Applied Physics Letters **68**(10) (1996) 1412-1414.

[Uch86] Uchitomi, M., M. Nagaoka, K. Shimada, T. Mizoguchi and N. Toyoda, Journal of Vacuum Science Technology B **4**(6) (1986) 1392-1397.

[Uch97] Uchibori, C. J., Y. Ohtani and T. Oku, Journal of Electronic Materials **26**(4) (1997) 410-414.

[Uek96] Uekubo, M., T. Oku, K. Nii, M. Murakami, K. Takahiro, S. Yamaguchi, T. Nakano and T. Ohta, Thin Solid Films **286** (1996) 170-175.

[Vel00] Veldman, S., A. M. Lemonds, K. Kershen, Y.-M. Sun, I. Emesh, K. Pfeifer, J. M. White and J. G. Ekerdt (2000). Advanced Metallization Conference San Diego, CA, Materials Research Society: 307-312.

[Vie02] Vieira, M. T., A. Cavaleiro and B. Trindade, Surface and Coatings Technology **151-152** (2002) 495-504.

[Vij99] Vijayendran, A. and M. Danek (1999). Materials Research Society Conference Proceedings,Vol.564,, Materials Research Society: 327-334.

[Vla195] Vlakhov, E. S., K. A. Gesheva, G. I. Stoyanov and G. D. Beshkov, Electronic & Electrical Engineering Research Studies, Electronic Materials Series 1994, **1**(Electronic, Optoelectronic and Magnetic Thin Films) (1995) 456-459.

[Vol85] Volpe, L. and M. Boudart, Journal of Solid State Chemistry **59**(3) (1985) 332-347.

[Vos78] Vossen, J. L. and W. Kern, Eds. Thin Film Processes,New York, Academic Press (1978)

[Vu90] Vu, Q. T., P. J. Pokela, C. L. Garden, E. Kolawa, S. Raud and M.-A. Nicolet, Journal of Applied Physics **68**(12) (1990) 6420-6423.

[Wag90] Wagner, C. D. Practical Surface Analysis, Volume 1: Auger and X-ray Photoelectron Spectroscopy. New York, John Wiley and Sons, (1990)

[Wan94] Wang, S. Q., MRS Bulletin **19**(8) (1994) 30-40.

[Wan00] Wang, D. Z., J. X. Chen, H. L. Zhang and N. K. Huang, Nuclear Instruments and Methods in Physics Research B **171** (2000) 465-469.

[Wan01a] Wang, S. J., H. Y. Tsai and S. C. Sun, Journal of the Electrochemical Society **148**(8) (2001a) C563-C568.

[Wan01b] Wang, S. J., H. Y. Tsai, S. C. Sun and M. H. Shiao, Journal of the Electrochemical Society **148**(9) (2001b) G500-G506.

[Wan03] Wang, Z., T. Ida, H. Sakaue, S. Shingubara and T. Takahagi, Electrochemical and Solid-State Letters **6**(3) (2003) C38-C41.

[Wei99] Wei, J., P. Hing and Z. Q. Mo, Wear **225-229** (1999) 1141-1147.

[Whi58] White, W. B., S. M. Johnson and G. B. Dantzig, Journal of Chemical Physics **28** (1958) 751-755.

[Whi91] White, F. M. Viscous Fluid Flow: Second Edition. New York, McGraw-Hill Inc., (1991)

[Wit80] Wittmer, M., Applied Physics Letters **36** (1980) 456-458.

[Wol86] Wolf, S. and R. N. Tauber. Silicon Processing for the VLSI Era. Sunset Beach, CA, Lattice Press, (1986)

[Wri89] Wriedt, H. A., Bulletin of Alloy Phase Diagrams **10**(4) (1989) 358-367.

[Xue98] Xue, Z., S. H. Chuang, K. G. Caulton and M. H. Chisholm, Chemistry of Materials **10** (1998) 2365-2370.

[Yan02] Yang, J.-M., I.-S. Choi, Y. S. Kim, J.-C. Park, S.-M. Lee, T.-E. Hong, Y.-B. Park, S.-Y. Lee and Y. W. Kim, Journal of Applied Physics **91**(12) (2002) 9788-9793.

[Yeh96] Yeh, W. K., K. Y. Chan, T. C. Chang, M. H. Tsai, S. H. Chen, M. C. Chen and M. S. Lin, Japanese Journal of Applied Physics **35**(Part 1, No. 2B) (1996) 1115-1119.

[You89] Young, C. M. and K. J. Voorhees, Preprints of papers - American Chemical Society, Division of Gas and Fuel Chemistry **34**(1) (1989) 280-287.

[Yu88] Yu, K. M., J. M. Jaklevic, E. E. Haller, S. K. Cheung and S. P. Kwok, Journal of Applied Physics **64**(3) (1988) 1284-1291.

[Zen00a] Zeng, Y., L. Chen and T. L. Alford (2000a). Materials Research Society Conference Proceedings, Vol.612, Materials Research Society: D9.11.1-D9.11.6.

[Zen00b] Zeng, Y., S. W. Russell, A. J. McKerrow, L. Chen and T. L. Alford, Journal of Vacuum Science Technology B **18**(1) (2000b) 221-230.

[Zha94] Zhang, S., C. D. Qin and L. C. Lim, International Journal of Refractory Metals & Hard Materials **12**(6) (1994) 329-333.

[Zha97] Zhang, Z., Synthesis and characterization of novel Group VI metal (Mo,W) nitride and oxide compounds, PhD Dissertation, Iowa State University, Ames,(1997)

[Zha99] Zhang, H. L., D. Z. Wang and N. K. Huang, Appl. Surf. Sci. **150** (1999) 34-38.

APPENDIX A
PROCESS FLOW DIAGRAMS FOR THE CVD SYSTEM

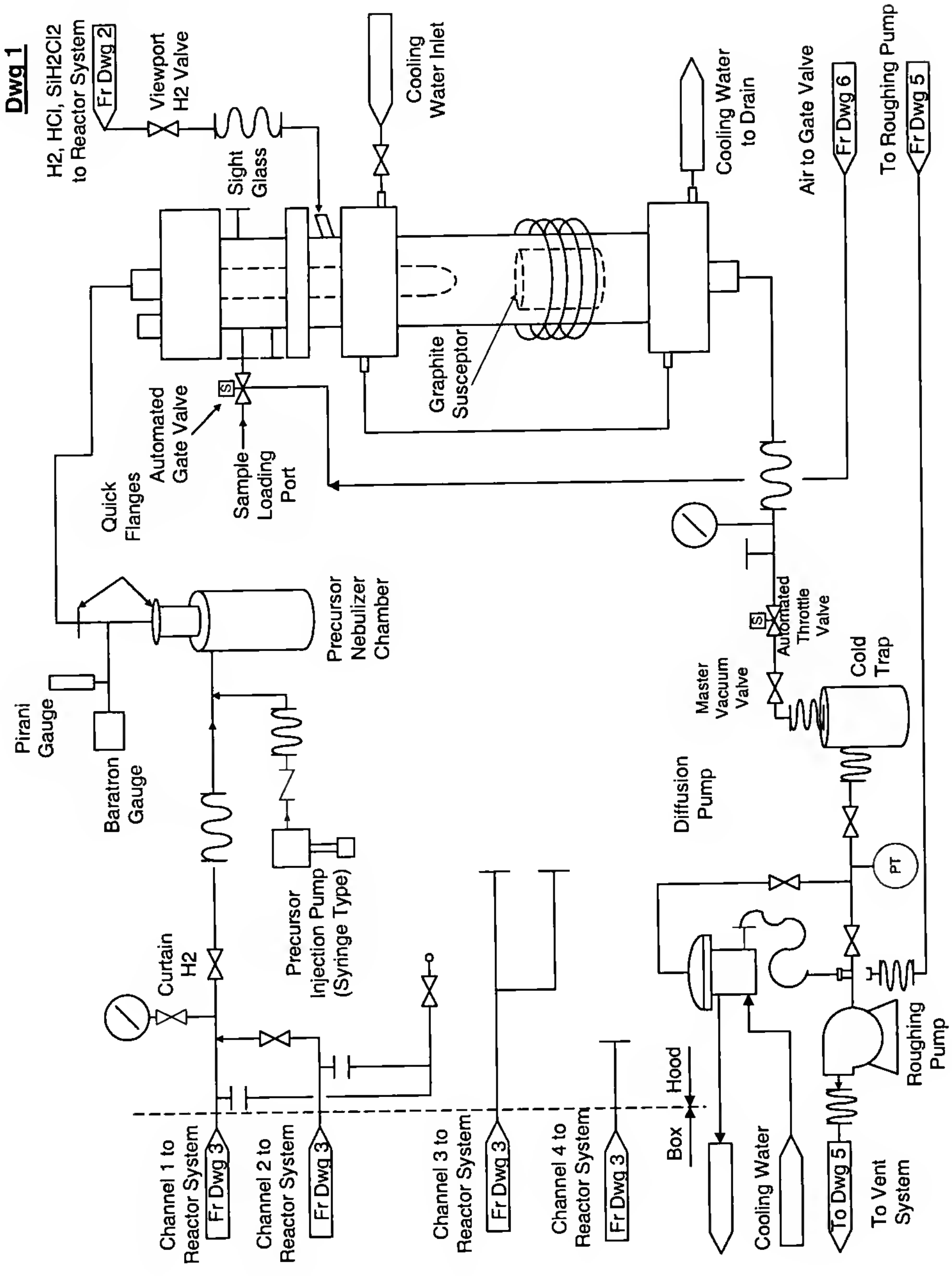
Dwg 1
H2, HCl, SiH2Cl2 to Reactor System
Fr Dwg 2
Viewport H2 Valve
Sight Glass
Cooling Water Inlet
Cooling Water to Drain
Air to Gate Valve
Fr Dwg 6
To Roughing Pump
Fr Dwg 5
Quick Flanges
Automated Gate Valve
S
Sample Loading Port
Graphite Susceptor
Precursor Nebulizer Chamber
Pirani Gauge
Baratron Gauge
Automated Throttle Valve
Master Vacuum Valve
Cold Trap
Diffusion Pump
PT
Precursor Injection Pump (Syringe Type)
Curtain H2
Roughing Pump
Hood
Box
Channel 1 to Reactor System
Fr Dwg 3
Channel 2 to Reactor System
Fr Dwg 3
Channel 3 to Reactor System
Fr Dwg 3
Channel 4 to Reactor System
Fr Dwg 3
Cooling Water
To Dwg 5
To Vent System

Figure A-1. Reactor, nebulizer and associated piping

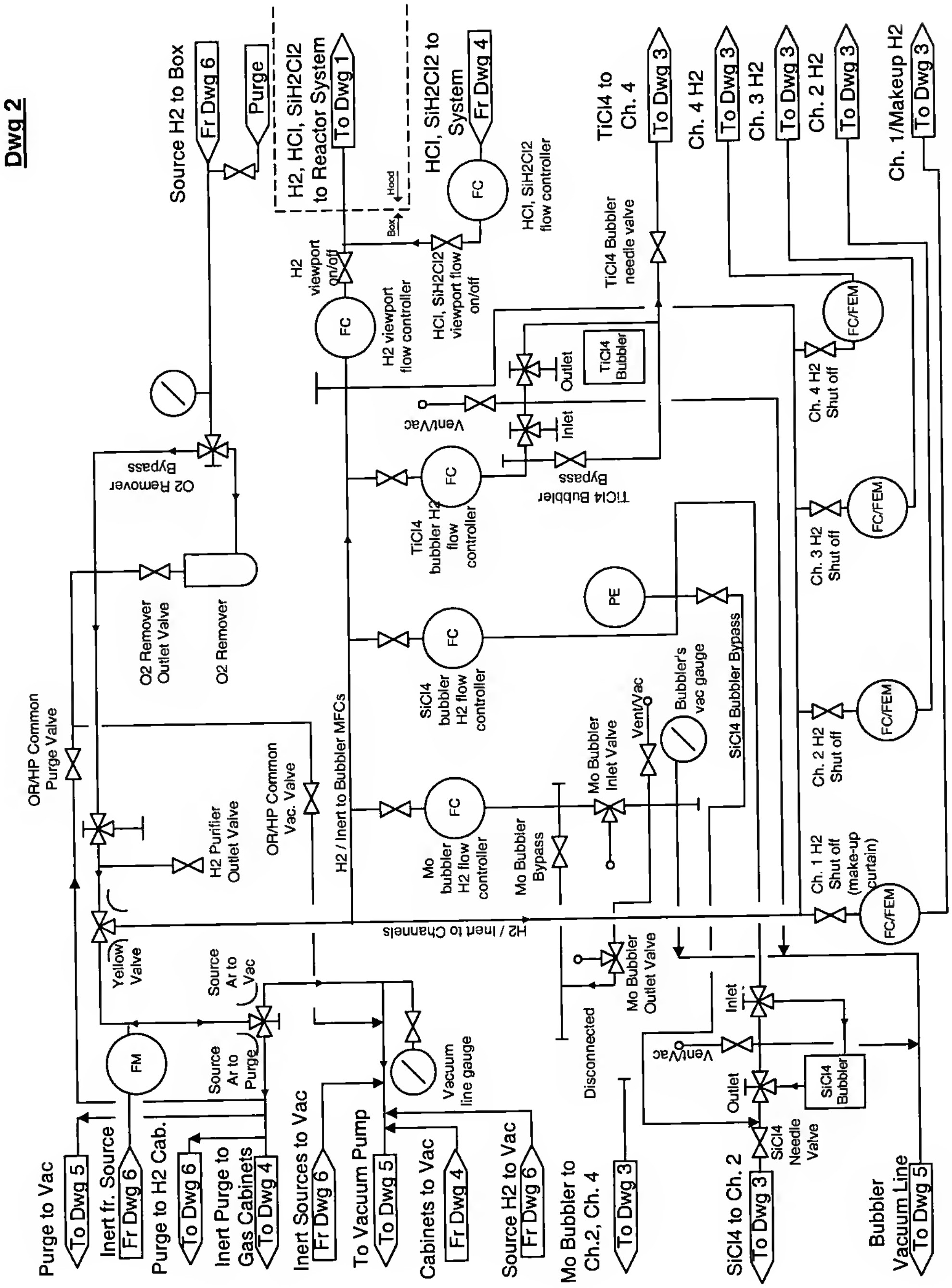
Dwg 2
Source H_2 to Box
Fr Dwg 6
Purge
H_2, HCl, SiH_2Cl_2 to Reactor System
To Dwg 1
HCl, SiH_2Cl_2 to System
Fr Dwg 4
$TiCl_4$ to Ch. 4
To Dwg 3
Ch. 4 H_2
To Dwg 3
Ch. 3 H_2
To Dwg 3
Ch. 2 H_2
To Dwg 3
Ch. 1/Makeup H_2
To Dwg 3
Box
Hood
FC
HCl, SiH_2Cl_2 flow controller
H_2 viewport on/off
HCl, SiH_2Cl_2 viewport flow on/off
FC
H_2 viewport flow controller
$TiCl_4$ Bubbler needle valve
Outlet
$TiCl_4$ Bubbler
Inlet
Vent/Vac
FC/FEM
Ch. 4 H_2 Shut off
O2 Remover Bypass
FC
$TiCl_4$ bubbler H_2 flow controller
$TiCl_4$ Bubbler Bypass
FC/FEM
Ch. 3 H_2 Shut off
O2 Remover Outlet Valve
O2 Remover
PE
FC
$SiCl_4$ bubbler H_2 flow controller
Bubbler's vac gauge
$SiCl_4$ Bubbler Bypass
OR/HP Common Purge Valve
OR/HP Common Vac. Valve
H_2 / Inert to Bubbler MFCs
Mo Bubbler Inlet Valve
Vent/Vac
FC/FEM
Ch. 2 H_2 Shut off
H_2 Purifier Outlet Valve
FC
Mo bubbler H_2 flow controller
Mo Bubbler Bypass
Ch. 1 H_2 Shut off (make-up curtain)
FC/FEM
Yellow Valve
H_2 / Inert to Channels
Source Ar to Vac
Mo Bubbler Outlet Valve
Disconnected
Inlet
FM
Source Ar to Purge
Vacuum line gauge
Vent/Vac
$SiCl_4$ Bubbler
Outlet
$SiCl_4$ Needle Valve
Purge to Vac
To Dwg 5
Inert fr. Source
Fr Dwg 6
Purge to H_2 Cab.
To Dwg 6
Inert Purge to Gas Cabinets
To Dwg 4
Inert Sources to Vac
Fr Dwg 6
To Vacuum Pump
To Dwg 5
Cabinets to Vac
Fr Dwg 4
Source H_2 to Vac
Fr Dwg 6
Mo Bubbler to Ch.2, Ch. 4
To Dwg 3
$SiCl_4$ to Ch. 2
To Dwg 3
Bubbler Vacuum Line
To Dwg 5

Figure A-2. Bubblers, mass flow controllers and associated piping

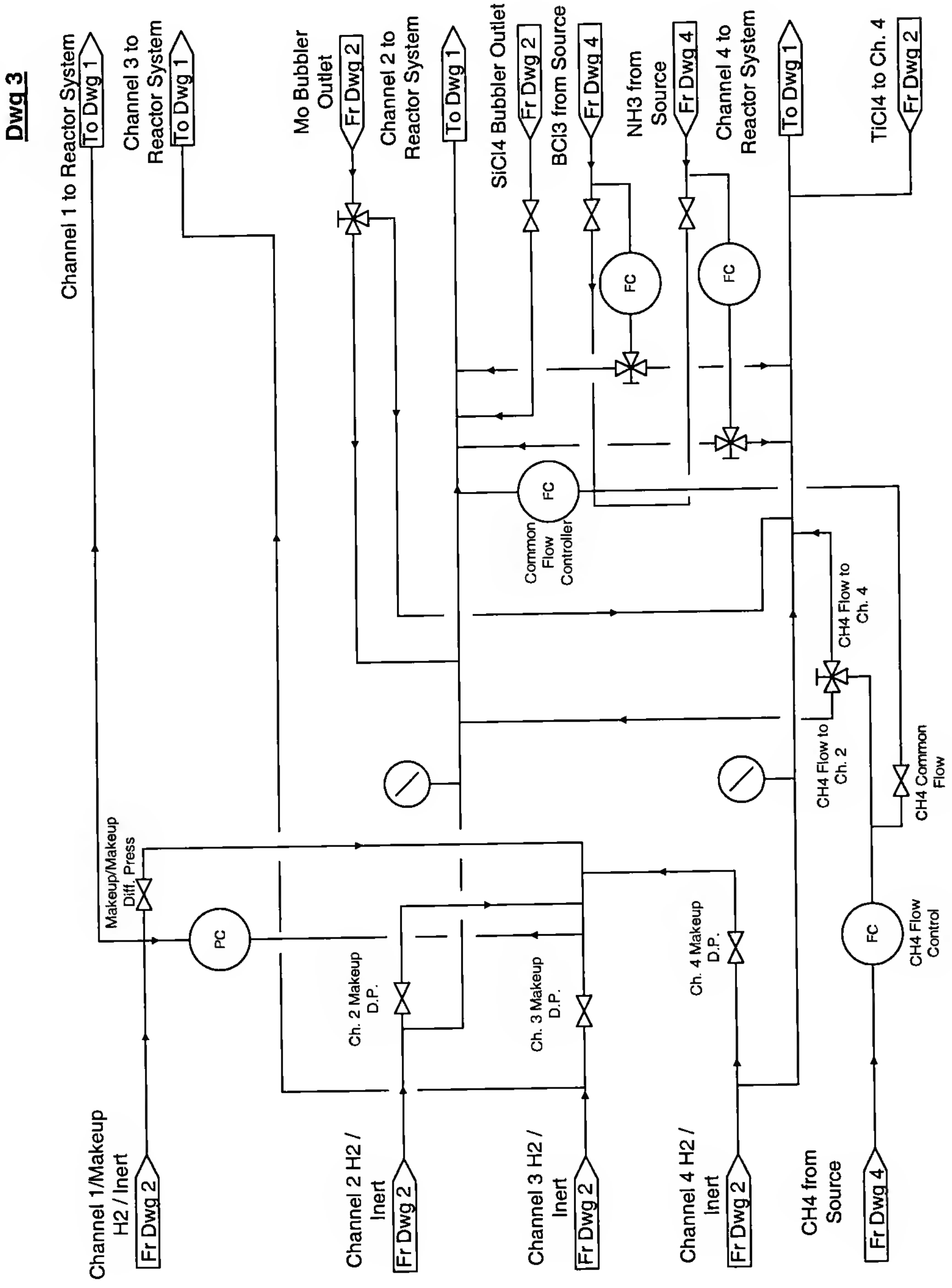
Dwg 3
Channel 1 to Reactor System
To Dwg 1
Channel 3 to Reactor System
To Dwg 1
Mo Bubbler Outlet
Fr Dwg 2
Channel 2 to Reactor System
To Dwg 1
SiCl4 Bubbler Outlet
Fr Dwg 2
BCl3 from Source
Fr Dwg 4
NH3 from Source
Fr Dwg 4
Channel 4 to Reactor System
To Dwg 1
TiCl4 to Ch. 4
Fr Dwg 2
FC
FC
FC
Common Flow Controller
CH4 Flow to Ch. 4
CH4 Flow to Ch. 2
CH4 Common Flow
Makeup/Makeup Diff. Press
PC
Ch. 2 Makeup D.P.
Ch. 3 Makeup D.P.
Ch. 4 Makeup D.P.
FC
CH4 Flow Control
Channel 1/Makeup H2 / Inert
Fr Dwg 2
Channel 2 H2 / Inert
Fr Dwg 2
Channel 3 H2 / Inert
Fr Dwg 2
Channel 4 H2 / Inert
Fr Dwg 2
CH4 from Source
Fr Dwg 4

Figure A-3. Channel headers and associated piping

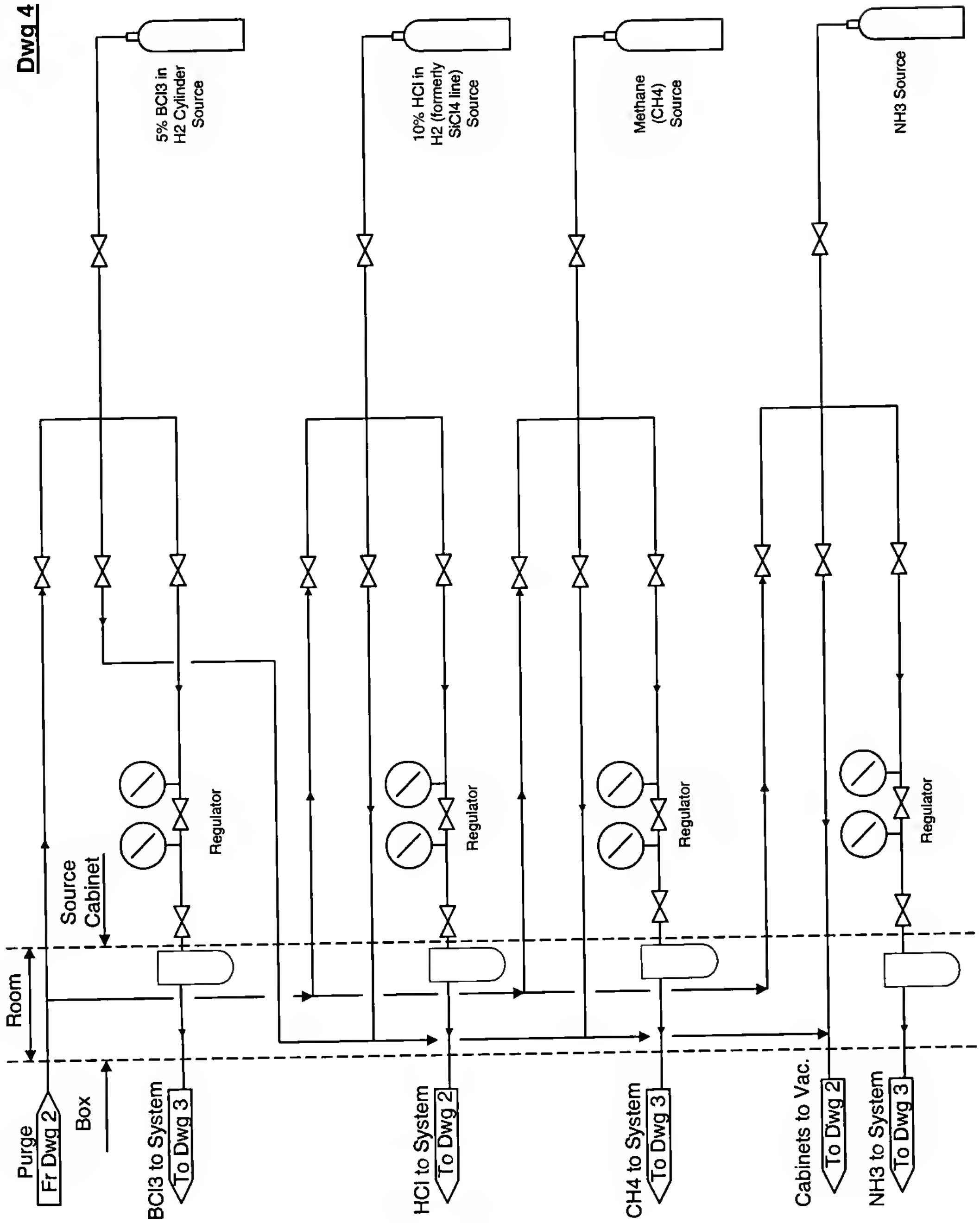
Dwg 4
5% BCl3 in H2 Cylinder Source
10% HCl in H2 (formerly SiCl4 line) Source
Methane (CH4) Source
NH3 Source
Regulator
Regulator
Regulator
Regulator
Source Cabinet
Room
Box
Purge
Fr Dwg 2
BCl3 to System
To Dwg 3
HCl to System
To Dwg 2
CH4 to System
To Dwg 3
Cabinets to Vac.
To Dwg 2
NH3 to System
To Dwg 3

Figure A-4. Gas cylinders and associated piping

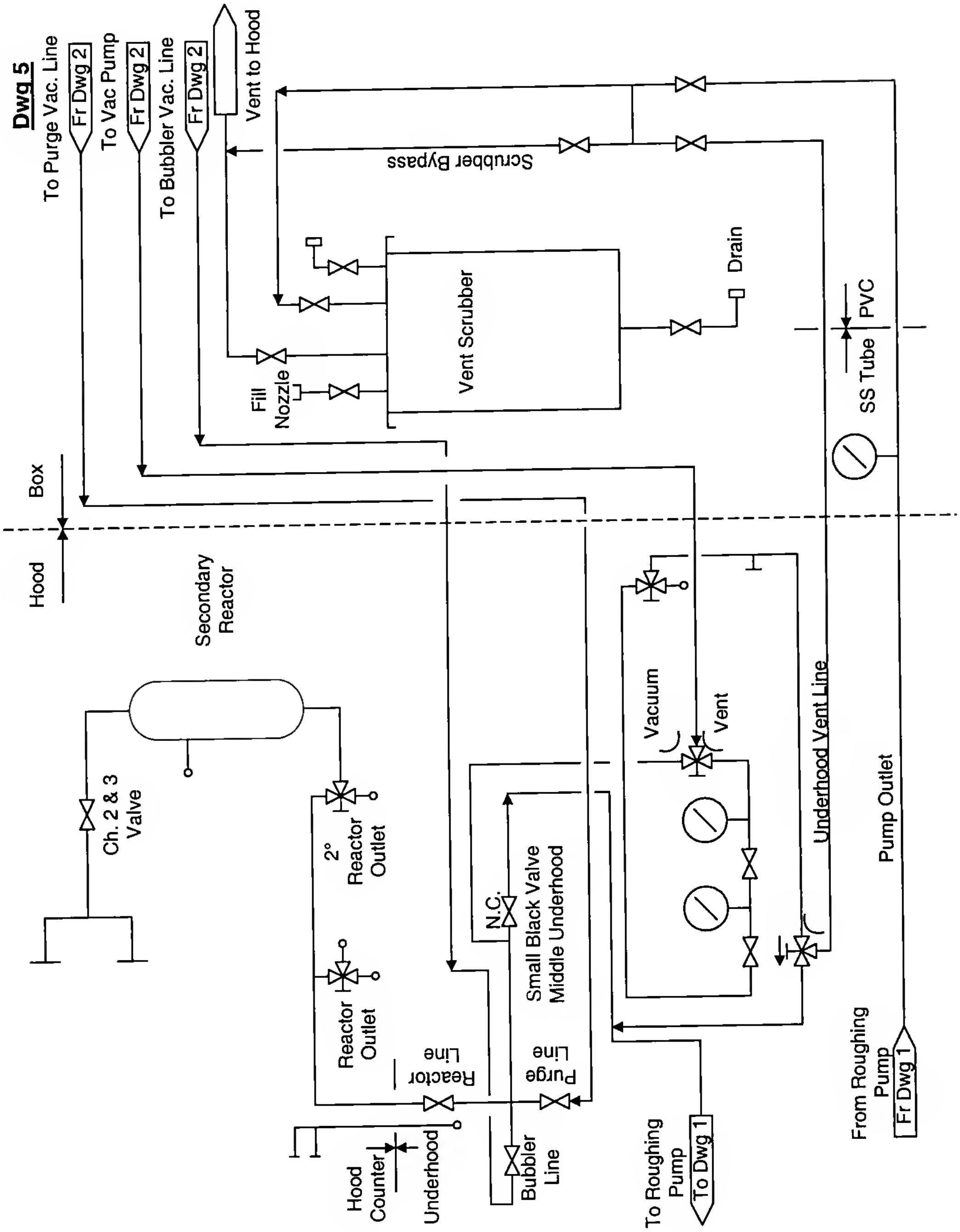
Dwg 5
To Purge Vac. Line
Fr Dwg 2
To Vac Pump
Fr Dwg 2
To Bubbler Vac. Line
Fr Dwg 2
Vent to Hood
Scrubber Bypass
Drain
Vent Scrubber
Fill Nozzle
PVC
SS Tube
Box
Hood
Secondary Reactor
Vacuum
Vent
Underhood Vent Line
Pump Outlet
Ch. 2 & 3 Valve
2° Reactor Outlet
N.C.
Small Black Valve Middle Underhood
Reactor Outlet
Reactor Line
Purge Line
Hood Counter
Underhood
Bubbler Line
To Roughing Pump
To Dwg 1
From Roughing Pump
Fr Dwg 1

Figure A-5. Vent scrubber, secondary reactor and associated piping

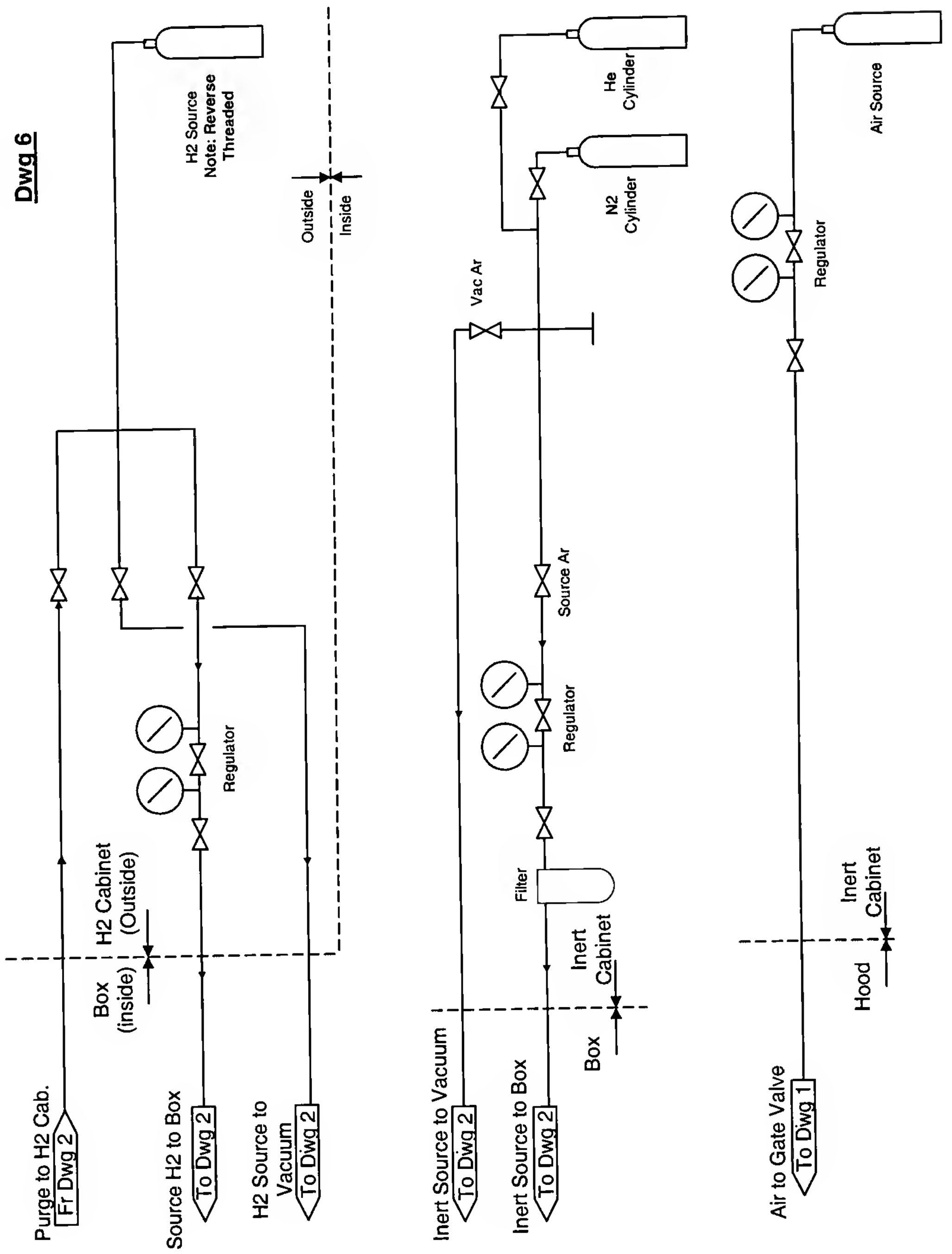
Dwg 6
H2 Source
Note: Reverse
Threaded
Outside
Inside
Purge to H2 Cab.
Fr Dwg 2
Box
(inside)
H2 Cabinet
(Outside)
Regulator
Source H2 to Box
To Dwg 2
H2 Source to
Vacuum
To Dwg 2
Inert Source to Vacuum
To Dwg 2
Inert Source to Box
To Dwg 2
Vac Ar
He
Cylinder
N2
Cylinder
Source Ar
Regulator
Filter
Inert
Cabinet
Box
Air Source
Regulator
Inert
Cabinet
Hood
Air to Gate Valve
To Dwg 1

Figure A-6. Carrier and inert gas cylinders and associated piping

APPENDIX B
OTHER PRECURSORS TESTED

Below is a list of precursors that have been tested to check their performance in growing tungsten nitride (WN_x) thin films. Dr. McElwee-White's group at the University of Florida's Department of Chemistry generated the precursors. The precursors have been listed in order of promise, with the first precursor/solvent pair showing us the best results thus far. Structures of the precursor molecules have been included, as well as the delivery system type (solid source vs. nebulizer) and the experimental temperature range for each precursor. In some cases, especially those using solid-source delivery, flux of the precursor to the reactor was minimal. In other cases using nebulizer delivery, flux to the reactor was adequate, but film deposition was minimal.

Table B-1. Other precursors tested for MOCVD of WN_x

Precursor Structure	Deposition Temp. Range (°C)	Delivery Method	Promising? (Yes/No)	Notes
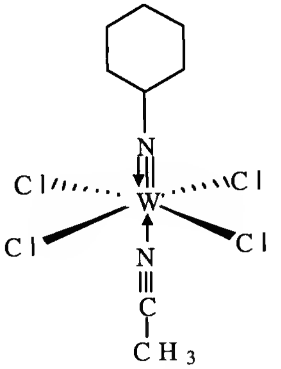	575-600	Nebulizer	Yes	Film composition similar to that for i-Pr precursor **1b**
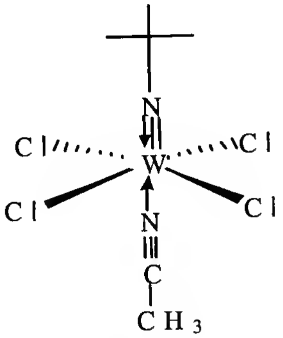	700-800	Nebulizer	Yes	Purification during precursor synthesis was an issue
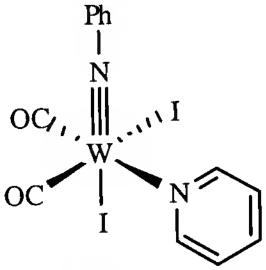	650 –700	Solid Source	No	Minimal precursor transport caused by low vapor pressure
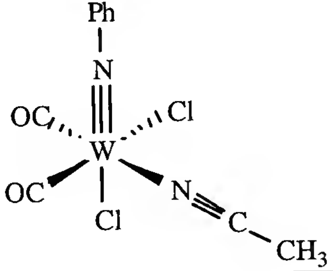	700	Solid Source	No	Minimal precursor transport caused by low vapor pressure

Table B-1. Continued

Precursor Structure	Deposition Temp. Range (°C)	Delivery Method	Promising? (Yes/No)	Notes
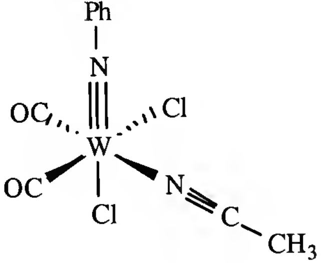	1000	Nebulizer	No	Minimal deposition
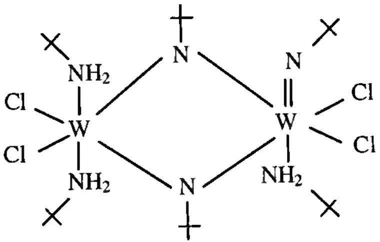	850	Solid Source	No	Minimal precursor transport caused by low vapor pressure
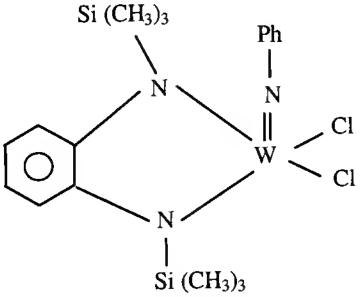	700	Solid Source	No	Minimal precursor transport caused by low vapor pressure
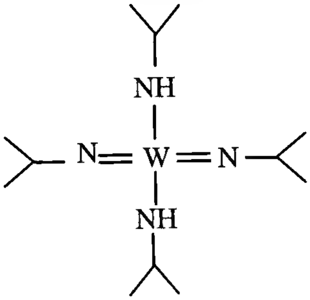	800	Nebulizer	No	Minimal deposition
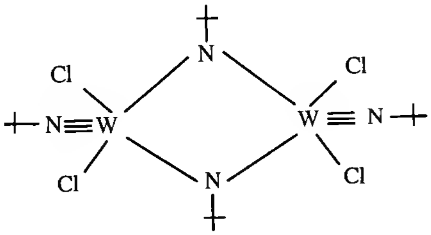	500	Nebulizer	No	Minimal deposition

Table B-1. Continued

Precursor Structure	Deposition Temp. Range (°C)	Delivery Method	Promising? (Yes/No)	Notes
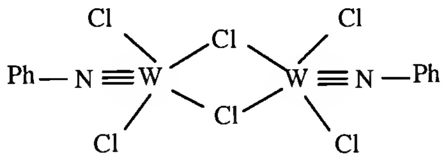	500	Nebulizer	No	Minimal deposition
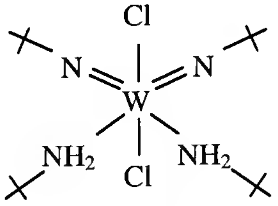	500	Nebulizer	No	Minimal deposition
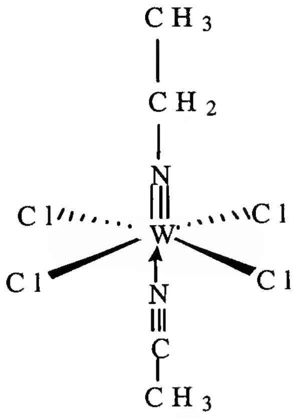	550-650	Nebulizer	No	Minimal deposition

BIOGRAPHICAL SKETCH

Omar James Bchir was born on October 31, 1974 in St. Petersburg, Florida. He is the son of Sara and Hachemi Bchir, and has an older sister, Annissa. He graduated in 1992 from the International Baccalaureate (IB) program at St. Petersburg Senior High School, receiving both the high school and IB diplomas. Following high school, he attended the Georgia Institute of Technology, graduating with a bachelor's degree in chemical engineering in March 1997. Upon graduation, he worked for more than two years as a process engineer for Fluor Daniel, Inc. in Greenville, SC. In the summer of 1999, he left Fluor Daniel to start graduate school at the University of Florida, pursuing his doctoral degree in chemical engineering. Upon graduation, he will work as a senior engineer at Intel Corporation in Chandler, Arizona.

I certify that I have read this study and that in my opinion it conforms to acceptable standards of scholarly presentation and is fully adequate, in scope and quality, as a dissertation for the degree of Doctor of Philosophy.

Timothy J. Anderson
Chair, Professor of Chemical Engineering

I certify that I have read this study and that in my opinion it conforms to acceptable standards of scholarly presentation and is fully adequate, in scope and quality, as a dissertation for the degree of Doctor of Philosophy.

Lisa McElwee-White
Professor of Chemistry

I certify that I have read this study and that in my opinion it conforms to acceptable standards of scholarly presentation and is fully adequate, in scope and quality, as a dissertation for the degree of Doctor of Philosophy.

Paul H Holloway

Paul H. Holloway
Distinguished Professor of Materials
Science and Engineering

I certify that I have read this study and that in my opinion it conforms to acceptable standards of scholarly presentation and is fully adequate, in scope and quality, as a dissertation for the degree of Doctor of Philosophy.

Fan Ren

Fan Ren
Professor of Chemical Engineering

This dissertation was submitted to the Graduate Faculty of the College of Engineering and to the Graduate School and was accepted as partial fulfillment of the requirements for the degree of Doctor of Philosophy.

August 2004

Pramod Khargonekar

Pramod P. Khargonekar
Dean, College of Engineering

Kenneth Gerhardt
Interim Dean, Graduate School

LD
1780
20 04
. B364

UNIVERSITY OF FLORIDA
3 1262 08554 2990